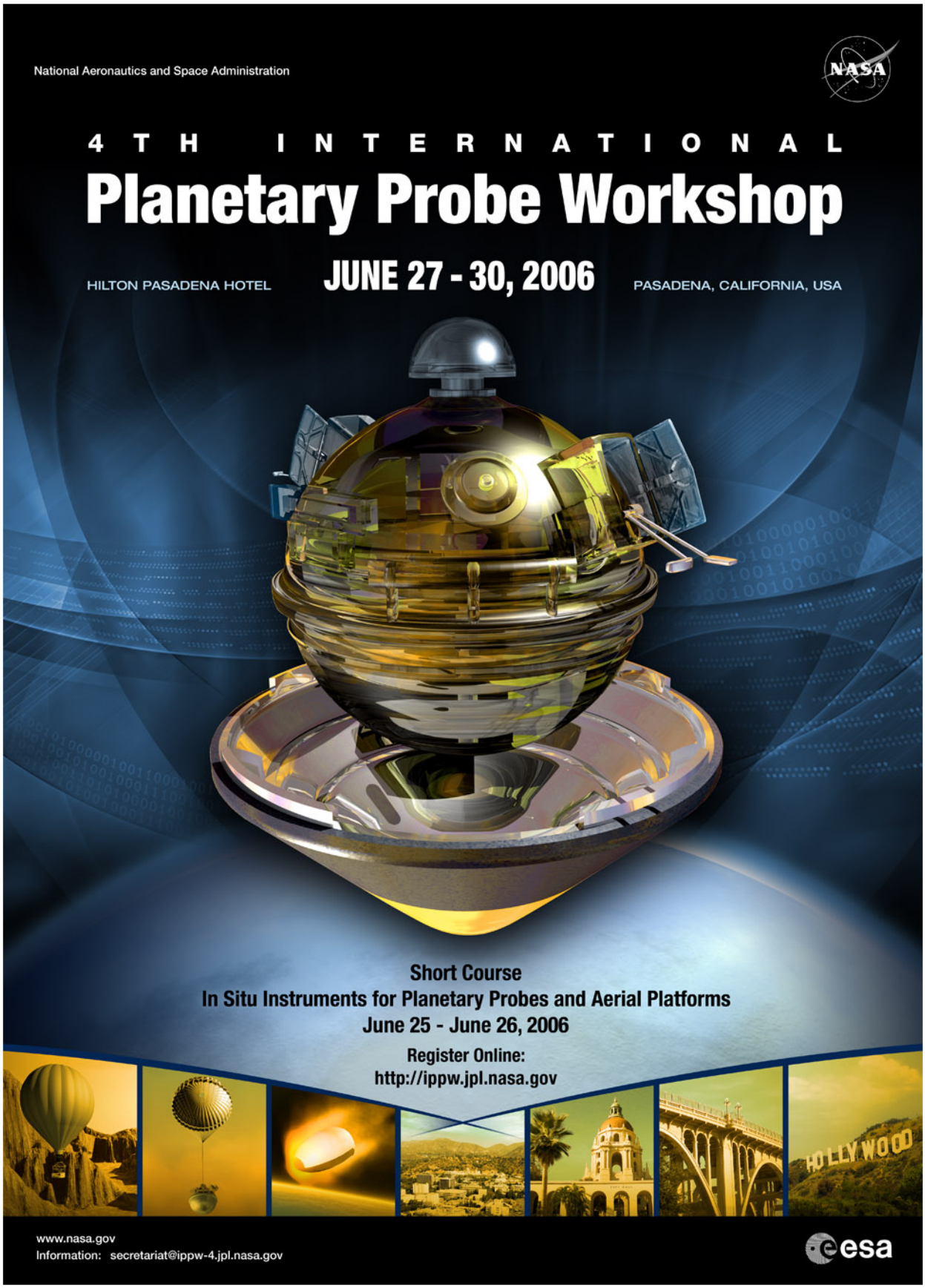

Proceedings

SESSION 1

CURRENT OUTLOOK FOR PROBE MISSIONS

Chair:
Jean-Pierre Lebreton, ESA, Netherlands
Melissa McGrath, NASA, USA

Update on the NASA Solar System Exploration Roadmap

J.I. Lunine for the Solar System Roadmapping Team

We summarize progress on the NASA roadmap for the exploration of the solar system, excluding the Moon and Mars, which are covered in other roadmaps. The roadmap is drawn for a thirty year planning horizon, against the backdrop of the Presidential Initiative “Moon, Mars and Beyond”". The roadmap builds on previous NASA Roadmaps and the NRC Decadal Survey of Solar System Exploration. A preliminary report was completed in May 2005. That report was reviewed by the NRC Panel on Science Strategy Road Maps in the summer of 2005. This Interim Final Report responds to the NRC review and to new scientific, technical and programmatic developments that have taken place in the last year. The final report is scheduled to be completed by May 30, 2006.

SESSION 2

SCIENTIFIC RESULTS FROM PROBE MISSIONS

Chairs:
Eric Chassefiere, Service d'Aeronomie, Univ. P&M Curie, France
Ralph Lorenz, U. Arizona, USA

Huygens Mission Overview

J.-P. Lebreton , Planetary Missions Division/RSSD, ESA-ESTEC, Keplerlaan 1, 2200 AG, Noordwijk, Netherlands,

The Cassini-Huygens mission to explore in detail Saturn's system was launched in October 1997, with the Huygens Probe riding on the back of the Orbiter. After a 7-year interplanetary trajectory, the spacecraft was inserted in orbit around Saturn on 1st July 2004. The Huygens Probe was successfully released on 25 December 2004 for its encounter with Titan 3 weeks later on 14 January 2005. After a descent of about 2½ hour under parachute, Huygens safely landed and continued to function flawlessly on the surface for slightly more than 3 hours. Data were received by the Cassini Orbiter for the whole descent and another 72 minutes from the surface. Earth-based radio telescopes received the Huygens carrier for the whole descent and another 3h14min from the surface. During entry, accelerometer measurements enabled the determination of the atmospheric structure profile from an altitude of about 1500 km above the surface down to 160 km altitude. After parachute deployment at 155 km altitude, all instruments were making their measurements. *In situ* measurements were made of the physical properties of the atmosphere, its composition and meteorology. Atmospheric haze was observed during the whole descent all the way down to the surface. Clear images of the surface were acquired below 50 km. They revealed a frozen earth-like world where organic chemistry is trapped in a pre-biotic stage. In this world, methane takes the role of water on Earth. Huygens descended over the boundary between a bright icy terrain, laced with narrow channels and rivers and a darker terrain covered with cm-size ice-pebbles in a dry river or lake-bed covered with a layer of organic matter. Zonal winds blew the probe eastwards by more than 250 km during its descent under parachute. Optical and radar observations of the Huygens landing site area allowed placing the Huygens surface mosaics in their wider context. The coordinates of the Huygens landing site, which are still being refined at the time of writing, are about 10.3S and 192.7W. The Huygens mission was unique in many respects. After giving an overview of the mission the main scientific results will be highlighted. A lessons-learned exercise is being conducted among all components of the Huygens team in order to fully exploit all the results of the mission including management, engineering, operational and scientific return aspects. A brief review of the status of this activity will also be provided. Huygens is the ESA-provided element of the Cassini-Huygens mission, which is a joint NASA-ESA programme in cooperation with the Italian Space Agency.

The Huygens Atmospheric Structure Instrument (HASI) results at Titan

M. Fulchignoni[1,2], F. Ferri[3], G. Colombatti[3] & the HASI team

[1]LESIA, Observatoire de Paris, 5 Place Janssen, 92195 MEUDON, France
[2]Université Denis Diderot – Paris 7, Paris France
[3]CISAS « G. Colombo », Università di Padova, Corso Venezia 15, 35131 Padova, Italia

The Huygens Atmospheric Structure Instrument (HASI) is a multi sensor package which measured the main physical characteristics of the Titan atmosphere in all the phases of the Huygens probe mission at Titan: entry, descent and impact.
The HASI instrument package had a total mass of 5.7 kg. The accelerometers package (ACC) was mounted at the center of mass of the Probe and the temperature sensors (TEM) and the pressure probe inlet were mounted on a stem outside of the Probe. Two deployable booms carrying Permittivity ad Wave electrodes stowed under the thermal shield of Huygens, has been deployed at the beginning of the descent into Titan's atmosphere.
HASI's suite of sensors measured the physical and electrical properties of Titan's atmosphere. Profiles of temperature, pressure, density, atmospheric conductivity have been determined along the Huygens descent trajectory.. HASI investigated the electric properties and the nature of the surface at the Huygens landing site . The accelerometers (ACC sensors) provided data from the very beginning of the entry phase (1500 km altitude) allowing us to obtain the density profile from which we derived pressure and temperature profiles under the assumption of hydrostatic equilibrium.
Temperature and pressure profile were obtained by direct measurements of T (TEM sensors) and P (PPI package) during descent (from 162 km down to the surface) and for half an hour at the surface, providing us with hints on the vertical structure of Titan’s lower atmosphere and local meteorology.
The Permittivity and Wave Analyzer sensors measured the electron and ion conductivities as well as the complex permittivity of the atmosphere at 45 Hz and searched for electric wave activity including lightning. Acoustic signals collected by the HASI microphone were processed by the on board FFT and their amplitude and main frequency, averaged over two minutes, were transmitted to the ground. The radar altimeter return signal recorded in the range of altitude 0-30 km have been processed by the HASI data processing unit in order to perform spectral analysis (FFT), providing us with information both on the elevation of the Probe in the last part of the descent and on some physical properties of Titan’s surface.
Furthermore the ACC recorded the signature of the impact of the Probe at the surface of Titan.
In addition to its own scientific data, HASI provided unique data for the reconstruction of attitude and trajectory of the Huygens probe and calibration information of use by other instruments on Huygens and by remote sensing observations from the Cassini orbiter.

Huygens probe entry trajectory reconstruction using Kalman filtering

Aboudan Alessio, Colmbatti Giacomo, Francesca Ferri, Francesco Angrilli, Marcello Fulchignoni

Space probes entering into planetary atmosphere can be used for in-situ study of its structure. During the entry phase aerodynamic forces exerted by a probe are related to atmospheric density. As a consequence acceleration measured by on-board sensor can be used to derive atmospheric density, pressure and temperature profiles as well as the probe trajectory. Huygens probe that has entered Titan's atmosphere is a perfect example of this technique. In this work acceleration data acquired by HASI (Huygens Atmospheric Structure Instrument) have been used to reconstruct probe trajectory and Titan's atmospheric structure at altitudes from 1570 km down to 160 km, where no direct measurements was possible due to the presence of the heatshield.

Initial attitude conditions have been estimated from accelerometers measurements before atmospheric entry, confirming probe spin around 7 rpm.

Entry state at 1570 km is obtained by comparing simulated deceleration profile with the one retrieved from accelerometer data and correcting the nominal entry vector as given by Huygens Project. A very accurate six degree of freedom model of the entry phase of the mission has been developed and a new reconstruction technique based on Kalman filtering is presented.

The algorithm gives an estimation of position, velocity, angular rate and attitude of the probe and of the physical parameters of the atmosphere. Drag forces acting on the probe depend strongly on atmospheric density and probe velocity: this relation allows to update the preflight atmospheric density and pressure profiles based on accelerometer measurements.

Reconstructed trajectory is consistent with profiles obtained from other approaches and preflight models. Used technique produces also an estimate of the probe attitude which is consistent with measured data.

HASI ACCELEROMETER KALMAN BASED ALTITUDE RECONSTRUCTION OF HUYGENS DESCENT PHASE

C.Bettanini[1], HASI Team*, ESA RADAR Team*

1 - Center for Studies an Activities for Space “G.Colombo”, University of Padova, Italy
* - correct co authors list to be provided at time of meeting

This work presents the results of a new reconstruction effort for the determination of Huygens altitude profile during the descent phase, in which the probe was successfully parachuted from an altitude of around 160 kilometer to ground. This work is based on Kalman filtering and relies mainly on reverse HASI Servo Accelerometer integration from impact up to start of the descent phase. In order to contain altitude uncertainties related to direct double integration, probe motion is propagated through state equations, which model probe dynamics and is corrected with both accelerometer data and PPI (Pressure Profile Instrument) total pressure measurements, which contain the possible drift in descent velocity.
Comparison of result with PPI derived altitude and RADAR altitude profiles is presented as well as a confrontation of uncertainties related with pressure based and accelerometer based reconstruction strategies.

IN-SITU INVESTIGATION OF ATMOSPHERIC ELECTRICITY AND ACOUSTICS: LESSONS LEARNED FROM THE SUCCESSFUL FLIGHT OF THE HUYGENS ATMOSPHERIC STRUCTURE INSTRUMENT PERMITTIVITY, WAVE AND ALTIMETRY EXPERIMENT

R. Trautner, Research and Scientific Support Department, ESA/ESTEC, Keplerlaan 1, 2200AG Noordwijk, The Netherlands, email: Roland.Trautner@esa.int

K. Schwingenschuh, Space Research Institute, Austrian Academy of Sciences (IWF), Schmiedlstrasse 6, 8042 Graz, Austria, email: konrad.schwingenschuh@oeaw.ac.at

J.J. López-Moreno, Instituto de Astrofisica de Andalucia IAA-CSIC, Camino Bajo de Huetor, 50, 18008 Granada, Spain, email: lopez@iaa.es

Peter Falkner, Science Payload and Advanced Concepts Office, ESA-ESTEC, European Space Agency, Keplerlaan 1, 2200AG Noordwijk, The Netherlands, email: Peter.Falkner@esa.int

R. Hofe, Space Research Institute, Austrian Academy of Sciences (IWF), Schmiedlstrasse 6, 8042 Graz, Austria, email: robinhofe@yahoo.de

The Permittivity, Wave and Altimetry (PWA) experiment, a sub-unit of the Huygens Atmospheric Structure Instrument (HASI), was designed to investigate atmospheric conductivity, electric fields, lightning activity, and acoustic phenomena in the atmosphere and on the surface of Saturn's biggest moon, Titan. The processing of Huygens Radar Altimeter data was implemented as an add-on in order to support scientific exploitation of the data delivered by this probe system. The performance of the instrument, as observed in terrestrial tests and during the successful mission, allows identifying a number of possible improvements in both instrument design and data processing which will be beneficial for future planetary probe missions employing similar types of sensors.

The basic design of the instrument is introduced. The individual sensors, their characteristics and measurement capabilities are presented. Processing of data by the PWA signal processor is explained. Data from terrestrial tests as well as data from the Huygens descent on Titan are shown. Instrument design features and their impact on the scientific investigations are presented, and improvements of the sensor design are suggested. The influence of probe motion and environmental effects is discussed. The importance of additional data sources for the interpretation of the science data is explained, and new and improved instrument features for future atmospheric probes are suggested.

VLBI TRACKING OF PLANETARY PROBES AS A MISSION TOOL AND SCIENTIFIC EXPERIMENT

L. I. Gurvits, S. V. Pogrebenko, I. M. Avruch, R. C. Campbell, JIVE, P.O. Box 2, 7990 AA, Dwingeloo, The Netherlands, lgurvits@jive.nl
and Huygens VLBI tracking team

Very Long Baseline Interferometry (VLBI) technique offers an unrivalled angular resolution reaching fractions of a milliarcsecond (mas) in studying structures and defining positions of celestial radio sources. Developed originally for astrophysical studies of natural sources of radio emission, VLBI entered the field of space flight science and engineering as an efficient tool for ultra-precise determination of coordinates and parameters of motion of planetary probes and other spacecraft. This application of the technique was introduced in the 1970s (Thornton and Border 2003). VLBI tracking was demonstrated for the VEGA (Venus – Halley Comet) mission in the mid 1980s (Preston et al. 1986, Sagdeev et al. 1992). Recently, the VLBI technique was applied to tracking of the Huygens Probe during its parachute descent in the atmosphere of Titan and on the planet's surface (Lebreton et al. 2005).

In this presentation we review VLBI tracking methodology using the Huygens VLBI experiment as an example. This experiment required development of the technique to the limit defined by the present day technology. It necessitated development of a novel software VLBI correlator enabling sub-Hz spectral resolution and use of the disk-based direct-access VLBI recording systems. Data processing of the Huygens VLBI tracking required introduction of a relativistic model in the near-field interferometry – a modification of the technique seldom used in the earlier VLBI spacecraft tracking applications. VLBI tracking of the Huygens Probe resulted in the sub-mas accuracy of determination of the transmitter position that corresponds to the random error of about 1 km. The Huygens VLBI processing also enabled independent verification of Doppler measurements of the winds in the atmosphere of Titan conducted by the Doppler Wind Experiment (Bird et al. 2005).

Future developments of VLBI tracking of planetary probes will be discussed in the light of their synergy with the progress of radio astronomy technologies. In the near future, VLBI will be able to detect radio transmission of distant spacecraft at Ka-band (32 GHz), a considerable improvement in terms of angular resolution comparing to standard nowadays S-band (2.3 GHz) and X-band (8.4 GHz) radio links. Large collecting areas of the prospective VLBI antennas combined with a wider band VLBI data streams (corresponding to data rates 1 Gbps and higher) will make it possible to use weak natural background sources as "anchors" for spacecraft tracking virtually anywhere on the celestial sphere. We will briefly discuss these perspectives emphasising both scientific and engineering aspects of the experimental technique.

References

Bird M.K. et al. 2005, Nature 438, 800
Lebreton J.-P. et al. 2005, Nature 438, 758
Preston R.A. et al. 1986, Science 231, 1414
Sagdeev R.Z. et al. 1992, Astronomy and Astrophysics 254, 387
Thornton C.L and Border J.S. 2003, *Radiometric Tracking Techniques for Deep Space Navigation*, John Wiley & Sons, Hoboken, NJ

HUYGENS ATMOSPHERIC STRUCTURE INSTRUMENT ENTRY ACCELEROMETER: APPLICATION TO MARS AND VENUS

A.J. Ball, PSSRI, The Open University, Walton Hall, Milton Keynes MK7 6AA, UK. A.J.Ball@open.ac.uk
I. Müller-Wodarg, Space and Atmospheric Physics Group, Imperial College London, Prince Consort Road, London SW7 2BW, UK. i.mueller-wodarg@imperial.ac.uk
S. R. Lewis, PSSRI, The Open University, Walton Hall, Milton Keynes MK7 6AA, UK. S.R.Lewis@open.ac.uk
J. C. Zarnecki, PSSRI, The Open University, Walton Hall, Milton Keynes MK7 6AA, UK. J.C.Zarnecki@open.ac.uk
B. Hathi, PSSRI, The Open University, Walton Hall, Milton Keynes MK7 6AA, UK. B.Hathi@open.ac.uk
M. R. Leese, PSSRI, The Open University, Walton Hall, Milton Keynes MK7 6AA, UK. M.R.Leese@open.ac.uk
M. C. Towner, PSSRI, The Open University, Walton Hall, Milton Keynes MK7 6AA, UK. M.C.Towner@open.ac.uk
F. Ferri, CISAS G. Colombo, University of Padova, Via Venezia 15, 35131 Padova, Italy. francesca.ferri@unipd.it
G. Colombatti, CISAS G. Colombo, University of Padova, Via Venezia 15, 35131 Padova, Italy. giacomo.colombatti@unipd.it
M. Fulchignoni, LESIA, Observatoire de Paris, 5 Place Janssen, 92195 Meudon, France. marcello.fulchignoni@obspm.fr

Abstract

An assessment will be made of the performance achievable if the Huygens entry accelerometer (HASI ACC Servo) were applied to Mars and Venus atmospheric entry. In particular, the cases of ESA's *ExoMars* mission and Venus Entry Probe study are considered. In both cases there is an excellent prospect of improving on previous entry accelerometry data, not least in terms of the maximum altitude at which the atmospheric deceleration is sensed. Some modifications are of course necessary for the Mars and Venus cases, however, with respect to that of Titan.

HUYGENS ATMOSPHERIC STRUCTURE INSTRUMENT ENTRY ACCELEROMETER: FLIGHT PERFORMANCE

A.J. Ball, PSSRI, The Open University, Walton Hall, Milton Keynes MK7 6AA, UK. A.J.Ball@open.ac.uk
M. R. Leese, PSSRI, The Open University, Walton Hall, Milton Keynes MK7 6AA, UK. M.R.Leese@open.ac.uk
B. Hathi, PSSRI, The Open University, Walton Hall, Milton Keynes MK7 6AA, UK. B.Hathi@open.ac.uk
M. C. Towner, PSSRI, The Open University, Walton Hall, Milton Keynes MK7 6AA, UK. M.C.Towner@open.ac.uk
J. C. Zarnecki, PSSRI, The Open University, Walton Hall, Milton Keynes MK7 6AA, UK. J.C.Zarnecki@open.ac.uk
P. Withers, Center for Space Physics, Boston University, 725 Commonwealth Avenue, Boston, MA 02215, USA. withers@bu.edu
F. Ferri, CISAS G. Colombo, University of Padova, Via Venezia 15, 35131 Padova, Italy. francesca.ferri@unipd.it
G. Colombatti, CISAS G. Colombo, University of Padova, Via Venezia 15, 35131 Padova, Italy. giacomo.colombatti@unipd.it
M. Fulchignoni, LESIA, Observatoire de Paris, 5 Place Janssen, 92195 Meudon, France. marcello.fulchignoni@obspm.fr
+ more?

Abstract

This abstract will concern the performance of the high-sensitivity servo accelerometry system of the Huygens Atmospheric Structure Instrument (HASI), which operated during cruise, atmospheric entry, descent and on the surface of Titan. An updated assessment of its noise and offset performance will be made, with respect to the work reported at the first probe workshop (Zarnecki *et al.*, 2004).

HASI ACCELEROMETER KALMAN BASED ALTITUDE RECONSTRUCTION OF HUYGENS DESCENT PHASE

C.Bettanini[1], HASI Team*, ESA RADAR Team*

1 - Center for Studies an Activities for Space “G.Colombo”, University of Padova, Italy
* - correct co authors list to be provided at time of meeting

This work presents the results of a new reconstruction effort for the determination of Huygens altitude profile during the descent phase, in which the probe was successfully parachuted from an altitude of around 160 kilometer to ground. This work is based on Kalman filtering and relies mainly on reverse HASI Servo Accelerometer integration from impact up to start of the descent phase. In order to contain altitude uncertainties related to direct double integration, probe motion is propagated through state equations, which model probe dynamics and is corrected with both accelerometer data and PPI (Pressure Profile Instrument) total pressure measurements, which contain the possible drift in descent velocity.
Comparison of result with PPI derived altitude and RADAR altitude profiles is presented as well as a confrontation of uncertainties related with pressure based and accelerometer based reconstruction strategies.

THE ATMOSPHERIC TEMPERATURE PROFILE OF TITAN RECONSTRUCTED FROM PRESSURE DATA

J. Leinonen[*], jussi.leinonen@fmi.fi
T. Mäkinen[*], teemu.makinen@fmi.fi
A.-M. Harri[*], ari-matti.harri@fmi.fi

[*]: F innish Meteorological Institute, Space Research, P.O. Box 503, FIN-00101 Helsinki, Finland

We introduce a new method for analyzing atmospheric sounding observations: the reconstruction of the vertical temperature profile from in situ pressure measurements accompanied with rough knowledge of the atmospheric composition and the aerodynamic response properties of the descent vehicle. This method can be useful to construct the temperature profiles when no reliable temperature sensors are available, as well as to verify the consistency of the data from redundant independent instruments. We applied the method to the measurements of Titan's atmosphere made by the Huygens probe, obtaining the relevant aerodynamic properties using the measurements of the radar altimeter. We discovered that the temperature profile computed in this manner is within a 10% error margin from the data from the temperature sensor (TEM) of the probe, giving an apparent tropopause altitude slightly above 50 km and a surface temperature of about 98 K. The notable difference between the reconstruction and direct observations likely implies an inconsistency between Huygens instrument measurements.

FAILURES OF PLANETARY PROBES

Ralph D Lorenz, Lunar and Planetary Lab, University of Arizona, AZ 85721
rlorenz@lpl.arizona.edu

Not every probe mission is successful. A number of probes have been lost completely (e.g. Mars Polar Lander, DS-2,) Other probes and landers have suffered mild to severe degradation due to subsystem failures (e.g. telemetry commutator and radio system failure on Venera 7 ; progressive degradation of Pathfinder/Sojourner ; MER file handling anomaly) Still other missions have suffered science loss due to instrument failure (e.g. Viking seismometer ; Pioneer Venus external sensors) or instrument operation outside calibration range (Pathfinder APXS ; Galileo probe instruments.)

Lessons can be drawn from failures, when their occurrence is acknowledged and documented (which is not always in the parochial interests of those involved). This poster presentation offers a brief survey of probe mission failures and what can be learned – the particular problems of planetary probes (e.g. EDL systems and environmental uncertainty) are discussed.

D. M. Harland and R. D. Lorenz, Space System Failures, Praxis-Springer April 2005 400p
A. J. Ball, J. R. C. Garry, R. D. Lorenz and V. V. Kerzhanovich, 'Planetary Landers and Entry Probes' , in production for publication in late 2006, Cambridge University Press

SESSION 3

IN SITU MEASUREMENTS OF EARHT'S ATMOSPHERE

Chairs:
George Durry, Institut Pierre-Simon-Laplace, France
Peter Jenniskens, SETI, USA
Maartin Roos-Serote, U. Lisbon, Portugal

Title: Challenges and Strategies for Sustaining TPS/Entry Technology in the era of focused projects and programs

Abstract: The challenges that faces entry technologist, especially in Thermal Protection System, are one of providing robust and cost-effective solutions to missions that are infrequent, and yet meet the mission planners and science community expectation of having the capabilities and expertise readily available to enable these future missions. In this presentation, we will review NASA's past history in this regard and look at current mission drivers and challenges that are being addressed in the TPS technology area via project-focused developments both for the Mars and Human Exploration projects. Current Crew Exploration Vehicle (CEV) design and development, which is key to enable NASA’s vision of Moon, Mars and beyond, is clearly benefiting from the past planetary missions. Future planetary missions can equally benefit from the current investment to varying degree in a large number of scenarios. In other cases, up-front investment is needed in order to have enabling capability readily available from emerging technology areas. Strategic planning is needed in order to maintain current infrastructure and expertise as well as develop new ones that can enable future missions. This talk will address these possible strategies the TPS technology community need to pursue in order to enable both the near term missions and longer term vision.

Authors: Ethiraj Venkatapathy, Bernie Laub and Robert Manning

The Stardust Sample Return Capsule reentry observing campaign

Peter Jenniskens (SETI Institute, Mountain View, CA), D. Jordan, D. Kontinos, M. Wright, J. Olejniczak, G. Raiche, P. Wercinski, E. Schilling (NASA Ames Research Center), M. Taylor (Utah State University at Logan), R. Rairden (Lockheed Martin), H. Stenbaek-Nielsen (University of Alaska at Fairbanks), M. G. McHarg (U.S. Air Force Academy), S. Abe (Kobe University, Japan), M. Winter (Universität Stuttgart, Germany), D. O. Revelle (Los Alamos National Laboratory), R. Dantowitz (Clay Center Observatory at Dexter and Southfield Schools)

The entry of probes into the atmosphere of a planet offer an opportunity to study the physics of reentry, the physical processes in natural meteors, physical properties of that atmosphere, and the performance of thermal protection materials. We will describe a N.E.S.C. and E.M.S.D. sponsored observing campaign to study the reentry of the STARDUST sample return capsule in Earth's own atmosphere on 2006 January 15. The probe returned on a cometary orbit from a visit to comet 81P/Wild 2, with a sample of cometary dust collected during a flyby. Because the probe had to match the comet orbit, the entry in Earth's atmosphere was the fastest on record, at a speed of 12.8 km/s (at 135 km altitude), comparable to natural meteoroids. The thermal protection material used was a Phenol-Impregnated Carbon Ablator (PICA), developed for the purpose of such fast reentry at NASA Ames Research Center. An observing campaign was organized to deploy an array of remote sensing instruments onboard the NASA DC-8 Airborne Laboratory, which provided an airborne platform above clouds and weather. The campaign proceeded much as planned and the results are now being analyzed. The presentation will focus on the anticipated signatures during the reentry that will be used to study the surface temperature, intensity of shock radiation, and the ablation process. Some preliminary results will be presented, to be discussed at the 2nd *Workshop on Reentry Emission Signatures* at the SETI Institute in Mountain View, CA, on July 6-7 (http://reentry.arc.nasa.gov).

Probing the meteoroids environnment of planets

J. Vaubaillon, CalTech, SSC, 1200 East California Boulevard, Pasadena, CA91125, USA

The detection of the first Martian meteor in 2004 by Selsis et al. (Nature, 435, Issue 7042, pp. 581, 2005) opened the doors to the detection of meteoroids in other places tan in the vicinity of the Earth. The interest resides in the fact that meteoroids are very hard to detect by other means than meteors or direct infrared observations of cometary trails. If the meteoroid environnement of the Earth is known thanks to the study of meteor showers, it is very poorly known in other planets, or in the whole Solar System to be true. Nature offers us sevral planets having an atmosphere able to reveal the meteoroids through the creation of meteors. We will list all the scientific interests of the detection of meteoritic activities in other atmospheres, i.e. the detection of not only meteors but also their signature in the atmospheric layers. This emerging topic is studied through the collaboration of scientist from NASA, ESA, UWO (Canada) and Armagh Observatory (UK).

Improving Mission Survivability and Science Return with Onboard Autonomy

Ashley Gerard Davies[(1)], Steve Chien[(1)], Thomas Doggett[(2)], Felipe Ip[(3)] and Rebecca Castaño[(1)]

[(1)]Jet Propulsion Laboratory-California Institute of Technology, ms 183-501, 4800 Oak Grove Drive, Pasadena, CA 91109-8099 (USA). Email: Ashley.Davies@jpl.nasa.gov
[(2)]Department of Geological Sciences, Arizona State University, Tempe, AZ 85287-1404 (USA). Email: tcd@asu.edu
[(3)]Department of Hydrology and Water Resources, University of Arizona, Tucson, AZ 85721 (USA). Email: felipe@hwr.arizona.edu

ABSTRACT

The ability to autonomously process data to generate information onboard a spacecraft and to make decisions based on the onboard analysis to control and, where necessary, change subsequent spacecraft and instrument operations, is now a reality, having been demonstrated by the NASA New Millennium Program Autonomous Sciencecraft Experiment. Spacecraft autonomy is a necessity for spacecraft survival in a dynamic environment; to operate in the most efficient manner to conserve resources; and to maximise science return through recognition of events of particular scientific value without overwhelming onboard and downlink resources. ASE data classifiers will soon be operating on the Mars Exploration Rovers and Mars Odyssey. Scientists and engineers designing the next generation of spacecraft and instruments should consider incorporation of autonomy at early stages of the design process.

1. TRADITIONAL MISSION OPERATIONS

For much of the era of spaceflight, robotic spacecraft have collected data according to pre-planned operations sequences. After acquisition, the collected data was returned to Earth, and analysed on the ground before the next observation sequence was planned, often of another planetary body, for flyby missions. In the case of planetary flyby missions like *Mariner*, *Pioneer* and *Voyager* the observations obtained were the first high-resolution look at the surfaces, revealing strange new worlds. This was the discovery phase of planetary exploration. All of the data collected were of high value due to their uniqueness, and allowed the planning of the next stage of exploration, reconnaissance missions such as *Viking* and *Galileo* to further investigate planets and satellites. Again, regardless of usefulness, all data collected were returned within the limits of downlink. In the case of *Galileo*, downlink was severely restricted, and a significant amount of data collected was not returned.

Even today, *Cassini* observations, including instrument settings, are pre-planned and firmly established, and unalterable, weeks before encounter.

More and more missions today have moved beyond the reconnaissance phase and mapping phases into a deeper investigative mission role, driven primarily by high-level science goals. Prime examples are the fleet of assets in orbit around and on the surface of Mars, currently consisting of the Mars Exploration Rovers (MER), Mars Odyssey (MO), Mars Global Surveyor (MGS), Mars Express (ME) and Mars Reconnaissance Orbiter (MRO).

Vast amounts of data are being generated by these missions, and it is impossible to return all of the data collected. The use of onboard autonomy, which is capable of processing large data sets, recognizing events of particularly high science value, preferentially returning those data of interest, and retasking of assets to obtain more data of the phenomenon in question, would remove the time delay in the discovery process by removing the need to data downlink, analysis, and re-sequencing of assets from the ground, a process that leads to missed opportunities for higher temporal resolution data, for example.

2. OPERATIONS WITH AUTONOMY: ASE

Autonomous spacecraft operations have been successfully demonstrated by the New Millennium Program Autonomous Sciencecraft Experiment (ASE) flying on the Earth Observing 1 spacecraft (*EO-1*) [1]. This new, flight-tested capability allows operations decisions to be made onboard the spacecraft, including resource allocation and fault detection and mitigation. Sequenced operations commands can be altered as a result of onboard data analysis, with science goals driving mission operations.

ASE routinely detects dynamic events and retasks *EO-1* to obtain further data, and the planner developed for ASE is currently used for routine *EO-1*

operations, overseeing over 5000 datatakes, greatly reducing operations cost while increasing system flexibility and allowing rapid, autonomous operations changes [1]. ASE uses classifiers to process Hyperion hyperspectral imaging data to detect dynamic events. Hyperion collects data at 220 wavelengths between 0.4 and 2.5 microns, at 30 m/pixel. ASE is being used to detect thermal emission from active volcanism [2], changes in the cryosphere, for example, where ice is forming or breaking up [3], and flooding events [4], as well as assessing cloud cover [3]. A précis of the most important data is returned in hours, rather than the weeks taken to obtain data with previous 'normal' operations [2]. On a positive detection of one of these processes of interest, an ongoing volcanic eruption, or detection of the onset of ice break up on a frozen lake, the onboard planner reschedules the spacecraft to obtain additional observations at a higher temporal resolution, at the next available opportunities. Having also determined cloud cover, the option exists to repeat observations at a later date if the target is obscured.

With a view to increasing temporal coverage of events, making the best use of other available resources, ASE and *EO-1* have been incorporated into a sensor web [5] that utilizes multiple detection and classification systems to detect events, which then are used to trigger *EO-1* observations. The sensor web is autonomously operating, seamlessly integrated into the *EO-1* operation planner, and affords rapid response to detections of volcanic activity [6], cryosphere changes, and flooding.

3. ASE ON MARS

ASE classifiers are being readied for uplink to Mars Odyssey THEMIS instrument to monitor the edge of the martian ice caps, detect clouds, and search for thermal anomalies [7], and making use of data for which there is insufficient downlink to return. Similar algorithms for detecting dust devils and clouds were uplinked to MER in the fall of 2006 [8]. In the case of the THEMIS experiment, a large proportion of collected data (~40% of nighttime data) are not returned due to downlink constraints. The ASE classifier will process all relevant THEMIS data to determine the position of the edge of the polar ice caps, and returning not the whole dataset but the edited dataset containing the edge information. In this way, at very little resource use, additional science value is returned. The ASE THEMIS data classifiers will also search through the data for pixels of anomalous surface thermal emission on the surface, possible evidence of hydrothermal or volcanic activity. This is a very low-cost operation looking for a very low-probability occurrence, but with a very high potential scientific value if such activity is discovered. In MER Panoramic Camera (Pancam) data, ASE algorithms search for clouds and dust devils, sending down only those images, or even portions of those images, where such phenomena are detected [8]. This allows more images to be taken and only the most valuable to be returned.

4. ENHANCED SCIENCE RETURN EXAMPLE

The benefits of Artificial Intelligence and spacecraft autonomy onboard a deep-space mission can be illustrated by considering how best to detect and monitor a dynamic, unexpected event of high science interest, such as an ongoing, large-scale but short-lived volcanic eruption [9]. The jovian moon Io is intensely volcanic, and although studied extensively by the NASA *Galileo* spacecraft, many questions remain as to the precise nature of the composition of the erupting lavas, specifically, whether very-high temperature ultramafic lavas are present [10, 11]. Ultramafic lava would apply strong constraints on the thermal and chemical evolution of Io's interior [12]. The science objective would therefore be to determine the temperature of Io's lavas and constrain possible compositions.

Given the nature of thermal emission from active volcanism, the best opportunity for detecting high-temperature lavas comes from rare lava-fountain events, where relatively large areas at or close to magma liquidus temperatures are exposed. Even from a great distance away, even from the orbit of Europa, it is possible to determine a lower limit on magma temperature, a very strong constraint on composition. For *Galileo*, engaged in multiple fly-bys of the Galilean satellites, each encounter observation sequence was planned well in advance. Instrument setting and exposure times were pre-ordained. Although lava fountains were observed, in one case at high spatial resolution, observations were planned to image the non-thermally active background and the intense thermal emission saturated both the visible imaging system (SSI) and infrared imager (NIMS). There was no opportunity to quantify the intensity of the thermal emission and change observation sequencing and instrument settings. By the time data had been returned to Earth and analysed, the spacecraft had moved on and the science event was over.

An onboard AI would do things very differently. Onboard data processing would quickly identify an intense thermal source at a great distance, calculate the opportune moment to make observations (with visible and infrared imagers in the 0.4 to 10

micron range to capture the full thermal emission spectrum), and set the appropriate instrument gain state or exposure time to obtain unsaturated data. Additional instrumentation can be brought to bear on the new eruption: an ultraviolet spectrometer would be used to study erupting gas. Subsequent orbits would flag this location for in-depth visible and infrared study to determine composition spectroscopically.

The science content of the returned data is therefore increased from an acquisition queue using preset observation sequencing, the need for communications (data transfer and commands, and accompanying time lag) between spacecraft and Earth for spacecraft re-tasking is eliminated, the use of bandwidth is optimised, and an important science question can be answered by making decisions on the spot.

A mission to Europa, such as the Europa Explorer concept now being studied by NASA, would spend at least two years in the Jovian system. This will allow considerable lengths of time for monitoring Io.

5. EUROPA

Detection of active resurfacing processes on Europa would be a major discovery. Such detections are best accomplished by either detecting plumes or by detecting anomalous thermal signatures on the surface in the thermal infrared [13]. Data classifiers based on the cryosphere and thermal detectors on ASE would fly on the Europa Mission, processing hyperspectral data and data from other instruments to detect such spectral features [13], a low-cost process with a potential huge science return.

6. MISSIONS REQUIRING AUTONOMY

The use of autonomy need not be as aggressive as described in the example in the previous section. The degree of autonomy has to be tailored to the environment in which the spacecraft will operate, and the science goals of the mission.

Some degree of autonomy is a necessity for missions inserted into a dynamic environment. Examples include balloons, blimps (a steerable balloon) or aerobots (rigid flying machines) in planetary atmospheres. A blimp exploring the atmosphere of Mars, Venus [e.g. 14], or Titan [e.g., 15], can process data onboard and return to sites, descending to the surface if necessary, to carry out a closer investigation of a target of interest identified during onboard data processing. This is especially important on missions where the lifetime of the probe is limited, and communications might be sporadic. Onboard autonomy allows continual operations, far removed from remote control, with accompanying time lag.

Another possible operational scenario is that of a Venus Atmosphere/surface blimp or balloon. Detecting a feature of interest from a relatively high, (and cool) altitude, the probe could make a rare descent into the much hotter, hostile environment for a quick high-resolution observation or sample collect before retreating back to safety at higher altitude.

For missions to active bodies such as comets, the level of autonomy can be tailored to the goal of the mission: is it important to head for a plume erupting from a comet to collect a sample, or are plumes to be avoided at all costs? In either case, the plume has to be identified first.

Thusly, these and others missions can benefit from onboard processing to focus on features and processes of greatest interest, allowing modification of instrument and spacecraft goals during monitoring or mapping phases. Another example would be on the aforementioned Europa mission. A spacecraft orbiting Europa has a limited operational lifetime because of the hostile radiation environment. Processing of data onboard can increase the science return by returning products from data that would otherwise not be returned in full, allows rapid identification of high-priority phenomena on the surface (thermal emission signifying possible volcanic activity, for example), and retasking of instruments and resources to gather data of these locations at higher temporal, spatial and spectral resolutions. Detection by a low data-volume instrument could be used to trigger observations by a high data-volume instrument, for example, an imager detecting a new hot spot triggering the spacecraft radar.

The same techniques for identifying and reacting to detections of active volcanism can be used to search for and investigate other phenomena on other planets, for example, on a dedicated mission to the Saturn moon Enceladus (detecting plumes, thermal anomalies on the surface), on Triton in the Neptune system (volcanic plumes and changes in ice caps), and on Titan and Venus missions (searching for volcanic activity and compositional outliers, for examples).

7. INCORPORATING AUTONOMY

The new ASE technology allows a step in the normal planetary exploration timeline to be removed. Now, instead of a discovery being investigated by the next mission, further investigations can be performed on the spot, driven by onboard science data analysis applications controlling resource allocation.

When designing a mission, therefore, it is important to consider how autonomy can enable the

achievement of science goals early in the concept and design process. Spacecraft autonomy can enhance what a mission can achieve, as shown by ASE [1-4] but to gain maximum benefit, it is preferable to integrate autonomy into the hardware, software and operational concept design sooner rather than try to bolt it on at a later stage. In particular, data classifier efficiency is a factor of available processing speed and data storage capacity, and data product type, as well as a function of the complexity of the data processing task.

Further information about ASE and contact information for the ASE Team are available at http://ase.jpl.nasa.gov.

8. ACKNOWLEDGEMENTS

This work was carried out at the Jet Propulsion Laboratory-California Institute of Technology, under contract to NASA.

9. REFERENCES

1. Chien, S. *et al.,* Using Autonomy Flight Software to Improve Science Return on Earth Observing One, *Journal of Aerospace Computing, Information, & Communication*, AIAA, 2, 196-216, 2005.
2. Davies, A. G. *et al.,* Monitoring active volcanism with the Autonomous Sciencecraft Experiment (ASE), *Rem. Sens. Env.*, 101, 427-446, 2006.
3. Doggett, T. *et al.,* Autonomous detection of cryospheric change with Hyperion onboard Earth-Observing 1, *Rem. Sens. Env.*, 101, 447-462, 2006.
4. Ip, F. *et al.*, Detecting, mapping and monitoring floods through the Autonomous Sciencecraft, *Rem. Sens. Env.*, 101, 463-481, 2006.
5. Chien, S., *et al.,* An Autonomous Earth Observing Sensorweb, *IEEE Intelligent Systems*, May-June 2005, pp. 16-24, 2005.
6. Davies, A. G., *et al.,* Sensor web enables rapid response to volcanic activity, *Eos*, 87 (1), 1&5, 2006.
7. Wagstaff, K., *et al.,* Dust storms and water ice clouds: feature detection for use onboard THEMIS, *Lunar. Plan. Sci. Conf. XXXVII*, abstract 2287, 2006.
8. Castano, A. *et al.,* Feature detection onboard Mars rovers: automated cloud and dust devil detection, *Lunar. Plan. Sci. Conf. XXXVII*, abstract 2059, 2006.
9. Davies, A. G., Increasing deep-space mission science return through onboard identification of dynamic events: examples from planetary volcanology, *Eos Trans. AGU, 87(36), Jt. Assem. Suppl.,* Abstract IN43E-02, 2006.
10. McEwen A. S. *et al.*, High-Temperature Silicate Volcanism on Jupiter's Moon Io, *Science*, 281, 87, 1998.
11. Davies, A. G., *et al.*, Thermal signature, eruption style and eruption evolution at Pele and Pillan on Io *J. Geophys. Res.*, 106, E12, 33,079-33,104, 2001.
12. Keszthelyi, L. P. *et al.* A post-*Galileo* view of Io's interior, *Icarus*, 169, 271-286, 2004.
13. Doggett, T. C., A. G. Davies and R. Greeley, Detectability of cryo-volcanism with thermal infrared spectroscopy, *Lunar. Plan. Sci. Conf. XXXVII* abstract 2243, on CD-ROM, 2006.
14. Gilmore, M. *et al.,* Investigation of the application of aerobot technology at Venus, *Acta Astronautica*, 56, no. 4, 477-494, 2005.
15. Lorenz, R. *et al.*, Science autonomy on a Titan airborne platform, *Eos Trans. AGU, 87(36), Jt. Assem. Suppl.,* Abstract IN43E-07, 2006.

A family of Balloons to study Earth atmosphere

Christian Cazaux
Centre National d'Etudes Spatiales
France
christian.cazaux@cnes.fr

Every year CNES is launching around 40 balloons to study the atmosphere. For this purpose, a family of balloons was developed and is available . We have, in the stratospheric family, Zero Pressure Balloons allowing a wide range of missions in term of carried mass and flight profile, Infrared Montgolphieres allowing to flight several weeks between 18 (night) and 30 (day) km with 50 kg of payload and Super Pressure Balloons allowing to carry during several months at constant altitude (around 20 km) up to 50 kg of payload. The tropospheric family includes the Boundary Layer Super Pressure Balloon and the Aeroclipper flying over the sea to study the interaction between ocean and atmosphere.
The presentation will be focused on the characteristics of the balloons family and typical atmospheric missions will be described. In addition, information on past studies and tests on planetary balloons will be given.

SYSTEM DESIGN OF SPACE VEHICLE FOR SMALL SIZE ORBITAL DEBRIS OBSERVATION

Yunir Gataullin

Ruhr University Bochum, University str. 150, Bochum 44801, Germany
Phone: +49 (0)1737870838 e-mail: yunirgataullin@yahoo.com

Abstract

World astronautics has made more than 4000 space launches for the last 45 years, and has generated approximately 13 000 trackable objects in near-Earth space orbits. Only some six to seven hundreds of these are operational spacecrafts; the remainder constitute is space debris, and many are traveling fast enough to seriously damage or destroy anything they hit. The space debris problem is significant and has to be solved. There are also approximately 150 000 small objects, which are not trackable easily.

Solution for this problem can be an observation of space debris directly from the orbit, using space-based radar. Small debris objects are typically defined as objects smaller than 10 cm in size. Such objects are not capable of being tracked from Earth, and therefore represent a considerable danger for the space operations.

In this work, preliminary system design of a spacecraft is carried out. The spacecraft can be based on its own platform or exiting platforms can also be made suitable. The following subsystems are included into the system, besides payload: mechanical structure, thermal subsystem, communication subsystem, altitude and dynamic control subsystem, propulsion subsystem, energy subsystem, scientific instrument subsystem. And, *active radar subsystem* as a payload.

Above represented method is the possibility to track approximately 10 to 25% of existing small debris population on LEO.

SESSION 4

MISSION CONSEPTS AND STUDIES

Chairs:
Sushil Atreya, U. Michigan, USA
Gerhard Schwehm, ESA
Tom Spilker, JPL, USA

Europe's concept and plans for a Venus Entry Probe Mission

E. Chassefière[1] & the VEP team

[1]Service d'Aéronomie, Pôle Système Solaire (IPSL), CNRS & Université Pierre et Marie Curie, 4 place Jussieu 75252 Paris Cedex 05, France

In May 2006 the European Space Agency's Science Programme plans to issue a Call for Ideas in the context of the Cosmic Vision (CV15-25) 2015-2025 (ESA publications BR-247). The CV15-25 programme is centred on four scientific questions: (i) What are the conditions for planet formation and the emergence of life? (ii) how does the Solar System work? (iii) What are the fundamental physical laws of the Universe? (iv) How did the Universe originate and what is it made of? In preparation for reacting to this Call for Ideas, we have organized the first international Venus Entry Probe Workshop (VEPW) on January 19-20 2006, at ESA/ESTEC. We feel that the further exploration of planet Venus, in the follow-up of Venus Express, now in orbit around Venus, and the japanese VCO orbiter, can address parts of the first two of the CV15-25 questions, in particular the following crucial questions :

- How can the detailed knowledge of the atmosphere of Venus, compared to that of the two other terrestrial planets, help in understanding observations of Earth-like extra-solar planet atmospheres and searching for habitability, and possibly life, signatures?
- Did Venus, which is the most Earth-like planet of the Solar System, offer suitable atmospheric and geological conditions for life to emerge at some time in the past ? Why did it evolve differently from Earth, and will Earth evolve toward a Venus-like state in the future?
- How does the Sun interact, through its radiation and particle emissions, with Venus' atmosphere, and what has been the influence of the Sun and of its evolution on the climate history of Venus?

The main measurement objectives of the proposed mission are :

- The *isotopic composition*, especially that of noble gases, which provides information on the origin and evolution of Venus and its atmosphere.
- The *chemical composition below the clouds and all the way down to the surface* with more detail than is possible using remote sensing, in order to fully characterize the chemical cycles involving clouds, surface and atmospheric gases.
- The *surface composition and mineralogy* at several locations representing the main types of Venus landforms and elevations.
- A *search for seismic activity and seismology on the surface*, and measurements at multiple locations to sound the interiors.
- *In situ* investigation of the *atmospheric dynamics*, for instance by tracking the drift of floating balloons.
- The *composition and microphysics of the cloud layer* at different altitudes and locations, by direct sampling.
- *Solar wind-atmosphere interaction processes and resulting escape* as a function of solar activity.
- *In situ* determination of the *surface heat flow* of different landforms and structure-elements.
- The *electromagnetic activity* monitoring and mapping of the planet.

The mission scenario is not completely defined at the present time. The mission will consist of a set of entry probes (descent probes and balloons) and an orbiter. An atmospheric sample return is also considered as an option.

Dual Balloon Concept For Lifting Payloads From The Surface Of Venus

Viktor.V. Kerzhanovich, Andre.H.Yavrouian, Jeffery.L.Hall and James.A.Cutts
Jet Propulsion Laboratory, 4800 Oak Grove Dr., Pasadena, CA., 91109

Two high-rated Venus mission concepts proposed in the National Science Foundation Decadal Survey require a balloon to lift payloads from Venusian surface to high altitudes: Venus Surface Sample Return (VESSR) and Venus In-Situ Explorer (VISE). In case of VESSR the payload is a canister with the surface sample plus a Venus ascent vehicle (VAV), which is a rocket that takes the sample into orbit for rendezvous with an Earth return vehicle. VISE is envisioned as a more limited precursor mission where the surface sample is only taken to high altitudes so that non time-critical analyses can be performed. From the balloon point of view, the only difference between these two missions is that the VESSR payload to be lifted is very much larger than VISE because of the inclusion of the VAV.

A key problem is that at the time the decadal survey was published, no high temperature balloon technology existed to implement either mission. Prior technology development efforts had concentrated on a single balloon that could operate across the entire 0-60 km altitude range, tolerating both the sulfuric acid aerosols and the extreme temperatures of -10 to +460 ºC. However, this problem was unsolved because no combination of sufficiently lightweight balloon material and manufacturing (seaming) technology was ever found to tolerate the high temperatures at the surface. The authors describe a solution to the problem based on the idea of using a two-balloon approach. One balloon is optimized for high temperature service in the lower atmosphere, while the second is optimized for high altitude performance. Both balloons can be made from available materials with known fabrication technology. The near-surface balloon will be a metal bellows made of stainless steel or other suitable alloy. The relatively high mass of metal material is allowable in this architecture because only small balloons are needed to lift significant payloads in the dense lower atmosphere of Venus. The second, high-altitude balloon will be made of a more conventional Teflon-coated Kapton film. This much lighter material enables the large balloon volumes needed for expansion in the low density upper atmosphere while the Teflon coating simultaneously provides sulfuric acid protection throughout the ascent.

In operation, the metal bellows balloon will be inflated with either helium or hydrogen gas during the initial descent and landing of the overall vehicle. During the descent and the short stay on the surface, the second, high altitude balloon remains in a thermally insulated container along with the vehicle avionics and other sensitive components. Once the sample has been collected, the payload and the two balloons will be released from the lander and begin to ascend. At a crossover altitude of approximately 12 km, the temperature will be low enough (~370 C) to deploy the high-altitude balloon from its insulated container. The valve that connects the two balloons will then be opened to allow the buoyancy gas from the metal bellows balloon to transfer to the high altitude balloon. The metal bellows balloon will be released once this gas transfer is complete, and the remaining vehicle will ascend to its floating altitude of approximately 60 km while the bellow will float at much lower altitude.

Detailed calculations have been performed to design the two balloon vehicle and quantify its performance during all phases of the mission. The paper includes key results from these trade studies for balloon sizing and mass, crossover altitude, and payload temperature.

EXOMARS Mission and Spacecraft Architecture

V. Giorgio[1] A. Gily[2], C.Cassi[3], G.Gianfiglio[4]

[1] [2] [3] Alcatel Alenia Space- Italia –Turin Plant Strada antica di Collegno 253 – 10146 Torino – Italy
[1]Tel. +39-011-7180 777; Fax: +39-011-7180 312; e-mail vincenzo.giorgio@alcatelaleniaspace.com
[2]Tel. +39-011-7180 933; Fax: +39-011-7180 319; e-mail alessandro.gily@alcatelaleniaspace.com
[3]Tel. +39-011-7180 623; Fax: +39-011-7180 998; e-mail carlo.cassi@alcatelaleniaspace.com
[4]ESA / ESTEC, Keplerlaan 1, NL-2201 AZ Noordwijk - The Netherlands
Tel. +31-565-4744; Fax: +31-565-8103; e-mail giacinto.gianfiglio@esa.int

MISSION DESCRIPTION

The ExoMars Mission is the first **ESA** led robotic mission of the Aurora Programme approved by the ESA Council at ministerial level on 6 December 2005 and combines technology development with investigations of major scientific interest. Italy is by far the major contributor to the mission through the strong support of the Italian Space Agency **ASI**.
ExoMars will search for traces of past and present life, characterise the Mars geochemistry and water distribution, improve the knowledge of the Martian environment and geophysics, and identify possible surface hazards for future human exploration missions.
ExoMars will also validate the technology for safe Entry, Descent and Landing (EDL) of a large size spacecraft on Mars, the surface mobility and the access to subsurface.
The ExoMars project is presently undergoing its B1 phase with **Alcatel Alenia Space-Italy** as Industrial Prime Contractor.

Launch and Transfer To Mars

The current mission baseline foresees the launch of a Carrier spacecraft and a Descent Module (DM) by means of a Soyuz 2b launcher lifting from Kourou.
An alternative launch date has been defined, with departure between mid-May and mid-June 2013, for which the mission and system design shall be compatible. The arrival in this case is in March 2015 and a DSM is also required.

Entry Descent and Landing

The Descent Module will separate from the Carrier with a relative velocity of 1 m/s and start the so called Entry, Descent and Landing phase.
No Mars Avoidance Manoeuvre for the Carrier is foreseen, due to the need to save propellant; this is pending confirmation that the Planetary Protection measures taken on the Carrier are sufficient to avoid Mars surface biological contamination.

Mars Operations

After landing on the Mars surface the ExoMars Descent Module will deploy two science elements on the Martian surface: a high-mobility Rover and a fixed station — the Geophysics/Environment Package (GEP).
The ExoMars Rover will carry a comprehensive suite of analytical instruments dedicated to exobiology and geological research: the Pasteur Payload. Over its planned 6-months lifetime, the Rover will ensure a regional mobility (several kilometres) searching for traces of past and present life. It will do this by collecting and analysing samples from surface and from underground, down to a depth of 2 meters by means of a Driller and a Sample Preparation and Distribution System.

The challenges of the mission

The Exomars mission presents a number of unique technological and programmatic challenges to the European space community; the following mission objectives represent new achievements for Europe:

- landing of a large spacecraft on Mars
- development of a Mars rover
- drilling of soil samples from under the Martian surface (this has never been achieved so far), and analysis of the samples for identification of possible traces of life
- achievement of a very high degree of sterilisation of the complete landing spacecraft, this again was never achieved by any mission in the past. The complete sterilisation is necessary in order to avoid the contamination of the Martian samples by terrestrial micro-organisms.

GUIDED MARS BALLOON PLATFORMS

Alexey A. Pankine, Kim M. Aaron, Nathan C. Barnes, Kerry T. Nock
Global Aerospace Corporation, Altadena, CA, 91001, global@gaerospace.com

ABSTRACT

We outline a new Mars exploration concept for guided balloons that integrates balloon flight path guidance and autonomous navigation and control. These balloon platforms could observe Mars in collaboration with orbiters and surface rovers on global scales. We summarize the overall system concept, show how these balloons can be guided, and describe potential science mission scenarios illustrated with an example trajectory simulation using realistic systems and winds. We also discuss some of the system aspects of autonomous balloon platforms for Mars, in particular, entry, deployment and inflation (EDI).

1. INTRODUCTION

Balloons have been long recognized as unique, low-cost scientific platforms due to their relatively low cost and low power consumption. The successful Venera-Vega Project [1] demonstrated technical feasibility of deploying a balloon at another planet and performing scientific observations from it. Numerous concepts and technologies enabling planetary balloon exploration have been developed [2-7] in the last 15 years.

Guided Mars balloons are a new exploration concept that extends these past balloon ideas and augments and enables new measurements not possible from existing types of platforms. For example, orbiters are not *in situ* nor can they achieve the resolution of aerial vehicles. Landers do not move. Rovers, despite their recent unqualified success, have very limited range. Airplanes and gliders can remain aloft for only a few hours or minutes, respectively. Airship propulsion makes them very heavy and difficult to deploy at Mars. Finally, free balloons are totally at the mercy of the Martian winds. This innovative system concept, developed under support from the NASA Institute for Advanced Concepts (NIAC), enables long duration targeted planetary exploration on a global scale with in situ and remote observation capabilities [8].

The guided Mars balloon platform is highly adaptive and capable of observing planetary atmospheres and surfaces over long periods of time without consuming much power. The guided Mars balloon platform "orbits" the planet using the prevailing atmospheric winds as its trajectory is modified according to observational objectives. Studies of atmospheric dynamics, atmospheric chemical, and radiative processes on other planets could become possible at an advanced level. Microprobes would be deployed over the target areas and perform a multitude of tasks at the surface or while descending, such as chemical, biological, meteorological, or thermal analyses, high-resolution imaging, measuring seismic activity, etc.

2. CONCEPT OVERVIEW

At the heart of this revolutionary concept for Mars exploration are long-duration planetary balloons with flight path guidance and control capabilities. A conceptual drawing of the guided Mars balloon platform is shown in Fig. 1. The drawing is for illustration purposes. The tether below the gondola is not to scale: the tether will be several km long. The figure shows a balloon in a shape of a 1:2 ellipsoid with a gondola and a deployed single-wing Balloon Guidance System (BGS) on a long tether below it. The single-wing BGS is a wing and a rudder attached to horizontal boom.

An ellipsoidal rather than a spherical balloon is employed for this example to improve performance of the BGS by reducing the aerodynamic drag on the balloon. We envision superpressure balloons that do not require carrying and dropping ballast to keep the balloon aloft. The ellipsoidal balloon in Fig. 1 reduces drag force by factor of two lower than for a spherical balloon of the same volume, and for an area and mass penalties of only about 10%.

The gondola, below the balloon houses scientific instruments, power, communication devices, etc. Below the gondola is the microprobe magazine that could hold a few to tens of miniature payloads. For this example system concept only 5 microprobes are shown.

The Balloon Guidance System (or BGS) is attached to the gondola via very strong, very long (3-8 km) tether. The BGS requires very little power (about 1 W on average) to operate, when it is not being reeled up to avoid terrain obstacles, and it can be made very light. This Mars BGS is expected to incorporate low-Reynolds number airfoil designs. The science payload could be split between the gondola and the BGS, e.g. the BGS in Fig. 1 illustrates cameras attached to it just below the large wing structure.

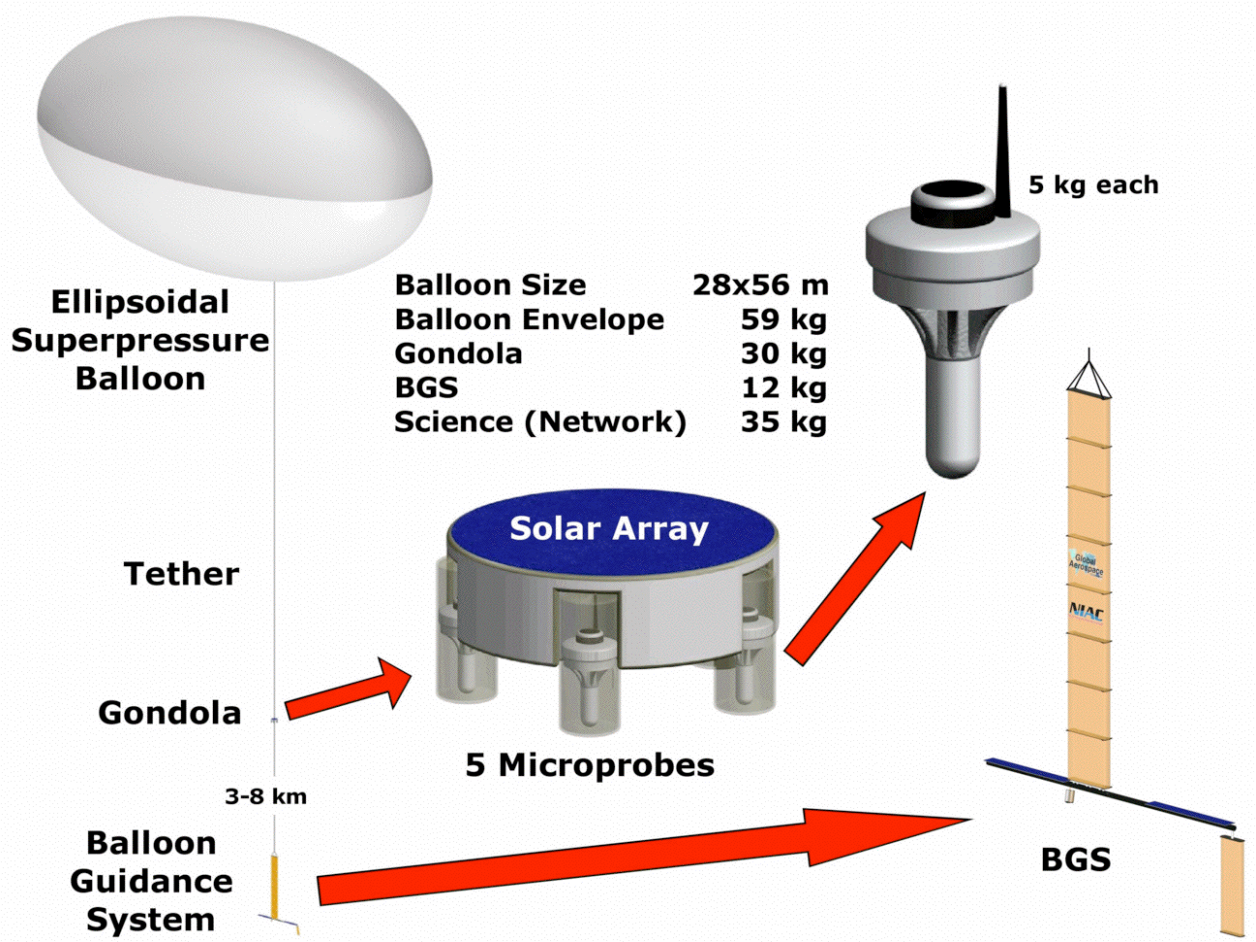

Fig. 1. Example guided Mars balloon system concept

3. BALLOON GUIDANCE SYSTEM (BGS)

In the past, the inability to control the path of Mars balloons has limited their usefulness, and therefore scientific interest in their use. Without flight path guidance technology, a Mars balloon has a high probability of impacting high topography and it cannot be commanded to observe a particular region of interest. The BGS vastly expands the capabilities of balloons for Mars exploration by providing the means to control their paths in the Martian atmosphere. In addition, a BGS reduces the risk of mission failure by avoiding regions with high topography.

A BGS exploits the natural wind field variation with altitude, generally observed on planets with atmospheres, to generate passive lateral control forces on a balloon using a tether-deployed aerodynamic surface below the balloon. A lifting device, such as a wing on end, is suspended on a tether well beneath the balloon to take advantage of this variation in wind velocity with altitude. The wing generates a horizontal lift force that can be directed over a wide range of angles. This force, transmitted to the balloon by a tether, alters the balloon's path providing a bias velocity of a few meters per second to the balloon drift rate. A BGS enables a balloon to fly over surface targets for high-resolution reconnaissance or for deployment of microprobes, to steer around mountains to avoid collisions, to sample the atmosphere to map the abundance of trace gases that could lead to locating possible surface sources of these gases, and to explore a planet on regional and global scales. No longer are planetary balloons totally at the mercy of the winds.

Features of a BGS include the ability to:

- Passively exploit natural wind conditions
- Operate day and night
- Control balloon direction of balloon flight path in various wind conditions
- Be made of lightweight materials and inflatable structures
- Operate with very little power and without consumables

The difference in winds at different altitudes in the atmosphere creates a relative wind at the altitude of the wing (stronger winds are usually found at higher altitudes on Mars). An example of a wind profile at Mars is shown on Fig. 2 (from Mars-GRAM 2001 [9]). The BGS wing in the relative wind generates a lifting force that is directed sideways. The lifting force depends on the size of the wing, its aerodynamic properties, density of the atmosphere and strength of the relative wind.

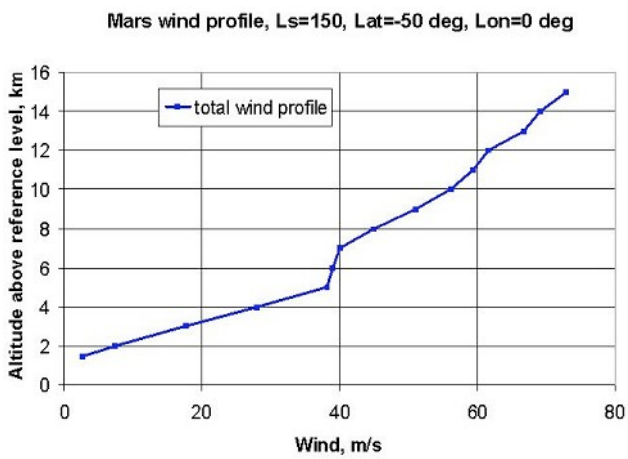

Fig. 2. Mars atmospheric wind profile.

The horizontal component of the total force produced by the wing can be used to change the path of a balloon in the winds. For this example wind profile the wind at 10 km altitude, where the balloon would be floating, is about 56 m/s while the wind at 3 km, where the BGS would be situated, is about 18 m/s. The resultant relative wind is therefore 38 m/s. This level of relative wind could apply a cross-wind delta-V to the balloon of the order of 4 m/s for an 8 m^2 wing operating with a lift coefficient of 0.8.

The aerodynamic surface of a Mars BGS will be operating at low Reynolds numbers (~1000). For these low Reynolds numbers, drag coefficients are significantly higher and maximum lift coefficients are a little lower than for airfoils at higher Reynolds number operation. The reduced Lift-to-Drag ratio is quite a challenge for systems, which must generate their lift aerodynamically while providing power to overcome the drag. However, for the BGS, the weight is supported by buoyancy. The "lift" from the wing is directed close to horizontal and predominantly across the flight path of the balloon. The drag acts mostly to slow the balloon down, and is relatively unimportant to the operation of the system.

The performance of the generic BGS technology has been demonstrated in scale model tests at Earth where the stability, dynamics and aerodynamic performance has been verified for Earth-based systems [10].

4. EXPLORATION CAPABILITIES

At Mars, guided balloons could float close to the surface (6-12 km, depending on location and season) and could provide a wealth of new and unique observations. Some observations, such as the magnetic anomalies on Mars, are, quite possibly, only feasible from a suborbital platform. They could provide spatial coverage comparable to that of satellites, but they additionally enable opportunities for *in situ* atmospheric and surface analysis with deployable science packages and high-resolution surface imaging.

The extended range and long flight duration (~700 days) of guided Mars balloons could provide opportunities for highly adaptive observations during science missions. Just like rovers, if an interesting target is found, a balloon can be commanded to reposition itself to observe it. In this case, the range is the entire planet, not the immediate vicinity of a landing site. A platform can deploy small rovers, miniature geo-chemical laboratories, or it can distribute small surface and atmospheric sampling probes over Mars at particular sites of interest.

Small thermal-emission spectrometers and high-resolution cameras onboard these platforms could image the surface and map mineralogical abundances at the spatial scales of centimeters on the global scale. Magnetic field measurements from altitudes of just 3 to 12 km will provide an unprecedented opportunity to study Martian geology and geophysics, and evolution of the planet. With these platforms, we can visit Polar Regions to closely observe sublimation of polar caps during the spring and the genesis of local dust storms, and then migrate towards tropical regions to observe the formation of dust devils or trace the plumes of atmospheric water vapor. We could release ice penetrators over the polar cap to study the layering in the ice sheets, miniature weather and seismological stations, small rovers and crawlers while flying over highlands and lowlands, and subsurface penetrators over the areas where shallow subsurface ice could be present.

A guided Mars balloon can participate in the reconnaissance of the landing sites rich in usable resources (such as water ice) for robotic or human base. Small navigational beacons and atmospheric sensors could be deployed over potential landing sites to mark and monitor landing zones for incoming piloted spaceships.

Potential science mission applications, described below, include search for the origin of atmospheric methane,

crustal magnetic anomalies mapping, precise emplacement of surface networks, polar night studies, and efficient sample return assist.

4.1 Mission to Search for Origin of Methane

One objective of a guided balloon mission could be to determine the nature of the source of the methane in the atmosphere of Mars [11] – is the source biologic or not? – and to locate the source of methane emission. To distinguish between biologically and abiologically produced methane, instruments onboard of the platform would measure isotopic fractionation of the methane isotopes in the atmosphere of Mars using a Tunable Laser Spectrometer (TLS). The measurement would look at the isotopic ratio of carbon in the methane (C^{12}/C^{13}) and isotopic ratios in other trace gases (water vapor and others).. This measurement can provide clues to the presence of life at Mars. Methane-making organisms discriminate between isotopes as they feed on a global reservoir of CO_2. These organisms are consuming the lighter isotope of CO_2, $C^{12}O_2$, while the heavier isotope, $C^{13}O_2$, is avoided. If the ratio of C^{12}/C^{13} in methane were different from that in CO_2, it would offer strong evidence for a biological source.

The TLS instruments could be housed in the gondola of the platform. Several instruments may be needed as isotopes of the other atmospheric constituents may need to be measured. Guided balloon platforms could also carry a magnetometer for simultaneous measurements of the magnetic field anomalies. Crustal magnetic anomalies at Mars may be indicative of preservation of subsurface structures that harbor methane-producing biota or outgas methane into the atmosphere.

The platform could float over the southern highlands performing isotopic and magnetic field measurements. The preferred seasons for the observations is late southern spring (Ls=200º-250º) or late southern summer (Ls=330º-360º), to avoid the season of major dust storms. The platform could circumnavigate Mars several times at different latitudes, mapping isotopic ratios and methane concentrations. This would enable establishing gradients of methane concentrations in the atmosphere and to locate the source of methane on the surface.

4.2 Mission to Characterize Crustal Magnetic Anomalies

Mars Global Surveyor (MGS) discovered strong magnetic anomalies in the Southern Hemisphere during its aerobraking phase [12]. However, crustal magnetic field anomalies measurements from orbital altitudes lack resolution needed to resolve the question of origin of the anomalies. In addition, weak crustal magnetic field anomalies are obscured by the solar wind.

The plot in Fig. 3 shows Southern Hemisphere map of the crustal magnetic anomalies from MGS. There are no anomalies in the Northern Hemisphere, which may have implications for the origin of the anomalies. To study the anomalies high resolution and higher sensitivity observations are needed.

A mission objective for characterizing these magnetic anomalies could be to study the history of the Mars internal magnetic field and the crustal accretion process, and the detection of subsurface water reservoirs. One or two vector magnetometers and attitude sensors could be positioned at the gondola and/or along the tether. Simultaneous high-resolution visible and infrared imaging of the surface could be performed to link the measurements of the magnetic field and subsurface water to topographic features.

The balloon platform could complete several "orbits" over southern highlands, producing multiple traverses of the anomalies. As a result, the measurements would enable characterization of the spatial frequency of the magnetic anomaly pattern, the depth, thickness and lateral extent of the sources. The relations of the magnetic features to topography would be established and the subsurface water reservoirs will be mapped.

Guided balloon platform equipped with an array of magnetometers can enable high resolution observations by being much closer to the surface and can have higher sensitivity than orbital measurements by using magnetic filed gradient measurements.

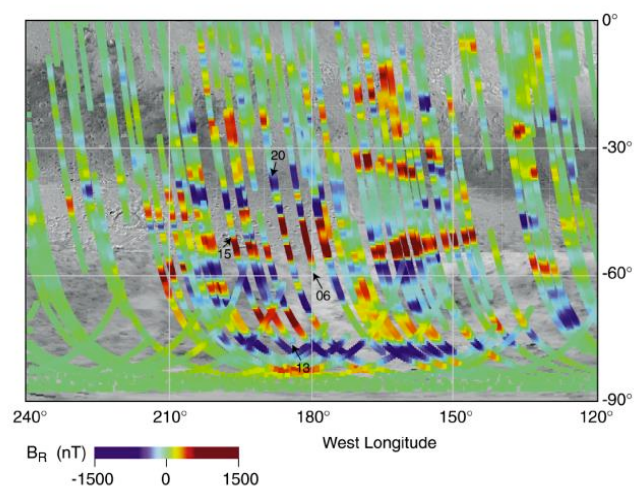

Fig. 3. Map of crustal magnetic anomalies on Mars (NASA GSFC)

4.3 Mission to Emplace a Surface Network

Guided balloons could carry many lightweight microprobes that would be dropped to the surface over

target areas. Unlike microprobes entering the atmosphere from space, these would not require an atmospheric entry heat shield for each probe. Emplacement from a guided balloon avoids several constraints on landing site latitude inherent to deployment of lander from direct entry. Also there are fewer limitations on elevation of landing site since one does not need thick atmosphere above the site for deceleration of a probe. Guided balloon microprobes can be targeted much more precisely than when deployed from orbit since entry uncertainties are no longer in play. Finally, the microprobes could be placed in different Martian regions; polar, floor of large depression (Hellas basin), "narrow" canyon (Valles Marineris), highlands, lowlands; in order to give a full global picture of the atmospheric changes, or to enable seismological sounding of the planets interior from a global network.

One objective of the Surface Network Emplacement mission could be the establishment a network of 4 combined seismological and meteorological stations (a SeisMet Network) on the surface of Mars. A guided balloon could carry up to 5 microprobes that could weigh 5 kg each and be capable of operating for 1 year on the surface. Mars microprobes, including a meteorological and seismometer mini-lab, would rely on Deep Space 2 (DS-2) [13] and NetLander [14] technology heritage. Surface penetration speeds could be as low as 40-60 m/s (1 m^2 decelerator, 5 kg probe from 10 km). Each microprobe could carry a seismometer, a simple soil analyzer and meteorological sensors (pressure, temperature, humidity and winds). A mission profile could consist of the balloon flying to pre-selected sites and deploying the microprobes and then continuing with an imaging mission afterwards. Preferred positions for the surface stations are at the nodes of a tetrahedron. This mission would produce a map of the internal structure of Mars and validate atmospheric circulation models.

Fig. 4 displays one 60-sol simulation of a guided balloon deploying a SeisMet Network. The trajectory is plotted over a filled contour plot of surface topography. The contours are plotted with 1 km interval. The color scale of the height contours is shown on the legend in the figure. The simulated trajectory is shown by the black curve, sites of the surface stations are shown by red triangles and a square. The highest locations on the map are the Tharsis rise and Olympus Mons (latitudes from –30° to 20°, longitudes from –140°E to -90°E). The lowest location on the map is the Hellas Basin (centered on -40° latitude and 70°E longitude).

The simulation starts on July 13, 2013 at the latitude of 50º and longitude of 55º. The date corresponds to the arrival date for the lowest energy Earth-Mars Type I trajectory of the 2013 opportunity. The season is almost equinox (Ls=356º). The geographic location for the start of the trajectory is consistent with potential entry location for the 2013 opportunity. Wind data for the simulation is supplied by Mars-GRAM 2001[9].

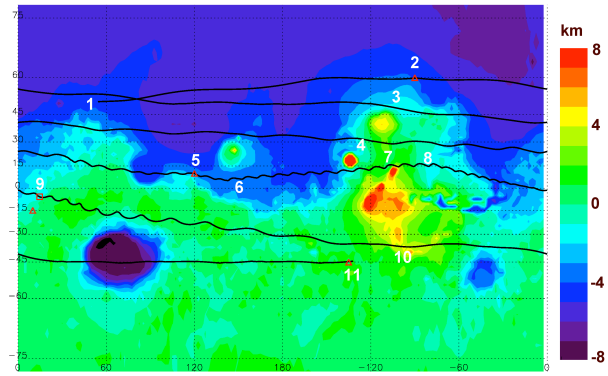

Fig. 4. Simulated guided balloon trajectory.

As discussed earlier, these microprobes can be deployed with great targeting precision, an important goal for future small landers. Fig. 5 shows a map of a portion of the Martian canyon with a narrow band of the olivine outcrop on the bottom (shown in purple). The yellow ellipse shows the landing error ellipse for a direct-entry probe landing from approach to the planet (the ellipse's dimensions are approximately 120 by 20 km, typical of the failed DS-2 probe landing accuracy). This example shows that interesting geology on Mars, with spatial dimensions on the order of a kilometer, would be very hard to target with conventional, direct-entry probes. Guided balloons, on the other hand, can target geologic features with deployable science packages with greater precision.

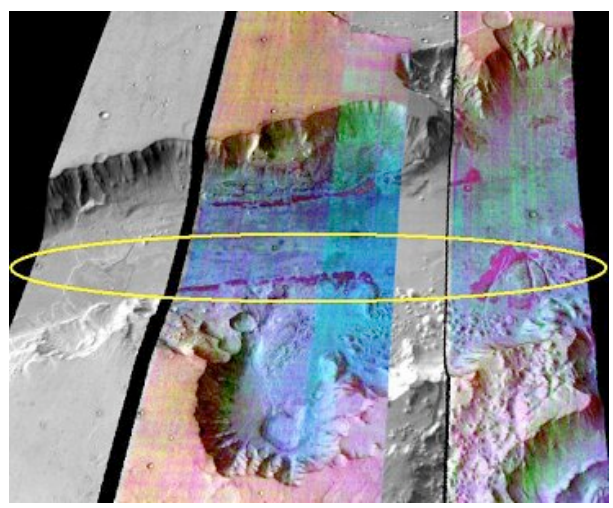

Fig. 5. Olivine outcrop and landing ellipse for existing space probes, like DS-2 (NASA/JPL/ASU)

4.4 Mission to Explore the Polar Night

An objective of a mission to explore the polar night could be to study polar winter processes – such as CO_2 accumulation, formation of clouds, etc. A guided balloon platform could carry a thermal spectrometer to measure atmospheric and surface temperatures and deployable microprobes to sample and analyze the underlying terrain. These balloons, flying in the dark for days on end, would need to rely on non-solar photovoltaic power sources, which may need to include radioisotope or wind power approaches. A mission of this type could produced observations to validate CO_2 cycle models and provide insights into formation of the polar terrains.

4.5 Mission to Support Mars Sample Return

Guided balloons could provide logistical support to Mars Sample Return missions. One objective of such a support mission could be to perform site surveillance to assist orbiters in site selection. Another, more direct, objective could be to enable sample return from multiple sites on a single return vehicle. This objective would utilize the cooperative capabilities offered by the guided balloons and sample acquisition rovers. In this mission profile, illustrated by Fig. 6, multiple rovers could collect samples at different sites across Mars. The rovers are able to search local terrain and to select samples for return to Earth. The samples are packaged into a container and transferred to a guided balloon that could overfly the sample collection sites. The actual transfer mechanism may involve a long, lightweight tether that is being snatched from the air by the guided balloon's BGS, as illustrated in Fig. 6, or many other approaches. After sample collection by the guided balloon, it overflies the site of the sample return vehicle and drops the sample canister for collection by a rover. The rover then transfers the canister to the Sample Return Vehicle that will take the samples to Earth. The sequence repeats until several samples from different sites on the planet are placed onto the sample return vehicle. The sample return vehicle then takes off and returns the samples to Earth. This mission would enable return of samples from several distinct sites on a single return vehicle, maximizing mission scientific return. In this way several samples from widely separated sites on Mars can be delivered to Earth on a single return vehicle.

5. GUIDED BALLOON PLATFORM SYSTEMS

Here we discuss one example platform design based on near-term technology (i.e. 3-10 year technology horizon) and the mission scenario to emplace a surface network. A Mars guided balloon platform consists of a superpressure balloon envelope; a gondola; a BGS; science instrumentation; and entry, descent and inflation (EDI) hardware. Since we have already discussed the BGS, a key element to the capability, we will focus this discussion on the balloon, gondola, EDI, and the overall flight system.

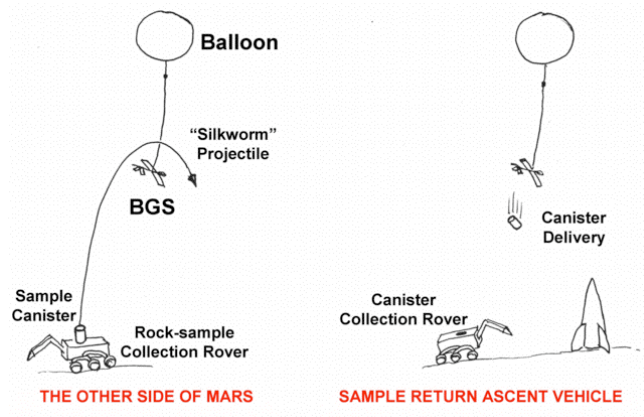

Fig. 6. Mars Sample Return Mission support

5.1 Balloon System

The balloon system is made up of the envelope and top and bottom fittings. One promising option for balloon envelope material is a composite material consisting of 1-micron Mylar, a 38-Denier PBO thread and a 3-micron PE film. The surface density of this material is estimated at 0.012 kg/m^2. A similar, but thicker, material was proposed in a previous Mars balloon study [5]. The need for a composite material arises from the fact that it is impossible to find all the needed mechanical properties in a single material. Hence, in this proposed composite material Mylar provides substrate stiffness, Polyethylene provides fracture toughness and pinhole resistance, while the scrim provides high-strength at low surface mass.

The shape of the envelope could be spherical, or ellipsoidal. The shape of the balloon has implications on material strength requirements, since it is super-pressurized, and on the aerodynamic drag it creates as it is pulled around in the air by the BGS. One attractive shape is ellipsoidal with the long axis in the direction of the balloon's relative wind in order to minimize aerodynamic drag.

5.2 Gondola

A gondola is suspended below the balloon and contains science instrumentation, communications gear, power subsystems (solar array and batteries), thermal protection equipment, attitude knowledge sensors, the BGS winch hardware, central computer control, and mechanical structure and mechanisms. Fig. 1 displays an example computer drawing of the gondola for a network emplacement mission.

5.3 Entry, Deployment and Inflation

Entry, deployment and inflation (EDI) is the sequence of events by which the entry probe decelerates in the atmosphere and the balloon system is deployed and inflated. Fig. 7 illustrates one concept for a sequence of events that take place during EDI.

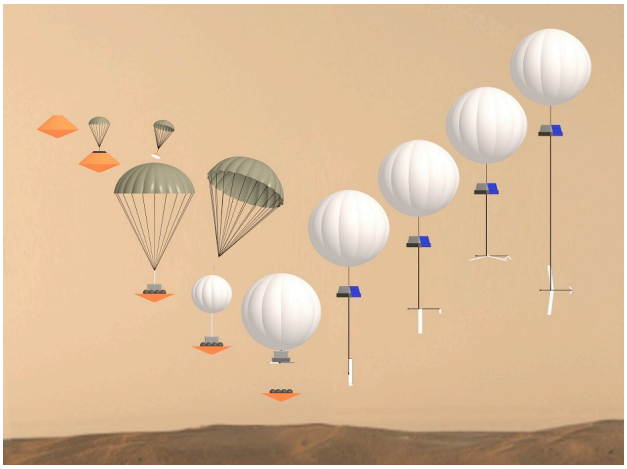

Fig. 7. An example EDI sequence

Fig. 8 shows one example for the packaging of the entry vehicle. The aft (top) part of the entry vehicle is occupied by the parachutes and a canister the houses the balloon envelope. The gondola is shown below the balloon envelope canister and above a folded BGS wing (inflated, rigidized versions are also possible). In this version, the wing separates from the gondola and unfolds, while being lowered on a winch upon ascent to the floating altitude during the EDI.

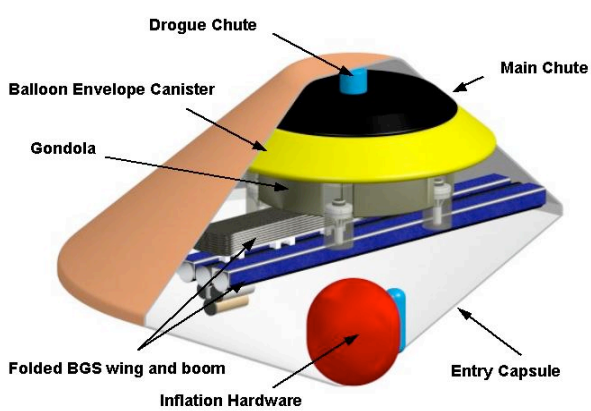

Fig. 8. Guided Mars balloon entry probe

Below the folded BGS is a cryogenic, hydrogen balloon inflation subsystem. The gondola houses the circular solar panel at the top, five deployable surface stations positioned on the circumference of the gondola, the winch and stored tether of the BGS. The folded envelope and supporting structure of the inflatable BGS wing and the folded boom of the BGS are attached to the bottom of the gondola.

The entry and descent phases (see Fig. 7) would be very similar to previous Mars lander missions. A blunt conical heat shield reduces the enormous interplanetary velocity and absorbs the heat generated by passing through the atmosphere. The aft cover is released and a supersonic parachute is deployed at a Mach number of ~2. This slows the descent rate significantly into the low subsonic range to the point the internal components no longer need protection from the ram air and the heat shield can be dropped. As the system approaches terminal velocity on the parachute, the inflation phase commences. The gondola and attached equipment are lowered, and the weight is used to stretch out the balloon envelope vertically. A load member inside the balloon could absorb the shock generated during deployment as the envelope goes taut. The inflation equipment is mounted below the balloon, and will be jettisoned when the inflation of the balloon is complete. An inflation tube is used to carry the gas up to the initial inflation bubble towards the upper end of the balloon and could also support the deployment shock. Once the balloon has reached a size comparable to the parachute, the parachute will be cut away. Upon completion of inflation, the inflation hardware will be released, and the system will ascend towards an equilibrium float altitude, at which point the BGS can be deployed. Mars balloon EDI technology is currently being studied by NASA.

The cryogenic inflation hardware (the tanks holding the buoyant gas, valves and pipes) can have a substantial mass. For this reason, we assumed the use of hydrogen instead of helium as a buoyant gas and stored in a cryogenically cooled container. Warming up cold hydrogen for inflation requires additional equipment, however the estimated savings in mass are still substantial – we estimate the mass of cryogenic inflation hardware for 8.3 kg of hydrogen at about 16 kg. Table 1 summarizes the entry vehicle mass breakdown.

Table 1. Entry vehicle mass summary

Component	Mass, kg
Main parachute	25
Heat shield	62
Back shell	67
Inflation hardware	16
Balloon flight system	140
Contingency (9%)	30
Total	**340**

5.4 Flight System Summary

The flight system mass was estimated including appropriate contingency for so early in the development process. Table 2 summarizes the mass and power budget for this example flight system design.

Table 2. Flight system mass budget

BGS & Balloon		***71***
BGS and Winch	12	
Buoyant Gas	9	
Envelope	50	
Gondola		***30***
Structure	15	
Communications	5	
Power	5	
Thermal	5	
Science Payload		***35***
Microprobes (5)	25	
Camera Systems	9	
Magnetometer	1	
TOTAL		**136**
Allowable Mass		**140**

6. SUMMARY

A concept for planetary exploration is described in the context of Mars exploration. The key elements of the concept are: long-duration-flight autonomous balloons, balloon flight path guidance, lightweight power generation and storage, and multiple, deployable microprobes for atmosphere and surface exploration. A relatively small and light balloon guidance system would enable repositioning the platform on a global scale for *in situ* analysis and targeted deployment of atmospheric and surface microprobes. Deployment of microprobes from balloons eliminates atmospheric entry and deceleration hardware thus reducing overall mass and permitting more science payload or more microprobes. This concept could enable low-cost, low-energy, long-term global exploration of the atmosphere and surface of Mars and other planets.

7. REFERENCES

1. Sagdeev, R. Z. et al., "Overview of the VEGA Venus balloon in situ meteorological measurements", *Science*, Vol. 231, pp. 1411-1422, 1986.
2. Cutts, J. A. et al., "Venus Aerobot Multisonde Mission", *AIAA Balloon Tech. Conference*, pp. 1-10, 1999.
3. Greeley, R. et al., "The Mars Aerial Platform Mission Concept", *AIAA paper 96-0335*, 1996.
4. Jones, J. A. and Heun, M. K., "Montgolfier Balloon Aerobots for Planetary Atmospheres", *AIAA Paper 97-1445*, 1997.
5. Nock, K.T. et al., "Overview of a Mars 2001 Aerobot/Balloon System", *12th AIAA Lighter-Than-Air Technology Conference*, San Francisco, 1997
6. SAIC, "Titan exploration with advanced systems", *NASA CR-173499*, 1983.
7. Tarrieu, C., "Status of the Mars 96 Aerostat Development", *44th Congress of the International Astronautical Federation*, paper IAF-93-Q.3.399, 1993
8. Justus, C. and D. L. Johnson, "Mars Global Reference Atmospheric Model 2001 Version (Mars-GRAM 2001): Users Guide", NASA/TM-2001-210961, April 2001.
9. Pankine, A., K. Aaron, N. Barnes, K. Nock, "Sailing the Planets: Planetary Science from Guided Balloons," 16th ESA Symposium on European Rocket and Balloon Programmes and Related Research, ESA SP-590, Sandefjord, Norway, May-June 2005.
10. Aaron, K., K. Nock, M. Heun, A. Pankine, "A Method for Planetary Balloon Flight Path Guidance", 4th International Planetary Probe Workshop, Pasadena, CA, July 2006.
11. Mumma, M., et al., "Detection and mapping of methane and water on Mars", *Bull. AAS*, Vol. 36, p. 1127, November 2004.
12. Connerney, J. et al., "Magnetic Lineations in the Ancient Crust of Mars", *Science*, Vol. 284, Issue 5415, pp. 794-798, 1999
13. Smrekar, S. et al., "Deep Space 2: The Mars Microprobe Mission", *Journal of Geophysical Research*, v. 104, No. E11, p. 27,013, 1999.
14. Counil, J-L, et al., "NetLander mission to Mars - Payload and scientific objectives", 52nd *IAC*, Toulouse, France; 1-5 Oct. 2001.

Not Afraid to Ride the Wind: Titan by Balloon

Jonathan Lunine, LPL/U.Arizona, USA and INTA-IFSI, Italy

Saturn's moon Titan has a dense atmosphere with hazes of organic molecules that obscure the surface and make mapping from Earth and space difficult. The ongoing NASA/ESA/ASI Cassini mission has revealed Titan to be a complex, perhaps recently active, world, and the most Earthlike of solar system bodies in terms of the balance of geologic and atmospheric processes. Though profoundly cold and hence likely devoid of Earth-like life, Titan is rich in methane, nitrogen, and organic products of these simple compounds. It has winds and rain that have shaped the surface, producing vast areas of dunes and a diversity of fluvial features from drainages extending over tens or hundreds of kilometers to locally cut streambeds that have carried ice pebbles down to the plains where Huygens landed. Features that look like volcanic domes, chains of mountains, mysterious pits, and circular features hint at a complex geologic past, while kidney-shaped lakes and bays—perhaps dry today—stand as mute testament to a past that might have included seas of liquid hydrocarbons.

Titan can be explored in a variety of ways, but future missions that both extend our knowledge of this planet-sized world and capture the imagination of the public could use the dense atmosphere to enable unique means of exploration. The extended nature of the atmosphere allows spacecraft to aerobrake into desired orbits, and provides relatively benign entry conditions compared to the giant planets, and even Earth. Particle radiation is low around Titan and absent in the environment near surface. The air density at lower altitudes is higher than on Earth, the air is cold and mostly stable nitrogen, and the winds relatively light and predictable below 10-20 kilometers. The most economical, elegant, and reliable way to navigate this environment is with a hot air balloon that uses the varying winds at different altitudes to cruise across the landscape and sample interesting regions. Here we describe the Titan Planetary Explorer mission, a hot-air balloon that could cruise with the wind at jetliner altitudes, circumnavigating the globe, while occasionally descending to the surface to sample sites of particular interest from the point of view of organic chemistry and the exotic geology of a giant water-ice world. Slow north-south winds would allow drift from one latitude region to another. Vistas that the mission would relay to Earth, based on the evocative scene imaged by Huygens, could well prove to be among the most hauntingly familiar yet exotically different landscapes viewed by humankind since the first images of our neighboring planets were returned some four decades ago from the Moon and Mars.

SATURN PROBES: Why, Where, How?

Sushil K. Atreya

Department of Atmospheric, Oceanic, and Space Sciences, University of Michigan, Ann Arbor, MI 48109-2143, USA,
Email: atreya@umich.edu Homepage: http://www.umich.edu/~atreya

Proceedings, International Planetary Probe Workshop, IPPW-4, Pasadena, California, June 2006
(Date of Submission: 8 August 2006)

ABSTRACT

While the critical heavy element abundance data for Jupiter will exist following the measurements on deep water (O/H) from Juno in 2016/2017, together with the 1995 Galileo Probe results on other key heavy elements, no such possibility currently exists for Saturn. At the same time, it is essential to have equivalent set of measurements at both gas giant planets, in order to build robust models for the formation of the giant planets, in particular, and the solar system, in general. In an earlier paper, Atreya et al. [1] presented a scenario of *shallow* entry probes combined with microwave radiometry (MWR), as an alternative to deep atmospheric probes for composition measurements at Saturn. This paper builds on, updates, and reinforces the conclusions of that earlier paper [1], especially that a Saturn Probe mission that combines Microwave Radiometry is suitable at Saturn, and that probes deployed to only 10 bars – shallow probes – can provide the needed data [1]. Such a mission is likely to fit within the cost cap of NASA's New Frontiers program. The Saturn Probe with Microwave Radiometry should be considered as the highest priority giant planet mission for the near term. The need for and scenarios of multiprobe missions to the other giant planets, Neptune, Uranus, and Jupiter are also discussed.

1. INTRODUCTION

Comparative planetology of the giant planets is key to the origin and evolution of the solar system and, by extension, extrasolar systems. Although many measurements contribute to the constraints on planetary formation models, "bulk" composition in general, and abundance of the heavy elements (mass > ^{4}He), in particular, is most critical. Its determination is also most challenging technologically. This is because the bulk composition may be found only in the well-mixed part of the atmosphere, which lies in an extreme environment of high pressure and high temperature for the principal reservoirs of certain key elements. Measurements are generally difficult to carry out, and transmission of data poses major obstacles. Just as the Voyager 1 and Voyager 2 flyby observations of Jupiter provided the fuel for *in situ* measurements at this gas giant and led to the Galileo Probe mission, the Voyager flybys and Cassini orbiter observations of Saturn have reinforced the case for return to Saturn with entry probes. In fact, the Cassini-Huygens mission was initially conceived of as a dual probe mission, with one probe into Saturn and another into Titan. However, budgetary constraints resulted in the demise of the Saturn probe. Despite the unprecedented wealth of data collected by the Cassini orbiter about Saturn's upper atmosphere and magnetosphere (p <1 bar), the elemental abundances in the well-mixed atmosphere will continue to remain mysterious (except for C/H) even after the Cassini extended mission. However, it is precisely the heavy element abundance that is critical to acquire for an understanding of the formation of Saturn and its atmosphere. Together with similar data at Jupiter, this information will prove powerful in constraining the models of the formation of the solar system and the origin of planetary atmospheres. Although it is not known where the well-mixed region of Saturn is, pertinent data for Jupiter and their interpretation with formation models can provide a good guide. Therefore we will first review briefly the known composition information for Jupiter and Saturn and then make predictions for Saturn's well-mixed region. This will be followed by a discussion of possible scenario of a probe mission at Saturn.

2. ATMOSPHERIC COMPOSITION

Amongst the outer planets, the atmosphere of Jupiter has been studied extensively due to observations from several flyby spacecrafts, an orbiter, and an entry probe, the Galileo Probe which entered the planet's atmosphere in December 1995. The detailed composition of Jupiter has been presented previously [2, 3, 4, 5, 6]. Here we will focus on the composition as it relates to the heavy elements (mass greater than helium, or m/z > ^{4}He), since the heavy elements provide critical constraints to the planetary formation scenarios. An insight into this

can be gleaned by revisiting briefly the currently accepted model for the formation of the Jupiter (and the other giant planets). According to this model, generally known as the core accretion model, the core of the planet formed first from grains of refractory material, rock, metal and ice, which also trapped gases from the protoplanetary nebula. Once the core grew to a critical mass of 10-15 M_E (earth masses), gravitational collapse of the surrounding remnant protoplanetary nebula occurred, leading to the capture of most volatile of gases, H_2, He, and Ne, on to the planet. The atmosphere was formed from these gases and those released from the core during accretionary heating phase. The heavy elements make up most of the original core, based on the elemental abundance in the Sun. The planetesimals that formed Jupiter must be cold, whether in the form of amorphous icy planetesimals [≤30K; 4, 7] or clathrate-hydrates [≤38K; 8]. For Jupiter, abundances of the heavy elements, except oxygen, became available from the Galileo Probe mass spectrometer in December 2005. The Probe entered a meteorologically anomalous region of Jupiter – the Sahara Desert of Jupiter – where water was found to be depleted but its well-mixed region was not reached [2,3,4,5,6]. The determination of the water abundance, hence O/H, is critical to the formation models, as water was presumably the original carrier of the heavy elements to Jupiter. Thus, it was presumably also the largest contributor (50-70%) to the heavy element (hence, core) mass. Although, the water abundance in the well-mixed atmosphere of Jupiter is not available yet, the abundances of the heavy elements that were measured provide clues to the possible range of the water abundance, based on different models of the formation of Jupiter, as discussed below.

As seen in Table 1a, and graphically in Figure 1, the heavy elements at Jupiter are enriched relative to their solar proportions (to H), but the enrichment factor is non uniform for different species, ranging from a factor of 2 to 6 relative to their solar values. For the sake of convenience, we assume that the elemental enrichment at Jupiter is 4±2× solar (previously, 3±1× solar, based on earlier solar values of Anders and Grevesse). Since water was presumably the original carrier of heavy elements, the cold icy planetesimal hypothesis predicts nearly equal enrichment for all heavy elements, so that water, hence O/H, is predicted to be enriched also by a factor of 4±2× solar. This hypothesis assumes the form of ice to be amorphous [4, 7]. It has been argued that the amorphous ice planetesimals may not survive the formation of the solar nebula, and would be converted to crystalline ice in the process of evaporation and recondensation [8]. Crystalline ice has poor trapping efficiency. An alternative is that the heavy elements were delivered by clathrates hydrates in the cooling, feeding zone of Jupiter [8,9]. Since large quantities of water are required to trap volatiles in the molecular cages of water ice lattice, this model predicts a huge enrichment of water, with O/H ≥ 15× solar [8; adjusted for the new solar elemental abundances]! The Galileo and Cassini imaging observations [10,11] and the Galileo near infrared data [12,2] provide evidence that water is at least solar at Jupiter, but presently we cannot tell what its exact enrichment relative to solar (expressed as O/H) in the well mixed atmosphere is. Water in Jupiter is like dark matter or dark energy in the universe – we know it's there, but don't know how much or where. This is about to change, at least in the case of Jupiter. The microwave radiometry experiment on the 2011 Juno mission is designed to determine the water abundance to pressures greater than one hundred bars.

Unlike Jupiter, information on the heavy elements on Saturn is sparse – limited to just carbon from CH_4 ($CH_4/H_2 = 5.1\pm1.0 \times 10^{-3}$, by CIRS on Cassini [12]) – and it will continue to remain so even after the Cassini extended mission. The currently available elemental and isotope abundances for Saturn is also presented in Tables 1a and 1b. and graphically shown in Figure 1. For the sake of completeness and comparison, we also present the known and "suspected" elemental abundances at Uranus and Neptune. However, the situation at the two ice giant planets is nearly as hopeless as at Saturn. As on Saturn, as the only heavy element whose abundance has been measured is carbon (but with large uncertainty) from ground-based observations of CH_4.

The trend of increasing enrichment factors from Jupiter to Neptune is consistent with the basic principle of the core accretion model. However, the assumption of *equal* enrichment over solar for all heavy elements at Saturn, Uranus and Neptune is biased by the icy planetesimal model. Therefore, one should exercise caution when using the tabulated values where data are presently lacking. Nevertheless, the tabulated values represent our current best guess, which is important for the purpose of mission design studies.

3. WHERE IS THE WELL-MIXED ATMOSPHERE OF SATURN?

The well-mixed region for condensible gases in the atmospheres of the outer planets lies below the bases of their respective cloud layers. Under conditions of thermodynamic equilibrium, this region should exist "just" below such cloud bases. Unlike Earth where a single volatile, water, undergoes condensation, the giant

planets are expected to have multiple cloud layers, composed of different species. Thus, there is no single base of the clouds. Clouds of each condensible species would have their own bases. The deepest clouds in the upper tropospheres of all four giant planets are predicted to be made up of water (see below). Thus the base of water clouds determines not only the level below which water is well-mixed under conditions of equilibrium thermodynamics, it also represents the well-mixed atmosphere for all heavy elements. As mentioned above, the determination of the water abundance in the well-mixed atmosphere is crucial, since water was presumably the original carrier of heavy elements to the giant planets, Since variations in the abundances of condensible volatiles can exist to depths below their equilibrium cloud bases, it is important to make their measurements to depths well below the cloud bases in order to arrive at the elemental abundance. Thus, water, hence the oxygen elemental ratio (i.e. O/H), places the biggest constraint on the depth to which composition measurements must be made by entry probes or other means, since water clouds are the deepest. In the following paragraphs, we first present a brief summary of the cloud models, in order to ascertain the well-mixed atmosphere. Then, a discussion of the required measurement is given, followed by recommendations.

Table 1a. Elemental Abundances [(1)]

Elements	Sun (protosolar)	Jupiter/Sun	Saturn/Sun	Uranus/Sun	Neptune/Sun
He/H	0.09705	0.807±0.02	0.56–0.85 [(2)]	0.92–1.0	0.92–1.0
Ne/H	2.10×10^{-4} [(3)]	0.059±0.004	?	20–30 (?)	30–50 (?)
Ar/H	1.70×10^{-6}	5.34±1.07	?	20–30 (?)	30–50 (?)
Kr/H	2.14×10^{-9}	2.03±0.38	?	20–30 (?)	30–50 (?)
Xe/H	2.10×10^{-10}	2.11±0.40	?	20–30 (?)	30–50 (?)
C/H	2.75×10^{-4}	3.82±0.66	9.3±1.8 (CIRS)	20–30	30–50
N/H	6.76×10^{-5}	4.90±1.87	2.6–5	20–30 (?)	30–50 (?)
O/H	5.13×10^{-4}	0.48±0.17 (hotspot)	?	20–30 (?)	30–50 (?)
S/H	1.55×10^{-5}	2.88±0.69	?	20–30 (?)	30–50 (?)
P/H	2.57×10^{-7}	1.21	5–10	20–30 (?)	30–50 (?)

Table 1b. Relevant Isotopic Abundances

Isotopes	Sun	Jupiter	Saturn	Uranus	Neptune
D/H	$2.1\pm0.5\times10^{-5}$	$2.6\pm0.7\times10^{-5}$	$2.25\pm0.35\times10^{-5}$	$5.5\ (+3.5, -1.5)\times10^{-5}$	$6.5\ (+2.5, -1.5)\times10^{-5}$
$^{3}He/^{4}He$	$1.5\pm0.3\times10^{-4}$	$1.66\pm0.05\times10^{-4}$			
$^{15}N/^{14}N$	$\leq2.8\times10^{-3}$	$2.3\pm0.3\times10^{-3}$			

[(1)] Updated from Atreya and Wong [2], using new protosolar elemental abundances [13].
The protosolar elemental abundances are calculated from the present-day solar photospheric values [13], after adjusting for the effects of diffusion at the bottom of the convective zone on the chemical composition of the photosphere, together with the effects of gravitational settling and radiative accelerations, as discussed in [13]. The new solar values [13] represent an improvement over the previous conventional standard [14]. The new solar values [13] result from the use of 3D hydrodynamic model of the solar atmosphere, non-LTE effects, and improved atomic and molecular data. The Jupiter values are from the Galileo Probe Mass Spectrometer. See Figure 1 and text for explanation of elemental abundances at the other giant planets.
[(2)] The Saturnian helium is based on the reanalysis of the Voyager remote sensing data [16]. The Cassini (CIRS) measurements of He indicate smaller He/H of perhaps as low as 0.4× solar [M. Flasar, personal comm., 2006], shown by the vertical dashed line for Saturnian He in Fig 1. However, in the absence of in situ measurements, uncertainties will remain large.
[(3)] The Ne/H is based on the X-ray spectral measurements of nearby solar-type stars [15], as the abundance of neon in the Sun is poorly determined. The previous protosolar Ne/O = 0.1513 [13] was simply to maintain consistency, i.e. neon was revised downward by the same factor as oxygen in [13]. Adoption of the new Ne/O = 0.41 – which is 2.7 times the value in [13] – also results in an excellent agreement between the solar interior models and helioseismology data [15].

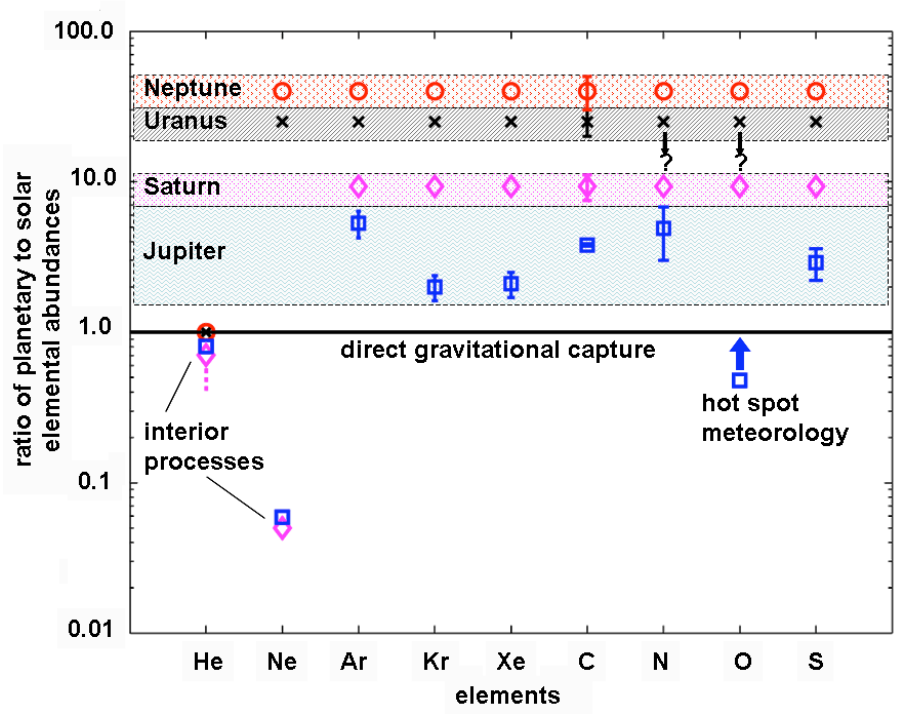

Fig. 1. Elemental abundances (relative to H) in the atmospheres of the giant planets compared to the *proto*solar values (see also Table 1 and its footnotes). The Jupiter results are those measured by the Galileo Probe Mass Spectrometer (GPMS). Solid horizontal line shows that direct gravitational capture would result in elemental abundances (ratioed to H) being the same as in the Sun. However, at Jupiter the heavy elements, Ar, Kr, Xe, C, N, and S are all found to be enriched by a factor of 4±2 (note that the factor in previous publications was 3±1, which was based on the solar elemental abundances of Anders and Grevesse [14]; the factor given here is based on the new solar values of Grevesse et al., [13]. The only heavy element measured at Saturn, Uranus and Neptune is carbon, which is shown with error bars. The other elements shown by the diamonds (Saturn), crosses (Uranus) and circles (Neptune) do not represent data, but are based on the icy planetesimal model predictions that they would be similarly enhanced as carbon (see text). Saturn's $CH_4/H_2 = 5.1\pm1.0 \times 10^{-3}$, based on the Cassini CIRS observations (Flasar, et al., 2005), results in C/H = 9.3±1.8, using the Grevesse et al. [13] *proto*solar C/H. Condensation of helium into droplets in the 3-5 megabar region of Jupiter's interior reduces the He/H ratio to approximately 80% solar in the upper troposphere. Neon is depleted to 6% solar, as neon dissolves into helium droplets. As on Jupiter, helium and neon are expected to be depleted in the upper troposphere of Saturn. He condensation could be greater in Saturn's colder interior, resulting in its greater depletion in the troposphere, as shown by the vertical dashed line for He [see footnote 2 to Table 1]. On the other hand, helium condensation is not expected in the interiors of the ice giants, Uranus and Neptune, due to their smaller masses and evolutionary history. This means that the He/H ratio would be solar or nearly solar in the upper tropospheres of these two planets, as is implied indirectly also by ground-based data on CO and HCN in the atmospheres of these ice giants [2]. The lack of helium droplets also implies that neon will not be removed either in the interiors of Uranus and Neptune, resulting in at least solar Ne/H, or it could also be enriched by similar factors as the other heavy elements, i.e. 20-50 times solar. Thus, the Ne and He measurements at the two ice giant planets are important tracers of interior processes. The presence of a putative water-ammonia ionic ocean at tens to hundreds of kilobar level would severely deplete water and ammonia above such an ocean, resulting in greatly subsolar O/H and N/H in the upper troposphere [2,17,18,19,20].

3.1 Well-mixed atmospheres: Equilibrium cloud condensation model (ECCM)

ECCM's date back to the pre-Voyager epoch. The model was first developed by Weidenschilling and Lewis [21], and has undergone further development, as described in Atreya and Romani [22] and Atreya [23]. The lifting condensation level (LCL), i.e. the base of the cloud, is calculated by comparing the partial pressure (e) and the saturation vapor pressure (e_c) of the condensible volatile. The LCL is reached at the altitude where relative humidity (e/ e_c) of 100% is attained. The amount of condensate in the ECCM is determined by the temperature structure at the LCL and vicinity. The release of latent heat of condensation modifies the lapse rate, hence the temperature structure, of the atmosphere. Thus, the composition and structure of the clouds depend on the composition of the atmosphere, and in particular the distribution of condensible volatiles.

Thermochemical equilibrium considerations suggest that NH_3, H_2S and H_2O are the only species that are likely to condense in the upper tropospheres (to pressures less than a few hundred bars) of Jupiter and Saturn. In the gas phase, H_2S can combine with NH_3 to form NH_4SH, i.e., $NH_3(g) + H_2S(g) \rightarrow NH_4SH$, or ammonium sulfide, $(NH_4)_2S$, which is less likely. NH_4SH would condense as a solid in the environmental conditions of all giant planets. NH_3 could also dissolve in H_2O, resulting in an aqueous solution (droplet) cloud. The extent of such a cloud depends on the mole fractions of NH_3 and H_2O. Additional cloud layers are possible at Uranus and Neptune.

As shown in Table 1, N/H (from NH_3) and S/H (from H_2S) are enriched relative to solar, but O/H (from H_2O) is subsolar even at the deepest level in the region of entry of the Galileo Probe at Jupiter. If the original heavy element carrying water arrived at Jupiter as cold amorphous ice, O/H would be expected to be enriched by a similar factor as the other heavy elements, i.e. 4±2× solar [revised from the earlier values of 3±1× solar, as discussed in the caption to Fig.1]. If the heavy elements were delivered by clathrate hydrates, then the water abundance would be more than 15× solar in Jupiter's well-mixed atmosphere [see Table 1 for current solar elemental abundances]. In either case, condensation of water both as ice and droplets is inevitable in Jupiter's troposphere. The same condensation scenario is expected at Saturn, but at deeper levels due to greater enrichment of the heavy elements compared to Jupiter (based on C/H measured from the Cassini orbiter, Table 1) and twice the scale height compared to Jupiter's. The O/H at Saturn may be smaller if the solar nebula at Saturn's orbit was "ice-starved". However, for the purpose of determining the possible deepest level for well-mixed water at Saturn, we assume that the enrichment factor for O/H is the same as that of C/H. We will present the cases with different enrichment factors at Saturn, comparing them to Jupiter which is our guide.

We present in Figs. 2 and 3 model results on the bases and concentrations of possible condensates of ammonia ice, ammonium hydrosulfide-solid, water ice, and the aqueous-ammonia solution ("droplet") clouds of Jupiter and Saturn. The ECCM calculations for Jupiter shown in Fig. 2 are with the condensible volatiles taken as 1× solar and 3× solar. The base of the water cloud is found to be at approximately 5 bar, 6.5 bar and, 9 bar level (not shown), respectively, for 1× solar, 3× solar and 10× solar enrichment of the condensible volatiles. The ECCM calculations for Saturn are shown with the condensible volatiles taken as 1× solar, 5× solar and 10× solar. The 10× solar or greater enhancement of the heavy elements is the more likely scenario for Saturn, based on the Cassini CIRS determination of CH_4/H_2 = $5.1\pm1.0\times10^{-3}$ [12], which yields C/H = 9.3±1.8× solar (Table 1). The 10× solar case should be regarded as the nominal case for the purpose of mission design. For this case the ECCM calculations yield the base of the water cloud to be at approximately 20 bars. In thermodynamic "equilibrium" the region below 20 bars would then be the well-mixed region for water at Saturn. Since the atmosphere of Saturn is colder than Jupiter's, condensation of the species with equal enrichment factors occurs at much greater pressure levels. For example, with solar O/H, the base of the water cloud on Saturn (~12 bars) is at more than twice the pressure it is at Jupiter.

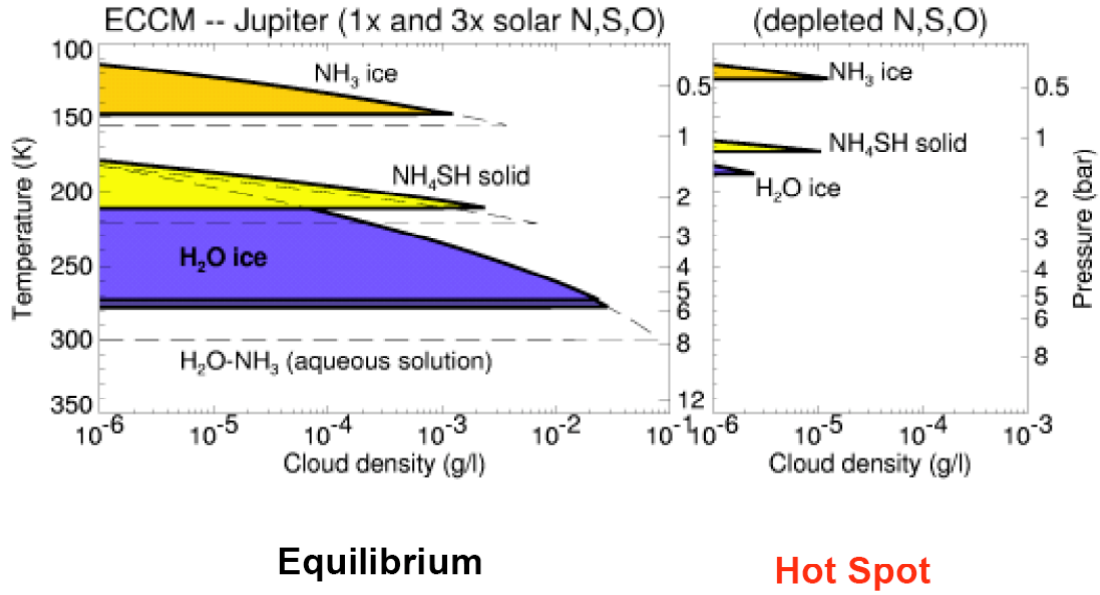

Fig. 2. Results of ECCM calculations for Jupiter, with 1x solar and 3x solar condensible volatile abundances in the left panel, and greatly depleted condensible volatiles in the right panel in order to simulate the LCL of the clouds detected in the Galileo Probe Entry Site (a 5-micron hot spot). Since the Galileo Probe entered a dry region, the condensible volatiles were found to be greatly depleted to levels well below their expected condensation levels. The cloud densities represent upper limits, as cloud microphysical processes (precipitation) would almost certainly reduce the density by factors of 100–1000 or more. However, the LCL's, i.e. cloud bases are expected to remain unaffected [5].

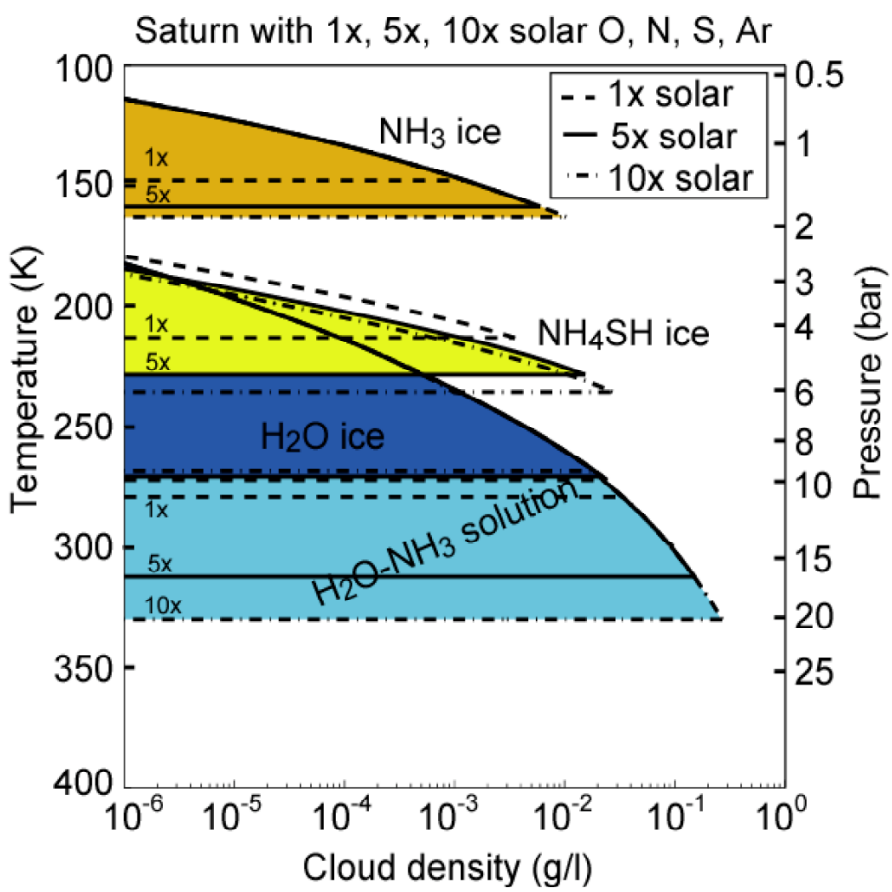

Fig. 3. Results of ECCM calculations for Saturn, with 1x solar, 5x solar, and 10x solar condensible volatile abundances. The 10x solar case should considered "nominal", based on model predictions of equal enrichment of all heavy elements. Only C/H = 9.3x solar has actually been determined. The cloud densities represent upper limits, as cloud microphysical processes (precipitation) would almost certainly reduce the density by factors of 100–1000 or more. However, the LCL's, i.e. cloud bases are expected to remain unaffected.

4. SATURN PROBES: DEEP OR SHALLOW?

The "Equilibrium" thermodynamics model discussed above predicts the well-mixed region for water at Saturn below 20 bars for the nominal case of 10x solar condensible volatile abundances. However, it could be well below this level. In fact, it is expected to be well below this level, since Saturn, like Jupiter, is a highly convective and stormy planet. This nature of Saturn is evident in the Cassini Imaging observations in the visible and the Cassini VIMS observations of 5-micron emission which originates from 6-8 bar level [K. H. Baines, personal comm., 2006]. Considerations of non-equilibrium thermodynamics and convection in the deep atmosphere are thus expected to push the well-mixed regions for water to much deeper levels, perhaps to 50-100 bars. The technological challenges of measurements at high pressures of 50-100 bars with correspondingly high temperatures of 400-500 K at Saturn are daunting. Survival of the probe structure and scientific payload in this environment and the difficulty of data transmission from such great depths are only two of a multitude of obstacles.

On the other hand, if water could be measured by another means than on entry probes, the technological challenges would not be insurmountable. Except for water, all other relevant heavy elements and isotopes can be accessed by probes deployed to approximately ten bars! The microwave radiometry (MWR) technique to be used on the Juno-Jupiter Polar Orbiter for measuring water appears to be the solution at Saturn also. MWR is a promising technique, designed to measure the water abundance to atmospheric pressures of several hundred bars at Jupiter [24]. Employing several antennas ranging in the wavelength coverage from 0.5 to 50 cm, both NH_3 and H_2O will be measured to high pressures by passive microwave remote sensing from an orbiting spacecraft, Juno. Although the peak of the weighting function for the longest wavelength (50 cm) is around 50 bars, the function is broad, making it possible to retrieve the information from as deep as several hundred bars.

Microwave radiometry from a flyby or orbiter spacecraft is expected to work well for measuring water at Saturn also. However, the MWR design, including the choice of wavelengths, remote sensing from spacecraft vs. from probes, achievable vs. desirable spatial resolutions, latitudinal/longitudinal coverage, etc. would require considerable modelling effort, beyond the initial, but very promising, work on possible architecture of such a mission [25]. The technological challenges associated with microwave radiometry are different at Saturn than at Jupiter. The radiation environment is less severe at Saturn, and Saturn's rings absorb much of the radiation. Thus, our preliminary analysis shows that plunging the spacecraft to low heights, such as 5000 km or so above the 1-bar level planned for Juno in order to fly inside the radiation belts of Jupiter, is not required at Saturn. On the other hand, flying close to the planet provides the best spatial resolution, but flying close may not be an option. Unlike Jupiter, the Saturn rings could pose a hazard, especially the D-ring debris. In that case the spacecraft may have to fly at approximately $2R_S$ or farther. Distant flying may also be required due to considerations of the delivery of and communication from the probes [25]. In that scenario, the spatial resolution achievable by the MWR could become undesirable. An alternative is to mount the antennas on the probe itself, and carry out the MWR experiment from the probes, rather than from the carrier spacecraft [25]. This might alleviate the above problem of low spatial resolution and the ring hazard, for example, but the coverage over the planet will be limited, unlike MWR from either a flyby or an orbiter spacecraft. The MWR experiment from the probe will need to be done during entry, then jettisoning the MWR payload before commencing the measurements of composition, etc. with the other payload instruments on the probe.

Communication from the probes is another challenging area. Conventional method is to transmit data from the probe to the flyby or orbiter spacecraft, which in turn relays it to the earth, as was done on the Galileo and the Huygens missions. The relay technique adds complexity, constrains the mission architecture, and requires extra resources. An alternative is direct-to-earth (DTE) communication from the probes, as proposed by Bolton and Owen [26]. However, consideration of mission architecture of the above Saturn flyby mission rule out direct-to-earth data transmission, even with potential availability of Square Kilometer Array (SKA), according to a recent study [25]. In another independent study of DTE [27], it is argued that even if a way could be found, e.g. by using UHF, improved DSN, etc., DTE without a reliable backup is not a desirable option, considering the chances of single-point-failure. Initial analysis also indicates that there is little advantage of any DTE over conventional relay technique [25]. In my opinion, minimum safe and desirable distance of spacecraft from Saturn, acceptable spatial resolution, and data transmission are critical issues science and mission

architecture issues that still require additional investigation and trade-off studies.

As mentioned above, preliminary studies show that microwave radiometry (MWR) is feasible on a probe mission to Saturn [25], not withstanding the architecture of such a mission. And, since MWR is expected to permit measurement of water in the mixed atmosphere of Saturn, the need for the probes to carry out measurements to deep levels is no longer there. Therefore, probes need not be deployed to more than 10 bars. *Shallow* probes will do the job just fine [1]. All noble gases, He, Ne, Ar, Kr and Xe, together with their isotopes, C, N, S, and D/H and $^{15}N/^{14}N$, and the disequilibrium species, CO, PH_3, AsH_3, GeH_4, SiH_4, can be measured at pressures less than or equal to 10 bars. Combined with O/H from microwave radiometer measurements of water, the data from the probes will provide the critical set of elemental composition information required for constraining the models of the formation of Saturn and the origin and evolution of its atmosphere. Comparative planetology with the other gas giant, Jupiter, will be even more valuable for understanding the formation of the solar system and, by extension, the extrasolar systems.

5. SUMMARY AND RECOMMENDATIONS

I recommend a Saturn Probe with Microwave (SP-MWR) mission as the highest priority giant planet mission for the near term. Such a mission could conceivably fit within the cost cap of NASA's New Frontiers class of planetary missions. At least two probes, one to an equatorial latitude and another to a midlatitude location, are most desirable in order to be able to sample a diversity of possible convective scenarios, and for mitigating risk. Although microwave radiometry from the spacecraft, rather than from the probes, is preferable, mission architecture scenarios might permit MWR only from the probes, which would probably not compromise critical science significantly, but needs to be studied further. I recommend a flyby mission, rather than an orbiter with probes. Besides being capable of delivering the required data sets, the Saturn Probe with Microwave Radiometry mission will be relatively less expensive, with fewer technological hurdles, and is possible to do in the near term. Moreover, another orbiter mission at Saturn cannot be justified now, scientifically or otherwise, in view of the highly successful Cassini orbiter mission. However, it is important to stress that the composition measurements recommended here for the next big scientific breakthrough at Saturn are independent of the nature of the mission, whether it is a flyby or an orbiter, with probes. Finally, multinational partnerships should be explored vigorously for maximizing and enhancing science return while realizing cost savings to NASA and to all nations interested in exploring Saturn.

The key measurement from the SP-MWR mission is composition of the well-mixed atmosphere. Deep winds and meteorology measurements are also most desirable for context, complementarity, and dynamics,. Determination of the core is another important science objective on such a mission. Accommodation of other secondary objectives will depend on the cost of the payload and resource requirements. For power, battery-assisted solar cell source is preferred in view of limited availability of the RPS/RTG material and other considerations. However, the effectiveness and feasibility of solar cells at Saturn still needs to be demonstrated. Although technological challenges of the Saturn probe mission do not seem daunting [25], they will require immediate, intensive studies and certain level of investment in enabling technology in order to be able to carry out a Saturn Probe with Microwave Radiometry mission in the near term.

What about the other giant planets?

Shallow probes at Uranus and Neptune can also collect most of the critical composition information. When combined with the data at Saturn and Jupiter, their scientific value will be enhanced greatly. Unlike at Jupiter and Saturn, microwave radiometry on Uranus and Neptune orbiters is not expected to be particularly useful, because of the requirement of accessing tens of kilobar region to find well-mixed water (and ammonia) if a water-ammonia ionic ocean actually exists, and to several kilobars to reach well-mixed water if it doesn't [1,2,20].

On the other hand, the rest of the critical elements and isotopes, including He, Ne, Ar, Kr, Xe, C, $^{15}N/^{14}N$, D/H and $^{3}He/^{4}He$, together with the disequilibrium species – PH_3, GeH_4, and AsH_3, CO – as tracers of internal processes, could be accessed and measured by entry probes at shallower depths with pressures of less than 10 bars [1]. Measurement of S/H may require going to approximately 50 bars. However, further studies are warranted on the criticality of the sulfur measurement, as well as on the possibility of dissolving H_2S in the purported water-ammonia ionic ocean in the deep atmosphere which may make the measurement of H_2S in the upper tropospheric non-representative of the true S/H value. Although O/H and N/H will most likely remain unknown even after the probe missions at the ice giants, their absence will not be a major impediment, as the trend will have been established by comparing all other heavy elements to the results at

Jupiter (and possibly Saturn). Unlike Jupiter and Saturn, the probe missions at Neptune and Uranus should be complemented with orbiters, not flybys, because of the dearth of complementary orbital science data. The Neptune polar orbiter probe mission will be even more attractive if a lander on Triton is also included. Clearly the probe mission at Neptune requires much additional work beyond that done under NASA's Visions Program. Such studies will benefit the architecture of a similar mission to Uranus as well.

A Jupiter multiprobe mission should be considered after data from Juno, especially on water, have been received and analyzed, as the Juno results will be valuable to the design of a multiprobe mission to Jupiter.

Multiple probes to all four the giant planets are needed for understanding the formation of our solar system, and by extension, extrasolar systems. However, such missions are technologically most demanding. An investment in enabling technology, especially in (a) TPS (thermal protection system, or heat shield) and the Giant Planet Facility for characterizing the TPS, (b) communication from microwave absorber-rich atmospheres of the giant planets, including DTE, (c) power, using battery-assisted solar cells, or conventional RTG/RPS (radioisotope) at Saturn, (d) operation in extreme environment of relatively high temperature and pressures, and (e) integrated payload systems, is essential now to realize the ambitious probe missions to the giant planets in the near and long term. Further studies on the feasibility of retrieval of deep water with microwave radiometers mounted on the Saturn probes or on flyby spacecraft are also required, and they will need to carried out hand in hand with modeling studies to encompass various composition and condensation scenarios based on formation and thermochemical models.

ACKNOWLEDGEMENTS

This study was supported by NASA's Planetary Atmospheres Program. Patricia A. Egeler helped with the preparation of Figs. 1 and 3.

6. REFERENCES

1. Atreya, S.K. et al., Multiprobe Exploration of the Giant Planets – Shallow Probes, Proceedings of Third International Planetary Probe Workshop, IPPW3, Anavyssos, Greece, July 2005, *ESA SP-WPP263*, 2006. See also Atreya's presentation to NASA's OPAG (Outer Planets Assessment Group) on 7 October 2005, "How Atmospheric Probes Fit into the Giant Planets Exploration": <http://www.lpi.usra.edu/opag/oct_05_meeting/agenda.html>

2. Atreya, S.K. and Wong, A.S., Coupled Chemistry and Clouds of the Giant Planets – A Case for Multiprobes, in *Outer Planets* (eds. Encrenaz, T., Kallenbach, R., Owen, C., Sotin), pp121-136, Springer-Verlag, 2005. Also in, *Space Sci. Rev.,* 116 (nos. 1-2), 121-136, 2005.

3. Niemann, H.B., Atreya, S.K., Carignan, G.R., Donahue, T.M., Haberman, J.A., Harpold, D.N., Hartle, R.E., Hunten, D.M., Kasprzak, W.T., Mahaffy, P.R., Owen, T.C. and Way, S.H., The Composition of the Jovian Atmosphere as Determined by the Galileo Probe Mass Spectrometer, *J. Geophys. Res.,* 103, 22,831–22,846, 1998.

4. Atreya, S.K., Wong, M.H., Owen, T.C., Mahaffy, P.R., Niemann, H.B., de Pater, I., Drossart, P. and Encrenaz, Th., A Comparison of the Atmospheres of Jupiter and Saturn: Deep Atmospheric Composition, Cloud Structure, Vertical Mixing, and Origin, *Planet. Space Sci.*, 47, 1243, 1999.

5. Atreya, S.K., Mahaffy, P.R., Niemann, H.B., Wong, M.H. and Owen, T.C., Composition and Origin of the Atmosphere—An Update, and Implications for the Extrasolar Giant Planets, *Planet. Space Sci.*, 51, 105–112, 2003.

6. Wong, M.H., Mahaffy, P.R., Atreya, S.K., Niemann, H.B. and Owen, T.C., Updated Galileo Probe Mass Spectrometer Measurements of Carbon, Oxygen, Nitrogen, and Sulfur on Jupiter, *Icarus*, 171, 153, 2004.

7. Owen, T., Mahaffy, P.R., Niemann, H.B., Atreya, S.K., Donahue, T., Bar-Nun, A. and de Pater, I., A Low-Temperature Origin for the Planetesimals That Formed Jupiter, *Nature*, 402, 269–270, 1999.

8. Gautier, D., Hersant, F., Mousis, O., Lunine, J.I., Enrichment in Volatiles in Jupiter: A New Interpretation of the Galileo Measurements, *Astrophys. J.*, 550, L227–L230, 2001. Correction in *Astrophys. J.*, 559, L183, 2001.

9. Hersant, F, Gautier, D., and Lunine, J., Enrichment in Volatiles in the Giant Planets of the Solar System, *Planet. Space Sci,*. 52, 2004.

10. Gierasch, P.J., Ingersoll, A.P., Banfield, D., Ewald, S.P., Helfenstein, P., Simon-Miller, A., Vasavada, A., Breneman, H.H., Senske, D.A., and the Galileo Imaging Team, 2000. Observation of moist convection in Jupiter's atmosphere', *Nature* 403, 628–630.

11. Dyudina, U.A., Del Genio, A.D., Ingersoll, A.P., Porco, C.,West, R.A., Vasavada, A.R., Barbara, J.M., 2004, 'Lightning on Jupiter Observed in the H-alpha line by the Cassini Imaging Science Subsystem', *Icarus* 10.1016/j.icarus.2004.07.014.

12. Flasar, M., and the CIRS Team, Temperature, Winds, and Composition in the Saturnian System, *Science*, 307, 1247, 2005.
13. Grevesse, N, Asplund, M., Sauval, J, The New Solar Composition, in Element Stratification in Stars, 40 Years of Atomic Diffusion (G. Alecian, O. Richard, S. Vauclair, eds.), *EAS Publications Series*, 2005.
14. Anders, E, Grevesse, N. Abundances of the elements: meteoritic and solar. *Geochimica et Cosmochimica Acta,* 53, 197-214, 1989.
15. Drake J. J., Testa, P., The "solar model problem solved by the abundance of neon in nearby stars, *Nature*, vol. 436/28 July 005/doi:10.1038/nature03803.
16. Conrath, B., Gautier, D., Saturn Helium Abundance: A Reanalysis of the Voyager Measurements, *Icarus*, 144, 124, 2000.
17. Atreya, S.K., Baines, K.H., Egeler, An Ocean of Water-Ammonia Ionic Ocean on Neptune and Uranus – Clues from Tropospheric Hydrogen Clouds Structure, *Bull. Am. Astronom. Soc.* Abstract, DPS/AAS Meeting, Pasadena CA, October 2006.
18. Atreya, S.K., Egeler, P.A., Wong, A.S., Water-Ammonia Ionic Ocean on Uranus and Neptune – Clues from Tropospheric Hydrogen Sulfide Clouds, *American Geophysical Union Meeting* Abstract P11A-0088, San Francisco, CA, 2005.
19. Water-Ammonia Ionic Ocean on Neptune and Uranus? S. K. Atreya, P. E. Egeler, K. H. Baines, Abstract, *European Geosciences Union Meeting*, Vienna, Austria, April 2006.
20. Atreya, S.K. and Wong, A.S., Clouds of Neptune and Uranus, in *Proceedings of Second International Planetary Probes Workshop NASA/CP-2004-213456* (ed. E. Venkatapathy, et al,), pp 107-110 2005.
21. Weidenschilling, S.J. and Lewis, J.S., Atmospheric and Cloud Structure of the Jovian Planets, *Icarus*, 20, 465–476, 1973.
22. Atreya, S.K. and Romani, P.N., Photochemistry and Clouds of Jupiter, Saturn and Uranus, in *Planetary Meteorology*, (ed. G. E. Hunt), pp. 17–68, Cambridge University Press, 1985.
23. Atreya S.K., *Atmospheres and Ionospheres of the Outer Planets and their Satellites*, Chapter 3, Springer-Verlag, New York-Berlin, 1986.
24. Bolton, S.J., Owen, T., Atreya, S.K., Guillot, T., *IPPW-3* Abstract, Anavyssos, Greece, 2005.
25. Balint, T. and SSEP Team, On the feasibility of a New Frontiers Class Saturn Probe Mission, *IPPW-4* Abstract, 2006.
26. Bolton, S.J., Owen, T., *IPPW-3 Proceedings*, 2006.
27. Atkinson, D.H., Spilker, T., Baines, K., Asmar, S., Oudrhiri, K., Bienstock, B., Sichi, S., Direct-To-Earth Communication for Outer Planetary Probe Entry Probe Missions, *IPPW-4* Abstract, 2006.

Mission Design Aspects of Planetary Entry Probe Missions

Thomas R. Spilker, Jet Propulsion Laboratory / California Institute of Technology

As planetary entry probes travel to and approach their destinations, their flight paths are governed by the fundamental and well-understood physics of macroscopic bodies in motion. This facet of physics, even its subtleties, can be modeled very precisely by relatively simple equations, so extreme accuracy is possible. But the first-order motion of entry probes is in no way subtle: speeds are at least kilometers per second, sometimes tens of km/s, occasionally more than 50 km/s. This, coupled with the limits of our technologies, means that mission design considerations can place rather severe constraints on where and when probes can enter a given planet's atmosphere. They also determine many more detailed aspects of the entry, such as minimum entry speeds, tolerable entry flight path angles, entry location uncertainties, data relay geometries, etc.

Entry probe mission design usually is considered complete when the probe begins experiencing significant aerodynamic forces. Most mission designers consider the remainder of the probe's flight path a problem for aerodynamicists and planetary atmospheric scientists. But after probe entry the flight path of associated vehicles such as data relay spacecraft are still the mission designer's bailiwick, and natural, physical constraints on those flight paths can have serious implications for the conduct of the probe's mission.

This presentation will cover many of the problems and choices facing the mission designer when conceiving new entry probe mission designs. Examples of topics addressed are the locus of feasible entries for a given approach, the cost of modifying natural approach circumstances, planetary rotation and its implications for prograde and retrograde entries, entry upon hyperbolic approach vs. entry after insertion into orbit, and communications geometries.

ON THE FEASIBILITY OF A NEW FRONTIERS CLASS SATURN PROBE MISSION

Tibor S. Balint
Jet Propulsion Laboratory, California Institute of Technology,
4800 Oak Grove Drive, M/S 301-170U, tibor.balint@jpl.nasa.gov

Participants of the SSEP Study
Jet Propulsion Laboratory, California Institute of Technology
& NASA Ames Research Center

The 2006 Update of NASA's Solar System Exploration (SSE) Road Map pointed to the possible inclusion of a New Frontiers (NF) class Saturn Probe mission to compete for the next opportunity against four other missions, including one targeting Jupiter with Deep Entry Probes. If subsequently selected, this new mission would provide compositional measurements of Saturn's atmosphere, ultimately addressing science questions about the formation of our Solar System. Since the SSE Road Map set other priorities for all Flagship class opportunities over the next three decades, a Saturn Probe mission would only be possible if it would fit under the NF category. Therefore, the selection of trade space options were driven by measures, which would potentially reduce mission cost. The science based baseline architecture calls for two shallow probes descending to 10 bar pressure elevation, utilizing Galileo probe heritage. One probe would target the equatorial region and the other one would aim towards mid-latitudes. In order to measure atmospheric composition to 100 bars, the flyby spacecraft would be equipped with a microwave radiometer, using Juno heritage. The explored mission architecture trade space options include both high-thrust ballistic and low-thrust Solar Electric Propulsion enabled trajectories. For communications, both Direct-to-Earth and relay though the flyby spacecraft are addressed. The spacecraft would be powered by batteries and solar panels, based on Juno heritage LILT technology. Thermal Protection System (TPS) availability and sizing are also discussed. The probe mission concept is costed for various mission architectures. Consequently, the results of this study provide a definitive answer on the feasibility of such a mission, which in turn could assist NASA with the decision making process regarding future NF Announcement of Opportunities.

THE JOVIAN ENTRY PROBE
A feasibility study of a minimum resource Jovian Entry Probe

Alessandro Atzei [(1)], Andrea Santovincenzo [(2)], Heiko Ritter [(3)], Frank Mazoué [(4)], Peter Falkner [(5)]
and the CDF JEP Team

European Space Agency, ESTEC, P.O. Box 299, 2200 AG Noordwijk, The Netherlands, E-mail:
[(1)] Alessandro.Atzei@esa.int, [(2)] Andrea.Santovincenzo@esa.int, [(3)] Heiko.Ritter@esa.int
[(4)] Franck.Mazoue@aoes.com [(5)] Peter.Falkner@esa.int

ABSTRACT

In the framework of the Technology Reference Studies, ESA's Science Payload and Advanced Concepts Office (SCI-A) has initiated a Concurrent Design Facility study to investigate the critical technologies and design issues related to a ballistic Jovian entry probe, with the aim of performing atmospheric measurements during descent and to survive to an ambient atmospheric pressure up to 100 bar.

For this study, the probe's objective was the in-situ measurement of the Jovian atmospheric composition to complement and extend data from the NASA Galileo probe. To this aim an entry probe was designed to penetrate the denser layers of the atmosphere, e.g. up to a pressure of 100 bar (Galileo deepest measurement was at 20 bar pressure), targeting a cloudy zone in contrast with the Galileo's regions, which was a so-called hot spot.

The goal of this study was to derive a 'minimum' entry probe design, to assess design, mass, size and telecommunications requirements and to identify the required enabling technologies, as well as to assess the impacts of such a probe on a potential combined atmospheric/magnetospheric mission to Jupiter. The design of the spacecraft accompanying the probe was beyond the scope of this study.

1. INTRODUCTION

The Jovian Entry Probe study was performed in the context of the Technology Reference Studies (TRS), an initiative of ESA's SCI-A department. The goal of the TRS's is to identify and, when possible, develop critical technologies required for future scientific missions. This is done through the study of several challenging and scientifically relevant mission concepts, which are not part of the current ESA science programme, and focus on medium term enabling technology requirements.

The JEP study is part of the Jovian Technology Reference Studies, which are intended to help identifying enabling technologies for future minimum resource missions to the Jovian system or similar challenging environments. These studies are also intended to support the scientific community in the field of Jovian exploration.

Presently two studies have been completed and a new one has been initiated:

- Jovian Minisat Explorer: Focussing on the exploration of Europa (this included a Europa polar orbiter and a Jovian equatorial relay S/C, implications of radioactive power sources, as well as small Europa impactors) [finished]
- Jovian Entry Probe: Study of the Jovian atmosphere with one or more entry probes, up to 100 bar [finished]
- Jovian System Explorer: Study of the Jovian magnetosphere (one or more magnetospheric S/C) [ongoing]

This paper focuses on the Jovian Entry Probe (JEP) study, which was performed by ESA's Concurrent Design Facility (CDF). This particular study aimed to understand the requirements for a minimum resource probe capable of entering the Jovian atmosphere up to a pressure level of 100 bar.

The following requirements and constraints applied to the study:

- Carry the probe to Jupiter and release it at the correct time
- Perform entry and descent into the Jovian atmosphere at near equatorial latitude (with an option of non-equatorial descent up to -30deg/+30 deg, if possible)
- Measure atmospheric properties in-situ down to a depth corresponding to 100 bar using a given Strawman payload
- Transmit the data in real time to the accompanying Orbiter
- Achieve a final orbit for magnetospheric measurements with the Orbiter
- Achieve multi-probe mission, if mass allows
- Use of highly integrated payload: 12 kg; 30 W; 5 l; 353 bps

- Launch vehicle: Soyuz Fregat 2-1b from Kourou
- Preferred launch dates: 2016 or 2023
- Avoidance of Jovian ring when defining probe approach, while not exceeding maximum allowable distance during comms
- Design shall be compliant with Beagle 2 Enquiry Board recommendations and Huygens Lessons Learned
- Maximum heat flux during entry: 500 MW/m^2 (assumed as maximum capability for present TPS technology)

2. MISSION DESIGN DRIVERS

This mission concept is driven by four main drivers: The Jovian atmosphere, the high entry velocity, launch mass restrictions and communications.

The main issue with the atmosphere is related to the uncertainties regarding the aerothermal phenomena. These uncertainties strongly complicate the design of the heat shield, since they impose significant margins to be added to the design, to compensate for these uncertainties. As a consequence, this leads to a likely over-dimensioned thermal protection system: depending on the entry latitude the resulting TPS mass fraction is in the order of 50% to 70%.

The entry velocity cannot be reduced below ~47 km/s. At these velocities and due to the previously mentioned limitations, the aerodynamic phenomena in the atmosphere cannot be properly computed, leading to uncertainties in the calculation of the heat fluxes. Further, the very high thermodynamic fluxes are at the limit of present TPS technology capabilities. The very high deceleration loads (in excess of 1700 m/s^2) additionally require dedicated qualification of the probe's components.

The relatively modest launcher provides the upper limit for the launch mass, while the fulfilment of the mission requirements provides the lower limit. This clearly poses a limit to the maximum TPS mass and therefore to the maximum entry velocity.

The high temperature and pressures in the atmosphere at lower altitudes further complicate the design of the entry probe, since the design needs to offer adequate protection against these conditions.

The strong attenuation of radio signals by the atmosphere below the 20 bar level impose stringent design requirements for the communication systems on both the probe and the orbiter. Furthermore, the trajectory of the carrier S/C will have to allow for a continuous communication with the probe during the deployment and relay phase.

3. MISSION ARCHITECTURE

The mission composite (Orbiter + Entry Probe) shall be launched by Soyuz-Fregat 2-1b into a highly elliptic orbit (HEO). The spacecraft is then inserted into a hyperbolic Jupiter transfer orbit by its own propulsion system with a two-burn sequence. The launcher performance into the optimal HEO is 2346 kg including adapter.
The Jupiter transfer trajectory is of the VEEGA type; including a Venus swing-by and two Earth swing-by's aiming at Jupiter impact for release of the entry probe. No mid-course manoeuvre is required except for navigation corrections.
Two cases have been considered: single probe or two probes onboard of the same Orbiter.

During cruise the probe is attached to the Orbiter S/C and uses the Orbiter's power supply to perform periodic instrument checkout and possibly software updates.

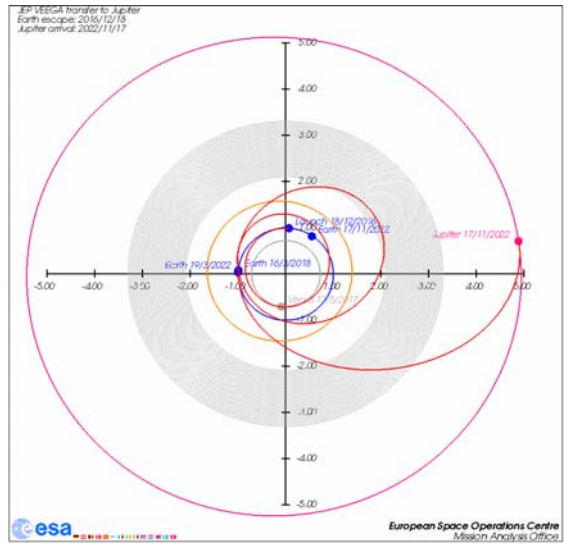

Figure 1: The VEEGA Transfer Trajectory

Sufficiently before Jupiter arrival, the Orbiter deploys the entry probe (in short sequence, should two probes be considered) and performs a deflection Manoeuvre (ODM) to get into a safe non-entry trajectory.
The time of probe release compared to the entry time sizes the delta-V cost of the ODM and the error on the Flight Path Angle (FPA) at entry which is constrained by probe TPS design. The selected release time is 90 days before entry with a delta-V cost of 89 m/s and a FPA error at entry of less than 1 deg.

During the coast phase, the probe is uncontrolled and unguided. It uses its own power system to perform communications with the Orbiter, and timer switches are used to activate automatic sequences.
While the probe coasts to its entry point, the Orbiter performs a Ganymede swing-by to reduce its incoming velocity and therefore reduce the delta-V cost of the Jupiter Orbit Insertion (JOI). The Insertion Orbit is the orbit from which the relay with the probe(s) is performed during their entry and descent. This is a 4x200 Jovian Radii (Rj) equatorial orbit around Jupiter (for near equatorial entry and descent). The perijove radius is a compromise between distance for probe relay (the closer, the lower the required power) and radiation protection (the closer, the higher the dose). The apogee corresponds to the required final orbit of 15x200 Rj. The JOI manoeuvre takes place 1 hour before perijove arrival, requires 570 m/s and its duration is about 0.5 hours.

The start of the probe entry phase is defined as the point where the probe reaches 450 km altitude above 1 bar (the 1 bar level is used as a reference zero level for altitude measurement). During this phase the probe relays flight instrumentation data (used for trajectory reconstruction) to the Orbiter with the exception of the period of blackout caused by the plasma sheath around the probe.

Due to Jupiter's massive gravity field, the spacecraft will accelerate considerably as it approaches perijove. The consequence for the entry probe is that the inertial velocity at entry will amount to around 60 km/s with only a weak dependency on the hyperbolic entry velocity. As Jupiter's rotation period is less than 10 hours, the equatorial atmospheric rotation speed is almost 12.6 km/s. Therefore, the actual atmospheric entry velocity depends strongly on the entry location. For a prograde, near-equatorial entry, the relative entry velocity is thus 47 km/s.

The science data relay phase occurs after the front heat shield and back cover have been released and the main parachute has been deployed. At this point all instruments will take measurements from the Jovian atmosphere and send them back to the Orbiter. The relay phase ends after the one hour communications window when the probe has reached 100 bar depth in the Jovian atmosphere. At this point the probe's mission is complete.

During the relay, the Orbiter needs a relatively slow, constant-rate slew manoeuvre (rate ca. 17 deg per hour), to keep its high-gain antenna trained upon the current probe location.

It is noted here that Direct-To-Earth communication from the probe is only possible during the early phases of entry. This is due to the low Earth elevation with respect to Jupiter's local horizon in the analysed 2022 arrival case; the very high rotation speed of Jupiter only allows for a short visibility time of the probe.

After the relay phase, the Orbiter will reach its final orbit for magnetospheric measurements, which has a line of apsides aligned with the sun direction. This is achieved by the combination of a propulsive manoeuvre of 500 m/s at apojove to increase the altitude of perijove and a Jovian satellite tour (a sequence of five Ganymede swing-by's) to rotate the line of apsides as needed.

Manoeuvre	1 probe Mission Delta-V (m/s)	2 probe Mission Delta-V (m/s)
Satellite tour/Apojove raise	30	30
Perijove raise (PRM)	500	500
Jupiter orbit insertion (JOI) 1 hr before perijove	570	570
Orbit deflection man. 70d before entry	N/A	120
Hyperbolic probe release	N/A	0
ODM 90d before entry	89	42
Probe release from hyperbolic	0	0
Mid-course manoeuvre	0	0
VEEGA	30	30
Escape from HEO	626	626
Inclination change	82	82
GTO to HEO	692	692
Total incl gravity loss Final total incl margin	2668 2801	2740 2878

Table 1: ΔV budget for baseline and option 1

The mission delta-V budget is shown in table 1 for a single probe and a two-probe mission. The table is based on the 2016 launch window, which is the worst case between the selected target launch dates.

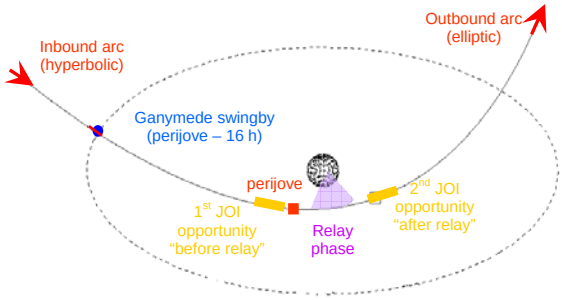

Figure 2: Swing-by augmented JOI

4. ALTERNATIVE OPTIONS

4.1 Two probes

A two probe mission would be preferable to enable different entry points and more data collection, and to allow for redundancy. Nonetheless, due to launcher mass constraints, the case of two probes is only considered feasible if the deepest altitude to each is reduced to 40 bar. In this case the two probes are deployed into approach orbits of different inclinations, leading to a difference in the entry and descent locations, the first probe aiming at a latitude of 3.6 deg N, the second at a latitude of 6.8 deg S. The relative entry velocity for both probes is slightly higher than 47 km/s.

4.2 Off-equatorial entry

The preferred probe entry latitude is non-equatorial between 30 deg N and 30 deg S. Entry at high latitude would require an approach from an inclined trajectory and an increase in delta-V to retarget the Orbiter for an equatorial insertion.

For the high-latitude probe, the inclination can be fairly low, which will limit the rise in relative entry velocity but would require a steeper entry. Or, the inclination can be larger, in which case a larger increase in relative velocity is incurred, but the entry angle could be kept relatively shallow.

This effect is due to the fact that the perijoves of the arrival hyperbolae are all close to equator and that shallower angles can only be achieved close to the perijove.

As an example, for a descent latitude of 15 deg South, the lowest inclination possible is 25 deg, leading to an entry FPA of -16 deg and an entry velocity around 49 km/s, while the larger inclination leads to –10 deg FPA and an entry velocity of about 50 km/s. In any case, heat fluxes occur in excess of 500 MW/m^2, exceeding available TPS capabilities. In addition, the high-latitude probe would require the communication relay to be conducted at an oblique angle with respect to the equatorial Orbiter. For these reasons, non-equatorial entry has been considered as non-affordable.

4.3 Release from orbit

Release from capture orbit requires a higher delta-V and gives an allowable probe mass of approximately 230 kg while it doesn't reduce the probe's entry speed enough to enable a lighter probe (46-47 km/s for capture vs 47.4 km/s for hyperbolic). Furthermore, the communications between the probe and the orbiter become much harder, as there cannot be a continuous one hour communication window, due to the eclipses caused by Jupiter. As there were no other clear advantages for the release from capture orbit, this option was discarded.

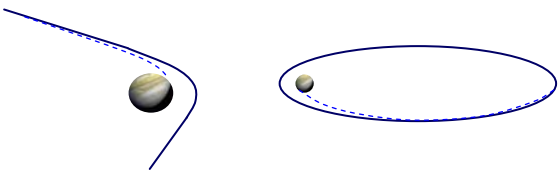

Figure 3: Hyperbolic release vs. from orbit

5. AEROTHERMODYNAMICS

The assumed probe shape is similar to the Galileo probe design, containing a front shield with a half cone angle of 45°, as shown in Figure 4:

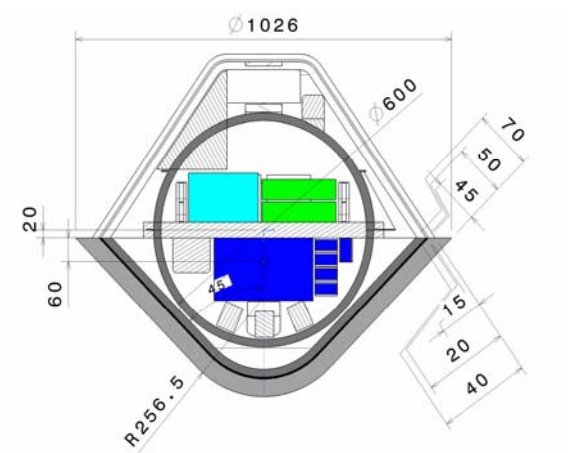

Figure 4: Probe geometry

The equatorial entry parameters are the following:

- Entry Altitude: 450 km
- Entry Velocity: 47.4 km/s
- Entry Angle: -7.5°

5.1. Equatorial entry

Two entry mass cases, 310 kg and 280 kg, have been studied depending on the final altitude respectively pressure level (100 bar and 40 bar). Figure 5 presents the entry and descent trajectories.

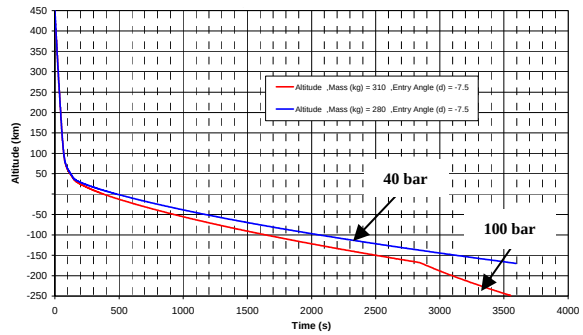

Figure 5: Altitude vs Time for equatorial entry

Relatively similar acceleration profiles are obtained for both cases with a peak around 1 700 m/s^2 at 69 s after the entry point (Figure 6). The smaller peaks correspond to the pilot chute deployment, release of the pilot / back cover / deployment of the main chute and the release of the front heat-shield.

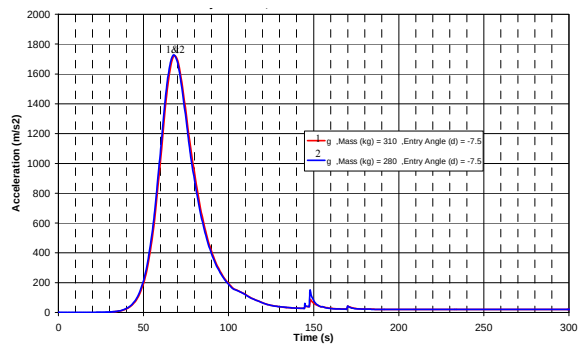

Figure 6: Acceleration vs Time for equatorial entry

The radiative heat fluxes at the stagnation point in both options are presented in Figure 7.

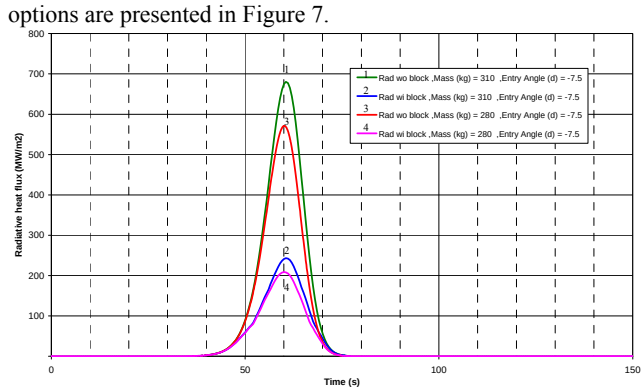

Figure 7: Heat Fluxes vs Time for an equatorial entry

The heat flux distribution along the front shield, at the stagnation point, mid-cone, edge and base point is presented in Figure 8 for the 100 bar option.

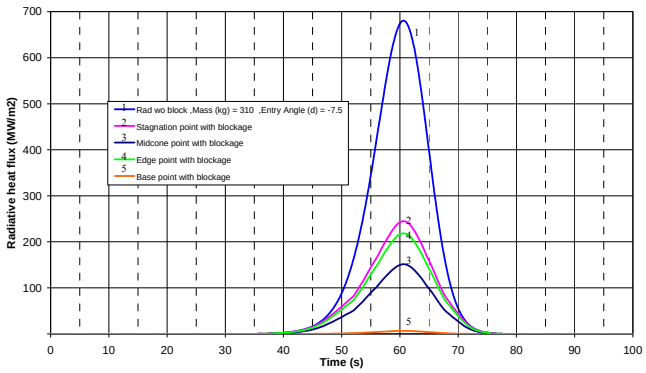

Figure 8: Heat Fluxes vs Time over the front shield surface for a Final pressure of 100 bar

Only 3-dof analyses were performed, therefore the probe stability during entry and descent could not be confirmed. The distance between the CoG location and the back cover/front shield interface is -38.7 mm which is about 3.8% of the base diameter and therefore lower than 4.5%, which was the requirement for the Galileo probe. This point would need to be addressed in further detail.

5.2. Non-equatorial entry

For a non-equatorial entry, the entry mass was assumed to be 500 kg in all cases. The used dimensions of the probe are 1.30m for the base diameter with a nose radius of 0.65m. The radiative heat fluxes are presented in Figure 9. Due to the very high level of the radiative heat fluxes (>1 GW/m2 even with blockage), the non-equatorial entry mission is beyond present technology capabilities.

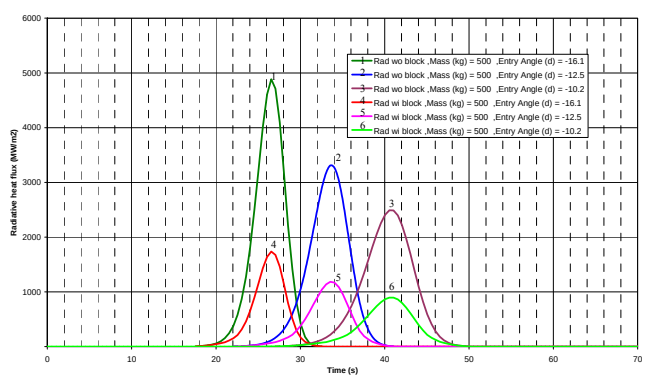

Figure 9:Heat Fluxes vsTime for non equatorial entry

6. THERMAL PROTECTION SYSTEM

One of the major feasibility drivers of the overall mission is the design of the thermal protection system and the availability of a suitable material capable to withstand the very high radiative and convective heat fluxes. A significant effort of the study was dedicated to the screening of potential heatshield concepts. As a result, a Galileo-like shield based on Carbon-Phenolic ablator still appears as the most promising solution.

The material considered as reference in this study is part of a family whose characteristics are close to the one used for the Galileo mission. The present availability of the material could not be confirmed. In any case, a dedicated development would be required for Europe.

Analysis has shown that if the ablator is applied using the SEPCORE concept (Figure 10), a mass reduction of about 25% can be achieved compared to a conventional ablator with a cold structure concept. This is mainly due to the fact that the ablator is mounted on a hot structure, which is insulated against the inner compartment using lightweight insulation, possibly fibres. Considerable mass savings are obtained due to reduced ablator thickness and the use of a more efficient insulation.

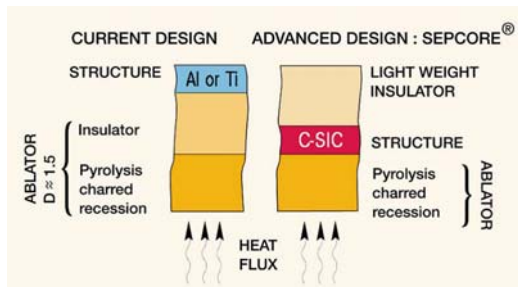

Figure 10: Classical vs SEPCORE TPS

Alternative options to be considered in later project phases are heatshields based on either Carbon-Carbon or Carbon-SiC ablators.
The TPS design is shown in the following figure:

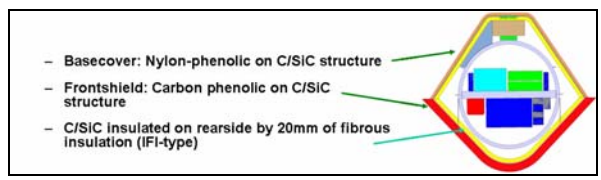

Figure 11: TPS schematic

Due to the uncertainties on the aerothermodynamic fluxes and loads as well as the TPS material characteristics in such entry environment, a robust margin philosophy has been applied (> 40% overall).

7. DESCENT SYSTEM

In the nominal case, the end of mission will occur when the probe reaches a depth corresponding to 100 bar. Due to communications constraints this will have to be achieved in less than one hour, otherwise measurements performed at low altitudes cannot be relayed back to the Orbiter. Therefore the requirement for the parachute system is to provide a flight time of around one hour to the final altitude. In addition, the parachute shall safely separate the probe from the heat shield by increasing the area of the separated elements, obtaining a ballistic coefficient that is sufficiently different (factor 2).
A minimum parachute designed to provide the above separation leads to a flight time in excess of 1 hour to achieve 100 bar altitude. Therefore, the parachute system

needs to include a release mechanism so that the probe can accelerate in the last part of the descent (see Figure 12)

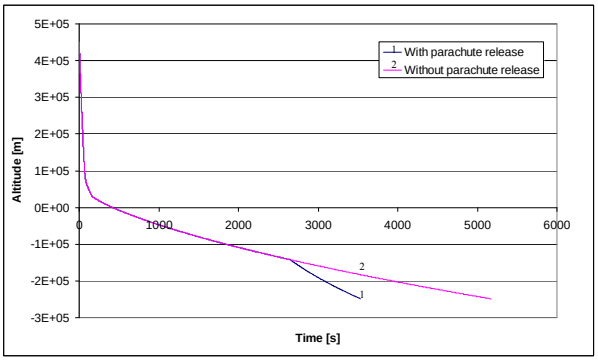

Figure 12: The descent trajectory

The descent system consists of a pilot parachute attached to the back cover with a diameter of 1.47m and a C_d of 0.52. The pilot is deployed at Mach 1.1 by a mortar, triggered by an accelerometer, g switches and a timer as backup. A main chute with a diameter of 2.28 m is deployed by the back cover once it is separated.

The descent module together with the front shield will continue the descent under the main chute for another 20 sec, allowing for stabilisation before a timer triggers the front shield release. The descent module will then continue its descent under the main parachute with the scientific payload operational. The main parachute is finally released after 47 min.

Conical ribbon technology was selected for the parachute due to its superior performances at high dynamic pressures (opening of the parachute occurs at q=12 kPa) and structural integrity. Furthermore, this type of parachute fulfils the stability requirement, although a small penalty has to be paid in terms of drag coefficient.
Dacron is proposed as the material for the canopy construction and Kevlar for the lines. At the time of release, the atmosphere temperature will still be sufficiently below the material performance limits.

8. COMMUNICATIONS

The following communication architecture is foreseen:

- *Coast phase:* data transmission to the orbiter occurs via a back cover antenna. Carrier recovery and Doppler tracking can be achieved by VLBI (Very Large Base Interferometry). To reduce the power consumption, a 3 hours total transmission time is assumed during the whole cruise phase at a data rate of 8 Kbps
- *Entry phase:* during this phase (~3 minutes) no transmission will be possible (black-out) due to attenuation by the plasma cloud
- *Parachute deployment and descent till 0.2h from entry:* after the back cover separation and parachute deployment, the Descent Module (DM) helix antenna will start to transmit. The TM signal will be received by the orbiter and VLBI until 0.2h after the entry. After that the Earth will be below the 'Jovian horizon' and VLBI can not detect the probe's carrier signal anymore
- *Descent, from 0.2h after the entry till 100 bar pressure altitude:* data transmission between probe and orbiter will take place via the DM patch array antenna. A minimum net data rate of 353 bps is required

A variable power system is foreseen to cope with the very strong atmospheric attenuation (up to ~24 dB at 100 bar). The maximum power consumption of one link is 225 W. Link redundancy (as in Galileo and Huygens), would imply unacceptable power consumption. Therefore, only cold redundancy has been assumed.

The frequency band selection is a trade-off between the conflicting factors of atmospheric attenuation and synchrotron radiation of Jupiter. The high atmospheric absorption is due to ammonia, water, sulphide and phosphine in the Jovian atmosphere (polar molecules). The synchrotron radiation originates in the Jovian magnetic field and depends on the geometry of the orbiter antenna orientation.
Frequencies below S-band (2GHz) need to be considered to limit attenuation. Therefore, the reuse of the Huygens frequency band (S-band) is not possible. On the other side, below 1.3GHz, the synchrotron radiation is expected to increase, overcoming the positive effect on signal attenuation. As a result of this trade-off, a 1.3GHz system (L-Band) has been selected for this mission.

All considered mission cases give a positive margin for a minimum data rate of 370 bps (353 bps + 5% margin), a maximum power of 100W and an antenna size on the Orbiter of 4m for the 100 bar cases. This antenna size will cause considerable accommodation problems for the carrier and needs to be properly understood if this concept is selected for further study. Because of the high attenuation, deeper altitudes into Jovian atmosphere would imply a significant increase of resources to maintain the link budget margins and is therefore considered unfeasible with the selected configuration.

9. DESCENT MODULE CONFIGURATION

A trade-off has been performed between several different structural concepts for the Descent Module (DM). In the end a spherical titanium sealed vessel was selected, with an internal pressure of 1 bar. The option of a fully internally pressurised DM (100 bar) has been rejected due to expected leakage during long cruise to Jupiter, the structural loads and the handling risks.
Under uniform external pressure, a thin-walled sphere buckles at a fraction of the pressure that would cause the same vessel to fail under uniform internal pressure. Therefore, the vessel has been stiffened with circular ring frames. These frames are also used to support the equipment shelf and serve as an attachment for the interface brackets of the DM to the front shield.

The DM features a single internal equipment shelf that hosts the entire internal equipment. In particular, the vessel contains the science payload, the CMDU, PCDU, Comms transponders and amplifiers, batteries as well as the L-Band patch and helix antenna on the outside. A volume reduction exercise of this equipment has been performed to decrease the required dimensions of the DM.

Figure 13: Exploded view of the probe+the DM

For stability during the descent of the DM into the Jovian atmosphere, vanes are added on the DM. Inlets and windows are added for the Strawman payload, as it is needed for its operation.
As the overall dimensions and mass of the probe result from the dimensions of the DM (which is sized by the equipment volume), the probe mass cannot be reduced below a certain threshold unless high electronics integration is pursued, something that should be kept in mind for further studies.

10. BUDGETS

10.1 100 bar probe mass budget

The minimum configuration mass budget is shown in the following table:

Structure	30.7
Thermal control	145.7
Mechanisms	9.3
Comms	6.8
Data handling	11.5
GNC	1.6
Power	18.1
Harness	10.1
Instruments	10.4
DLS	6.3
Total dry mass	250.5
20% system margin	50.1
Total mass with margin	300.6

Table 2: 100 bar probe mass budget (mass in kg)

10.2 Mission options comparison

The following table shows the available launch mass margin for the analysed mission options:

	Baseline	Two 40-bar probes	Larger P/L	Two S/C	From orbit
Total dV with margin	2801	2878	2801	2641	3002
Orbiter 1 dry (kg)	700	700	700	700	700
Orbiter 2 dry (kg)	--	--	--	700	--
Tot prop mass (kg)	1236	1409	1268	1903	1644
Probe 1 dry (kg)	300	268	350	--	300
Probe 2 dry (kg)	--	268	--	--	--
Total launch mass (kg)	2236	2646	2318	3304	2944
Launch margin SF 2-1b	24%	10%	21%	-12%	2%

Table 3: Mission architecture comparison with launch margin

The "larger P/L" option concerns a single probe with increased payload mass as a result of:

- 100% increase of the P/L mass
- 100% increase of the P/L volume
- 50% increase of the P/L power
- 50% increase of the P/L data rate

This option was analysed to assess the sensitivity of the probe design to changes in the payload.

Note, that all dry masses include 20% system margin.

10.3 Power budget

The following table shows the power requirements of the probe as a function of the different phases: passive coast (90 days prior to entry), check-out during coast (3 hours total) and the entry and descent phase (1.25 hours, including check-out).

The relevant power architecture is based on two different types of primary battery, LiSOCl2 for the timers during coasting and LiSO2 for the PCDU. This approach gives the minimum system mass.

Coast Phase	*90 days*		
DHS		0.3 W	
GNC		0 W	
Comms		0 W	
Check out during coast	*3h total*	648 Wh	
DHS		22 W	
Payload		5 W	
Comms		50 W	
		231 Wh	
Entry + descent	*1h 15*	**Average**	**Max**
Comms		104 W	225 W
DHS		22 W	22 W
Payload		28 W	29 W
GNC		22 W	22 W
		220 Wh	298 W
Total Wh (30% margin)		1429 Wh	
Total Pmax (30% margin)			388 W

Table 4: Power budget per phase

11. CONCLUSION

The study has shown that, for the given payload, a minimum Jupiter entry probe of about 300 kg can be designed reaching a depth corresponding to a pressure of 100 bars.

A smaller probe (about 10 % lighter) could be achieved if the requirement is relaxed to an altitude corresponding to a pressure of 20-40 bar. In this case, the mission mass capability would allow for two identical probes on one carrier (~700 kg dry mass) launched by a Soyuz-Fregat. Therefore, the requirement of atmospheric deep sampling needs to be traded against sampling in two different shallower atmosphere locations. On the other hand, lower altitudes corresponding to pressures in excess of 100 bar quickly become unfeasible because of the very high atmospheric attenuation and the associated low link margin or high communication power. Due to the very low resources and the atmospheric attenuation, communications are a major problem, driving the probe & S/C design. Furthermore, the distance between probe and relay S/C is limited to the ~4 Rj range to limit the required power to reach the carrier spacecraft.

Entry from a hyperbolic approach trajectory takes place 90 days after release. Only near equatorial latitudes can be targeted, as the study has shown that for higher latitudes the entry heat fluxes exceed the present capabilities of ablative thermal protection systems.

Jupiter entry probes face extreme aerothermodynamic challenges: the identification of adequate TPS is very challenging, therefore the probe design includes a generous margin for Thermal Protection System (TPS) design. This is mainly due to the large uncertainty that exists in the calculation of heat fluxes and performance of TPS in this thermal load range. Such uncertainties come from the fact that design and qualification will have to rely only on partial representation of the physical phenomena and on a reduced environment (testing in a representative environment is considered unfeasible, leading to large uncertainties in theoretical models).

High complexity and extreme test conditions are major cost drivers. The TPS design and qualification is the most critical issue of the mission. Therefore, a careful margin philosophy is required and the option of flying two identical probes may help reducing the mission risk. Next to this, highly integrated electronics will be required to minimise the required resource allocation.

12. ACKNOWLEDGEMENTS

The authors gratefully acknowledge the Concurrent Design Facility's JEP team that performed this study as well as Professor Chul Park (KAIST), for his advice on aerothermodynamics aspects and the ESTEC Huygens team for their inputs regarding the lessons learned.

11. KEY LITERATURE

Bagenal, F. et al, "Jupiter, The Planet, Satellites and Magnetosphere", Cambridge University Press, 2004

Huygens Science, Payload and Mission, SP-1177, 1997

Park, C., Overview of Radiation Problems in Planetary Entry, Proceeding of the International Workshop on Radiation of High Temperature Gases in Atmosphere Entry, ESA-SP-583.

Matsuyama, S., Ohnishi, N., Sasoh, A. and Sawada, K., Numerical simulation of Galileo Probe Entry Flow field with Radiation and Ablation, J. Thermophysics and Heat Transfer, Vol 19, No 1, Jan-March 2005.

Moss, J.N., Jones, J.J. and Simmonds, A.L., Radiative Heat flux Penetration through a Blown Shock Layer for Jupiter Entry, AIAA 78-908, 1978.

Sutton, K., Jones, J. and Powell, R.W., Effect of Probe Configuration on Radiative Heating During Jovian Entry, AIAA 76-471, 1976.

Williams, S.D. and Curry, D.M., Thermal Protection Materials – Thermophysical Property Data, NASA Reference Publication 1289, 1992

Park, C. and Tauber, M.E., Heatshield Problems of Planetary Entry, a Review, AIAA 99-3415, 1999

Laub, B. and Venkatapathy, E., Thermal Protection System Technology and Facility Needs for Demanding Future Planetary Missions, NASA Ames, 1st International Workshop on Planetary Probe Atmospheric Entry and Descent, October 2003

Moss, J.N., Jones, J.J., Galileo Probe Forebody Flow field prediction during Jupiter Entry, AIAA 82-0874

State of Affairs for Jupiter Deep Entry Probes, 3rd IPPW, by Balint, Young, Venkatapathy, Spilker and Kolawa., June 2005

CDF Study Report JEP Jupiter Entry Probe, CDF-43(A), December 2005

AUTONOMOUS TIER-SCALABLE RECONNAISSANCE MISSIONS FOR REMOTE PLANETARY EXPLORATION

Wolfgang Fink[(1)], James M. Dohm[(2)], Mark A. Tarbell[(1)], Trent M. Hare[(3)], Victor R. Baker[(2)], Dirk Schulze-Makuch[(4)], Roberto Furfaro[(5)], Alberto G. Fairén[(6)], Ty P.A. Ferré[(2)], Hideaki Miyamoto[(7)], Goro Komatsu[(8)], William C. Mahaney[(9)]

[(1)]California Institute of Technology, Visual and Autonomous Exploration Systems Research Laboratory, Division of Physics, Mathematics and Astronomy, Mail Code 103-33, Pasadena, CA 91125, USA, Email: wfink@autonomy.caltech.edu, mark@autonomy.caltech.edu, Website: http://autonomy.caltech.edu
[(2)]Dept. of Hydrology and Water Resources, University of Arizona, Tucson, AZ, USA, Email: jmd@hwr.arizona.edu, baker@hwr.arizona.edu, ty@hwr.arizona.edu
[(3)]United States Geologic Survey, Flagstaff, AZ, USA, Email: thare@usgs.gov
[(4)]Dept. of Geology, Washington State University, Pullman, WA, USA, Email: dirksm@wsu.edu
[(5)]Aerospace and Mechanical Engineering Dept., University of Arizona, Tucson, AZ, USA, Email: robertof@email.arizona.edu
[(6)]Centro de Biología Molecular, Universidad Autónoma de Madrid, Madrid, Spain, Email: agfairen@cbm.uam.es
[(7)]Department of Geosystem Engineering, University of Tokyo, Tokyo, Japan, Email: miyamoto@geosys.t.u-tokyo.ac.jp
[(8)]International Research School of Planetary Sciences, Università d'Annunzio, Pescara, Italy, Email: goro@irsps.unich.it
[(9)]Geomorphology and Pedology Laboratory, York University, Canada, Email: arkose@rogers.com

ABSTRACT

A "tier-scalable" paradigm integrates multi-tier (orbit⇔atmosphere⇔surface/subsurface) and multi-agent (orbiter(s)⇔blimps⇔rovers, landers, drill rigs, sensor grids) hierarchical mission architectures [1-4], not only introducing mission redundancy and safety, but enabling and optimizing intelligent, unconstrained, and distributed science-driven exploration of prime locations on Venus, Mars, Europa, Ganymede, Titan, Enceladus, Triton, and elsewhere, allowing for increased science return, and paving the way towards fully autonomous robotic missions.

1. INTRODUCTION

A fundamentally new scientific mission concept for remote planetary surface and subsurface reconnaissance recently has been devised [1-4] that soon will replace the engineering and safety constrained mission designs of the past, allowing for optimal acquisition of geologic, paleohydrologic, paleoclimatic, and possible astrobiologic information of Venus, Mars, Europa, Ganymede, Titan, Enceladus, Triton, and other extraterrestrial targets [5, 6]. Traditional missions have performed local, ground-level reconnaissance through rovers and immobile landers, or global mapping performed by an orbiter. The former is safety and engineering constrained, affording limited detailed reconnaissance of a single site at the expense of a regional understanding, while the latter returns immense datasets, often overlooking detailed information of local and regional significance.

A "tier-scalable" paradigm integrates multi-tier (orbit⇔atmosphere⇔surface/subsurface) and multi-agent (orbiter(s)⇔blimps⇔rovers, landers, drill rigs, sensor grids) hierarchical mission architectures [1-4], not only introducing mission redundancy and safety, but enabling and optimizing intelligent, unconstrained, and distributed science-driven exploration, allowing for increased science return and paving the way towards fully autonomous robotic missions [6].

In the highly automated scenario, the satellites command and control the airborne agents autonomously, and the airborne agents autonomously command and control the ground-tier reconnaissance agents (Fig. 1). This system integrates satellites with inexpensive balloons/blimps (airships) and ground-tier agents (rovers, fixed landers, e.g., Beagle 2, and sensors). The airborne and ground-tier agents can be inexpensive enough (in terms of capital cost and operational resources) to allow for the deployment of numerous agents that collectively can address specific science-driven questions. Multiple ground-tier and airborne agents collectively can explore the

same science target with a complementary suite of instruments.

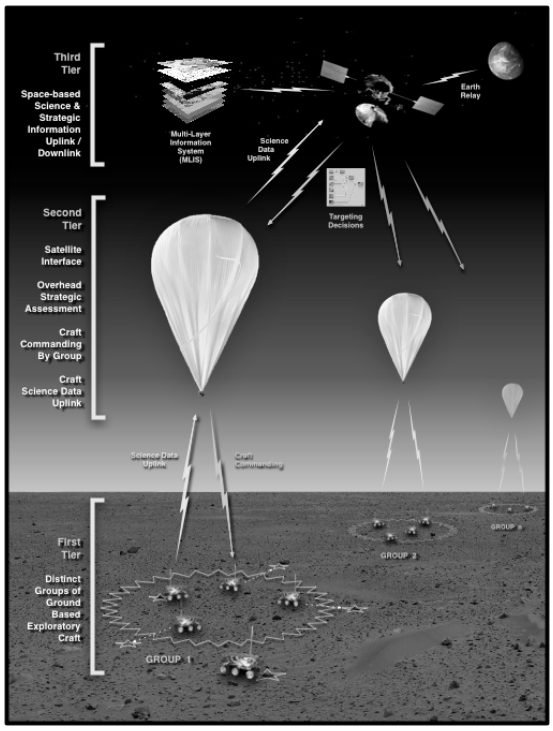

Fig. 1. Tri-level hierarchical multi-agent architecture for autonomous remote planetary exploration (from [1-4]).

To support such tier-scalable reconnaissance mission architectures, a high level of operation autonomy is required. Critical aspects of such operation autonomy are (1) to automatically map an operational area from different vantage points (i.e., space, air, surface/subsurface), (2) to automatically identify targets/regions of interest and to extract features of the identified targets/regions of interest within the mapped operational area [7], and (3) to automatically prioritize targets for close-up reexamination [7-11] (e.g., with ground-tier agents) based on preliminary (coarse) data, gathered (in transit) by, for example, space- and airborne sensor platforms, potentially coupled with existing information from previous missions.

Multiple prioritization scenarios can be conceived to evaluate the (scientific) importance of individual targets or combinations of targets to be further examined during reconnaissance missions (e.g., by a ground-tier agent such as a rover on Mars), which differ in their respective level of complexity. These scenarios can range from simple feature-based or feature-clustering-based prioritization (e.g., [12-14]) to prioritization via context-based clustering (e.g., [15]).

Based on previously gathered, coarse feature/reconnaissance data that has been pre-clustered using general purpose clustering algorithms (e.g., [12-14]) or clustering algorithms associated with special-purpose models (e.g., [15]), more advanced prioritization frameworks recently have been devised [8] for (1) the selection of single or multiple targets, and (2) the selection of instruments used for the close-up reexamination of these targets in an operational area for potential "knowledge gain" about the operational area. These prioritization frameworks are based on the method of "hypothetical probing" [8] that exploits current data only to infer the probability for a particular target or combination of targets to contribute to the "knowledge gain" of an operational area if reexamined more closely.

In addition, the full-scale and optimal deployment of agents as part of a tier-scalable mission requires the design, implementation, and architecture integration of an intelligent reconnaissance system capable of integrating existing and acquired "in-transit" information to automatically perform smart planetary reconnaissance, such as homing in on prime candidate sites for potentially life-containing habitats on Mars [9-11]. To enable a higher level of on-board automation, a fuzzy-logic theoretical framework can be exploited [9-11] to design a fuzzy-based expert system capable of autonomously reasoning over multiple layers of information gathered while en-route and performing smart assessment of the observed areas to help deciding the most appropriate hardware deployment (i.e., deployment of agents and sensors). Fuzzy logic is efficient in dealing with uncertainty and vagueness typical of real life scenarios and may represent an ideal platform to define the basic components of such an expert system. The tier-scalable geological approach, which compiles, synthesizes, and analyzes layers of diverse information (e.g., *Multi-Layer Information System (MLIS)* [1-3]) to identify prime targets for continued exploration [16, 17], is implemented as a set of IF-THEN rules representative of the desired expert knowledge [9-11]. Such rules can be effectively used by a fuzzy inference system to reason over water and/or life indicators to extract parameters such as "potential for water/life-containing", indicating the confidence exhibited by the system to find water and/or life at the observed locales.

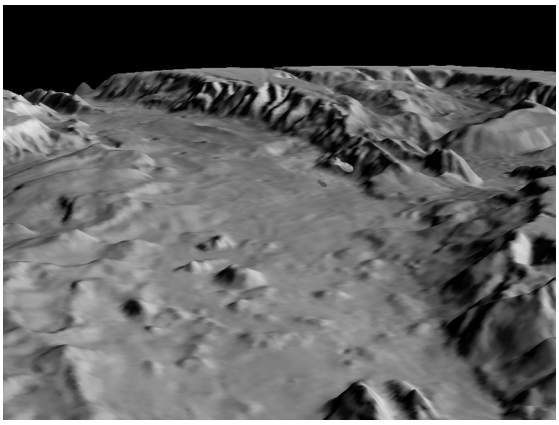

Fig. 2. 3-D oblique view, exemplifying an airborne agent (blimp/airship) performing intelligent reconnaissance over Melas Chasma (after [1]), the central part of the vast canyon system Valles Marineris on Mars. Part of the reconnaissance would include surveying the canyon walls, homing in on stratigraphic sequences, hovering above landslide and valley floor deposits, and identifying targets for subsequent deployment of ground-based agents such as miniature rovers and immobile sensors. Target features of special scientific interest may include: (1) geomorphic features and mineralogical/elemental signatures, indicative of past water activities; (2) diversity of rock types (e.g., site on Mars containing rocks that record the early, middle, and later parts of martian history); (3) elevated heat flow; (4) surface/near-surface water or moisture (including fog embankments); and (5) volatile plumes (e.g., methane). These target features contribute to the success in identifying potential life-containing habitats. (Note that for visual purposes the blimp/airship is not drawn to scale).

2. PRIME CANDIDATES FOR HIGH-RISK SCIENTIFIC EXPLORATION

Non-traditional autonomous missions to remote planetary bodies will be necessary [1-4, 6] primarily to allow intelligent and unconstrained access to scientifically interesting terrains on planetary bodies of the Solar System, not currently feasible with conventional mission designs, including: (1) canyons (e.g., Valles Marineris on Mars, or Devana Chasma, a big rift valley on Venus), (2) mountain ranges (e.g., Thaumasia highlands on Mars, Isthar Terra on Venus), (3) sites of suspected magmatic-driven uplift and associated tectonism and possible hydrothermal activity (e.g., plume-related activity such as hypothesized for the central part of Valles Marineris and the Warrego Valles rise on Mars [17-19], and Maxwell Montes on Venus), (4) polar ice caps (e.g., Mars), (5) suspected ice deposits within impact basins (e.g., Mercury and Moon) (e.g., [6]), (6) volcanoes of diverse sizes and shapes (e.g., Venus and Mars), (7) putative ancient accreted terrains and associated volcanism (e.g., Mars), (8) regions indicating potential recent hydrologic or hydrocarbon activities such as spring-fed seeps (e.g., Mars, Titan), (9) chaotic terrain (e.g., source areas of the circum-Chryse outflow channel system on Mars, Conamara Chaos on Europa), (10) liquid pools of ammonia-water mixtures associated with cryovolcanism or a recent impact cratering event (e.g., Titan, Triton, Enceladus), and (11) liquid hydrocarbon accumulation on the surface (e.g., Titan). All of these geologic terrains, including many other regions of interest on the planetary bodies of the Solar System, are particularly crucial for astrobiologic-oriented exploration in general, and sample return missions in particular [5, 6, 20].

3. APPLICATIONS OF TIER-SCALABLE MISSION ARCHITECTURES

A multi-tier, hierarchical mission architecture would overcome the inherent challenge of traditional geologic planetary surface exploration [1-3]: airborne agents (orbiters in conjunction with balloons/blimps) possess overhead perspectives at different length scales/resolutions, which could provide guidance to ground-based agents (e.g., mobile rover units).

In case of the central part of Valles Marineris: Melas Chasma (Fig. 2), the following deployment and reconnaissance sequence of such a reconnaissance mission is envisioned (see [1, 2, 6, 21-23] for further detail): Orbiter(s) with an embedded existing knowledge base (e.g., *Multi-Layer Information System (MLIS)* [1-3]) scout areas of scientific interest at a global scale, i.e., within Valles Marineris and subsequently Melas Chasma. They subsequently deploy airborne agents such as balloons, blimps, or airships, which deploy in mid-air above Melas Chasma for further scouting and testing of hypothesized conditions. If one (or more) of the airborne agents were to detect scientifically interesting features, such as volatile releases (methane plume or water vapor) and/or elevated heat flow, or transient geologic events (e.g., a giant landslide that initiates on the walls of Valles Marineris), hydrologic events (e.g., water seeps), atmospheric events (e.g., reoccurring fog embankment in a specific part of the canyon system), and/or unique rock assemblages (other than the typically reported basaltic/basaltic-andesite, sulfates, and hematite, e.g., [24, 25]), this

airborne agent(s) would then attempt to map out, for example, methane concentration profiles and acquire terrain images of the locales of ancient and extant hydrothermal or gas release activity (i.e., potential source regions).

The information acquired from the airborne vantage would subsequently be processed through automated feature-extraction algorithms such as with the *Automated Geologic Field Analyzer (AGFA)* [7]. The feature data would be autonomously/automatically analyzed by science prioritization algorithms while en route (e.g., [7-11]). This includes coupling existing information with the newly acquired information for comparative analysis (e.g., using a fuzzy-based expert system), to choose potential targets for in-situ investigation and sampling by subsequently deployed ground-tier agents (small rovers, drill rigs, networks of sensors, etc.) and for determining safe passages to their respective designated targets within the prime sites, as identified from the airborne vantage. At the respective targets, the ground-tier agents would conduct in-situ science experiments and thereby gather data that complement the remote sensing data obtained by the airborne agents. For example, the ground-tier agents would help identify, characterize, and map out sources of the volatile plumes (e.g., potential sites of extant hydrothermal activity). In addition, such a system could help direct ground-tier agents, potentially equipped with drills, to a locale of extant hydrothermal activity that records distinct elevated heat flow, mineral assemblages, near surface groundwater, volatile seepage such as water and methane vapors, etc., thereby paving the way for future sample return missions [6, 20].

4. IMPLICATIONS

Multi-tier multi-agent autonomous robotic planetary surface/subsurface reconnaissance will lead to an improved understanding of the various histories (e.g., geologic, geomorphic, pedologic, aqueous, climatic, and possible biologic) of Mars and other extraterrestrial targets, through the tier-scalable geologic approach. Importantly, this new paradigm in planetary reconnaissance will integrate disciplines such as geology, biology, chemistry, physics, mathematics, and engineering, allowing for optimal reconnaissance and testing of overarching theories [26]. This includes confirming working hypotheses such as in the case of Mars, whether (a) the mountain ranges contain a greater diversity of rock types than just volcanic; (b) sites of suspected hydrothermal activity are indeed hydrothermal environments; (c) prime candidate sites of potential life-containing habitability actually contain extant or fossil life or life forms [16, 27, 28]; or (d) close examination of surface/buried soils with sensors suitable for microscopic observation and chemical analysis of coatings on weathered sands might reveal important data on possible soil microenvironments, live microbes, or fossil forms (e.g., [28, 29]). Moreover, tier-scalable autonomous reconnaissance missions afford a first-of-a-kind opportunity to scout, discover, and characterize potential habitats and possible life [6, 20].

Prioritization frameworks for single and multiple (science) targets such as introduced in [8] may be useful for autonomously operating computer-based planning systems (e.g., onboard science craft such as satellite platforms, spacecraft, planetary orbiters, landers, rovers, etc.) to decide which previously detected and coarsely examined target or set of targets harbor the greatest potential for an overall "knowledge gain" about an operational area if revisited or examined more closely. In addition, prioritization frameworks for (science) instrument usage such as introduced in [8] may provide guidance as to which instrument out of a suite of available instruments onboard a science platform has the largest potential to contribute to the above "knowledge gain" if used on these targets. Since instruments may differ in power consumption, time of data acquisition (including total time to take measurements), and distance from the object to be examined (i.e., spatial association between instrument and target), etc., a planning system can take into account these constraints together with the prioritization probabilities and may come up with optimized "target-to-reexamine" and "instrument-to-use-for-reexamination" scenarios, thereby paving the way to more autonomous reconnaissance missions.

5. DISCUSSION & OUTLOOK

Following the published works by Fink et al. [1-3], NASA is now soliciting proposals calling for technology development of *"Sensor webs of the future [that] may include space-based, airborne, and in-situ sensors, all working together in a semi-closed loop system in which "smart" sensors sense what is happening per their designed sensing capabilities and feed that information into a control system. Based on the sensor inputs, the control system then modifies the environment (instrument pointing, data collection on or off, etc.) and causes the sensors to take in and provide new information to the control system."* (excerpt from Science Mission Directorate NASA Research

Announcement "Advanced Information Systems Technology" Solicitation: NNH05ZDA001N-AIST). Moreover, in testimony to Congress in May 2005, NASA Administrator Michael Griffin included the following statement: *"In the future, NASA plans to develop a "sensor web" to provide timely, on-demand data and analysis to users who can enable practical benefits for scientific research, national policymaking, economic growth, natural hazard mitigation, and the exploration of other planets in this solar system and beyond."* This followed the release of the February 2005 publication *The New Age of Exploration: NASA's Direction for 2005 and Beyond* that stated: *"NASA will develop new space-based technology to monitor the major interactions of the land, oceans, atmosphere, ice, and life that comprise the Earth system. In the years ahead, NASA's fleet will evolve into human made constellations of smart satellites that can be reconfigured based on the changing needs of science and technology. From there, researchers envision an intelligent and integrated observation network comprised of sensors deployed to vantage points from the Earth's subsurface to deep space. This "sensor web" will provide timely, on-demand data and analysis to users who can enable practical benefits for scientific research, national policymaking, economic growth, natural hazard mitigation, and the exploration of other planets in this solar system and beyond."*

There are individual components of the tier-scalable mission architecture proposed by Fink et al. [1-3, 21], which are either under development or have already been tested and proven in the "field". These include orbiters, balloons/blimps/airships (although not tested in a space environment so far), and ground-based agents such as rovers and landers as well as immobile sensor webs. The biggest challenge, however, appears to be not so much the hardware but the "intelligent" software that would enable all the components of a multi-tier multi-agent mission to be integrated and function autonomously. Some of the authors of this contribution are developing software (e.g., [7-11]) that would allow the orbiters, blimps, and rovers both to communicate with one another and to navigate and explore the planetary terrain with greatly reduced (and ultimately without) help from mission control on Earth, thus affording more mission autonomy/flexibility and increased science return.

We believe that it is possible to develop, test, and have ready multi-tier multi-agent hierarchical mission architectures within a 10-15 year timeframe to home in on prime targets such as potential volatile-enriched targets (e.g., water and methane sources), which include candidate sites of endogenic-driven hydrothermal activity on Mars. Integrated orbiter-airship missions, especially suitable for the exploration of Mars, Venus, and Titan, are envisioned to be feasible within a decade from now. Subsequent science-driven robotic exploration will couple this new paradigm in planetary reconnaissance with astronautic exploration and research.

6. REFERENCES

1. Fink W., et al., Next-Generation Robotic Planetary Reconnaissance Missions: A Paradigm Shift, *Planetary and Space Science*, 53, 1419-1426, 2005.
2. Fink W., et al., Next-Generation Robotic Planetary Surface/Subsurface Reconnaissance Missions: A Paradigm Shift [abstract 1977], in *36th Lunar and Planetary Science Conference Abstracts [CD-ROM]*, Lunar and Planetary Institute, Houston, 2005.
3. Fink W., et al., Next-Generation Robotic Planetary Reconnaissance Missions: A Paradigm Shift, *Geochimica et Cosmochimica Acta*, Volume 69, Number 10S, A533, 2005.
4. http://autonomy.caltech.edu/autonomy/tierscalable.html (by W. Fink).
5. Schulze-Makuch D. and Irwin L.N. *Life in the Universe: Expectations and Constraints*, Springer, 2004.
6. Schulze-Makuch D., et al., Venus, Mars, and the Ices on Mercury and the Moon: Astrobiological Implications and Proposed Mission Designs, *Astrobiology*, 5, 778-795, 2005.
7. Fink W., et al., AGFA: (Airborne) Automated Geologic Field Analyzer, *Geochimica et Cosmochimica Acta*, Volume 69, Number 10S, A535, 2005.
8. Fink W., Generic Prioritization Framework for Target Selection and Instrument Usage for Reconnaissance Mission Autonomy, *Proceedings of IEEE World Congress on Computational Intelligence (WCCI) 2006*, Vancouver, Canada, 11116-11119.
9. Furfaro R., et al., Multi-Layer Fuzzy Logic-based Expert System for Conducting Tier-scalable Planetary Reconnaissance [abstract 1257], in *37th Lunar and Planetary Science Conference Abstracts [CD-ROM]*, Lunar and Planetary Institute, Houston, 2006.
10. Furfaro R., et al., Fuzzy Logic Expert System for Tier-scalable Planetary Reconnaissance, *9th International Conference on Space*

Operations, AIAA, Rome, Italy, June 19-23, 2006.
11. Furfaro R., et al., Autonomy in Planetary Exploration: Fuzzy Expert System for Tier-Scalable Reconnaissance, abstract *25th International Space Development Conference 2006*, Los Angeles.
12. Duda, R.O., et al., *"Pattern Classification and Scene Analysis"*, John Wiley & Sons, 2nd edition, 2000.
13. Bishop, C.M., *"Neural Networks for Pattern Recognition"*, Clarendon Press, Oxford, 1995.
14. Williams, C.K.I., "An MCMC Approach to Hierarchical Mixture Modelling", *Advances in Neural Information Processing Systems* 12, S. A. Solla, T. K. Leen, K.-R. Mueller, eds., MIT Press, 2000.
15. Fink, W., et al., Clustering Algorithm for Mutually Constraining Heterogeneous Features, *Technical Report JPL-ICTR-01-5*, 2001.
16. Dohm, J.M., et al., The Northwestern Slope Valleys (NSVs) region, Mars: A prime candidate site for the future exploration of Mars, *Planetary Space Science*, 52, 189-198, 2004.
17. Dohm, J.M., et al., Geologic map of the Thaumasia region of Mars. *US Geol. Survey Map I-2650*, 2001.
18. Dohm, J.M., et al., Ancient drainage basin of the Tharsis region, Mars: Potential source for outflow channel systems and putative oceans or paleolakes, *J. Geophys. Res., 106*, 32 943-32 958, 2001.
19. Dohm, J.M., et al., Latent activity for western Tharsis, Mars: significant flood record exposed, *J. Geophys. Res., 106*, 12,301-12,314, 2001.
20. Schulze-Makuch D., et al., Sample Return Missions to Mars, Venus, and the Ices on Mercury and the Moon [abstract 1324], in *37th Lunar and Planetary Science Conference Abstracts [CD-ROM]*, Lunar and Planetary Institute, Houston, 2006.
21. Fink W., et al., Multi-tier Multi-agent Autonomous Robotic Planetary Surface/Subsurface Reconnaissance For Life [abstract 1433], in *37th Lunar and Planetary Science Conference Abstracts [CD-ROM]*, Lunar and Planetary Institute, Houston, 2006.
22. Dohm J.M., et al., Tier-scalable Reconnaissance To Test Overarching Geological Theories and Locate Prime Targets on Mars, abstract *25th International Space Development Conference 2006*, Los Angeles.
23. Fink W., et al., Tier-Scalable Reconnaissance for Remote Planetary Exploration, abstract *25th International Space Development Conference 2006*, Los Angeles.
24. Christensen P.R., et al., Morphology and composition of the surface of Mars: Mars Odyssey THEMIS results, *Science*, 300, 2056-2061, 2003.
25. Gendrin A., et al., Sulfates in Martian Layered Terrains: The OMEGA/Mars Express View, *Science, 307*, Published online 17 February 2005; 10.1126/science.1109087, 2005.
26. Baker, V.R., et al., A theory of early plate tectonics and subsequent long-term superplume activity on Mars, *Superplume International Workshop*, 312-316, 2002.
27. Fairén, A.G., et al., Prime candidate sites for astrobiological exploration through the hydrogeological history of Mars, *Planetary Space Science*, 53, 1355-1375, 2005.
28. Mahaney, W.C., et al., Ancient wet aeolian environments on Earth: clues to presence of fossil/live microorganisms on Mars, *Icarus*, 171: 39-53, 2004.
29. Mahaney, W.C., et al., Morphogenesis of Antarctic paleosols: martian analogue, *Icarus*, 154: 113-130, 2001.

DEVELOPMENT OF AUTOMATION & ROBOTICS IN SPACE EXPLORATION

27 - 30 June 2006, Pasadena, California, USA.

Paul Acquatella[(1)]

[(1)]INSA Lyon – Bat. H -410. 20, Av. Albert Einstein, 69100 Villeurbanne, France. - paul.acquatella@gmail.com

Abstract

Since the beginning of space exploration, the space community had the common belief that in the near future, the Automation & Robotics will be an important element for such missions. Today, this has become a reality. The implementation of this technology will play an important role in future missions, as robotic systems and "Artificial Intelligence" keeps developing further. The development of robotics arms as Canadarm and the ERA are citated as examples of contribution this kind of technology has made and how it will influence in the future. The main discussion in this paper is how this technology has been implemented in space exploration and how it will continuously keep contributing in such missions. A brief state of the art of how this technology has contributed to the space missions and a future approach for the coming years is proposed.

1. INTRODUCTION

Space exploration has been tremendously marked by the development of Automation & Robotics (A&R). Since the beginning of space exploration, the space community held the common belief that in the near future, the A&R will be an important element for such missions [1]. Today, we've seen this become a reality with all the applications and functionalities achieved as well as through the implementation of this technology in the space missions. The growth and evolution of complex spacecraft and space exploration missions demands a fast development of intelligent automated systems and robotic devices. This technology has to be adapted and developed in sense of reaching specific goals.

Robotics enables the exploration on orbit, deep space and planetary surfaces missions in addition to serving as a tool for complex in-space activities and missions. The development of this technology throughout the years has permitted an immense achievement in space missions and will continue to be an important and essential contributor to these activities.

For a successful development of space projects, A&R is a key technology. Automated processes and efficient robot implementation could lead to a better achievement in space missions, helping with their wide functionality and reducing the astronaut's workloads thus improving efficiency.

2. SPACE ROBOTICS

The "space robotics" is in many ways quite different than the standard "terrestrial" robots. In simplistic terms, the main difference would be the lack (or lower) of gravity, which is an important fact to consider in the whole system design reducing dynamic loads.

Fig. 1. The Canadarm2

It all begun with robots like the Surveyor, Mariner, Ranger and Lunakhod [2]. Since then, many proposals for robotic and automated applications in space missions have appeared. There is a wide range of functionalities and applications of robots in space; they can be listed as in [1]:

- Low Earth Orbit – Intra Vehicular Activities (IVA)

  - Payload Operations
    - Load/unload samples
    - Exchange measurement instrumentation
    - Inspect/monitor samples
    - Exchange of life – limited items

  - Payload Servicing
    - Preventive maintenance
    - Corrective maintenance
    - Cleaning
    - Diagnostics assistance
    - Calibration

  - Spacecraft Servicing
    - Inspection
    - Item replacement
    - Module exchange
    - P/L reconfiguration
    - Repairing

- Low Earth Orbit – Extra Vehicular Activities (EVA)

  - Mobile platform for EVA astronaut
  - ORU exchange
  - Inspection/diagnostics
  - Mechanical assistance
  - Connect/disconnect
  - Capture & berthing

- Polar Orbit

  Similar tasks as EVA in LEO, and in addition:

  - Instrument reconfiguration/exchange
  - Contingency assistance (deployment)

- Geostationary Servicing - GSV

  - Deployment assistance
  - Inspection, diagnostics assistance
  - Capture & berthing
  - Graveyarding

- Planetary surface exploration

  - Rovering
  - Instrument deployment
  - Sampling, shoveling
  - Building infrastructure

A&R will permit in an early future to have more "intelligent" space stations reducing the workload of astronauts, this will permit to improve efficiency.

3. ROBOTICS IN LOW EARTH ORBIT

The Low Earth Orbit (LEO) has been the domain of most manned spaceflights. Some of the spacecraft and space stations belonging to this class are the US Skylab, the Space Shuttle, the International Space Station, and the Russian space station Mir.

In LEO there are most of the in-space A&R applications, such as component assembly, maintenance and inspection, component replacement, and experiments in microgravity, which is the main purpose in such missions: research.

3.1 Intra-Vehicular Activity (IVA)

The Intra vehicular activities are all those related to payload operations, payload servicing and spacecraft servicing, as well as inspection and maintenance activities inside the spacecraft in space missions.

For example, the NASA has developed several concepts for IVA and microgravity experiments, as the Charlotte in 1995, and recently a concept for an internal payload tending robot to automate the routine logistics operations of microgravity facilities in the International Space Station called the Payload Tutor (PAT). It consists on a short 1 m. arm with five rotatory axes mounted on a vertical rail in front of a payload rack [3]. Once the robot has been "plugged in", no astronaut intervention is necessary anymore, since its routine payload tending operations will be automatically executed with high level commanding and monitoring from ground. The PAT concept allows to free the crew from tedious, repetitive payload tasks and thereby considerably increase the efficiency, cost and accuracy of standard payload operations.

Also, regarding the problem of the human resources shortage in space, especially in the International Space Station (ISS), NASA developed a small free flyer robot for IVA support, the PSA (Personal Satellite Assistant) which is equipped with several sensors and cameras and can easily communicate with the crew and observe experimental setups inside the ISS (figure 2).

In Japan, a new Intra-Vehicular Free Flyer System (IVFFS) was proposed in 2003 [4]. It has a mobility function similar to that of the PSA, and in addition, there is a manipulation function as well (allowing to perform contact tasks). A prototype called "Space Humming Bird" (SHB) has been introduced. It has a variably structured body which can adapt to and

perform various tasks and multiple SHB's can be combined to realize more complex tasks.

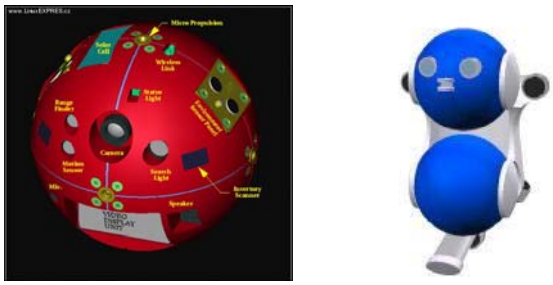

(a) (b)

Fig. 2. (a) the PSA. (b) IVFFS prototype SHB

Some other previous concepts have been developed for older missions and experiments as the German ROTEX robotic arm developed in 1993 by the DLR and the EMATS/AMTS developed by ESA for the European laboratory of the ISS which essentially consisted of one 7 - axes dexterous 2 m. arm whose base could move throughout the central aisle of the laboratory on a 3 – axes Cartesian gantry system [5]. However this concept was stopped before going into detailed design and manufacturing. Some other concepts for in-module experiments have been developed by ESA, as the BIOROB.

3.2 Extra-vehicular activity (EVA)

Regarding extra vehicular activities, many A&R systems have been designed. By using such robots, risk related to astronaut's EVA are reduced. The applications of this kind of robots are related to:

- Inspection/diagnostics
- Mechanical assistance
- Connect/disconnect
- Capture & berthing

Dextre [6], a recently concept for maintenance and servicing in EVA operations, will be launched to the International Space Station in 2007 (Fig.3). Developed by the Canadian Space Agency, Dextre works by grabbing an ISS stabilization point to anchor itself. It will do the hard and delicate tasks in EVA that astronauts are capable of, reducing their long and exigent activities outside de station, permitting them to dedicate more time for inside operation or IVA.

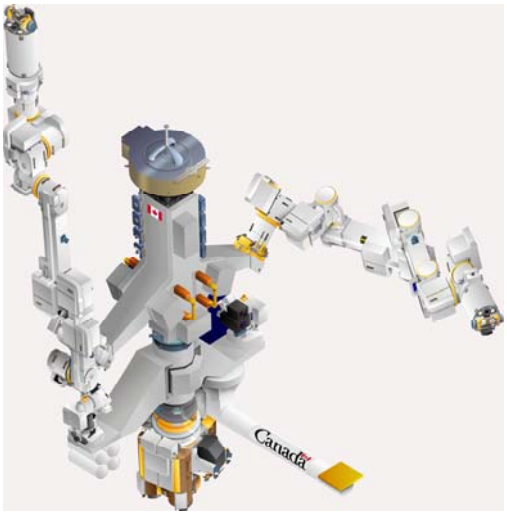

Fig. 3. The DEXTRE

3.2.1 Space Shuttle robotics

The Remote Manipulator System (RMS), or Canadarm (Fig. 4), is the most known and famous robot in the space. It is used in widely applications but most common are for in-space assembly operations, releasing satellites into space and for EVA support. The capture and repair of the Hubble Space Telescope has been possibly the most impressive use of the RMS [5]. It consists of a 480 kg. – 15 m. length robotic arm capable of transporting and operate payloads of 30.000 kg.!

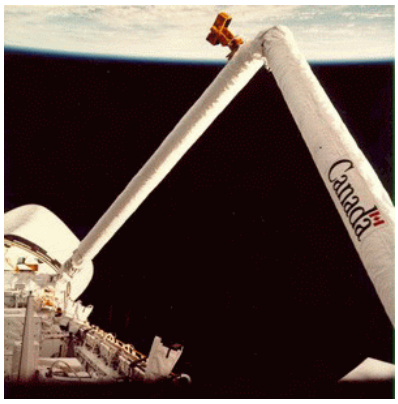

Fig. 4. The RMS

3.2.2 Robotics in the Russian space station MIR

For the Russian Space Station "MIR" there have been also wide robotic applications for system servicing, assembly and inspection operations.

PELIKAN, developed in Russia in 1998 it's an external system servicing robot, to install and remove

payloads. Also JERICO (Fig. 5) developed in 1999 by ESA, an external payload tending and inspection robot [5].

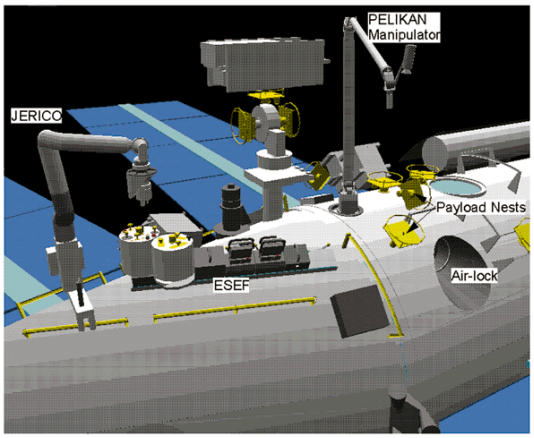

Fig. 5 PELIKAN and JERICO in MIR

3.2.3 Robotics in the International Space Station

The International Space Station (ISS) offers a unique infrastructure to enable scientists and engineers to conduct their experiments over a large timescale and to gain experiment results on a regular basis [futapps]. For a number of reasons, manipulative tending of payloads and servicing of the Space Station system elements cannot be completely performed by astronauts. This is why robotic systems are expected to play an ever increasing role in the operation of the ISS.

As mentioned in the survey paper [5], the applications of robotics on the ISS can be classified into four categories:

-Internal payload tending robots to automate the routine logistics operations of microgravity facilities (as seen before in the IVA section).
-External payload tending robots, doing the same for facilities on exposed payload platforms like the JEM-RMS (Japan), and the PELIKAN (Russia) and the EVA robots we've mentioned before.
-External system servicing robots with attached base, used to assemble larger Space Station structures and to exchange whole modules or platforms.
-External system servicing robots on free flying vehicles, for inspection and maintenance of Space Station elements.

There are three main robotic elements in the ISS (Fig. 6). The Space Station Remote Manipulator System (SSRMS) developed in Canada, a 7- m., 7-DOF robotic arm. The Special Purpose Dextrous Manipulator (SPDM), a smaller 2- m., 7- DOF robotic arm that can be used independently, or attached to the end of the SSRMS. And the Mobile Base System (MBS) which is used as a support platform and will also provide power and data links for both the SSRMS and the SPDM [7].
The MSS is used for assembly, external maintenance, to deploy, service, and retrieve external payloads on the Space Station.

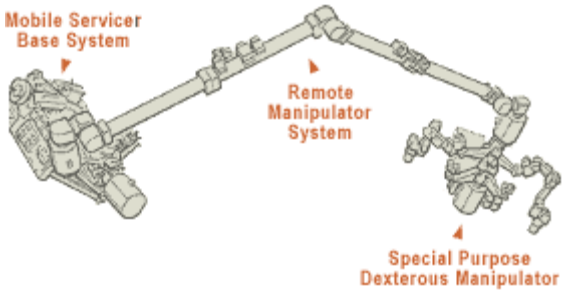

Fig. 6. ISS Remote Manipulator System

Also, for the Russian modules of the ISS, the European Robotic Arm (ERA) has been developed by ESA in 1999. It consists of a 630 Kg, 11.3 m. length robotic arm (Fig 7). ERA [9] is designed to perform missions like:

-Assembly of large station elements
-Installation and exchange of ORU's.
-Support to EVA astronauts in a variety of tasks.
-Installation of scientific payloads.
-Inspection of the Space Station exterior.

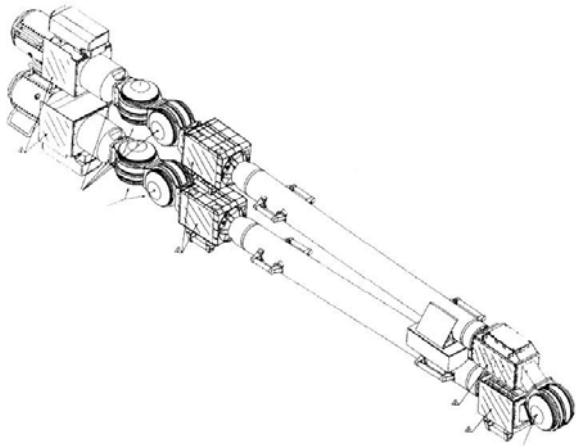

Fig. 7. ERA in folded configuration.

We can also find some external system servicing robots (from a free flying base) for systematic inspection of

the Space Station shell and for preventive/corrective maintenance like the OMV, the Ranger and the Spider [5].

3.2.4 In-space experiments

The in-space experiment is a field which evolutes real fast as A&R technologies and Artificial Intelligence (AI) concepts keeps developing more and more within the years. The Ranger [2], which was developed in the US to repair and upgrade orbiting satellites, particularly the Hubble, is one beautiful example of robotics applications in space operations. In fig. X a ground testbed for the Ranger to simulate the repairing of the Hubble Telescope is showed.

Fig. 8. A diver works on a model of the Hubble Telescope, assisted by the Ranger robot.

Other space robots for experiments such as ROTEX [8] and AERCam, has demonstrated dexterous operations and the usefulness of tele-operated robots for inspection tasks. Ground testbeds have demonstrated teleoperated robots performing fine assembly operations, like the Robonaut [2] developed by NASA (Fig. 9). The Robonaut project seeks to develop and demonstrate a robotic system that can function as an equivalent EVA astronaut. It has five-fingered, multi-jointed hands permitting to work with a real human mobility.

Fig 9. Robonaut

4. ROBOTICS IN GEOSTATIONARY EARTH ORBIT (GEO)

The Geostationary Earth Orbit (GEO) is where most communication and Earth observation satellites are placed. The orbit is important because it allows a satellite to orbit the earth at a fixed point viewed from the earth, so communications and earth observations are well suited with this orbit. Regarding the geostationary servicing robots, there have been concept studies for Geostationary Vehicles (GSV) which flies around GEO performing operations such as:

- Deployment assistance
- Inspection, diagnostics assistance
- Capture & berthing
-Graveyarding

In 1998 Japan developed the Engineering Test Satellite ETS -7 to perform simple repair tasks in GEO. Also in Germany, the Experimental Servicing Satellite (ESS) was developed for a servicing demonstration and de-orbiting of expired satellites.

5. ROBOTS FOR PLANETARY SURFACE EXPLORATION

Planetary surface exploration is another domain of research in space missions. A&R are widely applied in this field. Actually, most of these kinds of missions are unmanned, so this is viewed as a big challenge for A&R systems.

The robots for this category are expected to do such activities as:

- Rovering
- Instrument deployment

- Sampling, shoveling
- Building infrastructure
-Search for life

The pioneers are the Lunakhod 1&2 (Soviet Union, 1970-1973 respectively) which were developed to explore, rove, deploy instrument, and for sample collection [5]. Also the Viking arm (NASA, 1976) for the same purposes and in addition to search for past life.

Concerning Mars exploration, since the successful and popular Pathfinder mission by NASA, many concept studies have been treated to explore this planet. The most representative is the Sojourner, launched almost ten years ago in 1997 [1], also there is the family of Mars Exploration Rovers (Fig. 10), which are optimized versions of previous rovers. They are both autonomous within small local segments, with images sent back from Mars each day and a rigid sequence of robot motions uploaded for the following day. MERs will be more capable due to a larger size, greater science instruments, and a better communications infrastructure, but otherwise will be operated in a similar manner.

Fig. 10. Mars Exploration Rover

In Mars exploration there is also the proposals from Russia and Germany: The Marsokhod and the Nanokhod, respectively.

Some studies for comet/asteroid landing have been developed as well. For example the Rosetta Satellite (Fig 11) by ESA [5] which will be the first space mission to journey beyond the main asteroid belt.

Fig. 11. The Rosetta Satellite

Shortly after its arrival at the comet, the Rosetta Orbiter will dispatch a robotic Lander (Fig. 12) for the first controlled touchdown on a comet nucleus.

As it arrives on the comet, the Rosetta Lander uses three different techniques (self-adjusting landing gear, harpoons and a drill) to ensure that once it has arrived on the surface of the comet, it stays there [10].

Fig. 12. The Rosetta Lander

6. CONCLUSIONS

This “review” paper has showed and summarized the different A&R applications in space missions, and the evolution of robotic devices for spatial research. It gives a brief overview of the most impressing robots sent to space and some of the ground testbed for future research.

The space robotics has been and will always be necessary as an important key for space missions. Due to the development of the technology concerning A&R, space robots will keep being proposed for many purposes, and in a near future, most of them will highly assist in-space operations and reduce the “low intelligence” tasks of astronauts and allow safer EVA operations, for instance.

Planetary exploration seems to be a field which will be more and more researched since actual rovers are very effective in this kind of missions. Also, the

research on asteroids and comets will be an important field of research in the near future.

For a future approach, as space robots go further and further, many others applications and technologies should be studied. For instance, nanotechnology applied in small robots for surface exploration could lead to future mission's approaches. On the other hand, artificial intelligence could contribute by making space robots "learn" while being in orbit, creating smart robots "communities" which would be more and more independent from human assistance to do their tasks. Also, flying deployable robots for surface inspection, observation and exploration with solar array-wings are expected to be studied further.

7. REFERENCES

[1] W. De Peuter. Development programme on space automation and robotics. Intl Symposium "Artificial Intelligence, Robotics and Automation in Space". Toulouse, September 1992.

[2] L.Pedersen, D. Kortenkamp, D. Wettergreen, I. Nourbakhsh. *A survey of Space Robotics*. NASA Exploration Team. 2003

[3] S. Di Pippo, G. Colombina, R. Boumans, P. Putz. *Future potential applications of robotics for the International Space Station*. Journal of Robotics and Autonomous Systems 23 (1998) 37 – 43.

[4] Y. Tsumaki, M. Yokohama, D. Nenchev. *Intra-Vehicular Free-Flyer System*. Proceedings of the 2003 IEEE/RSJ Intl. Conference on Intelligent Robots and Systems. Las Vegas, Nevada. October 2003.

[5] P. Putz. *Space robotics in Europe: A survey*. Journal of Robotics and Autonomous Systems 23 (1998) 3-16.

[6]http://www.space.gc.ca/asc/fr/iss/mss_spdm.asp

[7] C. Sallaberger. *Canadian Space Robotic Activities*. Elsevier Acta Astronautica Vol. 41. pp 239 246, 1997.

[8] B. Hannaford, A. Bejczy, P. Buttolo, M. Moreyra, S. Venema. *Mini-Teleoperation Technology for Space Research*. Proceedings of MIMR-95, Sendai Japan, September 1995.

[9] R. Boumans, C. Heemskerk. *The European Robotic Arm for the International Space Station*. Journal of Robotics and Autonomous Systems 23 (1998) 17- 27.

[10] World wide web. www.esa.int

Interplanetary Mission Design Using Multi-Disciplinary Design Optimization

Richard J. Baun and Dr. Periklis Papadopoulos
Department of Mechanical and Aerospace Engineering
San José State University
One Washington Square
San Jose, CA 95192-0080, USA

ABSTRACT

A detailed discussion is presented for a software tool developed to conduct interplanetary mission design trade studies and to identify optimum mission parameters. The Interplanetary Design Framework Software (IDFS) code supports these trade studies by determining optimum interplanetary missions using a diverse set of user inputs. A Graphical User Interface accepts trade parameters selected from the IDFS database or from direct user input. Both graphical and tabular output is provided. IDFS core components include: (i) Launch vehicle performance calculation, (ii) Planetary ephemeris propagation, (iii) Planetary position and velocity vector computation, (iv) Interplanetary trajectory determination, (v) Delta velocity calculation, (vi) Usable payload mass and time of flight computation, and (vii) Optimization of delta velocity, usable payload mass, and time of flight using Multidisciplinary Design Optimization (MDO) techniques. Benchmarking results are also presented. Finally, IDFS is utilized to identify an optimum interplanetary mission and the trade results are presented, discussed, and evaluated.

1. INTRODUCTION

Not since the Apollo Program of the late 1960s and early 1970s has there been such an earnest effort to place men on the surface of a distant body. This is due in large part to President George W. Bush's 2004 announcement of an initiative to explore Mars via a permanent Moon base [1]. The President's proposal, in conjunction with the recent backing of Congress, places both manned and unmanned interplanetary travel at the forefront of future space endeavors [2].

In parallel with the renewed interest in interplanetary exploration, the MDO technique has continued to come to the forefront as a formal method used in the design of complex systems. MDO allows the effects of coupling between various interacting design variables to be numerically explored and the sensitivity of a design to each factor to be investigated.

Several numerical MDO methods currently exist and are well documented in the public domain. Further, there exists a serious worldwide effort to expand MDO technology and theory. For example, the AIAA has formed a technical committee to act as a forum for those active in development, application, and teaching of MDO. Similarly, NASA-Langley has an MDO branch whose mission is to lead in the identification, development, and demonstration of MDO methods.

While the Moon and Mars are the current focus of NASA planning, several other possible interplanetary missions are also of extreme interest. Saturn's moons Enceladus and Titan and Jupiter's moon Europa are of particular significance due to the likely presence of liquid water on the surface of those bodies [3]. As Jupiter is the closest of the outer planets, robotic "Mars like" missions to explore that planet and her many intriguing satellites must also be seriously considered.

Motivated by the heightened interest in interplanetary missions, the myriad of other possible high value interplanetary missions, and the rise of MDO, a software tool has been developed. The tool, known as IDFS, enables first order analysis of interplanetary mission design trade studies to be conducted efficiently and accurately. In addition, IDFS uses MDO methods to allow the complex trade space of interplanetary missions to be readily evaluated numerically.

2. BACKGROUND

The IDFS tool, whose high level flow is illustrated by Figure 1, is a MATLAB® based software program. IDFS is principally comprised of a mathematical model that determines a series of transfer orbit trajectories from Earth to any planet in the solar system across a user specified launch and arrival day windows. The corresponding departure and arrival ΔVs, departure and arrival propellant requirements, launch and arrival dates, and the resulting Payload System Mass (PSM) are computed for each unique trajectory. The results produced by this model are then analyzed, using the Simplex and Matrix Experiment MDO techniques, to identify the most advantageous case. The optimum case identified is a function of the user inputs and which of the six optimization options identified below is selected by the user.

- Find maximum Payload Systems Mass
- Find minimum Time of Flight
- Goalseek Payload System Mass

- Goalseek Time of Flight
- Find minimum Time of Flight for a given Payload System Mass
- Optimize Low Earth Orbit Altitude for Maximum Payload System Mass

2.1. METHODOLGY

At a high level, IDFS uses a MATLAB® mathematical model to calculate launch vehicle performance, determine planetary positions, identify interplanetary trajectories, compute ΔVs, derive propellant and payload system masses, and determine of the resulting optimum mission as outlined below:

- Launch vehicle performance – The Energy equation or a curve fit to manufacturer performance data
- Planetary orbital position – Keplerian orbit elements
- Interplanetary trajectories – Lambert's Problem
- ΔV computations – Patched-Conic Approximation
- PSM derivation – Rocket engine equation
- Optimum case determination – MDO Simplex and Matrix Experiment techniques

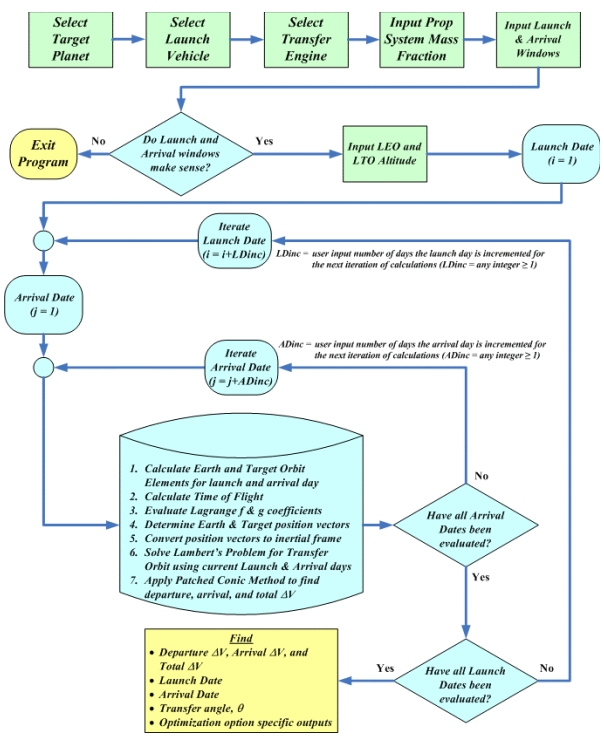

Fig. 1: IDFS High-Level Flow Diagram

2.1.1. Launch Vehicle Performance

IDFS allows the user to either select one of 12 launch vehicles from a database or to input launch vehicle performance directly. For the provided launch vehicles, performance is modeled using one of two approaches; performance curves or the energy equation.

For those launch vehicles that have published performance curves, the Least Squares Fit utility provided by MATLAB® is used to derive a second order mass to LEO altitude. These equations provide the launch vehicle throw weight, in kg to LEO where LEO altitude, h in kilometers, is input by the user. The performance as a function of altitude, known as Total System Mass (TSM) or $m_{TSM,}$ for 3 of the launch vehicles is provided by the Eqns. 1-3 below [4]-[6].

$$m_{TSM\text{-}AtlasV} = 21436.632 - 4.638h + 0.00064h^2 \quad (1)$$

$$m_{TSM\text{-}Angara5} = 25543.911 - 5.359h + 0.0007h^2 \quad (2)$$

$$m_{TSM\text{-}DeltaIV} = 25712.256 - 3.546h + 0.00024h^2 \quad (3)$$

Performance estimates for the remaining launch vehicles use the circular orbit velocity equation, (Eq. 4), the energy equation (Eq. 5), and manufacturer performance data. Once the energy to the reference orbit is known, the performance (m_{TSM}) to any low Earth orbit can be approximated by assuming E is constant, using the user provided altitude h, and Eq. 5 to derive a result for the total system mass, m_{TSM}. Eq. 6 shows the result of this derivation.

$$v = \sqrt{\mu_{earth} \big/ (r_{earth} + h)} \quad (4)$$

$$E = \frac{1}{2} m_{TSM} v^2 + m_{TSM} gh \quad (5)$$

$$m_{TSM} = \frac{2E}{v^2 + 2gh} \quad (6)$$

2.1.2. Planetary Position Calculation

Six Keplerian orbit elements are used to calculate the heliocentric radius vector of the Earth and the target planet for each Launch Day/Arrival Day pair. The six elements include: 1) Semi-major axis, a; 2) Inclination, i; 3) Eccentricity, e; 4) Longitude of the Ascending Node, Ω; 5) Longitude of Perihelion, $\tilde{\omega}$; and 6) Mean Longitude, L. The J2000 values and change rates per day for each of the six elements for all nine planets are obtained from NASA-Goddard's website [7].

To compute planetary position IDFS acquires the launch and arrival window dates from the user in the Gregorian calendar format. IDFS converts the launch

and arrival dates to Julian format and propagates the six orbit element values from epoch forward in time. Eqns. 7 and 8 calculate the elapsed time since the epoch with T_1 = launch day at Earth (elements with a subscript of 1) and T_2 = arrival day at the target (elements with a subscript of 2). Eqns. 9-10 illustrate orbit element propagation forward from the epoch.

$$T_1 = LaunchDay - epoch \tag{7}$$

$$T_2 = ArrivalDay - epoch \tag{8}$$

$$a_1 = \left(a_{epoch1} + a_{rate1}\right)T_1 \tag{9}$$

$$a_2 = \left(a_{epoch2} + a_{rate2}\right)T_2 \tag{10}$$

After the Earth and target orbit elements are updated to the launch and arrival days, Mean Anomaly, M, Eccentric Anomaly, E, and True Anomaly, ν are calculated as shown by Eqns. 11-13. Using True Anomaly from Eq. 13, the heliocentric radius vectors for earth and the target are computed using Eqn. 14. The heliocentric Cartesian coordinates for the planetary radius vectors **r** (r_x, r_y, and r_z) are given by Eqns, 15 – 17 [8]. Note Eqn. 12 is solved by Newton's Method.

$$M = L - \tilde{\omega} \tag{11}$$

$$E = E - e\sin(E) \tag{12}$$

$$\nu = 2\left(a\tan\left[\tan\left(\frac{E}{2}\right)\sqrt{\frac{(1+e)}{(1-e)}}\right]\right) \tag{13}$$

$$r = a\left[\frac{1-e^2}{1+e\cos(\nu)}\right] \tag{14}$$

$$r_x = r\left[\cos(\Omega)\cos(\nu+\tilde{\omega}+\Omega) - \sin(\Omega)\sin(\nu+\tilde{\omega}-\Omega)\cos(i)\right] \tag{15}$$

$$r_y = r\left[\sin(\Omega)\cos(\nu+\tilde{\omega}+\Omega) + \cos(\Omega)\sin(\nu+\tilde{\omega}-\Omega)\cos(i)\right] \tag{16}$$

$$r_z = r\left[\sin(\nu+\tilde{\omega}-\Omega)\sin(i)\right] \tag{17}$$

Following Earth and target heliocentric radius vector calculation, the heliocentric velocity vectors are found for both planets. The magnitude of the velocity vector is determined using Eq. 18. The result of Eq 18 is used in Eqns. 19 – 21 to find the heliocentric x, y, and z components of the two velocity vectors [8].

$$V = \sqrt{\mu_{sun}\left(\frac{2}{r} - \frac{1}{a}\right)} \tag{18}$$

$$V_x = V\left[-\cos(\Omega)\sin(\nu+\tilde{\omega}+\Omega) - \sin(\Omega)\cos(\nu+\tilde{\omega}-\Omega)\cos(i)\right] \tag{19}$$

$$V_y = V\left[-\sin(\Omega)\sin(\nu+\tilde{\omega}+\Omega) + \cos(\Omega)\cos(\nu+\tilde{\omega}-\Omega)\cos(i)\right] \tag{20}$$

$$V_z = V\left[\cos(\nu+\tilde{\omega}-\Omega)\sin(i)\right] \tag{21}$$

2.1.3. Interplanetary Trajectory Determination

IDFS utilizes a MATLAB® math model that solves Lambert's Problem to calculate the interplanetary trajectories. This approach allows the minimum energy trajectory to be found, using time of flight and the two planetary positions, even though an infinite number of trajectories exist between departure and arrival points.

IDFS begins at the first day in the launch window and calculates the Earth's position for that day as described above. Similarly, the target's position is calculated for the first day in the arrival window. Time of Flight (ToF) is determined from the elapsed time between those two days. Once the time of flight, t_f and the departure arrival positions are known, the solution to Lambert's Problem is determined using Lagrange's formulation (Eq. 22), where N is the number of revolutions about the sun for the transfer orbit, and α and β are defined by Eqns. 23 and 24 [9].

$$t_f = \sqrt{\frac{a^3}{\mu_{sun}}}\left[2N\pi + \alpha - \beta - \left(\sin(\alpha) - \sin(\beta)\right)\right] \tag{22}$$

$$\sin(\alpha) = \sqrt{\frac{s}{2a}} \tag{23}$$

$$\sin(\beta) = \sqrt{\frac{s-c}{2a}} \tag{24}$$

IDFS implements a modified Battin algorithm to solve Lambert's Problem. The approach was developed by the European Space Agency's (ESA) Advanced Concepts Team (ACT) and is superior to other methods in that it avoids the singularity that commonly occurs at a transfer angle of 180º [10]. To solve Lambert's Problem by the ACT method, the transfer angle θ between the Earth's and target planet's position vectors is determined as shown by Eq. 25. Once θ is known, the chord length of the transfer orbit, c, the semi-perimeter length of the transfer orbit, s, and the minimum energy semi-major axis length, a_m, of the transfer orbit are all computed using Eqns. 26-28. From the results of Eqns. 26-28, the dimensionless parameter λ is found by Eq. 29.

$$\theta = a\cos\left[\frac{r_{1x}r_{2x} + r_{1y}r_{2y} + r_{1z}r_{2z}}{r_1 r_2}\right] \tag{25}$$

$$c = \sqrt{1 + r_2^{\,2} - 2r_2\cos(\theta)} \tag{26}$$

$$s = \frac{1 + r_2 + c}{2} \tag{27}$$

$$a_m = \frac{s}{2} \tag{28}$$

$$\lambda = \frac{\cos\left(\frac{\theta}{2}\right)\sqrt{r_2}}{s} \tag{29}$$

Following the determination of θ, c, s, a_m, and λ the transfer orbit solution conic is found using these values to solve Eqns. 22-24. Once a transfer orbit solution is found for the unique launch day/arrival day pair the Patched Conic Approximation method (see Figure 2) is used to calculate the departure and arrival ΔVs.

In this method, spacecraft motion is simplified by assuming only two bodies exist in the problem at any point in the transfer orbit. The fundamental premise of the two-body system is that only the spacecraft and the celestial body it orbits need be considered since the dominating influence on the spacecraft's motion is the celestial body whose "sphere of influence" it is within.

Using this two-body concept, the velocity of the transfer orbit with respect to both the Earth and the target, V_{Depart} and V_{Arrive}, are determined by finding the Lagrange *F* and *G* coefficients from Eqns. 32-35 and using those results in Eqns. 30 and 31 [8]. Note, P is the semi-latus rectum of the transfer ellipse.

$$V_{Depart} = \frac{1}{G}\left(r_2 - F r_1\right) \tag{30}$$

$$V_{Arrive} = \dot{F} r_2 + \dot{G} \; V_{Depart} \tag{31}$$

$$F = 1 - \frac{r_2}{P}\left[1 - \cos(\theta)\right] \tag{32}$$

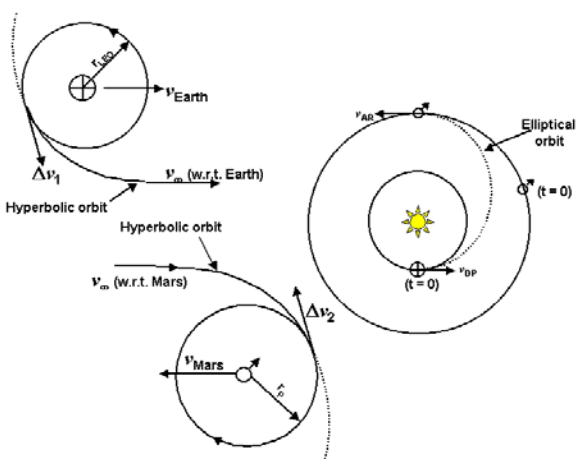

Fig. 2: The Patched-Conic Method [11]

$$G = \frac{r_1 r_2 \sin(\theta)}{\sqrt{\mu_{sun} P}} \tag{33}$$

$$\dot{F} = \sqrt{\frac{\mu_{sun}}{P}}\left[\tan\left(\frac{\theta}{2}\right)\left(\frac{1-\cos(\theta)}{P} - \frac{1}{r_2} - \frac{1}{r_1}\right)\right] \tag{34}$$

$$\dot{G} = 1 - \frac{r_1}{P}\left[1 - \cos(\theta)\right] \tag{35}$$

The methodology developed by ACT and implemented in IDFS, overcomes the known singularity problem at θ = 180°. The approach provides a generic orbit solution to the boundary problem as shown by Eq. 36. Using Eq. 23 to find α and substituting the result into Eq. 36 yields accurate values of ΔV versus ToF for the entire real axis. This occurs as the method avoids the use of Langrage coefficients as required for the solution to Eqns. 32-35. However, the algorithm in Eq. 36 will not converge at θ = 0° as log(0) is indeterminate [10].

$$X = \log\left[1 + \cos\left(\frac{\alpha}{2}\right)\right] \tag{36}$$

2.1.4. Delta Velocity Computation

Once the departure and arrival velocities are found, the required ΔV for each trajectory can be computed. IDFS finds these velocities using vector subtraction, as shown by Eqns. 37 and 38, to account for both the hyperbolic velocity on the transfer ellipse and the velocity of the Earth and target planet (see also Fig. 2).

$$\vec{V}_{E\infty} = \vec{V}_{Depart} - \vec{V}_{Earth} \tag{37}$$

$$\vec{V}_{T\infty} = \vec{V}_{Arrive} - \vec{V}_{Target} \tag{38}$$

Once the transfer orbit velocity of the spacecraft with respect to Earth and the target planet are computed, ΔV can be found. In each case ΔV is the difference between the spacecraft's velocity around the planet and the velocity of the spacecraft with respect to the planet. The circular orbit velocities are found by using the user provided orbital altitudes, h, in Eq. 39. Once the orbital velocities are known ΔV_{Depart}, ΔV_{Arrive}, and ΔV_{Total} are found from Eqns. 40-42 respectively.

$$V_{Orbit} = \sqrt{\frac{\mu_{Planet}}{h}} \tag{39}$$

$$\Delta V_{Depart} = V_{E\infty} - V_{LEO} \tag{40}$$

$$\Delta V_{Arrive} = V_{T\infty} - V_{LTO} \tag{41}$$

$$\Delta V_{Total} = \Delta V_{Depart} + \Delta V_{Arrive} \quad (42)$$

The ΔVs are then saved for future evaluation and the entire process is repeated for the next launch /arrival day pair. The next iteration is performed by holding the launch day constant and incrementing the arrival day until each case in the arrival window is considered. Once each arrival day has been used, the launch day is incremented and the process is repeated until the ΔVs for all possible pairs have been calculated.

2.1.5. Payload System Mass Calculation

Payload System Mass (PSM), m_{PSM}, is the mass of the "usable" Payload delivered to the target. Propellant and Propulsion Subsystem mass are not included in the computed PSM. The propellant needed to complete the mission is calculated by IDFS while the engine and propellant tank mass are found from user inputs. Before calculating PSM, the required propellant for both the departure and arrival ΔVs must be determined using Eq.43 (derived from the rocket engine equation).

$$m_1 = m_0\left(1 - e^{-\Delta V / gI_{sp}}\right) \quad (43)$$

To find the required departure propellant, m_{TSM} is obtained from Eqns. 1-3, 6 or by user input. TSM is then substituted into Eq. 43 with specific impulse, I_{sp}, obtained as a user input or from the database. The result of Eq. 44, $m_{prop\text{-}depart}$ yields the propellant required to depart Earth. The wet departure mass, $m_{wet\text{-}depart}$, is then calculated as shown in Eq. 45 with the result used in Eq. 46 to compute the propellant required to generate the arrival ΔV.

$$m_{prop-depart} = m_{TSM}\left(1 - e^{-\Delta V_{Depart} / gI_{sp}}\right) \quad (44)$$

$$m_{wet-depart} = m_{TSM} - m_{prop-depart} \quad (45)$$

$$m_{prop-arrive} = m_{wet-depart}\left(1 - e^{-\Delta V_{Arrive} / gI_{sp}}\right) \quad (46)$$

Once the mass of the propellant needed to perform the arrival ΔV is known, the total arrival mass, $m_{total\text{-}arrive}$, is obtained utilizing Eq. 47. When the wet arrival mass is determined, Eq. 48 is used to calculate the PSM. In Eq. 48, the engine mass is again from the database or a user input, the propellant tank mass is computed using the total propellant mass (Eq. 49), and the propellant tank mass fraction, m_{pmf}, is provided by the user. The IDFS default m_{pmf} is 4% based on the propellant mass tank fraction of the Space Shuttle's External Tank and the Apollo Command Service Module.

$$m_{total-arrive} = m_{wet-depart} - m_{prop-arrive} \quad (47)$$

$$m_{PSM} = m_{wet-arrive} - m_{engine} - m_{\tan k} \quad (48)$$

$$m_{\tan k} = m_{pmf}\left(m_{prop-depart} + m_{prop-arrive}\right) \quad (49)$$

2.1.6. Optimum Case Identification

IDFS allows the user to select from one of six possible optimization options. These options include: 1) Find maximum PSM; 2) Find minimum ToF; 3) Goalseek PSM; 4) Goalseek ToF; 5) Find minimum ToF for a specified PSM; and 6) Optimize LEO altitude for maximum PSM. In each case, IDFS optimizes only within the constraints of the user input parameters.

2.1.6.1. Find Maximum Payload System Mass

To find the maximum PSM, IDFS performs a two-step optimization process. IDFS first calculates the arrival, departure, and total ΔVs. It then employs the MDO Simplex approach to identify the minimum total ΔV, (which corresponds to the maximum PSM case). When the minimum total ΔV is identified, PSM is calculated as discussed above.

2.1.6.2. Find Minimum Time of Flight

IDFS identifies the minimum ToF by using the input parameters only. The tool merely determines minimum ToF by finding the elapsed time between the launch window end and the departure window start. The associated departure and arrival ΔVs are computed to determine the total ΔV for the ToF. Once the total ΔV is found, the PSM is calculated.

2.1.6.3. Goalseek Payload System Mass

The IDFS Goalseek PSM routine allows the user to specify a range of Payload System Masses to be delivered to a remote planet. The algorithm evaluates the user input parameters to determine if such a goal can be met. The goal is found by using the MDO Matrix Evaluation technique. IDFS first calculates the total ΔV.

Once the total ΔV is found PSM is determined and compared to the PSM goal. If the current PSM is within range of the PSM goal, all information associated with that launch day/arrival day pair, including the ToF, is saved. On subsequent iterations, the last saved PSM is compared to the PSM for the current launch day/arrival day pair. If the PSM from the current iteration is in range and closer to the PSM

goal than the last saved PSM, the current PSM and its related information are saved. However, if the two PSMs are equal, the mission with the shortest ToF, and it associated design characteristics, is saved.

2.1.6.4. Goalseek Time of Flight

Like the PSM Goalseek, IDFS uses the MDO Matrix Evaluation method to find the ToF goal. Similar to the previous optimization techniques, the total ΔV and PSM for each launch/arrival day pair is determined. If the ToF calculated for the current iteration is within the goal range, all launch/arrival day pair data is saved.

On succeeding iterations, the last saved ToF is compared to the current ToF for the launch/arrival day pair. If the latest ToF is closer to the ToF goal then the saved ToF, it and the related information are saved. However, if the two ToFs are equal, then the PSMs are compared and the case with the greatest PSM is saved.

2.1.6.5. Find Minimum ToF for a Given PSM

Perhaps the most useful IDFS tool for the planning of manned interplanetary missions is the Find Minimum ToF for a Given PSM optimization routine. IDFS, using both the standard set of input parameters and a range of acceptable PSMs provided by the user, identifies the minimum ToF for the given PSM.

In a fashion identical to the routines described earlier, the total ΔV, PSM, and ToF for the current launch /arrival day pair are found. As before, if the PSM calculated for the current iteration is within the goal range, the data associated with that pair is saved.

On subsequent iterations, the last saved PSM is contrasted against the current PSM. If the current PSM is within the specified range and its associated ToF is shorter than the saved ToF, then the current iteration's information is saved. If however, the two ToFs are equal, the mission with the greatest PSM is retained.

2.1.6.6. Optimize LEO for Maximum PSM

The optimum LEO case is found by first computing the maximum PSM, based on the user input mission design parameters, at a LEO of 150 km. LEO is then stepped at 50 km increments to an altitude of 1000 km. At each altitude, the maximum PSM is again calculated and compared to the previous case. The optimum case is identified and data saved and output for that case.

3. RESULTS

PSM is of course fundamental to the design of all interplanetary missions. That is, the PSM that can be delivered to the target planet is essential to the design and success of any mission. All aspects of the mission design are affected by this very limited resource. Consequently, every mission necessarily seeks to optimize PSM so to maximize the benefit.

Conversely, for crewed space missions, reducing the ToF, and thus the overall exposure of the crew to space environments, is also a mission design driver. ToF can also drive cost for unmanned missions as longer missions require additional mission ground support.

Unfortunately, the optimum method of shortening ToF is to traverse high-energy interplanetary trajectories. These high-energy interplanetary trajectories require massive propellant loads that consume a large fraction of the mass and thus diminish the utility of the mission. Further, delivering large propellant loads, even to LEO, equates to high launch costs. Accordingly, minimizing the ToF and maximizing the PSM are two goals that are diametrically opposed. This dichotomy of ToF vs. PSM for space mission design illustrates the need for tools like IDFS to find optimum mission designs.

The conclusion that PSM and ToF are the two most important aspects of mission design shaped the design of IDFS. The tool could merely have calculated trajectories and ΔVs, but this information is only moderately relevant. Each of the optimization tools was developed with the goal of helping the user find the best combination of PSM and ToF.

3.1. IDFS Outputs

IDFS produces outputs in two forms. The input trade parameters and the results of the trade are provided as text in the MATLAB® command window. In addition, each IDFS optimization routine generates six plots that illustrate the results of the input trade parameter analysis. Two example plots are shown in Fig. 3 and 4.

Each optimization routine echoes the user input parameters to the command window so that the user can view the values input in conjunction with the results. This facilitates iteration of trade parameters. Input parameters displayed by IDFS include the launch vehicle, target planet, number of launches, aerobrake ΔV, launch and arrival windows and window step size, LEO and LTO altitudes, rocket engine specifics, and propellant tank mass fraction.

The IDFS MATLAB® command window outputs include launch vehicle performance, total, departure, and arrival ΔV, optimum mission launch and arrival days, PSM and ToF for the optimum case, optimum mission transfer angle θ, departure and arrival propellant mass, and propulsion system mass.

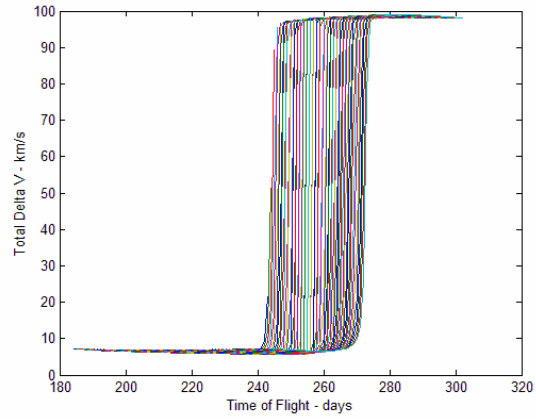

Fig. 3: Total ΔV vs. ToF

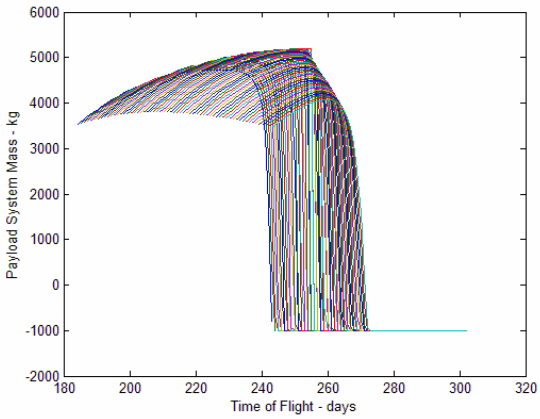

Fig. 4: PSM vs. ToF

Several indicators of the trade parameter validity can be assessed from the tool outputs. Specifically, a small or negative PSM occurs when there are large arrival or departure ΔVs or both. Small PSMs ultimately result from a θ not near 180° (a Hohmann transfer). Small θs (less than ~90°) imply launch and arrival windows too close together or that, due to the relative motion of the planets, the window locations are not optimal.

Finally, IDFS produces negative PSMs when that result is driven by the inputs. Though negative PSMs do not make sense physically, they are provided so that an increase in even a negative PSM, suggests to the user in which direction to adjust the launch and/or arrival windows such that the ToF should move in a direction that produces a larger PSM. Note that a negative PSM is the result of subtracting the larger Propulsion system mass from the smaller resulting PSM (see Eq. 48).

3.2. Benchmarking

Benchmarking of IDFS was performed by two separate code-to-code comparisons. The first validated IDFS planetary position calculations by contrasting the results produced by IDFS and JPL's Horizons website [11]. The results in Table 1 show IDFS accurately calculates, to 0.1 m, all planetary position vectors.

A second code-to-code comparison was performed on the IDFS ΔV calculations. This evaluation, whose results are provide in Table 2, is based on the output of a software model utilized by industry analysts to perform first order interplanetary mission trajectory design. As can be seen from the results below, the ΔV determined by IDFS is extremely accurate [12].

Table 1: Planetary Position Benchmark

Radius (km)	Mercury			Venus		
	IDFS	JPL	% Err	IDFS	JPL	% Err
Rx	52638550.8	52638550.8	0.0%	-54092361.3	-54092361.3	0.0%
Ry	-22688214.2	-22688214.2	0.0%	92784072.7	92784072.7	0.0%
Rz	-6683556.1	-6683556.1	0.0%	4391857.2	4391857.2	0.0%
Radius (km)	Earth			Mars		
	IDFS	JPL	% Err	IDFS	JPL	% Err
Rx	95541839.9	95541839.9	0.0%	103303558.3	103303558.3	0.0%
Ry	-118007885.5	-118007885.5	0.0%	-182950046.9	-182950046.9	0.0%
Rz	2227.6	2227.6	0.0%	-6371754.3	-6371754.3	0.0%
Radius (km)	Jupiter			Saturn		
	IDFS	JPL	% Err	IDFS	JPL	% Err
Rx	-772138493.7	-772138493.7	0.0%	635076135.5	635076135.5	0.0%
Ry	243284053.6	243284053.6	0.0%	-1355728654.5	-1355728654.5	0.0%
Rz	16269944.9	16269944.9	0.0%	-1671976.7	-1671976.7	0.0%
Radius (km)	Uranus			Neptune		
	IDFS	JPL	% Err	IDFS	JPL	% Err
Rx	2966641523.4	2966641523.4	0.0%	3704547277.0	3704547277.0	0.0%
Ry	-485416521.3	-485416521.3	0.0%	-2538175432.8	-2538175432.8	0.0%
Rz	-40136794.8	-40136794.8	0.0%	-33237926.6	-33237926.6	0.0%
Radius (km)	Pluto					
	IDFS	JPL	% Err			
Rx	671955176.4	671955176.4	0.0%			
Ry	-4767573386.5	-4767573386.5	0.0%			
Rz	315848193.6	315848193.6	0.0%			

Table 2: ΔV Benchmark

Item	Case 1			Case 2		
	IDFS	LM	% Diff	IDFS	LM	% Diff
Departure ΔV	5.989	5.989	0.00014%	3.839	3.840	0.00055%
Arrival ΔV	7.839	7.839	0.00000%	2.634	2.634	0.00000%
Total ΔV	13.828	13.828	0.00006%	6.473	6.473	0.00033%
TOF (days)	149	149	0.00000%	200	200	0.00000%
Launch Day	2/8/2018	2/8/2018		3/12/2016	3/12/2016	
Arrival Day	7/7/2018	7/7/2018		9/28/2016	9/28/2016	
Target	Mars	Mars		Mars	Mars	
Low Orbit Alt	400	400		400	400	
Item	Case 3			Case 4		
	IDFS	LM	% Diff	IDFS	LM	% Diff
Departure ΔV	10.369	10.369	-0.00009%	6.459	6.459	0.00017%
Arrival ΔV	10.699	10.699	-0.00006%	10.407	10.407	-0.00002%
Total ΔV	21.068	21.068	-0.00007%	16.866	16.866	0.00005%
TOF	289	289	0.00000%	956	956	0.00000%
Launch Day	12/7/2015	12/7/2015		7/19/2011	7/19/2011	
Arrival Day	9/21/2016	9/21/2016		3/1/2014	3/1/2014	
Target	Venus	Venus		Jupiter	Jupiter	
Low Orbit Alt	200	500		300	150000	

4. Trade Study Results

To provide a use case for IDFS, a detailed trade study was conducted to identify the maximum PSM that could be delivered to Mars using an Atlas V-552

launch vehicle, and an RL-10D rocket engine, in the 2010 to 2020 time frame.

The trade was conducted holding all input parameters fixed except for the launch and arrival windows. Starting 1 January 2010, six months launch and arrival windows were defined and placed back to back in time. IDFS was then run for each window pair sliding by six months to the right in each case. In total, twenty cases were run and those with large PSMs were identified.

Following the initial performance of all twenty cases, 7 cases were identified for further study. For those cases the results of the initial run where evaluated, the launch and arrival windows were refined such that they were short and centered on the optimum values from the first run, and the step size minimized. The second round of runs identified Case 4b as the optimum solution for the trade space. Trade results are provided in Table 3.

Trade Parameter/Variable	Units	Window 4	
		Case 4a	Case 4b
Launch Vehicle	-	Atlas V Heavy	Atlas V Heavy
Target Planet	-	Mars	Mars
Number of LV launches	#	1	1
Minimum Total ΔV	km/s	6.5210	5.7280
Earth Departure ΔV	km/s	3.7693	3.6427
Total Mars Arrival ΔV	km/s	2.7517	2.0853
Aerobrake ΔV	km/s	0.0000	0.0000
Net Mars Arrival ΔV	km/s	2.7517	2.0853
Launch Window	Date	7/1/11-12/31/11	10/1/11-12/31/11
Launch Window Step Size	Days	10	1
Launch Date	Date	11/18/2011	11/13/2011
Arrival Window	Date	1/1/12-6/30/12	5/1/12-7/31/12
Arrival Window Step Size	Days	10	1
Arrival Date	Date	6/19/2012	7/23/2012
Time of Flight	Days	214.0	253.0
Transfer Angle θ	Deg	156.52	178.18
Low Earth Orbit	km	200.0 km	200.0 km
Low Mars Orbit	km	500.0 km	500.0 km
Total Spacecraft Mass to LEO	kg	20534.53	20534.53
Engine Type	-	LOX/H_2	LOX/H_2
Engine I_{sp}	secs	472.0 secs	472.0 secs
Departure Propellant Mass	kg	11436.43	11184.27
Spacecraft Wet Departure Mass	kg	9098.09	9350.26
Arrival Propellant Mass	kg	4076.32	3390.37
Propellant System Mass	kg	802.51	764.99
Propellant Tank Mass Fraction	kg	4.0%	4.0%
Payload System Mass	kg	4219.26	5194.90

Table 3: Trade Study Results Summary

5. CONCLUSIONS

This study has shown that MDO methodologies can be utilized to aid in the interplanetary mission design process. Further, IDFS avoids a known issue with the solution to the Lambert Problem by implementing the ESA ACT's improved Battin Method.

IDFS is an extremely useful and accurate tool that identifies optimum interplanetary mission parameters. It is easy to operate, provides flexibility to manipulate input trade parameters, offers a database on which to base input parameters, and delivers a comprehensive set of data and graphical outputs to evaluate the results. Finally, IDFS demonstrated its utility by quickly identifying a possible Earth to Mars mission.

5.1. Future Enhancements

Possible future enhancements to IDFS include:

- Aerobrake and ballistic entry software that includes a descent ΔV and shield mass calculations
- Change propellant load calculation from impulsive thrust to thrust over time so that high specific impulse/low thrust engines can be studied
- Provide the ability to calculate mission results using direct injection by the launch vehicle
- Allow LEOs other than circular so that departure burns can be performed at a transfer orbit apogee
- Calculate results for an Earth return mission

6. REFERENCES

1. Bush, G. "A Renewed Spirit of Discovery," The White House, Office of the Press Sec, 14 Jan 04.
2. Roach, J. 2006. "NASA Budget Diverts Funds From Science to Spaceships," *National Geographic News*.
3. Nemiroff, R. and Bonnel, J. "Astronomy Picture of the Day, Enceladus Near Saturn," NASA Website, 22 March 2006.
4. International Launch Systems (ILS). 1999. "Atlas Launch System Mission Planner's Guide, Atlas V Addendum," ILS.
5. The Boeing Company. 2000. *Delta IV Payload Planner's Guide*. The Boeing Company.
6. International Launch Systems. 2002. "Angara Launch System Mission Planner's Guide," ILS.
7. Williams, D. 2006. "Planetary Fact Sheet – Metric," NASA Goddard Space Flight Center.
8. Prussing, J. and Conway, B. 1993. *Orbital Mechanics*. Oxford University Press, Inc. pp. 124-128.
9. Shen, H. and Tsiotras, P., "Optimal Two-Impulse Rendezvous Using Multiple-Revolution Lambert Solutions," *AIAA Journal of Guidance, Control, and Dynamics*, January 2003, pp. 50-51
10. Izzo, D., "Advance Concepts Team", European Space Agency, 28 May 2004
11. Leong, J. and Papadopoulos, P., "A Search for Viable Venus and Jupiter Sample Return Mission Trajectories for the Next Decade," San Jose State University, May 2004, p. 2.
12. Gill, J., et. al., "A Manned Mission to Mars", San Jose State University, 2 July 2003

Summary of the AGU Chapman Conference on Exploring Venus as a Terrestrial Planet
Larry W. Esposito and Dimitry Titov, Convenors

The AGU Chapman conference held 13-17 February in Key Largo, Florida, has the following objectives:
Review the current knowledge of Venus including surface and interior processes, atmospheric circulation, chemistry, and aeronomy; Compare the evolution of Venus with that of Earth and Mars; Preview observation plans and results expected from Venus Express; Identify objectives for future research and missions.
We will summarize major findings, and any updates proposed to the NRC and other strategic documents.

4th International Planetary Probe Workshop
27 June- 30 June, 2006, Pasadena, California, USA

Integrated OLAP Cubes Database driven Aerothermodynamic Trajectory Analysis for Planetary Probes

Periklis Papadopoulos , Prabhakar Subrahmanyam
ppapado1@email.sjsu.edu , prasub@gmail.com
Center of Excellence for Space Transportation & Exploration
Department of Mechanical and Aerospace Engineering
One Washington Square, San Jose State University,
San Jose- 95192, California, USA

Abstract

A novel approach to perform trajectory and aerothermodynamic analysis using the state-of-the-art OLAP multi-dimensional database technology will be presented in this publication. An Online Analytical Processing (OLAP) Database Management System integrated to a trajectory code has been developed. The database contains a list of planetary probe architectures and includes vehicle dimensions, trajectory and aero-thermal data. Material properties for several thermal protection systems are also populated into the OLAP database. The user interface allows for a selection from a list of existing planetary probe configurations. In addition, probe design specifications can be changed, including, trajectory, and entry conditions. Vehicle design parameters such as the geometric configuration, flight path angle, entry velocity, entry mass and ballistic coefficient can be varied through the interface. The specified design is dynamically linked to the trajectory code. The trajectory is computed and the database is populated back for the selected specifications of the chosen vehicle architecture. Once a trajectory is run, the data is analyzed from within the OLAP DB using a drill-down approach and can be plotted for comparative data analysis. The framework employs the fourth order Runge-Kutta integration for trajectory calculations. To study the aerodynamic heating, Fay-Riddell and Tauber-Sutton empirical correlations have been modeled for the stagnation point heat transfer computations. In addition, the OLAP database (DB) provides dynamic links to compressible flow solvers (CFD++, GASP, CFD-RC, LAURA, SPARTA) and allows for aerothermodynamic CFD modeling.

I. Introduction

A complete computational design framework is necessary that automates the calculations for stagnation point heating, TPS design so that better probes can be built with this analysis. An integrated planetary probe design framework that generates trajectory data for planetary probes given vehicle geometry and several different entry trajectory flight conditions is presented in this paper.

SPARTA is a platform independent Graphical User Interface (GUI) based, relational database-driven JAVA tool hat accurately predicts aerodynamic and heating entry environments. The aero-heating environment depends on the trajectory flown, size and shape of the vehicle. Figure 1 shows the software architecture of SPARTA. A comprehensive database of different ballistic reentry vehicles has been developed using the Planetary Mission Entry Vehicles manual [1]. This includes vehicle dimensions and trajectory data for all the capsules that has been flown in the past. The SPARTA GUI provides the capability to choose from a list of flight vehicle geometric information and entry trajectories. From the GUI, it is possible to choose the atmospheric model and the empirical convective and radiative stagnation point analysis. An approach is presented for dynamic TPS design. Materials properties like Carbon, Silicon and Carbon-Phenolic based Ablators have been obtained from the NASA Ames Thermal Protection Materials and System Branch TPS*X* Internet Database and modeled into the local OLAP database and integrated with the user interface. Any previously flown planetary probe can be chosen from the user interface and tied to an Ablator from the list in the interface and a trajectory case can be run for a planet that's available in the database. This populates the trajectory data back into the database.

Figure 1: SPARTA Software architecture.

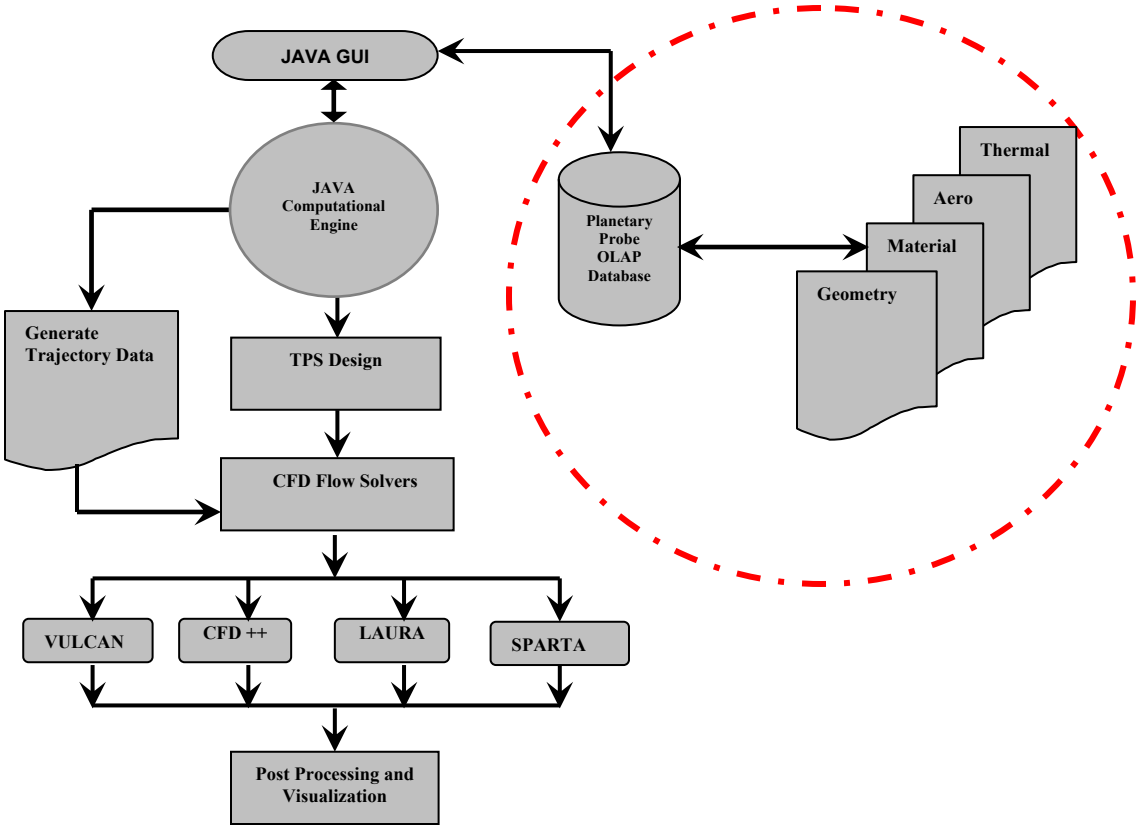

II. Software Architecture

The overall software architecture is shown in Figure 1. The front GUI allows the user to provide inputs for trajectory, geometry and grid generation computations. It is connected to an extensive planetary probe database and a Java computational engine, which is used to generate flight trajectory data. Based on the flight conditions and probe specifications, the geometry engine constructs the vehicle configuration. With the emerging Information Technology growth, heterogeneous systems are rapidly developing and this presents a need for distributed analysis system. So, with this in mind a platform independent tool has been developed. This architecture neutral code has the capability to execute in any platform for analysis without having to recompile.

Two different Ablators can be chosen for the same probe and the tool can run two different trajectories and the aerodynamic heating is computed for comparative data analysis. Two different ablators from two different categories like Carbon Ablator and Silicon based ablators can also be chosen for TPS Sizing analysis. The JAVA graphical user interface is shown in figure (5). The purpose of this research is to investigate the aerothermodynamics environment of atmospheric entry probes and to generate an automatic computational trajectory database populated by OLAP cubes and to provide flow field analysis for such probes.

III. OLAP Database Cubes and Multidimensional Analysis

An OLAP cube has been constructed for multidimensional trajectory analysis. A cube is a store of multidimensional data; it is defined by dimensions and measures. Different dimensions are populated in the database. Several measures are populated in the database for each of these dimensions. These variables that are characterized as measures: Effective Nose Radius (R_{eff}), Nose radius (R_n), Shoulder radius (R_s), Corner radius (R_c), vehicle's mass (m), initial flight path angle (γ_e) and initial entry velocity (V_e). Once these dimensions are specified as different values in the cube and the 3-DOF trajectory engine is run, it populates the database with all these different permutations and combinations of the design parameters and the data can be fetched from the database either by specifying a query or by choosing the appropriate design parameter for a set of flight conditions.

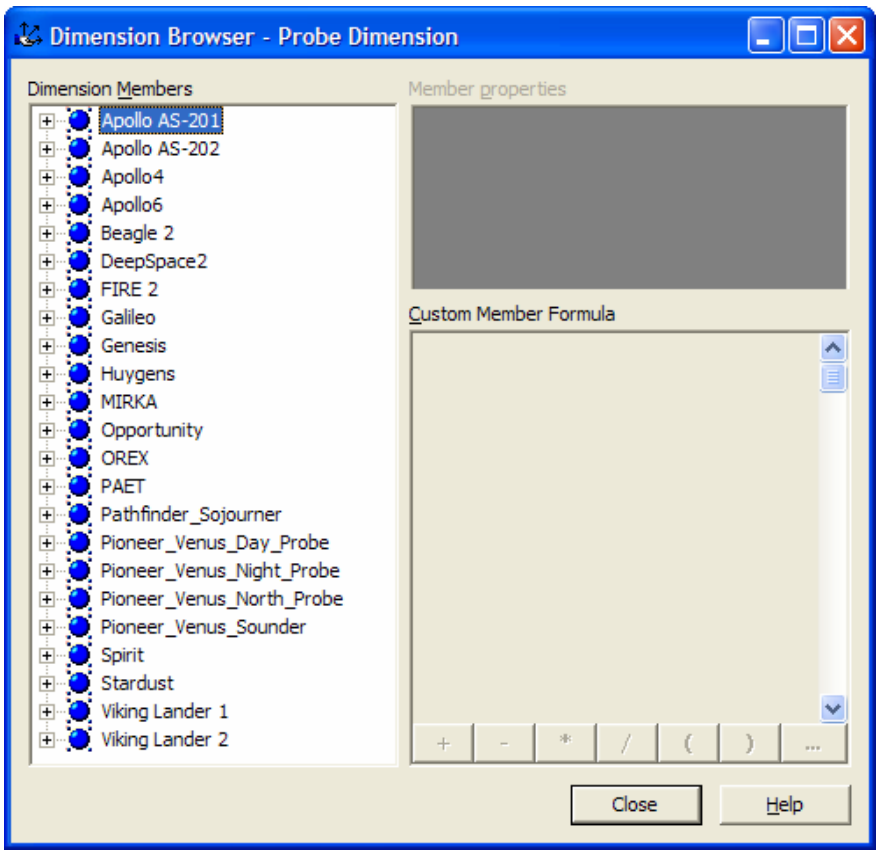

Figure 2: Planetary probes modeled in OLAP DB

OLAP cubes are constructed as dimensions and measures. Measures are the design parameters that are modeled in the OLAP database. These design parameters can be changed and forms the basis for multi dimensional data analysis capability. Figure 2 shows 23 different probes that are modeled as the dimension members in the cubes. Once the design parameters for these probes are modeled in the database as measures, from the trajectory graphical user interface, the flight vehicle is chosen, the appropriate dimensions and the measures from the OLAP cubes are loaded as inputs for the trajectory. Once the trajectory is run, data is generated from the 3-DOF trajectory engine and populated back into the database. From this point, it's data mining to retrieve the data for the specified set of flight conditions, thus for a change in the initial entry velocity for instance, a new run is not necessary, it's just a fetch from the OLAP cubes by browsing the dimensions data.

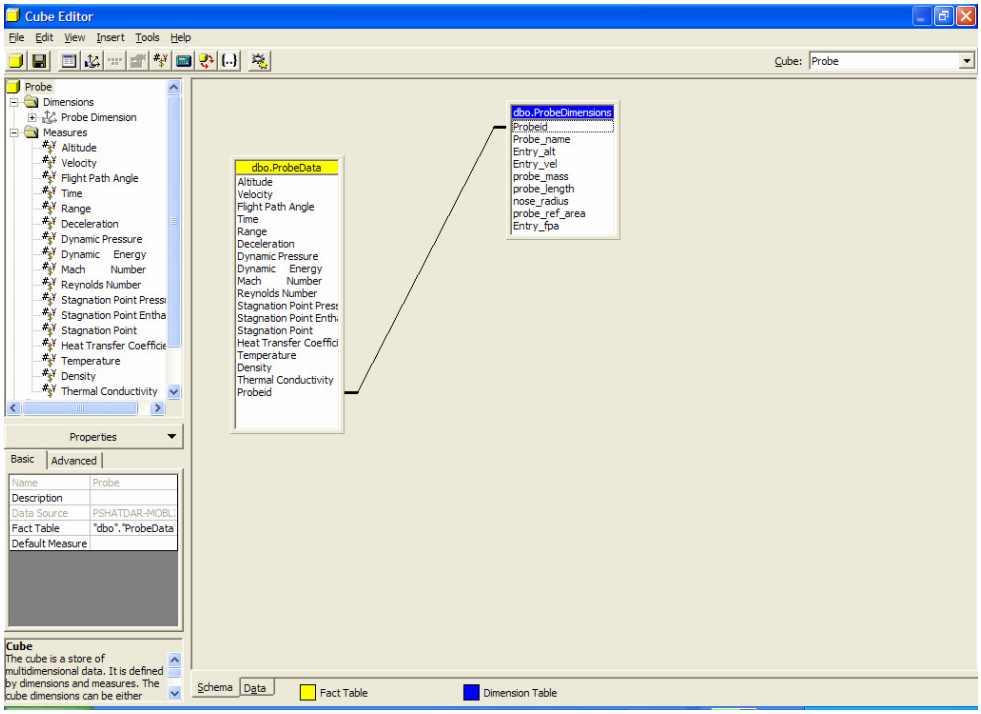

Figure 3: Measures (design parameters) modeled in OLAP Cube for planetary probes

Cubes are the logical storage medium for an OLAP database. The cube to an OLAP database what the table is to an RDBMS. A cube presents to the outside world, users and front-end applications, a potential intersection point, i.e. a cell, for every member from every dimension with every member of every other dimension. Cubes give the ability to model multiple loops in the trajectory code without having to write loops. Several values for three dimensions are changed in SPARTA cubes which are linked to the trajectory code. They also provide a capability to change up to 64 design parameters. The trajectory code is run once and the data-warehouse is populated by varying these design parameters. Data mining techniques are employed to drill-down the data and queried for specific flight conditions or entry design values from the database.

SPARTA Cubes have multiple values for these three dimensions: (a) initial flight path angles, (b) Initial entry velocity and (c) Nose radius. The term cube implies *three dimensions*. In fact OLAP server cubes can contain up to 64 dimensions. The Trajectory engine takes a little longer if more dimensions are included in the simulation. Each variable can have a maximum of up to five values. If each variable has five different values, then in this case each variable forms a separate loop and the trajectory engine is run within these three loops populating the data for 125 permutations and combinations of these design variables for each single point in the altitude. This whole setup is populated for the entire altitude integration in the database. Hence a drill-down approach to fetch the data from the OLAP database becomes necessary if several dimensions are specified for the trajectory simulation run.

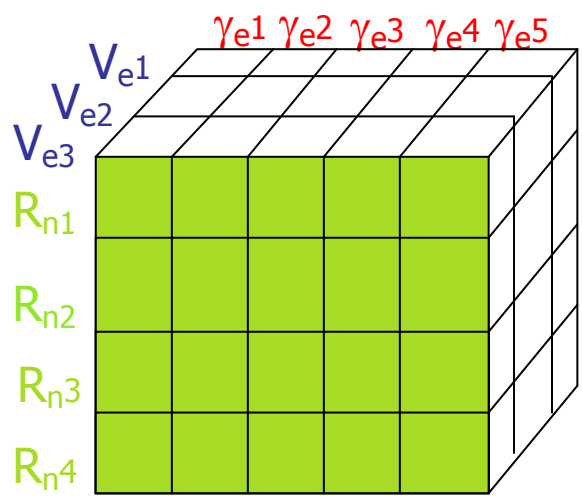

Figure 4: SPARTA OLAP Cube as modeled in the database

Table 1 is the data queried (drill-down approach) from the OLAP Cubes database that has been populated by varying five different values for the entry angles, entry velocities and nose radii (three

of the 64 dimensions that can be modeled). Also, SPARTA cubes have can fetch the best trajectory based on either the minimum heating loads or the minimum g-forces that is chosen in the optimization section from the graphical user interface.

Table 1: OLAP driven Trajectory Analysis at different Entry Angles, Velocities and Nose radii

Apollo 4, **Entry angle: -12.0°, Entry Velocity:22500 ft/s, Nose Radius: 4.69m**

Altitude (ft)	Velocity (ft/sec)	Flight Path Angle γ (deg)	Mach Number	Reynolds Number	Stag Point Pressure (lbf/ft²)	Stag Point Heat Transfer rate $\dot{q}_{conv}$ (W/cm²)
250000.00	22513.69	12.00	23.83	65486.33	30.70	391.30
249000.00	22512.32	12.00	23.80	68432.20	32.16	395.82
248000.00	22510.96	12.01	23.77	71501.97	33.69	400.44

Apollo 4, **Entry angle: -6.93°, Entry Velocity: 36545 ft/s , Nose Radius: 5.69m**

Altitude (ft)	Velocity (ft/sec)	Flight Path Angle γ (deg)	Mach Number	Reynolds Number	Stag Point Pressure (lbf/ft²)	Stag Point Heat Transfer rate $\dot{q}_{conv}$ (W/cm²)
250000.00	36545.00	6.93	33.75	106364.35	81.02	482.53
249000.00	36544.30	6.92	33.75	111144.56	84.87	482.90
248000.00	36544.00	6.91	33.70	116125.59	88.89	483.01

Data in table 1 has been fetched (or queried) from a user specified query in the OLAP Analysis Manager and can be specifically tailored to suit one of the entry conditions that has been used in the OLAP cubes to populate the database. So the idea is to run the trajectory engine only once for several different design conditions and populate the database and later retrieve the data for specified flight and design conditions so that the database has all the different permutations and combinations of trajectory data pertinent to a flight vehicle. The initial entry flight conditions in the OLAP Cubes for the Apollo vehicles were taken from Apollo Experience Report [2]

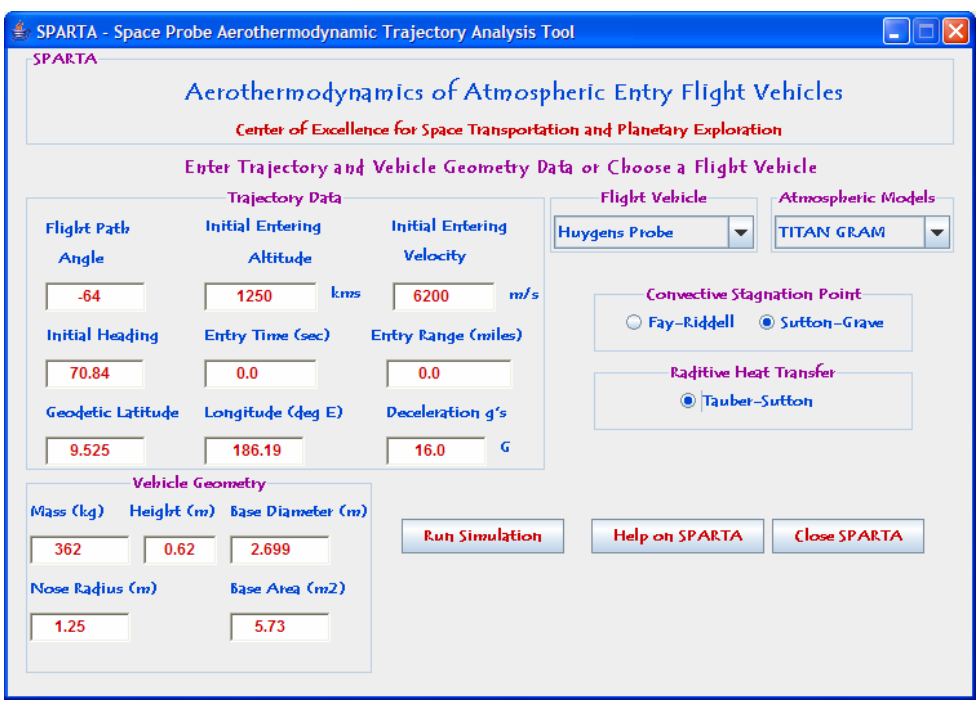

Figure 5: JAVA based GUI for Aerothermodynamic Trajectory Analysis

IV. Trajectory Optimization Analysis

The probe model developed for this trajectory is a point-mass model with two translations and one

rotation (3-DOF) around a spherical planet. It integrates the equations of motions of a vehicle on a ballistic entry trajectory so that no lift is generated and the body acts only on gravity. Figure 6 shows the various aerodynamic forces acting on the body. The vehicle model is build from a number of parameters defining the geometry of the probe including body diameter, cone half-angle, nose and shoulder radius. The aerodynamic properties of the probe are subsequently derived from the geometry of the vehicle as shown in figure 6. The graphical user interface is tied to the OLAP database at the backend. When a flight vehicle is chosen, appropriate geometry and initial trajectory values are fetched from the database and populated in the GUI. The user has the flexibility to change it or use the values from the database,

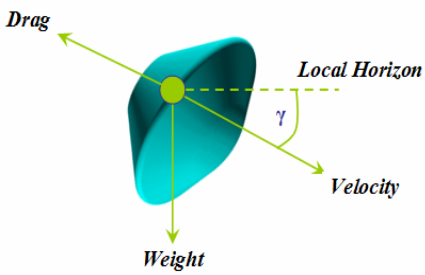

Figure 6: Aerodynamic forces acting on the atmospheric vehicle

Based on the capsule's entry interface, flight path angle and the vehicle shape and geometry, the trajectory engine is able to do multiple simulations involving undershoot, overshoot and finally recommend the optimal trajectory to reduce either the maximum convective heat or deceleration loads based on the optimization factor that is chosen during the simulation. The critical aerothermal conditions in the velocity-altitude plane are identified, in terms of the highest temperature surface points that correspond to the Thermal Protection System material that is chosen for modeling. The code adjusts in the trajectory automatically when it encounters a state when the peak heat exceeds the maximum allowable stagnation point temperature of the material that is chosen thus stabilizing the trajectory to a "*low-risk trajectory*".

During the reentry process, the aerodynamic parameters are first characterized by free molecular flow and then the trajectory engine allows the simulation to follow a gradual transition to continuum flow as the capsule descends into the denser parts of the atmosphere. Thus, despite being a 3-DOF model, the code can reliably simulate trajectories for reentry vehicles having predictable body dynamics. Modified Newton Flow Theory (NFT) is used to evaluate the pressure coefficient C_p around the body and derive the drag coefficient C_d of the configuration. The Modified NFT states that

$$C_p = C_{pmax} \sin^2\theta \qquad \textbf{(1)}$$

where θ is the angle between the flow and the body surface and C_{pmax} is evaluated as the maximum pressure coefficient found behind a normal shockwave at the stagnation point. The Ballistic Coefficient (β) of the probe is derived from the aerodynamic model as per equation (2)

$$\beta = m/(C_d)(A) \qquad \textbf{(2)}$$

where Cd, m and A are respectively the capsule coefficient of drag, mass of the vehicle an average cross-sectional area in the direction of the air flux.

Introducing the average specific heat [3], constant Lewis and Prandtl-Number (Le=1 and Pr=0.71), Fay and Riddell proposed an empirical correlation to define the stagnation point heat flux (*heating rate per unit area*) towards a fully catalytic, hot wall. The convective heat transfer to the stagnation point along the trajectories of the reentry capsule for Earth has been modeled using Sutton-Grave and correlation [3] Fay-Riddell theory [4] as described in equation (3) which gives the heat flux as

$$\dot{q}_{conv} = k\sqrt{\frac{\rho}{R_n}}\left(\frac{V_\infty}{1000}\right)^3 \qquad \textbf{(3)}$$

where $\dot{q}_{conv}$ is the convective heat-transfer rate into the flight body, per unit area, k is a constant based on the planetary atmosphere, ρ is the freestream density, and V_∞ is the flight velocity. The heating rate for $\dot{q}_{conv}$ is in W/cm^2 if the velocity is given in m/s and the density in kg/m^3. Radiative heat transfer is computed using the Tauber-Sutton Radiative heating correlation for Earth and Mars [5] as given in equation (4)

$$\dot{q}_{rad} = C r_n^{\,a} \rho^b f(V) \qquad \textbf{(4)}$$

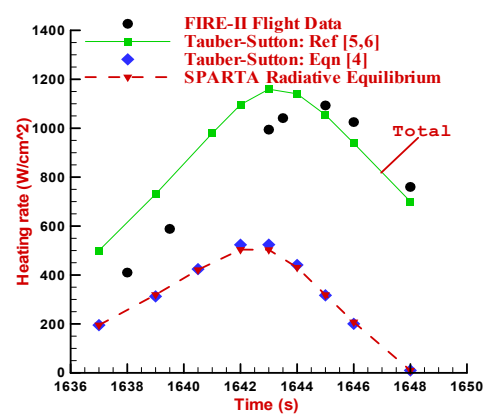

Figure 7: Radiative stagnation point heating of FIRE II data at a reentry velocity of 11.37 km/s

The plots in figure 7 show the comparison of calculated Radiative heating with Fire II flight data and the engineering correlations described by Tauber in [5] and [6]. The vehicle configuration for FIRE II is an axisymmetric, 66° sphere cone and truncated spherical forebody, with a small corner radius. This trajectory point corresponds to the first FIRE II heatshield, with a nose radius of 0.935 m.

High temperatures in high-speed atmospheric flight require that the properties behind a shock wave must be obtained using an equilibrium chemically reacting air model instead of a calorically perfect air model. The temperature and density ratios in the shock layer along some trajectory points were obtained from the results of Huber [7] that give the variations of shock temperature and density with velocity and altitude. The equilibrium composition of air at the corresponding temperature and density of the shock layer was computed using the Chemical Equilibrium with Applications (CEA) code [8]. Briefly, this code solves for chemical equilibrium using the minimization of the Gibbs free energy, which is the equivalent of finding the point where the maximum net work obtainable has been extracted from the system.

V. Ablative TPS Sizing and Materials Property Database

The objective of the convective and Radiative heating point calculation is to finally do the Ablative thermal protection system sizing. Currently, the heat shield materials used on a space vehicle such as Space Shuttle can withstand a total heat flux of the order of 50 W/cm^2 without causing ablation of the material. Advanced heat shield materials are believed to be able to withstand up to about 70 W/cm^2. When the sum of the convective and radiative heat fluxes exceeds such a maximum allowed heat flux value, the heat shield material ablates. In the ablation process, the heat energy is converted into the latent energy of vaporization.

For a hypersonic reentry vehicle entering the Earth's atmosphere on return from a planetary mission, its entry velocity is hyperbolic, that is greater than the escape velocity of 11.3 km/sec. From the Apollo flights experience, we know that the hyperbolic entries will produce a massively ablating environment. For a Martian entry, for which the escape velocity is 5.1 km/sec, a massively ablating environment may occur if the entry speed is greater than 8km/sec, and if the nose radius of the vehicle is large of the order of 3 m or larger. Thus, it is imperative to accurately model the ablation temperature for TPS materials.

Vehicle thermal response is calculated by an approximate method that uses heat of ablation data to estimate heat shield recession during entry. This analysis is coupled to a one-dimensional finite-difference calculation that determines in-depth thermal response. The in-depth solution accounts for material decomposition, but does not account for pyrolysis gas energy absorption through the material. As inputs, the method relies on trajectory data, including relative velocity, atmospheric density, pressure, and convective heat rate as a function of time.

The tool calculates radiative heating, recovery enthalpy, wall enthalpy, surface pressure, and heat transfer coefficient. Ultimately, the tool determines recession thickness, total thickness, and heat shield area mass based on thermal response at the stagnation-point. A uniform thickness heatshield is modeled. In the existing atmospheric reentry RDBMS, a material database has been constructed and added for common ablative thermal protection and substructure materials. User-defined materials can be easily added to the database without having to modify the thermal protection systems subsection code of the Reentry tool.

Stored constants for ablative materials include the decomposition kinetic constants used in the Arrhenius formulation for density decomposition, the resin volume fraction, the heats of formation, thermal conductivity, specific heat, emissivity, and heat of ablation curve fit constants. There are two components to the approximate technique presented here. The first component makes use of a steady state ablation assumption and employs the heat of ablation, or Q^*, to estimate recession during entry. The second component involves calculating the in-depth temperature response to predict the amount of material required as insulation to keep the bond-line temperature below a specified limit.

Calculating the in-depth temperature response is accomplished using a finite-difference formulation for the in-depth conduction through the material. Using the heat of ablation, the recession rate at any instant in time can be calculated by equation (5). The total recession is then found by integrating the recession rate over the entire trajectory. This formulation is conservative and will generally over predict recession rate.

$$\dot{S} = \frac{\dot{Q}_{hw}}{\rho Q^*} \qquad \textbf{(5)}$$

where $\dot{S}$ is the recession rate, $\dot{Q}_{hw}$ is the hot wall heat flux, ρ is the material density and Q^* is the heat of ablation. The one dimensional heat conduction equation can be written along with the surface energy balance as shown in the following equations (6) and (7).

$$\rho c_p \frac{\partial T}{\partial t} = \frac{1}{A}\frac{\partial}{\partial x}\left(\kappa A \frac{\partial T}{\partial x}\right) \quad \textbf{(6)}$$

$$\dot{q}_{conv} + \alpha \dot{q}_{rad} - \dot{q}_{cond} - \varepsilon \sigma T^4{}_w = 0 \quad \textbf{(7)}$$

where T is the temperature, T_w is the surface temperature, κ is the thermal conductivity, x is measured from TPS surface, ρ is the instantaneous material density, C_p is the material specific heat, $\dot{q}_{conv}$ is the convective heat flux, $\dot{q}_{rad}$ is the radiative heat flux, ε is the material emissivity, α is the material absorptivity and σ is the Stephen-Boltzmann's constant.

Table 2 shows the thermal and material properties for Avcoat-5026-39 and RCC. Because of the high thermal conductivity (κ) of the nose cap wall and the thinness of the wall when compared to the radius of the nose cap, the Biot number is small and the nose cap wall is effectively modeled as a "lumped-mass" structure with constant temperature throughout.

Table 2: Material and Thermal Properties of Avcoat-5026-39 and RCC

Material	Density (ρ) (kg/m^3)	Thermal Conductivity (κ) (watt/m-°k)	Specific Heat (C_p) (J/kg-°k)	Heat of Ablation (H) MJ/kg	Ablation Temperature (Ta) °k
Avcoat-5026-39	512.6	25.0	1110.0	47	835
RCC	1650.2	120.0	1312.0		

The wall thickness is defined as the depth of the ablative layer and the RCC thickness and the average head capacity of the wall is the thickness weighted heat capacity of the ablative and RCC wall layers. The "lumped-mass" temperature approximation for this wall segment can be written as

$$\dot{q}_{in} - \dot{q}_{out} = [\rho_{Avcoat} Cp_{Avcoat} t_{Avcoat} + \rho_{RCC} Cp_{RCC} t_{RCC}]\dot{T}_w \quad \textbf{[8]}$$

where $\dot{q}_{in}$ is the heat flux into he wall, $\dot{q}_{out}$ is the heat flux out of the wall, $\dot{T}_w$ is the time rate of change of the wall temperature and the remaining terms in the brackets is the average heat capacity of the wall segment. The only to significantly vary the heat capacity is to change the material thickness since the values of specific heat and density are thermal properties of the material.

V. Benchmarking SPARTA

SPARTA has been compared and evaluated against the industry standard tools like POST [9]: Program to Optimize Simulated Trajectories and TrajOpt: Trajectory Optimization tool. POST uses more traditional direct shooting approach that calculates the state variables as a function of time throughout the entire trajectory and this guarantees that the physics of the problem are accurate at all times during the simulation. This makes POST a perfect candidate for benchmarking against SPARTA.

Table 3: Benchmarking Analysis for Apollo 6 at an Entry Angle Of -5.9°

Codes	Velocity at Peak heating (km/s)	Altitude at Peak heating (km)	Maximum Deceleration [g's]	Mach Number
POST	8.45	24.01	12.15	26.40
TrajOpt	7.98	23.00	11.16	24.93
SPARTA	8.32	23.16	11.96	26.00

The flight vehicle configuration that was evaluated in POST, TrajOpt and SPARTA for the benchmark analysis was Apollo 6 reentry profile. Velocity at peak heat was found to be 8.32 km/s in

SPARTA calculations and around 8 km/s in the other trajectory tools that were used for benchmarking.

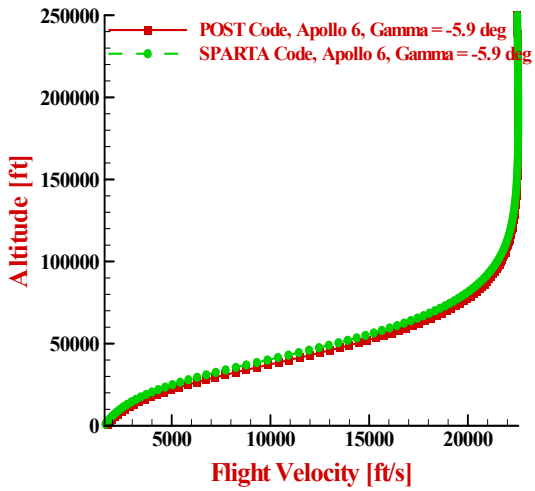

Figure 8: SPARTA Vs POST: Reentry Flight Velocity Vs Altitude

Conclusions

A platform-independent engineering level analysis, OLAP database-driven JAVA GUI based application has been developed for preliminary investigation of reentry vehicles. The code calculates all flight conditions along the trajectories including aerodynamic and Aerothermodynamic stagnation point quantities and populates the data back into OLAP database for comparative analysis capability. A fourth order Runge-Kutta integration is employed for trajectory calculations. In addition, a comprehensive database of existing planetary probe designs has been developed and integrated with the 3-DOF GUI tool. An algorithm to optimize trajectories is embedded in the code for undershoot, overshoot and optimal low-risk trajectory.

References

[1]. C. Davies, "Planetary Mission Entry Vehicles," Quick Reference Guide, Ver. 2.1, NASA-ARC, 2002.

[2]. J. E. Pavlosky and Leslie G. St. Leger, "Apollo Experience Report – Thermal Protection Subsystem", NASA TN D 7564

[3]. K. Sutton, R.A Graves, "A General Stagnation Point Convective Heating Equation for Arbitrary Gas Mixture", NASA TR-376, 1971

[4]. J. Fay and F. Riddell, "Theory of Stagnation Point Heat Transfer in Dissociated Air" *Journal of Aeronautical Sciences* 25 (2), Feb 1958.

[5]. Tauber, M. E., Sutton, K., "Stagnation Point Radiative Heating Relations for Earth and Mars Entries", *Journal of Spacecraft and Rockets*, Vol 28, No 1, 1991, pp.40-42

[6]. Tauber, M. E., "A Review of High-Speed, Convective Heat Transfer Computation Methods", NASA TP-2914, July 1989.

[7]. P. W. Huber, "Hypersonic Shock-Heated Flow Parameters for Velocities to 46,000 Feet per Second and Altitudes to 320,000 Feet, NASA TR-163, December 1963.

[8]. S. Gordon, B. J. McBride, Computer Program for Calculations of Complex Chemical Equilibrium Compositions and Applications Analysis, NASA RP-1311, October, 1994

[9]. G. L. Brauer, D. E. Cornick, and R. Stevenson, "Capabilities and Applications of the Program to Optimize Simulated Trajectories (POST)," NASA CR-2770, Feb. 1977.

ENDURANCE: THE REWARDS AND CHALLENGES OF LANDING A SPACECRAFT ON EUROPA

A. Rager[(1)], T. R. Hanley[(2)], C. Calvin[(3)], T. Balint[(4)], D. Santiago[(5)], J. Anderson[(6)], T. Cassidy[(7)], D. Chavez-Clemente[(8)], B. M. Corbett[(9)], H. Hammerstein[(10)], A. Letcher[(11)], E. M. McGowan[(12)], D. S. McMenamin[(13)], N. Murphy[(14)], M. D. Obland[(15)], J. S. Parker[(16)], T. Perron[(17)], N. Petro[(18)], M. Pulupa[(19)], R. Schofield[(20)], and H. G. Sizemore[(21)]

[(1)] UNLV, Dept of Geoscience, Las Vegas, NV 89154-4010 (U.S.A.), Email: ahrager@unlv.nevada.edu
[(2)] Georgia Institute of Technology, School of Electrical and Computer Engineering, Atlanta, GA, 30332-0250, (U.S.A.), Email: gtg237n@mail.gatech.edu
[(3)] Brown University, Dept of Geo Science 324 Brook Street, Box 1846, Providence, RI 02905, (U.S.A.), Email: Christina_Calvin@brown.edu
[(4)] JPL/CalTech, 4800 Oak Grove Drive Mail Stop 301-170U, Pasadena, CA 91109 (U.S.A.), Email: Tibor.Balint@jpl.nasa.gov
[(5)] UC Santa Cruz, Dept of Earth Sciences, Santa Cruz, CA 95064 (U.S.A.), Email: santiago@es.ucsc.edu
[(6)] Winona State Univ, Dept of Geosciences, Winona, MN 55987 (U.S.A.), Email: JLAnderson@winona.edu
[(7)] Univ of Virginia, Dept of Environmental Sciences, Charlottesville, VA 22904-4123 (U.S.A.), Email: tac2z@virginia.edu
[(8)] Stanford Univ, Dept of Aeronautical Engineering, Stanford, CA 94305-4035 (U.S.A.), Email: dchavez@stanford.edu
[(9)] Univ of Denver, Dept of Engineering and Materials Science, Denver, CO 80208 (U.S.A.), Email: bmyers@du.edu
[(10)] Gulfstream Aerospace, Gulfstream Aerospace Corp., Savannah, GA 31407, (U.S.A.), Email: Heidi_Hammerstein@hotmail.com
[(11)] Stanford Univ, School of Earth Sciences, Stanford, CA 94305 (U.S.A.), Email: aletcher@stanford.edu
[(12)] UMass, Amherst, Dept of Geosciences, Amherst, MA 01003-9297 (U.S.A.), Email: emcgowan@geo.umass.edu
[(13)] UMass, Amherst, Dept of Geosciences, Amherst, MA 01003-9297 (U.S.A.), Email: dianna@geo.umass.edu
[(14)] Univ of Colorado, Dept of Astrophysics and Planetary Science, Boulder, CO 80309 (U.S.A.), Email: nmurphy@lasp.colorado.edu
[(15)] Montana State Univ, Department of Physics, Bozeman, MT 59717 (U.S.A.), Email: obland@physics.montana.edu
[(16)] Univ of Colorado, Aerospace Engineering Sciences, Boulder, CO 80309 (U.S.A.), Email: parkerjs@colorado.edu
[(17)] UC Berkeley, Department of Earth & Planetary Science, Berkeley, CA 94720 (U.S.A.), Email: perron@eps.berkeley.edu
[(18)] Brown University, Dept of Geo Science 324 Brook Street, Box 1846, Providence, RI 02905 (U.S.A.), Email: Noahpetro@brown.edu
[(19)] UC Berkeley, Space Sciences Lab, Berkeley, CA 94720-4767 (U.S.A.), Email: pulupa@ssl.berkeley.edu
[(20)] Univ of Colorado, NOAA-David Skaggs Research Center, Boulder, CO 80309 (U.S.A.), Email: Robyn.Schofield@noaa.gov
[(21)] Univ of Colorado, Dept of Astrophysics and Planetary Science, Boulder, CO 80309 (U.S.A.), Email: hanna.sizemore@colorado.edu

ABSTRACT

The possibility that a water ocean exists beneath Europa's icy shell makes it one of the most likely places in our solar system for life to have formed and prospered. In this study, we discuss "Endurance," a proposed lander mission to Europa, and the issues involved in landing a spacecraft on the surface of Europa. Our lander was designed to meet the science objectives laid out in the Jupiter Icy Moons Orbiter (JIMO) Science Definition Team (SDT) Report [1], namely to: 1) assess the habitability of the environment beneath the surface of Europa; 2) assess the geochemical and physical structure of the surface of Europa and provide ground truth for orbital studies; and 3) provide ground based geophysical studies of Europa's icy shell. Additionally, the mission is designed to

assess surface conditions, such as surface structure and radiation levels, for future Europa lander missions. Although much can be learned from this mission, landing on Europa presents many challenges such as radiation, extreme cold, and the need to decontaminate the spacecraft to meet planetary protection requirements. Despite the harsh environment, the Endurance lander demonstrates the feasibility of landing and collecting valuable scientific data of the surface of Europa.

1. INTRODUCTION

In July, 2005, 20 Ph.D. students and recent Ph.D. graduates attended NASA's 17th Annual Planetary Science Summer School at the Jet Propulsion Laboratory. During this one-week intensive team exercise, the primary goal was to learn the process of developing a robotic mission concept into reality through concurrent engineering. Thus, with the guidance of Tibor Balint (JPL) and with the help of Team X, our team carried out a design exercise for a Europa lander mission concept.

This paper describes the science objectives, science payload, landing site selection, mission design, and lander design that resulted from this effort. In addition, the challenges of designing such a mission are discussed.

2. SCIENCE OBJECTIVES

Science objectives for this mission are adapted from [1] and [2] and include astrobiological, geophysical, and geochemical and physical structure of Europa's surface. In addition, a major objective of this study is to gather information that will help develop mission requirements for future missions.

2.1 Astrobiology

If Europa's subsurface is composed of liquid water, Europa will be one of the most likely places in the solar system for life to have developed. Therefore, astrobiological studies are at the forefront of this mission. These studies are loosely grouped into two types. The first looks for direct evidence that life existed on Europa in the past and/or continues to thrive today. These indicators, which are measured through direct chemical analysis at the surface, include the presence of complex and/or chiral compounds, stable isotopic signatures, etc. The second type of study will look at the conditions necessary for life to develop. This includes assessments of the physical properties of the subsurface, the magnetic field at the surface, etc.

2.2 Geophysics

The nature of Europa's physical structure provides a great number of unanswered questions including how thick is Europa's crust, what is the chemical and physical nature of the mantle beneath the icy shell, how does the magnetic field vary at the surface relative to orbital data, and how does the crust of Europa deform. This mission will constrain the answers to these questions through a combination of seismic and magnetic studies at the surface. Tab. 1. List of instruments and the science objectives they support.

Tab. 1. Instruments and Associated Science Objectives (A = Astrobiology; B = Geophysics; C = Geochemistry & Geomorphology; and D = Future Mission Support)

Instrument	**Science Objective** (*DS* = Direct Support; *IS* = Indirect Support)			
	A	**B**	**C**	**D**
Seismometer	*IS*	*DS*	*IS*	*IS*
Magnetometer	*IS*	*DS*		
Cameras	*IS*		*DS*	*DS*
Surface Grinder	*IS*		*IS*	*IS*
Microscopic Imager	*DS*		*DS*	
Geochemical Analysis Device	*DS*		*DS*	
Radiation sensor	*IS*		*IS*	*DS*

2.3 Geochemistry/Geomorphology

Current understanding of Europa's surface comes from orbital data. However, several important issues remain including the nature of salts integrated into the icy matrix, the ratio of contamination in the ice, etc. Developing an understanding of the chemical nature of the icy crust and interior will allow models of tectonic activity of Europa's crust to be refined. In addition, chemical studies of Europa's crust will provide ground truth for orbital missions.

2.4 Future Mission Support

In addition to these scientific objectives, this mission is designed to assess surface conditions for future missions. Placing a lander on the surface of Europa comes with many complex challenges. The cold surface temperature means that the surface is extremely hard, the lack of atmosphere makes landing a significant challenge, and the high

radiation means that the instruments have a short life span once they reach the surface. Therefore, this mission will gather data on surface conditions such as temperature, radiation level, ice structure and hardness. This will allow designs for future lander missions to be tailored to the specific hazards of Europa's surface.

3. SCIENCE PAYLOAD

The payload of Endurance consists of a suite of seven instruments capable of addressing the previously stated objectives. There is redundancy in the instruments that allows for the majority of each science objective to be met even in the event of a single instrument failure. The original design called for a ground penetrating radar, but due to mass and size constraints it was determined that radar would be a greater asset on an orbiter.

3.1 Broadband Seismometer

The broadband seismometer is the most important instrument on Endurance in that it either directly or indirectly addresses all four of the science goals. The seismometer is tri-axial and determines the amplitude and direction of high and low frequency seismic waves. It can verify the existence of a subsurface ocean by characterizing seismic activity, including high frequency oscillations due to ice cracking and surface impacts and low frequency flexing due to the Jovian gravitational field. It has a relatively high mass (2.3 kg) and requires a deployment mechanism to place it in solid contact with the Europan surface. It would also require several days of operating time to measure tidal flexing during the 3.5 day revolution period.

3.2 Magnetometer

The other instrument that addresses the geophysical goals of the mission is a magnetometer. A magnetometer would be able to verify and characterize Europa's magnetic induction field due to a subsurface ocean and the time varying field of Jupiter's origin while producing continuous time series records of the vector magnetic field near Europa. Two light-weight fluxgate magnetometers (~0.2 kg each), one placed on a boom halfway down its length, and the other at the tip would be capable of measuring at least 10 vectors/second. The magnetometers operate on DC and require low power (1 W) electronics within the bus.

3.3 Cameras

Endurance is equipped with four cameras with multispectral imagers and a descent imager used for hazard avoidance, landing site determination, and geomorphology characterization. The original design called for a panoramic camera mounted on a mast, but the mast exceeded the mass allocations. Instead, four cameras were chosen, three equidistant on the center support structure and one mounted to view a footpad for surface characterization. Each camera weighs approximately 0.26 kg, uses 3 W of power and is of similar heritage to the HazCam flown on MER. The cameras are used mainly for broadside-looking surface imaging and are an excellent tool for education and public outreach.

3.4 Microscopic Imager

For a closer look at the Europan surface, Endurance uses a microscopic imager mounted on the underside of the spacecraft. The 0.5 kg device uses about 3 W of power and will allow greater insight into the surface composition and structure as well as any potential astrobiological finds.

3.5 Surface Grinder

A surface grinder similar to the Rock Abrasion Tool (RAT) flown on MER is also included in the Endurance design. This apparatus would be lowered from the spacecraft to abrade the surface to assess its hardness and to release particles that could be characterized by the microscopic imager. The grinder has a mass of approximately 0.7 kg and uses 11 W of power. Additional development is required to allow the grinder to be able to efficiently abrade the cold, hardened surface.

3.6 Geochemical Analysis Device

In order to assess the Europan surface composition, a geochemical analysis device similar to the Plasma Experiment for Planetary Exploration (PEPE) flown on Deep Space I was chosen. The geochemical analysis device is capable of measuring and resolving the velocity distribution of electrons and ions and the mass composition of ions near Europa and in the Jovian magnetosphere in general. It resolves energy, angle, and mass & charge composition by using toroidal electrostatic angular scanning and energy/charge analyzers coupled to a linear-electric-field time-of-flight ion mass/charge analyzer. The instrument has a mass of approximately 5.5 kg, and requires less than 10 W of power, with a maximum data rate of 1.0 kbps. It has pointing requirements and preferred mounting locations on the spacecraft.

3.7 Radiation Sensor

The greatest asset Endurance provides to future mission planning is the data taken by its radiation sensor. It is able to measure high energy radiation doses while using very little power, mass, and volume. The radiation sensor would run

continuously, generating 172,800 bits of data per day. Additional data on the surface radiation environment would be obtained through the degradation of the cameras' optics, and potential degradation of electronics inside the vault.

4. LANDING SITE SELECTION

Europa's rugged terrain makes landing site selection difficult. Fig. 1 shows a variety of rough textures that dominate the surface of Europa. Locating a safe landing site which will also support Europa science objectives is even more challenging. A landing site must be relatively smooth and flat and encompass an area large enough for a landing ellipse. The authors followed the recommendation of Castalia Macula by Prockter and Schenk [3] as a landing site (Fig. 2).

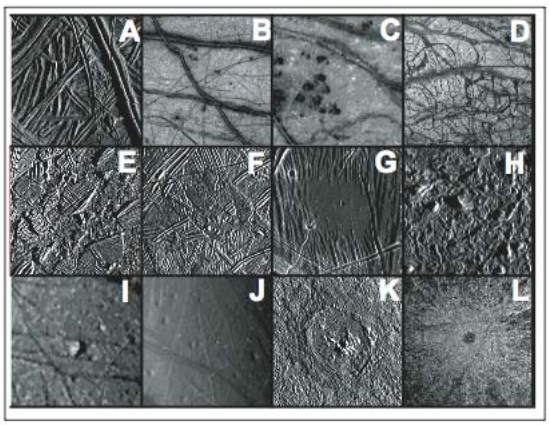

Fig. 1. Various Landscapes and Features on Europa: A = Ridges and Lineaments (27 m/pixel); B = Triple Bands (1.6 km/pixels); C = Dark Spots; D = "Pull-apart" Terrain (1.6 km/pixel); E = "Raft" Terrain (250 m/pixel); F = Flows (225 m/pixel); G = "Puddle" (27 m/pixel); H = Mottled Terrain (35 m/pixel), I = Knobs (1.6 km/pixel); J = Pits (1.6 m/pixel), K = Crater (300 m/pixel), L = Crater Ejecta. (Adapted from NASA Planetary Science Photojournal Image PIA00746 (http://photojournal.jpl.nasa.gov)

Prockter and Shenk [3] recommended Castalia Macula (Fig. 2) as a landing site for a future lander mission to Europa for two reasons. First, Castalia Macula is a relatively low-risk place to land. Second, topographic and geologic mapping of the Macula indicates it may include material that has been recently erupted from the subsurface, making it a good place to sample material that may have been in communication with Europa's putative subsurface ocean.

Castalia Macula (1.6° S, 225.7° W) is a depression about 350 m deep and 30km in diameter [3]. The Macula encompasses about 600m^2, making it large enough to accommodate the landing ellipse. Its smooth texture indicates the Macula is relatively smooth and flat. The smooth texture and large size make Castalia Macula a relatively safe place to land.

The dark and reddish material filling the Macula stands out against its lighter and more textured surroundings [3]. Castalia Macula is bounded by two large uplifted domes to the north (900 m high) and south (750 m high). Although superposition and topographic relationships indicate that Castalia Macula is older than the adjacent domes and the relatively young Pwyll impact crater, the albedo, color, and lack of cross-cutting features suggest that the Macula and domes are relatively young [3].

Fig. 2. Castalia Macula ((1.6˚ S, 225.7˚ W). (Image from PDS Map-A-Planet, http://pdsmaps.wr.usgs.gov/maps.html).

In addition to providing a relatively safe landing site, Castalia Macula meets many of the criteria for meeting astrobiological science goals on Europa set forth by [4] including evidence of high material mobility, concentration of non-ice components, and relative youth. These features also make it a good location to support the geochemistry science objective. The relatively smooth, flat surface should ensure safe deployment of the seismometers and promote communication with the orbiter to support the geophysics science objective.

Although Castalia Macula is a topographic depression, it is surrounded by high domes; this large variation in topography should enable the cameras to image the landscape in support of the geomorphology science goal.

5. MISSION DESIGN

This section summarizes the Endurance Lander mission and associated challenges and assumptions.

5.1 Challenges

Design of a lander mission to Europa poses many challenges including planetary protection, radiation shielding, and landing.

Since determining whether chemical evidence of life exists on Europa is a primary science goal, forward contamination is of utmost concern. However, the one-week time frame for design of this mission did not afford us an opportunity to adequately address this issue.

Because it is situated within Jupiter's magnetosphere, Europa has an extremely high radiation environment. This makes it necessary to include radiation shielding around the instruments and electronics, essentially enclosing them in a vault. In spite of the shielding, the high radiation environment results in shorter lifespan for instruments.

Europa has virtually no atmosphere. Therefore, a propulsive landing is required. The increased mass from radiation shielding and greater delta V increases the wet mass of the propulsion system.

5.2 Assumptions

The Endurance lander was designed during the first one-week session of the 2005 NASA/JPL Planetary Science Summer School. The orbiter was designed by another team of students during the second one-week session. The Endurance lander and mission design are based upon several assumptions about the orbiter. These assumptions include (1) 110° retrograde orbit, (2) 100 km circular orbit, (3) Orbital period = 125.6 minutes, (4) ~30 day nominal mission, (5) ~5.25 AU from Earth, (6) Will provide landing site validation, and (7) Science payload will complement lander.

5.3 Mission Design Summary

Fig. 3 summarizes the Endurance Lander mission launch and VEEGA cruise. Separation of the Endurance Lander from the orbiter and the lander's entry, descent, and landing are summarized in Fig. 4 and Fig. 5.

The Endurance orbiter/lander mission will launch on December 2, 2014 with a VEEGA Cruise lasting 7.76 years. The spacecraft will intercept Jupiter's orbit on about September 5, 2022; Europa Orbital Insertion will occur about June 7, 2023. The spacecraft will orbit Europa approximately 8 days during which time it will gather images to validate the primary landing site within Castalia Macula.

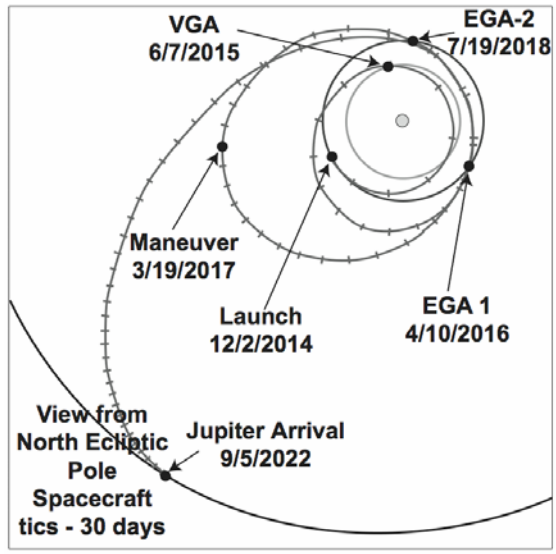

Fig. 3. Endurance launch and VEEGA cruise schedule.

Landing will occur on about June 15, 2023. Endurance's deorbit burn will begin 30 sec after separation from the orbiter at a 100 km parking orbit and last 42 sec. After exiting the 100 km parking orbit, Endurance will coast for 49.3 min and execute its stop burn for 668 sec. At the end of the stop burn at an altitude of 2 km, Endurance will reorient for landing. Endurance will then go through a 50 sec free fall to an altitude of 700 m with a radar altimeter and descent imager active. During a powered descent lasting 20 seconds, the Endurance lander will have hover and ~2000 m divert capability. Engine cutoff will occur at 10 m altitude with touchdown at T = 62.35 min after separation. Most science instruments have a 3.5-day lifetime, while the seismometer has a 7 – 14 day lifetime.

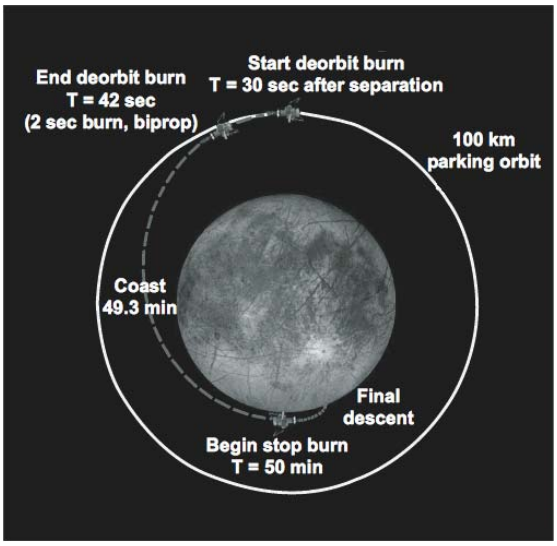

Fig. 4. Endurance lander separation from orbiter, entry, and descent.

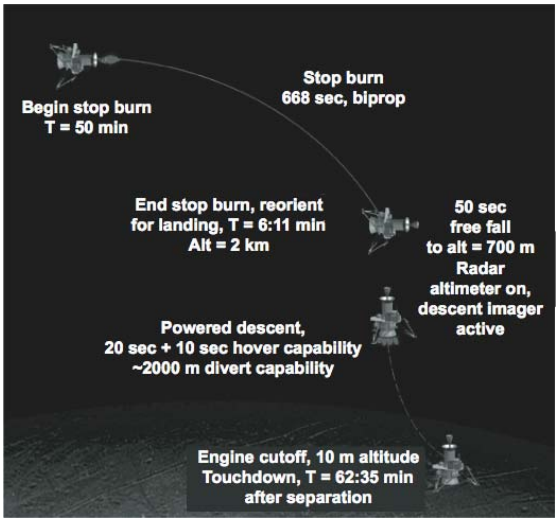

Fig. 5. Endurance landing.

6. ENDURANCE LANDER

JPL/NASA Planetary Science Summer School students who co-authored this paper worked with JPL's TeamX to design the Endurance Europa lander. The lander and its launch and landed configurations are shown in Fig. 6 and Fig. 7.

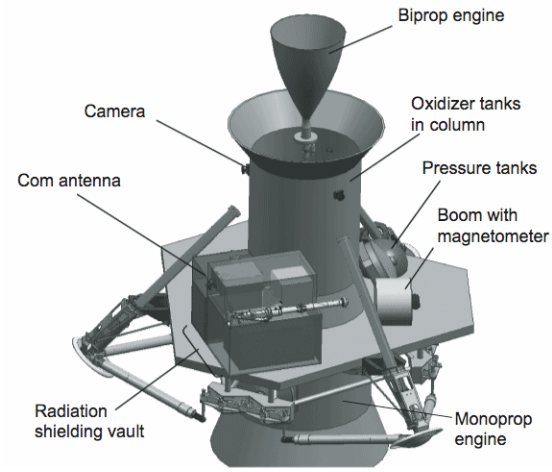

Fig. 6. Endurance Europa lander.

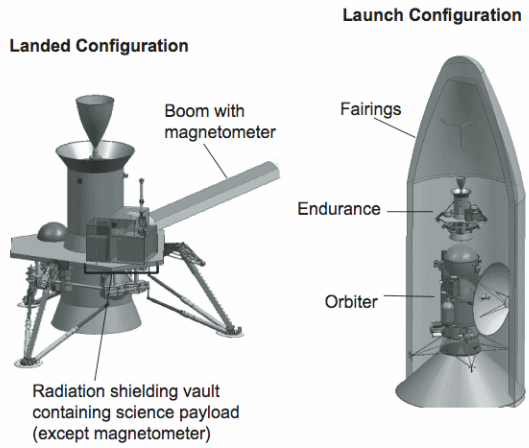

Fig. 7. Endurance landed configuration and launch configuration.

Fig. 8 shows the final mass budget for the Endurance lander. The final mass of the Endurance lander is about 820 kg, 320kg more than the 500kg goal (Fig. 9).

In an attempt to reduce the mass of the lander to 500kg or less, some instruments were descoped. Mass of a Europa lander with a minimum number of instruments to cover the science floor was about 680 kg (Fig. 9). Finally, all instruments, except those required for landing (i.e., altimeter and descent imager) were dropped. The result was an "empty box" with a mass of about 640 kg (Fig. 9).

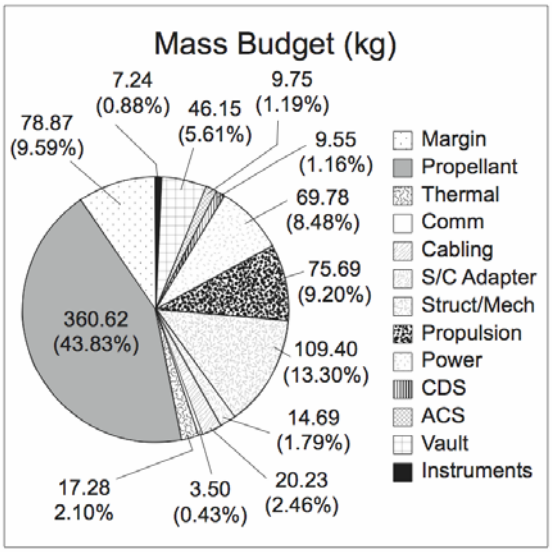

Fig. 8. Endurance mass budget with complete science package.

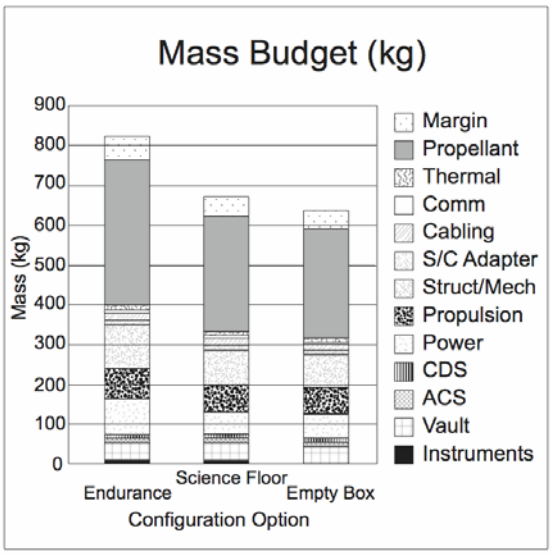

Fig. 9. Mass budget for Endurance lander with complete science package, lander with science floor option, and lander with no sensors to support the science package. None of the options met the 500 kg requirement.

7. CONCLUSIONS

Exploration of the Jovian system, including Jupiter and Europa, is a high priority science goal, which also presents significant technological difficulties.

The extreme environment of Europa can be characterized by high radiation and low temperatures. These must be mitigated. The proposed Europa Geophysical Explorer mission was identified in [5] as the highest priority first decade flagship mission. This orbiter could also include a small lander to provide in-situ validation of remote sensing measurements.

Previous assessments assumed 375 to 500 kg mass allocation for add-on Europa landers. The present study resulted in a lander mass allocation requirement of ~640 to ~820 kg. However, the current study had limited scope and resources, thus the design was not optimized.

It is recommended to carry out follow-on studies to refine the findings and to optimize the design.

8. ACKNOWLEDGEMENTS

Funding for the NASA/JPL Planetary Science Summer School was provided by the NASA Science Mission Directorate. We would like to thank the following individuals and groups for their help and hard work in making the Planetary Science Summer School such a rewarding experience for all of us: Anita Sohus (Task Manager), Corinne Karpinski (Coordinator and Escort), James Harrington (Goddard Space Flight Center/Mu-SPIN Program), Daniel Sedlacko (Webmaster and Escort), Jean Clough (Escort), Kay Ferrari (Solar System Ambassador Program), JPL Team X (Robert Carnright, Adrian Downs, Luke Dubord, Michael Etters, Gerardo Flores, Gani Ganapathi, Robert Haw, David Hansen, Cate Heneghan, Robert Kinsey, Gerhard Klose, Masashi Mizukami, David Mulier, Mark Schwochert, Abhijit Sengupta, Parthasar Shakkottai, William Smythe, Christopher Swan, Farinaz Tehrani, Yu-wen Tung, Keith Warfield, and Daniel Winterhalter), and our reviewers (James Cutts, Celeste Satter, David Senske, William Smythe, Theodore Sweetser, and Greg Wilson).

9. REFERENCES

1. Greeley, R. and Johnson, T. (2004), *Report of the NASA Science Definition Team for the Jupiter Icy Moons (JIMO)*. Technical Report, National Aeronautics and Space Administration, February 13, 2004.
2. Balint, T. (2004), Europa Surface Science Package Feasibility Assessment. 60 p. JPL D-30050, NASA Jet Propulsion Laboratory / California Institute of Technology, Pasadena, CA, September 22, 2004.

3. Prockter, L, Schenk, P (2004), Origin and Evolution of Castalia Macula, An Anomalous Young Depression on Europa, Eos Trans. AGU, 85(47), Fall Meet. Suppl., Abstract P31A-0962.
4. Figueredo, P. H., Greeley, R., Neuer, S., Irwin, L., and Schulze-Makuch, D. (2003),
Locating Potential Biosignatures on Europa from Surface Geology Observations, *Astrobiology*, vol 3, pp 851-861.
5. NASA. *Solar System Exploration*. JPL 400-1077, Office of Space Sciences, National Aeronautics and Space Administration, Jet Propulsion Laboratory / California Institute of Technology, Pasadena, CA, 2003.

TITAN ORBITER WITH AEROROVER MISSION (TOAM)

E. C. Sittler Jr.[(1)], J. F. Cooper[(1)], P. Mahaffy[(1)], J. Esper[(1)], D. Fairbrother[(2)], R. Farley[(1)], J. Pitman[(3)], D. R. Kojiro[(4)], M. Acuna[(1)], M. Allen[(5)], G. Bjoraker[(1)], J. Brasunas[(1)], M. J. Burchell[(6)], M. Burger[(1)], G. Chin[(1)], A. J. Coates[(7)], W. Farrell[(1)], M. Flasar[(1)], B. Gerlach[(8)], S. Gorevan[(9)], R. E. Hartle[(1)], Eastwood Im[(5)], D. Jennings[(1)], R. E. Johnson[(10)], W. T. Kasprzak[(1)], H. W. Kunow[(11)], S. Livi[(12)], H. Niemann[(1)], J. Nuth[(1)], D. J. McComas[(13)], R. MacDowall[(1)], B. McKibben[(14)], R. Pfaff[(1)], F. Raulin[(15)], D. Reuter[(1)], F. Robb[(16)], D. Schulze-Makuch[(17)], R. Wimmer-Schweingruber[(18)], P. Siegel[(5)], D. E. Smith[(1)], A. Steele[(18)], J. Trombka[(1)], Y. Yung[(19)], and J. C. Zarnecki[(20)]

[(1)]NASA Goddard Space Flight Center, Greenbelt, MD, 20771, USA, Email: Edward.c.sittler@nasa.gov
[(2)]NASA-GSFC Wallops Flight Facility, Wallops, VA, USA, Email: Debora.A.Fairbrother@nasa.gov
[(3)]Lockheed Martin-ATC, Palo Alto, CA, USA, Email: joe.pitman@lmco.com
[(4)]NASA Ames Research Center, Moffett Field, CA, USA, Email: dkojiro@mail.arc.nasa.gov
[(5)]Jet Propulsion Laboratory, Pasadena, CA, USA, Email: mark.allen@jpl.nasa.gov
[(6)] University of Kent, Canterbury, Kent CT2 7NH, UK, Email: m.j.burchell@ukc.ac.uk
[(7)] Mullard Space Science Laboratory, University College London, Dorking, UK, Email: ajc@mssl.ucl.ac.uk
[(8)] Rockwell Collins Deutschland GmbH, Grenzhöfer Weg 36, Heidelberg, Germany, Email: bernd_bs@gmx.de
[(9)] Honeybee Robotics, Ltd., New York, NY, USA , Email: gorevan@honeybeerobotics.com
[(10)] University of Virginia, Charlottesville, VA, USA, Email: rej@virginia.edu
[(11)] University of Kiel, Keil, Germany, Email: kunow@physik.uni-kiel.de
[(12)] Applied Physics Laboratory, Laurel, MD, USA, Email: stefano.livi@jhuapl.edu
[(13)] Southwest Research Institute, San Antonio, TX, USA, Email: dmccomas@swri.edu
[(14)] University of New Hampshire, NH, USA , Email: Bruce.McKibben@unh.edu
[(15)] LISA- University of Paris, France, Email: raulin@lisa.univ-paris12.fr
[(16)] University of Maryland Biotechnology Institute, Baltimore, MD, USA, Email: robb@umbi.umd.edu
[(17)] Washington State University, Pullman, WA, USA, Email: dirksm@mail.wsu.edu
[(18)] Carnegie Institution of Washington, D. C., USA, Email: a.steele@gl.ciw.edu
[(19)] California Institute of Technology, Pasadena, CA, USA, Email: yly@mercu1.gps.caltech.edu
[(20)] Open University, Milton Keynes, UK. Email: j.c.zarnecki@open.ac.uk

ABSTRACT

We propose to develop a new mission to Titan called Titan Orbiter with Aerorover Mission (TOAM). This mission is motivated by the recent discoveries of Titan, its atmosphere and its surface by the Huygens Probe, and a combination of in situ, remote sensing and radar mapping measurements of Titan by the Cassini orbiter. Titan is a body for which Astrobiology (i.e., prebiotic chemistry) will be the primary science goal of any future missions to it. TOAM is planned to use an orbiter and balloon technology (i.e., aerorover). Aerobraking will be used to put payload into orbit around Titan. The Aerorover will probably use a hot air balloon concept using the waste heat from the MMRTG ~ 500 watts. Orbiter support for the Aerorover is unique to our approach for Titan. Our strategy to use an orbiter is contrary to some studies using just a single probe with balloon. Autonomous operation and navigation of the Aerorover around Titan will be required, which will include descent near to the surface to collect surface samples for analysis (i.e., touch and go technique). The orbiter can provide both relay station and GPS roles for the Aerorover. The Aerorover will have all the instruments needed to sample Titan's atmosphere, surface, possible methane lakes-rivers, use multi-spectral imagers for surface reconnaissance; to take close up surface images; take core samples and deploy seismometers during landing phase. Both active and passive broadband remote sensing techniques will be used for surface topography, winds and composition measurements.

1. INTRODUCTION

Titan is presently listed as a high-priority future mission in the 2003 *Solar System Decadal Survey*, as well as in the June 2006 draft of the emerging *NASA Science Plan*. The Cassini/Huygens results have further elevated scientific priority for a mission to Titan. In this mission an orbital spacecraft 1200 km above Titan's extended atmosphere, works in concert with a hot air balloon, the Aerorover, globally traversing Titan at about 10km/hr. The mission will feature global radar

sounding, both passive and active laser remote sensing from the orbiter, global sampling of Titan's surface and atmosphere, along with close-range reconnaissance from the Aerorover.

In the case of Titan, there is now evidence of methane river beds, lakes and surfaces possibly saturated with methane and other hydrocarbons [1]. Titan's upper atmosphere and ionosphere is now known to be dominated by a very rich hydrocarbon chemistry [2, 3] producing precipitates raining down to Titan's surface where further complex chemistry can take place. The presence of methane in the atmosphere (detected *in situ* by the Huygens probe [4]), ~ 2% in upper atmosphere and ~ 6% at surface, means it must be continuously replenished (lifetime ~ 10 Myrs; [5]) from Titan's interior and thus Titan must be geologically active. There is indirect evidence from observation of horizontal clouds [6] that cryo-volcanism may be an ongoing process at Titan. Evidence for fluvial processes has been detected by Cassini cameras and radar [7,8], while Huygens cameras show evidence of methane rain [1] and constant methane drizzle [9]. Recently, Cassini radar has discovered methane or ethane lakes at Titan's North Polar Cap [*Cassini-Huygens News Release 2006-097*].

Originally, a Titan only mission called "Titan Orbiter Aerorover Mission" (TOAM) was put forth in a Goddard-led proposed 2003 *Vision Missions* Study by *Sittler et al.,* [2003] [10]. In that study, reviewed in our Figures 1, 2 and 3, they proposed a hot air balloon concept. The advantage of the hot air balloon is that the mass of the inflatable gas is not brought from Earth. Furthermore, over time the gas will eventually diffuse across the walls of the balloon and escape, thus limiting the balloon lifetime. A hot air balloon has an infinite reservoir of gas, so long as the energy source duration is unlimited, essentially true for an RTG power source. An orbiter is needed to avoid long blackout periods when the balloon is not facing Earth and the orbiter can provide global positioning information for the balloon's navigation system.

As presently conceived, TOAM is a multi-faceted mission with launch using a Delta IV Heavy for high C3 interplanetary orbit injection, possible Jupiter flyby, Solar Electric Propulsion (SEP), orbit injection around Titan via aerobraking at Titan, probe entry with balloon technology (i.e., aerorover phase) and finally a landing phase. Mission phase durations include 5-9 years for cruise to Saturn, and six months each for orbiter reconnaissance, aerorover global reconnaissance, aerorover global surface science and aerorover landing. There could be an extended phase for orbiter-lander science operations.The orbiter is planned to be powered by 3 MMRTGs and Aerorover by a single MMRTG. The Aerorover will probably use a hot air balloon concept using the waste heat from the MMRTG ~ 500 watts.

Our orbiter-Aerorover approach is unique and provides assurance for a successful long-term mission. Autonomous operation and navigation of the Aerorover around Titan, which will include descent near to the surface to collect surface samples for analysis, is in itself a very complex process and will require nearly continuous tracking and navigation updates. Only an orbiter can provide this capability as a relay station and GPS role so that the Aerorover will be able to navigate safely within Titan's environment, while maintaining nearly continuous communication with ground stations. Although very complex, our goal is to keep the Aerorover as simple as possible in order to enhance the likelihood of success. Experience has shown that such complex missions will develop unexpected problems, for which a balloon concept allows for it to safe itself by going to high altitudes. This allows teams on the ground the necessary time needed to work around such problems. New technologies will need to be

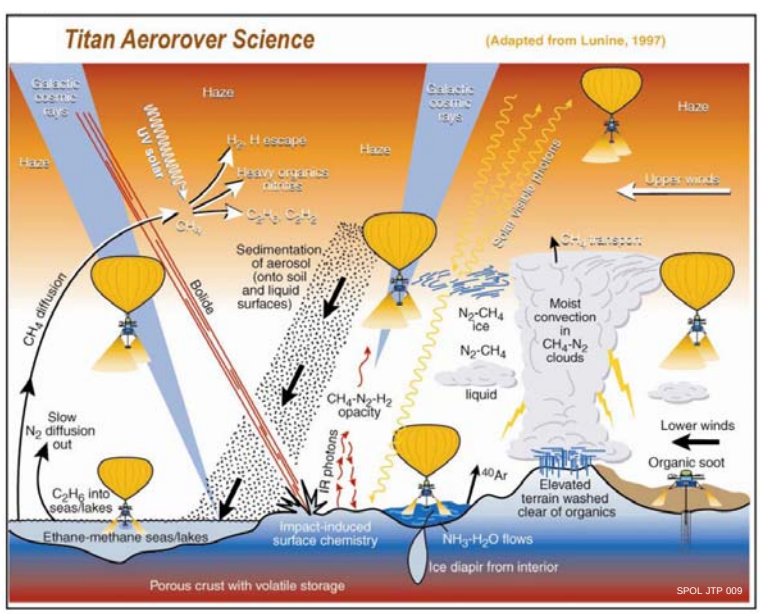

Figure 1 TOAM Aerorover Science Concept

developed and miniaturization will be required to maintain functionality while controlling mass, power and cost. Duty cycling will be used. The orbiter will combine altimetry, radio science and remote sensing instruments to measure the global topography, sub-surface structure and atmospheric winds during its recon phase. The Aerorover can then use this information to navigate safely around Titan and identify prime sites for surface sampling and analysis. In situ instruments will sample the upper atmosphere which may provide the seed population for the complex organic chemistry on the surface. The Aerorover will have all the instruments needed to sample Titan's atmosphere, surface, and possible methane lakes-rivers. In flight it will also use multi-spectral images for surface reconnaissance and take close up surface images. Surface core sampling and seismic measurements can be carried out during the final landed phase.

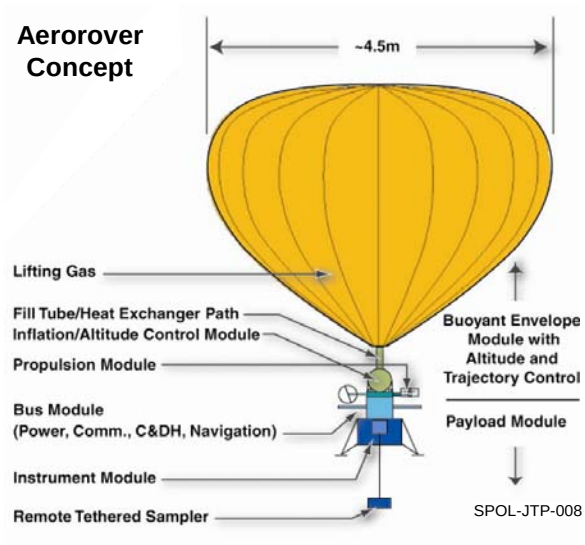

Figure 2 TOAM Aerorover Concept Design

3. IMPLEMENTATION APPROACH

3.1 Mission Design

TOAM leverages the planned maturation of a number of advanced technologies. They range from advanced chemical propulsion systems to power generation and aerocapture, advanced imaging systems, miniaturized instruments and aerorover technologies. This section summarizes major elements.

Mission operational phases will be:

- Launch and orbit injection; (after 2013)
- Cruise and midcourse corrections, which may include gravity assist maneuvers; (5 to 9 years)
- Saturn/Titan orbit insertion with possible tour with Enceladus as primary target and then obit insertion at Titan
- Orbiter science/reconnaissance; (6 months)
- Aerorover science; (12 months)
- Surface science; (6 months).

Total science mission operations is 2 years, from Titan orbit insertion to end of surface operations. Extended science operation capabilities from the orbiter would be included.

Transfer orbit from Earth to Titan can be achieved using either chemical propulsion alone or a combination of solar electric (SEP) and chemical propulsion. Preliminary studies indicate the SEP option will deliver a higher payload mass for a given launch vehicle and hence is the baseline. In this case, the low-thrust trajectory assumes the SEP

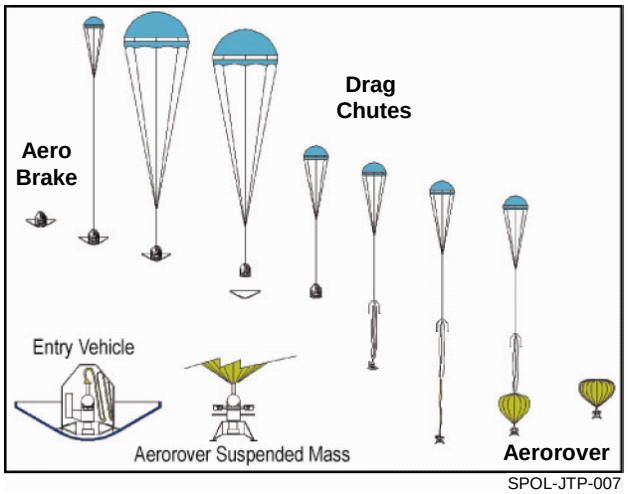

Figure 3 TOAM Aerorover Insertion

system will only be operated within 2 to 3 AU from the Sun, and ejected beyond. The spacecraft then continues operating with its chemical propulsion system. The Titan orbit will be achieved using a combination of chemical propulsion and aerodynamic forces. Aerocapture into the Saturnian system is the baseline scenario. Titan will be used to provide the initial aerocapture ΔV for injection into either a Saturn or a direct Titan orbit. The former requires a lower expenditure of fuel initially but necessitates a second pass near Titan for orbit insertion. The latter implies a larger initial ΔV and aerothermodynamic heat loads but may provide for a quicker start to science operations. Delayed Titan orbit entry allows opportunities for flybys of other high-interest Saturn moons including Enceladus.

For one study we had the Earth-Saturn trajectory for a SEP case with no gravity assist. The initial 14-hour elliptical polar science orbit (also shown) affords a close approach to Titan for radar and radio science measurements, and provides for an extended picture of its particles and fields environment. The orbit would then be circularized for surface mapping and aerorover release and tracking. Orbit radius may be raised to minimize blackout periods for aerorover.

Aerorover entry into Titan's atmosphere occurs after a 6-month period of orbital surface mapping and science reconnaissance. The entry sequence is shown in Figure 3, and includes aerodynamic braking with the aeroshell, parachute deployment, buoyant envelope deployment, and parachute release. This marks the onset of one year of science operations, leading to the 6-month surface landing phase. Landing may be achieved by slowly deflating the buoyant envelope until touchdown, and immediately detaching the envelope module to prevent the material from covering the payload module. The Aerorover phase then ends and transitions to the final fixed lander phase with continuing support from the orbiter.

3.2 Titan Orbiter

The orbiter houses the remote-sensing instruments, provides health and safety services to the aerorover during the cruise and orbit phases, transmits data to and from the aerorover, and communicates with the Deep Space Network (DSN). It also executes concurrent science operations during the aerorover and surface phases.

The baseline communications approach is to use Ka-band to downlink science data and X-band for uplink of commands and downlink of engineering telemetry. This approach also provides the required dual-band coverage for radio science observations. Assuming a 2-m high gain antenna (HGA), Reed-Solomon encoding, a maximum compressed data volume of 1.5 Gbits, a DSN 70-m equivalent antenna, and 86 kbps downlink rate, downlink time is about 5 hours. Data acquisition management and advanced encoding techniques are also assumed. Alternatively, use of optical communications will be explored during the study.

Three Multi-Mission Radioisotope Thermo-electric Generators (MMRTGs) yield ~ 300W of power. Details of a power management scheme using these and alternative radioisotope power systems need to be developed. A single Stirling Radioisotope Generater (SRG) probably would be used for the aerorover with ~ 100 W of electricity and ~ 500 W of waste heat..

The combined spacecraft-Aerorover payload is housed within a protective aeroshell, which provides thermal protection during aerocapture. The aerorover will have its own heat shield for entry into Titan's atmosphere. Modular and reconfigurable spacecraft architecture design principles are an important technology identified for future development.

3.2.1 Candidate Orbiter Science Instruments

Advanced remote sensing with high spatial and spectral resolution is essential to achievement of orbiter science goals. A facility class telescopic system, such as Lockheed Martin's Multiple Instrument Distributed Aperture Sensor (MIDAS) payload (see Figure 5), will be required for active and passive imaging. Lidar technologies will be used to produce surface topology maps needed for Aerorover navigation near the surface.

Titan Radio Science (TRS) will use both X- and Ka-band systems with ultra-stable oscillators for atmosphere-ionosphere radio occultation measurement, and use a "two-way" coherent tracking mode for gravity measurements. The combination of MIDAS-Lidar and TRS will provide the topographic and gravity measurements to allow detection of a subsurface ocean and determine crustal thickness [11, 12, 13]. The combination of the Titan Submillimeter Limb Sounder (TSLS), and Titan Infrared Spectrometer (TIRS), both integrated with MIDAS, and use of the wind equation will allow measurement of the global zonal wind pattern down to the surface. TSLS will use a two-channel submillimeter wave heterodyne radiometer system, while TIRS is an improvement to the Cassini Composite Infrared Spectrometer.

The fields and particles instrument package deals with the complex interaction of Saturn's magnetosphere (or solar wind/magnetosheath) with Titan's upper atmosphere and the corresponding upper atmospheric organic and elemental composition. This instrumentation also addresses induced complex current systems that can affect Aerorover measurement of electric and magnetic fields near the surface. Furthermore, the package quantifies the role of cosmic rays in Titan's middle atmosphere in providing ionization energy to the organic chemistry.

3.3 Aerorover

The Aerorover provides the platform to conduct *in-situ* sampling of Titan's atmosphere and surface at multiple locations. Aerorovers are ideally suited for this type of mission because these airborne platforms can travel above the surface at controlled altitudes and can cover greater areas than traditional surface vehicles. Close-up surface imaging of Titan; chemical, atmospheric and magnetometer measurements; and periodic surface sampling are all possible with the Aerorover regardless of surface composition.

The Balloon Program Office (BPO) at GSFC's Wallops Flight Facility (WFF) is NASA's center for ballooning technology development, design, and operations management. With its long and successful history of scientific ballooning, from conventional zero-pressure balloons to current superpressure ultra long duration balloon (ULDB) development, BPO is developing advanced balloon technologies for both terrestrial and Mars applications. Our partnership with Lockheed Martin will provide extensive knowledge in the balloon technology area from their High Altitude Balloon Program.

3.3.1 Aerorover Requirements

Science mission goals drive the following preliminary Aerorover requirements:

- Altitude control at 0-10 km;
- Highest priority scientific instruments;
- Ground track trajectory control;
- Survival of 5 to 9 year cruise, orbit insertion, and atmospheric deployment;
- Acquisition and analysis capability for surface and subsurface samples.

3.3.2 Candidate Aerorover Science Instruments

We now list possible candidate aerorover instruments, for which some were derived from the Huygens instrument package [14]. Resources will be a limiting factor for instrument selection. To begin, Gas Chromatigraph Mass Spectrometer (GCMS) measurements are key to achieving the TOAM requirements relating to the nature and complexity of prebiotic chemistry at Titan. The Aerosol Collector Pyrolyzer (ACP) uses a stainless steel filter to collect aerosols and retract into a chamber for later analysis by the GCMS. Microarray Assay for Titan Exploration (MATE) can detect large complex organic molecules such as peptides, proteins, and DNA fragments. The Titan

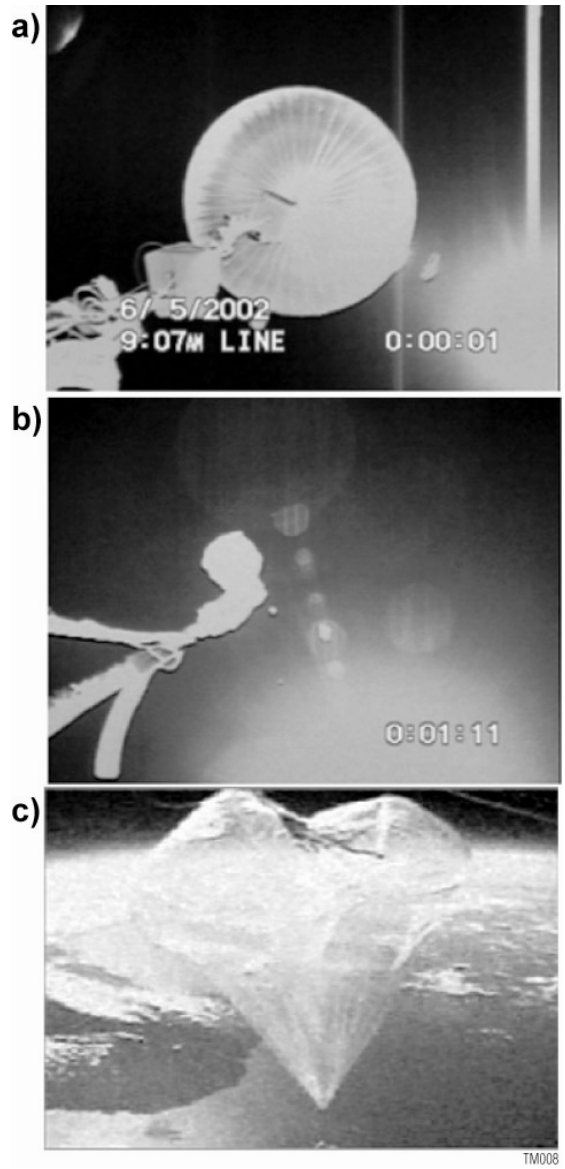

Figure 4 Successful aerial deployment and inflation of Goddard/Wallops prototype Mars pumpkin balloon. (a) upward view of carrier balloon just prior to deployment; (b) upward view of prototype balloon just after deployment; (c) side view of Mars prototype during descent (island of Hawaii in background).

Ice and Dust Experiment (TIDE) instrument will be used to collect both liquid and surface samples, store these in appropriate canisters, and then use, for example, pyrolosis to deliver the effluent gases to the GCMS. The Titan Neutron/Gamma-Ray Instrument (TNGRI), lowered near the surface by tether, will measure elemental and mineralogical chemistry to ~10 cm depth. The Atmosphere Properties Unit (APU) is composed of accelerometers, electric and magnetic field probes, a temperature sensor, pressure gauge, and acoustic and conductivity sensors. The Liquid Properties

Unit (LPU) uses sonar for lake depth and speed of sound measurements, temperature and density sensors for fluids, and a tiltmeter for measurement of surface waves and tides [15]. The Surface Properties Unit (SPU) will measure surface stiffness, uniformity and granular structure (sands, grit, gravel) [15] and have a magnetometer to measure crustal magnetism [16] and conduct induced magnetic field surveys in conjunction with external field measurements by the orbiter. A miniature version of LM's MIDAS would be used for Lidar altimetery and wind measurements (i.e., Doppler off of aerosols) and multi-spectral measurements for surface composition to name a few.

3.3.3 Aerorover Development Approach

The Aerorover must be stowed for several years, receive power and data from the orbiter, and deploy and inflate while descending through the Titan atmosphere. After deployment, the Aerorover must travel about Titan, obtain detailed imaging of Titan's surface, collect and analyze surface samples at numerous locations, and transmit the information to the orbiter. At the end of the aerial portion of the mission, the instrument package must safely land to collect and conduct detailed analyses of surface and subsurface samples. The data are then transmitted to the orbiter for relay to Earth.

The proposed concept poses several key Aerorover design and operational questions:

- What buoyant envelope design will permit the required altitude control?
- What trajectory control system will provide the greatest mission flexibility?
- What materials will survive transit, atmospheric entry and, deployment and perform in the Titan environment?
- What level of autonomy is required for Aerorover operations?
- How and when will information be exchanged between the orbiter and the Aerorover?
- How will the Aerorover safely land the instrumentation package on the surface?
- How will the Aerorover be constructed and handled to ensure that its surfaces are free of bioburden?

Mission requirements and extreme environmental conditions present unique vehicle design challenges and opportunities. The extreme temperatures of Titan require buoyant envelope materials to perform at temperatures that are much lower than any previously studied. If hot air balloon concept is not used, then lifting gas must be transported from Earth or generated *in-situ.* The vehicle must be capable of autonomous or semi-autonomous trajectory control for latitude, longitude and altitude control. The aerorover must be capable of interacting with Titan's surface to collect and analyze surface samples.

With regard to deployment, Titan's dense atmosphere enables sufficient time for the entry, deployment, and inflation sequence, as shown in Figure 3. BPO's ability to aerially deploy and inflate a planetary balloon for Mars was successfully demonstrated in June 2002 as shown in Figure 4. This experience, combined with research in packaging technologies will aid in providing a sound basis for continuing development.

Finally, any future mission to Titan with entry vehicle will require consideration of planetary protection.

4. TECHNOLOGY DEVELOPMENT

Our goal is to fit within the cost cap of New Frontiers for our TOAM concept. Our approach to achieving this goal is to establish partnerships with industry such as Lockheed Martin's MIDAS concept, High Altitude Balloon technology, missile defence technologies for atmospheric entry probes and RTG technologies. We will also take advantage of the capabilities offered by Ames Research Center (ARC) when it comes to astrobiology, aerocapture technologies, and planetary protection. Finally, we will look to develop new technologies in the area of miniaturization such as microelectronics, MEMS technology, sensor miniaturization and nanotechnology. We want to reduce mass, power

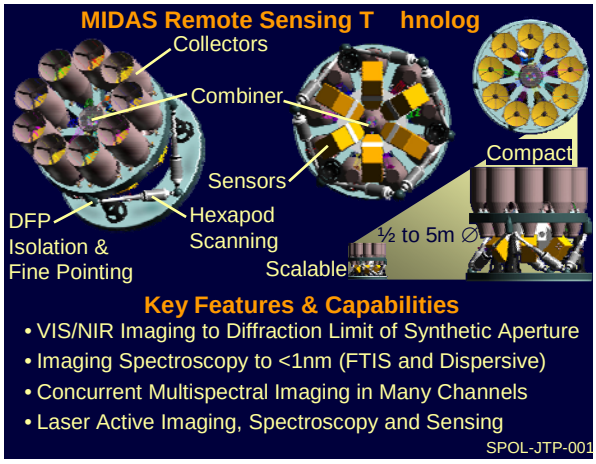

Figure 5 LM MIDAS Payload Technology

and volume while maintaining functionality. Work is already in progress when it comes to spacecraft miniaturization [17] and we plan to take advantage of these new technologies. Such technologies would be used for both the orbiter & Aerorover. We will briefly describe three key technologies actively being considered.

4.1 MIDAS Concept

Reconnaissance is a major element of the TOAM concept with active and passive imaging playing a major role in this process. LM's MIDAS testbed system [18, 19] can be considered a facility of telescopes which can be used individually and together as a phased array to provide affective aperture sizes ~ 1 meter. This technology has been developed by LM for a number of applications. This will greatly reduce the risk and cost of our TOAM mission. We plan to develop the interfaces between passive (spectroscopic measurements) and active (Lidar) imaging concepts. For the orbiter we would use a version of MIDAS having an effective aperture ~ 1 meter and for the balloon a lightweighted version with an effective aperture ~ 30-50 cm. The MIDAS telescope system has the capability to isolate itself from the spacecraft with 60bD of broadband attenuation, featuring precise pointing needed for its very high resolution active and passive imaging of Titan, Enceladus and the Saturnian system, before and during the Titan orbiter phase. This vibration isolation is very important as the Aerorover moves through atmospheric turbulence. On the balloon, a mini-version of MIDAS can provide altimetry data so that balloon can provide direct altimetry data, also supplemented by radar and sonar techniques, to assure safe navigation near the surface and avoidance of potentially hazardous surface topography, such as hills and cliffs. The gondola of the balloon will slowly rotate so that the imagers can get a panoramic view of the surface and atmosphere (i.e., MIDAS can look within a ±30° conical FOR). Tracking of the balloon will also provide local wind velocity data. The distributed aperture system minimizes risk, since single mirror failure cannot result in total imaging system failure, and this system can be then reconfigured with only minor reduction in capability.

4.2 Lidar Imaging

We plan to establish the interfaces between Goddard developed Lidar systems and Lockheed's MIDAS development effort. This is another technology that can be considered already established.

Lidar measurements during the recon phases are required for surface topography and atmospheric winds down to the surface, so that the balloon can navigate safely around Titan. Here, we note that the Huygens probe cameras clearly showed rolling hills with 100 meter heights present at probe's landing site [1], while the Cassini orbiter is only expected to provide ~ 20-30% radar coverage (i.e., topography) of Titan's surface. The Cassini imagers only provide albedo variations on the surface (i.e., no topography information). Lidar altimetry and atmospheric profiling will be done on the orbiter to get the big picture of Titan's surface, atmosphere and haze. The balloon, which will use microwave communications with the orbiter for GPS, is best suited for high resolution Lidar altimetry (topography), Doppler (winds), atmospheric haze and surface composition due to it is close proximity to the surface ($z < 10$ km). This balloon application is similar to Lidar techniques used with airplanes at Earth. In the case of composition measurements, broad-band passive spectroscopic techniques maybe more suited, since lasers can only cover specific molecular lines of interest. The Lidar measurements will look for sites of interest on surface. Active imagery will not be as sensitive to Titan's haze as it is for passive imagery, but we will explore usage of Titan's Near-IR windows that have been used by Cassini cameras and Earth telescopes. Cassini/Huygens measurements of the haze will be used. Techniques have been developed at GSFC to measure winds at Earth from airplanes by bouncing photons off aerosol particles and using Etalon filters [20].

4.3 Sensor Miniaturization

Goddard provided the GCMS for the Huygens Probe [21]. Goddard is developing miniature versions of the IMS as shown in Figure 6. This concept uses carbon nanotubes to provide field emission of electrons for its electron impact ionization source which requires very little power when compared with thermionic emission techniques. It also uses time-of-flight (TOF) technique for the mass determination and miniature ASIC TOF chip which digitizes the measured TOF. ARC is developing miniaturized GC columns [22]. By combining these two technologies one has a GCMS with similar capabilities as that flown on Huygens but with much less mass, power and volume. Other sensor reduction strategies will be explored.

5.0 CONCLUSION

We have described a mission concept for a new mission to Titan with astrobiology being the primary science objective. The mission would involve an orbiter and Aerorover (hot air balloon) with aerobraking being used to put payload in orbit around Titan. The Aerorover will provide 4π *in situ* coverage of the atmosphere and surface of Titan.. The surface is expected to be the most important when it comes to prebiotic chemistry. It is also the

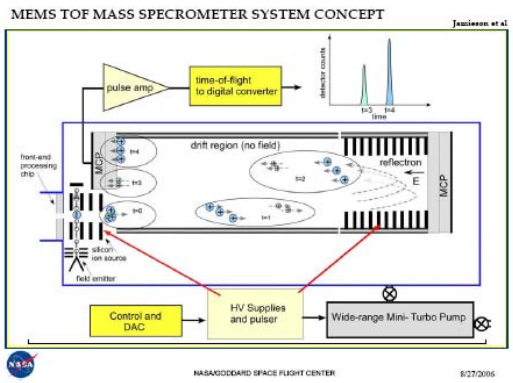

Figure 6. MEMS Ion Mass Spectrometer being developed at GSFC. It uses carbon nanotubes for field emission of electrons to ionize neutral gas entering instrument.

least known. We described most of the technology hurdles to be overcome and plan to reduce risk and cost by partnering with industry, using miniaturization strategies and new technology concepts such as nanotechnology. The recent Cassini/Huygens results have underscored the importance of a new mission to Titan and should be actively considered by the planetary community for the upcoming New Frontiers 2008 opportunity or later strategic flagship opportunities.

6.0 REFERENCES

1. Tomasko, M. G., et al., Rain, winds and haze during the Huygens probe's descent to Titan's surface, *Nature*, **438**, 765-778, 2005.
2. Waite, J. H., et al., Ion Neutral Mass Spectrometer results from the first flyby of Titan, *Science*, **308**, pp. 982-986, 2005.
3. Crary, F. J., et al., Dynamics and composition of plasma at Titan, *Science*, in review, 2006.
4 Niemann, H. B., et al., The abundances of constituents of Titan's atmosphere from the GCMS instrument on the Huygens probe, *Nature*, **438**, 779-784, 2005.
5. Schulze-Makuch, D. and D. H. Grinspoon, Biologically enhanced energy and carbon cycling on Titan?, *Astrobiology*, **5**, 560-567, 2005.
6. Sotin, C., et al., Release of volatiles from a possible cryovolcano from near-infrared imaging of Titan, *Nature*, **435**, 786, 2005.
7. Porco, C. C., et al., Imaging of Titan from Cassini spacecraft, *Nature*, **434**, 159-168, 2005.
8. Elachi, C., et al., Titan Radar Mapper observations from Cassini's T_3 fly-by, *Nature*, **441**, 709-713, 2006.
9. Takano, T., et al., Methane drizzle on Titan, *Nature*, **442**, 432-435, 2006.
10. Sittler, E. C., Jr., et al., Titan Orbiter Aerorover Mission (TOAM), proposal submitted in response to NRA 03-OSS-01-VM, Call for Mission Concepts: Space Science Vision Missions, 2003.
11. Rappaport, N., et al., Doppler measurements of the quadrupole moments of Titan, *Icarus*, **126**, 313-323, 1996.
12. Smith, D. E., et al., Mars orbiter laser altimeter: Experiment summary after the first year of global mapping of Mars, *J. Geophys. Res.*, **106(E10)**, 23689-23722, 2001.
13. Tyler, G. L., et al., Radio science observations with Mars Global Surveyor, *J. Geophys. Res.*, **106(E10)**, 23327-23348, 2001.
14. Lebreton, J.-P. and D. L. Matson, The Huygens Probe: Science, Payload and Mission, *Space Sci. Rev.*, **104**, 59-100, 2002.
15. Zarnecki, J. C., et al., Huygens' surface science package, *Space Sci. Rev.*, **104**, 593-611, 2002.
16. Acuna, M. H., et al., Global distributions of crustal magnetization discovered by the Mars Global Surveyor MAG/ER Experiment, *Science*, **284**, 790-793, 1999.
17. Carlisle, C. C., G. Le, J. A. Slavin, J. T. VanSant, E. H. Webb, Space Technology 5 – Technology Validation Update, *IEEEAC*, paper #1521, 2005.
18. Pitman, J. T., et al, Multiple Instrument Distributed Aperture Sensor (MIDAS) for planetary remote sensing, *Proceedings of SPIE – Volume 5660 Instruments, Science and Methods for Geospace and Planetary Remote Sensing*, C. A. Nardell, P. G. Lucey, J. Yee, J. B. Garvin editors December 2004, 168-180, 2004.
19. Kendrick, R. L., et al., Wide-field Fizeau imaging telescope: experimental results, *Applied Optics*, Vol 45, 4235-4240, 2006.
20. Gentry, B. M. and H. Chen, The Goddard Lidar Observatory for Winds (GLOW), 23rd ILRC in Nara Japan, 24-28 July, 2006.
21. Niemann et al., The Gas Chromatograph Mass Spectrometer Aboard Huygens, *Huygens Science Payload and Mission, ESA Publication SP-1177,* 85, 1997.
22. Kojiro, D., MiniGC-IMS, *15th International Conference on Ion Mobility Spectrometry, July 23-28, 2006, Honolulu, HA,* 2006.

AN ENTRY HANDBOOK FOR THE CONCEPTUAL DESIGN OF MARS MISSIONS

Grant Wells[(1)], Robert Braun[(2)]

[(1)]*Guggenheim School of Aerospace Engineering, Georgia Institute of Technology, Atlanta, Georgia, USA, Email: gtg315z@mail.gatech.edu*
[(2)]*Guggenheim School of Aerospace Engineering, Georgia Institute of Technology, Atlanta, Georgia, USA, Email: robert.braun@ae.gatech.edu*

ABSTRACT

The purpose of this investigation is to investigate trends in Mars entry, descent and landing conceptual mission design and propose a method of presenting this information as a handbook for conceptual design. The premise of the project is that Mars entry, descent and landing can be parameterized with five variables: (1) entry mass, (2) entry velocity, (3) entry flight path angle, (4) vehicle aeroshell diameter, and (5) vertical lift-to-drag ratio. For combinations of these input parameters, the following trajectory information will be determined: peak deceleration, peak heat rate, heat load, and the altitude at which Mach 2 is reached (for parachute deployment).

1. INTRODUCTION

A Mars entry, descent and landing (EDL) mission design handbook would serve as the initial basis for planetary probe EDL in the same manner that a Mars interplanetary mission design handbook serves as the initial basis for launch vehicle selection and mission timelines. As with interplanetary mission design handbooks, an EDL mission design handbook could be constructed for each planet of interest.

The premise of this investigation is that Mars EDL can be parameterized with five variables: (1) entry mass, (2) entry velocity, (3) entry flight path angle, (4) vehicle aeroshell diameter, and (5) vertical lift-to-drag ratio. For combinations of these input parameters, the following trajectory information would be determined: peak deceleration, peak heat rate, total heat load, and the altitude at which Mach 2 is reached (for parachute deployment). The data would then be assembled and presented as a series of "pork chop" (contour) plots with the five EDL variables on the x and y axes and the trajectory information shown by the contours.

The central idea is that if a mission designer knows the entry conditions, size and aerodynamic properties for a particular planetary probe, the peak deceleration, peak heat rate, total heat load, and the altitude at which Mach 2 is reached for the trajectory can all be determined without having to run trajectory simulations. Similarly, the effects on the trajectory due to changes in the input parameters could quickly be determined. For example, the change in the Mach 2 altitude from an increase in entry mass could quickly be assessed.

2. METHODOLOGY

2.1 Major Variables

Ranges for the five parameters used to characterize Mars entry are shown in Table 1. The maximum value of the entry mass range was chosen based the expected entry mass for the Mars Science Lander (MSL) of approximately 2000 kg [1], which is currently the heaviest Martian planetary probe planned. The range of entry velocities and flight path angles were chosen to encompass the range of entry velocities seen by several successful probes, specifically for entry velocity: Viking 1 (4.61 km/s) [2] and Pathfinder (7.26 km/s) [3] and for entry flight path angle: Viking 2 (-17.027°) [2] and the Mars Exploration Rovers (MERs) (-11.5°) [4]. The range of aeroshell diameters bounds probes from Pathfinder (2.65 m) [3] to the largest probe which can pass through the environmental test chamber at the Jet Propulsion Laboratory (approximately 4.5 m allowing for handling equipment). The range of vertical lift-to-drag ratios encompasses ballistic entry (0) to a possible maximum value for blunt bodies (0.5).

Since both entry mass and aeroshell diameter are independent parameters in this investigation, a wide ballistic coefficient range is assessed as shown in Table 2. An alternative approach to this investigation might have been to use either entry mass or diameter as one independent variable and a packing density as the other variable. Packing density is a measure of how much mass could be put into an aeroshell of a given shape. The packing density could be used to determine either the aeroshell diameter for a given entry mass (by photographically scaling the aeroshell), or the entry mass for a given diameter of the aeroshell (by increasing the mass until the desired packing density was reached). The shaded ballistic coefficients in Table 2 show the range of values for a low packing density based on Viking and a high packing density based on MER.

Table 1: Ranges for the variables used to characterize Mars entry.

Input Parameter	Min	Max	Increment
Entry Mass (kg)	200	2000	200
Entry Velocity (km/s)	4	9	1
Entry Flight Path Angle (°)	-15	-10	0.5
Aeroshell Diameter (m)	2	5	1
Lift-to-Drag Ratio	0	0.5	0.1

Table 2: Ballistic coefficients based on entry mass and aeroshell diameter.

Ballistic Coefficient (kg/m²)		Diameter (m)			
		2	3	4	5
Mass (kg)	200	37.9	16.8	9.5	6.1
	400	75.8	33.7	18.9	12.1
	600	113.7	50.5	28.4	18.2
	800	151.6	67.4	37.9	24.3
	1000	189.5	84.2	47.4	30.3
	1200	227.4	101.1	56.8	36.4
	1400	265.3	117.9	66.3	42.4
	1600	303.2	134.7	75.8	48.5
	1800	341.0	151.6	85.3	54.6
	2000	378.9	168.4	94.7	60.6

Shaded values show the range of values for a low packing density based on Viking and a high packing density based on MER.

2.2 Commonalities between Trajectory Simulations

All 15,840 trajectories were simulated using the Program to Optimize Simulated Trajectories (POST) [5]. Each planetary probe was assumed to have a constant hypersonic drag coefficient of 1.68 [6] typical of 70° sphere-cone planetary probes. The vertical lift coefficient for the vehicle was determined by multiplying the drag coefficient with the vertical lift-to-drag ratio. For vehicles in banked flight, the lift coefficient would represent the portion of lift in the vertical direction.

All trajectory simulations used a common atmosphere. The atmospheric density on Mars varies significantly with time-of-year, time-of-day, dust-level (atmospheric opacity) and latitude. To account for the effects of each of these variables, a design atmospheric density profile was constructed from approximately one-thousand runs of Mars-GRAM 2005 [7] in which month, time of day, dust level, and latitude for the years of 2030 and 2031 were randomly varied. The results of the Mars-GRAM runs covered the range of densities shown in Fig. 1.

A cumulative distribution function of density was constructed for 0 km MOLA. The density at the 30% point on the 0 km cumulative distribution function (0.0124 kg/m³) as shown in Fig. 1 was chosen as the basis for the atmosphere. The atmosphere from the Mars-GRAM runs having a 0 km density of 0.0124 kg/m³ with the lowest 4 km density was then chosen for this investigation. The resulting atmosphere (shown in Fig. 2) was chosen for this investigation.

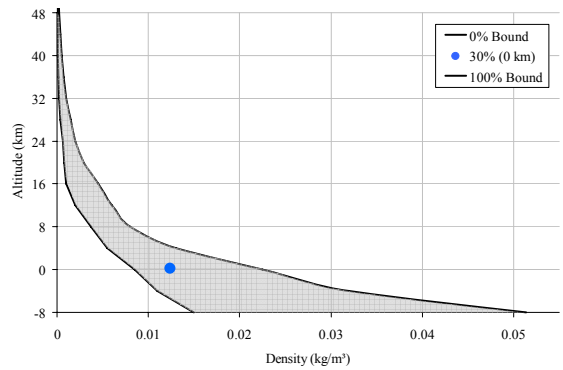

Fig. 1: The range of densities resulting from over 1000 runs of Mars-GRAM 2005.

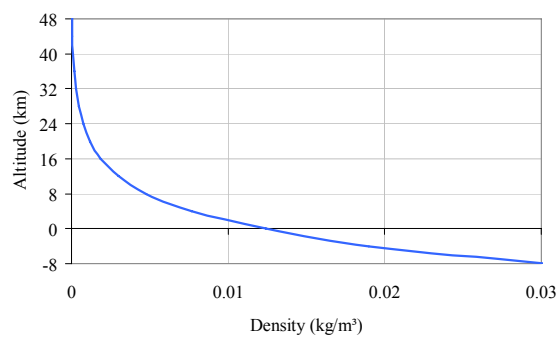

Fig. 2: Martian atmospheric density profile used for trajectory simulations.

2.3 Plots of Trajectory Data

After a trajectory for one combination of the input variables shown in Table 1 was run, the peak deceleration, peak heat rate, heat load, and Mach 2 altitude (for parachute deployment) were recorded. This data was then plotted against two of the major input variables (e.g. entry mass and flight path angle), while the other three major input variables (e.g. entry velocity, aeroshell diameter, and lift-to-drag ratio) were held constant. The data takes the form of contours in the plot such as that shown in Fig. 3 for peak deceleration.

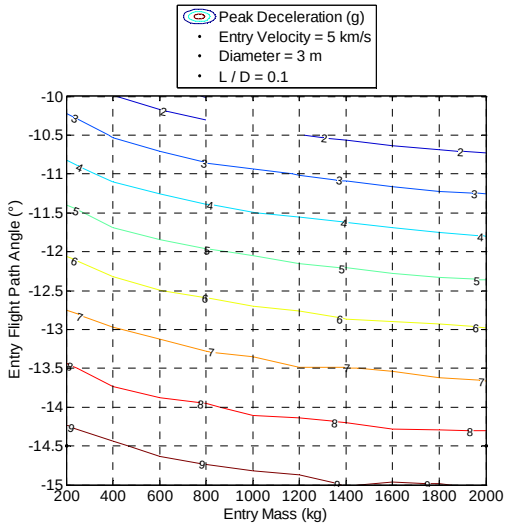

Fig. 3: An example plot of peak deceleration. The blank region between 800 and 2000 kg and -10° and -10.5° represents a region where the trajectory showed the probe skipping out of the atmosphere for a flight path angle of -10°, so contours cannot be plotted in this region.

Intersections of the gridlines on the contour plots show the specific points for which a trajectory simulation was run. Blank regions of the contour plots indicate combinations of major variables for which the simulations showed the probe skipping out of the atmosphere. Data was not recorded for cases which skipped out of the atmosphere. In order for contours to be plotted in any rectangular region bounded by the gridlines, the cases at the four vertices cannot have skipped out of the atmosphere, so contours cannot be plotted in these regions as shown in Fig. 4.

For example, in Fig. 3, the contour plot shows how peak deceleration varies with entry mass and flight path angle when entry velocity is held constant at 5 km/s, aeroshell diameter is held constant at 3 m, and the lift-to-drag ratio is held constant at 0.1. For this particular combination of entry velocity, aeroshell diameter, and flight path angle, the -10° flight path angle cases with masses from 1000 kg to 2000 kg skipped out of the atmosphere.

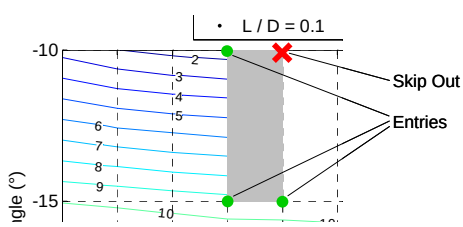

Fig. 4: Contour plots require successful entries for each of the four cases bounding regions of the plot.

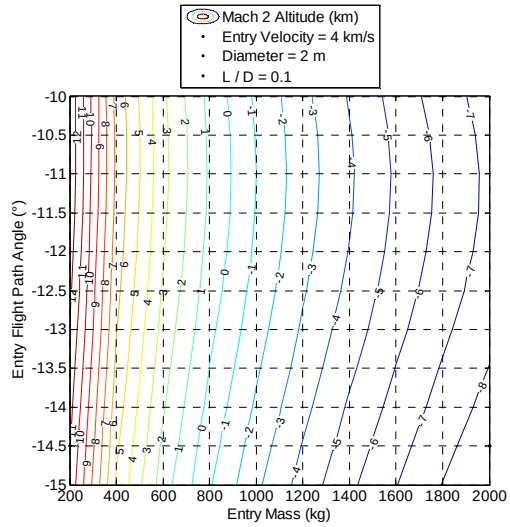

Fig. 5: An example plot of Mach 2 altitude. Mach 2 altitudes below -8 km were not plotted as the lowest point on Mars, located in Hellas Planitia, has an altitude of -8.18 km. [9]

The lowest point on Mars [9] has an elevation of -8.18 km, so Mach 2 altitudes lower than -8 km were not plotted on the contour plots as shown in Fig. 5.

3. RESULTS

The following paragraphs discuss some trends that can be seen in the results of the trajectory simulations. A sampling of the contour plots for peak deceleration, peak heat rate, heat load, and Mach 2 altitude are shown below. Note that plots were generally not made for combinations of variables which did not result in any successful entries (e.g. skip-out trajectories) that could be presented as a contour plot.

3.1 Peak Deceleration

As can be seen from Fig. 6, peak deceleration is generally not a strong function of entry mass when the entry velocity, aeroshell diameter, and lift-to-drag ratio are all fixed. Entry flight path angle, however, does significantly affect the peak deceleration of the entry trajectory when the other three major variables are fixed. Fig. 7 shows that peak deceleration is also a strong function of entry velocity in addition to entry flight path angle for a fixed entry mass, aeroshell diameter, and lift-to-drag ratio. However, for an entry flight path angle of approximately -12.7° in this investigation, peak deceleration is somewhat independent of entry velocity.

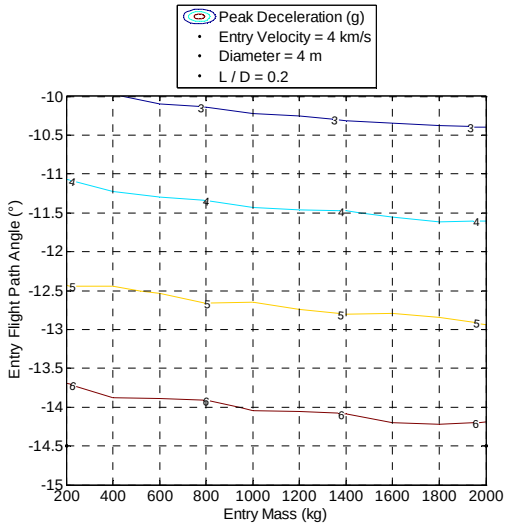

Fig. 6: Peak deceleration as a function of entry mass and flight path angle.

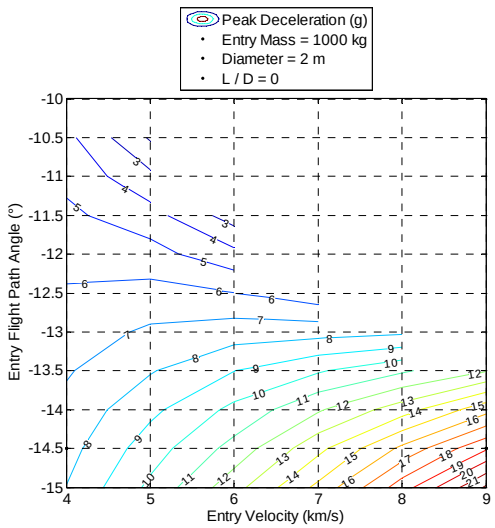

Fig. 7: Peak deceleration as a function of entry velocity and flight path angle.

3.2 Peak Heat Rate

The laminar stagnation point heat rate was calculated for each trajectory. Radiative effects were included for entry velocities above 6 km/s. [8] Peak heat rate increases with entry mass and slightly increases with entry flight path angle as shown in Fig. 8 for a fixed entry velocity, aeroshell diameter, and lift-to-drag ratio. Increasing entry velocity significantly increases peak heat rate as depicted in Fig. 9 for a fixed entry mass, aeroshell diameter, and lift-to-drag ratio. This is as expected since the major variables affecting heat rate are velocity, atmospheric density and the stagnation point radius.

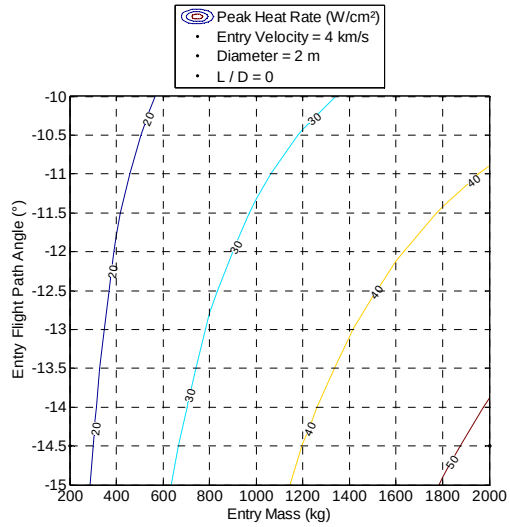

Fig. 8: Peak heat rate as a function of entry mass and flight path angle.

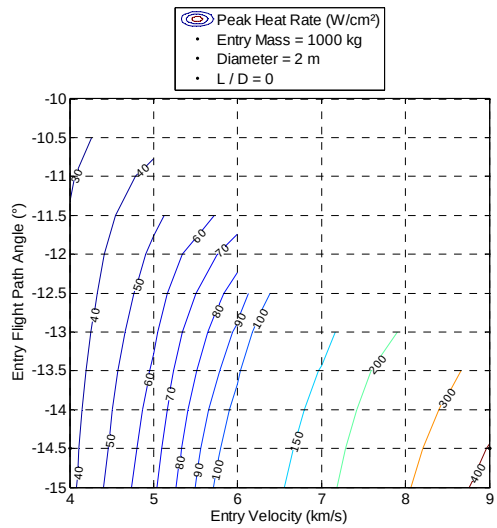

Fig. 9: Peak heat rate as a function of entry velocity and flight path angle.

3.3 Heat Load

Fig. 10 shows that heat load increases with entry mass and decreases with steepening of the entry flight path angle. As entry mass increases, heat load increases more quickly with entry mass at shallower entry flight path angles than at steeper flight path angles. Fig. 11 also shows that heat load increases with both entry velocity and shallower flight path angles, though more so with entry velocity, due to the higher heat rates experienced by the planetary probe, for a fixed entry mass, aeroshell diameter, and lift-to-drag ratio.

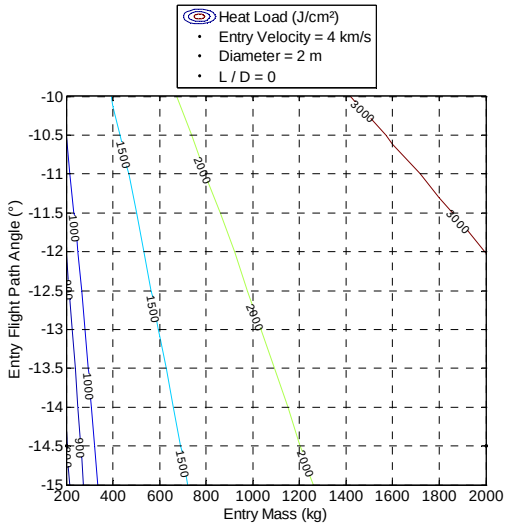

Fig. 10: Heat load as a function of entry mass and flight path angle.

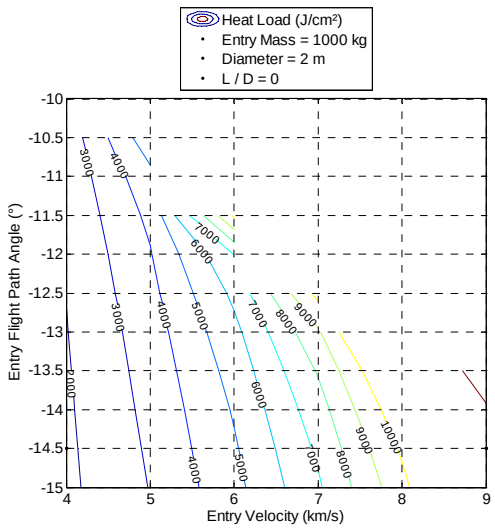

Fig. 11: Heat load as a function of entry velocity and flight path angle.

3.4 Mach 2 Altitude

Fig. 12 shows that the altitude at which Mach 2 is reached is strongly affected by the entry mass and less significantly affected by entry flight path angle when entry velocity, aeroshell diameter, and the lift-to-drag ratio of the planetary probe are all fixed. Fig. 13 also shows that the Mach 2 altitude generally increases as the aeroshell diameter of the probe increases. The larger diameter allows the planetary probe to slow down higher in the atmosphere and remain at a higher altitude when Mach 2 is reached.

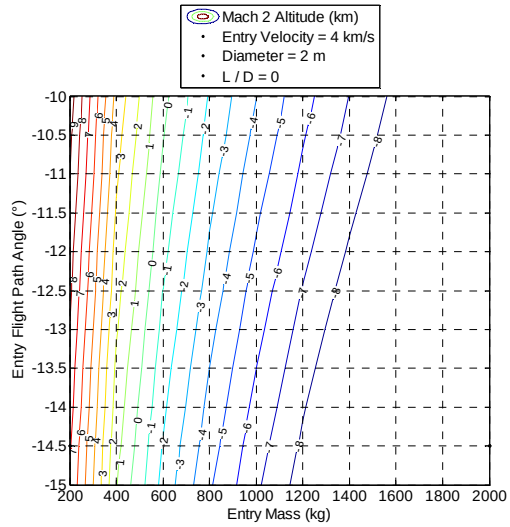

Fig. 12: Mach 2 altitude as a function of entry mass and flight path angle.

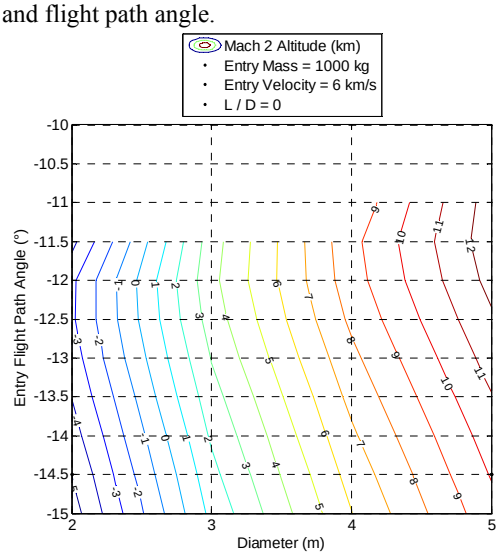

Fig. 13: Mach 2 altitude as a function of aeroshell diameter and entry flight path angle.

3.5 Conceptual Design

Once trajectory data has been compiled, as in this investigation, the data can be used to generate contour plots showing how design variables such as entry mass and lift-to-drag ratio can affect peak deceleration and peak heat rate. Table 3 lists design parameters for a conceptual Mars probe.

Table 3: Example parameters for a conceptual mission.

Parameter	Value
Entry Mass (kg)	200
Entry Velocity (km/s)	4
Entry Flight Path Angle (°)	-15
Aeroshell Diameter (m)	2
Lift-to-Drag Ratio	0

Contour plots specific to this conceptual mission, such as Fig. 14 and Fig. 15, show how changes in entry parameters can affect this conceptual mission. Note that the red dot in each figure represents the baseline mission. For example, Fig. 14 shows how increasing the flight path angle can impact peak deceleration, while Fig. 15 shows that changing the entry mass will affect the peak heat rate, but changing the lift-to-drag ratio in the vertical direction will not significantly change the peak heat rate.

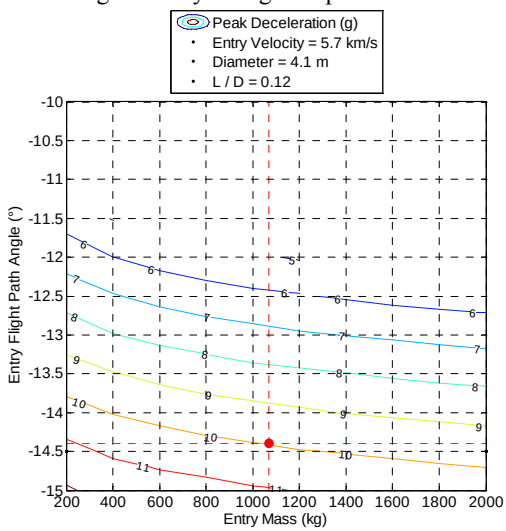

Fig. 14: How entry mass and flight path angle can impact the peak deceleration of a conceptual mission.

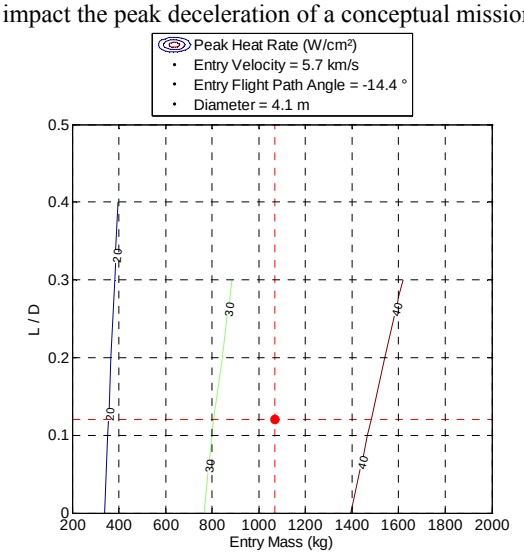

Fig. 15: How entry mass and lift-to-drag-ration can impact the peak heat rate of a conceptual mission.

4. CONCLUSIONS

Contour plots (or pork-chop plots as they are called by interplanetary mission designers) can be used to study trends in entry trajectories when major variables change. However, the number of independent major variables is more than can easily be represented in 2- or 3-dimensional plots, which makes looking at the effects of multiple variables difficult. Collections of contour plots such as those shown in this investigation can form the basis of entry mission design handbooks (the equivalent of interplanetary mission design handbooks). The contour plots in these handbooks can be general, or tailored to specific missions as shown in Fig. 14 and Fig. 15.

5. REFERENCES

1. Braun, R.D., Manning, R.M., "Mars Exploration Entry, Descent and Landing Challenges," *2006 IEEE Aerospace Conference*, IEEEAC paper #0076, Big Sky, Montana, March 2006.
2. Ingoldby, R. N., Michel, F. C., Flaherty, T. M., Doty, M. G., Preston, B., Villyard, K. W., Steele, R. D., "Entry Data Analysis for Viking Landers 1 and 2 Final Report", Martin Marietta Corp., NASA TN 3770218, NASA CR 159388, November 1976.
3. Spencer, D.A., Blanchard, R.C., Braun, R.D., Kallemeyn, P.H., Thurman, S.W., "Mars Pathfinder Entry, Descent, and Landing Reconstruction", *Journal of Spacecraft and Rockets*, Vol. 36, No. 3, May-June 1999.
4. Desai, P.N., Knocke, P.C., "Mars Exploration Rovers Entry, Descent, and Landing Trajectory Analysis," *AIAA/AAS Astrodynamics Specialist Conference and Exhibit*, AIAA-2004-5092, Providence, Rhode Island, August 16-19, 2004.
5. POST, Program to Optimize Simulated Trajectories, Ver. 5.2, NASA Langley Research Center, Hampton, Virginia, Martin Marietta Corporation, Denver, Colorado, 1997.
6. Gnoffo, P., Braun, R.D., Weilmuenster, K.J., Mitcheltree, R.A., Engelund, W.C., Powell, R.W., "Prediction and Validation of Mars Pathfinder Hypersonic Aerodynamic Database," *7th AIAA/ASME Joint Thermophysics and Heat Transfer Conference*, AIAA-1998-2445, Albuquerque, New Mexico, June 1998.
7. Mars-GRAM, Mars Global Reference Atmospheric Model, Ver 2005, Computer Sciences Corporation, Huntsville Alabama, NASA Marshall Spaceflight Center, Alabama, 2005.
8. Tauber, M.E., Sutton, K., "Stagnation-Point Radiative Heating Relations for Earth and Mars Entries", *Journal of Spacecraft and Rockets*, Vol. 28, pp. 40-42, January-February 1991.
9. Mars, The Red Planet Reference Map," Copyright © 2001 *National Geographic Society*, Washington, DC.

"Probes to Saturn and Beyond" Panel Discussion Report
IPPW-4, Friday, 30 June 2006

Submitted by
Sushil K. Atreya

Department of Atmospheric, Oceanic, and Space Sciences, University of Michigan, Ann Arbor, MI 48109-2143, USA,
Email: atreya@umich.edu Homepage: http://www.umich.edu/~atreya/

Proceedings, International Planetary Probe Workshop, IPPW-4, Pasadena, California, June 2006
(Date of Submission: 8 August 2006)

Panel Members: Sushil Atreya (U. Michigan, Chair), Alessandro Atzei (ESTEC), Tibor Balint (JPL), Christian Cazaux (CNES), Jean-Pierre LeBreton (ESTEC), Paul Mahaffy (GSFC), Thomas Spilker (JPL). Absent: Scott Bolton (SWRI).

The panel discussion focused on
(1) Scientific justification for probe missions to the giant planets
(2) Potential architecture for a Saturn probe mission
(3) Status of key enabling technology
(4) Importance of integrated systems approach
(5) Potential areas of international collaboration

The panel members were selected on the basis of their expertise in one or several of the above areas. The panel discussion lasted approximately one hour, with valuable input from the audience. The main findings of the discussion are summarized below.

The fundamental questions of the formation of the giant planets and the origin of their atmospheres require determination of the heavy element abundances (mass > ^{4}He). With the exception of carbon (in CH_4), such elements can be accessed *only* by in situ measurements from entry probes.

Comparative planetology of the gas giants (Jupiter and Saturn) and the ice giants (Uranus and Neptune) is essential for constraining fully the models of the origin and evolution of the solar system. Hence, probes are needed at all four giant planets.

A Saturn flyby mission which combines the capabilities of entry probes and microwave radiometry (MWR) must be considered as the highest priority giant planet mission for the near term (next 5-7 years). Recent studies done at JPL indicate that such a mission is very promising as a New Frontiers (NF) class ($700 Million) mission.

A minimum of two shallow probes will be required to meet the science goals of the Saturn mission, and they can be accommodated under the NF cost cap. In order to achieve reasonable spatial resolution, preliminary studies indicate that the MWR experiment will need to be carried out from the probes, rather than from the flyby spacecraft. Studies done at JPL indicate that the mission architecture requires flying the spacecraft at $2R_S$ or beyond, which would result in essentially planetary-scale spatial resolution, i.e. only disk-average results from MWR if mounted on the spacecraft. This needs to be looked into more carefully.

Direct-to-earth (DTE) transmission of data from the probes has been found not feasible. Besides not buying us much, even if possible, it would be very risky as the only means of data transmission, considering the possibility of single point failure. Nevertheless, it is desirable to include DTE as an "added" capability, and to ensure that enhancement to the DSN, SKA capability, etc. are being carried out in a timely manner.

For the longer term, Flagship class ($1 billion plus) missions to Neptune – Neptune polar orbiter with probes, with an option of a Triton lander – and Uranus orbiter with probes are required. A Jupiter multiprobe mission will benefit from the results of Juno; therefore its architecture is best decided after 2016/2017.

Thus, the IPPW-4 conclusion for future exploration of the giant planets is consistent with that of the OPAG (Outer Planet Assessment Group of NASA). For all probe missions, an integrated payload system approach should be looked into seriously, for savings in resources, minimizing complexity, and improving performance and capability. Presently, there are limits to such an approach, so early investment in technology development will be required. Investment is also required for communications, heat shield development and characterization, including the Giant Planet

Facility (except for the Saturn probes, for which sufficient left over material from the Galileo probe seems to exist), etc.

Finally, all agreed international collaboration on the probe missions is the way to go. However, ITAR rules have made such a collaboration highly challenging. A "clean interface" of hardware approach may still allow meaningful international collaboration. Some possibilities considered are in the area of solar panels, communication hardware, star trackers, etc. This will need to be settled and agreed upon rather rapidly, in order to meet the proposal and schedule timelines. The Panel strongly endorsed continued preparatory work for a Saturn probe with microwave mission, as an immediate goal for the near term.

SESSION 5

SENSORS, INSTRUMENTS AND SAMPLE ACQUISITION SYSTEMS

Chairs:

Ball, Andrew, The Open University, UK
Jamieson, Brian, NASA GSFC, USA
Laan, Erik, Dutch Space, Netherlands
Mahaffy, Paul, NASA GSFC, USA

GENTNER – a miniaturised LIBS/Raman instrument for the comprehensive *in-situ* analysis of the Martian surface

A. Del Bianco[(1)] I. Rauschenbach[(2)], V. Lazić[(3)], E.K. Jessberger[(4)] and the GENTNER Team

[(1)]*IPAC – Improve Process Analysis and Control GmbH, Europastraße 8, A-9524 St. Magdalen/Villach, Austria. Email:* delbianco@ipac.at.

[(2)]*Institut für Planetologie, Westfälische Wilhelms-Universität Münster, Wilhelm-Klemm-Straße 10, D-48149 Münster, Germany. Email:* irausch@uni-muenster.de

[(3)]*ENEA, Centro Ricerche Frascati, Unità Tecnologie Fisiche Avanzate, Via Enrico Fermi 45, I-00044 Frascati (Roma), Italy. Email:* lazic@frascati.enea.it

[(4)]*Institut für Planetologie, Westfälische Wilhelms-Universität Münster, Wilhelm-Klemm-Straße 10, D-48149 Münster, Germany. Email:* ekj@uni-muenster.de

ABSTRACT

We introduce a novel instrument to determine in-situ rapidly and with relatively high sensitivity (down to 10 ppm) the concentrations of many elements in Martian rock, coarse fine and soil samples with a lateral resolution of <1 mm. At the same time the instrument will provide information on possible organic components as well as mineralogical information. Detection of the life-related elements like H, C, N, O, P, S and Fe and investigation of their 3D-distributions as well as their occurrences in the various Martian materials may be indicative of biological activity.

The proposed instrument is a combination of Laser Induced Breakdown Spectroscopy (LIBS) and Raman Spectroscopy and meets the requirements concerning advanced in-situ analytical tools, like short measurement duration, high sensitivity, high repetition rate, high reproducibility, low mass, size and resource needs and high flexibility with respect to type, shape and size of sample material.

1. INTRODUCTION

The European Space Agency (ESA) recently started a program of exploration of Mars with the ultimate goal to have a manned mission to the planet within the year 2050. However, before getting to this ambitious and challenging task, a thorough exploration of the planet is needed both for scientific purposes and for the identification of hazards and local resources for the human exploration activities by detecting ions or radicals adsorbed on the environment and characterise the geochemical composition of the rocks. In the first phase, a major task will be to look for evidences of the existence of life, either extinct or extant.

There are two major avenues to hunt for potential past or present life on Mars. One is to directly search for evidence of biological activity such as organic matter or bio-mineralisations. Alternatively and complementarily, the study of the exogenic dynamics stored in the Martian sedimentary record will provide constraints on conditions, under which past or present life may have existed. The investigation of the sedimentary archive is based on the detailed characterisation of the chemical and mineralogical constitution of primary materials and its weathering products. Furthermore, it is essential to determine the chemical and mineralogical fractionation trends that occurred during disintegration and weathering of primary materials, during sediment transport and deposition since the nature of the chemical fractionations and mineralogical transformations will provide insight into the respective processes degrading the primary material and forming the sediments which in turn mirror the surface environmental conditions on ancient Mars. Thus the main goal will be to identify chemical trends or mineral phases that are diagnostic for specific processes and environments. Weathering under warm and wet conditions would have produced typical secondary mineralogical remnants such as clay minerals; hydrothermal activity and acid fog weathering would produce sulphates and chlorides; biological activity could be the source of carbonates and iron oxides such as magnetite.

The analysis should not be limited to the surface: because active plate tectonics probably ended many millions of years ago, the Martian sedimentary record represents the long-term exogenic cycle. A subsurface characterisation will allow to derive information on the evolution of surface conditions during the geologic past by applying sedimentological principles to soil profiles. In particular, the variation of element concentrations with depth will allow to reconstruct past changes in the contributions from different source materials. Given that the evolution of the meteoritic infall rate with time is known, a Ni-concentration depth profile in Martian regolith may provide insight into the evolution in the rate of soil formation during the geologic past. In addition, the depth distribution of the elements S, Cl,

Br, Li, Zn and Ba may reveal the effects of volcanic aerosols and hydrothermal activity.

To efficiently carry out these studies, several instruments are needed to perform a complete molecular and elemental analysis (see the study of the Exobiology Team of the ESA for a complete review [1]). The instruments proposed include Mössbauer spectrometers [2,3], chromatographic instrumentation [4,5], alpha proton X-ray spectrometers [6], Raman spectrometers [7, 8], mass spectrometers [9], X-ray diffractometers [10], electromagnetic subsounding devices [11] and a drill to analyse samples not oxidised by the intense UV radiation reaching the planet's surface.

For the molecular analysis a Raman spectrometer presents a number of advantages because of his high

Fig. 1. Raman spectrum of meteorite ALH8401(white matrix) showing silicates and carbonates peaks.

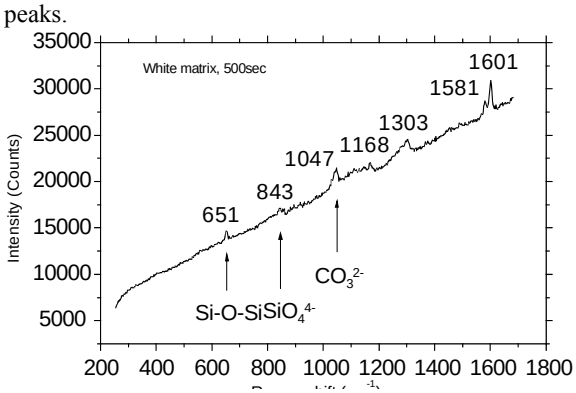

Fig. 2. Raman spectrum of meteorite ALH8401 (grey/black matrix) showing silicates, carbonates and sulphates peaks as well as the presence of organic contamination and humidity.

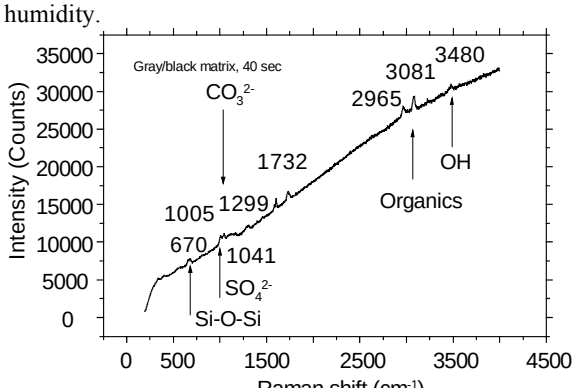

spatial resolution, sensitivity, relatively short integration time and non destructiveness which allow to analyse the same sample also with other techniques. It has, however, some drawbacks. First of all, the excitation laser beam may excite a fluorescence emission of the sample which, being usually several orders of magnitude stronger than the the Raman signal, can hide the information. Another disadvantage is paradoxically the extreme sensitivity of the technique. Raman scattering is heavily influenced by both the molecular composition and the geometrical arrangement of the sample[12]: even when the chemical composition is the same, the position of the lines varies depending on the molecular geometry. Furthermore, the position of Raman lines is also influenced by the phase of the sample and by its reological properties. To study unambiguously and completely a sample, its elemental content should therefore be independently known.

A solution to this problem can be found by using Laser-Induced Breakdown Spectroscopy (LIBS) which can quickly provide a full elemental analysis of the sample. Furthermore, LIBS and Raman can share a large number of subsystems thus allowing the saving of resources in the payload.

Fig. 3. LIBS spectrum of Andesite under Martian conditions.

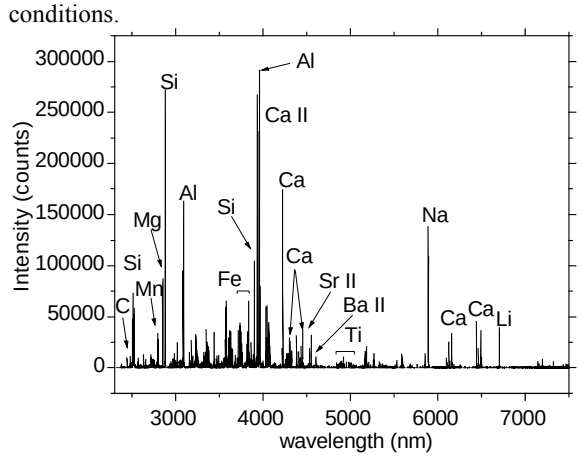

A combined Raman/LIBS spectrometer can therefore perform an important role in the context of planetary exploration –see Fig. 1 – 3 for examples of the potentialities – for its advantages:

1. No sample preparation needed;
2. Fast *in-situ* determination of the element concentrations down to 100 ppm and with a lateral resolution above 100 µm of all kinds of samples encountered *via* LIBS;
3. Elemental analysis immune from interferences from dust layers;
4. Elemental depth profiling;
5. Raman spectroscopy provides information on the mineral composition;

6. Raman spectroscopy provides information on the presence and molecular composition of organic components;

7. Raman spectroscopy can be used as probe technique for reactions of chemicals with Martian materials on microchips.

The possibility of such an integration has been thoroughly analysed in a theoretical exercise called LIRAMIS [13]. A prosecution of that study is ongoing [14]and will lead to a fully functional breadboard by the end of 2006. The innovative instrument, named GENTNER after the physicist and cosmochemist Wolfgang Gentner (1906 – 1980), greatly profits from synergistic effects, sharing the optical spectrometer, the lasers, and on-board data reduction facilities [15].

2. SPECIFIC GENTNER SCIENCE

The complementary nature of the chemical and structural information that GENTNER will return from a single spot on the target material renders unequivocal phase identification, which will be greatly enhanced by linking the sets of complementary data through the application of mineralogical concepts. Pristine, cosmic material, which is continuously delivered to the Martian surface through meteoritic infall, contains considerable quantities of organic matter – the prerequisites for the evolution of life. Organic material has, however, not yet been detected on the surface of any planet. The absence of organics on the Martian surface despite of this continuous meteoritic delivery is ascribed to the reactivity of the Martian soil. This reactivity that possibly involves adsorbed super-oxide is obviously a result of an intense atmosphere-surface interaction under strong solar UV radiation. It has important implications for future human space-flight and for Exobiology in general. Super-oxide species, however, are not yet identified on Mars. The GENTNER instrument can identify, at least qualitatively, such radicals. High quality mineralogical characterisation is a prerequisite for the identification of surface adsorbed molecular or ionic species by means of Raman spectroscopy. Radicals not only drive the degradation of organic matter, they also contribute to oxidative weathering of primary minerals. From earlier missions we know that in the Martian regolith iron and sulphur occur in their highest oxidation states. Provided, that this is not the case in the magmatic and meteoritic precursor materials, the Martian surface acts as an oxygen sink and in this respect has a considerable effect on the composition of the Martian atmosphere. Although GENTNER will not be able to directly distinguish between oxidised and reduced iron and sulphur it provides the basis for normative calculations to identify the minerals, which host these species.

Given the present day ambient and subsurface environment, precipitates such as water ice, solid CO_2 and gas hydrates such as clathrates may be stable on Mars. The Raman spectroscopy part of GENTNER is a powerful tool to identify and characterise such species. Cryo-volcanism – instead of liquid water – may have played an dominant role in the formation of the channel features on the Martian surface. Vertical profiling of ices and clathrates could help to unravel this intensely debated uncertainty.

Table 1 summarises the possible applications of GENTNER in the different disciplines inherent the planetary exploration.

Discipline	***Measurement***	***Science***
Exobiology	Signatures of organic species	Analysis of molecular structures; Analysis of biofilm; Presence of present or past life
Organic chemistry	Reaction of materials with specific reagents	Presence and analysis of organic matter
Atmospheric Science	Adsorbed neutrals, ions and radicals	Interaction of Martian weather with solids
Mineralogy	Bio-mineralisations	Identification of mineral phases; Grain size distribution; Viscosity; Mechanical processes
Geochemistry	Bulk chemical composition	Abundances of major, minor and trace elements; Depth profiling; Geologic and geochemical history; Discrimination between surface species and bulk rock and minerals

Table 1. Range of applications of GENTNER instrument.

3. GENTNER CONCEPT

In the view of the deployment of the GENTNER instrument in an actual lander several experimental scenarios are foreseeable:

1. The instrument should analyse the material extracted from the drill in real time and outside the lander to take decisions on the opportunity to continue or stop the excavation phase;

2. The device should help to preselect which samples to be passed to subsequent and time-intensive instruments such as mass spectrometers or chromatographs inside the lander [16].

It is clear that the design should be kept flexible and modular to be able to accomodate these different needs. The basic design idea was to separate the main part of the instrument or Instrument Module (IM) and the needed optics for delivery/collection of the light or Sensor Head (SH), the two main subsystem being connected by fibre optic links. The IM contains the main subsystems composing the device: the excitation lasers, the spectrometer whilst the SH contains all the optics needed to shape the excitation beams, to collect the emitted radiation and to provide a visual image of the sample to ease the interpretation of the results.

This concept also allows to connect more than one head to the IM allowing to measure in more than one location with the same instrument (*e.g.* inside and outside a lander).

4. INSTRUMENT MODULE

4.1. Excitation lasers

Two different laser sources are needed owing to the different wavelengths and regimes of operation. For both Raman and LIBS measurements, a careful analysis of the scientific requirements is needed to select the proper source.

The efficiency of Raman scattering is inversely proportional to the the fourth power of excitation wavelength. Although a blue-green laser may appears the best choice, this is not the case because such a laser will also excite a considerable fluorescence in the sample.

Excitation wavelength (nm)	***Raman spectral range shift 200 – 3100 cm-1 (nm)***	***Normalised Raman efficiency***
532	538 – 637	100
633	641 – 848	50
660	669 – 830	42
670	679 – 846	40
705	715 – 902	32
720	731 – 927	30
750	761 – 977	25

Table 2.Spectral ranges corresponding to a shift 200 - 3100 cm^{-1} and scattering efficiency for some wavelengths.

Furthermore, one has to consider that the most useful Raman signal will be shifted towards longer wavelengths with respect to the laser line. The maximum shift allowable depends on the molecules that are investigated. For the scientific requirements of the mission one can assume a maximum shift of 3100cm^{-1} which covers all major geological and biological features. This imply that the laser line should be selected so that the maximum shift will be detectable with a Silicon detector to be able to use the same detector for both Raman and the LIBS measurements. Table 2 shows the Raman spectral ranges corresponding to shifts 200 – 3100cm^{-1} as well as the corresponding scattering efficiencies for a selection of laser lines. It is quite evident that a laser source that simultaneously satisfy all the requirements should have emission in the range 600-720 nm.

The selected laser should be ideally monochromatic and free of mode hopping since Raman measurement are done relatively to the laser frequency. Since a reasonable bandwidth for the expected samples is about 8 cm^{-1} (~0.5nm in the spectral range of interest), the wavelength should be stabilised within ±0.2nm .

A laser emitting in this range can be either a wavelength-stabilised laser diodes or diode pumped solid state lasers (DPSSL). In the latter case a frequency-doubled Nd:YAG laser exploiting the line at 1348 nm will be used. Both lasers can be used with a proper design of the sensor head. The power required to collect Raman spectra in a reasonable time is about 5 mW.

Also in case of LIBS trade-offs have to be considered. The LIBS signal in given experimental conditions mainly depends on the sample ablation rate which is in turn determined by the sample physical and chemical properties such as optical absorption, thermal coefficients, grain size, surface roughness , matrix composition. Given the variety of the geological materials that could be found on Mars, and their different physical characteristics – *e. g.* dust, naturally or artificially compacted material, rocks, soil mixtures with CO_2 ice, etc. very different ablation rates and consequently LIBS signals are to be expected.

Although also for LIBS short wavelengths look attractive, a Q-switched Nd:YAG laser operating at standard λ=1064 nm should be used since the advantages to use shorter wavelengths will be offset by the increase of the system complexity (weight, volume) and of the sensibility on misalignment. Furthermore, the laser should be focused with a spot size in the range 50 – 500 μm to increase the ablation rates that can be obtained by a given laser pulse energy.

The laser energy should then be selected so that the energy density is above the ablation threshold for all the types of samples that are expected on Mars surface or subsurface (drilling cores), thus allowing for LIBS determination of at least principal constituents and major elements. Although different recent publications

report LIBS measurements in simulated Martian environment, they were performed by using very different experimental configurations and spectrometers/detection systems, and were considering mainly the soil samples, which are easier to ablate than the compact rocks such as basaltic rocks. So, the straightforward comparison between the results of different authors is not possible.

In the case of basaltic rock – the most difficult sample expected – the ablation of the sample and the LIBS emission has been reported [17] with an energy density of 1.05J/cm^2 over 10ns pulses. For soil samples, the LIBS signal increases and more elements can be detected by applying the same laser energy. The ablation rates in simulated Martian conditions are reported in table 3.

Material	***Ablation rate per shot (µm)***
Weathered basaltic layer	0.6 – 1.2
Dust (sand)	0.1 – 0.25

Table 3: Ablation rates per shot in simulated Martian conditions as reported in ref. [17].

Knight [17] also reported the limits of detection for the major constituents of expected samples as shown in table 4.

Element	Ba	Cr	Cu	Li	Ni	Pb	Sn	Sr
LOD (ppm)	21	39	43	20	224	95	84	1.9

Table 4: Limits of detection for the main constituents of the Martian rocks as reported in ref. [17].

Other elements, elements such as C, N, and O represent a special case. Their LOD is expected to be above 1% due to interference of the surrounding atmosphere on LIBS signal. Also for S, a LOD above 1% might be expected [18]

In conclusion for LIBS in Martian conditions a Nd:YAG laser emitting 4mJ and pulse length of 5 ns is sufficient to ablate the Martian rocks when focused in a spot smaller than 250µm.

The current baseline for GENTNER sources is summarised in table 5.

	LIBS	***Raman***
Operation mode	Pulsed	Continuous wave
Wavelength Wavelength stability	1064 nm Uncritical	600 – 700 nm < 0.2nm
Sample irradiance	>500 MW/cm^2	<1KW/cm^2
Spot size	50 – 100 µm	20 – 50 µm

Table 5. Main characteristics of the laser sources needed for GENTNER.

4.2. Spectrometer system

Giving the required technical inputs in terms of spectral range and resolution, the expected intensities of the lines to be detected and the need to have a one-shot measurement as LIBS destroys the first layer of the samples more than one spectrometer design can be devised. In any case, if the full spectral range needed for LIBS and Raman (200 – 1000nm) is to be measured with a spectral resolution of 0.1nm which is required to resolve the plasma lines, there is no alternative to the use of high diffraction orders which will give superimposed spectra. To separate the orders there are two approaches: the first foresees a multiple order spectrometer concept with a single entrance slit. This spectrometer uses one grating to cover the full spectral range by measuring either the 1st, 2nd or 3rd spectral order. The proper order is selected by an optical filter array placed immediately behind the entrance slit and driven by a piezoelectric motor. In this spectrometer design, short wavelength spectra are analysed by higher diffraction orders (*e.g.* 2nd and 3rd), whereas long wavelength spectra are analysed by the fundamental order. Obviously also several laser shots are required to cover the entire spectra range for a LIBS measurement. This spectrometer has been extensively used in the LIRAMIS project [15].

Parameter	***Raman***	***LIBS***
Echelle grating	RGL 413 E 27 grooves/mm, 70° blaze angle	RGL 407 E 46.1 grooves/mm, 32° blaze angle
Order	20	92
Slit size f/#	200x200µm f/10	40x40µm f/10
Specral resolution per 3 pixels	25pm@200nm, 125pm@1000nm	0.20nm@720nm, 0.25nm@900nm
Detector	EMCCD DV885 1002x1004	EMCCD DV885 1002x1004

Table 6. Key specification of the twin Echelle spectrometer.

The most interesting design foresees the use of an Echelle spectrometer. An Echelle grating is coarse, but is used at very high diffraction orders (typically 10 – 100). In comparison to the other spectrometer configuration, this design simultaneously produces spectra of many diffraction orders that are superimposed to each other at the focal plane. The separation between the different orders is obtained by using another diffraction element dispersing the light in the normal direction respect to the first one. Such element can be another grating, a prism or a combination of the two (grism). The problem of this configuration lays in the

different requirements for the optimisation of the UV and IR portion of the spectra. The solution is to use a twin spectrometer in a so-call "butterfly" configuration. In this configuration, two slits are used for the short and the long range so that both ranges are separately optimised. The preliminary design of this spectrometer allowed to draw the specifications listed in table 6.

5. SENSOR HEAD

For the design of the SH the starting point is the choice of the geometrical scheme of illumination detection. Considerations of mechanical stability towards variations of temperature and of ease of alignment, prompt for a coaxial arrangement in which the light of the two lasers is combined in a single beam. This configuration offers several advantages:

- Identical spots are measured with both analysis;
- The spot on the sample does not move if the distance changes slightly as in LIBS depth profiling;
- Distance control can be achieved by a simple mechanical stop. The mechanical stop can be also used as a shield against environmental light (for example, a conical tube around the measurement beam);
- No opto-mechanical elements for focusing are needed.

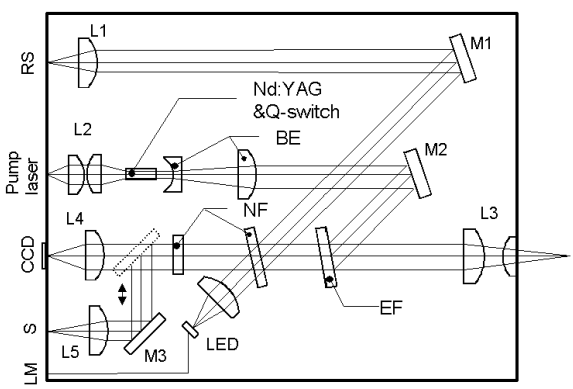

Fig. 4. Block scheme of the sensor head with Bragg grating filtered laser diode as source for Raman. RS Raman excitation from the instrument module; Pump Laser emission from the pumping laser diode; Nd:YAG &Q-switch laser active medium and passive Q-switch crystal; M1, M2, M3 mirrors; L1 collimator, L2 coupling optics, L3 front optics for focusing/collection; L4, L5 focusing optics, BE beam expander, EF dichroic edge filter, NF notch filters, LED laser monitor. M3 is movable to switch between the visual inspection and the spectral operational modus.

The current baseline for the design of the SH is shown in Fig. 4 and foresees a Bragg grating wavelength-stabilised laser diode and a Q-switched Nd:YAG laser as sources for Raman and LIBS measurements, respectively. The design keeps into account the possibility of integration with a microscope and/or close up imager that will share its objective lens with the beam delivery subsystem.

The wavelength-stabilised Raman source is placed inside the cavity as well as the pumping diode for the Nd:YAG laser where the environment temperature is less severe and they are connected by fibre optic links to the sensor head. The laser cavity of the Nd:YAG laser is however placed inside the sensor head to reduce the problems of coupling high peak power densities into the optic fibres. Special solarisation-resistant tapered optic fibres will be used to further reduce the power density on the fibre surface and to decrease the sensitivity to lateral misalignments. These fibres can be gold-plated to withstand the severe Martian conditions.

For what concerns the Raman branch, the light is first collimated and the beam is deflected by a folding mirror onto a notch filter. This filter reflects the light in an extremely narrow band around the laser line and is highly transmissive for all the other wavelengths. After passing through a high-pass edge filter, which has the function to combine the two laser beams, the light is finally focused onto the sample. On the other side of the notch filter an LED is foreseen as laser power monitor. Its output will be used to normalise the detected Raman signals removing any influence of the excitation power fluctuations.

For the LIBS branch, the pumping light will be coupled in the active medium in a standard stable laser cavity with intracavity passive Q-switching crystal. The infrared laser emission will be shaped by the beam expander BE which has the double role of reducing the power density on the dichroic edge filter EF and to reduce the spot size on the sample since the spot size is given by

$$w = \frac{2f}{D} \tag{1}$$

where w is the spot size, f is the focal length of the lens and D is the diameter of the area of the lens illuminated by the laser beam. The laser beam is then coupled in the front optics L3 whose focal length will be of the order of few centimetres to prevent the deposition of Martian matter on the lens surface during the LIBS measurements.

When starting from the sample, the emitted radiation is collected by the same optics used for the focusing. With this configuration, the coincidence between the

illuminated spot and the detection area is ensured even if for some reason a slight misalignment should occur the only consequence being a decrease of the intensity. After crossing the edge filter, the radiation is filtered by a couple of notch filters which provide an attenuation of the Raman line of the order of 10^{-8}. A movable mirror allows the selection between a spectral channel where an optical fibre is used to connect the measurement head to the spectrometer and an inspection channel where a proper focusing optics is used to form an image on CCD sensor. This inspection channel can be designed either to work as close up imager. The illumination of the sample will be carried out by using LEDs.

It should be pointed out that to the best of our knowledge, no space testing has been carried out on the Bragg grating wavelength-stabilised laser diode. Therefore, other alternative designs have been taken into account in the case that the suggested laser diode could not be used in the space environment. The backup solution has been identified in using a frequency-doubled $Nd:YVO_4$ laser operating at λ= 664nm. the Raman branch will be conceptually identical to the LIBS one with the pumping laser diode in the IM and a laser cavity and beam expander in the SH. However, giving the tight tolerances in the alignment of the $Nd:YVO_4$ and of the frequency doubling crystals a stable alignment is not easy to realise. Therefore, this approach shows some risks and additional work on the laser design is to be foreseen.

6. BUDGETS

Finally the budgets of GENTNER for what concerns the mass, power consumption, thermal power dissipated and data generation are shown in tables 7– 10. For completeness also the data pertinent to the optional colour imager are reported.

Subunit	***Mass (g)***
Instrument Module	
Laser drive unit	172
Pump laser	295
Raman laser system	41
Spectrometer	333
Spectrometer detector	59
Proximity electronics	141
Housing	157
External interconnections	47
Subtotal	*1245*
Sensor Head	
LIBS/Raman system	215
Imager	94
Subtotal	*309*
Total	**1554**

Table 7. Foreseen mass budget of GENTNER.

Measurement	***Peak Power (W)***	***Energy(Wh)***
LIBS spectrum acquisition	6.8	0.057
Raman spectrum acquisition	7.2	0.060
Data transfer	4.3	
Idle mode	2.5	N/A
Colour image acquisition	3.2	0.054

Table 8. Power absorption of GENTNER

Measurement	***Instrument Module (W)***	***Sensor Head (W)***
LIBS spectrum acquisition	5.3	1.5
Raman spectrum acquisition	7.0	0.2
Data transfer	4.1	0.1
Idle mode	2.4	0.1
Colour image acquisition	2.5	0.7

Table 9.Thermal power dissipated during GENTNER operation.

Measurement	***Data, uncompressed***	***Data compressed (libgzip)***
LIBS spectrum	158 kByte	70kByte
Raman spectrum	52.5kByte	21kByte
Colour image	4.096MByte	450kByte
Housekeeping	200Byte	N/A

Table 10 Data budget of GENTNER.

7. CONCLUSIONS

GENTNER is in advanced stage of development and a fully functional breadboard is expected to be ready at the end of 2006. The breadboard will be available to all scientists of the team to develop proper databases prior the deployment of the device in the Martian environment.

8. ACKNOWLEDGEMENTS

The work has been financed by Deutsches Tentrum für Luft- und Raumfahrt.

This paper is the result of the efforts of a large team of 26 scientists and engineers from 6 different European countries and from academic and industrial environments. Although the complete list is too long to be reported in this paper, their contribution has been invaluable to draft the scientific needs for GENTNER.

9. REFERENCES

1 ESA Exobiology Team Study, *Exobiology in the Solar System & the Search for Life on Mars*, ESA SP1231 (1999).

2 G. Klingelhöfer, B. Fegley Jr., R.V. Morris, E. Kankeleit, P. Held, E. Evlanov, O. Priloutski, *Mineralogical analysis of Martian soil and rock by a miniaturised backscattering Mössbauer spectrometer*. Planet. Space Sci. **44**, 1277-1288.n (1996).

3 R.V. Morris, S.W. Squyres, J.F. Bell III, P.H. Christensen, T. Economu, G. Klingelhöfer, P. Held, L.A. Haskin,A. Wang, B.L. Jolliff, R. Rieder, *Analysis of Martian Surface Materials during the Mars Surveyor 2001 mission by the ATHENA instrument payload*. In *Lunar and Planetary Science XXIX*, Abstract #1326, Lunar and Planetary Institute, Houston, USA (CD-ROM) (1998).

4 A. Afflalaye, R. Sternberg, D. Coscia, F. Raulin, C. Vidal-Madjar, *Gas chromatography of Titans atmosphere. VIII: Analysis of permanent gases with carbon molecular sieve packed capillary columns.* J. Chromatogr. **A76**, 195-203 (1997).

5 H.B. Niemann, S. Atreya, J. Bauer, K. Biemann, B. Block, G.R. Carignan, T. Donahue, L. Frost, D. Gautier, D. Harpold, D. Hunten, G. Israel, J. Lunine, K. Mauersberger, T. Owen, F. Raulin, J. Richards, S. Way, *The gas chromatograph mass spectrometer aboard Huygens*, ESA SP-1177, 85-107.e (1997).

6 R. Rieder, T. Economou, H. Wänke, A. Turkevich, J. Crisp, J. Brückner, G. Dreibus, H.Y McSween Jr., *The Chemical Composition of Martian Soil and Rocks Returned by the Mobile Alpha Proton X-ray Spectrometer: Preliminary Results from the X-ray Mode*. Science **278**, 1771-1774 (1997).

7 A. Wang, L.A.Haskin, E. Cortez, *Prototype Raman spectroscopic sensor for* in situ *mineral characterisation on planetary surfaces*. Appl. Spectrosc. **52(4)**, 477-487 (1998).

8 S.K. Sharma, P.G. Lucey, M. Ghosh, H.W. Hubble, K.A. Horton, *Stand-off Raman spectroscopic detection of minerals on planetary surfaces.* Spectrochimica Acta part A **59,** 2391 - 2407, 2003

9 W.B. Brinkerhoff, P.R. Mahaffay, T.J. Cornish, A.F. Cheng, H.B. Niemann, D. Harpold, S.P. Gorevan, S. Rafeek, D. Yucht, *Dual source mass spectrometer and sample handling system*, Lunar and Planetary Science **33**, 1544-1545 (2002).

10 L. Marinangeli, A. Baliva, E. Piluso, G.G. Ori, I. Casanova, A. Lenti, C. Ponzoni, E. Cavazzuti, L. Isabella, *X-Ray Diffraction instrument For in Situ Analysis of Martian Rocks*, Bull. of the American Astronomical Society, **31(4)**, 1083, 1999

11 G. Vannaroni, R. Filippini, E. Pettinelli, A. Cereti, G. Della Monica, D. Del Vento, A. M. Di Lellis, R. Di Maio, A. Galli, A. Menghini, R. Orosei, S. Orsini, C. Ottonello, S. Pagnan, F. Paolucci, A.R. Pisani, G. Schettini, M. Storini, G. Tacconi, *MUSES: MUlti-sensor Soil Electromagnetic Sounding,* Planetary and Space Science **52** , 67 – 78, 2004

12 K. Nakamoto, *Infrared and Raman spectra of inorganic and coordination compounds,* John Wiley and Sons, Inc., New York (USA) 3 – 101, 1976

13 R. Bertrand, A. Del Bianco, E.K. Jessberger, I. Mann, P. Peuser, D. Rost, K. Schneider, T. Stephan, I. Weber, *Flight Model Instrument Concept, LIRAMIS-TN22-03, issue 1.0*, ESTEC Contract No.: 16475/02/NL/HB, 2003.

14 E.K. Jessberger et.al., *GENTNER – a Miniaturised Laser Instru-ment for Planetary in-situ Analysis,* submitted in response to ESA's Call for Ideas *Pasteur Instrument Payload for the EXOMARS Rover Mission*

15 R. Bertrand, A. Del Bianco, E.K. Jessberger, I. Mann, P. Peuser, D. Rost, K. Schneider, T. Stephan, I. Weber, *LIRAMIS Instrument Definition Document. LIRAMIS-TN4-10c, Issue 1.0*, ESTEC Contract No.: 16475/02/NL/HB, 2003.

16 R. Bertrand, A. Del Bianco, E.K. Jessberger, I. Mann, P. Peuser, D. Rost, K. Schneider, T. Stephan, I. Weber, *Technical Data Package*, ESTEC Contract no. 14866/00/NL/LVH, 2001.

17 A.K. Knight, N.L. Scherbarth, D.A. Cremers, M.J. Ferris, *Characterization of Laser-Induced Breakdown Spectroscopy (LIBS) for Application to Space Exploration*, Appl. Spectr. **54(3)**, 331-340 (2000)

18 F. Colao , R. Fantoni, V. Lazić, A. Paolini, *LIBS application for analyses of martian crust analogues: search for the optimal experimental parameters in air and CO_2 atmospher,* Appl. Phys. A, **79(1)**, 143 – 152 (2004)

GaN-based Robust Micro Pressure and Temperature Sensors for Extreme Planetary Environments

K. Son[1], B. Yang[1], Y. Liu[2], P. P. Ruden[2], N. Biyikli[3], X. Ni[3], J. Xie[3] H. Morkoç[3], R. E. Young[4], and A. Colaprete[4]

[1]Jet Propulsion Laboratory, Pasadena, CA 91109, kson@jpl.nasa.gov

[2]Dept. of Electrical & Computer Engineering, University of Minnesota, Minneapolis, MN

[3]Dept. of Electrical Engineering, Virginia Commonwealth University, Richmond, VA

[4]NASA Ames Research Center, Moffett Field, CA 94035

We are developing a robust AlGaN/GaN-based microsensor that is capable of simultaneous temperature and pressure measurements in harsh planetary atmosphere. The AlGaN/GaN sensor has small volume (<1cm^3), low mass (<5g), and low power requirement (<10 mW) and can operate at extreme temperatures (-250 to 600 °C) and pressures (0 bar to 10 Kbar) and in strong radiation (> 5 Mrad) environments. Measuring the thermal structure of a planet's atmosphere under extreme conditions, the AlGaN/GaN microsensor can be a key element for future entry probes for *in situ* planetary atmospheric investigation.

The III-nitride compounds based on the AlGaN alloy have large band gaps (3.4-6.1 eV) and strong atomic bonds. Consequently, these semiconductors exhibit favorable mechanical, thermal, and chemical stabilities with minimal problems arising from the unwanted optical or thermal generation of charge carriers. Therefore they are ideal materials for constructing sensors for applications in extreme and harsh environments. One of the unique advantages of GaN-based devices is that AlGaN/GaN heterostructures develop sheet charges at the hetero-interfaces due to the piezoelectric and spontaneous polarizations between AlGaN and GaN layers. Applied stress modulates this interfacial polarization charge due to differences in the piezoelectric coefficients of AlGaN and GaN, and therefore the barrier height (that controls transport across the interface) is modulated. We utilize this stress-induced modulation of the barrier height for pressure sensing. Mobility of the electrons in the polarization sheet changes with temperature due to scattering. We use this temperature-induced mobility change for temperature measurements.

Among the various AlGaN/GaN heterostructure devices, we have investigated n-GaN/$Al_xGa_{1-x}N$/n-GaN (n-I-n) vertical transport devices and high electron mobility transistors (HEMTs) for pressure and temperature sensing applications. Theoretical modeling of n-I-n sensors performed with various compositions (x = 0.1, 0.15, & 0.2) of $Al_xGa_{1-x}N$ suggests that electrical currents will decrease with increased pressure and this effect becomes more significant with higher AlN compositions in the $Al_xGa_{1-x}N$ layer. The effects of hydrostatic pressure on the electrical properties of n-GaN/$Al_{0.15}Ga_{0.85}N$/n-GaN structures measured over the range of 0-6 kbar show that the current decreases linearly and reversibly with increasing pressure.

The current-voltage characteristics of various $Al_{0.3}Ga_{0.7}N$/n-GaN HEMT sensors have been measured under hydrostatic pressure of 0-2 kbar. The results show that the drain current increases with pressure and the maximum relative increase occurs when the gate bias is near threshold and drain bias is slightly larger than saturation bias. The increase of the drain current is associated with a pressure-induced shift of the threshold voltage by -8.0mV/kbar. The linearity and reversibility in pressure response observed with both n-I-n and HEMT sensors suggest that they are promising for pressure sensor applications in extreme environments. Temperature effects on electrical properties of the GaN-based sensors have also been measured, and detailed analysis on the results is in progress.

Miniature Mass Spectrometer with Direct Ion Detection

Mahadeva P. Sinha
Jet Propulsion Laboratory, California Institute of Technology, Pasadena, CA 91109
and

Mark Wadsworth
Tangent Technologies, Inc., Monrovia, California 91016

Abstract

A high performance, focal plane miniature mass spectrometer (MMS) of Mattauch-Herzog geometry with a CCD-based array detector for the direct and simultaneous measurements of different mass ions has been developed in our laboratory* Miniaturization (10cm x 5 cm x 5cm, 395 g) was accomplished by using high-energy-product magnet material (Nd-B-Fe alloy) and a high permeability yoke material (V-Co-Fe Alloy) for the fabrication of the magnetic sector. The electrostatic sector was machined from a single piece of machinable ceramic (MACOR). The modified-CCD based ion detector array has 1000 elements (25 µm x 2mm) and was invented in our laboratory. The photosensitive part of the CCD was replaced with a metal-oxide-semiconductor (MOS) capacitor for ion detection. The ion sensing capacitor plates are connected to the CCD gates that are operated in the fill-and spill mode providing a gain in the charge domain for the signal ions and minimizing various noises during measurements. The MMS with the array detector can measure masses up to 250 u with a unit mass resolution. The results of mass spectral measurement with this detector array and MMS will be presented.

The above attributes make MMS suitable for space applications for isotopic and chemical analysis and also for field applications on earth. A novel methodology for the determination of isotopic composition of Fe and O in minerals has also been developed. The application of the methodology in combination with MMS for the determination of biosignature and paleoenvironmental conditions of planetary bodies will also be discussed.

* Rev. Sci. Instrum. **76**, 025103 (2005)

TECHNOLOGY DEVELOPMENTS TOWARDS A COMBINED XRD-XRF INSTRUMENT FOR PLANETARY SURFACE ANALYSIS

N. Nelms[1], A. Holland[2], D. Talboys[1], I. Hutchinson[2], D. Simpson[2], G. Cressey[3], P. Bland[4]

[1]*Space Research Centre, University of Leicester, Leicester, LE1 7RH, UK, nin@star.le.ac.uk.*
[2]*e2v centre for electronic imaging, Brunel University, Uxbridge, UB8 3PH, UK.*
[3]*Dept. Mineralogy, The Natural History Museum, Cromwell Road, London, SW7 5BD, UK.*
[4]*Dept. Earth Science & Engineering, Royal School of Mines, Imperial College, London, SW7 2AZ, UK.*

ABSTRACT

Geochemical analysis of the surface material of terrestrial type planets is of fundamental importance in understanding the geological context of the planetary environment. Consequently this analysis should be performed whenever possible and indeed this has occurred on a number of previous landers. Current techniques include X-ray fluorescence (XRF) and Rutherford back-scattering of alpha particles, which provide information on the elemental composition of the sample. However, geological understanding can be greatly improved if the mineral structure of the sample can also be determined. The dominant method used for mineralogical identification of geological samples in earth-based laboratories is X-ray diffraction (XRD), which analyses the crystal lattice structure to decipher the constituent minerals. When XRD is combined with XRF it creates a powerful tool for characterisation of the geochemical, mineralogical and, by inference, the petrological nature of geologic material. To date no XRD instrument has been operated on the surface of another planet but a number of combined XRD – XRF instruments for planetary surface operation are currently under development in the US, Europe and Japan. In this paper we describe a number of technology developments that are taking place in the UK aimed at developing an efficient excitation and detection system for such a combined XRD-XRF instrument.

1. INTRODUCTION

A combined X-ray diffraction/X-ray fluorescence instrument deployed on a planetary lander or rover is able characterise the mineralogical and geochemical makeup of local geological materials. Taken together these measurements can provide unambiguous mineral identification which can help determine the past conditions and context under which those samples were formed and so make an important contribution to interpreting the nature, origin and evolution of the geological environment. Such an instrument has never been deployed on another planetary surface but is currently baselined by both NASA for the Mars Science laboratory (Chemin) [1] and by ESA for the ExoMars rover [2]. In the case of Mars, the surface geochemistry has been measured by instruments on the two Viking landers, Mars Pathfinder's Sojourner Rover and the two Mars Exploration Rovers. The Viking landers made the first analyses of the Martian regolith [3]. The Pathfinder Sojourner rover was first to analyse rocks on Mars [4] while the two Mars Exploration Rovers detected chemical signatures in rocks that indicate alteration by water [5,6]. However, the use of this geochemical data to infer rock mineralogy (and hence petrology) involves some uncertainty since different mineral assemblages may have the same composition. In contrast, the X-ray diffraction technique probes the crystal structure of minerals and is able to make a direct measurement of mineralogy.

An XRD/XRF instrument deployed on a Mars rover can perform several science investigations but of considerable contemporary interest is the search for evidence of life. This consists of investigating the mineralogy of lithologies that may harbour fossilized life or extant life [7]. The instrument can also search for evidence that liquid water influenced the evolution of the landing site [8] which has important implications for the past or present biological habitability of the landing area [9]. Mineral deposits formed in the presence of liquid water detected from orbit, by TES [10] and OMEGA [11], can be investigated *in situ*. Ground truth measurements have a valuable role in constraining the interpretation of remote sensing data since it can provide definitive characterisation of the mineralogy of individual rocks.

A practical XRD instrument comprises three main elements – an X-ray source, a prepared sample and a detector. These can be arranged in a number of different ways around two main modes of operation – transmission or reflection (see figure 1). In transmission mode X-rays are diffracted (and fluoresced) by a prepared sample in the path of the incident X-ray beam while in reflection mode both the source and the detector are located on the same side of the sample. Each geometry has advantages and disadvantages based mostly on sample

presentation but both arrangements require a powdered sample that is well prepared in terms of consistent grain size. Current work described in this paper is concentrating for the most part on reflection geometry due to sample sharing with other instruments.

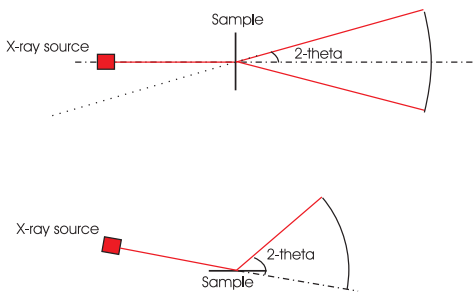

Figure 1. Transmission (top) and reflection (bottom) diffraction geometries showing sample orientation and 2-theta angle.

2. X-RAY SOURCE

XRD requires a coherent X-ray source that is both monochromatic and has low beam divergence. Preliminary studies have indicated little benefit from the use of X-ray optics for this application, and so beam collimation is more readily achieved using a simple pinhole placed at a suitable distance from the source. In our developments we are concentrating our efforts into the use of X-ray tubes rather than, for example, an ^{55}Fe radioactive source since it is possible to achieve much higher X-ray flux from the tube source. Initial trials using a standard Kevex X-ray tube with Cu anode have resulted in a flux of approximately 20,000 s^{-1} through an 80 µm hole in a tungsten foil (see figure 2) placed at a distance of 10 cm from the focal spot.

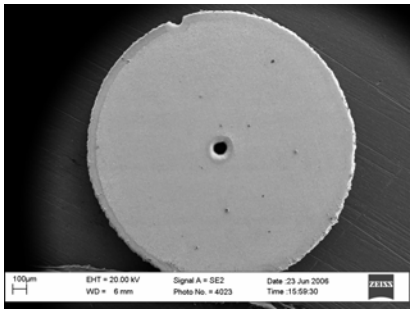

Figure 2. 80µm pin-hole in tungsten foil used for X-ray beam collimation.

Given the ~250 µm diameter of X-ray spot in the tube, this equates to a beam divergence of approximately 0.07° which is suitable for our requirements. We are initially conducting further trials using an Oxford Instruments Eclipse III portable X-ray tube [12], and later hope to use the planned micro-focus version with a target spot size of 50 µm. Using this tube, suitable collimation for a 0.1° beam divergence could be obtained using an 80µm pinhole placed at a distance of 50mm. This would result in significantly more flux (or lower power) than the flux measured to-date. The use of such an X-ray tube would need to pass qualification testing, particularly to survive the entry descent and landing, and the operating temperature. Diffraction is an inherently inefficient process (typically 10^{-4} or 10^{-5}) and even with a high incident flux detected count-rates can be very low.

3. DETECTORS

Solid-state semiconductor detectors for X-ray detection are available in a number of different formats, both single pixel and as 1D and 2D arrays. High-resolution laboratory X-ray diffractometers tend to use a silicon diode detector on a movable arm to measure the diffraction distribution. Mechanisms of any sort are not preferred for spacecraft operations due to inherent reliability problems. Consequently a position-sensitive detector (either 1D or 2D) provides a convenient method for detecting the diffraction pattern without movement – see figure 3.

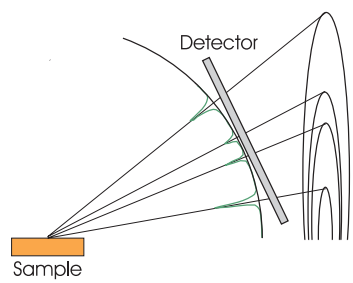

Figure 3. Diffraction measurement using position sensitive detector.

Charge coupled device (CCD) detectors have a long heritage in space operation as X-ray detectors [13]. With direct X-ray detection (in the 0.5 – 10 keV range), low noise operation and good spatial resolution (pixel size of order 10 – 40 µm) CCDs can make excellent detectors for XRD. When operated in photon-counting mode the energy of each X-ray can be determined allowing discrimination between fluoresced and diffracted photons. This enables simultaneous construction of an XRF histogram and an XRD diffractogram (figure 4), providing

information on both the elemental composition and the mineralogical structure.

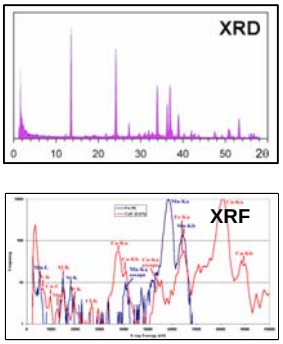

Fig. 4. Sample XRD 2θ diffractogram plot and XRF histogram.

Detector parameters have a large impact on the overall performance of an XRD instrument especially when a position-sensitive array is used. In terms of the diffraction pattern the choice of detector affects the area of the diffraction rings sampled and the angular resolution of the resultant diffraction pattern. Sampling the diffraction pattern with a 1D (linear) array or narrow 2D array minimises the raw data (due to the small number of pixels) and can provide high resolution. However, with predicted very low X-ray flux rates (see section 2) collecting area most probably needs to be maximised. This can be achieved by using a wider 2D array but for practical reasons of instrument volume, power and mass means that a lower angular resolution has to be accepted. As part of this development programme two different custom CCD designs are being produced by e2v technologies Ltd [14]. They are both frame-transfer CCDs, which allows effectively zero dead-time during operation and have small pixels (13.5 μm square). The frame-transfer region of both devices has a reduced area (25% instead of 50%) to maximise the collecting area of the CCD. The two devices are identical except for number of pixels (and hence area) – the two formats are shown in figure 5.

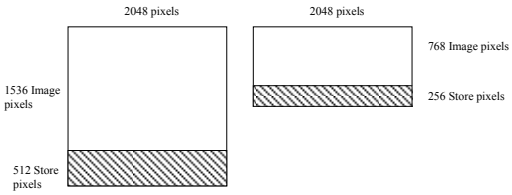

Fig. 5. Proposed CCD formats for development programme.

The devices are being manufactured using deep-depletion silicon in order to provide good X-ray quantum efficiency. They are front-illuminated and have inverted mode operation for reduced dark-current at non-cryogenic temperatures.

As discussed above the format of the detector affects the performance of the instrument. This argument can be extended to include the use of multiple detectors arranged in array. It is planned to study a number of different array geometries based on the two CCD structures shown in figure 5. The proposed arrangements are shown in figure 6.

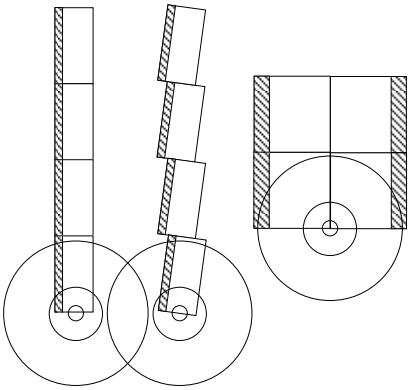

Figure 6. Proposed CCD detector array geometries. The interaction with (part of) the diffraction rings is shown.

The first two linear arrangements provide high angular resolution (~0.05° over a 60° range) coverage but with a narrow collecting area. The offset linear arrangement removes dead space between the detectors but further complicates diffraction pattern correction. The third 2x2 array presents the best collecting area but suffers from reduced angular resolution (~0.15° over a 60° range).

As stated above, low noise operation is necessary for X-ray photon counting and a prerequisite for this is to cool the CCD in order to reduce leakage (dark) current generation. Operating temperatures of order 173 - 243 K are typically required. At the higher end of this range more precise thermal control is required to prevent significant fluctuations in dark current levels. Typical total noise requirements are discussed in section 4.1.3. Read-out rates are driven by a number of factors including dark current generation, read-noise requirements and power consumption. With reasonable cooling (< 243 K) exposure times of order a few seconds can be tolerated with regard to dark current. On-chip binning can also be applied to reduce the number pixels that need to be read, in this case driven by angular resolution requirements and curvature of the diffraction pattern. For the CCDs being developed numbers of (binned) pixels to read are either 250,000 or 500,000. Read-out rates of 100

– 200 kpixels/second will meet the few second exposure time limit.

4. ELECTRONICS

Although CCDs are ideally suited to a combined XRD-XRF instrument they are not simple devices to operate. They require a range of bias voltages and a number of different clocks. For low noise operation, required for both XRD and XRF, the output signal from the CCD also needs to be processed. Figure 7 is a block diagram of a CCD detector array showing the typical drive signals for both the detector and the signal processing electronics.

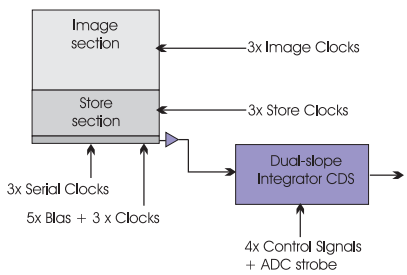

Fig. 7. Typical CCD control signals.

4.1 Bias Voltage Generation

e2v CCDs typically require bias voltages in the range of 0 to 35 V. Maximum current requirement is for the output drain of the on-chip amplifier, typically 2 – 5 mA (at 28 – 32 V). These can be easily generated using an operational amplifier buffer coupled with a low-pass filter to reduce noise injection. Once optimised for a particular CCD, the bias voltages do not usually need to be altered and can be fixed in the design.

4.1.2 Clock Waveform Generation

A number of approaches are possible for producing the clock waveforms that are required. For an application such as this, the clock pattern is essentially fixed with possible variable parameters for image integration time and on-chip binning. We are adopting an FPGA approach since space-qualified devices are readily available. The CCDs being used are of frame-transfer design which provides essentially zero dead-time during read-out. Consequently extra clocks are required to control the storage section of the detector. The clocking outputs from the FPGA are TTL level and need to be level shifted for correct CCD operation. Typical maximum clock levels for e2v devices are of order 15 V, with a 0 V minimum. Proprietary level shifters (clock drivers), with high current output, are available from Intersil (Elantec) although qualification for operation in a space environment needs to be verified. Bias generation is also required for the high-level of the clock driver, appropriately decoupled in order to provide the peak current requirements of the various clock loads.

4.1.3 CCD Signal Processing

The noise performance of the CCD depends upon a number of things, not least dark-current generation which is temperature dependent, and output read-noise. CCD noise performance is usually quoted as an equivalent noise charge (enc) in electrons rms. An enc < 10 electrons rms is typically needed in order to perform XRF with < 30 electrons for XRD. When the CCD is cooled and/or operated fast enough the read-noise is dominated by the CCD output node reset noise, i.e. the dc level of the CCD output amplifier is reset after each pixel charge is read and the uncertainty in this reset level is of order 100s electrons rms.

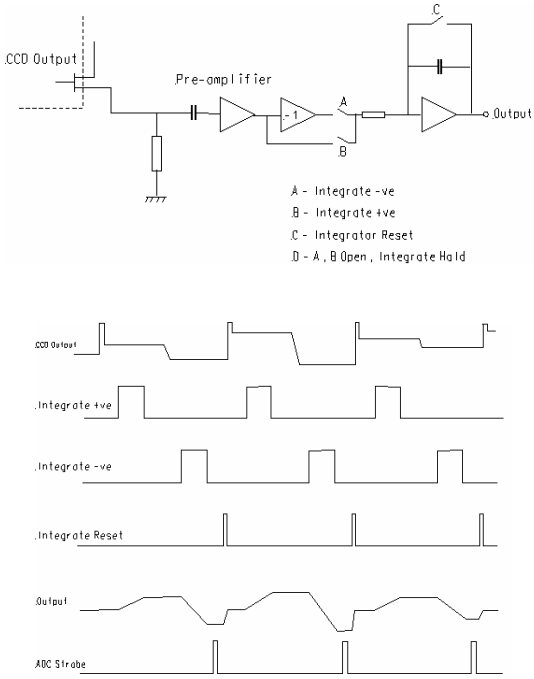

Fig. 8. CCD signal processing – dual-slope integrator technique. Top – typical dual-slope integrator schematic, bottom – associated control and output waveforms. The actual circuit also includes an input clamp to avoid saturation from reset feed-through.

Left like this the CCD would be incapable of X-ray photon energy analysis and construction of XRD diffractograms and XRF histograms would be impossible. The reset noise is removed using correlated double sampling (CDS). A number of

different schemes exist but they all perform the same function. The output amplifier of the CCD is reset and the reset level is sampled. The pixel charge is then clocked onto the output node and the output sampled again. These two samples are then differenced (or correlated) and the result is the pixel charge level independent of the uncertain reset level. As mentioned above a number of different schemes for CDS processing exist and we have chosen a dual-slope integration technique – see figure 8. This is not the fastest scheme but high-speed read-out is not required (see section 3) and the technique benefits from improved noise reduction provided by the integration technique. A single channel version of the dual-slope integrator CDS has been built and tested with noise performance of 5 electrons rms (over-scan) at 100 kHz when operating with an e2v CCD42 – see figure 9.

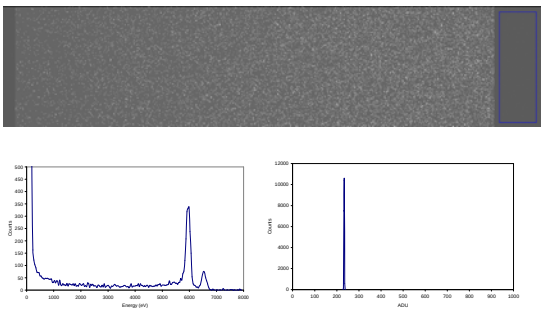

Fig. 9. Prototype dual-slope integrator performance. Top - CCD image with X-rays from ^{55}Fe source at 5.9 keV and 6.4 keV showing over-scan region at the right. Bottom left – X-ray histogram, FWHM at 5.9 keV is 200 eV. Bottom right – over-scan noise histogram, enc is 5 electrons rms. X-ray performance is limited by dark-current from CCD at -50 °C. 100 kHz pixel read-out rate with 2.8 μs integrator time.

For the flight-type CDS design we are developing a dual-channel hybrid circuit. One or two of these devices will be used depending upon the size of the detector array, either 2 or 4 CCDs. The hybrid circuit approach has a number of advantages over an ASIC design. The hybrid is cheaper for small quantities, it can be built around radiation-hard and/or space qualified devices and performance is easier to verify at the prototype stage. The hybrid is also usually housed in sealed metal package which contributes further to the environmental durability. Our design is based on Analog Devices OP42 amplifiers and ADG201HS analogue switches, both of which have radiation and environmental test data available. Both devices are of course available as dice. At the time of writing the hybrid design is complete and has been sent out for manufacture.

4.1.4 CCD Data Processing – Hardware

With an array of 4 CCD detectors operating in photon counting mode raw data rates can be high. In order to shield the uplink from excessive data quantities on-board processing can be performed. To this end we have included a digital signal processor (DSP) between the analogue to digital converters and the output bus (the laboratory prototype uses a USB output bus to facilitate PC interfacing).

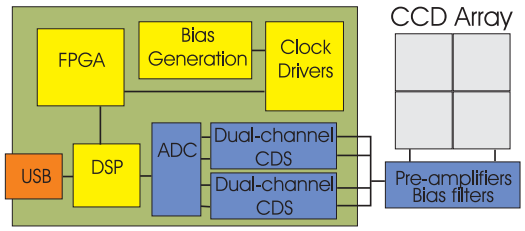

Fig. 10. Overall block diagram of proposed flight-type CCD array drive electronics. The USB interface is to facilitate laboratory testing.

As indicated in section 4.1.3 the CDS hybrid is already in manufacture. The design for the CCD drive electronics is underway (figure 10) and we aim to have a working prototype of the whole system by the end of 2006.

5. DATA PROCESSING

The reduction of data volumes (and consequently rates) requires some on-board processing and since event rates are low this can be performed in real-time. This is achieved using a dedicated DSP that will take digitised CCD data as an input and produce XRD diffractograms and XRF histograms as output.

The DSP will have a number of functions related to data processing including:

- Dynamic calibration – this is possible using the diffracted photons of known energy.
- Event reconstruction. X-ray photons that deposit their charge into more than one pixel can be 'reconstructed' to recover the original energy. These can then contribute to XRF and XRD histograms.
- Diffracted/fluoresced photon discrimination based on photon energy.
- Background rejection.
- Construction of XRF energy histogram.
- Diffraction pattern curvature correction.
- Construction of Kα and Kβ 2θ XRD diffractograms.

The DSP will also be responsible for CCD clock sequencer parameter setting since it provides the only interface to the outside world. A 'raw-data' mode will also be included for diagnostic purposes to allow direct visualisation of CCD images.

6. CONCLUSIONS

A combined XRD-XRF instrument that is able to perform *in situ* analyses on surface samples of another planet can provide the geochemical and mineralogical information with which to contextualise the local environment. It is also capable of providing valuable ground truth measurements for the current and future generations of orbital instruments. The technology developments described in this paper are aimed at enabling such an instrument to be produced initially for Mars but possibly also for the Moon and other terrestrial type surfaces.

7. REFERENCES

1. Blake, D.F., Sarrazin, P., Bish, D.L., Feldman, S., Chipera, S.J.,Vaniman, D.T., Collins, S.A. "Definitive Mineralogical Analysis of Mars Analogs Using the CheMin XRD/XRF Instrument", Lunar and Planetary Science Conf XXXV, 2004.
2. http://www.esa.int/esaMI/Aurora
3. Clark, B. C., A. K. Baird, R. J. Weldon, D. M. Tsusaki, L. Schnabel, M. P. Candelaria, "Chemical composition of Martian fines", J. Geophys. Res, 87, 10059-10067, 1982.
4. Rieder, R., T. Economou, H. Wänke, A. Turkevich, J. Crisp, J. Brückner, G. Dreibus, H. Y. McSween Jr., "The chemical composition of martian soil and rocks returned by the mobile Alpha Proton X-ray Spectrometer: Preliminary results from the X-ray mode", Science, 278, no. 5344, 1771-1774, 1997.
5. Rieder, R., R. Gellert, R. C. Anderson, J. Brückner, B. C. Clark, G. Dreibus, T. Economou, G. Klingelhöfer, G. W. Lugmair, D. W. Ming, S. W. Squyres, C. d'Uston, H. Wänke, A. Yen, J. Zipfel, "Chemistry of rocks and soils at Meridiani Planum from the Alpha Particle X-ray Spectrometer", Science, 306/5702, 1746-1749, 2004.
6. Gellert, R., R. Rieder, J. Brückner, B. Clark, G. Dreibus, G. Klingelhoefer; G. Lugmair, D. Ming, D, H. Wänke, A. Yen, J. Zipfel, S. Squyres, "The Alpha Particle X-Ray Spectrometer (APXS): Results from Gusev Crater and calibration report", J. Geophys. Res, 111/E2, 2555, 2006.
7. Vaniman, D., D. Bish, D. Blake, S. T. Elliot, P. Sarrazin, S. A. Collins, S. Chipera, "Landed XRRF/XRD analysis of prime targets in the search for past or present Martian life", J. Geophys. Res, 103/E13, 31477-31489, 1998.
8. Blake, D. F., P. Sarrazin, S. J. Chipera, D. L. Bish, D. T. Vaniman, Y. Bar-Cohen, S. Sherrit, S. Collins, B. Boyer, C. Bryson, J. King, "Definitive mineralogical analysis of Martian rocks and soil using the CheMin XRD/XRF instrument and the USDC sampler", Sixth international conference on Mars, 2003.
9. Harland, D. M., "Water and the Search for Life on Mars", Springer-Verlag, 2005.
10. Christensen, P.R., Bandfield, J.L., Clark, R.N., Edgett, K.S., Hamilton, V.E., Hoefen, T., Kieffer, H. H., Kuzmin, R. O. , Lane, M. D., Malin, M.C., Morris, R.V., Pearl, J.C.,Pearson, R., Roush, T.L. , Ruff, S.W. , Smith, M.D., "Detection of crystalline hematite mineralization on Mars by the Thermal Emission Spectrometer: Evidence for near-surface water", J. Geophys. Res, 105/E4, 9623-9643, 2000.
11. Bibring, J.-P., Langevin, Y., Gendrin, A., Gondet, B., Poulet, F., Berthe, M., Soufflot, A., Arvidson, R., Mangold, N., Mustard, J., Drossart, P. and the OMEGA team, "Mars Surface Diversity as Revealed by the OMEGA/ Mars Express Observations", Science, 307, 1576-1581, 2005.
12. www.oxfordxtg.com
13. Holland, A.D., "X-ray spectroscopy using MOS CCDs", Nucl. Instr. Meth. A, 377, 334-339, 1996.
14. www.e2v.com

X-RAY AND GAMMA RAY SPECTROMETER FOR THE HEAT FLOW AND PHYSICAL PROPERTIES INSTRUMENT (HP^3) ON THE *EXOMARS* GEOPHYSICAL AND ENVIRONMENTAL PACKAGE

R. M. Ambrosi [(1)], A. J. Ball [(2)], N. Nelms [(1)], D. Talboys [(1)], M. S. Bentley [(3)], T. Spohn [(4)], R. Nadalini [(4)], A. Hagermann [(2)], L. Richter [(5)], S. Calcutt [(6)], G. W. Fraser [(1)], J. Bridges[(2)], J. C. Zarnecki [(2)], C. S. Cockell [(2)], M. M. Grady [(2)], H. Simon [(7)], P. Siffert [(7)], M. S. Skidmore [(1)]

[(1)] *University of Leicester, Dept. of Physics and Astronomy, Space Research Centre, University Rd, Leicester, LE1 7RH, UK, rma@star.le.ac.uk.*
[(2)] *Planetary Space Science Research Institute, The Open University, Walton Hall, Milton Keynes, MK7 6AA, UK, a.j.ball@open.ac.uk.*
[(3)] *Cosine Research B.V., Niels Bohrweg 11, NL-2333 CA Leiden, The Netherlands.*
[(4)] *German Aerospace Center, DLR, Berlin-Adlershof, Rutherfordstraße 2, 12489 Berlin, Germany.*
[(5)] *German Aerospace Center, DLR, Linder Hoehe, 51147 Koeln, Germany.*
[(6)] *University of Oxford, Atmospheric Oceanic Planetary Physics, Clarendon Laboratory, Parks Road, Oxford, OX1 3PU, UK.*
[(8)] *EURORAD, CTT, 23 Rue du Loess, BP20, 67037 Strasbourg, Cedex 2, France*

ABSTRACT

In this study we highlight the enhancement of one of the proposed core experiments on the Mars Long-Lived Surface Package (ML2SP) proposal to the European Space Agency for the *ExoMars* Geophysical and Environmental Package (GEP). The instrument is the Heat Flow and Physical Properties Package (HP^3), led by Tilman Spohn at DLR Berlin (formerly at Institut für Planetologie, Münster). HP^3 is a sub-surface suite of sensors aimed at measuring planetary surface heat flow, an important geophysical parameter never before measured on Mars. The experiment comprises a suite of three sensor subsystems deployed from a surface station to a depth of several metres by means of a tethered mole. Mechanical properties are derived from measurements of the dynamics of mole penetration; thermal properties are measured using sensors distributed along the umbilical tether, and the bulk density profile is measured using a gamma-ray backscatter densitometer housed within a payload compartment at the lower end of the tether. The densitometer comprises a radioisotope source (^{137}Cs), high density shielding, two semiconductor gamma ray detectors and associated front-end electronics. The Open University and University of Leicester teams have been working on the development of a Monte Carlo model for the probe as well as the laboratory breadboard model. In this study we describe the laboratory programme and show some of the results obtained. The enhancement requires the inclusion of both X-ray and Gamma Ray spectrometers in the instrumented mole, which will provide details of the elemental composition of the Martian surface as a function of depth. The enhancement will also provide details of natural sources of radiation such as U, Th and K. The compositional information will allow for a more accurate estimate of the specific heat capacity of the material surrounding the mole, thus providing more accurate heat flow measurements.

1. INTRODUCTION

The Martian sub-surface preserves records of geological and climatic evolution and plays host to water ice, possibly habitable environments and perhaps, traces of life. The development and flight of a mole-deployed X-ray / γ-ray instrument for the *ExoMars* Geophysics and Environmental Package (GEP) will enable the geophysical and geochemical profiling of the first 5 m to 10 m of the sub-surface at the targeted landing site. Previous Martian missions, e.g. Viking Lander, have profiled no deeper than 30 cm and the results from Spirit and Opportunity indicate a small-scale compositional heterogeneity [1]. The X-Gamma experiment may be *ExoMars*' only opportunity to make geochemical measurements below the oxidant extinction depth, which has a global mean of 2 m to 5 m by some models [2], greater than the depth accessible by the *ExoMars* drill. A mole deployment system is already base-lined for the GEP.

2. SCIENCE OBJECTIVES

The proposed X-Gamma instrument has three simultaneous measurement modes (A) ~200 to 700 keV; (B) 1 keV to 20 keV; (C) 30 keV to at least 2.5 MeV; however, this limit could be increased above 6 MeV if a large volume detector is selected to measure gamma rays produced via neutron activation processes.

The instrument will perform a number of measurements on the structure and elemental compositions of the Martian sub-surface. Bulk density will be measured

using mode (A); elemental composition will be measured using modes (B, C). The instrument will determine the relative abundances of major rock-forming elements, modes (B, C); the abundance vs. depth of meteoritic nickel, modes (B, C); the presence of water/ice, from prompt neutron activation products, mode (C) [3]; the abundances of carbon and nitrogen, mode (C), phosphorus and sulphur, modes (B, C); radioactivity levels generated by particle-induced reactions, mode (C), and the concentration of natural radioisotopes (K, U, Th), mode (C). Detailed lists of elements detectable by complementary X-ray and neutron activation techniques more are given by Nair et al., 2004 [4] and Meyer (ed), et al. [5], 1995.

The neutron flux on the Martian surface has been reported to be higher than expected [6]. The estimated fluence at the surface of 1 MeV neutrons is of the order of $2x10^7$ neutrons cm^{-2} MeV^{-1} for the duration of a 1956 equivalent solar particle event. At thermal neutron energies the fluence levels are an order of magnitude higher. The continuous exposure of the surface to neutrons and the pulsed nature of the exposure due to solar events implies that both prompt and delayed activation products should be detectable.

To assess the habitability of the Martian sub-surface, the instrument will also carry out measurements of elements that are required as nutrients (C, N, P and S) and elements such as iron that might serve as energy supplies for organisms that use inorganic compounds for energy (chemolithotrophic organisms). Determining the relative abundances of these elements in the sub-surface is essential for a comprehensive understanding of habitability and how the potential habitability varies with depth.

The bulk density profile constrains the geological interpretation of the local deposits, e.g. fluvial and aeolian activity, volcanism, glaciation and erosion, the depth of loose deposits and bedrock, petrology and possibly sedimentary layering. Constraints on porosity, and thus permeability, are important for assessing the capacity of the sub-surface material for harbouring and transporting volatiles / liquids, atmospheric constituents and perhaps life. Through microstructural modelling and mechanical measurements from the mole, the bulk density constrains a host of other physical and geotechnical parameters. Together with thermal measurements, a 'ground truth' thermal inertia can be determined, both at the surface accessible by orbital measurements, but more importantly at depths greater than those accessible from orbit. Surface heat flow is currently known only for the Earth and rather poorly for the Moon [7, 8].

The principle for heat flow measurements is described in detail by [9, 10] and the thermal conductivity of the regolith, λ, can be calculated via the following expression:

$$\lambda = \kappa \rho c, \qquad (1)$$

where κ is the thermal diffusivity of the regolith, ρ is the bulk density of the regolith and c the heat capacity.

The bulk density profile is important in order to measure the surface heat flow on Mars. The error in heat flow measurements can be reduced by the composition measurement capability of the X-Gamma instrument. This profile will provide an improved measure of the heat capacity of the crust as a function of depth given that the heat capacity is element dependent [10]. Martian thermal evolution models will also be supported by X-Gamma's measurements of the natural radioisotopes.

Once deployed to the maximum possible depth by the mole, the instrument will continue to operate. This allows not only the elemental composition of the surrounding material to be measured very accurately, but also any changes to be monitored. These may arise from the seasonal exchange of atmospheric constituents and volatiles with the sub-surface, an important aspect of Martian astrobiology and meteorology. Fig. 1 shows an example of an X-ray spectrum that would be within the ranges to be used by X-Gamma, indicating the rich array of geochemical information obtainable at every measurement point (every few cm) examined by the instrument on its sub-surface journey. In addition the gamma ray mode will allow detailed evaluation of radioactive nuclei and neutron activation products.

3. THE X-GAMMA INSTRUMENT

3.1. The HP^3 Probe

The current incarnation of the HP^3 instrument is shown in detail in Fig. 2 and 3. In the schematic diagram (Fig. 2) the dimensions of the basic structure are visible in addition to the radioactive source and shielding. The CdTe detectors, supplied by Amptek Inc., USA, are 5 x 5 x 0.75 mm^3 (18.75 mm^3) in size and as shown in Fig. 2 there are 2 detectors for the bulk density measurements.

In Fig. 3 we see the engineering drawing of the final configuration of the breadboard model to be delivered to the European Space Agency later this year.

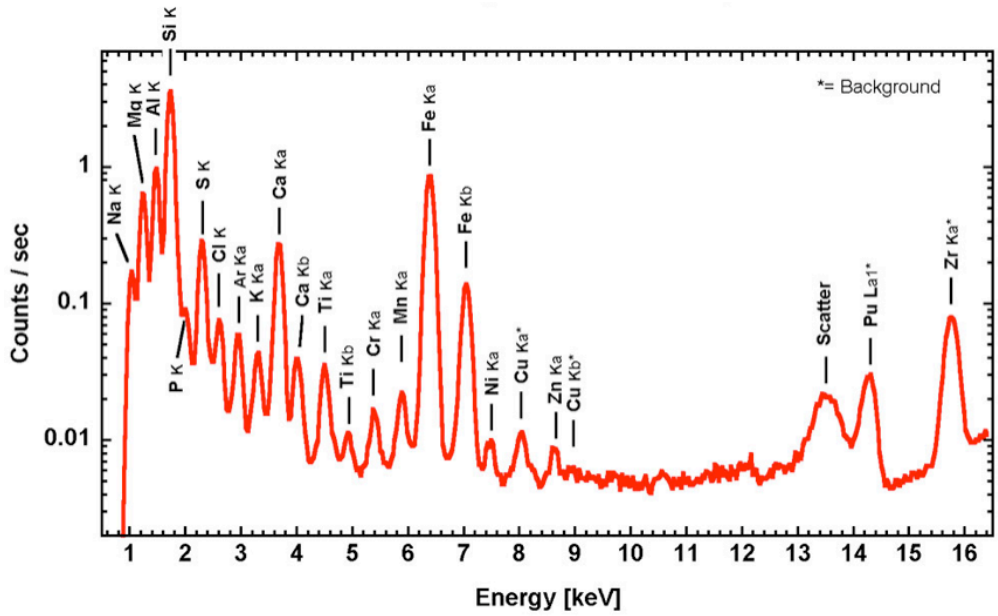

Fig. 1. MER APXS spectrum from Mars [1]. Prominent lines are labelled. Spectral artefacts from the instrument and characteristic elemental lines from the sample are present.

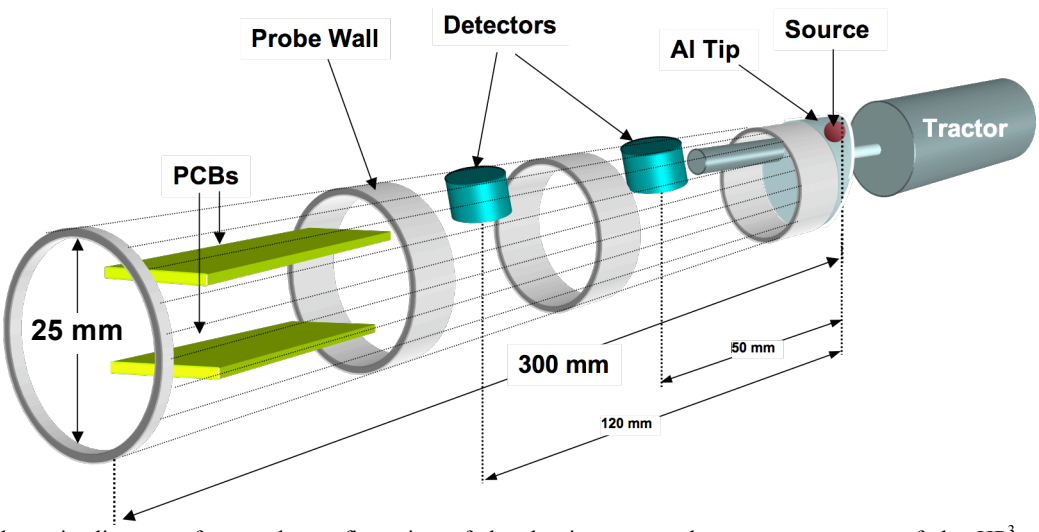

Fig. 2. Schematic diagram of an early configuration of the densitometer and tractor component of the HP^3 mole. This configuration was used in the development of early Monte Carlo models of the mole. Two 18 mm^3 CdTe detectors are visible along with the ^{137}Cs source and tungsten shield.

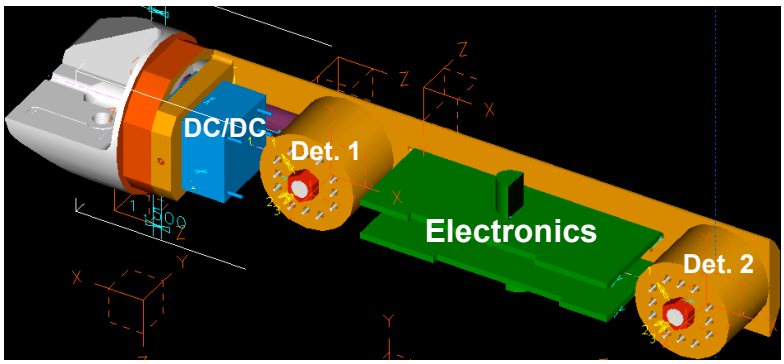

Fig. 3. CAD image of the breadboard configuration for delivery to ESA in 2006, showing (L to R) the tip of the payload compartment housing the source, shielding and DC/DC converter, the first detector, the preamplifier and bias filter boards, and the second detector. The flight model instrument would employ ASICs instead of the boards shown.

The probe tether will be used to facilitate the measurement of the heat flow on the planetary surface. The instrument makes use of the line heat source (LHS) method [9, 11, 12] or the self-heating effect of an internally heated long sensor, which is surrounded by the sample material. The LHS technique is a transient method and records the temperature rise within the sensor as a function of time and heating power per unit length. For the LHS method to work, the length of the sensor has to be greater than 30 times the magnitude of the radius of the sensor [9]. The LHS method works on the assumption that the surrounding medium can be approximated by an isotopic and homogeneous medium in both azimuthal and axial directions.

This tether is a 5 m long multilayer flexible copper and Kapton cable based on cables developed by Oxford University for use on Cassini, Meteosat Second Generation and at CERN. The cable is challenging largely because of the use of high spatial resolution copper tracks over a large area. This experiment consists of resistance thermometers and heaters distributed along the cable and implemented as high resolution etched patterns in the copper tracks. A complete prototype cable including sensors has already been manufactured.

Calibration of the densitometer was carried out at the Open University; this was done by inserting the prototype probe, incorporating the two detectors and the source, in cylindrical standards of varying density. The calibrations standards varied in density from 1 g cm^{-3} to 10 g cm^{-3}. Calibration spectra were recorded (See Fig. 4) and the ratio of the counts in each of the detectors calculated as a function of density. For the bulk density measurements we used the count rate of the continuum in a broad energy window, 250-500 keV, dominated by Compton scattering of the ^{137}Cs source's 662 keV photons in the surrounding material. In Fig. 4 we can see that as the bulk density increases, more photons are scattered into the detectors. This bulk density measurement technique was used in the 1960s and 1970s by the Soviet Union for surface density instruments for use on the Moon, Mars and Venus [13]. This technique is commonly used for terrestrial applications including well logging by the oil and gas industry, albeit with much larger and more massive instruments.

3.2. The Monte Carlo Model

A Monte Carlo model of the current version of the densitometer for HP^3 was developed using MCNPX™. The schematic diagram, Fig. 1, best describes the structure incorporated in the model. The model was used to generate a calibration curve for the densitometer. The calibration curve of count rate in the detectors versus density was compared to the data recorded with the breadboard model. And the results are shown in Fig. 5.

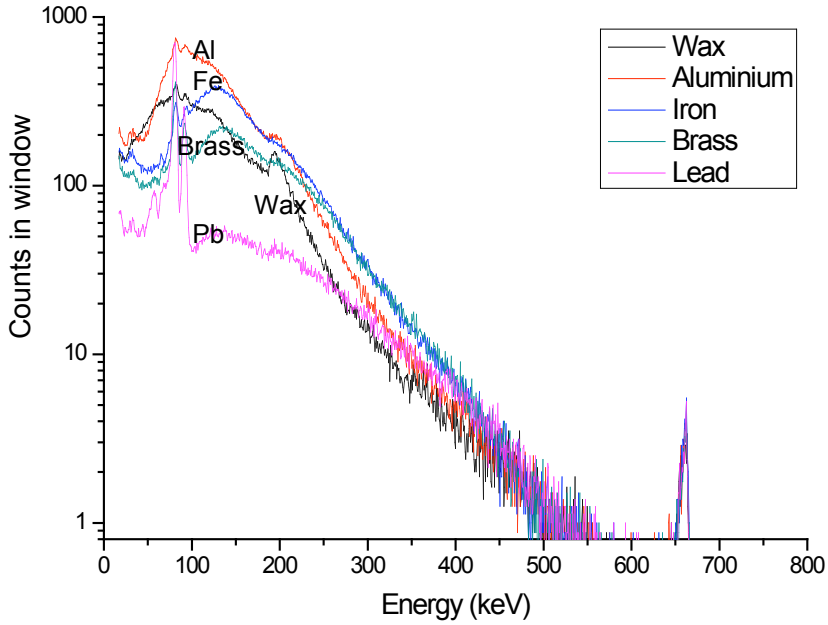

Fig. 4. Spectra obtained using the lab densitometer shown in Fig. 3. The count rate in the range 250-500 keV depends almost entirely on the bulk density of the material, due to the dominance of Compton scattering and the fact that for most elements (except H), A/Z~2. A peak from the 662 keV Cs source and lead fluorescence X-rays are also visible.

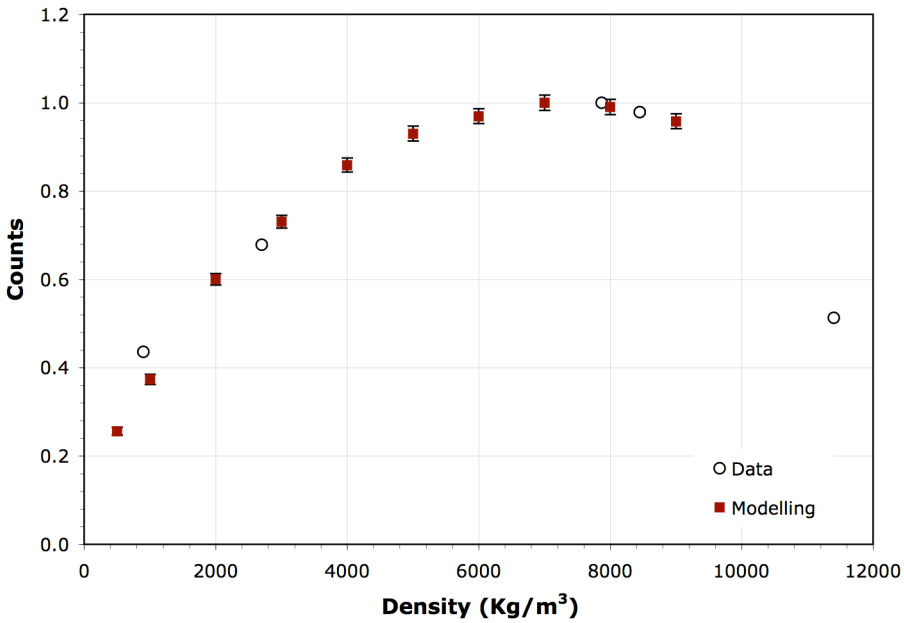

Fig. 5. Calibration graph, showing normalised count rate vs. bulk density. Good agreement is seen between the laboratory data and Monte Carlo model.

3.3. The Hybrid Detector Concept

The enhancements to the second generation HP^3 probe comprise larger volume gamma ray CdTe detectors, one of which will be combined with an X-ray Si detector.

CdTe is known for its high resolution 1% at 662 keV [14] and although a pulse shape processor is required to reduce any charge redistribution [15] there are no stringent cooling requirements with nominal operation at -20 ^{o}C to -30 ^{o}C.

A larger volume will expand the detectable gamma ray energy range beyond the current limit of 1 MeV. Recent experiments at the University of Leicester with a 500 mm^3 CdTe detector, supplied by EURORAD, indicated that we could increase the detection efficiency of our probe sensors to 2.5 MeV. Our aim is to go beyond 10 MeV.

In order to determine the feasibility of achieving some detection efficiency at such high gamma ray energies, we are developing a Monte Carlo model to test the efficiency of CdTe as a function of volume. In the model, a spherical CdTe detector was exposed to a number of discrete gamma ray energies ranging from ^{137}Cs 662 keV gamma rays to prompt activation products from nitrogen above 10 MeV. The initial results are shown in Fig. 6. The energy cut off for the current detectors used in the breadboard HP^3 is around 1 MeV; detection efficiency drops off rapidly at high energies. Increasing the volume to 500 mm^3 and possibly 2000 mm^3 (using 4 x 500 mm^3 units) the efficiency of the detector can be increased to energies above 10 MeV; however a more detailed model needs to be developed coupled with an experimental campaign, which begins later this year. In Fig. 6 we see some of the typical gamma ray energies one would hope to detect with the system.

The densitometer design shown in Fig. 2 could be modified to resemble what is shown in Fig. 7. Placing a large volume detector at the base of the mole and the ^{137}Cs source at the top of the mole should make better use of the mole volume (especially the hollow tip) and possibly allow a reduction in the overall length of the mole to less than 250 mm.

The enhanced X-Gamma system has an additional X-ray detector to facilitate X-ray fluorescence measurements of the regolith as a function of depth. The schematic diagram (Fig. 7) shows the X-ray source, which will stimulate the production of fluorescence X-rays that will greatly constrain the composition of the regolith. The X-ray source should stimulate X-ray emissions ranging in energy from 1 keV to 30 keV in order to detect a broad range of elements. Sources could include ^{55}Fe (5.898 keV), ^{109}Cd (88 keV), ^{241}Am (59 keV, 33 keV, 26 keV) or combinations of two sources. The X-ray transmission windows will be of a suitable material that will maximise the X-ray transmission efficiency at energies above 1 keV, without compromising the integrity of the probe. Materials such as Kapton, Uralene, Teflon, Mylar and polypropylene will be considered for the X-ray window; combinations of materials may be required to best protect the detector.

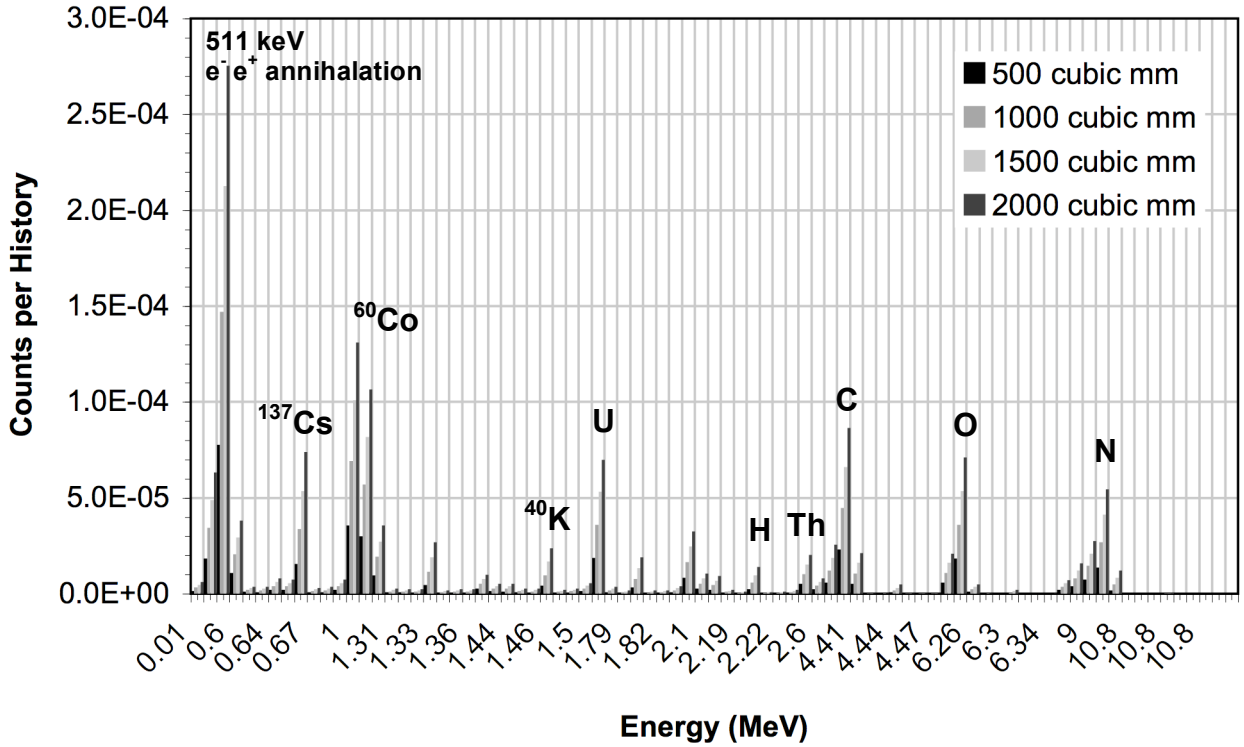

Fig. 6. Preliminary results from the computational model of detection efficiency versus detector volume as a function of energy. Typical gamma ray lines were included in the model to determine the relative increase in detection efficiency as a function of detector volume. The counts were normalised per photon history and the total number of histories was of the order of 4 x10^8 directed at the detector for the various simulations. The energy cut off for the current 18 mm^3 detectors incorporated in the densitometer, part of HP^3, is at 1 MeV.

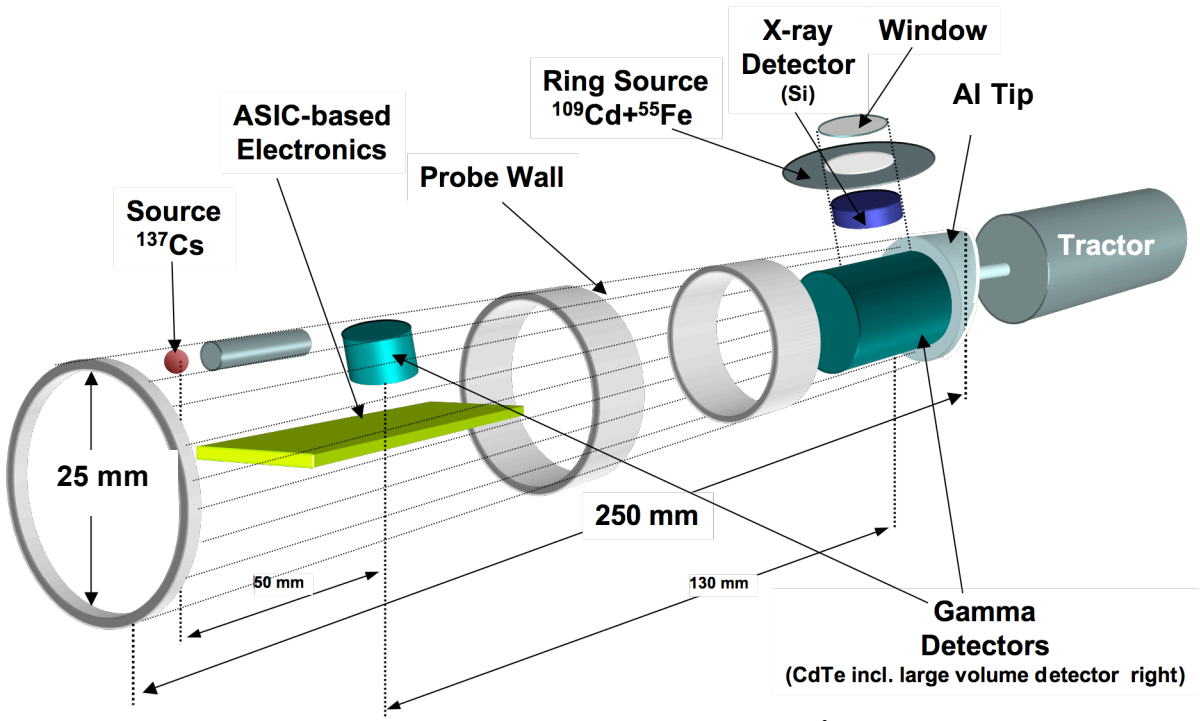

Fig. 7. Schematic diagram of the modified densitometer and tractor component of the HP^3 mole. This is a possible configuration for X-Gamma, with the large volume detector > 500 mm^3 at the base of the mole, hybridised with an X-ray spectrometer. The second gamma ray sensor ~500 mm^3 in size would be at the top of the mole close to the tungsten shield and ^{137}Cs source.

Elemental composition is measured by peak detection in the X-ray fluorescence and gamma spectra, while the bulk density is measured by using the technique described in Section 3.1.

4. CONCLUSION

In this paper we have outlined the current baseline breadboard design for a penetrometer aimed at measuring heat flow through a planetary regolith as a function of penetration depth. The instrument incorporates a densitometer for bulk density measurements using the well established gamma ray backscatter technique. We have proposed an enhancement to the probe in the form of a hybrid X-ray gamma ray detector consisting of a CdTe gamma ray spectrometer and a silicon-based X-ray sensor. This enhancement will enable a broad spectral analysis of the composition of the planetary surface as a function of depth. In addition we have proposed the inclusion of large volume gamma ray sensors in order to broaden the detection efficiency of one of the gamma ray sensors in order to detect gamma rays from the neutron activation of lighter elements such as carbon, oxygen and nitrogen.

A Monte Carlo model was developed to generate a calibration curve for the densitometer, part of HP3, and the results show good agreement with experimental data. In addition a Monte Carlo model is being developed for the case of the large volume detector. Preliminary results indicate that detector efficiency may exceed the required 10 MeV in order to detect gamma rays from light elements (C, O, N) activated by neutrons; however, experimental validation is required.

5. REFERENCES

1. http://marsrovers.jpl.nasa.gov.
2. Lammer H., Lichtenegger H. I. M., Kolb C., Ribas I., Guinan E. F., Abart R. and Bauer S. J., Loss Of Water From Mars: Implications For The Oxidation Of The Soil. *ICARUS,* Vol. 165 (1), 9-25, 2003.
3. Ambrosi R. M., Talboys D. L., Sims M. R., et al. Neutron activation analysis, gamma ray spectrometry and radiation environment monitoring instrument concept: GEORAD. *Nuclear Instruments and Methods A,* Vol. 539 (1-2), 198-216, 2005.
4. Nair A. G. C., Acharya R., Reddy A. V. R., et al. Elemental composition of Jagannath meteorite by neutron activation analysis, *Current Science*, Vol. 87, 654-657, 2004
5. Meyer C., Treiman A. H., Kostiuk T., editors, Planetary Surface Instruments Workshop, LPI Technical Report 95-05, 1995.
6. Clowdsley M. S., Wilson J. W., Kim M.-H. Y., et al. Neutron Environments on the Martian Surface, *Physica Medica*, Vol. 17, Supplement 1, 94-96, 2001.
7. Hagermann A., Planetary Heat Flow Measurements, *Philosophical Transactions of the Royal Society A*, Vol. 363 (1837), 2777-2791, 2005.
8. Spohn T., Ball A. J., Seiferlin K., Conzelmann V., Hagermann A., Kömle N. I. and Kargl G., A Heat Flow and Physical Properties Package for the Surface of Mercury, *Planetary and Space Science*, Vol. 49 (14/15), 1571-1577, 2001.
9. Healy J., de Groot J., Kestin J., The theory of. the transient hot-wire method for measuring thermal. Conductivity, *Physica C*, Vol. 82, 392-408, 1976.
10. Briggs M., Ambrosi R. M., Nelms N., et al. Proposed method to improve the accuracy of thermal conductivity measurements of a planetary regolith. *Nuclear Instruments and Methods A*, Vol. 541 (3), 651-656, 2005.
11. Seiferlin K., Kolme N. I., Kargl G., et al. Line heat-source measurements of the thermal conductivity of porous H2O ice, CO2 ice and mineral powders under space conditions, *Planetary and Space Science*, Vol. 44 (7), 691-704, 1996.
12. F D. Snyder, E. Gier, I. Carmichael, Experimental determination of the thermal conductivity of molten CaMgSi2O6 and the transport of heat through magmas, *Journal of Geophysical Research*, Vol. 99 (B8) 15503-15516, 1994.
13. Surkov Yu. A., Exploration of Terrestrial Planets from Spacecraft: Instrumentation, Investigation, Interpretation. 2nd ed., Wiley-Praxis, Chichester, 1997.
14. Vo D. T., Russo P. A., PC/FRAM plutonium isotopic analysis of CdTe gamma-ray spectra, *Nuclear Instruments and Methods A*, Vol. 486, 813-824, 2002.
15. Perez-Andujar, A., Pibida, L., Performance of CdTe, HPGe and NaI(Tl) detectors for radioactivity measurements, *Applied Radiation Isotopes*, Vol. 60, 41-47, 2004.

PLANETARY POLARIZATION NEPHELOMETSER

Don Banfield, Peter Gierasch, Cornell University, banfield@astro.cornell.edu
Maarten Roos-Serote, Observatorio Astronomico de Lisboa
Daphne Stam, Hester Volten, University of Amsterdam
Olga Munoz, Instituto de Astrofisica de Andalucia, CSIC
Michael Mishchenko, NASA GISS
Rich Dissly, Ball Aerospace and Technologies Corp.

We are developing a polarization nephelometer for use on future planetary descent probes. Significantly exceeding the capabilities of previous planetary nephelometers, it will measure both the scattered intensity and polarization phase functions of the aerosols it encounters descending through an atmosphere. These measurements will be taken at two wavelengths separated by about an octave (e.g., 1μm and 500nm). Adding polarization measurements to the intensity phase functions greatly increases our ability to constrain the size distribution, shape and especially the chemical composition of the sampled particles. The NRC Planetary Sciences Decadal Survey has identified probe missions to Venus and Jupiter as a priority. On both of these missions, our proposed instrument would be an excellent candidate for flight. We also expect that future probe missions to Saturn, Uranus, Neptune and Titan would employ our instrument. It could also find use in Earth and Mars *in situ* aerosol studies.

Atmospheric aerosols are key determinants of the global heat balances and atmospheric circulations on all of the above planets. They are as yet still poorly understood. There is a distinct need for polarization nephelometers on descent probes into these planetary atmospheres. For example, for Venus, we have some detailed knowledge of the cloud layers from remote sensing and also from earlier nephelometers placed in Venus' atmosphere on Russian and American probes. But in spite of this detailed knowledge of the clouds on Venus, there are still significant questions that can be answered with a polarization nephelometer at Venus. It would be crucial in fully quantifying the trace gases in Venus' atmosphere. If a probe only measured the gas phase abundances of sulfur bearing molecules it would exclude roughly 1/3 of the sulfur, which may be in aerosols. Current greenhouse models still leave open debates about the relative importance of various contributors to the observed temperature on Venus. The clouds represent a substantial absorber of solar and thermal energy on Venus, and defining their microphysical properties and vertical structure is critical in fully understanding the mechanisms that control the greenhouse. A prime example is that the upper cloud has a still unknown blue absorber, responsible for about 1/4 of all solar energy absorbed by Venus. Identifying this absorber is a task that our proposed polarizing nephelometer would be ideally suited to. For Jupiter, we know even less about the clouds than for Venus. Remote sensing has revealed significant facts about Jupiter's clouds, but important ambiguities still remain (e.g., West *et al*., 1986). An example of this is that we do not know the vertical structure of the clouds on Jupiter. For instance, the contrast-bearing cloud deck may be composed of either ammonia or ammonium hydrosulfide aerosols. Remote sensing studies have been unable to agree on this point, with visible wavelengths tending to support ammonia clouds bearing the contrast (e.g., Banfield *et al.,* 1998), and near-infrared wavelengths indicating ammonium hydrosulfide (e.g., Irwin *et al.*, 2001). A nephelometer on a Jupiter descent probe, entering a representative region of the planet would easily clarify the vertical structure and specific constituency of Jupiter's clouds.

We are using a technique to simultaneously measure intensity and polarization phase functions via polarization modulation of a light source. A similar technique has been implemented in laboratory settings, but not with considerations to the environment on a planetary descent probe. Using recently awarded NASA PIDDP funding, we are developing and building a flexible breadboard nephelometer to verify our approach and candidate components. This will be tested against well defined aerosols and other simple scatterers ensuring that it accurately measures their expected intensity and polarization phase functions. With the knowledge gained in this flexible design, we will design and build the breadboard polarization nephelometer more suited to integration on a planetary descent probe. All of these investigations are being carried out to enhance the likelihood of success and useful data return of our proposed instrument in its descent through a planetary atmosphere. Considerations are also being given to mass, volume, power and cost.

Rock Sampling using the Ultrasonic/Sonic Driller/Corer (USDC) for In-situ Planetary Exploration

Xiaoqi Bao, Yoseph Bar-Cohen, Zensheu Chang, Stewart Sherrit and Mircea Badescu

Jet Propulsion Laboratory, California Institute of Technology,
4800 Oak Grove Drive, Pasadena, CA 91109-8099[1]

ABSTRACT

Future NASA exploration missions to Mars, Europa, Titan, comets and asteroids are seeking to perform sampling, in-situ analysis and possibly the return of material to Earth for further tests. Existing drilling techniques are limited by the need for large axial forces and holding torques, high power consumption and an inability to efficiently duty cycle. Lightweight robots and rovers have difficulties accommodating these requirements. To address these key challenges to the NASA objective of planetary in-situ rock sampling and analysis, an ultrasonic/sonic driller/corer (USDC) was developed. The actuator of the USDC is an ultrasonic horn transducer that is driven by a piezoelectric stack. Unlike the typical ultrasonic drill where the drill stem is acoustically coupled to the transducer, the horn transducer in the USDC drives a free flying mass (free-mass), which bounces between the horn tip and a drill stem at sonic frequencies. The impacts of the free-mass create stress pulses that propagate to the interface of the stem tip and the rock. The rock fractures when its ultimate strain is exceeded at the rock/bit interface. This novel drilling mechanism has been shown to be more efficient and versatile than conventional ultrasonic drills under a variety of conditions. The low mass of a USDC device and the ability to operate with minimum axial load with near zero holding torque offers an important tool for sample acquisition and in-situ analysis. The details of the design, computer simulation and the test results of the USDC prototypes will be presented.

[1] Correspondence: Email **xbao@jpl.nasa.gov**; web: **http://ndeaa.jpl.nasa.gov**

ARES: an atmospheric electricity instrument proposed for EXOMARS

M. Hamelin, K. Szegö, M. Godefroy, J.J. Berthelier, F. Simões, and the ARES team

The Atmospheric Relaxation and Electric Field sensor (ARES) experiment on the Geophysical and Environmental Package (GEP) of the EXOMARS project is devoted to the investigation of atmospheric electric phenomena. It will measure the ionisation state of the atmosphere, the electric fields that result from various charging mechanisms and investigate the planet global electrical circuit. Atmospheric electrical phenomena are an important issue in dust transport and surface and atmospheric chemistry. Intense electric fields, possibly capable of producing electrical breakdown, are expected at the time of dust storms and in the vicinity of dust devils that could be the source of electromagnetic waves. Electrification processes may also affect a landed vehicle, such as the GEP or the EXOMARS rover, and could be an important issue for their safe and reliable operation and, more generally, for future landed systems in the context of the human exploration of Mars.

The proposed instrument, ARES, is a double probe with two cylindrical electrodes that can be installed on the meteorological mast. It measures the magnitude of the vertical component of the electric field and the potential of the GEP with respect to background from DC to 2 kHz up to ~ 250 V/m which can be increased to ~20 kV/m in dedicated modes of operation. The vertical electric component of electromagnetic waves and the AC fluctuations of the potential of the rover will be measured in the frequency range from 8 Hz to 4 kHz. This channel may also be used to detect the impacts of charged dust particles and infer their fluxes and charge distribution. Operated in the relaxation probe mode, the instrument will also provide a measurement of the atmospheric conductivity separately for positive and negative ions. We present the results obtained in the terrestrial atmosphere with prototypes of ARES on board stratospheric balloons.

METHOD OF CHARACTERIZING AMMONIA OPACITY IN JOVIAN ATMOSPHERES WITH APPLICATION TO ENTRY PROBE RADIO LINKS

T. R. Hanley [(1)] and P. G. Steffes [(2)]

[(1)] *Georgia Institute of Technology, School of ECE, 777 Atlantic Drive, Atlanta, GA 30332, USA, gtg237n@mail.gatech.edu*
[(2)] *Georgia Institute of Technology, School of ECE, 777 Atlantic Drive, Atlanta, GA 30332, USA, ps11@mail.gatech.edu*

ABSTRACT

The link budgets used when designing the communication system on a probe rely heavily on attenuation of the medium through which the radio signals travel. This is especially important in the denser atmospheres of the Jovian planets. Knowledge of the temperature, pressure and concentrations of the various atmospheric constituents all factor into determining the attenuation of a radio signal through a specified path length assuming a thorough understanding of each constituent's microwave absorbing properties. Ammonia is one of the most common and strongest microwave absorbing constituents found in the atmospheres of the Jovian planets, yet discrepancies in its current opacity models require that new experimental data be taken to better constrain its true properties.

1. INTRODUCTION

One of the major surprises of the Galileo Probe Mission to Jupiter was the determination of an ammonia abundance in the deep atmosphere which was 4 times the solar abundance in the 7-16 Bar pressure range. This abundance was retrieved from the signal attenuation measurements on the 1.387 GHz radio link from the entry probe to the Galileo Orbiter during the probe descent [1]. This result was problematic for atmospheric modelers, since earth-based observations of radio emission from the Jovian atmosphere indicated a significantly lower, disk-averaged, deep atmospheric abundance of ammonia, and the ammonia abundance retrieved from the Galileo Entry Probe Net Flux Radiometer (NFR) never exceeded 1.5x solar down to the 4 Bar pressure level with a maximum of 3x solar deeper in the atmosphere [2]. While this disparity could possibly be explained by a localized instability creating the elevated ammonia abundance detected by the entry probe radio link, [2] suggested that it may also be due to inaccuracies in the models for constituent radio opacities used by [1].

The models used by [1] for the opacity of ammonia in the Jovian atmosphere were from [3] and from [4]. While the opacity from ammonia predicted by the two models is consistent (within 5%) when calculated under the deep atmospheric conditions encountered by the Galileo Probe, both models are based on laboratory measurements which were made at significantly higher frequencies and at significantly lower pressures than those for the Galileo Probe radio link. An improved microwave measurement system has been developed at Georgia Tech (similar to that used by [5]) to measure ammonia opacity in a hydrogen and helium atmosphere at wavelengths from 1.1 to 20 cm, pressures from 0.5 to 16 bars and temperatures from 185 to 550 K.

One key problem with all previous measurements of ammonia is the uncertainty in mixing ratio due to adsorption of ammonia gas by the test chambers. At the higher pressures of these measurements, it is necessary to use a metallic pressure vessel to simulate the deeper atmosphere. Ammonia is easily adsorbed onto the metal surface during measurements, which makes knowledge of the measured ammonia concentration difficult, especially at colder temperatures. Our new laboratory system uses a glass Ka-Band Fabry-Perot resonator kept at room temperature (minimizing adsorption) enabling differential measurements of the gas mixtures both before and after admission to the pressure vessel. With this method we have been able to constrain the uncertainty in the ammonia concentration to a maximum of 10% of the stated value and generally less than 5% of the stated value.

This new measurement system will enable development of a more accurate model of ammonia opacity at microwave frequencies that can be used in the design of communications links between planetary probes and orbiters as well as improving the scientific return from Galileo Entry Probe data and future missions.

2. MEASUREMENT THEORY

The method used to measure the microwave absorptivity of a gas is based on the lessening of the quality factor (Q) of a resonance in the presence of a lossy gas. The technique of monitoring the changes of Q of different resonances of a cavity resonator in order to determine the refractive index and the absorption coefficient of an introduced gas or gas mixture (at those resonant frequencies) has been used for over one half of a century. (See, e.g., [6]-[9])

The Q of a resonance is a unitless quantity defined in Eq. 1 by [10] as

$$Q = \frac{2\pi\ f_0 \times \text{Energy Stored}}{\text{Average Power Loss}} \tag{1}$$

where f_0 is the frequency of the resonance and can be measured directly as the frequency divided by its half-power bandwidth (f_0/BW). The opacity or absorptivity (α) of a gas is related to the Q of that gas by

$$\alpha = \frac{\varepsilon''\pi}{\varepsilon'\lambda} = \frac{1}{Q_{\text{gas}}}\frac{\pi}{\lambda}(\text{Nepers/km}) \tag{2}$$

where ε' and ε'' represent the real and imaginary permittivity of the gas and λ is the wavelength in km [10]. The quality factor of a resonator loaded with a test gas can be represented by

$$\frac{1}{Q^m_{\text{loaded}}} = \frac{1}{Q_{\text{gas}}} + \frac{1}{Q_{\text{vac}}} + \frac{1}{Q_{\text{ext1}}} + \frac{1}{Q_{\text{ext2}}} \tag{3}$$

where $Q^{\text{m}}_{\text{loaded}}$ is the measured quality factor of the gas filled resonator, Q_{gas} is the quality factor of the gas itself, Q_{vac} is the quality factor of the evacuated cavity resonator, and Q_{ext1} and Q_{ext2} represent the external coupling losses from the antenna probes in the resonator [10]. Since only symmetric resonators are used, we can assume $Q_{\text{ext1}} = Q_{\text{ext2}}$. The Q_{ext} value can be calculated by measuring the transmissivity of the system, $t=10^{-S/10}$ where S is the insertion loss of the resonator in decibels, and using the relations [10]

$$t = \left[2\frac{Q^{\text{m}}}{Q_{\text{ext}}}\right]^2 \tag{4}$$

$$Q_{\text{ext}} = \frac{2Q^{\text{m}}}{\sqrt{t}} \tag{5}$$

where Q^{m} represents a measured quality factor. Substitution of Eq. 5 into Eq. 3 yields

$$\frac{1}{Q_{\text{gas}}} = \frac{1-\sqrt{t_{\text{loaded}}}}{Q^{\text{m}}_{\text{loaded}}} - \frac{1-\sqrt{t_{\text{vac}}}}{Q^{\text{m}}_{\text{vac}}} \tag{6}$$

with t_{loaded} and t_{vac} representing the transmissivities of the loaded and vacuum measurements respectively. Calculating Q_{gas} in this manner is slightly flawed, however, as this formula does not account for changes in the center frequency of a resonance when a gas is present. If measurements are conducted under relatively benign conditions, (e.g., 270 K - 400 K), it is possible to construct a tunable resonator which can be retuned to the original resonant frequency when the test gas is present. (See, e.g., [7] or [8]) However, under conditions of extreme temperature and pressure it is very hard to construct reliable tunable resonators. If "fixed-tuned" resonators are used, the frequency shift, which accompanies the introduction of the gas under test, changes the coupling of the resonator and consequently the quality factor, even in the absence of opacity. Known as dielectric loading (described in more detail in [3] and [11]), this effect requires an additional measurement to be made with an essentially lossless gas that causes the same frequency shift as that from the test gas. Using this measurement in place of that made under vacuum conditions in Eq. 6, substituting into Eq. 2, and converting from Nepers/km to dB/km (1 Np/km = 2 optical depths/km = 2*10 $\log_{10}$e (≈8.686) dB/km) gives the final formula for calculating absorptivity

$$\alpha = 8.686\frac{\pi}{\lambda}\left(\frac{1-\sqrt{t_{\text{loaded}}}}{Q^{\text{m}}_{\text{loaded}}} - \frac{1-\sqrt{t_{\text{matched}}}}{Q^{\text{m}}_{\text{matched}}}\right)\frac{\text{dB}}{\text{km}} \tag{7}$$

[12].

Measuring the refractivity of a gas is more direct than determining its opacity. Refractivity (N) is calculated as:

$$N = 10^6\,\frac{(f_{\text{vac}} - f_{\text{gas}})}{f_{\text{gas}}} \tag{8}$$

where f_{vac} and f_{gas} represent the center frequencies of a resonance measured with the system under vacuum and filled with the test gas mixture respectively [13]. This represents the refractivity of the entire gas mixture, which is the sum of the constituents' refractivities weighted by their percent concentrations. Refractivity is dependent on pressure and temperature and is often presented in a normalized form to exclude these dependencies. Normalized refractivity is calculated as:

$$N' = \frac{NRT}{P}\left(\frac{N - units \times cm^3}{molecule}\right) \tag{9}$$

where T is the temperature in Kelvin, P is the pressure in atmospheres and $R = 1.362344 \times 10^{-22}$ (atm*cm^3)/(molecule*K).

3. SYSTEM DESCRIPTION

The current system is composed of three major parts described herein:

3.1 Planetary Atmospheric Simulator

The planetary atmospheric simulator controls and monitors temperature and pressure along with handling the gases used. The main component of the atmospheric simulator is a pressure vessel capable of handling pressures from vacuum to 8 atm with a volume of approximately 31 liters. The vessel is cylindrical and made of stainless steel with a detachable top plate sealed by a Viton O-ring and vacuum grease. Gases are fed into the vessel through a series of regulators and valves. The pressure vessel itself is contained in a temperature chamber. For temperatures between 173 K and 218 K, the temperature chamber is a Revco ultra-low temperature freezer. At warmer temperatures between room temperature and 550 K, the vessel is placed in a digitally-controlled electric oven.

The temperature inside the pressure vessel is monitored by an Omega Model HH21 Microprocessor Thermometer connected to a T-type thermocouple probe inserted into a sealed and capped inverted 3/8" outer diameter pipe protruding into the vessel, but not in direct contact with the gases inside. The thermometer has a resolution of a tenth of a degree Celsius and an accuracy of 0.3% ± 0.6º C at temperatures below 0º C and 0.1% ± 0.6º C at temperatures above 0º C. The thermocouple itself has an accuracy of either 0.75% or 1º C, whichever quantity is greater. Positive pressures in the system are measured by an Omega DPG7000 Digital Test Gauge with a resolution of 1 mbar and accuracy of 10 mbar, capable of measuring pressures up to 300 psig, whereas pressures below one atmosphere are measured by a Hastings Model 760 vacuum gauge with a resolution of 1 torr and an accuracy of 1 mbar. A Precision Scientific vacuum pump Model 150 is used to evacuate the gases from the system from 1 bar down to a level of 0.1 mbar. Gases at higher pressures are ventilated through an exhaust valve. The evacuated gas can be sent through a chemical scrubber to remove toxicity as in previous uses with ammonia and phosphine. A combustible gas detector (GasTech model GP-204) can also be used to detect leaks from the pressure vessel when the system contains hydrogen. A glass tube tee capable of withstanding 3 atm of pressure is also connected to the gas handling system for mixture sampling and testing, but is maintained at room temperature.

A PortaSens II gas leak detector is used in the system to measure trace amounts of contaminants that may be left in the system due to lingering adsorption effects. It is attached to a long glass tube chamber that is used for mixing the test gases with air, because the electrochemical sensor module in the PortaSens II requires a minimum of 5% oxygen to operate. The PortaSens II is connected in a feedback configuration with the input sampling from a plastic tube extending to the bottom of the glass chamber and the output into the top of the chamber to maximize the accuracy of its measurement on a mixture of a limited volume.

3.2 Microwave Measurement Subsystem

At the heart of the microwave measurement subsystem are two stainless-steel cylindrical cavity resonators positioned inside the pressure vessel. These resonators have been plated with gold, so as to prevent reactions with corrosive acid vapors that have been measured previously. The larger of the two resonators measures 13.1 cm in radius and stands 25.3 cm tall, thus making it ideal for measurements from 1.5 to 10 GHz. It rests at the bottom of the pressure vessel, whereas the smaller resonator, measuring 2.5 cm in radius and 4.9 cm high, rests on a shelf suspended from the top of the pressure vessel. The small resonator is best used in measurements from 10 to 28 GHz. Each resonator contains two closed-loop antenna probes mounted on their top plates and oriented to maximize the Q or quality factor of TE_{0mn} modes. Both resonators are connected to hermetically-sealed bulkhead feed-throughs on the top plate of the pressure vessel. Each resonator has two horizontal slits on their circular sides near their top plates that act to suppress unwanted TM resonant modes, as well as allowing gases to enter them. The two ports for each resonator are symmetric.

The feed-through ports on the pressure vessel connected internally to the large resonator are also connected via low-loss flexible coaxial cables to a 2-port Agilent E5071B Vector Network Analyzer that operates from 300 kHz to 8.5 GHz. The feed-throughs corresponding to the small resonator have one port connected to an input from an HP 83650B Swept Signal Generator and the other to a high-resolution HP 8564E Spectrum Analyzer both via semi-rigid RG-405 coaxial cable. A ferrite isolator is placed between the signal generator and the small resonator to provide a minimum of 10 dB of isolation for measurements up to 18.5 GHz. At higher frequencies, the cables themselves provide enough isolation from reflected signals due to their attenuation. The spectrum analyzer is set in detector positive peak mode, which displays the maximum power level received during the integration time of each

point. The maximum resolution on the spectrum analyzer is 601 points in both the frequency and amplitude axes whereas the network analyzer offers higher precision up to 1601 points.

The signal generator and spectrum analyzer can also be connected to a Fabry-Perot resonator contained in the glass tube tee that operates at Ka-band from 28 to 40 GHz. The Fabry-Perot resonator is the same used by [14] and consists of two gold-plated mirrors. One mirror is flat and contains two symmetric WR-28 waveguide ports and the other mirror is concave, allowing reflection of signals from one port to the other through path lengths up to 10 meters. The waveguides are connected to waveguide-to-coax SMA adapters, which are connected to high-frequency flexible coaxial cables.

Ideally, a network analyzer that could measure up to 40 GHz would replace the signal generator and spectrum analyzer, but at this time it is too cost prohibitive. This would allow greater accuracy along with shorter measurement times.

3.3 Data Handling Subsystem

The data acquisition subsystem consists of a laptop computer connected to the spectrum analyzer, network analyzer, and swept signal generator via a general purpose interface bus (GPIB) connected to a National Instruments NI-488.2 interface card. The suite of instruments is controlled via Matlab and the Standard Commands for Programmable Instruments (SCPI) language. The primary function of the software is to control the instruments and retrieve resonance data from either the spectrum analyzer or network analyzer in the form of received power as a function of frequency. Each resonance is viewed with the amplitude axis extending 10 dBm and with the frequency axis being approximately twice the half-power bandwidth. This "zooming-in" on each resonance allows the best resolution without spreading the resonance over multiple screen widths. The resolution bandwidth (RB) of the spectrum analyzer is set to the value closest to $1/100^{th}$ of frequency span of a particular resonance under the resonance's broadest condition during the experiment. The value of RB is limited to 1 or 3 times any integer power of ten within the specifications of the device and is kept constant for all measurements of a specific resonance. The software used is similar to the PCSA program created by [15], but with the added flexibility of Matlab and the ability to process the incoming data to directly calculate absorptivity and refractivity.

One problem that arises with the measurements from the spectrum analyzer comes from sweep-on-scan nulls. Due to difficulty in synchronizing the swept signal generator to the spectrum analyzer, the signal generator is set to sweep at a fast pace while the spectrum analyzer is set at a slower rate. The sweep rate for the signal generator is set at 75 ms at which the device can put out a stable power level at all frequencies used. It can be made to sweep as fast as 10ms, but the signal is noisier. At 75 ms per sweep, in order for the spectrum analyzer to always detect the signal, there must be at least 75 ms during each of the 601 frequency measurement bins. The actual time between sweeps is greater than this, however, as the signal generator is not capable of operating at 100% duty cycle, because it takes a finite amount of processing time to begin each sweep. To detect this signal in each frequency bin it would take close to two minutes per sweep! For each resonance measurement it is beneficial to take multiple sweeps to decrease variance, so it is optimal to have shorter, more frequent sweeps and to use the computer to interpolate the value of the null points that are generated when the swept signal is not present during the measurement interval. If we limit the amount of time for each measurement to 200 seconds, the standard deviation of the set of measurements weighted by the statistical confidence coefficient is minimized for 5 sweeps of 40 seconds each. The data from each set of sweeps is saved in a unique file.

To compensate for this apparent loss of resolution, an algorithm is run to "stuff" the data. The algorithm sets the value of each point equal to the average of the ten nearest points (five higher and five lower) if it is less than that average. For the points within five of either end, the average is done on fewer than ten points to avoid the curve being leveled at the edges. This is done until an iteration is reached where the change at every point is less than 0.02%. This accounts for raising all the original null points but does not account for noisy spikes that stand above the data. To compensate for these, the same algorithm is used, except that it only changes points that are greater than the average of the ten nearest points until the change is less than 10%. This method allows for a smoother curve than doing a simple linear interpolation between the high points.

Once the sweeps have been stuffed, the software calculates the center frequency, half-power bandwidth, power level at the peak, asymmetry figure of merit, and Q of each sweep and averages those values. The standard deviation of each measurement becomes its 1σ uncertainty. The half power or 3 dB bandwidth is calculated by interpolating between the data points to give a frequency value that corresponds to exactly 3 dB below the peak power both higher and

lower than the peak frequency. The asymmetry figure of merit is calculated as in [15].

$$af = 100 \times \frac{(f_r - f_c) - (f_c - f_l)}{f_r - f_l}\% \qquad (10)$$

The asymmetry figure of merit is used to determine if any resonances are yielding questionable results. Resonances with asymmetry values greater than 15% generally suggest overlapping of nearby resonances and would likely yield inaccurate results. It is also important to make sure the asymmetry values of both the loaded and matched measurements for a particular resonance data point are consistent within ± 2%, or this may suggest that there is preferential broadening of one side of the resonance over the other. Resonances that do not meet these criteria are not used.

The measurements taken with the network analyzer are much quicker and require less processing. The network analyzer is capable of generating 30 null-free data sweeps each of both transmissive scattering parameters (S12 and S21) along with one sweep each of the reflective scattering parameters (S11 and S22) in one minute at 1601-point resolution with an IF bandwidth of 10 kHz. The primary data used is from S21, but the others are taken to ensure consistency and enable better examination of each resonance. These 62 sweeps are saved to the laptop and then undergo the same processing to calculate the average and standard deviation of the center frequency, half-power bandwidth, power level, asymmetry and Q.

4. COMPLEXITIES WHEN MEASURING AMMONIA

One complication that arises when measuring ammonia or other highly polarized molecules is its strong tendency to adsorb or stick to the surfaces of the metallic test chamber. This makes knowledge of the ammonia concentration in vapor phase during the measurements very difficult. As the ammonia cools, the molecules have less kinetic energy to escape the attraction to the metallic sides of the pressure vessel and resonators and thus bind themselves to the surfaces due to their large dipole moment. These adsorption effects are seen most strongly at colder temperatures that relate to the upper Jovian atmospheres.

In our measurements, we use a certified pre-mixed cylinder of gas containing hydrogen, helium and approximately 1% ammonia. At 188 K after 2 bars of this mixture have been added to the system, the gaseous ammonia concentration can drop to around 0.25%. To add to the complication, as the ammonia adsorbs in the vessel and resonators, the concentration of ammonia begins to vary inside the system. This is due to great differences between the surface area to volume ratios of the large resonator, the small resonator, and the rest of the pressure vessel as can be seen in Table 1.

Table1. Surface areas and volumes for the various regions inside the pressure vessel

	Volume (cm^3)	Surface Area (cm^2)	SA / V Ratio
Small resonator	~ 96	~ 116	~ 1.21
Large resonator	~ 13,600	~ 3160	~ 0.23
Remainder of vessel	~ 18,000	~ 9000	~ 0.50

The greater the surface area to volume ratio, the greater the amount of adsorption that will occur, since there will be more sites for the ammonia molecules to bind and less ammonia molecules in a smaller volume. Since the resonators only have two small slits through which to exchange gases, this means that the gases take a long time to thoroughly mix, especially at colder temperatures. This can be charted by monitoring the values of the Q's of resonances in both resonators until those values stabilize. For the coldest ammonia measurements planned (188 K) this stabilization can take upwards of 15 hours.

The Fabry-Perot resonator attached to the measurement system can be used as a means of comparison and verification of the ammonia mixing ratio. Since this resonator is comprised mostly of glass and is maintained at room temperature, the total amount of ammonia adsorbed is less than 1% of the amount added. By measuring the microwave properties of the mixture at Ka-band before the gas is added to the vessel and comparing them to that of the gas mixture that has been in the vessel, the degree of adsorption can be characterized.

5. MEASUREMENT PROCEDURE

Each experiment is designed to measure a gas mixture of a specified concentration at a constant temperature over a range of pressures and at resonances covering a wide range of frequencies. The first step is to make sure the gas handling system is sufficiently leak-proof. Any major leaks will add to the uncertainty of the experiment and in the case of toxic gases present a health hazard. With the system sealed, each resonance is measured under a vacuum of less than 1 torr. For every measurement, the temperatures and pressures inside the pressure vessel before and after each set of sweeps are recorded, averaged, and saved

along with the sweeps. Next, the test gas is slowly added to the pressure vessel until the desired highest pressure to be measured is reached, also providing for enough gas to fill the Fabry-Perot resonator and to allow for some small leaks, which are inevitable at the coldest measurements. The temperature inside the pressure vessel is monitored and the system is given time to thermally equilibrate and to thoroughly mix. The gas mixture is then allowed to enter the Ka-Band Fabry-Perot resonator. Once the mixture has stabilized throughout the system, measurements of each resonance, including six Ka-Band frequencies, are then executed with the test gas in the resonators. Next, the Ka-Band system is evacuated and purged. The gas in the pressure vessel, if at positive pressure, is then vented off or sent through a scrubber until the next desired pressure is reached. Measurements of all test resonances are again similarly carried out at each desired pressure.

A vacuum is once again drawn in the system and argon is added and vacuumed out numerous times to purge the system of any adsorbed ammonia. The argon that is added is periodically drawn off into the gas sensing chamber and mixed with ambient air. This allows for the connected ammonia gas sensor to detect the amount of ammonia that may still be present in the system. This purging process is continued until the ammonia concentration is less than 30 ppm. This minimizes the amount of contamination in the system for the dielectrically matched measurements. A long vacuum is drawn and the resonances measured once more, along the with straight-through cable transmissivities under the same conditions on the spectrum and network analyzers as the original measurements. This eliminates the variability in measured power that can occur under slightly different frequency and span conditions. Then, the process of dielectric matching is begun. The frequency that each resonance shifted to while the system was loaded with the test gas is calculated and a loss-less gas (argon) is added until each resonance has shifted to that same frequency. This usually requires a slightly different pressure of gas for each resonance. This is done for every resonance at each measured pressure. Lastly, a final vacuum is drawn and the resonances and transmissivities measured one last time.

6. DATA PROCESSING

The data processing begins after an experiment has been completed. Software was created that loads the experimental data, runs the data stuffing algorithm, and calculates the absorptivity and refractivity of the test gas at the measured frequencies, pressures, temperature and mixing ratio. Any major variation in cable transmissivity over the frequency range of a resonance is deconvolved from the measured sweeps. The transmissivity of the cables at the frequency of each resonance under each pressure condition is calculated by averaging the values of the average of each set of sweeps from the transmissivity measurements. This value is subtracted from the peak power measured from the test gas and matching gas and the result is the insertion loss (S). The first and last vacuum measurements are compared to the middle one for consistency, but the values of the middle vacuum measurement are the ones used in Eq. 7 because they are temporally closest to the loaded and matched measurements. Then, by using Eqs. 7 and 9, the absorptivity and normalized refractivity are calculated. These values are compared to current models to determine which models work best at each temperature, pressure, concentration, and frequency.

7. CONCLUSION

Planetary probes can provide a wealth of scientific information with in situ measurements that remote sensing options do not offer. In order for these measurements to be of use, the data taken by a probe must be transmitted either to an orbiting spacecraft or directly back to Earth, most often via UHF or microwave radio frequencies. By better constraining the microwave properties of ammonia in Jovian atmospheres, more efficient probe transceivers can be utilized and greater scientific information can be obtained from past as well as future missions.

The High-Sensitivity Microwave Measurement System described has evolved greatly from its first configurations where the measurement sweeps were read on the spectrum analyzer by eye. The sensitivities have vastly improved in response to a demand for more precise radiative transfer models and with more accurate equipment. The measurement procedure has also become more complicated to allow this greater precision, through an improved understanding of the adsorbing and mixing properties of gaseous ammonia.

There are plans to upgrade the pressure vessel in the near future to be able to withstand 16 atm of pressure. In a few more years, a pressure vessel similar to that described in [7] will be built that is capable of maintaining pressures up to 100 atm. After thorough characterization of ammonia is completed, water vapor will be measured to better constrain its microwave absorptive properties.

This work is supported by the NASA Planetary Atmospheres Program under the Grant NNGO5-GQ87G.

REFERENCES

1. Folkner W.M., et al. Ammonia abundance in Jupiter's atmosphere derived from the attenuation of the Galileo probe's radio signal, *Journal of Geophysical Research (Planets)*, Vol. 103, 22847-22855, 1998.
2. Atreya S.K., et al. A comparison of the atmospheres of Jupiter and Saturn: deep atmospheric composition, cloud structure, vertical mixing, and origin. *Planetary and Space Science*, Vol. 47, 1243-1262, 1999.
3. Spilker T.R., *Laboratory measurements of the microwave absorptivity and refractivity spectra of gas mixtures applicable to giant planet atmospheres*, PhD thesis, Stanford University, 1990.
4. Joiner J. and Steffes P.G., Modeling of Jupiter's millimeter wave emission utilizing laboratory measurements of ammonia (NH3) opacity, *Journal of Geophysical Research (Planets)*, Vol. 96, 17463-17470, 1991.
5. Hoffman J.P., et al. Laboratory measurements of the microwave opacity of phosphine: opacity formalism and application to the atmospheres of the outer planets, *Icarus*, Vol. 152, 172-184, 2001.
6. Bleaney B. and Loubser J.H.N., The inversion spectra of NH3, CH3Cl and CH3Br at high pressures, *Proceedings of the Physical Society, Section A*, Vol. 63, 483-493, 1950.
7. Ho W., et al. Laboratory measurements of microwave absorption in models of the atmosphere of Venus, *Journal of Geophysical Research*, Vol. 71, 5091-5108, 1966.
8. Morris E.C. and Parsons R.W., Microwave absorption by gas mixtures at pressures up to several hundred bars. I. Experimental technique and results, *Australian Journal of Physics*, Vol. 23, 335-349, 1970.
9. Steffes P.G. and Eshleman V.R., Laboratory measurements of the microwave opacity of sulfur dioxide and other cloud-related gases under simulated conditions for the middle atmosphere of Venus, *Icarus*, Vol. 48, 180-187, 1981.
10. Matthaei G. L., et al. *Microwave Filters, Impedance Matching Networks and Coupling Structures.* McGraw-Hill, New York, 1980.
11. Joiner J., *Millimeter-wave spectra of the Jovian planets*, Ph.D. thesis, Georgia Institute of Technology, 1991.
12. DeBoer D.R. and Steffes P.G., Laboratory measurements of the microwave properties of H_2S under simulated Jovian conditions with an application to Neptune, *Icarus*, Vol. 109, 352-366, 1994.
13. Tyler G.L. and Howard H.T., Refractivity of carbon dioxide under simulated Martian conditions, *Radio Science*, Vol. 4, 899-904, 1969.
14. Mohammed P.N. and Steffes P.G., Laboratory measurements of the Ka-band (7.5 to 9.2 mm) opacity of phosphine (PH_3) and ammonia (NH_3) under simulated conditions for the Cassini-Saturn encounter, *Icarus*, Vol. 166, 425-435, 2003.
15. DeBoer D.R. and Steffes P.G., The Georgia Tech high sensitivity microwave measurement system. *Astrophysics and Space Science*, Vol. 236, 111-124, 1996.

MICROSYSTEMS, INSTRUMENT ELECTRONICS, AND MOBILE SENSOR PLATFORMS

G. W. Hunter[(1)], R. S. Okojie[(2)], L. Oberle[(3)], M. Krasowski[(4)], G. M. Beheim[(5)], G. Fralick[(6)], J. Wrbanek[(7)], P. Greenberg[(8)], P. G. Neudeck[(9)], and J. Xu[(10)].

[(1)]NASA Glenn Research Center at Lewis Field, 21000 Brookpark Road, Cleveland, OH 44135, USA, Email: Gary.W.Hunter@nasa.gov
[(2)]Email: Robert.S.Okojie@grc.nasa.gov, [(3)]Email: Lawrence.G.Oberle@nasa.gov,
[(4)]Email:Michael.J.Krasowski@nasa.gov, [(5)]Email: Glenn.M.Beheim@nasa.gov,
[(6)]Email: Gustave.C.Fralick@nasa.gov, [(7)]Email: John.D.Wrbanek@nasa.gov,[(8)]Email: Paul.S.Greenberg@nasa.gov,
[(9)]Email: Neudeck@nasa.gov, [(10)]Email: Jennifer.Xu@nasa.gov

ABSTRACT

NASA Glenn Research Center is presently developing and applying a range of sensor and electronic technologies that can enable future planetary missions. These include space qualified instruments and electronics, high temperature sensors for Venus missions, mobile sensor platforms, and microsystems for detection of a range of chemical species and particulates. A discussion of each technology area and its level of maturity is given.

1. INTRODUCTION

NASA Glenn Research Center (GRC) is presently developing and applying a range of sensor and electronic technologies that, while initially developed for other applications, can enable future planetary missions. NASA GRC has extensive experience in space qualified electronics integrated with instrument systems. This experience ranges from the Material Adherence Experiment (MAE), which flew on the Mars Pathfinder Sojourner in 1996, to the recent Materials International Space Station Experiment 5 (MISSE-5) Forward Technology Solar Cell Experiment. World-leading development in harsh environment sensors and electronics is also on-going and uniquely positioned to contribute to future Venus missions. While the high temperature electronics capability is covered in another paper at this conference [1], this paper discusses in more detail a wide range of Microsystems based sensor technology for in-situ Venus measurement applications. Mobile sensor platforms are also being developed for sensor placement, as well as methods for communicating between roving platforms and a central command location. This work leverages commercially available equipment to miniaturize existing sensor platforms and produce mobile platforms that are compatible for planetary exploration. Finally, a range of Microsystems based sensors have also been developed for applications such as fire detection, leak detection, EVA, and environmental monitoring. These microsystems also have applications in planetary exploration missions.

The purpose of this paper is to describe the various microsystems, instrument electronics, high temperature sensors, and mobile sensor platforms available at NASA GRC and their possible application in planetary exploration applications.

2. SPACE QUALIFIED ELECTRONICS

NASA GRC has extensive experience in space qualified electronics integrated with instrument systems. The focus of this group's activity has been specialized in choosing parts and designing space qualified electronics systems based on commercial-off-the-shelf (COTS) electronics and integrating these systems with a range of instrumentation. These resulting electronics/instrument units are stand-alone systems with appropriate interfaces to be integrated with the rest of the flight system. A standard design feature is the assurance that failure of the instrument unit does not affect operation of other experiments or systems. Other design issues vary with the application, but include minimal power consumption and mass, as well as operation in space radiation environments. The following are examples of these space qualified electronics systems and associated instrumentation whose development and operation span over a decade.

The Material Adherence Experiment (MAE) flew on the Mars Pathfinder Sojourner in 1996 and measured the effects of dust on the rover's solar panel (Fig. 1). MAE, composed both of electronics and a corresponding dust measuring instrument, functioned in the harsh thermal and radiation surface environment on Mars. The sensor saturated early in the mission during a secondary egress

attempt for the rover, but during the mission the electronics continued to operate as required by mission parameters.

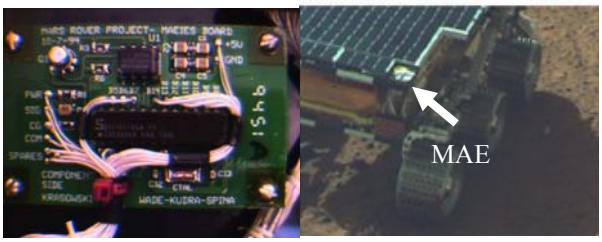

Fig. 1. The MAE circuit board and the location of the MAE on the Pathfinder Sojourner solar panel.

The Mars Array Technology Experiment (MATE) and Dust Accumulation and Removal Technology (DART) experiment were designed and qualified for the 2001 Surveyor Lander Mars In-Situ Propellant Precursor mission (Fig. 2). MATE and DART had an array of instruments for characterizing the solar and dust environment on Mars. This included sun position sensors, two radiometers, a microscope, visible and near infrared spectrometers, and a myriad of dust mitigation experiments. While the mission was cancelled, the MATE and DART design and qualification significantly broadened this group's experience in electronics and instrument design for planetary missions.

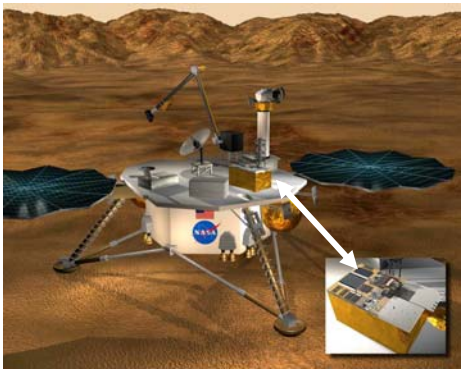

Fig. 2. The location of MATE and DART on the Mars Surveyor Lander

Most recently, this group took the radiation tolerant microprocessor core from MATE and DART and produced the Materials International Space Station Experiment 5 (MISSE-5) Forward Technology Solar Cell Experiment (FTSCE) (Fig. 3). FTSCE is currently operating successfully while mounted external to the International Space Station, exposed to the Low Earth Orbital environment on a nominal one year mission. This system operates autonomously or as directed by ground link from the U.S. Naval Research Labs. Data is archived on-board along with scheduled dumps to Earth receivers. It is designed to last for 2.4 years if its removal EVA is delayed for any reason. FTSCE is comprised of the core electronics board and nine data acquisition boards each displacing 75 cubic centimeters. Each is capable of interrogating numerous sensors and has been successfully sending data to Earth since its insertion on Aug. 3, 2005. Neither data corruption nor interruption of operations has occurred despite high radiation fluence from solar flare activity.

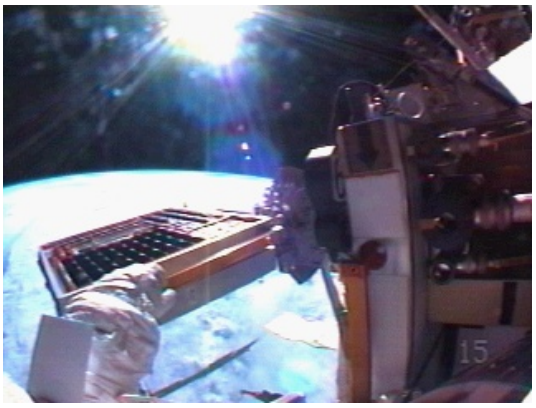

Fig. 3. The FTSCE experiment container being installed on the P6 solar panel strut on the ISS.

These activities demonstrate the capability to provide space qualified electronics capable of interfacing with a wide range of instrumentation. These space qualified electronics have been designed, qualified, and, in some cases, demonstrated operation in environments ranging from in-space to planetary. The need for space qualified electronics is prevalent across all planetary missions and is a prerequisite of a successful operational system. NASA GRC has the capability to provide such electronics for planetary exploration consistently on-schedule and on-budget.

3. HARSH ENVIRONMENT SENSOR TECHNOLOGY DEVELOPMENT

A range of sensor development applicable to Venus missions is on-going at NASA GRC. While related high temperature electronics work and application of sensors and electronics to a Venus Integrated Weather Sensor (VIWS) System is described in another paper in the workshop [1], this paper provides details on the high temperature sensors which can provide measurements in extreme environments. The sensor development includes pressure sensors, thin film sensors, and chemical sensors [2]. Each of these sensor types will be described in the subsections that follow.

3.1 High Temperature SiC Pressure Sensors

Conventional pressure sensors are temperature limited while SiC-based pressure sensors have a much wider temperature range. They also have the added benefit that high temperature SiC electronics can be integrated with the sensor. However, the difficulty of micromachining SiC to form a well-defined diaphragm structure, combined with the lack of reliable device packaging for these operating environments, has largely prevented the application of these devices. Progress has been made at NASA GRC in both SiC pressure sensor micromachining and packaging [3]. A SiC sensor die (2.1 x 2.1 mm^2) is mounted on an aluminum nitride (AlN) header (0.25 in. diameter) by the direct chip attach (DCA) method, as shown in Fig. 4, so that only the sensor's circular diaphragm is free to deflect in and out of the reference cavity. The design significantly limits the effect that stresses in the package can have on the sensor output.

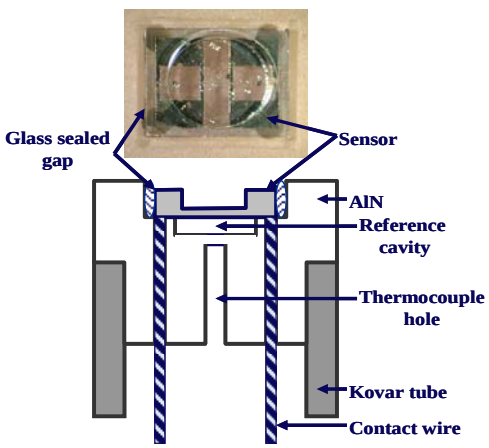

Fig. 4. Top and cross-sectional views of MEMS-DCA package featuring direct wire contact to sensor and thermocouple access hole for temperature compensation and calibration.

Fig. 5 shows the net bridge output and strain sensitivity for a typical SiC pressure sensor as a function of pressure at various temperatures. The data demonstrates the capabilities of the pressure sensor to withstand high temperatures with improved reliability. The sensor has an expanded temperature range beyond what is shown in Fig. 5, up to 600°C [4]. These temperature ranges are more than adequate for Venus applications.

The high temperature operation (600°C) of a SiC pressure sensor and anemometer has been previously demonstrated as separate discrete sensing devices [4]. Ongoing research effort is geared towards integrating three functionalities by the utilization of advanced SiC MEMS Microsystems technology: a pressure sensor, an anemometer, and a fully passivated resistance temperature differential sensor. [5]

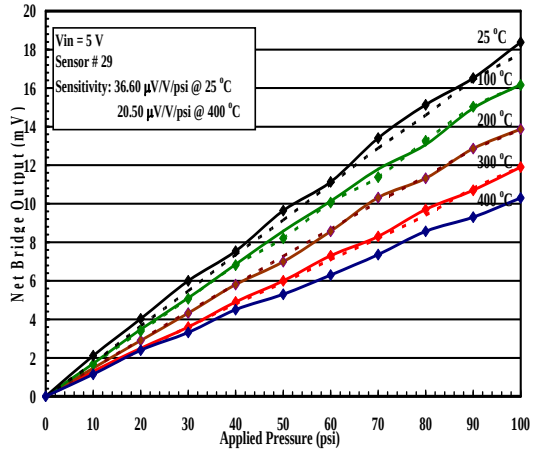

Fig. 5. Net voltage as a function of pressure for various temperatures. Solid and dashed plots represent heating and cooling excursions, respectively.

3.2 Thin Film Physical Sensors

NASA GRC has an in-house effort to develop thin film sensors for surface measurement in propulsion system research. The sensors include those for strain, temperature, heat flux, and surface flow which will enable critical vehicle health monitoring of future space and air vehicles [6,7]. The current challenges of instrumentation technology are to further develop specialized sensor systems, further develop instrumentation techniques on complex surfaces, improve sensor durability, and address needs for higher temperature applications exceeding 1000 °C. The use of sensors made of thin films has several advantages over wire or foil sensors. Thin film sensors do not require special machining of the components on which they are mounted, and with thicknesses less than 10 µm, they are considerably thinner than wire or foils. Thin film sensors are thus much less disturbing to the operating environment, and have a minimal impact on the physical characteristics of the supporting components. A broad array of thin film physical sensor technology is being developed.

One area of development is a patented thin film multifunctional sensor which integrates into one "smart" sensor the designs of individual gauges that measure strain magnitudes and direction, heat flux, surface temperature, flow speed and direction [8,9]. The entire gauge is microfabricated, enclosing a triangular area

approximately 1.5 cm on a side with 50-µm-wide features, and is shown in Fig. 6. Designed for applications in material systems and engine components testing, the sensor can provide minimally intrusive characterization of advanced propulsion materials and components in hostile, high-temperature environments, validation of propulsion system design codes, and experimental verification of computational models. Various prototypes of the gauge have been bench tested on alumina substrates [9]. Future testing will include measuring all of the parameters simultaneously on a component to be tested in an engine environment. Thus, in one sensor system, a range of physical parameters regarding the immediate environment can be measured in Venus relevant environments. Further, this microsensor system can provide information on structural properties of the vehicle in the harsh Venus environment.

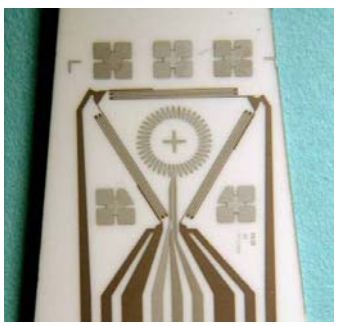

Fig. 6. A thin film multifunctional sensor in the geometry of an off-axis rosette.

3.3 Chemical Sensor Technology

The development of MEMS-based chemical microsensors to measure emissions in harsh environments has been on-going for a considerable time for emission monitoring applications [10]. The development of such a MEMS-based chemical sensors array, or High Temperature Electronic Nose, has begun using high temperature gas sensors being developed for a range of applications [10,11]. There are three very different sensor types that constitute the High Temperature Electronic Nose: resistors, electrochemical cells, and Schottky diodes. Each sensor type provides qualitatively very different types of information on the environment being monitored. This is in contrast to a conventional array of sensors that generally consists of elements of the same type, e.g., tin oxide (SnO_2) resistors doped differently for different selectivities. It is envisioned that the elements of the High Temperature Electronic Nose array (resistors, diodes, and electrochemical cells) will have very different responses to the individual gases in the environment.

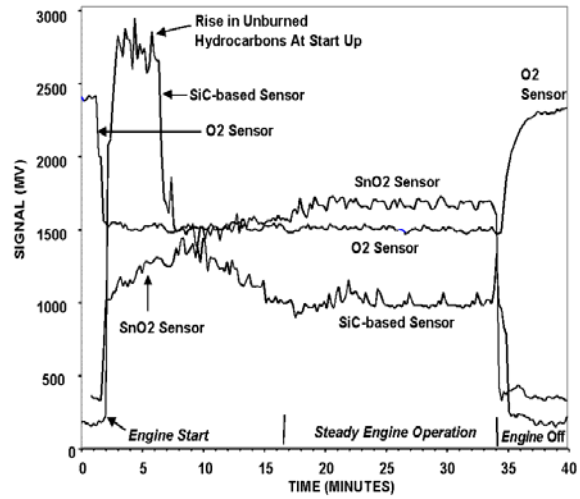

Fig. 7. The response of a sensor array composed of a tin oxide based sensor (doped for NO_x sensitivity), an oxygen sensor, and a SiC-based hydrocarbon sensor in an engine environment.

A first generation High Temperature Electronic Nose has been demonstrated on a modified automotive propulsion system. Fig. 7 shows the response of a nanocrystalline tin oxide based sensor (doped for nitrogen oxide or NO_x sensitivity), an oxygen (O_2) sensor, and a SiC-based hydrocarbon (C_xH_y) sensor. The figure shows the individual sensor responses during the initial start of the propulsion system, a warm-up period, a steady state operation period, and at the engine turn-off. The sensors were operated at 400°C while the engine operating temperature was 337°C. Each sensor has a different characteristic response. The results are qualitatively consistent with what would be expected for this type of engine. They also show the value of using sensors with very different response mechanisms in an electronic nose array: the information provided by each sensor was unique and monitored a different aspect of the engine's chemical behavior.

This data shows the capability to detect multiple chemical species in Venus relevant environments. Higher temperature operation has been achieved for some sensors and other species can be detected. Overall, a potential chemical sensor array can be tailored to measure chemical species specifically relevant for Venus applications.

4. MOBILE SENSOR PLATFORMS

Mobile sensor platforms are also being developed for

sensor placement, as well as methods for communicating between roving platforms and a central command location. This work, begun in the mid 1990's, leverages commercially available equipment to miniaturize existing sensor platforms and produce mobile platforms that are planetary exploration compatible. While initially envisioned for use in engine maintenance, the major thrust of this work was to produce systems of sturdy, simple design meeting a technology gap in methods to move sensors from one location to another. These mobile sensor platforms can be integrated with a range of instrumentation as well as potential alternate modes of locomotion for planetary exploration.

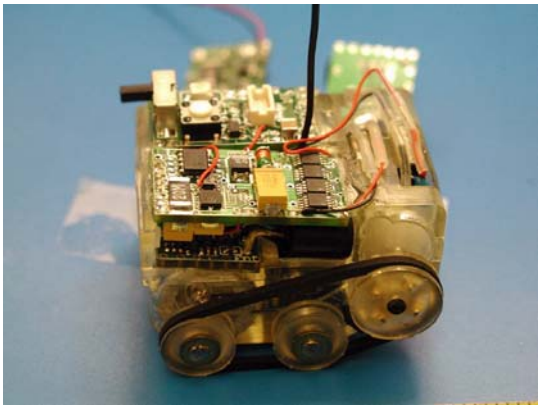

Fig. 8. Miniature Sensor Platform containing RF communications, video camera, and a temperature sensor.

In the nineties, a series of small rover initiatives were executed under aeronautics funding to look into the practicality of performing robotic inspection within airframe structures such as engines and fuel tanks. During these efforts, the technological hurdles overcome were the miniaturization of the platforms along with the embedment of sensors and communications. A sensor platform, as seen in Fig. 8, which carried two way RF communications, a video camera, and a temperature sensor and displaced less than 60 cubic centimeters was fabricated.

More recently, the Optical Instrumentation and NDE Branch at NASA GRC has been collaborating with academia to pursue other mobile sensor platform activities. A proposal under ROSES 05 titled Terrestrial and Extraterrestrial Astrobiology Science and Engineering Research Vehicles for Remote Sensing (TEA SERVERS): Advanced Mobile Sensor Platforms For Astrobiolology was submitted with Case Western Reserve University researchers and Dr. Penelope Boston of New Mexico Tech. Within this proposal, a biologically inspired walking robot named a Whegs, modeled after the common cockroach, was proposed in combination with a planetary instrumentation exploration suite (Fig. 9). It is envisioned that groups of these simple sensor platforms investigating an area of interest to scientists could add breadth of coverage to complement the activities of a larger, more heavily instrumented single large rover leading the group.

Fig. 9. Whegs Vehicle operating in uneven terrain using the locomotion approach of a cockroach (picture courtesy of Case Western Reserve University).

Fig. 10: NASA GRC Sensor Platform "Mule" for demonstrating technologies on the CMU Highlander.

Fig. 11. CMU Highlander Rover operation in simulated Lunar environments.

Most recently, a tracked "mule" or test robot (shown in Fig. 10) has been fabricated to develop and verify instrumentation, sensors, communications and control algorithms for the Carnegie Mellon University (CMU) Robotics Institute's Highlander Lunar Rover Initiative. The Highlander Lunar Rover system, shown in Fig. 11, has a range of subsystems whose operation and maturity need to be verified before operational deployment. To date, a Sterling Radioisotope Generator simulator for prototyping has been provided to CMU by GRC. Also, the Highlander is currently using GRC designed and built control and communications electronics which reside between the Highlander main CPU and the various actuators. NASA GRC has also provided the RF communications, onboard communications, the inertial measurement unit, and tilt and power monitoring sensors for the robot. The interface and control software was also developed by NASA GRC.

5. MICROSENSOR SYSTEMS

A range of Microsystems based chemical sensors have also been developed for applications such as fire detection, leak detection, EVA, and environmental monitoring. These microsensors have been demonstrated on a range of aerospace applications. This technology utilizes basic microsensor platforms that can be modified as needed for a given application. A range of gases of general planetary exploration interest can be measured including methane, ammonia, carbon dioxide, oxygen, and hydrogen.

This development also includes a "Lick and Stick" sensor package featuring sensors, power, signal conditioning, and telemetry on a near postage stamp size unit. The objective in the leak detection project is to produce a microsensor array, which includes hydrogen (H_2), O_2, and C_xH_y [10]. Thus, a range of potential launch vehicle fuels (hydrogen or hydrocarbons) and oxygen can be measured simultaneously. The array is being incorporated with signal conditioning electronics, power, data storage, and telemetry. The final system is envisioned to be self-contained with the surface area comparable to a postage stamp. Thus, this postage stamp sized "Lick and Stick" type gas sensor technology can enable a matrix of leak detection sensors placed throughout a region with minimal size and weight as well as with no power consumption from the vehicle. Sensor outputs are fed to a data processing station, enabling realtime visual images of leaks, and enhancing vehicle safety.

A prototype model of the "Lick and Stick" sensor system has been fabricated and is shown in Fig. 12 [12]. The complete system has signal conditioning electronics, power, data storage, and telemetry with hydrogen, hydrocarbon, and oxygen sensors. Fig. 13 shows the operation of the electronics plus the three sensor system simultaneously. In particular, the data highlights the response of a SiC-based hydrocarbon sensor at various hydrocarbon fuel (RP-1) concentrations. The oxygen concentration is held constant and the hydrogen sensor signal shows no response, suggesting a lack of cross-sensitivity between the hydrogen and hydrocarbon sensors to the detection of this hydrocarbon.

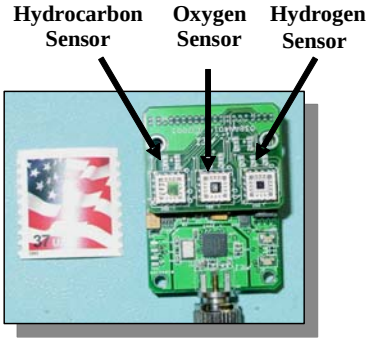

Fig. 12. A prototype version of a "Lick and Stick" leak sensor system with hydrogen, hydrocarbon, and oxygen detection capabilities combined with supporting electronics including signal conditioning and telemetry.

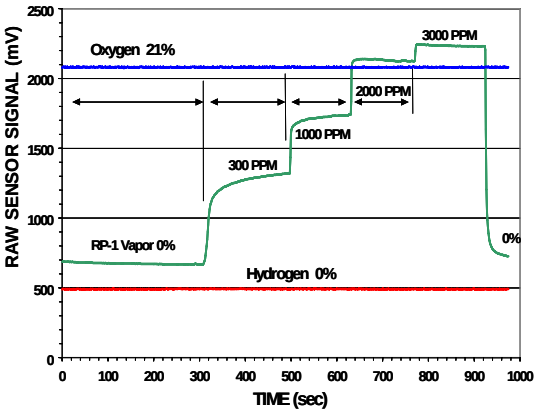

Fig. 13. Response of the three sensors of the leak sensor system to a constant oxygen environment and varying hydrocarbon (RP-1) concentrations. The sensor signal shown is the output from the signal conditioning electronics which processes the measured sensor current at a constant voltage.

Also being developed is a microfabricated particle classifier. The combination of a range of chemical species measurements with particle classification is a significant potential tool to broadly characterize a planetary sur-

face. The approach adopted here for the measurement of particle size distributions, number density, and ambient charge state is that of ion or electrical mobility classification (IMC or EMC) [13]. The EMC process exploits differences in individual particle mobilities to perform either spatial or temporal classification. One objective of the sensor development work is the fabrication of microscale particulate detectors and classifiers [14].

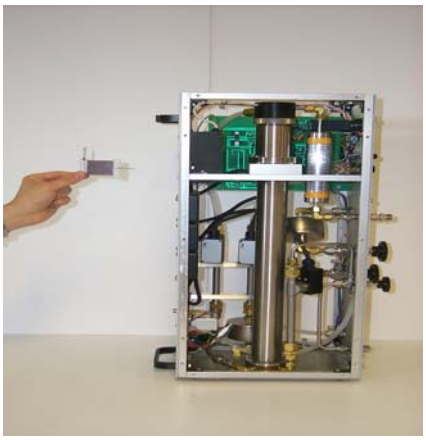

Figure 14. MEMS particulate classifier contrasted with traditional macroscale device.

A prototype MEMS particulate sensor is shown in Fig. 14. For comparison, this device is contrasted with the conventional macroscale device which it replaces. This sensor is in the form of a wafer stack, wherein the active channel is composed of a pair of silicon substrates separated by a dielectric spacer. All features of this device are fabricated using conventional thin film lithography and deposition techniques, combined with relatively standard MEMS wafer etching and micromachining methods. The combined approach of microchemical sensors and microparticulate detectors has been applied to cargo bay fire detection applications with the resulting system demonstration yielding a significantly decreased false fire alarm rate and a highly increased confidence in the measurement.

The application of these microsystems for planetary exploration would enable a broad-based instrument for understanding planetary environments and enabling the detection of the chemical signatures of life. Measuring chemical constituents of a sample should be done with as broad a simultaneous identification of as many species as feasible. The microsystem technology above provides a range of tools, from multiple chemical species to particulate analysis, to understand the planetary environment. Further, these tools are provided using Microsystems technology which minimizes size, weight, and power consumption.

6. SUMMARY AND POSSIBLE PLANETARY APPLICATIONS

This paper has presented a range of technologies which can enable planetary missions. This includes the electronics to process data and operate instruments, micro chemical and particulate sensors to measure multiple facets of the planetary environment, and mobile sensor platforms to move the electronics and sensors around a planetary environment. Harsh environment sensor technology will enable Venus missions and also monitor vehicle component conditions such as those of an engine.

A common thread associated with this electronics and instrumentation development is the enabling of small, smart, rugged, and mobile systems. Measurements at one location are likely not enough to be able to make conclusions regarding the presence of life. While it may occur that everything one needs to measure can be found at, for example, the lander's location, measurements at a variety of locations are more likely to provide a larger picture of planetary conditions as well as increase the probability of taking a measurement indicative of life. Such activities may be hampered by large, power consumptive systems.

Thus, there is a strong need for low power devices which can be mobile and provide substantial characterization of the planetary environment where and when needed. The sensors, electronics, and mobile platforms described here are uniquely capable of low power operation in relevant environments. While a given mission will require tailoring of the technology for the application, basic tools which can enable new planetary missions are being developed.

7. ACKNOWLEDGEMENTS

We gratefully acknowledge the contributions of those whose made this review paper and its contents possible: Dr. L. Matus, Dr. M. Zeller, and E. Benavage of NASA GRC, C. Blaha, J. Gonzalez, D. Androjna, M. Artale, B. Osborn, P. Lampard, K. Laster, M. Mrdenovich of Sierra Lobo/NASA GRC, A. Trunek and D. Spry of OAI, Carl W. Chang and D. Lukco of QSS, A. Powell of SEST/NASA, E. Savrun of Sienna Technologies, Inc., C.C. Liu and R. Quinn of Case Western Reserve University, D. Makel and B. Ward of Makel Engineering, Inc., P. Dutta and B. Patton of the Ohio State Univer-

sity, Dr. Penelope Boston of New Mexico Tech., R. Whitaker of Carnegie Mellon University.

8. REFERENCES

1. Hunter G.W., Neudeck P. G., Okojie R. S., Beheim G. M., Ponchak G, Chen L.Y., High Temperature Electronics, Communications, And Supporting Technologies For Venus Missions, Fourth Annual International Planetary Probe Workshop, Pasadena, CA, June 27-30, 2006.
2. Hunter G.W., Wrbanek J. D., Okojie R. S., Neudeck P. G., Fralick G. C., Chen L.Y., Xu J., and Beheim G. M., Development and application of high temperature sensors and electronics for propulsion applications, accepted for publication for the Proceedings of the SPIE Defense and Security Symposium, 2006 Sensors for Propulsion Measurement Applications Workshop, 2006.
3. Okojie R. S., Savrun E., Nguyen P., Nguyen V., Blaha C., Reliability Evaluation of Direct Chip Attached Silicon Carbide Pressure Transducers, *3rd IEEE International Conference on Sensors*, Vienna, Austria, October 24-27, 2004.
4. Okojie R. S., Beheim G. M., Saad G. J., and Savrun E., Characteristics of Hermetic 6H-SiC Pressure Sensor at 600 C, AIAA Space 2001 Conference and Exposition, AIAA Paper No. 2001-4652, Albuquerque, NM, August 28-30, 2001.
5. Okojie R. S., Fralick G. C., Saad G. J., Blaha C. A., Adamczyk J. J., and Feiereisen J. M., A Single Crystal SiC Plug-and-Play High Temperature Drag Force Transducer, *Digest of Technical Papers for Transducers '03*, IEEE Catalog Number 03TH8664C, p 400-403, The 12th International Conference on Solid State Sensors, Actuators and Microsystems, Boston, MA June 8-12, 2003.
6. Lei J. F., Martin L. C., Will H. A., Advances in Thin Film Sensor Technologies for Engine Applications, NASA TM–107418, Turbo Expo '97, Orlando, FL, June 2-5, 1997.
7. Martin L. C., Wrbanek J. D., and Fralick G. C., Thin Film Sensors for Surface Measurements, NASA/TM—2001-211149, September 2001.
8. Lei J. F., Fralick G. C., and Krasowski M. J., Microfabricated Multifunction Strain-Temperature Gauge, US Patent 5,979,243, November 9, 1999.
9. Wrbanek J.D., Fralick G. C., Martin L. C., Blaha C.A., A Thin Film Multifunction Sensor for Harsh Environments, NASA TM-2001-211075, AIAA–2001–3315, July 2001.
10. Hunter G. W., Liu C. C., Makel D., *MEMS Handbook*, CRC Press LLC, ed. M. Gad-el-Hak, Boca Raton, Florida, Ch. 22, 2001.
11. Hunter G. W., Neudeck P. G., Fralick G., Makel D., Liu C.C., Ward B., Wu Q. H., Thomas V., Hall G., Microfabricated Chemical Sensors For Space Health Monitoring Applications, AIAA 2001-4689, 2001.
12. Hunter G. W., Neudeck P. G., Xu J., Lukco D., Trunek A., Artale M., Lampard P., Androjna D., Makel D., Ward B., and Liu C. C., Development of SiC-based Gas Sensors for Aerospace Applications, *Mat. Res. Soc. Symp. Proc.*, Vol. 815, J.4.4.1-J.4.4.12, 2004.
13. Pui, D. Y. H., Direct-Reading Instruments for Workplace Aerosol Measurements, *Analyst*, Vol. 121, 1215-1224, 1996.
14. Chen, D. and Pui, D. Y. H., A High Efficiency, High Throughput Unipolar Aerosol Charger for Nanoparticles, *Journal Nanoparticle Research*, Vol. 1, 115-126, 1999.

A SMALL STUDENT-DESIGNED DESCENT PROBE

Cy Klein [(1)], Austin Howard[(2)], Jessica Malecha[(3)], Michelle Kalman[(4)], Byron Wong[(5)]

[(1)] College of Engineering, University of Idaho, Current Address: 505 S. Euclid Ave. Sandpoint, ID 83864, USA Email: cyklein@uidaho.edu)

[(2)] College of Engineering, University of Idaho, Current Address:123 ¼ Asbury St. Moscow, ID 83843, USA Email: austiey@gmail.com

[(3)] College of Engineering, University of Idaho, Current Address: 18125 Misty Falls Circle Eagle River, AK 99577, USA Email: male1738@uidaho.edu

[(4)] College of Engineering, University of Idaho, Current Address: 3580 Rialto Heights, APT 365 Colorado Springs, CO 80907, USA Email: michellek@idahovandals.com

(5) College of Engineering, University of Idaho, Current Address: 2688 E Red Cedar Ln Apt H102 Boise, ID 83716, USA Email: wong3972@uidaho.edu

ABSTRACT

The student-designed Venus descent probe team (V-Team) comprises two mechanical and three electrical engineering students. The team designed an aerodynamically stable instrumented descent probe that maintains structural, aerodynamic, and thermal integrity through release, descent, and landing. The probe is designed to freefall for a predetermined period of time before autonomously deploying a parachute for a survivable landing. The goal of the project is to demonstrate that a small, light weight, low cost instrumented descent probe designed to collect useful atmospheric data can be built with off the shelf components.

1.0 INTRODUCTION

1.1 Background

The Venus Instrumented Descent Probe is a University of Idaho senior design project sponsored by the NASA Ames Research Center in collaboration with the Idaho RISE (Research Involving Student Engineers and Educators) program. NASA Ames is one of the nation's premiere research centers. Its purpose is to conduct the fundamental research and technology development that make NASA missions possible. The client representing NASA Ames is Dr. Tony Colaprete. The Idaho RISE program is funded by the Idaho Space Grant Consortium (ISGC). The goal of Idaho RISE is to develop the capability to design, build, test, fly, and recover high altitude science and engineering instrumentation. The faculty advisor for this project is Dr. David H. Atkinson. NASA Ames and the Idaho Space Grant Consortium sponsored the NASA V-Team senior design group to design and implement the instrumented descent probe.

1.2 Objective

The NASA V-Team proposed to design a balanced and aerodynamically stable instrumented descent probe that would maintain structural, aerodynamic, and thermal integrity and survive impact upon landing. The NASA V-Team designed, built, tested, and implemented a data acquisition and data storage system. The acceleration data collected was used to illustrate the ability to derive temperature and pressure profiles.

1.3 Flight Procedure

The probe was designed to follow a pre-determined flight path. The flight begins with the launch of the balloon which carries the probe to 85,000 ft. At this altitude a microcontroller triggers a release mechanism to detach the probe from the balloon. Once the release mechanism is triggered data acquisition begins. All data is stored onboard and transmitted to ground in real time. The probe then free-falls for a specified period of time (≈ 120 seconds) before the microcontroller triggers parachute deployment. After parachute deployment, the probe continues data acquisition while descending to ground. The flight procedure is illustrated in Fig. 1.

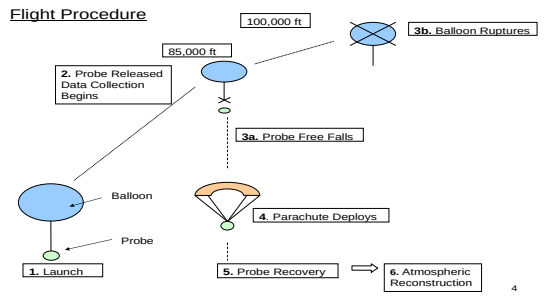

Fig. 1: Flight Procedure

2.0 PROBLEM DEFINITION

2.1 Client Needs

The client needs are highlighted in the list below:

- Perform atmospheric reconstruction using the acceleration data to obtain pressure and temperature profiles of the atmosphere.
- Use pressure and temperature sensors to compare and validate the pressure and temperature profiles derived from the acceleration data results.
- Include a telemetry system that transmits data from the probe to the ground.
- Write a detailed report containing an evaluation of the final product as well as results from the data reconstruction.
- Work within a budget of $2000.

2.2 Specifications
Tables 1 and 2 portray the project specifications for the NASA V-Team.

Table 1: Summary of Mechanical Specifications

Mechanical Specifications
Survive expected impact (velocity approximately 5m/s)
Aerodynamically stable (Pitch\Roll < 10º) for free fall descent
Reliable parachute deployment system (95% reliability)
Operate in low pressure (est. 21.3 mb at 26 km)
Operate in low temperature (-55ºC)
Position pressure and temp. sensors outside boundary layer
Minimize mass and size
Maximize free fall-time (≈ 120 sec minimum)

Table 2: Summary of Electrical Specifications

Electrical Specifications
Record 3-axis acceleration, probe orientation, temperature and pressure
Store sensor data onboard
Transmit sensor and GPS data to ground in real-time
Minimum sampling rate of 10Hz
Report position during flight derived from GPS (for tracking and recovery)
Detach probe from balloon at predetermined altitude (85,000ft)
Deploy parachute after free-fall

3.0 PRODUCT DESCRIPTION

3.1 Electrical

The electrical system features a single microcontroller. Fifteen of the ADC inputs of the microcontroller were used to input data from the instruments. The sensors package consisted of four accelerometers (1-3 axis, 1-2 axis, and 2-1 axis which yields seven measurements), three temperature sensors, two pressure sensors, and three gyroscopes. The microcontroller initiates analog-to-digital conversion of the sensor inputs every tenth of a second (10Hz). When analog-to-digital conversion is performed once for each of the 16 analog channels, a data packet of 32 bytes is formed. The first ADC channel is not used, so one data packet contains 30 bytes of useful sensor data. This data packet is transmitted through telemetry at 10Hz. The GPS data string received by the microcontroller is parsed to transmit altitude, latitude and longitude through the telemetry system at 1Hz. The data packet resulting from the analog-to-digital conversion is combined with the current altitude received from the GPS and saved in the external memory at 10Hz.

An additional GPS tracking unit was included in the final design to decrease the risk of losing the probe. The additional tracking unit is independent of the rest of the electrical system.

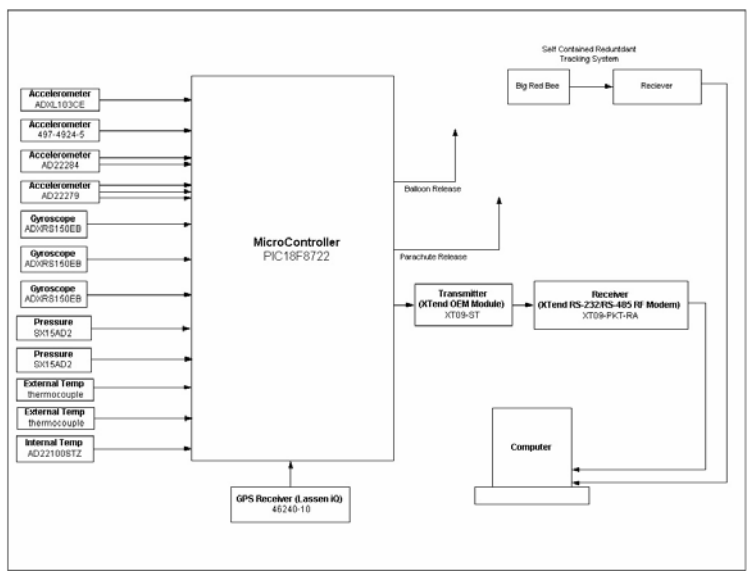

Fig. 2: Final Electrical Design

3.2 Mechanical

Following a prioritization and tradeoff study, the selected mechanical design comprises a spherical

geometry made from a plastic shell. The release mechanism consists of a nichrome wire heating element that burned through the cord(s) suspending the probe underneath the balloon. The parachute deployment mechanism consists of a mortar tube that upon triggering uses a controlled explosion to eject the parachute from the probe. The parachute design has a parachute with stability hole in the center for increased stability during descent. The pressure and temperature sensor arms are oriented in a cross pattern.

During the ordering and fabrication of the mechanical design, several problems and challenges with the selected design surfaced. These problems included the selection of a specific plastic material, the capability to machine the sphere shape, the mortar design, the parachute design, the orientation of the sensor arms, and the stability of the probe. These challenges are further outlined below.

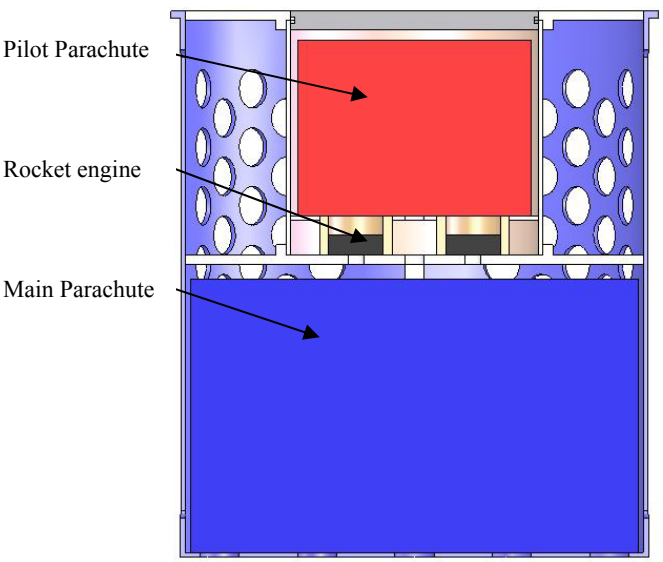

Fig. 3: Parachute Compartments

The first design decision the team faced was the selection of a probe material. After research, polycarbonate was selected. This material was a good choice because of its outstanding material properties for our application, including a high strength vs. weight ratio and a high fracture resistance.

Once we had selected a material for the shell, our team began to order parts. Our first focus was on the shell of the probe and it was soon determined that the University of Idaho machine shop was not capable of machining the desired sphere shape. The diameter of the shell was too big for the machine shop lathe. Also, if the shell was shaped from a large block of material then a large amount of waste would be produced. The team then began to look for available shells on the market that were injection blow molded. A 30 cm diameter prefabricated polycarbonate injection blow molded shell was selected for the probe body.

The next design change arose during the fabrication and testing process and required a modification in the parachute deployment system. The original design called for the parachute to be deployed by a large single mortar. However, after preliminary calculations and modeling it was clear that the size of explosion required to deploy the large (0.5 kg) parachute was not feasible for this project. The team then decided to use a smaller explosion to deploy a pilot parachute which would in turn deploy the main parachute. Standard model rocket engines were selected to deploy the pilot parachute and the rocket engines were modified to reduce the size of the blast. Also, even though one engine was sufficient, the new design called for two engines to deploy one pilot parachute for redundancy (Fig. 3).

Another necessary change was the parachute design. Originally, our design called for a round parachute with a hole in the center for added stability. However, the RISE class had a history of purchasing parachutes from a supplier that employed an alternative design shown in Fig. 4. This design is known for its stability and was a good choice for our team. [1]

Fig. 4: Parachute design

The next design change that the team made was to the shape of the sensor arms. Originally, the sensor arms were designed to place sensors outside of the boundary layer of air that surrounds the capsule during free fall. However, the dimensions that the arms needed to be were not known and the original design did not account for the velocity effects of air on the sensors. A new design was developed to eliminate the velocity effects and was molded after a standard pitot tube. This design is shown below in Fig. 5.

Fig. 5: Pitot tube

Once the fabrication process began it was determined that time constraints and lack of expertise prohibited the parts from being built as designed. Therefore, standard pitot tubes were purchased from a supplier. [2]

The final problem that arose in our project was the stability of the probe. To increase the stability and lower the center of mass we added a 0.5 kg lead weight to the probe and placed a battery pack (0.23 kg) at the bottom of the probe. These additions lowered the center of mass to the proximity of the sensor package (Fig. 6). Because a larger distance between the center of pressure and center of mass is desired to increase the stability of the probe we decided to add fins to the design. The idea was that the addition of fins would raise the center of pressure and further increase the stability of the probe.

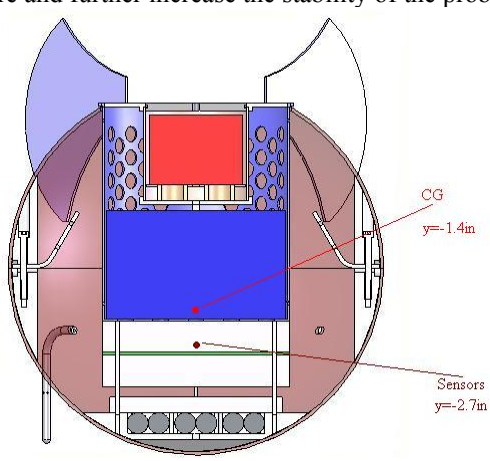

Fig. 6: Fins and Center of Mass

The finished probe design is shown in Figures 7 and 8. Several key features of the probe are: the shell, the parachute compartment, the pilot parachute compartment, the fins, the pitot tubes, the battery compartment, and the lead weight. More detailed pictures and explanation of the fabrication process of each part can be found on the V-Team website [3].

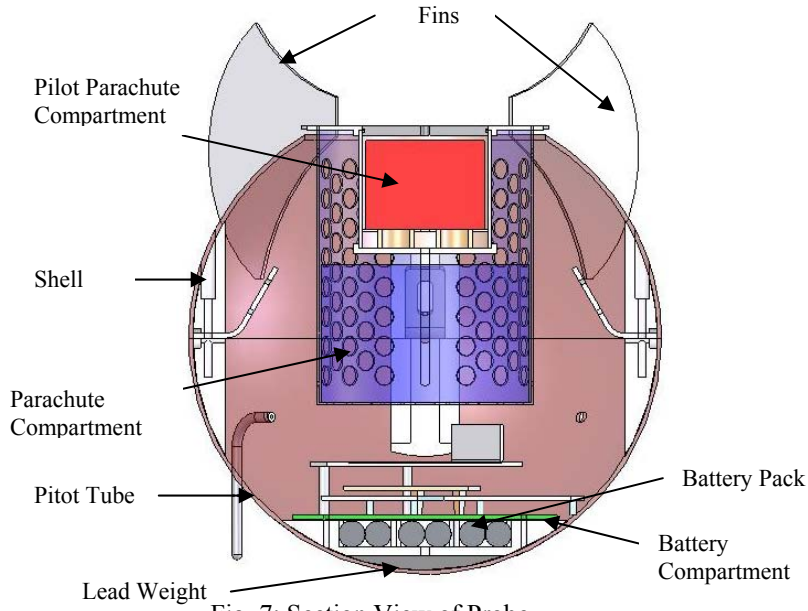

Fig. 7: Section View of Probe

The resulting probe is shown in Figure 8 and the finished electric equipment is shown in Figure 9. Additional pictures of the probe and testing processes can be accessed on the team's website. [3]

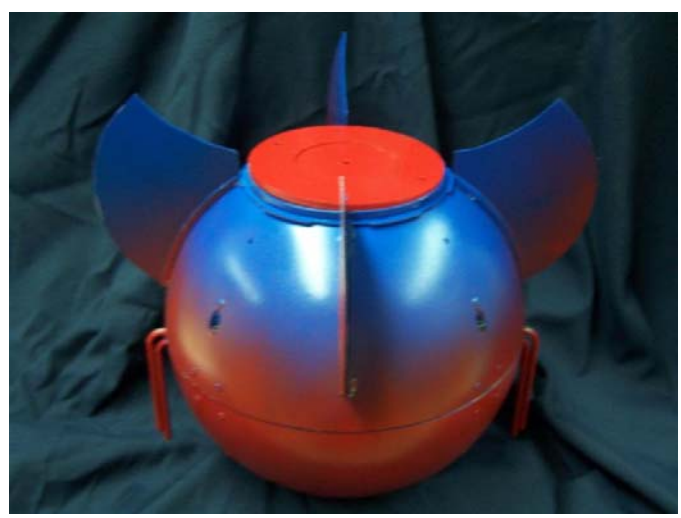

Fig. 8: Finished Probe

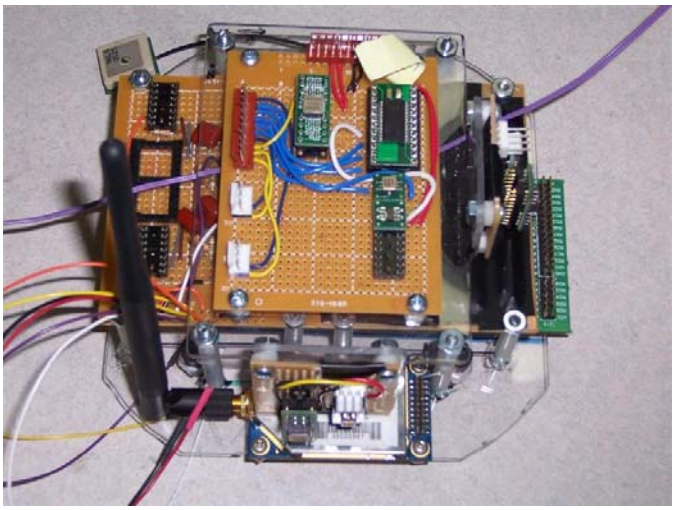

Fig. 9: Completed Electrical System

The V-Team probe design will continue to evolve as the Idaho RISE team continues to refine the electrical and mechanical design. Ultimately this will lead to a complete working probe that can demonstrate the use of acceleration, and pressure and temperature data to accurately reconstruct the profile of the atmosphere, and the probe descent trajectory.

4.0 UNRESOLVED ISSUES

A number of remaining open issues remain must be addressed prior to flight.

4.1 Tracking system

The tracking systems have not been fully demonstrated. The units themselves have been verified to be completely functional when operating external to the probe. However, once the GPS units are integrated into the probe they have difficulty receiving satellite signals. Relocating the antennas, possibly external to the probe, will improve the performance of the GPS units.

4.2 Telemetry system

The telemetry system has been verified to be fully functional in lab and during moored launches. However, the system has not yet been range tested. It is recommended that the system undergo extensive range testing prior to launch.

4.3 Balloon release mechanism

The balloon release system was demonstrated in lab testing, but failed during moored flight tests. In the first moored flight the failure of this system was due to an external connection failure. In the second moored flight, the release mechanism worked, but because of a programming error the nichrome wire was heated at the wrong time.

4.4 Parachute release mechanism

The parachute deployment system was successfully demonstrated in lab testing. The microcontroller successfully burned fuses at the correct times. The team also successfully tested the deployment of a pilot chute with a single rocket engine that was manually triggered. However, the parachute deployment mechanism failed during moored testing. This failure is believed to have been caused by a fuse failure when the components were integrated. The fuse likely failed or was broken when it was inserted into the rocket engine. Also, a failure could have occurred due to connection shorts when the probe was assembled.

4.5 Main parachute deployment

One of the major concerns in the project was the deployment of the main parachute by the pilot parachute. Our design called for the pilot parachute to be deployed by rocket engines. The pilot parachute was then designed to pull its compartment out of the probe and then deploy the main parachute. However, this deployment has not been tested. Additionally, concern was raised following the results of thermal testing. After the probe had been exposed to -20ºC for two hours the force required to deploy the pilot chute compartment from the probe was measured to be 3.6 kg. From wind tunnel testing, the pilot parachute could only generate 3.4 kg at the time of deployment. Further testing is required to gain confidence in the design.

5.0 CONCLUSIONS AND RECOMMENDATIONS

5.1 Conclusions

The results of this project demonstrate that a small, light weight, low cost instrumented descent probe designed to collect useful atmospheric data can be built with off the shelf components. From our research we believe that low cost microprobe entry science technology for planetary atmospheric science is feasible within the near future. The V-Team encountered many of the challenges that engineers face when attempting to develop miniature, low cost, descent vehicles, including aerodynamics, power, mass distribution, sensors (type, location, and configuration), and environment (pressure, temp) considerations. Some of the challenges were addressed by utilizing commercially available (off the shelf) components, lightweight materials, and mass reduction techniques.

The aerodynamic design of an entry probe is one of the critical factors due to the high velocity probes have when entering an atmosphere. This speed must be reduced quickly in the upper atmosphere in order to avoid unmanageable heating and accelerations that would occur if the high speeds were maintained down to the dense lower atmosphere. To most efficiently dissipate the energy of entry, entry probe aeroshells are designed with blunt bodies. The descent probe themselves, however, are often spherical or near-spherical in shape.

The V-Team probe's initial velocity is zero, so heating is not a major consideration in the aerodynamic design of the probe. However, the probe shape is still critical to the success of the design because one of the goals of the project is to construct the density, pressure, and temperature profiles of the Earth's atmosphere based on acceleration data. The more accurately the aerodynamic behavior of the probe is, the more accurate the atmospheric profiles will become. This consideration lead to selection of the spherical probe since the aerodynamic behavior of a sphere is the best understood of all geometries considered.

Another factor in the design of entry probes is the power supply and usage. Batteries are relatively heavy and their size is proportional to the power required. So the lower the power consumption of the instrumentation packages the lower the battery's mass. For the V-Team probe this was not a major problem because MEMS sensors and a low power microprocessor were used. Modern electronics continue to become more miniaturized and consume less power. If the space industry can certify this technology for space flight, entry probes can easily become smaller and possibly less expensive.

Traditionally engineers have thought of entry probes as vehicles for the instruments they carry. As entry probes get smaller and less expensive, engineers and scientist may start to view micro and pico probes as instruments in themselves. This shift in thinking may change the way engineers and scientist design and deploy entry probes in our solar system, and in turn will enable the collection of significantly more atmospheric data which is needed to further our understanding of the bodies in our solar system.

6.0 REFERENCES

[1] The Rocket Man. 1 Feb. 2006. Rocketman enterprises, inc. http://www.the-rocketman.com/

[2] Aircraft Spruce and Specialty Co. 1 March 2006. http://www.aircraftspruce.com/

[3] NASA V-Team website: http://seniordesign.engr.uidaho.edu/2005_2006/nasavteam/

7.0 SPECIAL THANKS

Tony Colaprete – NASA Ames Research Center

Dave Atkinson – University of Idaho

NASA Idaho Space Grant Consortium

Joe Law – University of Idaho

Russ Porter – University of Idaho

MICROSPECTROMETER FOR INTERPLANETARY MISSIONS AND ROVERS, 4th international Planetary Probe Workshop, 27 June- 30 June, 2006, Pasadena, California, USA

Dipl. Ing. Kruselburger Andreas

Department for Astronautics
Technische Universität München
Boltzmannstrasse 15
85748 Garching
Germany
Email: andi.krusel@t-online.de

ABSTRACT

Developments in micro technology over the last years offer the possibility for new instrument designs. These instruments could provide scientists with a complete new family of mission scenarios. This paper contains a summary of flying instruments and their main parameters, as well as a summary of new methods, technologies and elements for sensor development. This leads to new instrument designs. The present study analyzes the case for micro spectrometers.

In this presentation a couple of different micro spectrometer designs for potential interplanetary missions are presented. All of them have been realized as prototypes through the use of MEMS Technologies.

This new class of instruments provides opportunities for new mission concepts or improvements for existing mission scenarios. All space missions are strictly limited in mass, size, power and cost. The use of MEMS technologies provides the opportunity to dramatically decrease all of these factors. Instrument miniaturization also leads to mass reduction and power consumption minimization. Through the use of inexpensive reproduction methods, the fabrication cost for these instruments could be minimized.

One potential new mission concept is the use of a large group of miniaturized instruments connected to each other by means of a radio linked network. Small and simple mechanisms within each sensor element provide the ability to move around collecting data from different spots. Through this kind of mission it would be possible to explore caves and very rough terrains. Instead of sending one spacecraft with a selection of a few expensive, conventional experiments, these new instruments offer the possibility to send hundreds of small sensor packages to a planetary surface. A similar approach could be used to perform Aerobot missions, where instrument packages are dropped during flight through an atmosphere. For such missions to be successful, new miniaturized payloads are necessary. A novel micro spectrometer that combines the advantages of the waveguide and the programmable grating technology is described in this paper.

1. MEMS/ MOEMS

Through the use of MEMS technologies, new types of instrument design are possible. Mechanisms of the smallest dimensions and minimum power consumption are now feasible.

The main advantages of this relatively new type of technology are as follows:

- Production in large numbers at low cost
- Small size
- Low weight
- Extreme accuracy
- Complex mechanisms feasible

However, some disadvantages are connected with MEMS technologies. The basis for most of the process steps applied in this area is the use of masks. The layout and production of these masks is quite expensive which makes the production of a few units comparatively expensive. Therefore, applications where larger amounts of units are used could be of interest.

2. MISSION CONCEPTS

All previous space missions were one of the following types of main mission scenarios:

Flyby
Flyby missions have the advantage of smaller propulsion requirements. However, the shorter pass-over time limits the ability to observe the target in comparison to orbiters. An orbiter goes into orbit around a celestial body which allows long term observation of a target.

Lander
Landers touch the surface of a moon and/or a planet. Therefore, they offer much better ground resolution. These probes can apply in situ research methods rather than using remote sensing methods.

Rover
To improve the surface mobility, mobile rover systems like the Mars Exploration Rovers are applied.

Sample return
A sample return mission from moons, planets, or comets is of great interest for the interplanetary science community. Such a mission has only been completed a few times due to the propellant requirements and the mission complexity. One mission has been completed from the moon with interplanetary dust, and an unsuccessful attempt at a sample return from a comet has also taken place.

New concepts with improved capabilities are now a realistic alternative through the use of miniaturized elements and payloads. The concepts listed below will briefly be described in the following section.

Aerobots
Aerobots are simple probes that could be dropped from a balloon. Through this type of mission, atmospheric profiles could easily be realized. Potential targets for their use could be the atmospheres of Mars, Venus or Titan.

Balloons
Deeply connected to the Aeroprobes are potential balloons. Mars, Venus or Titan are interesting targets for this type of mission. Humankind has had both successful and unsuccessful experiences with orbiters and landers especially on Mars, and balloons could possess great potential for exploration. Balloons may provide the best opportunity to climb to different heights, which would allow for the collection of different measurements from varying altitudes and at the same time travel greater distances over the planet to obtain an overall picture. By decreasing the altitude during the night it would be possible to do in-situ surface science.
A further possibility would be the use of a blimp to further improve previous mission concepts through improved maneuverability.

Air vehicles
Aside from balloons, aerobots and blimps, there are other possibilities for atmospheric exploration missions. These could include other potential "Unmanned aerial vehicles". NASA is investigating this option with the ARES Airplanes. There are also various papers available on the use of micro helicopters.

Penetrators
A penetration system is a device that is driven through its own kinetic energy into the soil of a moon's or planet's surface. MEMS or MOEMS payload devices are, therefore, highly recommended because they can withstand enormous acceleration loads that would appear during such missions.

Surface vehicles
There are a large variety of mission concepts available that could be used for in-situ surface missions. The rovers used in the past had restricted movement and needed a relatively flat surface to land. New concepts could therefore offer great advantages.
An example of a surface vehicle could be a spider like robot that is able to climb very steep hills or walk through rough terrains.

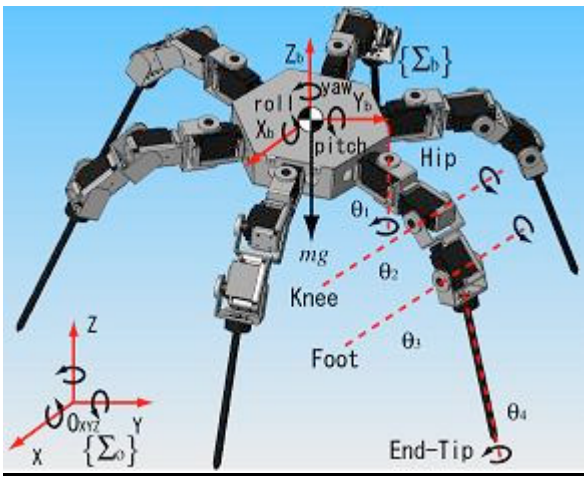

Fig. 1: Bio inspired surface vehicle developed at the Tohoku University [1].

Also, other types and designs of surface vehicles could be found on the drawing boards of universities and space agencies all over the world [2],[3].

Subsurface systems

The material of the top surface layers erode over billions of years due to wind, meteorites and other environmental influences.

Therefore, it is planned to send a small probe deep into the surface to collect data.

A "mole" is a tool that was developed for the Beagle 2 lander by DLR that would dig itself into the ground and transmit data.

Network-, Swarm- or Micro probes

Another new application is the use of groups of small spacecrafts. The idea behind this kind of mission is the use of hundreds of identical instruments that are all connected to each other via a radio linked network which allows communication between the spacecrafts. If single elements of the overall system fail, redundancy of the communication link is in place through the other elements of this network.

A potential application would be the use of small balls between the size of a ping pong and a tennis ball that has a spring inside. MEMS or piezo actuators contract this spring and release the mechanism which leads to a small jump of the device.

With such a mission approach it would be feasible to send a "Mars cave explorer" to the red planet. This mission could land near one of the great volcanoes where potential lava tunnels are expected. After finding a potential access to these caves, single hopper units can jump into the caves to collect data. Many astrobiologists think these specific places may be where life exists on Mars if it does.

Even if 40% of the total instrument packages were lost during such a mission, the overall mission is not endangered at all through the high redundancy within such a network.

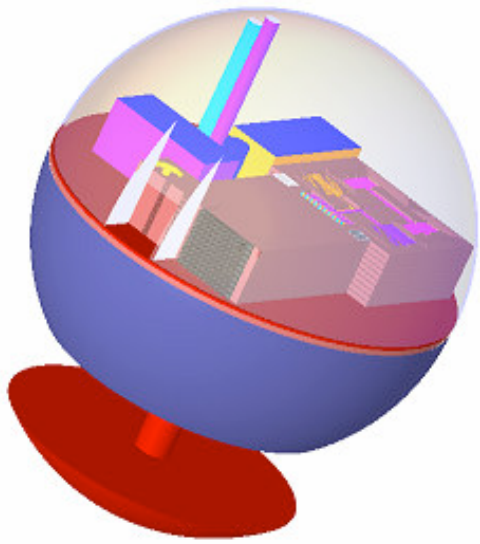

Fig. 2: Hopping micro probe for swarm applications for various targets [4].

3. ANALYSIS INSTRUMENT PARAMETER

To start the process of designing a new type of micro spectrometer the first step was to define the main instrument parameters required.

An analysis was made of various interplanetary instruments flown on different missions. This analysis covered the spectral range of the instrument and the possible spectral resolution. The overview led to average values for both numbers. These average values were targeted in this analysis as a required minimum performance for the new instrument.

Additionally, an overview of different studies on requirements for future instrument parameters was performed. These studies were done by the "Mars Exploration Programme Analysis Group" (MEPAG) and the "Astrogeology Programme Group". Furthermore, different papers on conferences regarding future science missions were considered. This includes the "Mars Infrared Workshop", "Spectroscopy on Mars" and a paper with recommendations on a Neptune mission.

The results of the survey of the different papers and the statistical analysis is summarized in the following table.

This overview led to a spectral "target" range of 0,4 - 2,5 µm and a desired spectral resolution of at least 10 nm.

	λ [µm]	Δλ[µm]	R=λ/Δλ
Analysis missions	0,4 - 2,1	18,3	3904
MEPAG	1,0 - 5,0	2,5	---
MARS IR Workshop	0,4 - 2,5	<15	---
Spectroscopy on Mars	0,4 - 2,5	<10	---
	2,5 - 5,0	---	250
Astrogeology program	1,2 - 4,8	---	---
Recommendat. Neptune	1,0- 5,0	---	300

Table 1: Overview Instrument requirements

4. INSTRUMENT CONCEPTS

During the research for this new concept, various other micro spectrometer concepts were found. These will briefly be described in the following section.

Micro Fourier- Transform- Spectrometer

A Fourier Transform Spectrometer uses a beamsplitter to divide the incoming radiation into separate rays. These rays travel different variable distances and are then recombined where they interfere. This interference is detected with the movement of the mirror that is responsible for the travel distance of one of the rays. A Fourier transformation of the detected signal then delivers the spectrum of the target. The following picture shows a prototype miniaturized Fourier-transform-spectrometer.

However, work on this type of a micro-Fourier-transform-spectrometer was canceled. The design and the production of a beamsplitter in this scale is quite a challenge, and this challenge caused the system to become obsolete which lead to the end of the project.

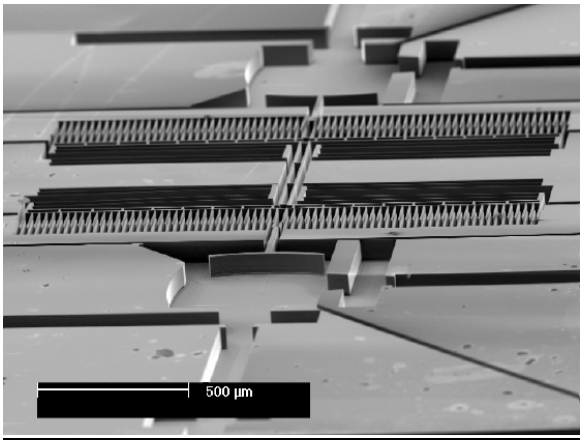

Fig. 3: Prototype of a micro Fourier transform spectrometer without beamsplitter [5].

Fourier lamellar grating

A similar approach is the use of lamellar grating. Instead of having two mirrors that are in a rectangular position to each other, the two mirror planes are parallel. Therefore, the beamsplitter could skipped. To avoid unplanned interference the two mirrors are split up into small pieces of mirrors that are overlayed as displayed in figure 4.

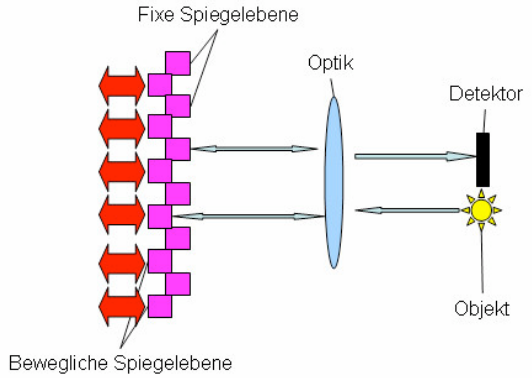

Fig. 4: Lamellar grating micro-spectrometer concept [2].

The purple rectangles display the two different mirror planes. The left row is the variable mirror plane. Through the movement of this plane it is possible to detect an interference signal similar to the Fourier transform spectrometer in a simplified instrument. Unfortunately, because of optical properties it is mandatory to use a relatively expensive optical system which makes the whole system less interesting in comparison to other options described in the following chapters.

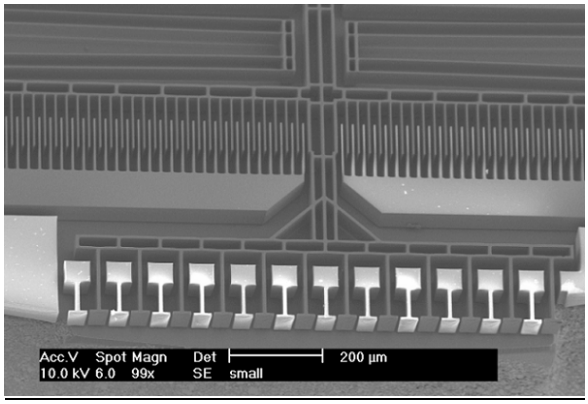

Fig. 5: Prototype of a lamellar grating micro-spectrometer [6].

Figure 5 shows a prototype of a lamellar grating for a micro spcetrometer. The light elements along the bottom are the fixed mirror plane, the dark elements in between are the variable mirror. All of the dark elements are connected with the electrostatically driven actuator in the upper part of the figure.

"Standing wave" spectrometer

A "standing wave" spectrometer is also a very specific form of a Fourier-transform-spectrometer. Here the sensor is combined with the beamsplittter, and one fixed mirror is used. The radiation first enters the partially transmissive

sensor element. About half of the radiation is absorbed or detected. The rest of the radiation passes the detector and is reflected from a mirror behind the detector and falls again on the backside of the detector. The difference in the travel distance is measured through the movement of the mirror.

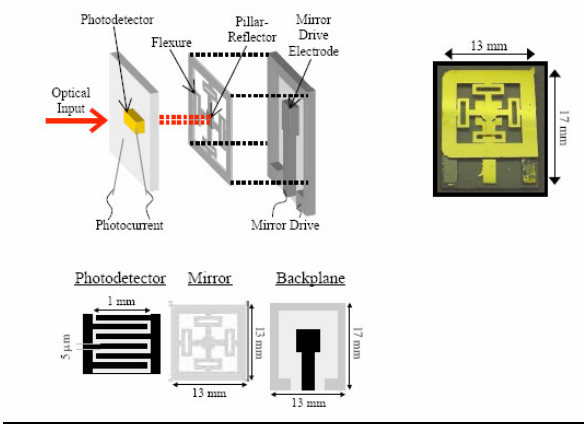

Fig. 6: "Standing wave" micro-spectrometer concept [7].

On the left side, Figure 6 shows the overall configuration of the device with the main dimensions of the parts. On the right the mirror element's mechanical structure is illustrated.
This is a very compact design for a spectrometer, and the technical requirements for the partially transmissive detector are quite high. Furthermore, the material properties of the sensor elements are highly dependent on the wavelength. Therefore, an application for a spectrometer that should work within a bigger wavelength range as required here is not viable.

Programmable grating

A very promising new technology is the use of a programmable grating. This is a normal grating spectrometer. Rather than a fixed grating, a micro mechanical device that can change its shape will be used. With such a device it would be possible to emphasize specific parts of the spectrum to get better information within this spectral area.
Another idea would be a completely new approach in spectroscopy. Through the change of the shape of the grating, very specific spectral ranges could be emphasized as mentioned above. Furthermore, the spectrometer has a database of different chemicals. Depending on the chemical of interest, the shape of the grating is adapted. The detector simply detects the main peaks within the spectrum. As opposed to detecting the whole spectrum, a "Yes-No" question is answered. Depending on the complexity of the grating and the size of the database, such a device would be able to answer the question of which specific chemicals are available. This type of system could dramatically reduce the amount of data to be transmitted back to Earth.

Waveguide spectrometer

The waveguide technology is also very promising for an application as a micro spectrometer. Similar to an optical fiber, a wave guide keeps radiation coupled into the core layer. A specific optical layout of the device allows very flexible designs. A specific structure along the sidewalls or a reflective surface establishes gratings or mirrors within this device.
With this simple technology, miniaturized and monolithic spectrometers can be produced.

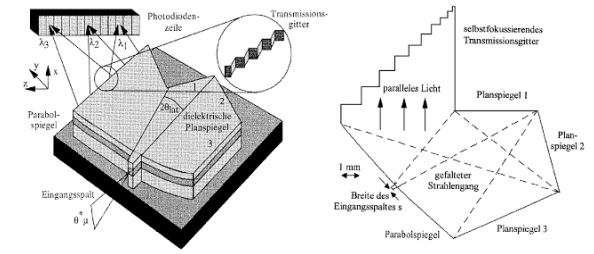

Fig. 7: "Standing wave" micro-spectrometer concept [4].

Figure 7 shows a potential design that includes three plain mirrors and one focusing mirror. On the upper left side of the device, there is a self focusing, transmissive grating. This technology offers great degrees of freedom to design the optical layout. This makes it very promising for an application for a new spectrometer.

Borehole spectrometer

This is not a specific concept for a spectrometer. However, because of its importance for future missions it will be mentioned briefly. Subsurface material is of great interest for the scientist. Surface material from radiation, erosion, weather, etc. was influenced over the millennia. Subsurface material, however, could provide clues about the original material. To obtain this data, new concepts on how to get there must be developed.
Common to all these concepts is the need for a miniaturized spectrometer in the diameter of a driller. Such an instrument could also be used for a mole mission similar to the DLR-payload for Beagle 2.

5. DEVELOPMENT PLAN

None of the technologies alone is sufficient enough to handle the requirements. The lamellar grating technology seems very promising. However, through the combination of a programmable grating and the waveguide technology a very interesting instrument can be designed. A potential stepwise development process will be described briefly.
The first step could be the design of a monolithic waveguide block with a reflective grating on one of the sidewalls. In Figure 8 this is illustrated in grey on the right side.

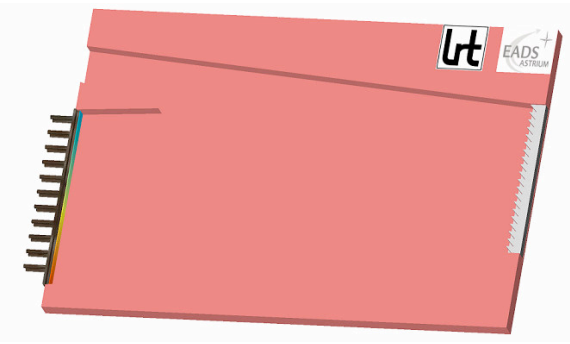

Fig. 8: Micro-spectrometer with fixed diffraction grating [4].

The input slit is on the left side next to the sensor element. After diffraction on the grating, the spectrum is on the detector on the left side in black.
The same layout could be used for an improved version where the grating is replaced through a programmable grating as described above. Figure 9 illustrates a simplified, variable, programmable grating. To use this technology a more detailed study must be performed on the various possible options to realize such a device.

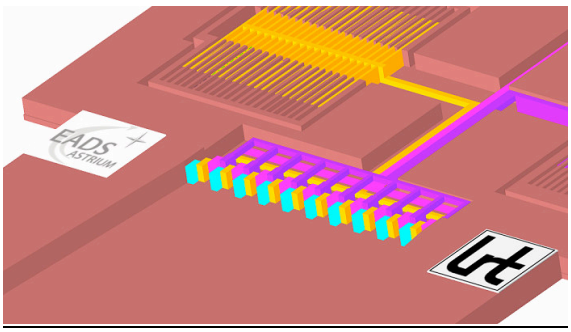

Fig. 9: Simplified programmable grating [4].

A further improvement could be the use of a light source to provide the opportunity to gather scientific data including data from the subsurface or in areas without sufficient sunlight. Such light sources could also be included in the substrate and, therefore, be part of the monolithic block which simplifies production. Missions as described under the chapter network/swarm missions would clearly benefit from such an instrument.

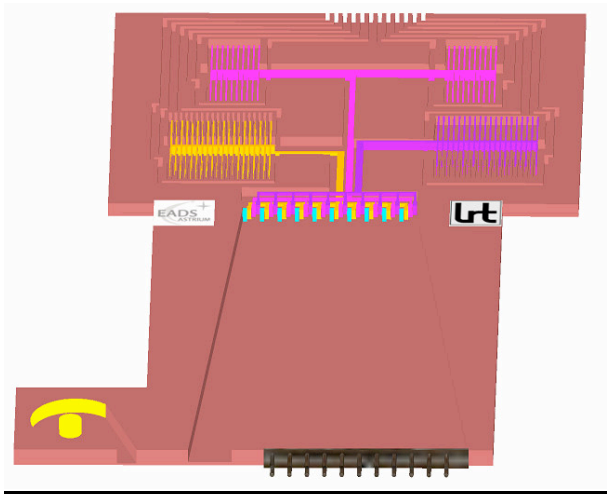

Fig. 10: Micro-spectrometer with programmable grating and integrated light source; approximate size 30mm by 10mm [4].

The basic layout with a single input fiber is able to observe one specific point. Therefore, no spatial information could be gained. MEMS elements like a small rotating micro mirror could provide the option to gain a line scan instead of a point observation. A two dimensional, moveable mirror could scan a two dimensional scene. However, the amount of data that has to be transmitted back to Earth increases dramatically.
Through the very thin design of the whole instrument the third dimension is almost not used at all. Therefore, a couple of instruments can be put on top of each other to provide mapping functions. Different types of spectrometers can be used together in the case of fixed gratings.

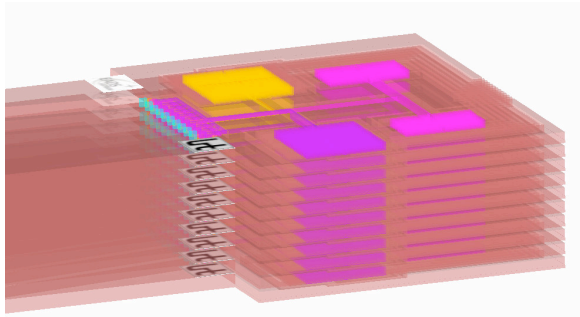

Fig. 11: Stack of micro- spectrometers [4].

6. CONCLUSION

This study showed the great potential for new miniaturized spectrometers and the possibilities such instruments provide. Different types of potential micro spectrometers were introduced, and as a result, a development process for a multifunctional miniaturized spectrometer was described. The main technologies used were the promising waveguide technology, programmable gratings and micro-electro-mechanical-system.

7. ACKNOWLEDGEMENT

Attendance to the workshop was funded through the IPPW4 student scholarship Programme.

8. REFERENCES

[1] M. Chacin, K. Nagatani, K. Yoshida; „*Next-Generation Rover Development For Asteroid Surface Exploration: System description*“; ISTS 2006-d-101p; Tohoku University, Sendai, Japan;

[2] K. Yoshida, M. Chacin, J. Merino, H. Yano ; „*Bio- mimetric Mechanism for Rovers Under Microgravity Surface Environment*“; Tohoku University, Sendai, Japan;

[3] G. P. Scott, A. Ellery; “*Biomimicry as Applied to Space Robotics with Specific Reference to the Martian Environment*”; Guildford, Surrey 2004;

[4] Kruselburger, A.; “*Micro-spectrometer For Interplanetary Missions And Rovers*”, Diploma thesis - Technische Universität München- EADS Astrium 2006;

[5] *MEMS- based micro-spectrometer*; KTI/CTI; Institute of Microtechnology, University of Neuchatal

[6] *Two concepts for Fourier transform Spectroscopy*; Institute of Microtechnology; University of Neuchatel;

[7] Alain, F.; *Simulation of Imaging Fourier Transform spectrometers Using DIRSIG*; Royal Military College of Canada, 1994

SPEX – A SPECTROPOLARIMETER FOR PLANETARY EXPLORATION ONBOARD THE EXOMARS ORBITER

4th International Interplanetary Probe Workshop (IPPW4), 27 June – 30 June, 2006, Pasadena, California, USA

Erik Laan [1,2], Daphne Stam[2,3], Ruud Hoogeveen[3], Gregory Bazalgette Courreges-Lacoste[4], Eric Boom[1]

[1]Dutch Space, Newtonweg 1, 2333 CP, Leiden, the Netherlands, Email:e.laan@dutchspace.nl, e.boom@dutchspace.nl

[2]Astronomical Institute 'Anton Pannekoek', University of Amsterdam, Kruislaan 403, 1098 SJ Amsterdam, The Netherlands, Email:dstam@science.uva.nl

[3]Netherlands Institute for Space Research (SRON), Sorbonnelaan 2, 3584 CA Utrecht, The Netherlands, Email:r.hoogeveen@sron.nl

[4] TNO Science & Industry, P.O. Box 155, 2600 AD, Delft, The Netherlands, Email:gregory.bazalgette@tno.nl

ABSTRACT

Despite the recent detailed observations of Mars, surprisingly little is known about the microphysical properties (size, shape, composition) of the dust and cloud particles in the Martian atmosphere. Information on these microphysical properties is crucial for understanding the atmospheric radiative and chemical balances, and the weather and climate system. In addition, knowledge on the dust particles is essential for future exploration missions. The Spectrometer for Planetary EXploration (SPEX) that is being developed by Dutch industry and scientists (Dutch Space, SRON, TNO and the University of Amsterdam) is tailored to study atmospheric aerosol (i.e. cloud and dust) particles.

SPEX is aimed for accomodation on the foreseen ExoMars orbiter platform and provides synergy with instruments on the ExoMars rover and lander. As an exploration instrument, SPEX will give crucial "planetary weather" information for the ExoMars rover and lander as well as for future landers. As a scientific instrument, SPEX will provide information on the optical and microphysical properties of the aerosol particles that cannot be obtained with the planned ExoMars ground-based instrumentation.

1. THE EXOMARS MISSION

[1] Establishing whether life ever existed on Mars, or might even be present today, is an outstanding question of our time. It is also a prerequisite to prepare for future human exploration of the red planet. To address this important objective, ESA plans to launch the ExoMars mission in 2011 (with arrival at Mars in 2013). ExoMars will also develop and demonstrate key technologies needed to extend Europe's capabilities for planetary exploration.

ExoMars will deploy two science elements on the Martian surface: the Pasteur rover and the stationary Geophysics & Environment Package (the GEP). The rover will search for signs of past and present life on Mars, and will characterise the water and geochemical environment by collecting and analysing surface and subsurface samples. The GEP will measure geophysical parameters that are important for understanding Mars's evolution and habitability, identify potential surface hazards to future human missions, and study the environment.

The lander part of the ExoMars mission has fully been approved at the European Ministerial conference for the ESA programme at the end of 2005. The orbiter part of the mission has not been approved yet but is believed to be a high probability candidate because of its science merits and especially from an overall mission success perspective, as it safeguards the critical communication link with the rover. Figure 1.1 shows an artist's impression of the ExoMars orbiter with the descent module and the rover.

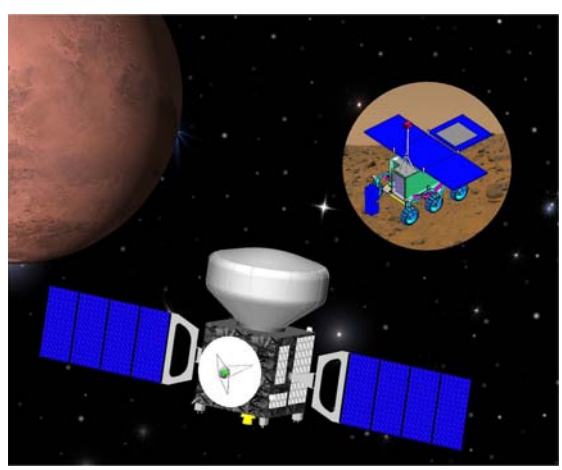

Figure 1.1: Artist's impression of the ExoMars orbiter with descent module and rover (credit: ESA)

The current baseline for communication with the ExoMars rover is NASA's Mars Reconnaisance Orbiter (MRO) which was placed into Mars orbit in March 2006, i.e seven years in advance of the earliest expected arrival of the ExoMars mission, and therefore doubtful for ExoMars service. A decision about the orbiter will be made by the end of 2006.

In support to their search-for-life-experiments, Pasteur and the GEP will have dedicated instrumentation to measure the geological context and the environment. This includes an in-situ dust characterisation experiment and water vapour analysis equipment. The payload(s) on an orbiter should provide synergy with the payload on the surface. As depositing dust could be one of the limiting factors for the lifetime of the rover, it appears to be sensible to propose to measure dust in the Martian atmosphere from orbit during the rover mission.

2. DUST AND CLOUDS IN THE MARTIAN ATMOSPHERE

On Mars, most of the atmospheric aerosol particles are dust particles that are swept up from the surface. Sometimes the airborne dust forms into relatively small, local events, such as the so-called dust devils that can reach altitudes of about 1000 m and that have cross-sections of a few hundred meters. Occasionally, however, regional or even planet encircling dust storms develop within a few days (usually during the Southern spring) that can last for weeks. During such storms, dust particles are lifted up into the Martian stratosphere (i.e. up to altitudes of about 40 km). The amount of airborne dust particles thus varies strongly both in time and in space, causing the colour of the Martian sky to range from bluish (when there is little dust) to orange, as observed by NASA's two Mars Exploration rovers.

Figure 2.1 shows a picture of Martian analogue palagonite particles; dust that was sampled near a Hawaiian volcano by American colleagues at NASA Ames. These particles are considered to be the best representative currently available for dust in the Martian atmosphere and scattering measurements of these particles, performed at the University of Amsterdam, now serve as input for radiative transfer modelling of the Martian atmosphere which include the polarization state of the light.

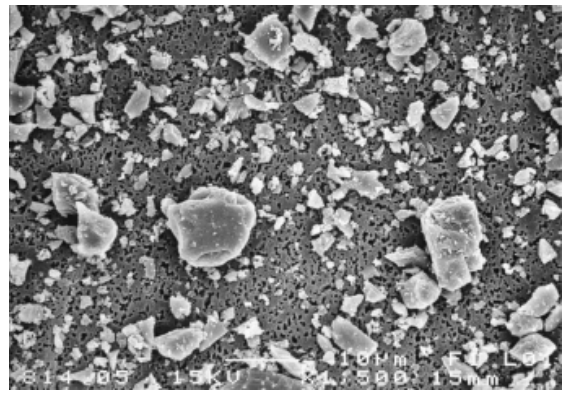

Figure 2.1: Martian analogue palogonite particles

The influence of aerosol particles on a planet and its atmosphere has many facets. To start with, aerosol particles scatter and absorb incoming solar radiation (visual to near-infrared wavelengths), and they absorb and emit thermal radiation, e.g. originating from the planetary surface, (at infrared wavelengths). Through their interaction with radiation, dust particles thus directly influence the planet's radiation and energy balance, as well as its weather and climate. In addition, dust particles can serve as condensation nuclei for atmospheric gases. Most of the clouds that are observed on Mars are cirrus-like ice clouds composed of H_2O-ice crystals. However, clouds of CO_2-ice crystals have also been detected, in particular over the polar ice caps. Figure 2.2 shows CO2-ice particles that formed in a laboratory (they have a bipyramidal shape).

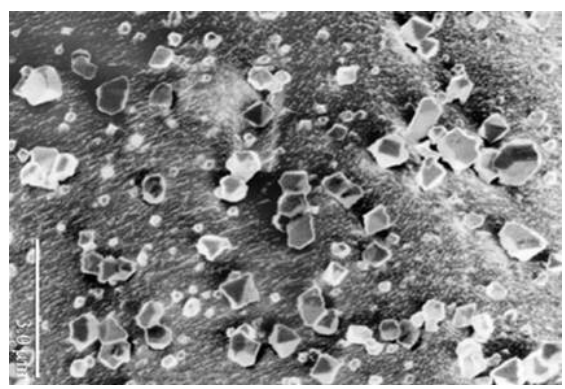

Figure 2.2: CO_2 ice particles (bipyramids)

Even clouds as thin as those found on Mars, play an important role in a planet's climate and radiation balance, because the clouds remove dust and other aerosol particles from the atmosphere. And, just like the aerosol particles themselves, the cloud particles that form on them interact with the radiation in the atmosphere. In addition, clouds provide the vertical and horizontal transport on Mars of condensates, such as water vapour. Interestingly, model studies show that the

formation of CO_2 clouds might have limited the development of a greenhouse effect on Mars, a finding that is crucial in understanding the early and current Martian climate.

Aerosol particles and the cloud particles that form on them also influence chemical processes, for example, by providing the surface area for heterogeneous reactions. Recent research has shown that heterogeneous chemical reactions on dust in the Martian atmosphere could significantly decrease the mixing ratio of methane, especially when the dust particles are electrically charged, as happens during dust storms. Without knowledge of the physical properties of the dust particles, methane observations such as those by a PFS-like instrument are thus hard to interpret.

Finally, in view of the Aurora program, studying the Martian dust is important for landing and habitability considerations, as not only the dust storms themselves but also the electrical discharges that can occur in them are potential hazards for human life on the Martian surface

On Earth, the climatic effects of aerosols have been recognized, and the spatial and temporal distribution of aerosol particles, such as soot and Saharan dust, are regularly monitored. Compared to the Earth with its surface pressure of about 1 bar, Mars has a very thin gaseous atmosphere consisting mostly of CO_2 with traces of H_2O: the surface pressure varies between about 0.006 bars during Northern winter to 0.01 bars during Northern summer. In addition, Mars lacks water bodies like oceans, which on Earth are strongly coupled with processes in the atmosphere, and which regulate e.g. temperature changes. As a result, on Mars, aerosol particles are generally thought to have a much larger relative impact on the atmospheric and climate processes than on Earth.

The precise contribution of aerosol particles to an atmosphere's radiation and chemical balances, as well as their role as condensation nuclei in cloud formation processes depends on their number density, their spatial and temporal distribution, and on their microphysical properties, such as their size, shape, and chemical composition or refractive index. A powerful tool for deriving information on the distribution and the microphysical properties of aerosol particles is the observation of sunlight that has been scattered within the planetary atmosphere. On the current Mars missions, there are various instruments that are capable of measuring the reflected sunlight, e.g. PFS and Omega on ESA's Mars Express orbiter. However, these instruments measure only the intensity of the scattered light, not its degree of polarization. The reflected intensity depends both on the amount of particles and on their optical properties, and as such it appears to be very difficult to untangle these two parameters. It should thus come as no surprise that although we now have some knowledge on the optical thicknesses of Martian dust and clouds (mainly derived by using pre-defined aerosol optical properties), there is still very little information on the microphysical properties of the particles.

Despite the important role of dust particles in the Martian atmosphere, surprisingly little is known about their microphysical properties. Consequently, in radiative transfer calculations that are used to interpret observations of Mars, various assumptions are made regarding the dust optical properties. For example, although dust particles on Earth are known to be irregularly shaped (see Figures 2.1 and 2.2), it is common to assume spherical or, more generally, spheroidal shaped dust particles. The optical properties of the particles are then calculated using, respectively, Mie-theory or e.g. the T-matrix method.The optical properties of spheroidal particles, however, differ significantly from those of irregularly shaped particles, even if their composition and/or size distribution is similar. Therefore, assuming spheroidal instead of irregularly shaped particles in radiative transfer calculations that are used to analyse observations, leads to significant errors in retrieved parameters, such as the dust optical thickness and/or the dust particle size distributions.

3. SPECTROPOLARIMETRY

We plan to design our instrument such that we can determine both the spatial distribution and the microphysical properties of atmospheric aerosol particles. We will achieve this by measuring both the intensity and the degree and direction of polarization of the reflected light, for a range of visible to near-infrared wavelengths. In particular the degree of polarization has proven to be very sensitive to the microphysical properties of atmospheric particles. By observing under different angles, we can derive for specific locations, the particle's phase functions in both the intensity and the polarization, the combination of which is very sensitive to the shape and size of the particles. By observing the intensity and polarization across a range of wavelengths, valuable information about the refractive index of the particles will be obtained. The aerosol parameters we will retrieve give information that is unique and complementary to that of other science instruments, both from orbit and on the surface.

Figure 3.1 illustrates the influence of particle shape on the scattered intensity and degree of polarization. The plot on the left shows that for irregularly shaped silicate particles, the dependence of the intensity with the scattering angle is very similar to that for spherical particles. The plot on the right, however, convincingly shows that the scattering angle dependence of the degree of polarization differs strongly between the irregularly and spherically shaped particles. Apparently, polarimetry is a strong and essential tool for reliably deriving the microphysical properties of atmospheric dust and cloud particles.

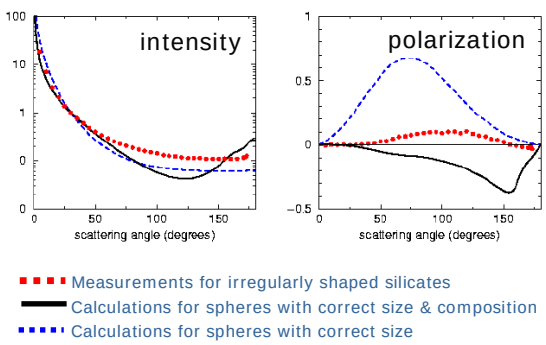

Figure 3.1: Intensity and polarization as function of the scattering angle for irregularly shaped silicates (measurements) and spherical particles (numerical simulations).

4. PRELIMINARY SPECIFICATIONS OF THE SPEX INSTRUMENT

The preferred spectral window for the detection of aerosol particles is the UV-visible. In the 290 nm – 800 nm wavelength region, the optimum conditions are reached both for the reflection of the solar light and for the detection using Silicon-based 2D detector arrays. A compact instrument design can be obtained by employing prisms as dispersive elements, yielding a relatively high spectral resolution of 1.6 nm at 300 nm and of about 26 nm at 800 nm. This resolution strongly limits the data rate in comparison with grating based spectrometers, and avoids overlapping grating orders.

The SPEX optical concept shown in Figure 4.1 consists of three telescopes, placed such to yield maximum angle-dependent information on the aerosol across the scene.

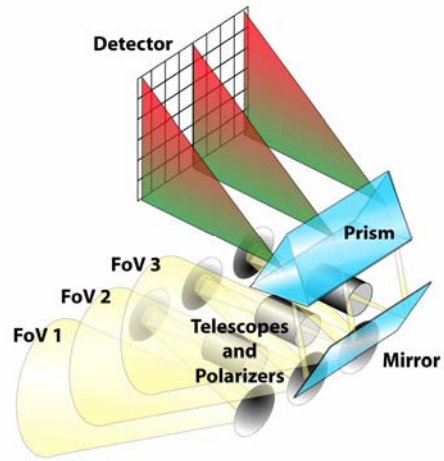

Figure 4.1: Optical concept of the Spectropolarimeter for Planetary EXploration

Each telescope system consists of a primary mirror which provides a telecentric beam on a slit. Behind the slit, efficient polarisation selection could occur by employing a stack of Brewster angle prisms, which, in a very wide wavelength band, effectively transmit light of a particular linear polarisation direction. The beams could next be imaged onto a single collimator for wavelength dispersion.

For detection and readout, a single detector instrument is proposed for the strawman instrument concept. The typical size of the detector would be 1024x1024 pixels. Employing CMOS technology would lead to less read-out electronics compared to CCD technology detectors.

On the square detector, all spectra of the three viewing angles and polarization directions will be imaged. In one image direction, the spatial information will be present, while the other direction will show the wavelength window. Each spectrum will be highly oversampled in the visible part of the spectrum. Co-adding data increases the signal-to-noise ratio, while reducing the data rate. In the spatial direction, the detector allows a swath of some 300 spatial pixels.

The orbit that will be chosen for an ExoMars orbiter will have a significant impact on the exact spatial resolution and coverage that can be accomplished with the SPEX instrument. For high coverage and small groundpixels, a Low Mars Orbit (LMO) is required. This allows a groundpixel resolution of about 5-10 km. Figures 4.2 and 4.3 show some global coverage statistics for sun-synchronous orbits around Mars. Figure 4.2 shows the global coverage time as a function of satellite altitude and total instrument Field Of View (FOV) in a push-broom mode.

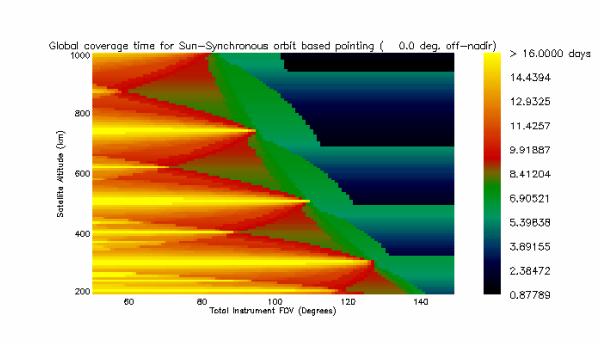

Figure 4.2: Global coverage time for a sun-synchronous circular orbit around Mars as a function of satellite altitude and total instrument FOV in a push-broom mode.

It is clear from Figure 4.2 that a large FOV combined with a high satellite altitude provides the best global coverage time, although it will compromise a compact telescope design and limited aperture, needed for a spatial resolution down to 5 km. Obviously, there are other attractive combinations of satellite altitude and instrument FOV that could be used. For example, at a satellite altitude of 600 km and a total FOV of 80 degrees, a global coverage time of about 4 days can be achieved.

Figure 4.3 shows the daily global coverage percentage as a function of the satellite altitude and total instrument FOV in push-broom mode. It shows that for the previously used example of a satellite altitude of 600 km and a total instrument FOV of 80 degrees, 80 % of the Martian surface can be monitored in a single day.

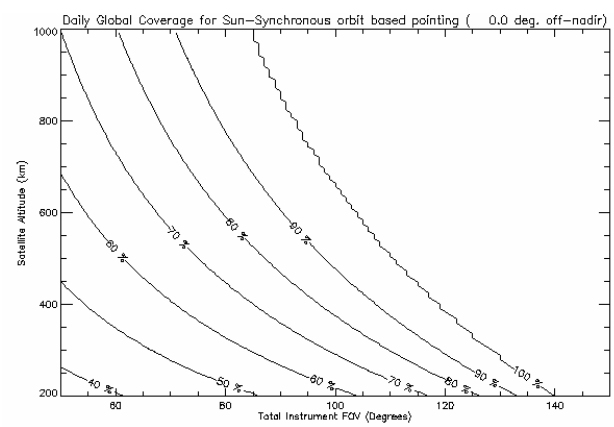

Figure 4.3: Daily global coverage percentage for a sun-synchronous circular orbit around Mars as a function of satellite altitude and total instrument FOV in push-broom mode

Although a circular orbit is advantageous for coverage and spatial resolution, circularizing the orbit from an interplanetary orbit injection is highly demanding for the fuel budget of the spacecraft to be inserted into Mars orbit. Nevertheless, an elliptical orbit (as the Mars Express orbit) could also provide some advantages.

Figure 4.4 shows a picture of a total instrument FOV of only 32 degrees from an apocenter altitude of 9000 km. It is clear that the entire width of the Martian globe can be observed in a single observation.

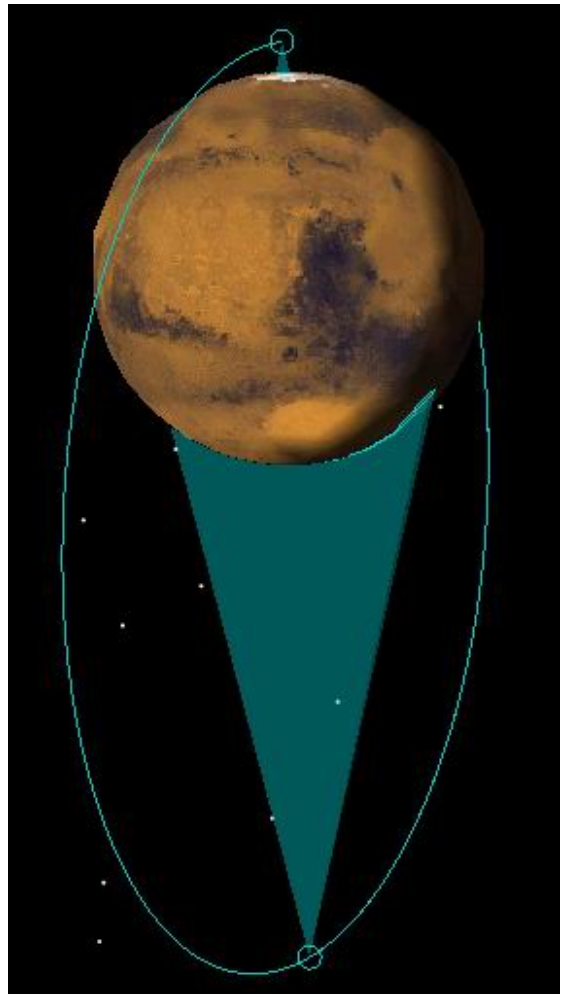

Figure 4.4: FOV of 32 degrees from an apocenter altitude of 9000 km

Using such a highly elliptical orbit, the spatial resolution varies between 3-5 km per ground pixel, when the orbiter is at the pericenter (at an altitude of 300-500 km), and about 100 km, when the orbiter is at the apocenter (at about 10000 km of altitude). Such an orbit would provide both the opportunity to do detailed observations, at either the northern or southern hemisphere, and the option to get a global overview, at the other hemisphere.

5. CONCLUDING REMARKS

SPEX (Spectropolarimeter for Planetary Exploration) is a compact spectropolarimeter to study dust and cloud particles in the Martian atmosphere. SPEX is aimed for accomodation onboard ESA's foreseen ExoMars orbiter.

Without dedicated observations of the dust and clouds in the Martian atmosphere, the weather and climate system of Mars – knowledge of which is essential for both exploration and comparative climatology - cannot be understood or predicted. It is generally recognized that studying other planets helps us to understand our own planet and to answer questions that cannot be solved by looking at only our own planet. This is certainly the case for atmospheric and climate studies. In particular, the Martian atmosphere and surface appear to form a relatively simple, homogeneous system (with a low surface pressure and no oceans) compared to the highly variable Earth's atmosphere and surface. We thus expect that on Mars the role of dust in heating and/or cooling of a planetary atmosphere and surface can be studied in a more straightforward manner than on Earth. The hence obtained knowledge can subsequently help in understanding the role of aerosol (comparative planetology) in the terrestrial climate (comparative climatology). Obviously, the instrumentation we propose to develop within this study can also well be used for atmospheric research of other planets or moons, such as the Earth, Venus and/or Titan.

6. REFERENCES

1. The Aurora programme, Europe's Framework for Space Exploration, ESA Bulletin, number 126, May 2006

THE LIFE MARKER CHIP (LMC) ONBOARD THE EXOMARS ROVER
4th Interplanetary Probe Workshop, 27 June – 30 June, 2006, Pasadena, California, USA

Erik Laan [(1)], Henk Leeuwis [(2)], Inge Loes ten Kate [(3)], Eric Boom[(1)]

[(1)]Dutch Space, Newtonweg 1, 2333 CP, Leiden, the Netherlands, Email:e.laan@dutchspace.nl, e.boom@dutchspace.nl
[(2)] LioniX, PO Box 456, 7500 AH, Enschede, the Netherlands, Email: h.leeuwis@lionixbv.nl
[(3)]Astrobiology Group, Leiden Institute of Chemistry, Leiden University, Einsteinweg 55, 2300 RA Leiden, The Netherlands, Email: tenkate@strw.leidenuniv.nl

ABSTRACT
The Life Marker Chip (LMC) on board the ExoMars rover is one of the key instruments to detect signs of past and/present life on Mars. The ExoMars mission is currently planned for launch in 2011 and will land its rover in 2013, which will be capable to acquire a sample of Martian subsurface soil at a depth of 2 mtr.

The LMC instrument basically consists of two parts which are the microfluidic lab-on-a-chip and the sampling processing unit which shall prepare samples for the aforementioned lab-on-a-chip

An ESA breadboard study for the microfluidic lab-on-a-chip is ongoing with English, German and US partners. (University of Leicester, University of Cranfield, Surrey Satellite Technology, QinetiQ, Open University, EADS-Astrium Stevenage, University of Kiel, Kayser-Threde, GeSim, DLR & Carnegie Institution) together with Dutch partners Dutch Space and LioniX. The University of Leiden acts as an intermediate for the Dutch scientists involved in the Life Marker Chip project.

1. THE EXOMARS MISSION
[1] Establishing whether life ever existed on Mars, or is still active today, is one of the great outstanding questions of our time. It is also a prerequisite to prepare for future human exploration of the red planet. To address this important objective, ESA plans to launch the ExoMars mission in 2011 (with arrival at Mars in 2013).

ExoMars will deploy two science elements on the Martian surface: a rover and a small, fixed package. The Rover will search for signs of past and present life on Mars, and characterise the water and geochemical environment with depth by collecting and analysing subsurface samples. The fixed package, the Geophysics/Environment Package (GEP), will measure planetary geophysics parameters important for understanding Mars's evolution and habitability, identify possible surface hazards to future human missions, and study the environment. Figure 1 shows an artist concept of the ExoMars rover.

Figure 1: Artist concept of the ExoMars rover as it drills into the Martian subsurface, on the search for signs of extant and/or extinct life. (artist concept: courtesy ESA)

2. THE LIFE MARKER CHIP – SCIENCE BACKGROUND
To understand the presence and evolution of organics within the Solar System and their modification by local environments and by life (if present) on suitable targets (e.g. on Mars and perhaps Jupiter's moon Europa) requires the

availability of in situ detection and characterisation of organic molecules. A new detection method for planetary exploration application is provided by immunodiagnostics found widely in the medical and biotechnology sectors and becoming established in the environmental sector for the detection of trace levels of organic pollutants. Such methods exploit the highly specific recognition and binding properties of molecular receptors such as antibodies (i.e. proteins) or fragments of them, and / or wholly artificial receptors such as molecular imprinted polymers [2].

The context for the detection of organics on Mars is complex. A simplistic view is that a significant organics inventory may have been delivered to early Mars from the solar nebula during the formation of Mars and the subsequent heavy bombardment phase. Additionally, organics have continued to arrive on the Martian surface up to the present day via cometary, meteorite and especially micrometeorite delivery. It can therefore be assumed that the organics inventory will have initially been similar to the organics found in representative meteorites present on Earth. The geological and climatic evolution of Mars will have modified the initial inventory by thermal, aqueous and other processes. Additionally, if life has been present on Mars, further modification of the inventory by biological processes will have occurred. It should however be noted that organic matter has yet to be detected in situ on Mars.

Current organic molecules related to life can be divided in 2 groups. Firstly, the so-called geomolecules, remnants of extinct life. In general, these molecules have lost their active groups and can be solved in organic solvents. Secondly, biomolecules, representatives of current life. In general, these molecules still have their active groups and can be solved in polar/acquaous solutions.

A typical example of a geomolecule is the hopane group. 2-methyl hopane has been found in 2.7 billion year old sediments [3]. Many bacteria are known to synthesize (bio)hopanoids as membrane stabilizing components. Other examples of molecules of interest for the LMC are pigment derivatives such as porphyrins and isoprenoids.

3. THE LIFE MARKER CHIP – THE INSTRUMENT

The design aim of the LMC is to detect ~20-25 specific molecules/classes on ~20-50 samples within the constraints set by mission resources and instrument design. The samples will be provided as crushed rock or regolith with a mass smaller or equal to 1 gram with particle sizes upto tens of microns. A sample processing system will extract the organic molecules (if any are present) from (within) the sample, concentrate them and provide them to the microfluidic chip part of the Life Marker Chip. The molecules will be measured via multiple single-use multiplexed immuno-assays. Each assay will perform ~100 simultaneous measurements (via a 100 spot micro-array) detecting molecules down to the level of parts per billion – assuming appropriate antibodies. To allow for controls (both positive and negative), redundancy/replicates etc. it is foreseen that ~20-25 target molecules can be simultaneously detected in any one assay/sample.

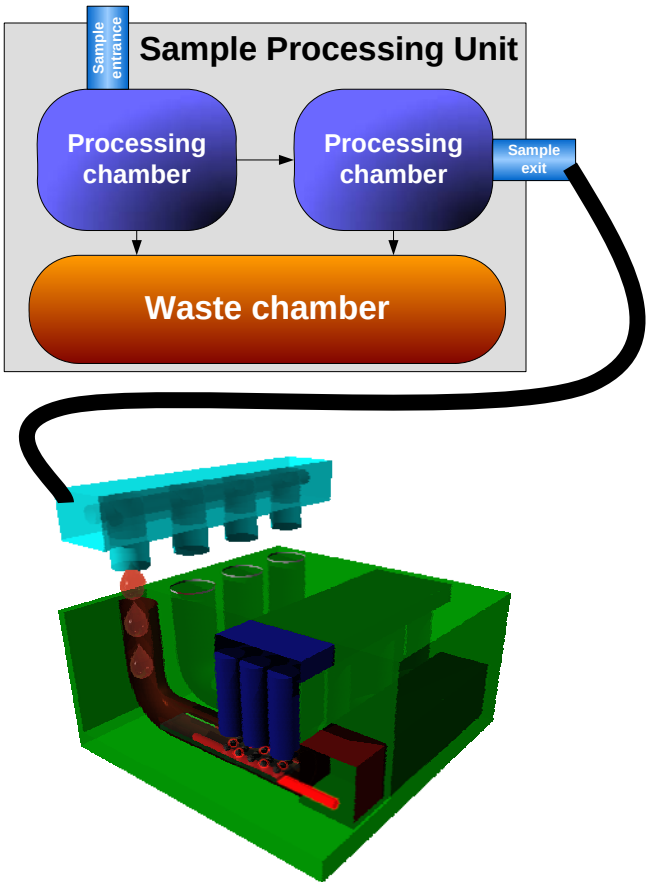

Figure 2: High level concept of the Life Marker Chip instrument. The top of the figure shows the Sample Preparation Unit. The bottom of the figure shows the microfluidic chip.

A list of 63 potential target molecules was derived using a team of consultants during a Biomarker workshop which was chaired by Prof. John Parnell of the University of Aberdeen and was held at the Space Research Centre, Department of Physics and Astronomy, University of Leicester in the UK from 24th - 26th May 2006.

Target molecules included those associated with pre-biotic chemistry, meteoritic and cometary impacts/infall, past life, present life and potential spacecraft contamination.

The targets are a mix of specific molecules and generic compound classes, in some cases with overlap both within the LMC and within the detection targets of the broader organics suite of instruments within the Pasteur instrument payload. This should allow flexibility in LMC assay design, antibody production and instrument design. The level of information obtained from the LMC will stem not from detection of a single compound, but from the detailed distribution of compounds, detected and not detected. The molecular targets have to a certain extent been selected with the other ExoMars instruments in mind to allow the "confirmatory and complementary" analysis process proposed for the Exomars organics package to be used.

4. TESTING CRITICAL TECHNOLOGIES – THE OPTICAL CHIP DEMONSTRATOR

One of the critical issues in the Life Marker Chip is the coupling of light into the biomarkers. This was already envisioned early in the conceptualisation of the Life Marker Chip and therefor Dutch Space & LioniX started a national technology development study in the summer of 2005 concerning an Optical Chip Demonstrator, managed by the Dutch Aerospace Agency NIVR. This chip basically contains a number of solutions of distributing light in a waveguide where the so-called evanescent wave field (external to the waveguide) is available for excitation of fluorophores bound to biomarker dots. Figure 3 shows the set-up that was built to test the OCD chips.

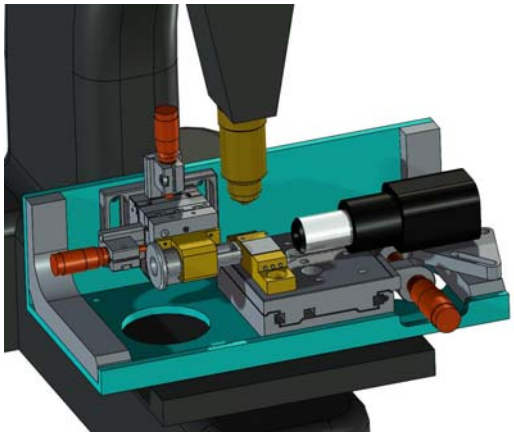

Figure 3: set-up to test the Optical Demonstrator Chip (OCD)

The set-up is built onto a microscope mounting. On the left, light can be coupled in, into a chip. This is performed with 2 microstages, able to position the light source within a micrometer in 2 directions. On the right, there is a camera measuring the output of the chip. The position of this camera can be set within 0.5 micrometer in the lateral direction. Then, for fluorescence measurements, the microscope is suited with an emission filter and a camera to make images of the fluorescence field.

One of the main test objectives is to validate a radiometric throughput model of the Optical Demonstror Chip.

5. CONCLUDING REMARKS

The Life Marker Chip (LMC) on board the ExoMars rover is one of the key instruments to detect signs of past and/present life from samples taken down to a depth of 2 mtr below the Martian surface. The ExoMars mission is currently planned for launch in 2011 and land its rover in 2013. Technology development is running to produce an operational breadboard of the instrument within an ESA contract by the end of 2007.

6. REFERENCES

1. The Aurora programme, Europe's Framework for Space Exploration, ESA Bulletin, number 126, May 2006

2. Sims, M.R., Cullen, D.C., Bannister, N.P., Grant, W.D., Henry, O., Jones, R., McKnight, D., Thompson, D.P., and Wilson, P.K., The Specific Molecular identification of Life Experiment (SMILE), 2005, Planetary and Space Science, 53, 781-791

3. J. J. Brocks, G. A. Logan, R. Buick, and R. E. Summons, Science, vol. 285, pp. 1033-6., 1999.

CARBON NANOTUBE-BASED VACUUM AND SEMICONDUCTING DEVICES FOR MICRO-INSTRUMENTATION AND ELECTRONICS

H. M Manohara,	Harish.Manohara@jpl.nasa.gov
M.J Bronikowski,	Michael.J.Bronikowski@jpl.nasa.gov
E.W Wong,	Eric.W.Wong@jpl.nasa.gov
R. Toda,	Risaku.Toda@jpl.nasa.gov
R.H Lin,	Rlin@merlin.jpl.nasa.gov
E. Schlecht,	Erichs@merlin.jpl.nasa.gov
E.M Luong,	Edward.M.Luong@jpl.nasa.gov
B.D Hunt,	Brian.D.Hunt@jpl.nasa.gov
P.H Siegel	phs@merlin.jpl.nasa.gov

Affiliation (all authors): JPL, 4800 Oak Grove Drive, Pasadena, CA 91109, USA

Introduction: High-current density field emission electron sources are the essential components to enable multiple miniature instruments for planetary probe missions, which include, XRD/XRF, XPS, miniature mass spectrometers, UV-Lasers for Raman spectroscopy, advanced THz sources for heterodyne spectroscopy, and vacuum microelectronics. Such sources increase the data collection rate, and reduce mass and power budgets, which makes them attractive for probe missions, especially to extreme environments such as Venus, where the mission lifetime could be very short.

Carbon nanotube (CNT)-based electronics are inherently radiation hard and find applications in high frequency as well as in control and communication electronics. It is possible to realize logic gates and zero-power consuming non-volatile memories using CNTs that can be employed for electronic applications in probe missions to high radiation Jovian environment.

This work focuses on the field emission and the electronics technology development using both multi-walled nanotubes (MWNTs) and single-walled nanotubes (SWNTs).

CNT Field Emitters: On the field emitter front, the high-current-density CNT bundle arrays have been developed and have been successfully integrated with extraction grids using either molybdenum or conductive silicon-on-insulator substrates. The recent Mo-gate samples have produced current densities > 4 A/cm^2 at the anode with emission efficiencies up to 95%. Further electron beam optics design and fabrication considerations will be shown.

CNT Schottky Dodes: In the CNT-Schottky diode development, we have produced devices with Pt or Pd Ohmic contacts and Ti Schottky contacts using angled evaporation technique. After annealing the devices have exhibited ideality factors (n) of 1.3 to 1.5. They still suffer from hundreds of kOhms series resistance and the aging effect when tested after a prolonged storage. Again, annealing was seen to restore/improve the device performance. Details of these results along with their application modes for planetary probe missions will be discussed.

Descent and Landing Rock Hazard Avoidance System (ROHAS) for the Mars Exploration Program Advanced Technologies (MEPAT) Program

Paolo Masini, Karl Blasius
Santa Barbara Remote Sensing
Raytheon Company
75 Coromar Drive
Goleta, CA 93117
805-562-7342
paolo@raytheon.com
and
Philip R. Christensen, Greg Mehall
Arizona State University
Tempe, Arizona

One of the key problems of entry, descent and landing for planetary probes and sensors is hazard detection and avoidance. This is especially critical when a mission must target very accurately (near pinpoint landing) a scientifically interesting, possibly unique, location on the surface of a planet or other celestial object. A cushioned landing such as Mars Pathfinder's, may result in bouncing and rolling to a significant distance from the target location. This could cause difficulty and potentially thwart key mission objectives. A controlled landing using accurate navigation is required for a precisely targeted mission. Raytheon SBRS in collaboration with Arizona State University is developing a navigation aid to support a controlled landing, with terminal navigation corrections, to a rock hazard-free location as near as possible to a nominal landing site. Differences in thermal inertia between fines (dust/sand) and rocks on Mars will cause hazardous (large) rocks to have distinctive temperatures in thermal IR images. Mixtures of fine dust/sand and rocks explain the thermal inertia signatures, measured from orbit, of the three Mars landing sites prior to the Mars Exploration Rovers. (Golombek, et al, 2001) At low altitudes, during controlled descent of a lander, thermal IR images could resolve individual rock hazards and thereby support navigation corrections to touchdown in a relatively safe location.

This development has been coordinated and funded as part of the Mars Technology Program (MTP), in support of the Mars Exploration Program Advanced Technologies (MEPAT) Program with NASA JPL. Raytheon SBRS in collaboration with Arizona State University is developing a breadboard demonstration to maturity (TRL 4) miniature IR camera-based system for mapping the locations of geologic hazards, including boulders and rock outcrops. Arizona State University is developing the terminal hazard mapping algorithms to be used for real-time navigation correction during descent and landing.

EXPERT AEROTHERMODYNAMIC FLIGHT INSTRUMENTATION ENVIRONMENT AND INTEGRATION
27 June – 30 June 2006, Pasadena, California, USA

J-M. Muylaert[(1)], H. Ottens[(2)], L.Walpot[(2)], F. Cipollini[(1)], F.Gavira[(1)], G, Marino[(1)], M. Caporicci[(1)]

[(1)]ESA-ESTEC, Keplerlaan 1, 2200 AG Noordwijk, The Netherlands, Email:Jean-Marie.Muylaert@ESA.int
[(2)]AOES-Group B.V.,Haagse Schouwweg 6G, 2332 KG Leiden, The Netherlands

ABSTRACT

The paper reports on the aerothermodynamic (ATD) environment of the EXPERT configuration associated with the planned first flight (5km/sec trajectory). A status report is given on the embarked flight measurement technique developments and qualification with emphasis on the thermal protection system (TPS) integration issues. Special attention is given to the design of the flight measurement sensors themselves, their integration into the TPS as well as to the measurement of the free stream parameters during re-entry using an Air Data System (ADS).

This paper addresses the EXPERT scientific payload that consists of a series of scientific flight measurement techniques such as:

- Flush Air Data System (FADS),
- Nose heating (Pyrex),
- Catalysis measurements,
- Natural and roughness induced transition,
- SWBLI upstream of the open flap and flow reattachment on the flap,
- Shock layer chemistry using emission spectroscopy (RESPECT),
- Base pressure and heat flux measurement,
- Skin friction gauges,
- Temperature and heat flux measurement on Sharp Hot Structures (UHTC)
- Boundary layer thickness, Pitot static probe

INTRODUCTION

EXPERT is an "in flight research" test bed (CLASS 1) i.e. a generic vehicle incorporating a series of critical phenomena requiring improved understanding so as to enhance the tools for design used for demonstrators (CLASS 2) and full-scale qualification flight vehicles (CLASS 3). These tools for design incorporate numerical tools including physical modeling, ground-based facilities including associated measurement techniques as well as the flight sensors and their integration themselves. EXPERT is a generic configuration that will perform a sub-orbital flight and re-enter the Earth atmosphere. The EXPERT vehicle will be equipped with state-of-the-art instrumentation and will provide flight measurements of critical aero-thermodynamic phenomena occurring during a hypersonic flight.

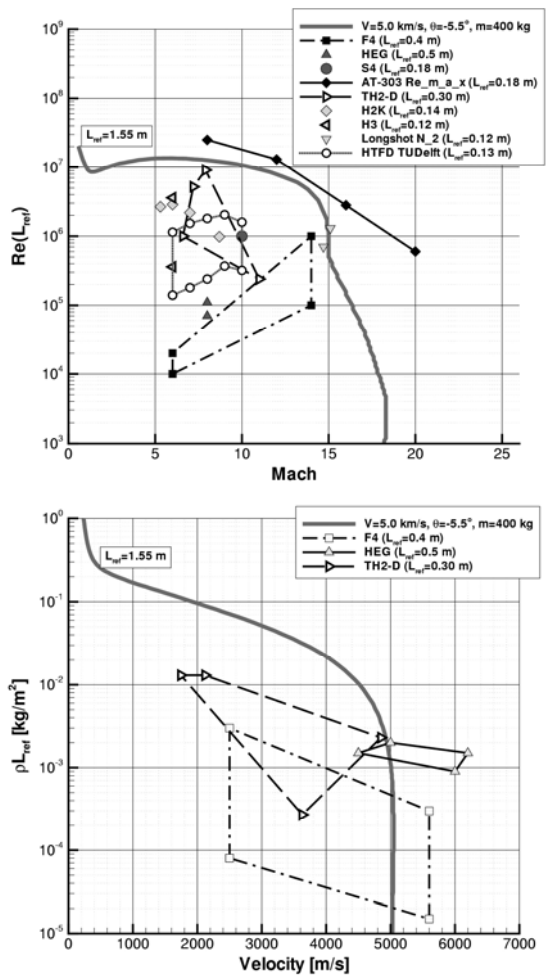

Fig. 1a and b: EXPERT trajectory with high-enthalpy- and some major perfect gas -facilities performance envelops.

The objective of the EXPERT mission is to perform a sub orbital flight for in-flight measurements of critical aerothermodynamic phenomena using state-of-the-art instrumentation.

A test bed is provided for validation of aerothermodynamic models, codes and ground test facilities in a representative flight environment, to improve the understanding of issues related to analysis, testing and extrapolation to flight. The flight data provided by the EXPERT mission will be used to study the wind tunnel-to-flight extrapolation and scaling methodologies at established high enthalpy facility and perfect gas facility crossing points (Fig. 1 a en b).

THE EXPERT VEHICLE

The EXPERT configuration has been optimized to enhance the phenomena of interest and at the same time respecting the constraints of mass and volume imposed by the VOLNA Launcher. The final configuration is shown in Fig. 2. A body of revolution with an ellipse-clothoid-cone two-dimensional longitudinal profile constitutes the basic shape cut by 4 planes incorporating 4 fixed flaps.

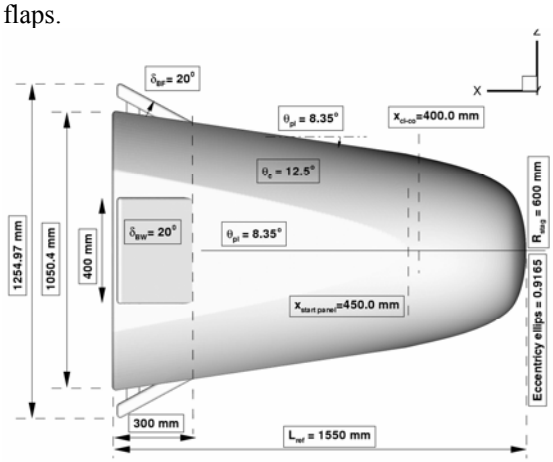

Fig. 2: EXPERT 4.5 side view.

The nose is an ellipse with an eccentricity of 0.9165 with a local nose radius of 0.60 m. The ellipse- cone junction is second order by using a clothoid to avoid pressure jumps. The cone has an angle θ_c=12.5° and features axisymmetric flow enabling two-dimensional sensitivity computations. The connection of the clothoid and the cone is located at x=0.40, exactly where the C-SiC TPS ends and PM-1000 TPS starts. So the C-SiC part covers completely the ellipse and the clothoid and the PM-1000 is just conical. The leading edge of the panels are located at x=0.45 m to avoid double curvature in the C-SiC part. The angle of the panels are θ_{pl}=8.35°. The four flaps have a width of 0.40 m and a projected length of 0.30 m and their deflection angles δ_{bf} are 20°. All flaps will be open to study 3D micro-aerodynamic effects on corners; base flow recirculation and non-convex reradiating wall effects. The reference length of EXPERT is L_{ref}= 1.55 m. with a wetted base area S_{ref}=1.1877 m^2.

THE SCIENTIFIC PAYLOADS

The EXPERT vehicle will carry state-of-the-art instrumentation for in-flight measurement of the critical aerothermodynamic phenomena: transition, catalysis, real gas effects on shock interaction, as well as blackout. Special attention will be paid to the design of measurement sensors, as well as to the gathering of the free-stream parameters during reentry.

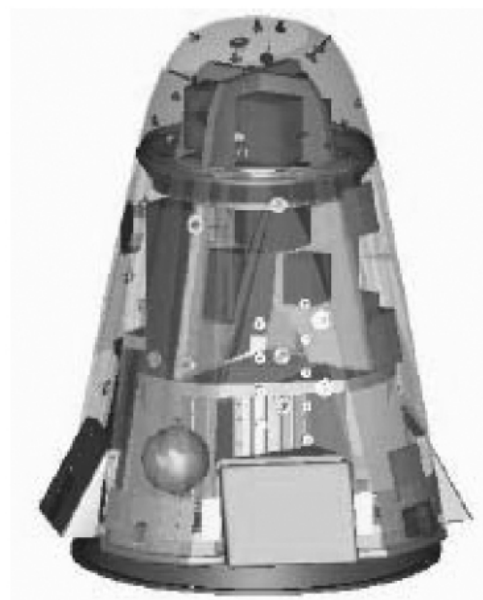

Fig. 3: EXPERT internal layout

Air Data System and Nose Heating

The nose of the vehicle, featuring high geometrical accuracy and a low surface catalicity, integrates both a Flush Air Data System and heat flux sensors PYREX (developed by IRS, Germany).

A pressure-based Air Data System (ADS) mounted on EXPERT's nose will provide free stream dynamic pressure, angle of attack and sideslip angle. Raflex gages will be used as ADS sensors featuring combined pressure and heat flux measurements. These heat flux measurements will be compared with those obtained from the PYREX measurements.

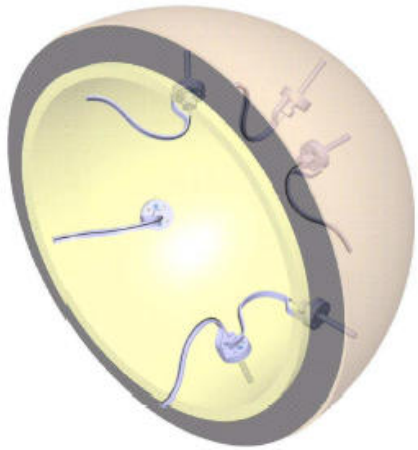

Fig. 4: Heat flux sensors (Pyrex) mounted in nose

The goal of the PYREX measurements is to determine the temperature history and corresponding heat fluxes at six locations on the nose (Fig. 4). Pyrometric sensors have been developed in the last years for temperature and consequently heat flux measurements based on collected thermal radiation intensity.

Among the pyrometric sensors developments within Europe, a particular system aimed at gathering relevant data on TPS rear surfaces, has reached an advanced design status. The experimental set-up, whose initial application was the rear surface of the X-38 Nose, is constituted by:

1) Sensor heads.
2) Fiber optics.
3) Sensor unit.

The optical signal from the sensors is led through an optical path to the sensor lens where it is focused; subsequently the fiber optics lead the optical signal to the conversion unit hosting the photodiodes and finally the electric signal is recorded by the electronic unit of the sensors

Catalysis measurements

The assessment of the catalytic gas-surface interaction is a major concern when designing a thermal protection system. The degree of catalicity of a material affects the heating of the surface (the higher the degree of catalicity, the higher the wall heat flux) and thus the design of the protection needed. Understanding this phenomenon calls for very complex modeling at the molecular level, which can be only partly validated in ground-based plasmatron facilities.

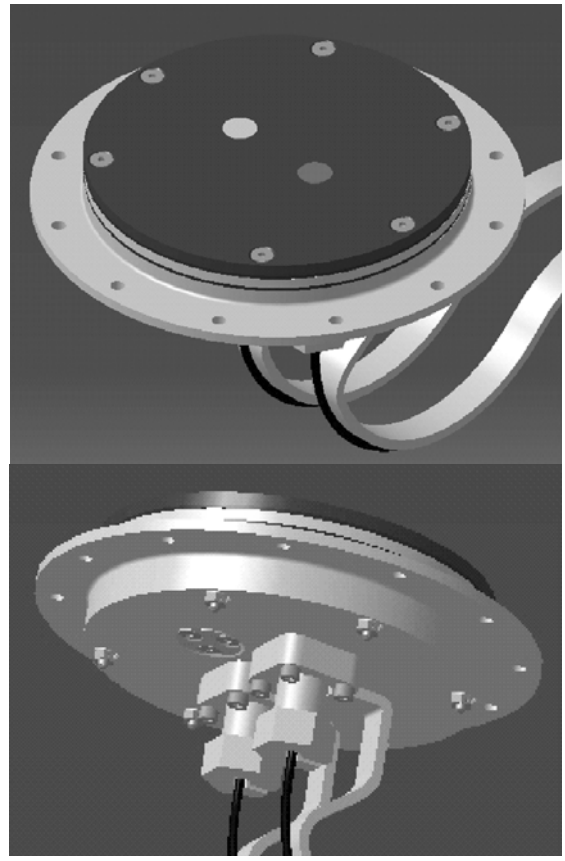

Fig. 5a and b: PHLUX sensor with thermocouples

For EXPERT the catalysis will be studied with the PHLUX sensor, which is depicted in Fig. 5.

Natural and roughness-induced transition

Laminar to turbulent boundary-layer transition is considered one of the most critical aerothermodynamic phenomena due to the associated local temperature peaks and drag increase; unfortunately, present day hypersonic methods are based on old correlations that need to be revisited. In fact, chemistry effects are difficult to simulate in ground facilities and cold hypersonic facilities are affected by external disturbances (wind tunnel related), which constitute dominant sources of perturbations for transition triggering.

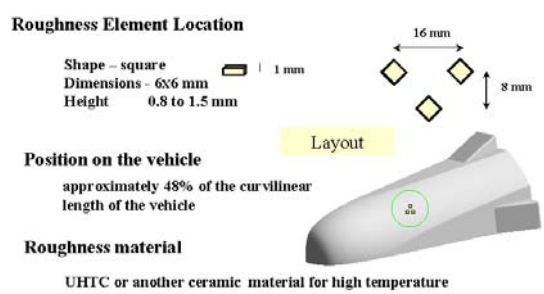

Fig. 6: Roughness elements on EXPERT

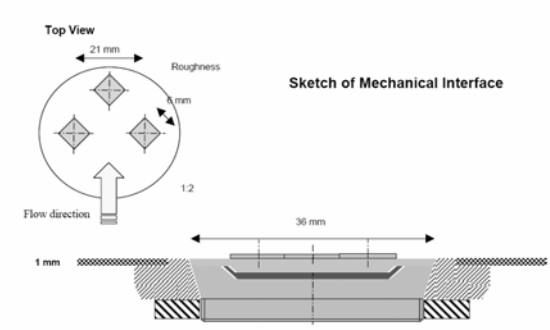

Fig. 7: Roughness elements in detail

Thus, only flight experiments with well-characterized disturbances (triggering transition where required) may provide essential information to be coupled with ground facilities data and numerical simulation results. Roughness-inducing boundary-layer transition elements will be mounted on the leading edges of EXPERT in diametrically opposite locations. Their position, size and number will be chosen such that transition occurs in the lower altitude, higher Reynolds number part of the flight. Heat flux sensors will detect transition.

The other conical edges will be kept smooth in order to have a reference clean condition to be compared against the induced transition behavior.
Fig. 6 and Fig. 7 show a typical roughness element layout, whereas Fig. 8 addresses typical roughness induced transition correlations, which need to be validated via new flight data.

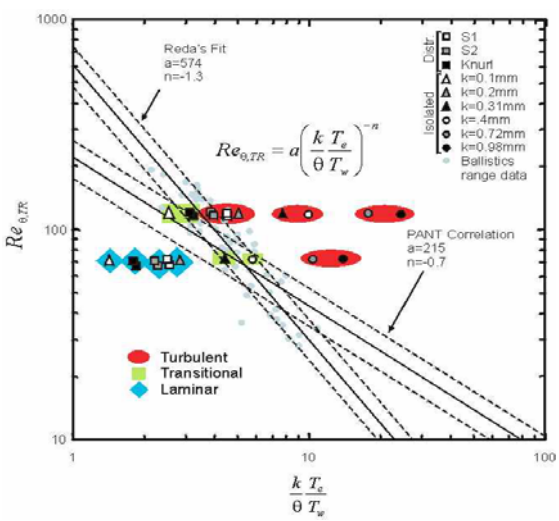

Fig. 8: Experimental activities on Roughness induced transition (courtesy VKI).

At this point, the importance of analyzing smooth surfaces has to be remarked: in fact, the experiment will be successful only if no transition is triggered by surface discontinuities upstream of the roughness elements are located. That is why this Payload addresses both surface discontinuities triggered transition and roughness element induced transition via CFD + stability analysis, wind tunnel test campaigns and flight tests.

<u>SWBLI upstream of the open flap and flow reattachment on the flap.</u>
It is widely known that boundary layer separation effects in front of deflected flap have a significant impact on re-entry vehicle controllability; moreover the heating associated with shear layer reattachment may affect to a great extent the TPS design of the relevant area.

Three dimensional effects, corner and gap heating, flow circulation, constitute critical issues that need to be addressed; the EXPERT vehicle is foreseen to be equipped with an experimental set-up including thermocouples, heat and pressure gages, strain gages in three different locations:

- Ahead of the open flap.
- Onto the open flap.
- In the cavity underneath the open flap.

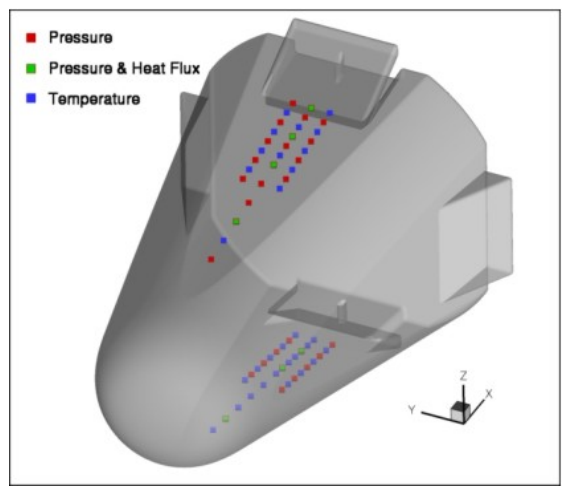

Fig. 9: Sensors located before the Open Flaps

Boundary-layer separation effects in front of a deflected flap (Fig. 9) affect not only the flap for control purposes, but also the heating associated with shear-layer reattachment. Three dimensional effects, corner and gap heating, base-flow circulation and wall cooling are all critical issues that need to be addressed in the design of control flaps. The set-up proposed for EXPERT consists of a space-vehicle ceramic flap with fixed actuator instrumented with simple but reliable devices such as thermocouples, heat and pressure gages and micro-pyrometers.

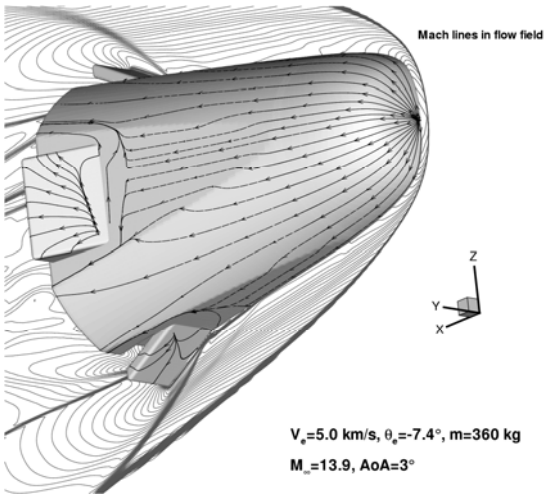

Fig. 10: Streamlines and Mach lines around EXPERT

In order to derive extrapolation-to-flight criteria able to reproduce both the mechanical and thermal loads acting on the control surface, a number of experimental tests will be performed. The EXPERT flight conditions in the flap region will be characterized by means of CFD and ground experimental activities. Also the flat faces upstream of the flap are foreseen to be instrumented.

Rear Face Infrared Thermography

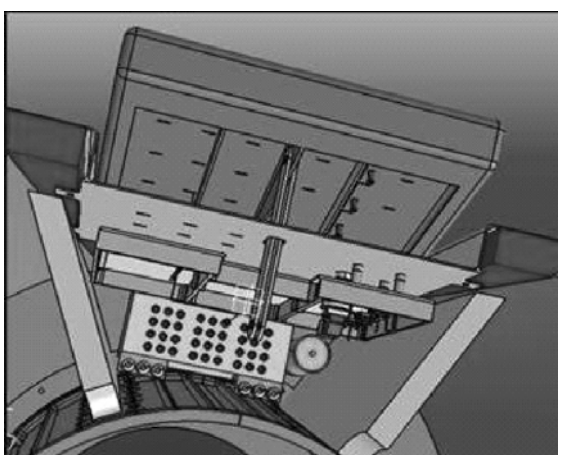
Fig. 11: Base view of the open flap.

The scientific objective of this measurement technique is to use a non-intrusive instrument based on Infrared technology to get a 3D thermal map of the rear face of a control surface evolving in time; this technique, accompanied by a validated non-linear inverse method, allows for the determination of the heat loads subjected to the flap.

Different European companies/research institutes (such as HTS, Switzerland and Onera, France) have been investigating this technique.

The selection of the operational wavelength regime coupled to the choice of the infrared camera (from the commercial market) constitutes a first step into the design of the overall experimental set-up.
One important characteristic that the camera is asked to have is the ability to feature variable exposure times, thus allowing measuring an extended range of temperatures.

At present a technical possibility would be to choose a quantum detector based on an InGaAs photodiode array operating in the NIR regime. With such a choice the achievement of a 2K-temperature resolution has been considered feasible if the integration times of the camera are adapted in the course of the measurement ranging from 700 to 1800 K.

It was found that, in order to maximize the scientific output of the assembly and to minimize the risks, the assembly needs to be equipped with a lens system allowing for sufficient coverage of the surface under investigation as well as to inhibit saturation of the detector and radiative overheating.

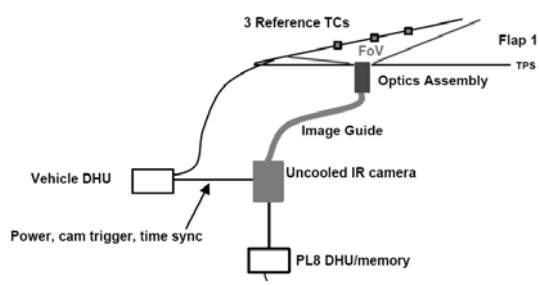

Fig. 12: Rare face infrared thermography schematics.

It is worth to highlight that the attainable accuracy on the temperature measurement is not only dependent on the selected detector but also on the intensity of the emitted radiation, which it self is a function of the temperature of the object and of the viewing angle. A rigorous calibration activity is mandatory so as to ensure reliable experimental data. To this end some “check” thermocouples in the field of view of the camera providing a calibration means have been incorporated into the flap. The overall accuracy would be a function of the thermocouples accuracy and would feature some geometrical dependence provided that the radiative properties are well known.

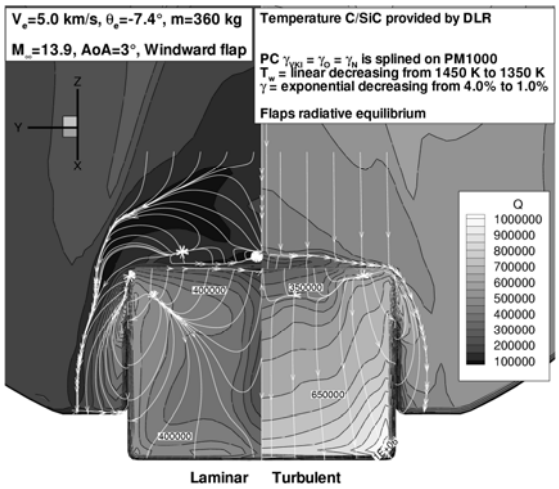

Fig. 13: Laminar and turbulent heat flux and separation bubble

Apart from the selected hardware, this measurement technique relies on the development and validation of a reliable rebuilding procedure based on a true multidisciplinary approach. Such a rebuilding procedure, currently under consolidation, is designed to take into account:

1) Convective heating of the control flap.
2) Conductive & radiative properties of the materials in the control surfaces area.
3) Re-radiative effects.
4) Flow/structure interaction.

Radiative properties of the measurement assembly affecting directly the signal to the detector (e.g. lens emissivity) will be taken into account.

The laminar and turbulent heat flux distribution on and around the leeward and windward flaps are presented in Fig. 13. The heat flux on the corner of the windward flap reaches 1.0 MW/m^2. The separation bubble is visualized with streamlines. The laminar separated bubble is much larger that the one computed assuming turbulent flow. Care should be taken, as it is known that a laminar separation combined with a turbulent reattachment provides a design case in which a transitional reattachment provides a higher heat flux than a fully turbulent case. The laminar flow show a much more complicated separated flow field then the turbulent flow, e.g. notice the secondary separation bubble. All these features hopefully will be detected in flight.

Shock-layer chemistry using emission spectroscopy: RESPECT

This instrument aims at collecting spectroscopic information during re-entry through spectrally resolved emission; the experimental data will then be compared with coupled flow field/radiation codes leading to the validation of thermo-chemical models. The RESPECT subsystem (Fig. 14 shows a two channel device) consisting of a miniaturized spectrometer, optical fibers and a lens system; the foreseen spectral range is 200-800 nm.

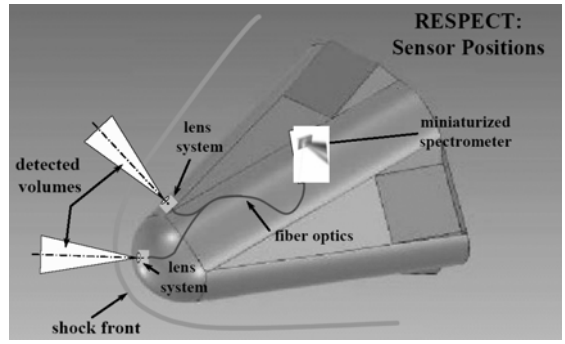

Fig. 14: RESPECT mounted on EXPERT (courtesy IRS)

The challenge of this flight instrument lies in the design of the electronics supporting the spectral measurement and the optical window through the heat shield. Preliminary activities performed at IRS demonstrated the feasibility of such a procedure.

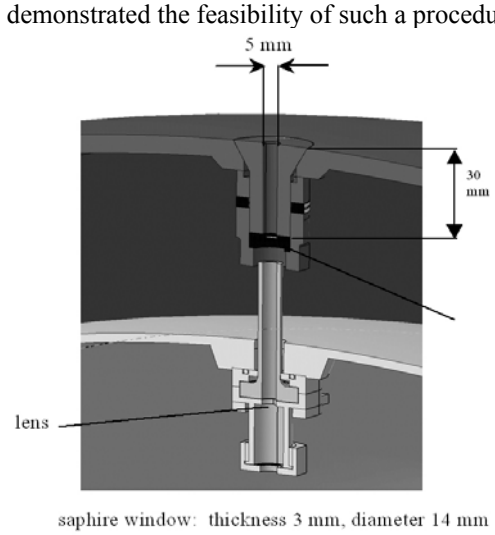

Fig. 15: Close view lens system RESPECT

Base flow measurements

This Payload aims at measuring base pressure. Local base pressure and heat flux measurements will be made to study the complex base recirculation flow field.

Skin Friction Measurements

A slip flow sensor is foreseen to be integrated in the EXPERT vehicle: this combined probe mainly designed for surface flow diagnostics in the slip- and rarefied flow regime may also be used in the laminar continuum flow regime. In the rarefied flow regime heat flux, particle flux to surface and

slip speed ratio will be measured as well as surface pressure, heat flux and skin friction during the continuum regime. The slip flow sensor has been designed with two inclined pressure taps, which are integrated in one caloric copper sensor head, ensuring same temperature for the cavities of both probes.

Sharp Hot Structures

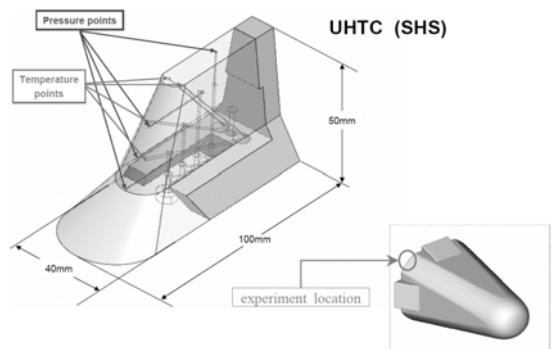

Fig. 16 Dimensions of the sharp hot structure

The objective of this payload is to fly an instrumented patch of UHTC material. The payload could be a bulk ceramic component or coated component (UHTC covered with anti-oxidation UHTC). The flight test aims at monitoring the thermal conditions of the structure. Two symmetric locations are foreseen for this Payload. The UHTC could be integrated on dummy winglets, similar to the Pitot static rakes or on a small-deflected surface at vehicle trailing edge.

Pitot static probe

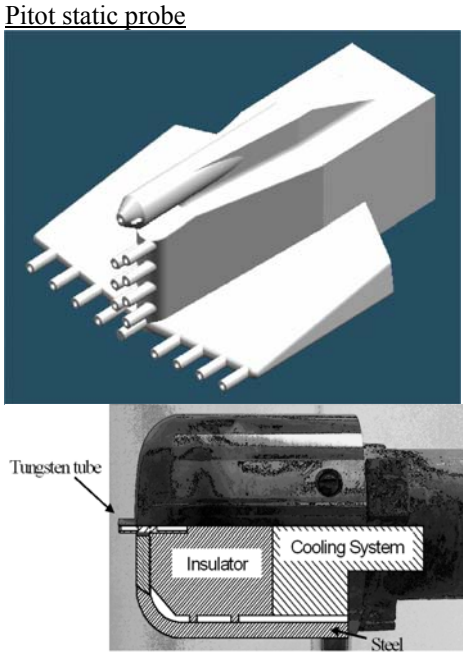

Fig. 17: Pitot static rakes and probe holder for Plasmatron testing.

EXPERT is currently foreseen to be equipped at trailing edge location with a Pitot static pressure rake in order to collect in-flight data on the boundary layer characteristics; the critical issues to be tackled are related to the conceptual design of the probe, the selection of the material, the definition of the attachment points and the location and type of transducers. The resulting characterization of the boundary layer at the trailing edge of the vehicle will further contribute to the understanding of the boundary layer laminar-to-turbulent transition phenomenon. Testing of probe elements will be performed in the VKI plasmatron; as shown in Fig 17.

CONCLUSIONS

EXPERT is an in-flight research programme, with the objective to improve our understanding of critical aerothermodynamics phenomena such as transition, real gas effects and shock wave boundary layer interactions associated with flap efficiency and heating. At present one ballistic flight (5 km/sec) is planned. If successful, it is believed that other flights are possible such as for higher speed (6 km/sec); future flights for the study of transitional flow phenomena and skipping trajectories, jet interaction, test beds for MHD/nose heat flux reduction schemes and flights for the study of advanced materials associated with high-speed re-entry.

REFERENCE

1. Muylaert, J-M.,et al, *Aerothermodynamic Environment of EXPERT and Flight Measurement Technique Integration*, IAC-05-2363, 2005.
2. Ottens, H., et al. *Aerothermodynamic Flight Measurement Techniques and Environment Issues of EXPERT*, IPPW-3, Anavysos, 2005.
3. Cipollini, F, et al, *European Activities on Advanced Flight Measurement Techniques for Hypersonic Space Vehicles,* AIAA 2006-3832, 2006
4. Massobrio, F., *Introducing the EXPERT System Features for Innovative TPS,* 5th European Workshop on TPS, 2006
5. Massobrio, F., *EXPERT: An Atmospheric Re-entry Test-bed*, ICA-04-C8.02, 2004

A mutual impedance probe for measuring the dielectric properties of the atmosphere and of the surface of planetary environments.

F. Simões[1], R. Trautner[2], R. Grard[2], M. Hamelin[1], J.-P. Lebreton[2]

[1]*Centre d'etude des Environments Terrestre et Planétaires (CETP), CNRS, 4 Avenue de Neptune, 94107 Saint Maur, France, Fernando.Simoes@cetp.ipsl.fr*

[2]*Research and Scientific Support Department (RSSD), ESA/ESTEC, Noordwijk, The Netherlands*

A mutual impedance probe is a suitable instrument for measuring the complex permittivity of a medium. A sinusoidal current is injected through two transmitting electrodes and the induced voltage is measured between two receiving electrodes. The variations of the amplitude and phase of the injected signal, with respect to their values in a vacuum taken as references, yields the permittivity and the conductivity of the medium. This technique has been successfully used on the Huygens Probe for measuring the atmospheric conductivity profile of the atmosphere and the dielectric constant of the surface of Titan. A similar instrument is included in the payload of Philae, the Rosetta lander, for measuring the surface properties of the comet Churyumov-Gerasimenko.

We describe different applications of the mutual impedance probe to the characterization of planetary environments. During the descent phase, this probe can possibly measure the complex permittivity of the ionosphere and the conductivity of the atmosphere. The sensor can also be mounted on landers, rovers, tails, drills and moles, for measuring the water/ice content of the soil and performing stratigraphic studies of the subsurface. Several electrode configurations are presented and discussed, depending upon scientific goals, host vehicle constraints, and performance requirements.

Mid-Infrared lasers for planetary explorations

Alex Soibel, Cory J. Hill, Kamjou Mansour, Yueming Qiu, Rui Q. Yang
Jet Propulsion Laboratory, California Institute of Technology, Pasadena, CA

The mid-infrared spectral range (3 - 20 μm) is of particular interest for in-situ and remote sensing of material composition as many chemical species have absorption features in this wavelength range that are associated with molecular rotational-vibration transitions. These include molecules such as H_2O, CO_2, N_2O, CH_4, CO, NH_3, NO_x, HCl, and many other compounds whose absorption spectra are shown in Figure 1a and 1b. Detection of these molecules is essential for many applications in space research, atmospheric chemistry, pollution control and industrial processing. Space research applications include in-situ and remote sensing of the gases in planetary atmospheres, isotope detection and the identification of the surface composition of planetary and lunar bodies. For example, water (H_2O) has strong absorption lines in the mid-IR spectral range, and is a critical component in biological activity. Detection of these gases with ppm and ppb concentration can be straightforwardly achieved with tunable laser spectroscopy in mid-IR.

Other applications are in Laser Reflectance Spectrometer (LRS) instruments for in-situ and remote measurements of chemical composition of solids. Spectroscopy in the 3 to 20-μm region has the potential to provide an incredible amount of information about the compositions of surfaces in the outer Solar System. However, the lack of sunlight and cold conditions, make reflected solar spectroscopy and thermal emission spectroscopy difficult to perform. Both solar illumination (<4% of the level at Earth) and thermal emission (10^{-2} to 10^{-4} the level at earth) are low in the mid-IR wavelength range. Therefore, an artificial mid-IR light source is needed. Mid-IR illuminator will enable one to determine the silicate and oxide mineralogy, ice composition, and the composition of organic materials on outer solar system surfaces.

The key components required to advance the development of mid-IR instruments are the compact, efficient and wide spectral coverage laser sources operating in 3 – 20 μm wavelength region. During the last decade, quantum cascade (QC) and interband cascade (IC) semiconductor lasers have been demonstrated and have emerged with reasonable optical powers over the entire mid-IR wavelength range of interest and have operating temperatures accessible with thermoelectric (TE) coolers. Both QC and IC lasers have recently been selected for the Tunable Laser Spectrometer (TLS) instrument on the Mars Science Laboratory, which is scheduled to launch in 2009.

Here, we will discuss our effort at JPL to develop advanced and reliable mid-IR QC and IC lasers to meet instrument demands for space exploration applications. Table 1 summarizes the operational parameters of mid-IR QC and IC lasers that were demonstrated at JPL. Challenges for their further development will be discussed.

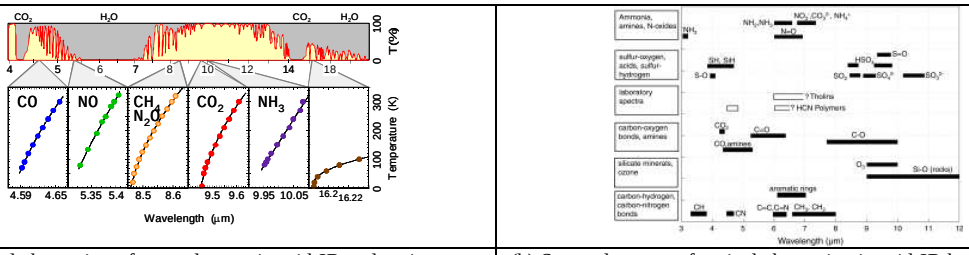

(a) Optical absorption of several gases in mid-IR and tuning range of QC lasers

(b) Spectral ranges of optical absorption in mid-IR by various chemicals

Figure 1

Laser type	Wavelength coverage	Cw operating temperature	Output power	Tunability	Power consumption
QC laser	5-12 μm	77-TE cooler	2- 400 mW	10-100 nm	2-5 W
IC laser	3-5 μm	77-264 K	1-12 mW for single-mode >400 mW for broad-area	>10 nm	0.02-1.2 W

Table 1

PLANETARY ATMOSPHERIC COMPONET MEASUREMENTS USING OSCILLATING MEMS BASED

P. W. Valek (pvalek@swri.edu),
S. Bolton (sbolton@swri.edu),
F. Crary (fcrary@swri.edu),
J. Helffrich (jhelffrich@swri.edu),
D. McComas (dmccomas@swri.edu),
J. Mitchell (jmitchell@swri.edu),
D. L. Strickland (dstrickland@swri.edu)

Southwest Research Institute,
6220 Culebra Rd
San Antonio, TX 78238

In a previous paper, we presented the concept of Micro-Electromechanical Planetary Probes (MEMPPs) [McComas et al, 2005]. MEMPPs use Micro-Electromechanical Systems (MEMS) to make highly integrated, mechanically robust probes with a much smaller size, mass, and power requirement than traditional planetary probes. These small probes allow for lower cost missions and for missions with large numbers of distributed probes. We are developing a MEMPPs sensor that will measure specific components of an atmosphere. This sensor consists of an oscillating beam with a treated surface. The surface treatment is tailored to adsorb a specific component of the atmosphere of interest, such as water or hydrogen sulfide. As material adsorbs on the oscillator, the increase in mass will cause the resonance to shift to lower frequencies. Measurement of the frequency shift tells us the concentration of the specific component in the atmosphere. This MEMPPS sensor is simple and robust, allowing it to be deployed to depths beyond that standard mass spectrometers could survive without a pressure vessel. MEMPPs including this sensor could be used to augment a traditional probe mission. A more traditional mass spectrometer would be used to make a thorough measurement of the atmospheric composition, while many MEMPPs probes focusing on a few key components of the atmosphere would be deployed with wide spatial coverage and to deeper depths than probes requiring pressure vessels.

McComas, D.J., S. Cerwin, F. Crary, J. Helffrich, J. Mitchell, D. Strickland, and P. Valek, Micro-electromechanical planetary probes (MEMPPs), *Proceedings of the 3rd International Planetary Probe Workshop*, 2005.

SESSION 6

THERMAL CONTROL AND PRESSURE VESSELS

Chairs:
Bernie Bienstock, Boeing, USA
Denis Lebleu, Alcatel, France

GALILEO PROBE THERMAL CONTROL

T. Rust, Boeing Satellite Design Center, PO Box 92919, MC W-S13-G357, Los Angeles, CA 90009, email thomas.rust-iii@boeing.com

Introduction

The Galileo spacecraft was launched in October 1989 and sent on its way to Jupiter by the Space Shuttle Atlantis. It arrived at Jupiter on December 7, 1995, where it made a successful encounter with the Jovian atmosphere. The Galileo Probe was provided by Hughes Space and Communication (HSC), which is now known as Boeing Satellite Design Center (BSDC). This study describes the Galileo Probe thermal control system performance throughout the mission, including its cruise while attached to the orbiter traveling around Venus and back around the Earth for gravitational assist along its way. A detailed review of the Probe's temperatures during its encounter with the Jovian atmosphere is presented, along with a comparison of how the temperatures compared to predicts and the ground testing prior to launch.

Cruise and Coast

Thermal performance of the Galileo Probe during both the cruise and coast phases was nominal. Temperature were within $\pm 3^{o}$C of pre-launch predictions and ground testing. Initial functional tests showed nominal performance of all Probe subsystems. After the High Gain Antenna (HGA) on the parent spacecraft failed to deploy in April 1991, warming and cooling cycles were performed by turning the spacecraft in an attempt to cycle the mechanism into releasing the stuck antenna. Probe temperatures during the thermal cycling were very closely monitored to insure no limits were exceeded. Unfortunately the thermal cycling was not able to free the stuck antenna, but no damage was done to the Probe in the efforts. A final Probe check-out was performed just prior to release from the orbiter in July 1995, again showing nominal performance of all Probe subsystems. The Probe release was completed flawlessly, and the Probe thermal control system performed nominally during the entire 150 day coast period.

Descent

Probe temperature telemetry indicated colder than expected temperatures during the early descent and warmer than expected during later descent. At the 13 bar level, the Probe RF units were at or below Qualification levels and all other science and engineering units were at or below Acceptance levels, but both were noticeably above predicts. The Galileo Probe mission was a resounding success in spite of the thermal extremes seen during its descent. The cause of the thermal extremes is believed to be higher than expected convective currents flowing through the Probe since it was not sealed and was subjected to significant buffeting during its descent. These temperature extremes were not seen during ground test since it was tested in a non-moving, stagnant environment. Additional detail on the Probe temperatures during descent is provided in the reference.

Reference

1997 AIAA Applied Aerodynamics, Plasmadynamics and Lasers, and Thermophysics Conference, 97-2456, "Galileo Probe Descent Post-Flight Thermal Correlation Analysis," Brian Mischel, Tom Rust, and Fred Linkchorst, June 23, 1997.

PRESSURE VESSEL TECHNOLOGY DEVELOPMENTS
4th INTERNATIONAL PLANETARY PROBE WORKSHOP
27 June – 30 June, 2006 Pasadena, California, USA

Michael Pauken[(1)], Elizabeth Kolawa[(1)], Ram Manvi[(1)], Witold Sokolowski[(1)], Joseph Lewis[(1)]

[(1)] *Jet Propulsion Laboratory, 4800 Oak Grove Dr. M/S 125-109, Pasadena, CA 91109, USA, Email: michael.t.pauken@jpl.nasa.gov*

ABSTRACT

Historically, titanium and aluminum have been used as structural shells or pressure vessels for extreme environment planetary probes and landers. Improvements in the state-of-the-art of pressure vessel materials are sought to reduce the mass of such components by 20 to 50% over titanium shells. The pressure vessel represents the single largest mass element for deep atmospheric probes at Venus, Jupiter and the other Gas and Ice Giants, or landers to the surface of Venus. The high loads on the spacecraft due to atmospheric entry, landing and external atmospheric pressure require high strength structures and new fabrication techniques. Significant improvements to the overall spacecraft design can be realized by reducing the overall mass of the pressure vessel to allow additional payload mass. New structural shell materials exhibit high strength and stiffness at elevated temperatures and are resistant to creep and buckling under high external pressures.

1. INTRODUCTION

The Decadal Survey identified missions to the surface of Venus and the Jupiter Deep Atmospheric Probe as 2 of the 6 highest priority science missions. The present state-of-the-art pressure vessel material, titanium, represents one of single largest mass elements for a Venus Lander or Deep Atmospheric Probe. Given that this material has been used since the early 1970s as the structural shell for these kinds of missions, it is worth examining material improvements over the last 3 decades to see if significant mass reductions can be realized with different shell materials. The pressure vessel for a Venus Lander mission about 1 m diameter would have a mass around 200 kg if it were made of titanium. Using new materials and manufacturing methods, it appears that mass reductions on the order of 50% can be realized over a monolithic (solid metal) titanium shell. However, the Technology Readiness Level (TRL) for these new materials and manufacturing methods as they would apply to a spherical shaped structural shell are typically around TRL 3 even though they may have significant heritage in other applications. Lighter weight pressure vessels impact the whole flight system by reducing the loads carried by the structures within the aeroshell, carrier spacecraft bus and the launch vehicle itself. This is especially significant when designing structures for handling the atmospheric entry loads encountered for missions to Venus or Jupiter which can have decelerations as high as 200 to 300 Gs. This paper describes an investigation into new materials and their associated manufacturing processes for fabricating a spherical shaped pressure vessel (or structural shell) that has potential for use in a space flight mission to the surface of Venus or through the atmosphere of any of the Gas Giant Planets.

2. HISTORICAL PERSPECTIVE

In 1961 the Soviet space agency started an extensive Venus exploration program that eventually included orbiters, atmospheric probes, landers and balloon missions. The program was very successful resulting in many completed missions but it took Soviets many years to learn how to survive and conduct science investigations in Venus environment. In the late seventies NASA conducted a multiprobe mission, Pioneer Venus, aimed at understanding Venus atmosphere.

The Soviet program lasted more than two decades from their first attempt to send a spacecraft to Venus – Venera 1 launched in 1961 to their last mission, VEGA1 and 2, in 1984 which included both a lander and a high altitude balloon on each of two vehicles. The two spacecraft continued to an encounter with Halley's Comet after deployment of their payloads at Venus.

The first spacecraft, Venera 1, had no provision for surviving entry. At that time, Venus was believed to have a much thinner atmosphere and benign temperatures than those we know today. As successive missions were launched they had increasing levels of capability and were equipped to deal with the more severe environmental conditions. In 1965, Venera 3

was the first successful spacecraft to land (by impact) on another planet. However, it was designed to withstand 5 bars external pressure and 80ºC temperature. From 1967 through 1969, Venera 4, 5 and 6 were sent to Venus and were designed to withstand 300ºC and 25 bar. When Venera 5 and 6 were sent, it was known that the surface temperature of Venus was 427ºC and the surface pressure was at least 75 bar. However, it was too late to change the design of those spacecraft. A drawing of the Venera 5 descent module is shown in Fig. 1.

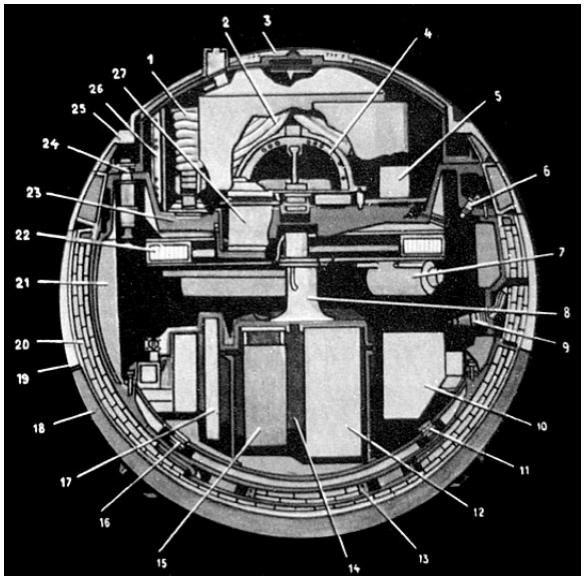

Fig. 1. Venera 5 Descent Module Layout showing all systems were protected by a pressure vessel with passive thermal control.

By 1970, Venera 7 was designed to survive 150 bar and 540ºC and used a titanium spherical pressure vessel. The earlier Venera landers used a hemispherical capsule. This spacecraft successfully survived on the Venus surface for 23 minutes becoming the first spacecraft to transmit from another planet. When Venera 8 was launched in 1972, scientists had accurate estimates of the temperature and pressure environment on Venus. The titanium pressure vessel was designed for surviving 490ºC and 100 bar. It transmitted data from the Venus surface for 50 minutes. A drawing of the Venera 8 descent module layout from [1] is shown in Fig. 2.

The remaining Venera missions 9-14 continued to use the same spherical pressure vessel design criteria as Venera 8, however, they were larger in diameter and were mostly successful missions. Venera 13 and 14 were launched in 1981. The limiting factor in the later missions was communication time with the flyby spacecraft. Fig. 3 shows a photograph of the Venera 13 Lander.

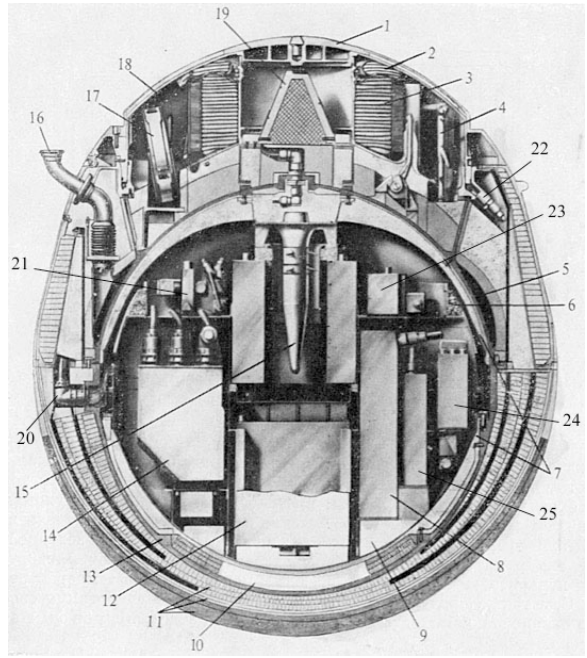

Fig. 2. Venera 8 Descent Module Layout showing the systems packed in a spherical pressure vessel.

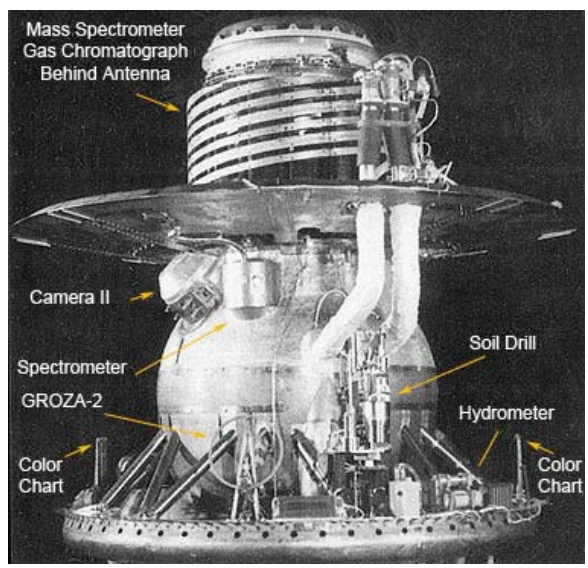

Fig. 3. Venera 13 external configuration photograph.

The only NASA mission to the Venus surface was Pioneer Venus which was launched in 1978. It consisted of one large probe and three small proves. The large probe had a 78 cm diameter titanium pressure vessel while the small probes at 47 cm diameter pressure vessels. Only one of the small proves survived on the surface; none of them were specifically designed

to survive landing. Fig. 4 as in [2] and [3] shows an inside view of the Pioneer Large probe.

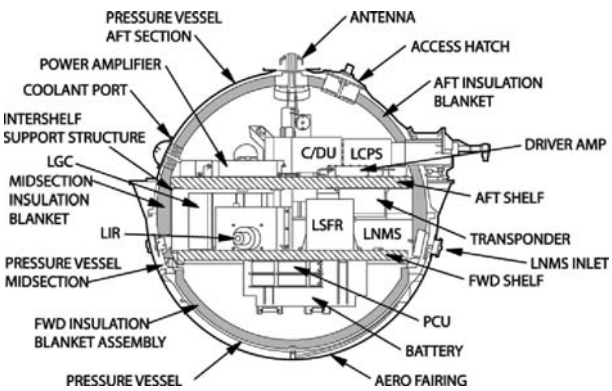

Fig. 4. Pioneer Venus Large Probe interior layout.

A summary of the general development trend in the pressure vessel ratings for missions to the Venus surface is shown in Table 1.

Table 1. Historical Summary of Pressure Vessel Ratings for Venus Landers

Mission	Launch	Pressure Rating
Venera 3	1965	5 bar
Venera 4	1967	20 bar
Venera 5,6	1969	25 bar
Venera 7	1970	150 bar Titanium
Venera 8-14	1972-1981	100 bar Titanium
Pioneer Large Probe	1978	100 bar Titanium
Pioneer Small Probe	1978	100 bar Titanium

PRESSURE VESSEL DESIGN GUIDELINES

A standard set of guidelines was established to compare different pressure vessel materials to one another. Three basic mechanical parameters were used to estimate pressure vessel mass for a given shell diameter. The shell must satisfy these criteria at a temperature of 500ºC: (1) No buckling at the ultimate load of 150 atm pressure using standard NASA knockdown factor of 0.14 for pressure vessels. The common industry standard knockdown factor is 0.30. Knockdown factors account for imperfections in the material and the manufacturing process which deviate from the ideal case. The elastic modulus determines the bucking limit. (2) No yielding at the proof load of 125 atm pressure. The yield strength determines the yield limit. (3) Total allowable creep in 10 hours under 100 atm external load must be less than 0.5%.

These criteria are evaluated based on compressive yield strength, compressive modulus, and creep strain rates. Additional necessary requirements for the pressure vessel material include impermeable to gases and compatibility with the Venus chemical environment. It is also desirable to have low conductivity, however, this requirement can be mitigated against through better insulation. Other factors to be considered in selecting shell materials include: fracture toughness, heat capacity, and thermal expansion coefficient.

Several material candidates were examined to determine their suitability for a spacecraft pressure vessel operating in a Venus environment. These materials were compared to the current state-of-the-art material titanium-6Al-4V. Materials were classified as metallics or composites and are listed below:

Metallic Materials

- Titanium Beta S
- Nickel-chromium alloys: Inconel 718, Inconel X and Haynes 230
- Nickel-chromium-cobalt alloys: Haynes 188
- PH stainless steels: 17-7 PH or 15-5 PH
- Beryllium I-220H

Advanced Composite Materials

- Silicon carbide fiber reinforced titanium matrix
- Boron fiber reinforced titanium matrix
- Inorganic Sialyte based composite
- Aluminum-sapphire carbide metal matrix
- Aluminum-silicon carbide metal matrix
- Epoxy Polymer matrix composite

MATERIAL EVALUATIONS

Inconel 718 showed the best performance in both creep and tensile property comparisons and is the best metallic candidate for a pressure shell using a honeycomb sandwich construction. The high density of nickel alloys prohibits them from being considered for monolithic shell designs. Ti-6Al-4V was the second best performer in the creep and tensile comparisons at temperature. This is the traditional Venus lander spacecraft pressure vessel material and is fabricated in a monolithic shell.

Haynes 188 was originally selected as a candidate because of its superior creep properties at high temperature. However the operating temperature of the pressure shell (500ºC) is not high enough to utilize the creep resistance of Haynes 188. The Haynes 188 alloy (cobalt base) was designed to perform in the 900ºC to 1100ºC range where it is clearly superior to the other

materials selected. At 500ºC it is no better than Inconel 718. Haynes 188 was not retained for further consideration.

15-5 PH showed reasonable creep properties at 500ºC, but the creep resistance falls very rapidly in this material above 500ºC leaving little margin. 15-5 PH was not retained for further consideration. Creep data was not available for 17-7 PH. However it is not expected to perform significantly better than 15-5 PH and was not be retained for further consideration.

Beryllium is lightweight and has high elastic modulus, high thermal conductivity and high specific heat but low creep resistance in tension at temperature. Toxicity issues raise concerns regarding fabrication; however established vendors are available to fabricate beryllium products.

In all the metal candidates, bucking was the limiting criteria except for beryllium because of its high elastic modulus. A comparison of elastic modulus as a function of material density at room temperature is shown in Fig. 5 for the metallic candidates. At 500ºC, the magnesium and aluminum alloys drop out of consideration. Beryllium clearly has the highest modulus per unit mass of all candidates even at 500ºC. It is limited by yield and creep.

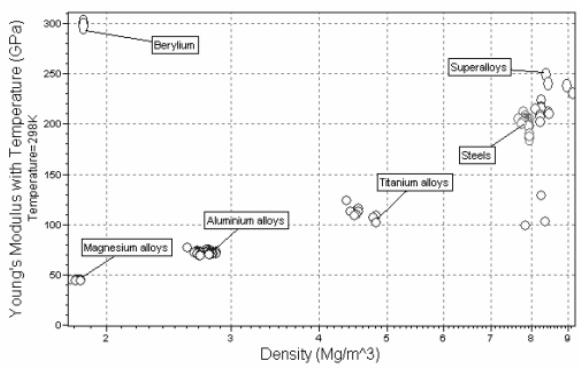

Fig. 5. Modulus comparisons of various metals at room temperature.

SiC/Ti matrix composite has superior strength/density performance compared to other materials. It is creep resistant at 500ºC. It is suitable for fabricating a monolithic shell configuration. Boron fiber titanium matrix composite has good strength to density performance but the boron fibers degrade significantly above 400ºC. It could possibly be used with an external insulation system that would keep the shell temperature below the degradation temperature limit; however it was decided not to pursue this option.

Sialyte is a trademarked inorganic resin product developed by Cornerstone Research Group. The resin is used to fabricate lightweight fiber-reinforced composite structural components. It has a low coefficient of thermal expansion, and relatively high compressive strengths offering consistent performance up to 900ºC. However, it did not have sufficient strength to be considered as a viable candidate for a Venus Lander pressure vessel.

The aluminum-sapphire carbide metal matrix and aluminum-silicon carbide metal matrix are fabricated by passing sapphire-carbide fibers or silicon carbide fibers through a bath of molten aluminum and then wrapped around a mandrel. The process is similar to the method used to make composite pressure cylinders. This allows lightweight tanks to be made without aluminum liners for gas retention. These materials/processes are worth consideration for a Venus Lander pressure vessel but they have not been thoroughly evaluated. The composite material properties are dependent upon the manufacturing technique which needs to be developed for a hemispherical geometry featuring flanges, feed-throughs, ports etc.

An epoxy polymer matrix composite material using the trademarked name Kiboko has been developed by Composite Technology Development Inc. to fabricate lightweight linerless composite wound pressure vessels. It has been primarily developed for storing cryogenic materials or for gases around room temperature. A novel toughened epoxy resin provides the sealing necessary to eliminate the need for a tank liner. Two issues with this material are similar to those above with the aluminum-silicon carbide material: (1) manufacturing a wound product into hemispherical shapes that incorporate many complicating features and (2) performance at high temperatures has not been demonstrated so it may require an exterior insulation system to prevent premature failure.

MANUFACTURING METHODS

Three different pressure vessel configurations have been identified based on the different materials that were considered in this study. Monolithic shells can be fabricated from titanium or beryllium, which has been the traditional manufacturing process for spacecraft landing on Venus' surface. Composite wrapped shells are commonly seen in pressure cylinders and the technology is well developed. This manufacturing technique would be used for aluminum/sapphire or aluminum/silicon carbide or Polymer Matrix Composite materials. Honeycomb sandwich shells are often

formed into curved geometries for aircraft engine cowlings for example. This is an appropriate fabrication technique for Beta S titanium or Inconel 718.

Fabricating a monolithic shell for a pressure vessel uses fairly common manufacturing processes. A titanium hemisphere can be shaped using spin forming. Flanges, windows, feed-throughs, brackets etc. can be welded onto the shell to create the spacecraft pressure vessel. An example of a three piece sphere is shown in Fig. 6. A three piece sphere allows two equipment shelves to be mounted to a central ring, while the forward and aft sections of the sphere serve as caps mounted to the center section.

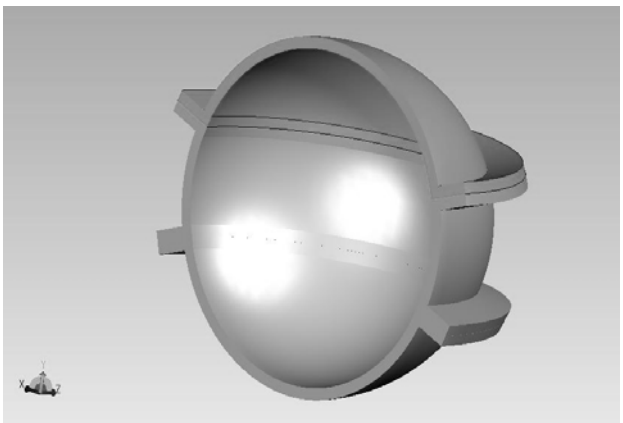

Fig. 6. Cut-Away sectional view of a 3 piece monolithic shell.

Fabricating a monolithic shell out of beryllium can be more difficult than out of titanium. Beryllium is a brittle material and cannot be shaped by spin forming. The spherical sections would have to be machined from solid billets. Flanges and windows etc. cannot be welded to a beryllium shell so these features would have to be machined as part of the shell from the parent billet material. A three piece spherical shell is preferred for beryllium because the billets for each section would be smaller than if it were made into hemispheres. It also would reduce rework costs if mistakes were made during the fabrication process by having to scrap say only 1/3 of the sphere instead of ½ of the sphere. Issues regarding toxicity of beryllium during fabrication processing are of concern and must be dealt with. Also, the vendors qualified to work with beryllium are limited.

Composite wrapped tanks are now commonplace and the latest innovations involve linerless tanks. The impermeable aluminum liner has been replaced by using resins that form a gas-tight barrier which resists microcracking as the pressure cylinder is loaded and unloaded over its lifetime. The manufacturing process consists of passing the wrapping fibers through wet adhesive such as molten aluminum or epoxy. The wetted matrix is then wrapped around a mandrel to form the tank shape. The composite wound tank is then cured at an elevated temperature to set the tank. A picture of composite wound linerless tanks is shown in Fig. 7. While this process is conducive to fabricating pressure cylinders or composite tubes, it has not be used to fabricate hemispherical sections. Thus the manufacturing process for creating a structural shell for a spacecraft with flanges, windows, feed-throughs etc still needs to be developed.

Fig. 7. Linerless composite tanks developed by Composite Technology Development Inc.

Honeycomb sandwich construction produces strong lightweight panels for many applications. While a large majority of honeycomb structures are flat panels, many curved components are fabricated with a honeycomb sandwich construction. To manufacture a spherical shaped segement using honeycomb requires forming the inner and outer facesheets into the desired shape using a bulge-form technique. A picture of a bulge forming tool is shown in Fig. 8. The honeycomb core is made by diffusion bonding thin corrugated sheet (ribbon) sliced to the desired web thickness. The core is then bulge-formed to match the inner and out facesheets. The core is assembled to the facesheets in a special toolset and a braze alloy is added to bond the facesheets to the core. For a titanium structure, TiCuNi braze alloy would be used, while for Inconel the braze alloy would be BNi-8. There are several methods of completing the brazing process, but typically the assembly would be placed in a vacuum braze furnace. A vacuum braze furnace is shown in Fig. 9. When the brazing process is complete, the tool set is removed and the part is ready for attaching features such as windows, flanges,

brackets, etc. Adding these components would require cutting the shell for openings and brazing in window ports for example. Flanges and brackets would be brazed on to the shell.

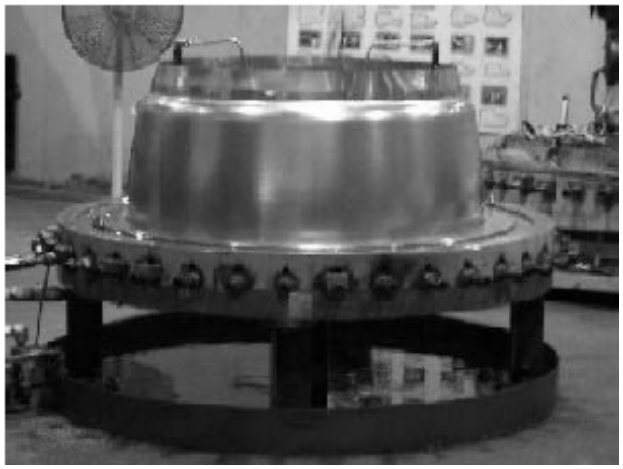

Fig. 8. A typical bulge forming tool for fabricating honeycomb facesheets.

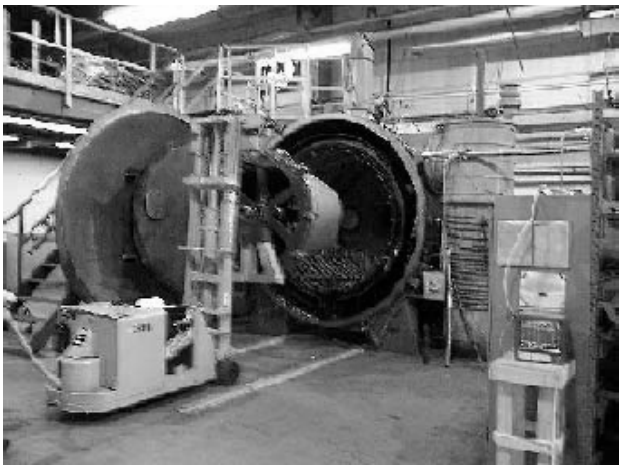

Fig. 9. A vacuum braze furnace for bonding honeycomb structures.

CONCLUSIONS

Development of improve materials and manufacturing methods for fabricating space qualified pressure vessels or structural shells is far from complete. Some of the remaining technology development tasks to improve the current state-of-the-art include: (1) Develop more detailed manufacturing engineering plans for the leading candidate materials. There are many issues involved in fabricating a simple hemispherical shape that can be sealed together with a mating part. Adding features such as optical windows, electrical feedthroughs, flanges, brackets etc. makes the manufacturability of a spacecraft shell even more challenging. (2) Estimate comparative fabrication costs for the different manufacturing technologies. This can help select which technologies are financially feasible to pursue further development. (3) Obtain samples/prototypes of shells from leading candidate materials to demonstrate that the technology is practical. And (4) Perform testing on subscale prototypes under Venus-like environmental conditions for temperature and pressure survivability. The materials and the manufacturing methods examined in this study have the potential for reducing the mass of titanium baseline pressure vessel for a mission to a high pressure/temperature environment by 30 to 50%.

ACKNOWLEDGEMENTS

This work was performed through an internal research and development effort at the Jet Propulsion Laboratory, California Institute of Technology under a contract with the National Aeronautics and Space Administration.

REFERENCES:

1. Kerzhanovich, V. and Pichkhadze, K., *Soviet Veneras and Mars: First Entry Probes Trajectory Reconstruction and Science,* International Workshop on Planetary Probe Atmospheric Entry and Descent Trajectory Analysis and Science, Lisbon Portugal, 2003.
2. Bienstock, B.J., *Pioneer Venus and Galileo Entry Probe Heritage,* International Workshop on Planetary Probe Atmospheric Entry and Descent Trajectory Analysis and Science, Lisbon Portugal, 2003.
3. Hennis, L.A. and Varon, M.N., *Thermal Design and Development of Pioneer Venus Large Probe*, Thermophysics and Thermal Control, Vol. 65 of Progress in Astronautics and Aeronautics, 1978.

RHU management for planetary probe thermal control

Denis LEBLEU, ALCATEL ALENIA SPACE, 100 boulevard du midi BP99 06156 CANNES La Bocca CEDEX, denis.lebleu@alcatelaleniaspace.com

Radioisotope Heater Unit is of major benefit for deep space missions:

- Constant (almost) heating dissipation all along the mission,
- No impact on power budget
- Easy implementation
    - Small volume
    - Easy spreading inside the probe
    - No wiring

This device allows simple and flexible thermal control for all of the deep space phases of the mission.

However, during the initial phases of the mission, where the thermal environment is relatively warm with regard to the deep space one, presence of RHU can induced severe constraints on the probe.
The number of RHU and their implementation inside the probe is defined considering the constraints in the coldest environment. During integration of the probe on ground, the particular configuration of entry probes could induce overheating, as the heat is trapped within the probe. Dedicated devices should be implemented for the on-ground phases, including the operation on the Launcher.

A comparison of the philosophy followed for different missions will be performed, including the HUYGENS probe to TITAN, and missions to Mars as the NASA MER, and the CNES NETLANDER mission for which ALCATEL was EDLS prime contractor before the mission cancellation.

Thermal Engineering for the Beagle 2 Mars Lander Surface Operations

Bryan Shaughnessy, Rutherford Appleton Laboratory, UK

Beagle 2 was a mission to place a scientific Lander on Mars to search specifically for evidence of past or present life and to conduct geochemical and environmental investigations. It was launched aboard the European Space Agency's Mars Express in June 2003 and was scheduled to land in the Isidis Planitia region of Mars in late December 2003.

The Rutherford Appleton Laboratory was responsible for the thermal engineering of Beagle 2. This presentation will summarise the development and testing of the thermal control sub-system for the landed operations.

RADIOISOTOPE POWER SYSTEMS FOR IN-SITU EXPLORATION OF TITAN AND VENUS

Tibor S. Balint
Jet Propulsion Laboratory, California Institute of Technology,
4800 Oak Grove Drive, M/S 301-170U
tibor.balint@jpl.nasa.gov

In-situ exploration of moons and planets are essential to answer questions about the formation of our solar system and habitability. NASA's Solar System Exploration Road Map, in line with recommendations by the National Research Council, identified five flagship class missions over the next three decades. Two of these would have months to years of operation at or near the surfaces of Titan and Venus, whose deep atmospheres greatly attenuate the amount of solar energy reaching the surface. These vehicles must operate under vastly different conditions. While the near surface environment of Titan is cold (-178°C), the temperature and pressure on Venus could reach +460°C and 90 bars, respectively. Their high density atmospheres lend themselves to air mobility mission architectures, two of which utilize balloons and airships. Space missions are typically mass and power limited. While balloons could significantly increase traversing – compared to surface rovers – the benefits would be offset by reduced payload mass. Therefore, the selection of suitable power sources for these missions is critical. Energy storage devices (batteries and fuel cells) greatly limit mission duration. Thus, it is expected that long lived in-situ missions to destinations where solar power is not available, would require internal power sources, such as Radioisotope Power Systems (RPS). On Titan, beside power generation, the excess heat from an RPS could be used to heat a Montgolfière (hot air) balloon; therefore, plutonium reduction for this mission would not be a key driver. However, the cold environment would necessitate re-sizing of the cooling fins of the Multi-Mission Radioisotope Power System (MMRTG), considered for this architecture. (An advanced RPS with improved specific power could increase power to the spacecraft, but would require technology development.) Conversely, on Venus, extreme environment mitigation would call for a new type of RPS; a Stirling Radioisotope Generator, which could generate power while providing active cooling to the instruments inside the pressure vessel. In this paper, further discussions are given on RPS requirements and possible configurations for these proposed Titan and Venus missions, performing in-situ science investigations and validation of remote sensing measurements.

(Note: document review pending)

SESSION 7

ELECTRONICS, COMMUNICATION AND BATTERIES

Chairs:
Jim Arnold, UCSC, USA (jarnold@mail.arc.nasa.gov)
Thierry Blancquaert, ESTEC, France (Thierry.Blancquaert@esa.int)
Wayne Johnson, Aurburn University, USA (Johnson@eng.aurburn.edu)

SILICON-GERMANIUM INTEGRATED ELECTRONICS FOR EXTREME ENVIRONMENTS

John D. Cressler

School of Electrical and Computer Engineering
777 Atlantic Drive, N.W., Georgia Tech, Atlanta, GA 30332-0250 USA
(404) 894-5161 / cressler@ece.gatech.edu

Invited Paper

The extreme temperature conditions on the lunar surface (at worst case, -230°C in shadowed polar craters, and across -180°C (night) to +120°C (day) with 28 day cycles) precludes the use of conventional electronics for sensing, actuation, and control. Currently, this need for protective electronic "warm boxes" critically limits the mission architect's ability to create a truly distributed, modular electronics systems, resulting in excessive point-to-point wiring, increased system weight and complexity, lack of modularity, and an overall reduction in system reliability. We intend to change this situation.

The overall goal of this project is to develop and demonstrate extreme environment electronics components required for electronic systems with distributed architecture, using low-cost, commercial silicon-germanium (SiGe) BiCMOS technology. Unlike other COTS integrated circuit technologies, SiGe BiCMOS offers unparalleled cryogenic temperature performance (to 4K), inherent total dose radiation tolerance, wide temperature range capability, and optimal monolithic mixed-signal circuit design flexibility, by offering power efficient high-speed transistors (SiGe HBTs) together on the same piece of silicon wafer with high density Si CMOS and a suite of passive components.

This NASA ETDP project directly addresses the development of: 1) low-power, radiation tolerant (to 300 krad to support Moon+Mars missions), integrated SiGe BiCMOS mixed-signal (digital + analog + power) electronic components for sensor/imager and control/actuator systems that can operate reliably across -180°C to +120°C; 2) High-density packaging of these SiGe BiCMOS electronic components (with integrated passives); and 3) modeling/CAD tools for both SiGe BiCMOS devices and packaging, to accurately predict and simulate the electrical performance, reliability, and radiation tolerance of these SiGe BiCMOS mixed-signal circuits and packages. This SiGe ETDP team includes: Georgia Tech (lead), JPL, Auburn University, University of Tennessee, IBM, Boeing, BAE Systems, Lynguent, University of Arkansas, Vanderbilt University, and the University of Maryland.

Acknowledgement

This work was supported by NASA, under grant NNL05AA37C, and the Georgia Electronic Design Center at Georgia Tech. We are grateful for the support of C. Moore, M. Watson, M. Beatty, L. Nadeau of NASA, E. Kolawa of JPL, and the IBM SiGe development group, as well the many contributions of the SiGe ETDP team, including: M. Mojarradi, B. Blalock, W. Johnson, R. Garbos, R. Berger, F. Dai, G. Niu, L. Peltz, A. Mantooth, P. McCluskey, M. Alles, R. Reed, A. Joseph, and C. Eckert.

ANALOG/DIGITAL CIRCUIT DESIGN IN SiGe FOR SPACE APPLICATIONS

Tiejun Cao, Electrical Engineering Dept., University of Arkansas, tcao@uark.edu
Richard Broughton, Electrical Engineering Dept., University of Arkansas, rbrough@uark.edu
Jayamadhuri Penumarthi, Computer Science and Computer Engineering Dept., University of Arkansas, jpenuma@uark.edu
Jia Di, Computer Science and Computer Engineering Dept., University of Arkansas, jdi@uark.edu
H. Alan Mantooth, Electrical Engineering, University of Arkansas, mantooth@uark.edu
Contact Author: Jia Di; ENGR 311, CSCE Dept., University of Arkansas; Fayetteville, AR 72701

***Abstract* – This paper reports on both analog and digital circuit designs in Silicon-Germanium (SiGe) that are designed to operate over the lunar temperature extremes. The design of a variable gain amplifier (VGA), and digital circuits using synchronous and asynchronous logic styles for comparison working under low temperatures are described.**

I. INTRODUCTION

Silicon-Germanium (SiGe) BiCMOS technology has demonstrated the capability to provide excellent high-performance characteristics with very low noise, high power gain, and excellent linearity. The bandgap engineering employed in the design of SiGe HBTs generally favors their operation at cryogenic temperatures. Thus, SiGe circuits hold much promise for applications to the extreme environments of space applications. Analog and digital circuits are designed in SiGe to operate over the lunar temperature extremes.

Sensor systems are critical parts for space exploration vehicles. In particular, to improve the accuracy of collected data, the signals output from sensors should be pre-processed prior to transmission and further processing. The high variability of the sensor's signal output has to be regulated so that a suitable signal level can be applied to subsequent circuitry such as analog-digital converters (ADCs). For that reason, the VGA plays a fundamental role in optimizing system capacity. Sensors are often exposed directly to the environment in order to perform their function. The environment of space can exhibit large temperature swings.

VGAs are widely used in wireless communications, industrial scanning, radar, ultrasound, and speech-analysis applications that require a wide dynamic range of a continuous voltage. There are many different topologies used to realize VGAs. Common approaches use analog multipliers [1]-[3], variable transconductance [4], [5], variable loads [4], [6], variable feedback [7], [8], and attenuator networks [9]. In this paper, a VGA for wide temperature applications is proposed. It is based on a variable gain transconductance topology. The gain of the VGA is designed to vary from 1 to 50 per requirements of the overall system.

While working under low temperatures, CMOS digital circuits are able to operate faster because of better carrier mobility in the device's channel. Since sometimes this performance enhancement is either not required or even unwanted, it provides the opportunity to reduce power consumption. The circuit will achieve the same performance under lower supply voltage while operating at low temperatures. Since power consumption of CMOS digital circuits is roughly proportional to V_{DD}^2, the use of lower supply voltage will produce much lower power consumption, which is a critical consideration for space applications. Asynchronous circuits have the potential for even better power efficiency than normal synchronous circuits. Synchronous circuits have to toggle clock lines and charge signals in those circuit blocks that are not processing useful data for a computation. For asynchronous circuits, even though they typically need more transistors to achieve equivalent functionality, only the transistors in the area of a current computation will be actively drawing power. Asynchronous circuits are also more adaptable to changes in temperature and supply voltages. A synchronous circuit would have to adjust its clock to the worse case critical path delay for the entire temperature and voltage range in which the circuit is to operate. Since asynchronous circuits use handshaking signals to sense completion, they automatically adjust to the delay changes caused by these variations.

Three simple pipelined circuits have been designed in synchronous logic and two asynchronous logic styles, namely, delay-insensitive and bounded-delay. The bounded-delay circuit used the traditional micropipeline structure approach [10]. In this methodology, standard Boolean-based combinational logic is combined with asynchronous control which employs C-elements. The delay-insensitive circuit design used NULL Convention Logic ™ (NCL) [11]. This type of asynchronous design employs dual-rail encoding to represent data and NULL states in order to incorporate control information to data as well as to provide hysteresis.

II. VGA CIRCUIT DESCRIPTION

The block diagram of the VGA is shown in Fig. 1. The VGA consists of a VGA core A1 and a buffer circuit A2. A1 is based on a classic differential pair, whose transconductance is adjusted by varying the tail bias current I_{CTRL}, as shown in Fig. 2 [12]. A2 can provide a single-ended output and cancel a common-mode voltage variation at the output of A1. In order to make the gain independent of temperature, "ratioing" of the resistors and currents is implemented. The gain of the VGA is

$$A = \frac{R_2}{R_1}\frac{I_{CTRL}}{I_1}\frac{R_L}{R_E} \tag{1}$$

A. VGA Core

The circuit of VGA core A1 has two stages. The first stage has a constant gain. The feedback within the first stage linearizes the overall circuit gain. The second stage is a traditional differential pair. The transconductance of the two transistors in this pair is controlled by I_{CTRL}, which is the current to control the gain of the VGA core.

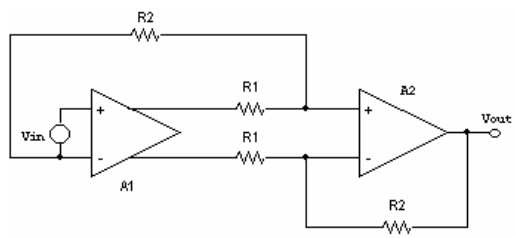

Fig. 1. The block diagram of the VGA circuit.

The gain of the second stage is

$$A_{V2} = -g_m R_L \tag{2}$$

where

$$g_m = \frac{I_{ctrl}}{2V_T}$$

thus,

$$A_{V2} = -\frac{I_{CTRL}}{2V_T} R_L \tag{3}$$

For the first stage, Q3, Q4, Q5 and Q6 act as a feedback circuit for the differential pair Q1and Q2. Transistor pairs Q3, Q5 and Q4, Q6 form CC-CE configurations with $g_m = \frac{I_1}{V_T}$.

Therefore, the feedback factor is given as follows,

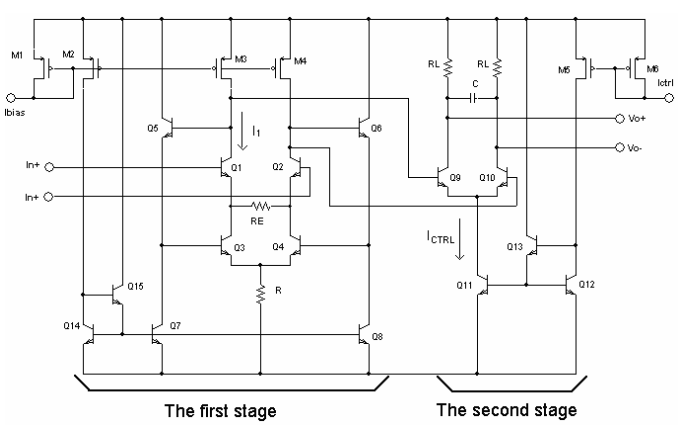

Fig. 2. The schematic of VGA core circuit.

$$\beta = g_m \frac{R_E}{2} = \frac{I_1}{V_T}\frac{R_E}{2}. \tag{4}$$

The open loop gain of the Q1-Q2 differential pair is assumed large, thus

$$A_{V1} \cong \frac{1}{\beta} = \frac{2V_T}{I_1.R_E}. \tag{5}$$

As a result, the overall gain is [10]

$$A_1 = A_{V1}A_{V2} = \frac{2V_T}{I_1.R_E}\frac{I_{CTRL}}{2V_T}.R_L = \frac{I_{CTRL}}{I_1}\frac{R_L}{R}. \tag{6}$$

To achieve a constant gain over a wide temperature range, the ratio $\frac{I_{CTRL}}{I_1}$ and $\frac{R_L}{R_E}$ must be held constant.

Reducing the mismatch between R_L and R_E is critical to maintaining a constant ratio. R_L and R_E are chosen as 4.4 kΩ and 1 kΩ, respectively. An off-chip current reference source was used to produce I_{CTRL} and I_1 for testing purposes, but an on-chip current reference is the subject of additional wide temperature design activity.

B. Buffer Circuit

The variable control current leads to a common-mode voltage variation at the output of the VGA core. A buffer (A2 from Fig. 2) shown in Fig. 3 is introduced in order to cancel this effect and provide a single-ended output.

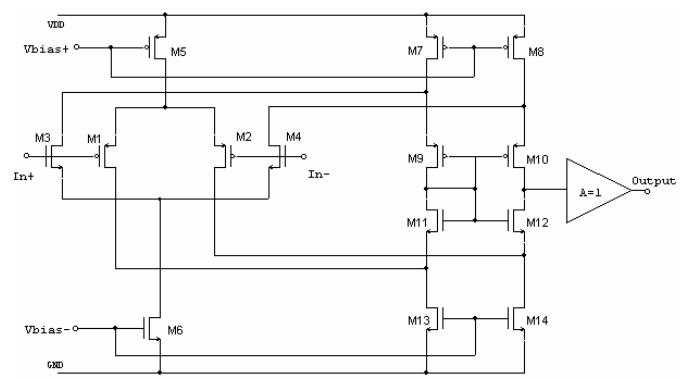

Fig. 3. The schematic of the buffer circuit (A2 in Fig. 1).

The folded cascode amplifier provides a wide-band frequency response and high gain with a single stage. However, its high output resistance makes it difficult to interface with other circuits. A unity gain buffer at the output of the folded cascode circuit addresses this issue.

The low frequency gain of the folded cascode stage is

$$A_V = G_m R_0 \tag{7}$$

where G_m is the total transconductance of the input stage, which is given by [13]

$$G_m = g_{m1} + g_{m3}. \tag{8}$$

The R_0 is the small-signal resistance looking into the drain of M10 and M12, thus (7) becomes

$$A_V = (g_{m1} + g_{m3})(g_{m10}r_{08}r_{010} // g_{m12}r_{014}r_{012}). \tag{9}$$

In order to achieve an open-loop gain over temperature that remains sufficiently large such that the closed-loop gain of A2 remains determined by the feedback factor (i.e., the ratio of two resistor values here), the authors chose to maintain a constant inversion coefficient (IC) (defined below). A constant inversion coefficient has the advantage of canceling out

temperature variation due to changing thermal voltage. For each transistor, the moderate inversion characteristic current I_S is given by,

$$I_S = \frac{2\mu C_{ox} V_T^2}{k}(\frac{W}{L}) \tag{10}$$

The *IC* for each transistor may be calculated as the ratio of drain current to the moderate inversion characteristic current as follows [14],

$$IC = \frac{I_D}{I_S} \tag{11}$$

A transistor having $IC > 10$ clearly operates in strong inversion region and has a transconductance proportional to the square root of drain current. A transistor having $IC < 0.1$ clearly operates in weak inversion region and has a transconductance proportional to the drain current. Generally, $IC = 1$ is the crossover point between weak and strong inversion.

In weak inversion, the transconductance of the transistors is

$$g_m = \frac{kI_D}{V_T} \tag{12}$$

where k is the subthreshold gate coupling coefficient. A typical value of k is 0.7. In strong inversion region, g_m is

$$g_m = \sqrt{2\mu C_{ox}(\frac{W}{L})I_D} \tag{13}$$

Therefore, the relative transconductance can be derived as follows,

$$\frac{g_m}{I_D} = \frac{kI_D/V_T}{I_D} = \frac{k}{V_T} \tag{14}$$

in weak inversion, and

$$\frac{g_m}{I_D} = \frac{\sqrt{2\mu C_{ox}(\frac{W}{L})I_D}}{I_D} = \sqrt{\frac{2\mu C_{ox}(\frac{W}{L})}{I_D}} \tag{15}$$

in strong inversion.

We can rewrite (9) in terms of the relative transconductance and drain current as follows,

$$A_V = (g_{m1} + g_{m3})\left[g_{m10}\frac{V_A}{I_{D8}}\frac{V_A}{I_{D10}} // g_{m12}\frac{V_A}{I_{D14}}\frac{V_A}{I_{D12}}\right] \tag{16}$$

Note that we have $g_{m10} = g_{m12}$, $I_{D8} = I_{D14}$, and $I_{D10} = I_{D12}$, Therefore, the gain of the buffer becomes

$$A_V = \frac{1}{2}\frac{g_{m10}}{I_{D10}}(\frac{g_{m1}}{I_{D8}} + \frac{g_{m3}}{I_{D8}}).V_A^2 \tag{17}$$

In strong inversion, the gain is

$$A_V = \sqrt{\frac{\mu_p C_{ox}(\frac{W}{L})_{10}}{2I_{D10}}}\left[\frac{\sqrt{2\mu_p C_{ox}(\frac{W}{L})_1 . I_{D1}}}{I_{D8}} + \frac{\sqrt{2\mu_n C_{ox}(\frac{W}{L})_3 I_{D3}}}{I_{D8}}\right]V_A^2 . \tag{18}$$

In weak inversion, the gain is

$$A_V = \frac{1}{2}\left(\frac{kV_A}{V_T}\right)^2\left[\frac{I_{D1}}{I_{D8}} + \frac{I_{D3}}{I_{D8}}\right]. \tag{19}$$

From (10), we have

$$\mu C_{ox}(\frac{W}{L}) = \frac{kI_S}{2V_T^2} . \tag{20}$$

Therefore, (18) becomes

$$A_V = \frac{1}{2}(\frac{KV_A}{V_T})^2\sqrt{\frac{1}{k}\frac{1}{IC_{10}}}\left[\sqrt{\frac{1}{k}\frac{1}{\eta_1}\frac{1}{IC_1}} + \sqrt{\frac{1}{k}\frac{1}{\eta_3}\frac{1}{IC_3}}\right] \tag{21}$$

where $\eta_1 = (\frac{I_{D8}}{I_{D1}})^2$ and $\eta_3 = (\frac{I_{D8}}{I_{D3}})^2$.

From (19), in weak inversion, we also have

$$A_V = \frac{1}{2}(\frac{kV_A}{V_T})^2\left[\sqrt{\frac{1}{\eta_1}} + \sqrt{\frac{1}{\eta_3}}\right] \tag{22}$$

Since the transistors are identical, η_1 and η_3 are constant over temperatures.

From (21) and (22), the open loop gain of the buffer over temperature is primarily affected by V_T if *IC* is kept constant. The overall gain of the buffer circuit depends on the ratio of the feedback resistors and thus the gain is constant over temperature.

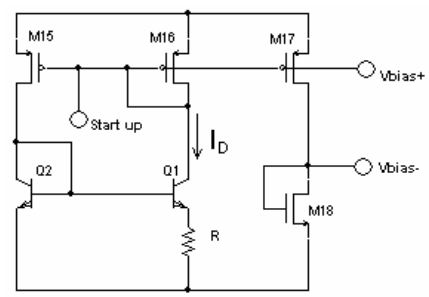

Fig. 4. The bias configuration for the buffer circuit.

To keep $IC = \frac{I_D}{I_S}$ constant, a proportional to absolute temperature (PTAT) current source bias is used. Because I_S depends on V_T^2 which is strongly dependent on temperature, I_S will increase when temperature increases. Therefore, the bias current I_D also has to increase with the temperature. From Fig. 4, we have

$$I_{C2} = \frac{V_T}{R}\ln(N) \tag{23}$$

where N is the ratio of base-emitter junction areas of Q1 and Q2.

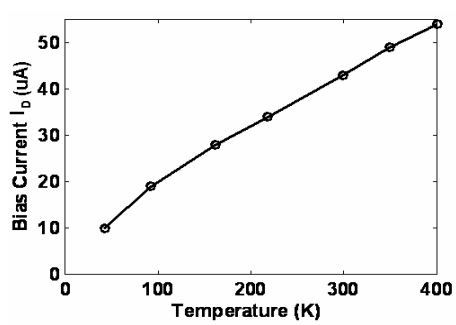

Fig. 5. The bias current of buffer circuit versus temperature.

Fig. 5 shows the relationship between the bias current and temperature. *N* equal to 5 is chosen from the simulation results in order to keep *IC* constant.

III. Experimental Results

The VGA circuit was fabricated in the IBM SiGe 5AM BiCMOS process. A die photograph of the VGA circuit is shown in Fig. 6. The circuit performed over a wide temperature range from 43 K to 300 K. There are four main specifications: gain (1-50), bandwidth (> 1MHz), slew rate (10 V/µs) and input capacitance (< 25pF). These measured results met the main design specifications. Fig. 7 shows the VGA gain characteristics at different temperatures. Fig. 8 describes the VGA slew rate characteristics over the wide temperature range.

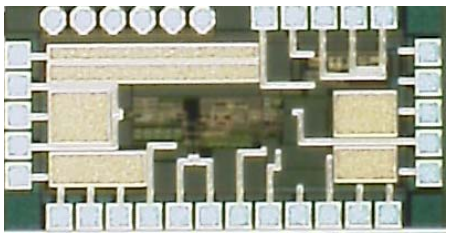

Fig. 6. Die photograph of the VGA.

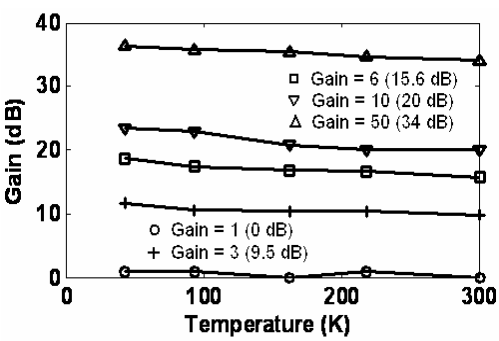

Fig. 7. VGA gain characteristics over cryo temperatures.

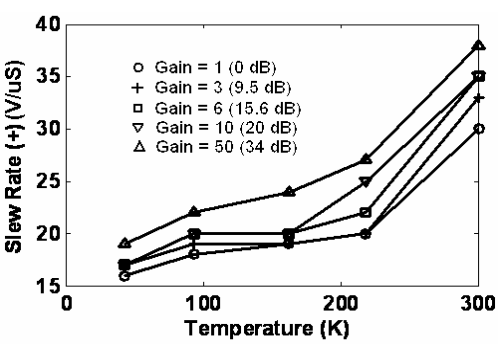

Fig. 8. VGA slew rate characteristics over cryo temperatures.

IV. Digital Circuit Description

A. Pipelined Circuit Comparison

A supply voltage scalability comparison of regular synchronous digital logic and the two asynchronous digital logic styles is being performed in order to determine which logic style would be best suited to extreme environment space application. So far simulations of simple pipelined circuit structures suggest that there is an advantage to using asynchronous logic.

Simple Pipelines Circuits

In order to make the comparison as fair as possible, the same circuit topology was constructed with all three design methods. The topology chosen was a small pipeline structure that is shown in Fig. 9 which contains three register stages with full adders between them. Thus the circuits performed the same function on the data, but each circuit was constructed based on its different design methodology.

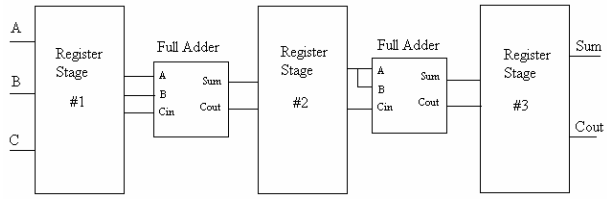

Fig. 9. Topology for comparison circuits.

Simulation Results

The lowest operating voltage levels for all three circuits at the three cold temperature points as well as room temperature are shown in Table 1. In these simulations the two asynchronous circuits were both able to operate at 0.2 volts lower supply voltage then the synchronous circuit at the colder temperatures. The NCL circuit performed particularly well in these simulations, and was able to operate at even lower supply voltages then the bounded delay circuit.

Table 1. Simulated lowest operating voltages

	25 °C	-111 °C	-180 °C	-230 °C
Synchronous Circuit	1.35 V	1.35 V	1.28 V	1.31 V
NCL Circuit	1.05 V	1 V	0.95 V	1 V
Bounded Delay Circuit	1.5 V	1.1 V	1.1 V	1.08 V

These circuits have been fabricated and experimental measurements will be taken to validate the results of the simulation. While this is happening, the comparison has been taken a step further by designing an asynchronous microcontroller to be compared to a synchronous counterpart.

B. Design of Asynchronous Microcontroller

A dual-Rail 8-bit asynchronous microcontroller has been designed using the delay- Insensitive NULL Convention Logic ™ (NCL) paradigm. The microcontroller mainly consists of Instruction Decoder, Arithmetic Logic Unit (ALU), and Register File. It has no memory and the opcode is the primary input. There are two interfacing circuits (wrappers) at the input and output to communicate with any synchronous devices.

Instruction Set:

Operation Type	*Instruction Type*	*Mnemonics*	*Description*
Data Transfer	LOAD	LD Rx	Store data into Rx register.
	MOVE	MOV Rx, Ry	The contents of Ry is copied to Rx
	OUT	OUT Rx	The contents of Rx are output from microcontroller
Logical	AND	AND Rx ,Ry	The operands of Rx and Ry are ANDed and result is stored in Rx.
	OR	OR Rx ,Ry	The operands of Rx and Ry are ORed and result is stored in Rx
	XOR	XOR Rx ,Ry	The operands of Rx and Ry are XORed and result is stored in Rx
Arithmetic	ADD	ADD Rx ,Ry	The operands of Rx and Ry are ADDed and result is stored in Rx
	NOT	NOT Rx	The operands of Rx are complemented.

The block diagram of the microcontroller is shown in Fig. 10.

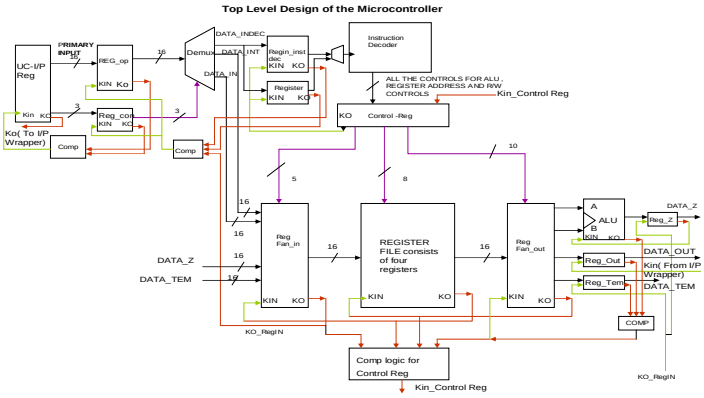

Fig. 10. The block diagram of the microcontroller.

Instruction Decoder

It's a combinational circuit consists of threshold gates. The instructions are the inputs and the outputs are the controls for the ALU and Register file.

ALU

The ALU consists of an adder, a logic unit and a NOT block. It's a pipelined structure. The adder is a 2NCL 8-bit Ripple Carry Adder which performs addition on the 8-bit dual-rail input. The Logic unit performs AND, OR and XOR operations.

Register File

The Register file consists of four general-purpose Registers and one temporary register. The general-purpose registers have consume/produce Structure, which consists of phase inverted storage /consume registration stage followed by a produce registration stage, both coordinated by a two value control. The temporary register supports the MOVE operation and is a simple ring structure.

At this time the cold temperature simulations of this asynchronous microcontroller as well as its synchronous counterpart are still being performed. The preliminary results show the asynchronous microcontroller is able to work at lower supply voltage under low temperature.

V. Conclusion

This paper demonstrated the operating principle and experimental results of a VGA circuit featuring temperature stable operation, as well as the advantage of asynchronous logic over synchronous counterpart on supply voltage scaling under low temperature for designing digital electronics for space applications. The circuit works over a wide range of temperatures. Maintaining a constant inversion coefficient provided a reasonable tradeoff to maintain gain versus temperature. Measurement results satisfy the main specifications. Future work includes circuit optimization and reducing noise.

References

[1] T. Pan, and A. A. Abidi, "A 50-dB Variable Gain Amplifier using Parasitic Bipolar Transistors in CMOS," *IEEE Journal of Solid-State Circuits*, vol.24, no.4, pp. 951-961, August 1989.

[2] M. Franciotta, G. Colli, and R. Castello, "A 100-MHz 4-mW Four-Quadrant BiCMOS Analog Multiplier," *IEEE Journal of Solid-State Circuits*, vol.32, no.10, pp.1568-1572, Oct. 1997.

[3] J. Hakkinen, T. Rahkonen, and J. Kostamovaara, "A 100-MHz to 1 GHz Variable Gain Amplifier in a 8 GHz 1.2mm BiCMOS Process," *Analog Integrated Circuits and Signal Processing,* vol.15, no.2, pp.169-181, Feb. 1998.

[4] R. Gomez, and A. A. Abidi, "A 50-MHz CMOS Variable Gain Amplifier for Magnetic Data Storage Systems," *IEEE Journal of Solid-State Circuits*, vol.27, no.6, pp.935-939, June 1992.

[5] J. J. Rijns, "CMOS Low-Distortion High Frequency Variable Gain Amplifier," *IEEE Journal of Solid-State Circuits*, vol.31, no.7, pp.1029-1034, July 1996.

[6] T.H. Hu, and P. R. Gray, "A Monolithic 480 Mb/s Parallel AGC/Decision/Clock Recovery Circuit in 1.2-mm CMOS," *IEEE Journal of Solid-State Circuits*, vol.28, no.12, pp.1314-1320, Dec 1999.

[7] J.N. Babanezhad, and R. Gregorian, "A Programmable Gain/Loss Circuit," *IEEE Journal of Solid-State Circuits*, vol.22, no.6, pp.1082-1090, Dec 1987.

[8] A.L. Wittenberg, M.L. Simpson and G. R. Young, "A CMOS Variable Gain Amplifier for PHENIX Electromagnetic Calorimeter and RICH Energy Measurements," *IEEE Trans. Nuclear Sci*, vol.44, no.3, pp.326-330, June 1997.

[9] J. Bales, "An BiCMOS Digitally-Controlled Variable Gain Wideband Amplifier," *Proceedings of the IEEE BiCMOS Circuits and Technology Meeting, pp. 84-87, 1997*.

[10] Ivan E. Sutherland, "Micropipelines" *Communications of the ACM*, vol. 32, no. 6, pp. 720-738, June 1989.

[11] K. Fant, *Logically Determined Design: Clockless System Design with NULL Convention Logic™*, 1st ed., New York: Wiley-Interscience, pp. 36-41, 2005.

[12] F. Carrara, P. Filoramo, and G. Palmisano, "High-dynamic-range decibel-linear IF variable-gain amplifier with temperature compensation for WCDMA applications," *Circuits and Systems, 2003. ISCAS '03.*, vol.1,SC-9, pp. I289-I292, May 2003.

[13] Adel S. Sedra, Kenneth C. Smith, *Microelectronic Circuits*, Oxford University Press, New York, 2004.

[14] D. M. Binkley, C. E. Hopper, S. D. Tucker, B. C. Moss, J. M. Rochelle, and D. P. Foty, "A CAD Methodology for Optimizing Transistor Current and Sizing in Analog CMOS Design," *IEEE Trans. Computer-Dided Design of Integrated Circuits and Systems*, vol.22, no.2, pp.225-237, Feb. 2003.

DEVELOPMENT OF AN EXTREME ENVIRONMENT DC MOTOR DRIVE FULL BRIDGE POWER STAGE USING COMMERCIAL-OFF-THE-SHELF COMPONENTS

John Garrett[1], Roberto Schupbach[1], H. Alan Mantooth[2], Alexander B. Lostetter[1]

[1]Arkansas Power Electronics International, Inc., 700 Research Center Blvd., Fayetteville, AR 72701, USA, Email: john@apei.net
[2]University of Arkansas, Fayetteville, AR 72701, USA, Email: mantooth@uark.edu

Abstract – Spacecraft electronic systems routinely experience extreme environmental conditions, including cryogenic temperatures. Radioisotope Heating Units (RHUs) are commonly used to keep the electronic systems at warmer temperatures; however, the RHUs continually produce heat, are expensive, and add complexity and weight to the spacecraft. Previous research efforts have shown several commercial-off-the-shelf (COTS) components, both active and passive, can perform well in cryogenic environments, thus allowing for lower weight and complexity of the electronic systems aboard spacecraft. This paper details the cryogenic testing (down to -184 ºC) of COTS components commonly used in DC motor drive power stages. The performance of silicon carbide (SiC) diodes and transistors at cold temperatures was evaluated, followed by the building and testing (down to -184 ºC) of a cryogenic 20 W full bridge power stage for motor drive applications.

1. INTRODUCTION

Spacecraft electronic systems which experience cryogenic temperatures in their mission lifetimes are normally heated to more suitable temperatures for operation (i.e. 20 ºC). This is done through the use of Radioisotope Heating Units (RHUs). Since RHUs constantly produce heat, thermal systems must be installed on the spacecraft to dissipate the heat when it is not needed, adding complexity and weight to the vehicle that could be better utilized. RHUs could potentially be eliminated through the use of commercial-off-the-shelf (COTS) components that have been found to operate reliably in these extreme environments. The COTS components studied in this research included the following elements that are commonly used in motor drives: resistors, capacitors, gate driver integrated circuits, diodes, and transistors. For each component, several technologies were evaluated in order to determine which technology could potentially yield the best performance at cold temperatures. Emerging silicon carbide (SiC) device technology was evaluated as well.

This paper is divided into seven sections. The second section discusses the overall test setup and the procedures followed for the cryogenic testing. The results of the cryogenic testing of the COTS components, component specific tests, as well as the additional equipment utilized to conduct the tests are presented in sections three and four. Section three details the passive elements tests and results, while section four details the active elements tests and results. The COTS components selection and the construction of the DC motor drive power stage are detailed in section five, followed by conclusions and references in sections six and seven, respectively.

2. TEST SETUP AND PROCEDURES

The cryogenic testing of the components and the power stage was conducted using a Delta Design 9028 environmental test chamber configured to use liquid nitrogen as a coolant to achieve the various cold temperatures down to -184 ºC. The components were placed inside the chamber and the tests were performed at different temperatures. The resistors, capacitors, high/low side gate drivers, and power stage were each tested at the following temperatures in the specified sequence: +25 ºC, 0 ºC, -55 ºC, -100 ºC, -125 ºC, -150 ºC, -175 ºC, and -184 ºC. The diodes and transistors were tested at the following temperatures in the specified sequence: +25 ºC, 0 ºC, -55 ºC, -100 ºC, -150 ºC, and -184 ºC.

Each component was allowed to soak at each temperature for 15 minutes to ensure that its internal temperature reached steady state before any test circuits were energized to investigate the component's performance. After cryogenic testing, each component was allowed to warm to room temperature (+25 ºC) and then retested to see what effects a single temperature cycle might have had on its performance.

3. PASSIVE ELEMENTS

3.1 Resistors

Resistors are a crucial part in gate drive and dead-time setting circuits. Nine resistor types were cryogenically tested in order to determine the performance of the different technologies at cryogenic temperatures, including; thick film, thin film, metal film, metal oxide, vitreous enamel, and metal foil resistors. The resistance of each resistor was measured with an HP 4261A LCR meter. Fig. 1 shows the results of the resistor tests versus temperature. In this figure, the resistances indicated are normalized to each individual resistor's room temperature resistance. It can be seen that most of the resistors demonstrated good performance over temperature, while a few did not. Most notably, the Ohmite thick film and the metal oxide resistors performed relatively poorly. When the resistors were retested at room temperature, it was observed that the single temperature cycle had little effect on most of the resistors. Two of the resistor types (Ohmite thick film and metal oxide) suffered some increases in resistance (0.01% and 0.36%, respectively) after the temperature cycle. From the results it can be seen that most of the resistors would be good for cryogenic applications except for the Ohmite thick film and the metal oxide resistors.

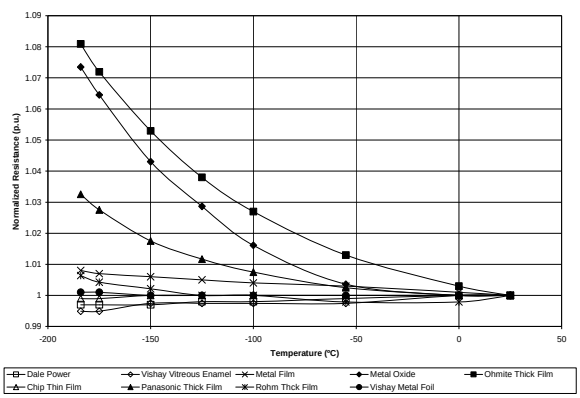

Fig. 1. Normalized resistance (p.u.) vs. temperature.

3.2 Capacitors

High performance capacitors are vital in most motor drive circuits. They are used for filtering and for providing instantaneous power to circuits under quick load changes.

Eight different types of capacitors were cryogenically tested in order to evaluate the performance of several capacitor technologies. These included the following: metallized polypropylene, polypropylene, polyethylene, NPO, X7R, and several tantalums. Both the capacitance and dissipation factor of each capacitor was tested with and without a 30 VDC bias placed across the capacitor using a HP 4261A LCR meter and an external voltage source. The LCR meter was operated with the test frequency selector set for 1 kHz.

Fig. 2 and Fig. 3 show the results of the capacitor tests versus temperature where each capacitor has a 30 VDC bias placed across it. In Fig. 2, the capacitances indicated are normalized to each individual capacitor's room temperature capacitance. It is observed that the NPO, metallized polypropylene, and polypropylene types of capacitors exhibited slight increases in capacitance as their temperature was lowered. The remainder of the capacitors exhibited a decrease in capacitance as the temperature was lowered. Notably, the polyethylene and all of the tantalum types showed a decrease of less than 10% of their room temperature capacitance, whereas the X7R type showed the worst performance, a capacitance at -184 ºC that was approximately 41% of its room temperature capacitance. In Fig. 3, the dissipation factor of each capacitor is shown. From the figure it can be seen that all three tantalum capacitors and the X7R performed relatively poorly compared to the other capacitors.

When the capacitors were retested at room temperature, it was observed that all but one was affected in terms of capacitance after a single temperature cycle. The X7R type suffered a 5.36% decrease in capacitance with no DC bias placed across it, and a 0.94% decrease in capacitance with a 30 VDC bias placed across it. There was no change observed in the dissipation factors.

From the results, it can be concluded that the metallized polypropylene, polypropylene, polyethylene, and NPO types would be the best choice for cold temperature applications. Tantalum types would also be good choices if the application requires higher energy storage capabilities, provided that the larger dissipation factors are acceptable.

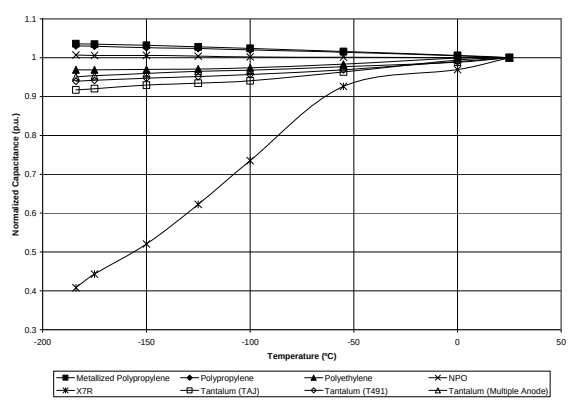

Fig. 2. Normalized capacitance (p.u.) vs. temperature.

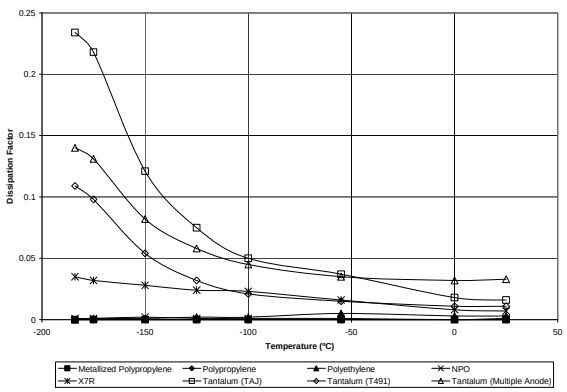

Fig. 3. Dissipation factor vs. temperature.

4. ACTIVE ELEMENTS

4.1 High/Low Side Gate Drivers

It is often necessary to use high/low side gate drivers in order to properly charge and discharge the large capacitances of power switching devices effectively, to provide isolation, and/or to generate a high side signal to drive the high side device in a half bridge.

Two different gate driver integrated circuit technologies were evaluated; silicon and silicon-on-insulator (SOI). Gate drivers based on BJT technology were not examined in this work due to recent research efforts indicating relatively poor performances of bipolar based integrated circuits at cold temperature [2,3]. Three gate drivers fabricated with silicon processes and one gate driver fabricated with an SOI process were chosen to be examined. The three silicon devices were the following: an IR2110S from International Rectifier, a L6385 from ST Microelectronics, and a MIC4100YM from Micrel Incorporated. The SOI gate driver chosen was the Phillips UBA2033. It is a high frequency full bridge driver IC designed as a commutator for high intensity discharge lamps, but can be configured to be a half bridge driver.

The performance of the gate drivers was evaluated by measuring the following time durations of the low side output while driving an external 1000pF capacitive load: turn-on propagation delay, turn-off propagation delay, turn-on rise time, and turn-off fall time. In addition, the supply current drawn by each gate driver was measured as the temperature was decreased. The measurement method used for the time duration measurements can be more clearly understood by referencing Fig. 4

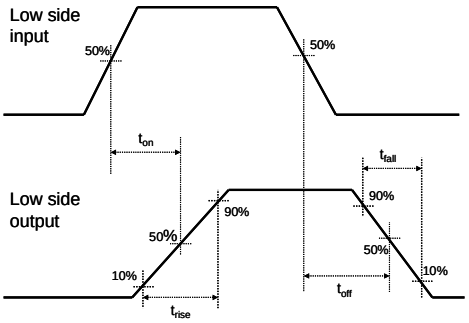

Fig. 4. Description of high/low side driver measurements.

A 20 kHz, 50% duty cycle square wave signal with an amplitude of 10 Volts was applied to the input of the drivers if independent low and high side inputs were available on the driver. If the driver did not have independent inputs, the same square wave signal would be applied to the single input available. A 15 VDC supply voltage was applied to the three silicon drivers, whereas a 13 VDC supply voltage was applied to the Phillips SOI driver. The input supply current was measured with a Tektronix DM 502A multi-meter. The cursor functionality of a Tektronix TDS 3014B oscilloscope was used to measure the turn-on rise time, turn-off fall time, turn-on propagation delay, and turn-off propagation delay of the low side output of each driver.

Fig. 5 through Fig. 8 show the turn-on propagation delay, turn-off propagation delay, turn-on rise time, and turn-off fall time of the gate drivers. From the results, it was seen that the Micrel MIC4100YM provided the best performance in terms of the change (smallest) in the time durations measured as the temperature was decreased. On the other hand, the SOI-based gate driver exhibited the largest change in the measured time durations as the temperature was decreased.

Fig. 9 shows the current supplied to each gate driver versus temperature. The IR2110S and the MIC4100YM both exhibited an increase in supply current as the temperature was decreased, whereas the ST L6385 showed a decrease in supply current as the temperature was decreased. The SOI driver exhibited both a rise and then a fall in the supply current as the temperature was decreased.

When the gate drivers were retested at room temperature, it was observed that the single temperature cycle had no effect on the gate drivers examined. From the test results, it can be seen that the silicon gate drivers provided the best performance when compared to the SOI gate driver at cryogenic temperatures. The Micrel MIC4100YM provided the best performance overall.

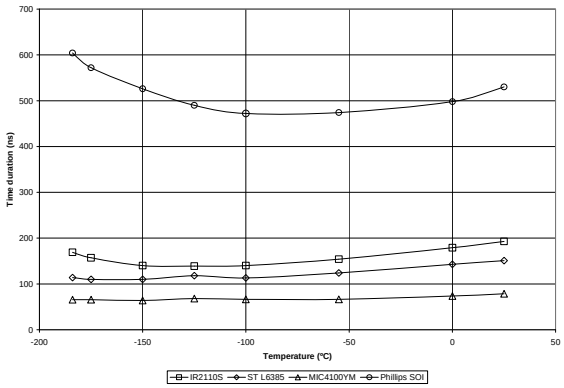

Fig. 5. Driver turn-on propagation delay vs. temperature.

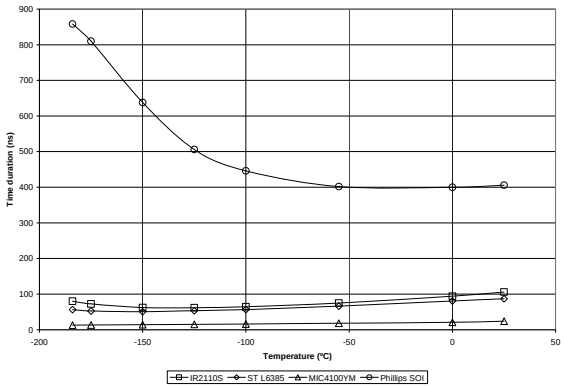

Fig. 6. Driver turn-off propagation delay vs. temperature.

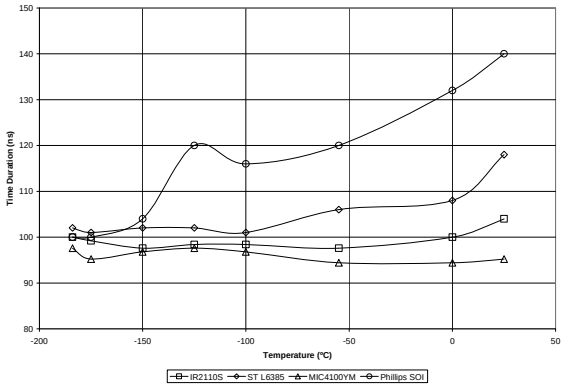

Fig. 7. Driver turn-on rise time vs. temperature.

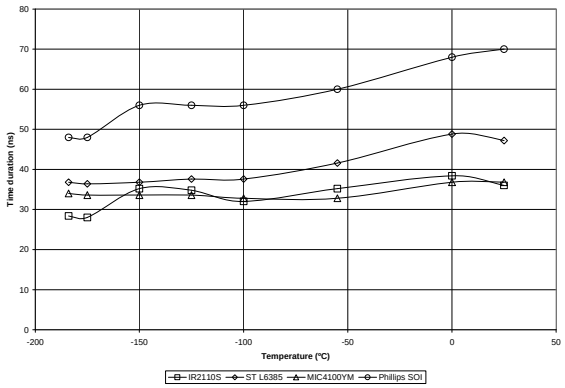

Fig. 8. Driver turn-off fall time vs. temperature.

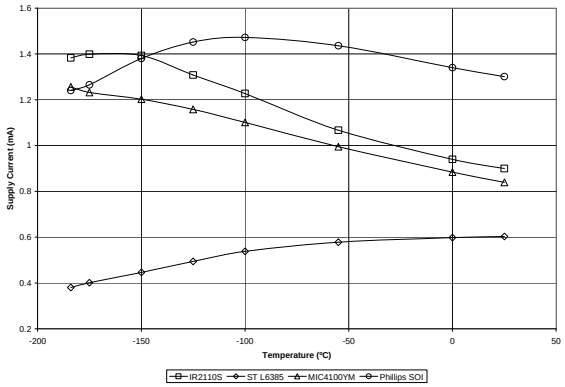

Fig. 9. Driver supply current vs. temperature.

4.2 Diodes and Transistors

Diodes and transistors that perform well at cryogenic temperatures are essential in order to efficiently and properly control the flow of power in power electronic circuits. For the diodes, three different technologies were evaluated: silicon schottky, silicon super-fast, and SiC schottky.

The following diodes were chosen to be tested: a 3 Amp 60 Volt silicon MBRS360TR schottky rectifier from International Rectifier, a 2 Amp 50 Volt silicon ES2A super-fast rectifier from Diodes Incorporated, and a 10 Amp 300 Volt SiC CSD10030 schottky diode from Cree. A Tektronix 371B programmable high power curve tracer was utilized to measure the forward voltages, on-resistances, and reverse breakdown voltages.

Fig. 10 through Fig. 12 show the diode forward voltages, on-resistances, and reverse breakdown voltages versus temperature. The results indicated that the silicon diodes followed roughly linear trends as the temperature decreased. On the other hand, the SiC diode did not follow this trend. In Fig. 10, it can be

observed that the forward voltage for each of the silicon diodes increased in a linear fashion as the temperature was lowered, whereas the forward voltage for the SiC diode increased in a non-linear manner. The on-resistances of the diodes, as seen in Fig. 11, show a similar behavior. Here, as the temperature is decreased, the on-resistances of the silicon diodes decrease almost linearly; however, the on-resistance of the SiC diode increases dramatically. In Fig. 12 the reverse breakdown voltages changed very little with respect to decreasing temperature. The silicon super-fast diode reverse breakdown voltage stayed approximately the same. The silicon schottky diode reverse breakdown voltage decreased slightly, whereas the breakdown voltage of the SiC schottky showed a small increase.

When the diodes were retested at room temperature it was observed that the diode forward voltages and reverse breakdown voltages were unaffected by the single temperature cycle; however, the on-resistances of each of the silicon diodes increased by approximately 14% after the single temperature cycle, and the on-resistance of the SiC diode increased by approximately 15% after the single temperature cycle. It is unknown at this point if this increase in on-resistance is a result of the temperature cycle on the packaging or the device itself, and it should be further investigated.

Based on the results, it can be concluded that silicon diodes are a good choice for cryogenic applications. The SiC diode, however, performed relatively poorly, primarily due to carrier freeze-out occurring at the low temperatures, and is not recommended for cryogenic applications.

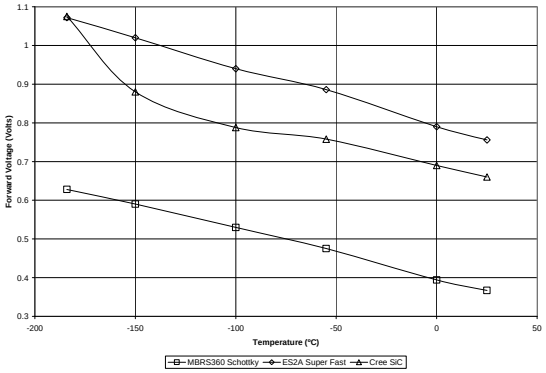

Fig. 10. Diode forward voltage vs. temperature.

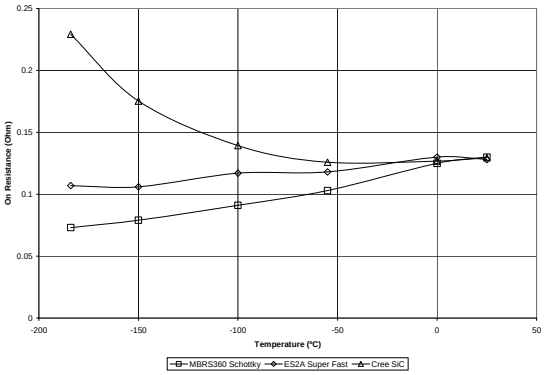

Fig. 11. Diode on-resistance vs. temperature.

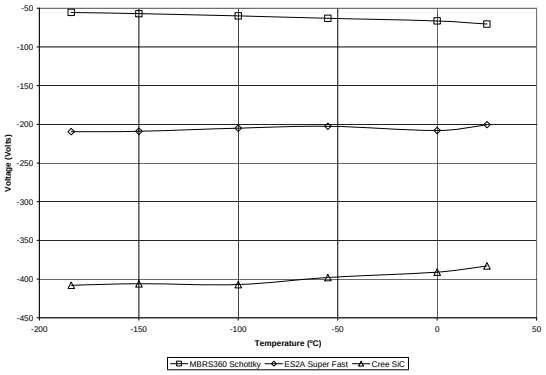

Fig. 12. Diode reverse breakdown voltage vs. temperature.

For the transistors, the following device technologies were examined: silicon MOSFET, SOI MOSFET, and SiC JFET. For each of the transistor technologies studied, the threshold voltages, on-resistances, and breakdown voltages were measured. BJT types of power devices were not investigated due to recent research efforts indicating poor performance of bipolar based parts when subjected to cold temperatures [1-3]. The following transistors were chosen to be tested: a 1.5 Amp 100 Volt silicon IRLL110 HEXFET power MOSFET from International Rectifier, a 1.5 Amp 55 Volt SOI HTNFET from Honeywell, and a 5 Amp 1500 Volt SiC cascode JFET from SiCED**.** The cascode "device" consists of a silicon MOSFET in a cascode configuration with a normally-on SiC JFET. In addition to the cascode configuration of this device, cryogenic testing was performed on the MOSFET and JFET, each individually isolated. A Tektronix 371B programmable high power curve tracer was utilized to measure the threshold voltages, breakdown voltages, and on-state resistances of the transistors.

The threshold voltages for the silicon IRLL110, the SOI HTNFET, and the SiCED cascode are shown in Fig. 13. The threshold voltage curve for the SiCED cascode is identical to the threshold voltage curve for the

MOSFET itself inside the SiCED cascode. From the figure it can be observed that as the temperature of these devices was decreased the threshold voltage increased. Fig. 14 shows the threshold voltage versus temperature for the normally-on SiC JFET itself within the SiCED cascode. It was observed that the threshold voltage for the SiC JFET decreased dramatically as the temperature was lowered. At room temperature (25 ºC), the threshold voltage for the JFET was approximately -25 Volts. At -184 ºC, the threshold voltage had decreased to approximately –51 Volts.

Fig. 15 and Fig. 16 show the on-resistance and breakdown voltage, respectively, for each transistor as the temperature was decreased. The results generally indicated a decrease in on-resistance for the silicon and SOI transistors as the temperature was lowered. The silicon MOSFET inside the SiC cascode exhibited a slight increase in on-resistance as the temperature was decreased. However, both the isolated SiC JFET and the SiC cascode circuit as a whole exhibited a slight decrease and then a dramatic increase in on-resistance as the temperature was lowered, much like the SiC schottky diode from Cree. It was observed that the primary change in on-resistance of the SiC cascode circuit was primarily dependent on the change in the on-resistance of the SiC JFET itself and not the MOSFET.

In the case of the breakdown voltages of the devices, the silicon and SOI transistor breakdown voltages both decreased slightly as the temperature was lowered. The breakdown voltage of the cascode MOSFET increased slightly, whereas the SiC JFET itself exhibited a relatively large change in breakdown voltage as the temperature was decreased. Fig. 16 shows that the breakdown voltage of the SiC cascode, was dominated largely by the change in the breakdown voltage of the JFET.

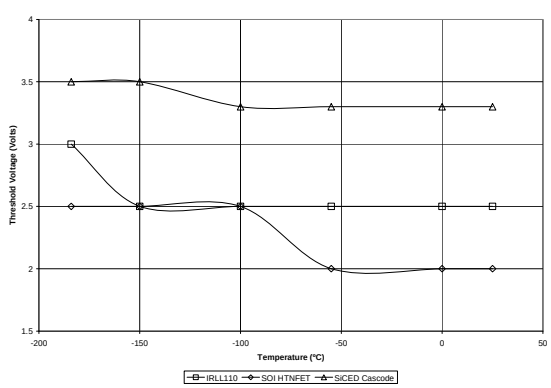

Fig. 13. Transistor threshold voltages for IRLL110, SOI HTNFET, and SiCED Cascode vs. temperature.

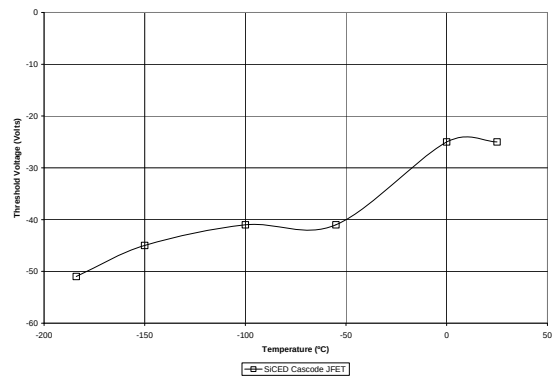

Fig. 14. Transistor threshold voltage for SiC JFET from SiCED Cascode vs. temperature.

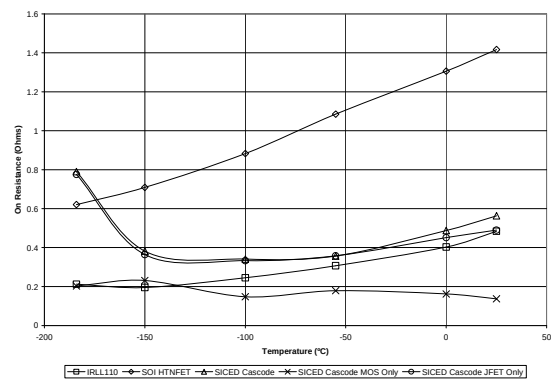

Fig. 15. Transistor on-resistance vs. temperature.

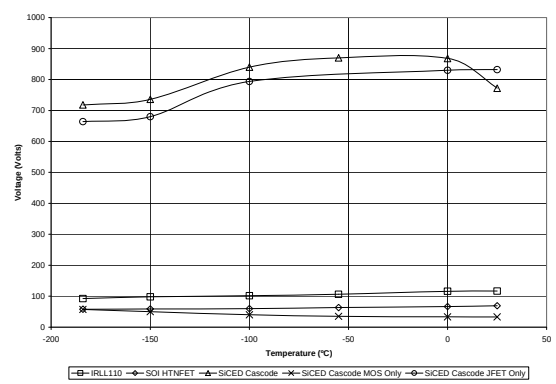

Fig. 16. Transistor breakdown voltage vs. temperature.

When the devices were retested at room temperature it was observed that the device characteristics were unaffected by the single temperature cycle.

Based on the results, it can be concluded that the silicon IRLL110 transistor would be the best choice for cryogenic applications, followed by the SOI transistor. The SiC transistor, however, performed relatively poorly, primarily due to carrier freeze-out occurring at

the low temperatures, and is not recommended for cryogenic applications.

5. DC MOTOR DRIVE POWER STAGE

A full bridge power stage was selected and designed to drive a 20 W Maxon RE 25 permanent magnet DC motor. The DC bus voltage was originally chosen to be 28 Volts in accordance with some of the DC bus voltages utilized in NASA rovers and probes; however, this was lowered to 24 VDC in order to not exceed the maximum continuous terminal voltage of the motor (i.e., 24 VDC).

The components for the power stage were chosen based upon the results of the cryogenic testing of the components. Because the power stage is a low voltage, low power design, the silicon IRLL110 transistors (MOSFETs) were chosen as the power switches for the full bridge. The gate resistors were chosen to be the thick film type manufactured by Rohm. Polyethylene capacitors were chosen to serve the purpose of the DC bus filter capacitors. The power stage was constructed on an in-house made FR4 substrate and the components were mounted to it using standard Pb/Sn solder. The cryogenic power stage is shown in Fig. 17.

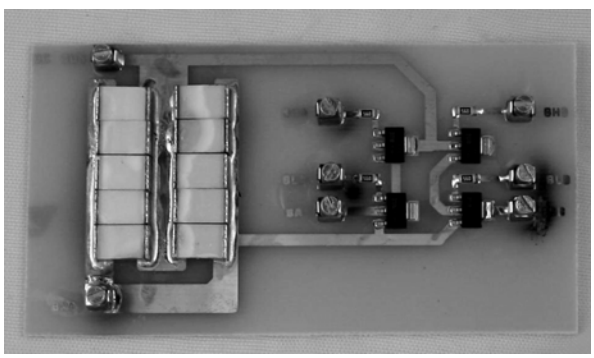

Fig. 17. Cryogenic power stage.

In order to test the power stage, the proper gate signals are needed to control the full bridge switches. These signals are generated from a control board which uses a L9903 motor bridge controller from ST Microelectronics. Since the controller has the capability to properly drive the gates of the IRLL110 power switches, separate gate drivers were not necessary. This controller was kept outside the environmental test chamber during cold temperature testing since the power stage itself was being tested.

The Maxon RE 25 DC motor was kept outside the cryogenic tester. A smoothing inductor was connected in series with the motor (to decrease the current ripple) and both were connected to the motor connection wires of the power stage. As previously mentioned, the controller board was placed outside the test chamber and it was connected to the power stage gate connection wires coming from the power stage inside the test chamber. Power was supplied to the controller board and the power stage using DC supplies and a PWM signal was supplied to the controller board using a function generator. Tektronix 3014B oscilloscopes were used to capture the waveforms of interest.

At each temperature test point, the power stage was energized and pressure was applied to the motor shaft in order to increase the output current delivered to the motor by the power stage to approximately 1 A average, which was followed by oscilloscope waveform captures. When the measurements at each temperature were compared with the room temperature measurements, the results indicated that there were no major changes to the power stage when operating at each temperature point.

After the final cold temperature measurement (at -184 ºC), the power stage was allowed to soak at this temperature (-184 ºC) for an additional 65 minutes with no power or signals applied to it. Following this long soak time, the power stage was again energized, pressure was applied to the shaft, and oscilloscope waveforms were captured. This longer soak time was implemented to see if being turned off while at an extreme low temperature for a longer period of time had any effect on the power stage operation. The results indicated that there were no detrimental effects caused by this additional soak time.

Following the additional soak time, the power stage was allowed to warm to room temperature and was again tested. This was done to determine what effects the complete temperature cycle might have had on the power stage. It was observed that there were no major changes to the power stage when subjected to one cold temperature cycle.

Fig. 18 shows the drain-to-source voltages of the power stage transistors when operating at room temperature (25 ºC). Fig. 19 shows the input and output voltages and currents of the power stage also operating at room temperature (25 ºC). In this waveform capture, channel 1 is the power stage input voltage, channel 2 is the power stage input current, channel 3 is the power stage output voltage, and channel 4 is the power stage output current.

Fig. 20 shows the drain-to-source voltages of the power stage transistors when operating at -184 ºC after the long soak time. Fig. 21 shows the input and output voltages and currents of the power stage when operating at -184 ºC after the long soak time. In this waveform capture the oscilloscope channel arrangements are identical to those as given in Fig. 19.

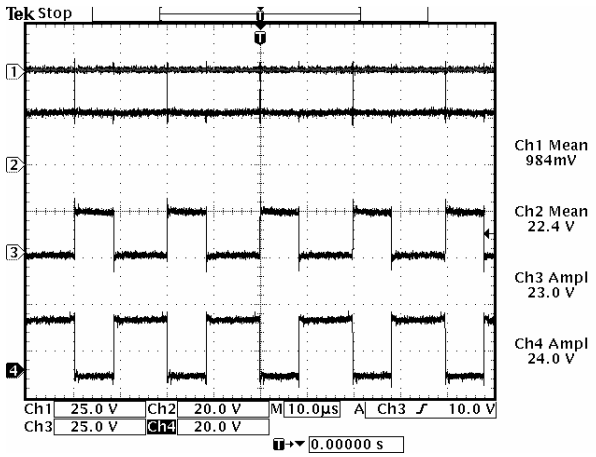

Fig. 18. Power stage drain-to-source voltages at 25 ºC.

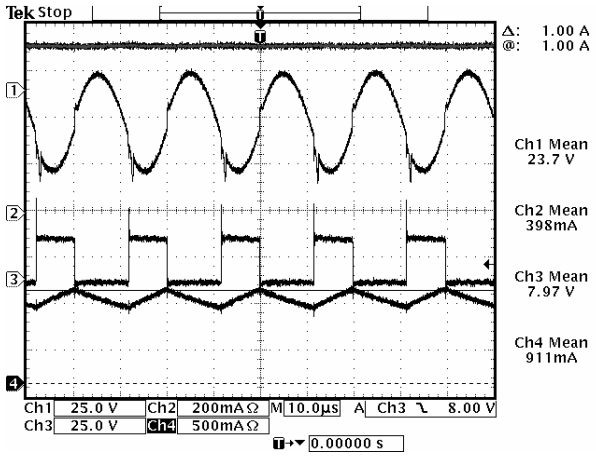

Fig. 19. Input voltage, input current, output voltage, and output current of power stage at 25 ºC.

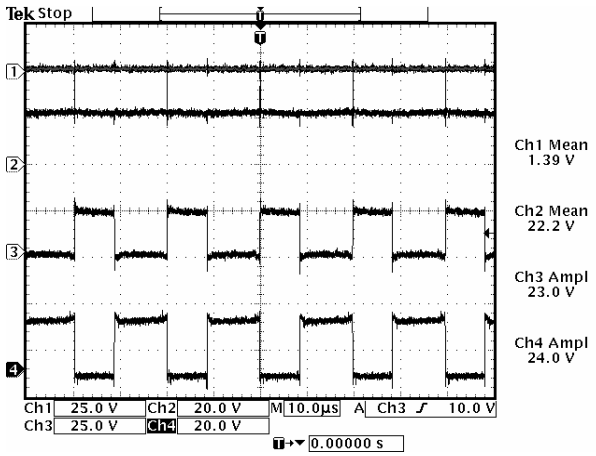

Fig. 20. Power stage drain-to-source voltages at -184 ºC

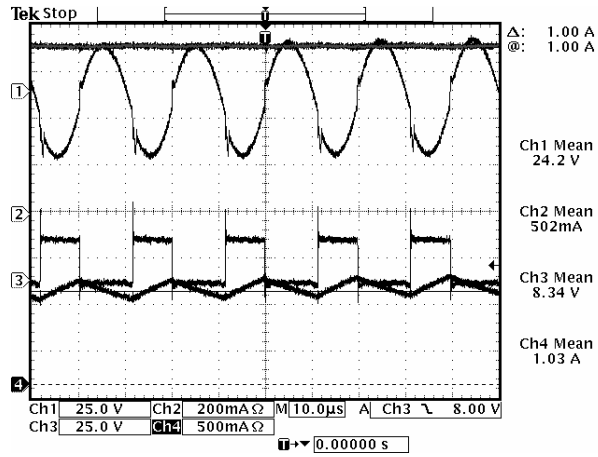

Fig. 21. Input voltage, input current, output voltage, and output current of power stage at -184 ºC.

6. SUMMARY

In this research the performance of commercially available passive and active components of varying technologies were cryogenically tested (down to -184 ºC), including; resistors, capacitors, high/low side gate drivers, diodes, and transistors. Based upon the results of the cold temperature component testing, a 20 W DC motor drive full bridge power stage was constructed. The power stage was then successfully tested down to -184 ºC while driving a permanent magnet DC motor.

7. REFERENCES

1. Elbuluk M., et al. "Power electronic components, circuits and systems for deep space missions", *IEEE Conference on Power Electronics Specialists*, Recife, Brazil, 2005, 1156 - 1162.
2. Elbuluk M., et al. "Performance of high-speed PWM control chips at cryogenic temperatures", *IEEE Transactions on Industry Applications,* Vol. 39, 443 – 450, 2003.
3. Elbuluk M., Hammoud A., "Power electronics in harsh environments", *IEEE Industry Applications Conference, 2005, Fortieth IAS Annual Meeting, Conference Record of the,* Hong Kong, China, 2005, 1442 - 1448.
4. Patterson R., et al. "Evaluation of capacitors at cryogenic temperatures for space applications", *Electrical Insulation*, *Conference Record of the 1998 IEEE International,* Washington, DC, United Stages, 1998, 468 - 471.
5. Hammoud A., Overton E., "Low temperature characterization of ceramic and film power capacitors", *Electrical Insulation and Dielectric Phenomena, 1996. IEEE 1996 Annual Report of the Conference on,* Millbrae, CA, United States, 1996, 701 - 704.

CMOS COMPATIBLE SOI MESFETS FOR EXTREME ENVIRONMENT ELECTRONICS

J. Ervin [1, 2], A. Balijepalli [2], V. Kushner [2] A. Shanmugam [2], B. Bakkaloglu [2] and T. J. Thornton [1, 2]

[1] SJT Micropower, 16411 N. Skyridge Lane, Fountain Hills, AZ 85268, USA, sjt-micropower@cox.net
[2] Arizona State University, Dept. of Electrical Engineering and Center for Solid State Electronics Research, PO Box 876206, Tempe, AZ 85287, USA, t.thornton@asu.edu

ABSTRACT

Silicon-on-insulator MESFETs have been fabricated using standard CMOS process flows and their characteristics have been measured over a temperature range of –180°C to + 300°C. From the measured data a TOM3 Spice model has been extracted. The Spice model has been used to simulate a two-stage operational transconductance amplifier and a voltage controlled oscillator. The circuit simulations show good performance over a temperature range consistent with lunar missions. In addition, MESFETs fabricated using a government SOI CMOS foundry demonstrate good radiation tolerance up to 5 Mrad(Si).

1. INTRODUCTION

Metal-semiconductor field-effect transistors, or MESFETS, have a number of advantages compared to silicon CMOS that make them attractive for extreme environment applications. These include intrinsic radiation hardness and higher breakdown voltages. MESFETs are also capable of very low power operation with excellent RF characteristics and low noise. Current MESFET technology is based on compound semiconductors and is limited to low integration levels and cannot be integrated with digital CMOS.

We have demonstrated that Si-based MESFETs can be fabricated with no changes to existing CMOS process flows. We have used a government SOI CMOS foundry [1] as well as a commercial foundry [2-4] to fabricate SOI MESFETs. The device characteristics were qualitatively identical in either case. A photograph of a MESFET used for RF measurements is shown in Fig. 1.

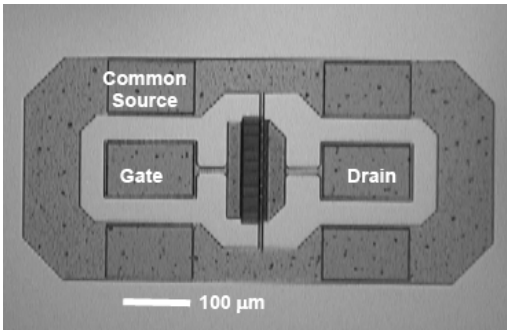

Fig. 1. Plan view of a multi-finger gate MESFET used for RF measurements.

We present results from SOI MESFETs measured in the temperature range –180°C to +300°C. The measured data has been used to extract a Spice model that is valid over the lunar temperature range of –180°C to +130°C.

2. DEVICE FABRICATION

Unlike MOSFETs, which make use of a metal-oxide-semiconductor gate to form an inversion layer channel, a MESFET uses a metal-semiconductor Schottky gate that controls the current flowing in a lightly doped channel by depletion. The Schottky gate behaves as a rectifying contact and is tolerant of relatively large current flow. This fact makes the MESFET more robust than a deeply scaled MOSFET which is prone to gate breakdown if large electric fields are developed across the gate oxide. The fabrication of the Schottky gate electrode is the key step in the MESFET process and is outlined below. More details of the processing can be found in [3].

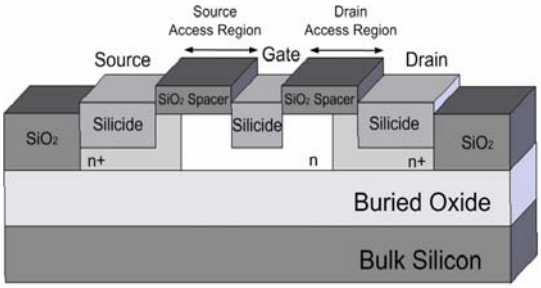

Fig. 2. Schematic cross-section of the CMOS compatible SOI MESFET.

A schematic diagram showing the cross-section of the MESFET is given in Fig. 2. The MESFET Schottky gate is made of $CoSi_2$. The $CoSi_2$ is commonly used in CMOS processing to form the low resistance contacts to the heavily doped source and drain regions. In the case of the MESFET, the $CoSi_2$ is also formed above a lightly doped n-well, resulting in a nearly ideal rectifying Schottky contact. The key step here is the availability of a 'silicide-block' step. The silicide-block is typically used to form resistive components in either silicon or poly-silicon. For the MESFETs it is used to

define the oxide spacers that separate the $CoSi_2$ that forms the Schottky gate from the $CoSi_2$ that forms the low resistance contacts to the source and drain.

The dimensions of the oxide spacers and their separation define the length of the gate, as well as the length of the channel access region from the gate to the doped source and drain regions, as shown in Fig. 2. The minimum access length was chosen to be a conservative 0.6 μm. We note that a smaller separation between the oxide spacers could probably be achieved with this 0.35 μm CMOS process, leading to shorter MESFET gate lengths.

Unlike MOSFETs, the contacts to the MESFETs are not self-aligned and the distance between the gate and the source and drain contacts (the channel access length, L_a) is controlled by the dimensions of the oxide spacers. A range of channel access lengths, L_a = 0.6, 1, 2.2, 5 and 10 μm, were defined for different devices. The channel access length between the drain and the gate controls the breakdown voltage of the MESFET and is akin to the drift region of the LD-MOSFET [5].

3. DEVICE CHARACTERIZATION

The SOI MESFETs have been tested over a wide range of temperatures. For lunar and Martian applications, we have characterized the devices over the temperature range -180°C to +150°C. This data has been used to extract an accurate device model suitable for circuit design simulators such as Cadence. For higher temperature applications we have extended the measurements to 300° C.

3.1 SPICE Model for -180°C < T < 150°C

The drain current of the MESFET follows a good square-law dependence above threshold i.e.

$$I_d^{sat} \propto (V_{GS} - V_{th})^2 \qquad (1)$$

Below threshold an exponential dependence is observed i.e.

$$I_d^{sat} \propto \exp(V_{GS} - V_{th} / nU_T) \qquad (2)$$

This device behavior is well-described by existing SPICE MESFET models such as the Curtice and TOM3 models. We have chosen to extract parameters for a TOM3 model [6] which is the most advanced MESFET model available. The model parameters are extracted from the device measurements using the IC-CAP extraction tool from Agilent [7]. More details of the model and extraction procedure can be found in [4].

Fig. 3 below shows the turn-on characteristics of the MESFET at the two extremes of temperature, i.e. –180° and +150° C. The solid lines are the measured data while the dashed lines are the simulated results. In this above-threshold regime the difference between the measured data and the model results is never more than 5% and is generally considerably less.

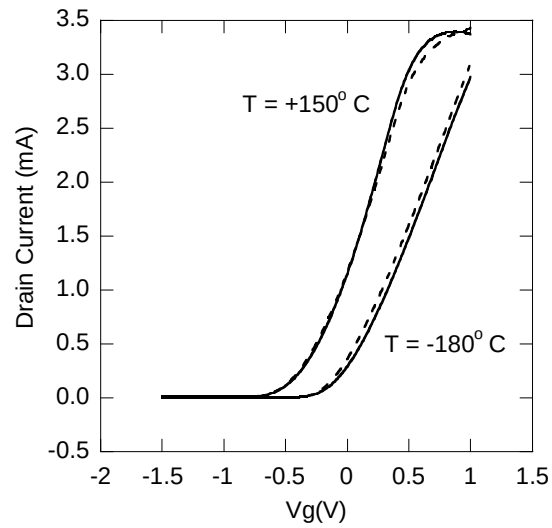

Fig. 3. The drain current as a function of gate voltage at the temperature extremes of – 180°C and +150°C. The solid lines are measured data, the dashed lines are the results from the simulation. The drain voltage in each case is 2 V.

The sub-threshold drain current is illustrated in Fig. 4 for a number of different temperatures. Again, very good agreement is seen between the measured and simulated results over a wide range of temperatures and currents. The only exception would be for the off-state current at the lowest temperatures, which we attribute to parasitic leakage paths. We note that the deviations are considerably less than 1 nA and therefore make little impact upon the results described here.

The MESFETs operate as depletion mode devices, and the threshold voltage, V_{th}, varies linearly with temperature as shown in Fig. 5. The linear temperature variation is well reproduced by the TOM3 model as shown by the solid line in Fig 5.

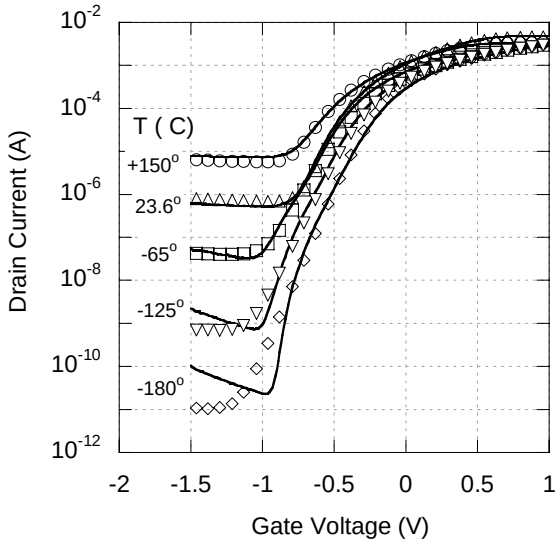

Fig. 4. The drain current plotted on a log-scale as a function of gate voltage for different temperatures. The solid lines are the measured data while the symbols are the simulated results.

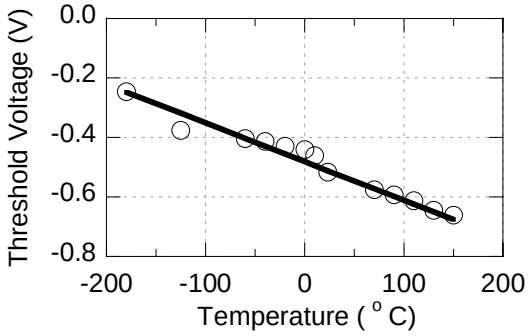

Fig. 5. The threshold voltage as a function of temperature. The solid line is the linear relation extracted for use in the TOM3 Spice model.

As a final demonstration of the MESFET SPICE model we show the measured and simulated family of curves in Fig. 6. The model has been developed to describe the small-signal and large-signal properties of a 0.6 μm gate length MESFET with L_a = 0.6 μm and a total width of 100 μm from 20 gate fingers. The breakdown voltage of this device exceeds 12 V. The data in Fig. 6 once again demonstrates the very reasonable agreement between measurements and modeled results over the entire range of temperature and bias voltage. Of course there is still room for optimization, as indicated by the somewhat higher current drive at room temperature and the higher output resistance at the lowest temperatures. Further optimization is possible, but the current model is sufficiently accurate to proceed with the circuit design.

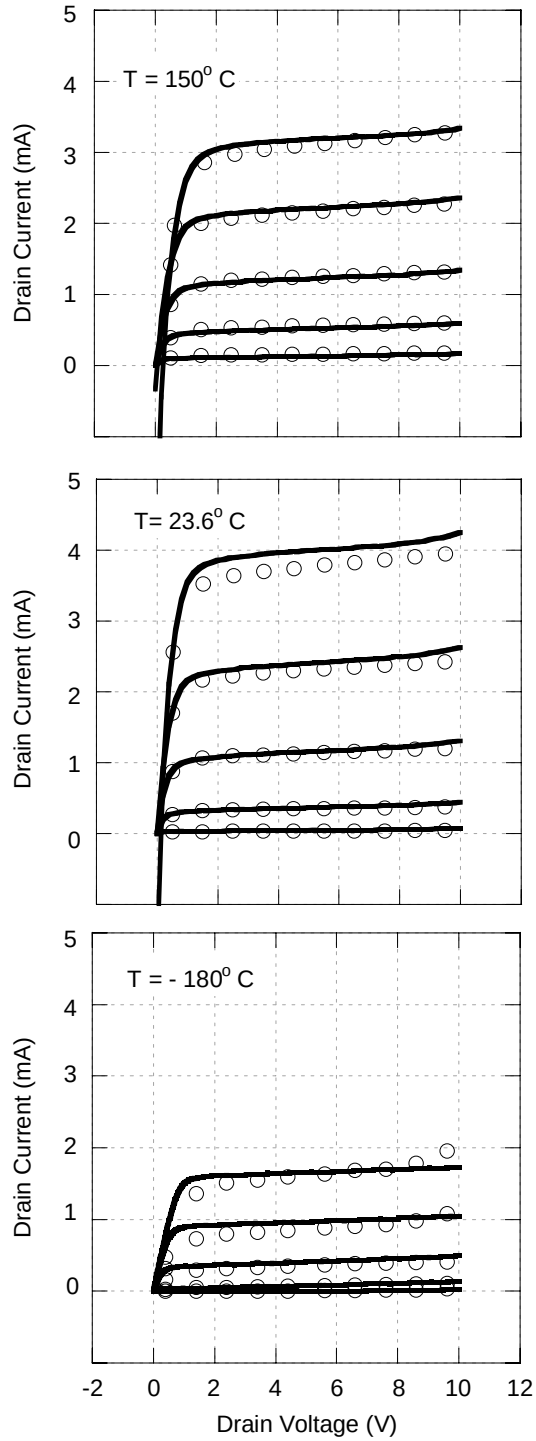

Fig. 6. The $I_d - V_{ds}$ family of curves at -180° C, room temperature and +150° C. The gate voltages used in each case are 0.5, 0.25, 0, -0.25 and -0.5V from top to bottom. The solid lines are the measured data while the open symbols are the simulated results.

4. CIRCUIT SIMULATION

To illustrate potential applications of the SOI MESFETs we have simulated two analog circuits one being an operational transconductance amplifier (OTA) and the other a voltage controlled oscillator (VCO). The OTA is a key component in an instrumentation operational amplifier and the VCO would be used in an RF Transceiver. Both circuits have been completed to a first order design, and simulated over the temperature range -180°C < T < +130°C. Only slight variations in performance were observed. We point out here that the CMOS models are likely to be valid only over the military temperature range of -55°C to +125°C. As a consequence, although we believe that the MESFET models are accurate over the entire range, there may be discrepancies when the temperature extends beyond the limits of the available CMOS models. However, recent work has confirmed that SOI CMOS can be used for wide temperature range bias circuits using the constant inversion coefficient approach [8]

4.1 Two Stage OTA

A two stage operational transconductance amplifier (OTA) that uses MESFETs as the input differential pair in the first stage with a PMOS common-source amplifier with NMOS active load is shown in Fig. 7. The gain and phase as a function of frequency is plotted for room temperature and the two extreme temperatures of –180ºC and 130ºC in Fig. 8. The supply voltage was chosen to be V_{DD} = 3.3V, to be consistent with the SOI CMOS process. This circuit illustrates one of the main advantages of the SOI MESFET, namely the fact that they can be integrated with standard CMOS devices.

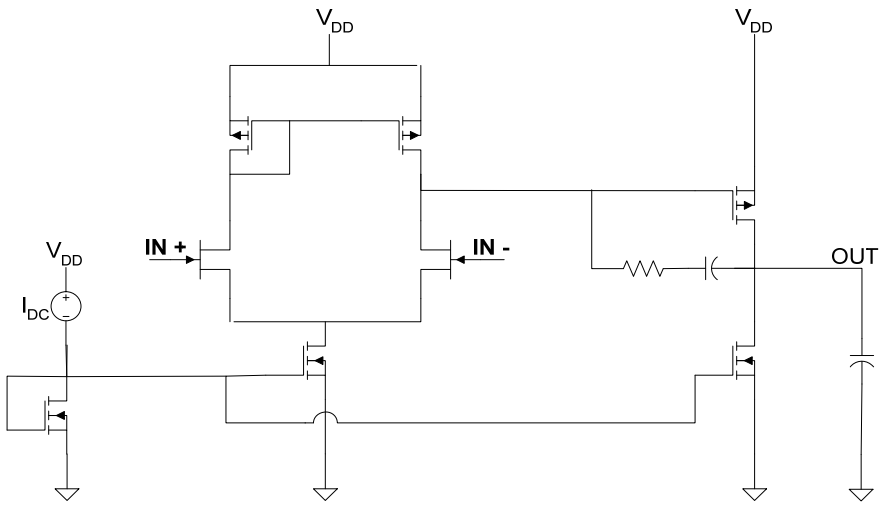

Fig. 7. Schematic circuit diagram of the MESFET+CMOS operational transconductance amplifier.

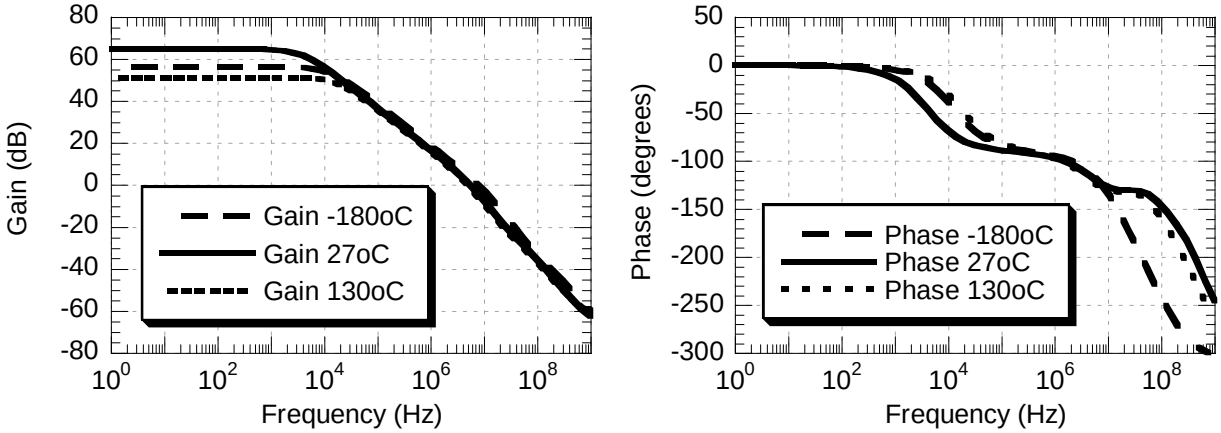

Fig. 8. Gain and phase of the MESFET OTA as a function of frequency.

The biasing of the OTA was chosen such that the tail current was 25 μA with a further 25 μA flowing in the common-source PMOS second stage with I_{DC} = 5 μA. These bias levels place the OTA in the sub-threshold (i.e. micropower) regime for all temperatures in the range -180°C to +130°C – see Fig. 4. The DC gain, unity-gain bandwidth and power consumption at RT and the temperature extremes are given in Table 1. Further optimization of the design will allow a reduction in the power consumed but without significant impact on the gain and bandwidth.

Table 1: The gain, bandwidth, current bias and power consumption of the 2-stage OTA. V_{DD} = 3.3V.

Temp	DC Gain	Gain*BW Product	DC current	Power
-180°C	57 dB	7.6 MHz	76.65uA	0.252mW
27°C	66 dB	5.4 MHz	55.67uA	0.183mW
130°C	52 dB	4.9 MHz	62.3uA	0.205mW

4.2 Voltage Controlled Oscillator

As a demonstrator of the RF applications of the MESFETs we have designed an LC tank-oscillator with a frequency of 1.5 GHz based on a Clapp oscillator architecture. The circuit topology is shown in Fig. 9, with the output response shown in Fig. 10. Note that with a V_{DD} of 3.3 V the output voltage swing of the VCO is ~ 7V. This would exceed the breakdown voltage of the SOI MOSFETs, and demonstrates one of the significant advantages of the MESFET based approach. To first order, the frequency and amplitude of the Clapp oscillator are controlled by the properties of the LC tank, although the start-up condition depends upon transconductance which varies by a factor of 2 over the temperature range. There is no significant shift in the frequency or amplitude of the response. With the change in temperature, the circuit current bias changes, thereby changing the power usage. The properties of the VCO are detailed in Table 2. We note that for this preliminary design no effort was made to minimize the power consumption of the Clapp oscillator.

Table 2: The frequency, output swing, current bias and power consumption of the Clapp VCO. V_{DD} = 3.3V.

Temp	f (GHz)	Output Swing (V)	DC current	Power
-180°C	1.5029	-0.41 to 7.02	671.75uA	2.22mW
27°C	1.5032	-0.4 to 7.01	671.801uA	2.22mW
130°C	1.5035	-0.185 to 6.8	773.142uA	2.55mW

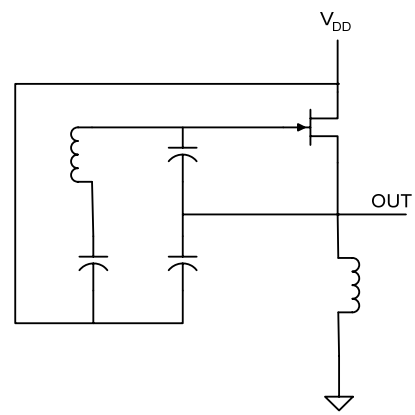

Fig. 9. The Clapp circuit topology used for the VCO design

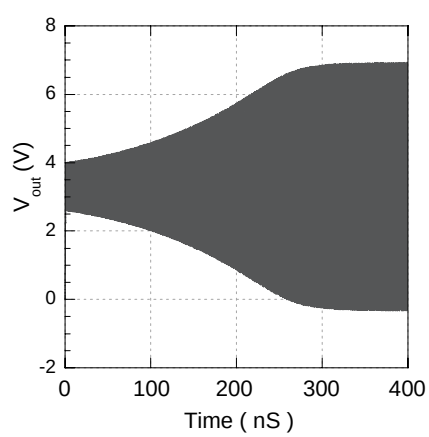

Fig. 10. Envelope function of the VCO output response. T= 27°C.

5. CHARACTERIZATION UP TO 300°C

To better understand the temperature limits of the SOI MESFETs we have extended the high temperature measurements to 300°C. The gate and drain currents as a function of gate voltage are shown in Fig. 11. At room temperature the ratio of on-state to off-state drain current is ~ 4000. This ratio falls to ~ 3 at 300°C. The increase in off-state drain current with increasing temperature can be attributed to the increase in the reverse bias gate leakage current. It is apparent from the data in Fig. 11 that the Schottky gate becomes more conducting at elevated temperatures and the non-linear (i.e. rectifying) nature of the gate is diminished. We attribute much of the gate leakage current to edge effects and with further optimization it might be possible to further decrease the off-state drain current. However, from these measurements we speculate that the highest operating temperature for MESFET-based circuits will be 250°C where the off-state ratio is > 10. We note here that the MESFETs appear to suffer no permanent damage after several hours of heating to 300°C. The drain and gate currents were re-measured at room temperature after thermal cycling and only minimal changes were observed.

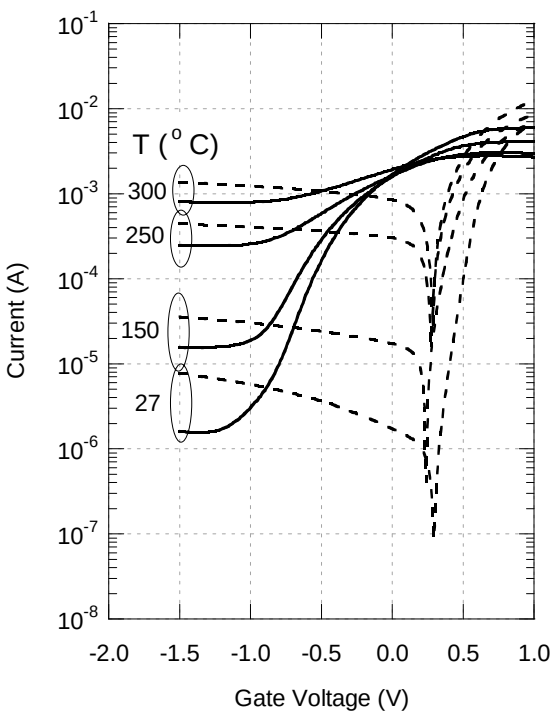

Fig. 11. The drain currents (solid lines) and gate currents (dashed lines) as a function of gate voltage measured at elevated temperatures. V_{ds} = 2V.

6. RADIATION TESTING

The radiation response of SOI MESFETs fabricated using the government CMOS process have been tested by exposure to 50 keV x-rays up to a total ionizing dose of 5 Mrad(Si). These results are summarized below. More detail can be found in [1].

The turn-on characteristics of the MESFETs are shown in Fig. 12. Prior to irradiation the threshood voltage of the device was approximately – 0.5V. To better understand the operation of the device, we have developed a numerical model for the SOI MESFET - see [1]. The values of device parameters that are accurately known, such as gate length, SOI thickness, channel doping etc., are used for the simulation. The parameters that are not known prior to simulation are the fixed oxide charge density, N_{ot}, and the interface trap density, N_{it}, both of which are associated with the non-ideal interfaces between the SOI channel and the BOX layer below and the spacer oxides above. These parameters are used as fitting parameters in the model. To reproduce the pre-radiation data shown in Fig. 12 we have used a fixed charge density, N_{ot} of 0.4×10^{11} cm^{-2}, and an interface state density N_{it}, of 6×10^{11} cm^{-2}. A single trap level at an energy 0.48 eV below the conduction band edge was used, although the precise location of the trap level did not change the simulation significantly. Although this assignment of interface trap states is empirical it adequately reproduces the slope of the I_d vs V_{gs} curve.

Radiation tests were performed on unpackaged die using an Aracor 4100 Semiconductor Irradiation System. The Aracor system emits x-rays at energies from 10 to 60 keV and these x-rays are then directed out of an aperture towards the chuck and the sample. For these experiments, the electron energies were 50keV. During irradiation, the devices were contacted using a probe card and electrical measurements were made immediately after irradiation. Arbitrary bias could be applied during the irradiation but for the results described here all contacts were grounded during the x-ray exposure. The total dose test plan selected follows the military standard 883E, method 1019.6. The dose rate is set to 20 krad(Si)/min up to 400 krad(Si) total dose. Beyond 400 krad(Si) the dose rate is increased to 40 krad(Si)/min.

The SOI MESFET has a buried oxide that will be susceptible to radiation induced trapped charge. The spacer oxide on the top surface of the MESFET (see Fig. 2) will also be susceptible to radiation. To model the effect any such trapped charge will have on the

threshold voltage of the MESFET, we assume that it can be treated as fixed charge, N_{ot}, because previous work on SOI BOX charge trapping indicates that generated carriers do not travel far from their generation site [9], [10]. The data in Fig. 12 shows the turn-on characteristics (I_d vs. V_{gs}) of the MESFET after the device has received a total ionizing dose of 5 Mrad(Si). After irradiation the threshold voltage has shifted to approximately – 1 V.

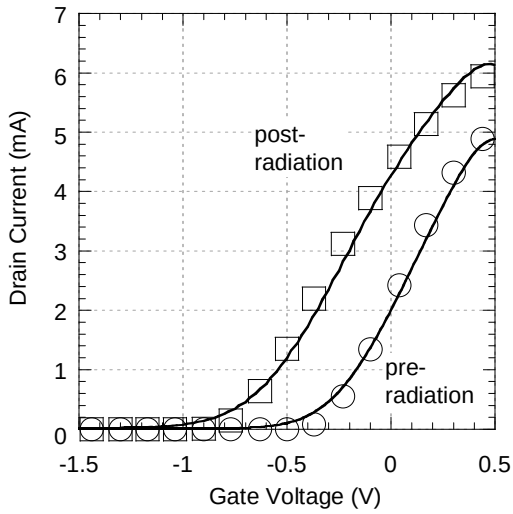

Fig. 12. The drain current as a function of gate voltage for a MESFET of gate length 0.6 μm. Prior to irradiation the threshold voltage is approximately – 0.5 V. After a TID of 5 Mrad(Si) it shifts to –1 V. The circles and squares show the simulated results before and after irradiation, respectively. V_{ds} = 0.5V.

The observed shift in threshold voltage is consistent with an increase in the fixed oxide trapped charge density in the buried oxide and, presumably, in the surface spacer oxide. The fixed oxide charges will be positive, and extra free electron charge will be attracted into the channel from the n^+ source/drain contacts to ensure charge neutrality. A larger reverse bias will have to be applied to the gate to deplete the increased free electron concentration in the channel, resulting in a more negative threshold voltage. The shift in threshold, ΔV_{th}, due to an increase in trapped oxide charge, ΔN_{ot}, can therefore be written as

$$\Delta V_{th} = - e\, \Delta N_{ot} / C_{gate} \qquad (3)$$

where C_{gate} is the gate capacitance per unit area. We have taken the model used to describe the pre-irradiation data and modified it to fit the data after a TID of 5 Mrad(Si). The data in Fig. 12 suggests a simple translational shift in the I_d vs V_{gs} curve as a result of a change in threshold voltage. There is no obvious shift in the slope of the I_d vs V_{gs} curves and for this reason we believe that any increase to the interface trap density after irradiation is negligible. Indeed, the fit to the data after irradiation shown by the open squares in Fig. 12 was obtained simply by increasing N_{ot} from 0.4×10^{11} cm^{-2} to 3.4×10^{11} cm^{-2}.

The shift in threshold voltage, ΔV_{th}, is plotted as a function of TID in Fig. 13. The data in Fig. 13 suggests that the threshold voltage shift is initially linear with increasing TID but eventually saturates for a high enough TID. This saturation in the threshold shift has been observed in SOI MOSFETs [11], [12] and is attributed to a saturation in the fixed oxide charge density at high radiation doses.

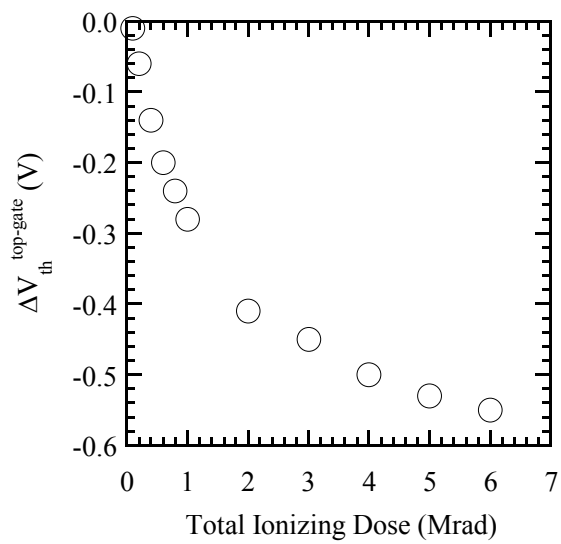

Fig. 13. The shift in the threshold voltage of the Schottky top gate as a function of total ionizing dose.

7. CONCLUSIONS

We have demonstrated that CMOS compatible MESFETs can be fabricated alongside conventional CMOS. The MESFETs show excellent device performance over the wide temperature range -180°C to + 150°C. We have extracted an accurate Spice model and applied it to the design of a two-stage OTA and a 1.5 GHz VCO. The MESFETs operate up to 300°C although high off-state current limits the useful application of the current generation of devices to 250°C. With further optimization it may be possible to

extend the operating temperature. The MESFETs show good radiation tolerance with a – 0.5 V shift in threshold voltage after exposure to a TID of 5 Mrad(Si). The high voltage capability, combined with the wide temperature operating range and radiation tolerance suggest that CMOS compatible SOI MESFETs will be suitable for applications that require high-performance extreme environment electronics.

8. REFERENCES

1. J. Spann, V. Kushner, T. J. Thornton, J. Yang, A. Balijepalli, H. J. Barnaby, X. J. Chen, D. Alexander, W. T. Kemp, S. J. Sampson, and M. E. Wood, "Total Dose Radiation Response of CMOS Compatible SOI MESFETs," *IEEE Trans. Nuc. Sci.* pp. 2398-2402, 2005.

2. J. Vandersand, V. Kushner, J. Yang, B. Blalock, and T. Thornton, "CMOS Compatible SOI MESFETs for Extreme Environment Applications," presented at *IEEE Aerospace Conference*, pp 1-7 Big Sky, Montana 5-12 March, 2005.

3. J. Yang, A. Balijepalli, T.J. Thornton, J. Vandersand, B.J. Blalock and M.E. Wood, "Integrated SOI MOSFETs and MESFETs" accepted for publication in the *Journal of High Speed Electronics.*

4. A. Balijepalli, J. Ervin, P. Joshi, J. Yang, Y. Cao, and T.J.Thornton, "High-Voltage CMOS Compatible SOI MESFET Characterization and Spice Model Extraction," presented at the *IEEE MTT-S International Microwave Symposium,* San Francisco, CA June 11-16, 2006.

5. B. Jayant Baliga *"Silicon RF Power MOSFETs"* published by World Scientific, 2005.

6. R. B. Hallgren, P. H. Litzenberg, "TOM3 capacitance model: Linking large- and small-signal MESFET models in SPICE", *IEEE Trans. Microwave Thoery Tech.,* vol. 47,no. 5, pp 556-561,1999.

7. Agilent 85190A *IC-CAP 2004 User's Guide*, August 2004.

8. B. Blalock, University of Tennessee, Knoxville, *private communication*

9. R.K. Lawrence, "Radiation effects in SOI isolation oxides," *2001 IEEE Semiconductor Device Research Symposium*, p.461, 2001.

10. J.R. Schwank, V.Ferlet-Cavrois, M.R. Shaneyfelt, P. Paillet, P.E. Dodd, "Radiation effects in SOI technologies," *IEEE Trans. on Nuclear Science,* Vol. 50, p. 522, 2003.

11. S. T. Liu, W. C. Jenkins, and H. L. Hughes, "Total Dose Radiation Hard 0.35 micron CMOS Technology" *IEEE Trans. on Nuclear Science*, Vol. 45, pp. 2442 – 2449, 1998.

12. Y. Li, G. Nu, J. D. Cressler, J. Patel, S. T. Liu, R. A. Reed, M. M. Mojarradi, B. J. Blalock "The Operation of 0.35 micron Partially Depleted SOI CMOS Technology in Extreme Environments" *Solid-State Electronics*, Vol. 47, pp 1111-1115, 2003.

A COMPARISON OF SiC POWER SWITCHES FOR HI-REL APPLICATIONS

J.B. Casady, SemiSouth Laboratories, Inc., 201 Research Blvd, Starkville, MS 39759, **jeff.casady@semisouth.com**

M.S. Mazzola, SemiSouth Laboratories, Inc., 201 Research Blvd, Starkville, MS 39759, **mike.mazzola@semisouth.com**

W.A. Draper, SemiSouth Laboratories, Inc., 201 Research Blvd, Starkville, MS 39759, **will.draper@semisouth.com**

Three principal switch types based on silicon carbide have achieved a reasonable level of maturity for Hi-Rel applications. They are the vertical junction field effect transistor (VJFET), the metal-oxide-semiconductor FET (MOSFET), and the bipolar junction transistor (BJT). The VJFET is principally valued for having demonstrated the highest current and voltage combinations, positive temperature coefficient over the entire applications range of -40 C to 300 C; and other features that are either inherent to the simplicity of the VJFET or to their somewhat greater technology readiness level, such as the lowest reported specific on-resistance, rugged radiation tolerance, and good reliability at operating temperatures well above 175 C. In principal, this makes the VJFET the preferred solution for Hi-Rel applications in the defense, aerospace, and commercial sectors, but the perception remains that the VJFET is a normally on device that is not compatible with typical circuits and methods in power electronics. However, the large built-in potential of the SiC pn-junction gate, a liability in power diodes, is an asset for VJFET power switches for expanding the design options for threshold voltage to include positive threshold voltage (meaning normally off devices).

HIGH TEMPERATURE ELECTRONICS, COMMUNICATIONS, AND SUPPORTING TECHNOLOGIES FOR VENUS MISSIONS

G. W. Hunter[(1)], R. S. Okojie[(2)], P. G. Neudeck[(3)], G. M. Beheim[(4)] , G. E. Ponchak [(5),] G. Fralick[(6)], J. Wrbanek[(7)], and L.-Y. Chen[(8)]

[(1)]NASA Glenn Research Center at Lewis Field, 21000 Brookpark Road, Cleveland, OH 44135, USA, Email: Gary.W.Hunter@nasa.gov
[(2)] Email: Robert.S.Okojie@grc.nasa.gov, [(3)] Email: Neudeck@nasa.gov, [4)] Email: Glenn.M.Beheim@nasa.gov
[(5)]Email: George.E.Ponchak@nasa.gov, [(6)]Email: Gustave.C.Fralick@nasa.gov, [(7)]Email: John.D.Wrbanek@nasa.gov
[(8)] OAI, 22800 Cedar Point Road, Cleveland, OH 44142, USA, Email: Liangyu.Chen@grc.nasa.gov

ABSTRACT

NASA Glenn Research Center is presently leading the development of electronics and sensors capable of prolonged stable operation in harsh 500°C environments. These technologies are being developed for engine environments but also have Venus planetary exploration applications. This paper discusses these high temperature electronic and sensor technologies as well as their relevance to Venus missions. A specific application describing a Venus instrument, a Venus Integrated Weather Sensor (VIWS) System, is described.

1. INTRODUCTION

NASA Glenn Research Center (GRC) is presently leading the development of electronics and sensors capable of prolonged stable operation in harsh 500°C environments. These technologies are being developed for engine environments but also have Venus planetary exploration applications. Given the previous lack of electronics that could collect and transmit scientific data in Venus's 450°C lower-atmosphere, almost all proposed missions to explore this important planetary environment were based on very limited duration (on the order of hours) of data collection and return. The ability of a spacecraft (including its electronics) to function and return useful data for far longer time periods (months) would undoubtedly greatly improve the scientific return gained from Venus surface missions.

For example, the recent emergence of wide bandgap semiconductors, including silicon carbide (SiC), diamond, and gallium nitride (GaN), has enabled short-term electrical device demonstrations at temperatures from 500°C to 650°C [1]. Until recently however, these wide bandgap devices have demonstrated only a few minutes to a few hours of durability when electronically operated at these high temperatures. In order to support the needs of long-duration Venus surface operations, wide bandgap electronics technology must first demonstrate that it can achieve stable, long-term operation under electrical bias at 450°C temperature without significant changes in electrical operating parameters.

NASA GRC is a world-leader in harsh environment electronics and sensor technology [2] and is uniquely positioned to contribute to future Venus electronics systems. NASA GRC has developed SiC-based transistor technology (including packaging) that has demonstrated continuous electrical operation at 500°C for over 2000 hours [2,3]. No other reported semiconductor transistor has demonstrated such continuous prolonged electrical operation in an ambient comparable to or exceeding Venus atmospheric temperature. In contrast to other proposed high temperature electronics approaches (such as miniature vacuum tubes), the NASA GRC SiC transistor technology is inherently compatible with integrated circuit manufacturing techniques, so that increasingly complex electronics could be implemented on a single SiC chip.

Development of high temperature wireless communication based on SiC electronics has also been on-going at NASA GRC. This work has concentrated on the SiC electronic devices as well as the passive components such as resistors and capacitors needed to enable a high temperature wireless system.

This paper discusses the development of SiC based electronics and wireless communications technology and its possible application in Venus missions. This electronics development includes the supporting technologies such as device contacts and packaging. Further, characterization of Venus surface conditions also requires durable lightweight sensor technology which can operate in harsh environments. A brief overview of relevant sensor technologies and their compatibility with SiC based electronics will be given. It is concluded that the base technologies being developed for engine applications can have a significant effect on possible Venus missions.

2. HIGH TEMPERATURE ELECTRONICS AND COMMUNICATIONS

The ability to process, amplify, and even wirelessly transmit signals directly from the point of harsh-environment sensing would have clear benefits in a variety of aeropropulsion systems. To be useful, such electronics need to be as small, lightweight, and non-intrusive as possible; in addition, it should preferably operate without thermal management overhead in hot regions, such as cooling, at or near very hot combustion chambers and exhaust gas streams. While conventional semiconductors have enabled quite complex room-temperature circuits to be miniaturized onto small chips, the extension of this technology to temperatures above 300 °C appears impractical using silicon semiconductors [4,5].

Silicon carbide (SiC) presently appears to be the strongest candidate semiconductor for implementing 400-600 °C integrated electronics, as competing high temperature electronics technologies are either physically incapable of functioning at these high temperatures (silicon and silicon-on-insulator), or are significantly less-developed (GaN, diamond, etc.). Single-crystal wafers of either the 6H or 4H crystal structures of SiC are commercially available with sufficient quality and size to enable foundry mass-fabrication of semiconductor discrete devices and integrated circuits. SiC devices such as pn junction diodes, Junction Field Effect Transistors (JFETs), and Metal-Oxide-Semiconductor Field Effect Transistors (MOSFETs) have previously demonstrated reasonable electrical functionality at high temperatures for relatively short time periods [4,5]. However, for such electronics to be useful in engine applications, much longer lifetimes at 400 to 600 °C must be realized. Acceptable levels of durability and reliability must be attained before high temperature electronics will qualify for beneficial insertion into a broad variety of systems. Therefore, more than any other metric such as transistor power, gain, or frequency, NASA GRC's SiC electronics technology development is focused on realizing increasingly prolonged 400-600°C electronic operation.

The operational lifetime of SiC-based transistors at 400-600 °C is not limited by the semiconductor itself, but is instead largely governed by the reliability and stability of various interfaces with the SiC crystal surface. The physical degradation of the metal-semiconductor ohmic contact interface limits the 600 °C operating lifetime of all devices, while high temperature MOSFET operating lifetime is also limited by the electrical integrity of the oxide-semiconductor interface. Thus, junction-based transistors without gate insulators appear more feasible in the nearer term. Of the candidate junction-based transistor technologies that might be used to implement SiC integrated circuits, the pn junction gate JFET seems closest to demonstrating long-term operation at 400-600°C.

(a)

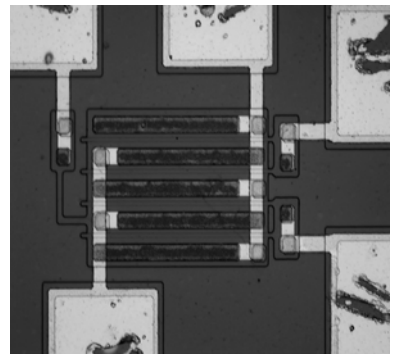

(b)

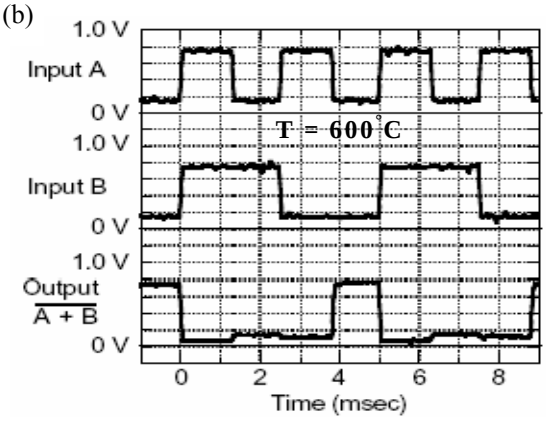

Fig. 1. (a) Optical micrograph and (b) 600 °C functional electrical testing waveforms of 6H-SiC JFET-based NOR logic gate. Supply voltages used for electrical testing were V_{DD} = 3.5 V, V_{SS} = 0 V, and $V_{substrate}$ = -1.8 V [6].

An example of the maturity level of SiC JFET technology over seven years ago was the demonstration of 600°C digital logic using SiC JFETs (Fig. 1) [6]. A resistive load Direct-Coupled FET Logic (DCFL) approach was adopted to demonstrate simple 600°C digital logic using SiC JFETs. A mesa-etched epitaxial gate JFET design was chosen over that of a planar ion-implanted structure, largely to alleviate the challenging process of sufficiently activating high-dose p+ ion implants in SiC. The two-level interconnect approach used oxidation-resistant silicon nitride as the dielectric passivation along with oxidation resistant gold for the metal interconnect. However, because non-optimized ohmic contact metals were employed in this experiment, the devices failed after less than an hour of 600°C operation.

Because metal-semiconductor contacts were the primary factor limiting high temperature operational lifetime, focused fundamental (i.e. low technology readiness level) research efforts to develop more durable SiC high-temperature ohmic contacts were undertaken. These efforts produced a novel and remarkably durable $Ti/TaSi_2/Pt$ multilayer contact to n-type SiC that has demonstrated stable ohmic properties over the course of 1000 hours of annealing at 600°C in air [7]. It is important to note that such demonstrated durability in oxidizing air ambient is significant and unique. Almost all other published reports of high temperature contacts study contact durability only in oxygen-free inert-gas or vacuum environments. Durable functionality in oxygen-containing air ambient simplifies high temperature packaging challenges by reducing the need to obtain a perfectly hermetic package seal against oxygen penetration (which by itself is quite a difficult challenge given large temperature extremes). It also simplifies the design of SiC-based electronic sensing elements desired to monitor high temperature processes, such as pressure sensors and gas sensors described elsewhere in this paper.

Using the $Ti/TaSi_2/Pt$ high temperature n-type ohmic contact discussed above, a high temperature n-channel 6H-SiC metal semiconductor field effect transistor (MESFET) demonstrated previously unattained 500°C transistor electronic durability. Fig. 2a shows a scanning electron micrograph of the device, whose fabrication and characterization are described in much greater detail elsewhere [3]. Fig. 2b compares the operating characteristics before (black) and after (gray) 558 hours of continuous electrical operation at 500°C. For the first 500 hours, the device underwent less than 10% change in operational transistor parameters. The dominant degradation mechanism of this MESFET was due to annealing of the metal-semiconductor gate interface. The inability of the transistor to turn-off completely (including the slope in the Fig. 2 drain I-V characteristics) was caused by a simple fabrication error [3]. By implementing a relatively minor process change, the degrading metal-semiconductor gate can be replaced with a pn junction gate, thereby forming a more durable junction field effect transistor.

Such JFETs are presently being fabricated at NASA GRC. Aside from the gate-related degradation, all other aspects of the MESFET demonstrated excellent harsh-environment stability while operating for over 2000 hours under prolonged electrical bias at 500°C. The prolonged high temperature electrical testing of the MESFET was enabled by packaging technology discussed elsewhere in this article, as probe-station testing over long time periods at 500°C is largely impractical.

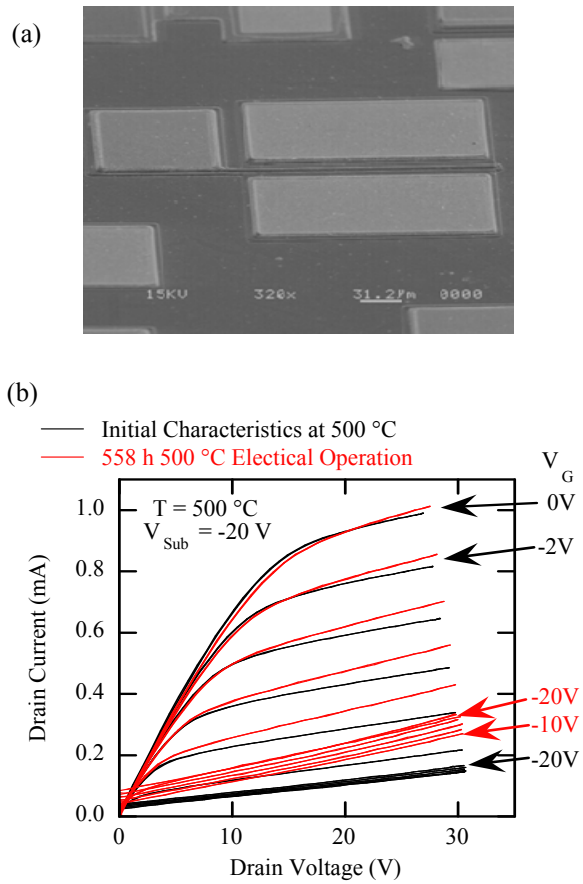

Fig. 2. (a) Scanning electron micrograph and (b) drain current-voltage characteristics of a 6H-SiC transistor that electrically operated continuously for over 500 hours at 500 °C in oxidizing air ambient with minimal device degradation [3]. The initial (black) and final (gray) I-V curves differ slightly due to degradation of the metal semiconductor gate contact, a mechanism which can be eliminated by implementing a pn junction gate transistor process (see text).

Integrated circuits require interconnects to carry electrical signals between the various transistors on the semiconductor chip. However, long-term electrical operation of dielectrics with microscopically patterned metal traces in an oxidizing 400-600°C environment has not (to the best of our knowledge) previously been demonstrated. Therefore, NASA GRC is also pursuing fundamental materials and processing development of this critical building block needed to implement extreme temperature integrated circuit electronics.

Recently, a high temperature, low frequency common-source voltage amplifier based on a SiC MESFET, SiC resistors, and high temperature ceramic packaging was successfully demonstrated at 500°C [8]. Both voltage

gain and frequency response were reasonably stable during the entire testing period of 1100 hours at 500°C.

Work has also been on-going to integrate SiC electronics with high temperature passive devices to produce a high temperature wireless communications system. The passive devices include capacitors and resistors able to work at high temperatures and frequencies. The objective is to eliminate wires associated with high temperature sensors which add weight to a vehicle and can be a cause of sensor unreliability.

A high-temperature measurement system capable of performing on-wafer microwave testing of semiconductor devices has been developed [9]. This high temperature probe station can characterize active and passive devices and circuits at temperatures ranging from room temperature to above 500°C. The heating system is comprised of a ceramic heater mounted on an insulating block of NASA shuttle tile material. The temperature is adjusted by a simple graphical computer interface and is automatically controlled. The system is used with a Hewlett-Packard 8510C Network Analyzer to measure scattering parameters over a frequency range of 1 to 50 GHz. The microwave probes, cables, and inspection microscope are all shielded to protect them from heat damage. The high temperature probe station has been successfully used to characterize gold transmission lines on silicon carbide at temperatures up to 540°C.

Passive devices for communication purposes which have been formed include thin film nickel chromium (NiCr) resistors, metal-insulator-metal (MIM) capacitors, and spiral inductors fabricated on a high purity semi-insulating 4H-SiC substrate [10]. The devices have been experimentally characterized through 50 GHz at temperatures up to 500°C. The NiCr resistors are stable to within 10% to 300°C while the capacitors have a value stable within 10% through 500°C. Inductors are expected to be fully stable through 500°C with a redesign of the associated air bridges.

A critical component of a wireless sensor system is the local oscillator that generates the RF signal, which will be modulated by the sensor and data will be transmitted to cooler environments. Integration of passive components with a commercially available SiC MESFET was performed to demonstrate the ability to design the circuit, the operability of the passive components, and the integration of the components with a SiC device [6,11]. The temperature characteristics of the Cree SiC MESFET were measured and used with temperature-dependent characteristics of the passive components to design the oscillator.

The first design was a differential oscillator designed to operate at 1 GHz instead, which operated at 500 MHz due to drift in the transistor capacitance with temperature. However, this circuit did operate at 475˚ C with an output frequency of 453 MHz [6] into a non-50 Ω load. A second circuit, a Clapp Oscillator that has less dependence on the transistor capacitance, was designed and is shown in Fig. 3. Testing showed that it operates at 1 GHz into a 50-Ω load over the temperature range of 30 to 200˚ C. with an output power of 21.8 dBm at 1 GHz and 200°C. The frequency variation over the temperature range is less than 0.5%. The efficiency at 200°C is 15%. Modeling predicted that the circuit should have operated through 300˚ C, but increased loss in the passive devices limited the operation.

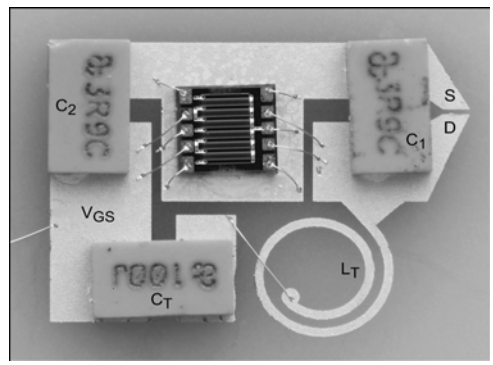

Fig. 3. Photograph of oscillator comprised of SiC MESFET, ceramic chip capacitors, a spiral inductor, and gold wire bond interconnects.

This oscillator was a proof-of-concept device to show the viability of the design approach. It also showed that greater gain is required from the transistors if they are to operate at 1 GHz and temperatures above 300˚ C. Moreover, it is noted that the transistor characteristics varied over time at high temperature. A critical aspect of oscillator performance is noise generation by the circuit because noise will limit the data rate of the wireless system. While the literature indicates that further research on noise performance of SiC transistors is required, preliminary studies show that low frequency noise of SiC transistors initially increases with increasing temperature, but that after a maximum is reached, the noise spectral density decreases with temperature. Therefore, noise performance of SiC transistors does not appear to be a limiting factor in performance [12].

As noted, work is on-going at NASA GRC to advance the state-of-the-art of the SiC devices, and work is planned to improve the passive devices. Overall, the ability for high temperature wireless communication to operate up to Venus temperatures is envisioned within

the next 5 years at the present rate of development (and sooner if concentrated effort is applied to the problem). Communication at lower temperatures, e.g., below 250°C, is envisioned to be achievable in a shorter time frame using techniques such as silicon on insulator or SiGe.

A parallel approach to using a SiC MESFET is to use atomically flat SiC as a substrate for growing gallium nitride (GaN) and then using GaN on SiC for communication purposes. This approach allows use of the favorable properties of GaN, provided durable high temperatre operation can be obtained with this material. Recent data has shown a significant decrease in defects of GaN on SiC by using atomically flat SiC with a world-record 100 fold defect reduction [13].

3. PACKAGING OF HARSH ENVIRONMENT SENSORS AND ELECTRONICS

The operation of electronics and sensors in propulsion environments requires packaging technologies beyond those for conventional electronics and sensors. For *in situ* monitoring of aerospace engines, sensors and electronics must operate at temperatures of 500°C and above. Thus, the packaging materials and basic components, such as substrate, metallization material(s), electrical interconnections (such as wire-bonds), and die-attach must be operable and reliable in high temperature (500°C) and chemically reactive (especially oxidizing and reducing) environments. These packaging components may also experience high dynamic pressure and high acceleration, depending on the application. These harsh operation environments are far beyond those which commercially available packaging technologies can withstand; therefore, development of high temperature, harsh environment packaging technologies is necessary to implement high temperature sensors and microelectronics in aeronautic and space propulsion systems as well as Venus missions.

Ceramic substrates and precious metal thick-film metallizations have been proposed for packaging of harsh environment electronics and sensors, based on their excellent stability at high temperatures and in chemically reactive environments [14,15]. As a packaging substrate material, aluminum oxide has acceptable variation of dielectric constant and dielectric loss in the temperature range from 25 to 500°C for a wide frequency range. Aluminum nitride was proposed to package high temperature SiC MEMS and power devices because it possesses a low thermal expansion coefficient [16] and high thermal conductivity.

Recently, ceramic (aluminum nitride and aluminum oxide) substrates and gold (Au) thick-film metallization based chip-level electronic packages (Fig. 4a) [2,17] and printed circuit boards (Fig. 4b) have been designed and fabricated for testing high-temperature devices. The electrical interconnection system of this advanced packaging system, including the thick-film metallization and wirebonds, has been successfully tested at 500°C in an oxidizing environment for over 5000 hours with DC electrical bias. Electrically conductive die-attach materials with low curing temperature are being developed for packaging of SiC devices.

(a)

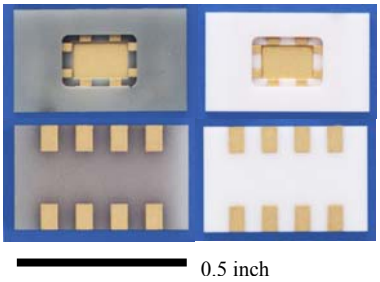

(b)

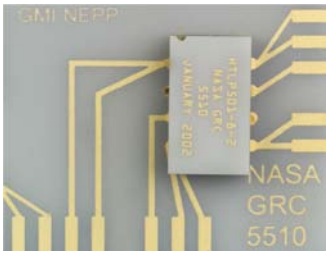

Fig. 4. (a) AlN (left) and Al_2O_3 (right) high temperature chip-level packages. (b) AlN PCB designed for AlN packages.

An 96% aluminum oxide based packaging material system was successfully used to facilitate the test, previously described above, of an in-house-fabricated SiC MESFET under electrical bias in a 500°C air ambient for more than 2000 hrs [2,3]. Fig. 2b shows the transistor current-voltage characteristics at the start of the test and after 558 hours of continuous electrical operation in air at 500°C. The packaging components continued to successfully operate without observable electrical degradation for the full duration of the 500°C test that exceeded 2000 hours in duration. Further, the demonstration of a functional 500°C amplifier, discussed above, highlights the most recent progress in printed circuit board level packaging and passive devices for 500°C [8] and is a significant step towards 500°C and Venus relevant applications. The board packaging is shown in Figure 5.

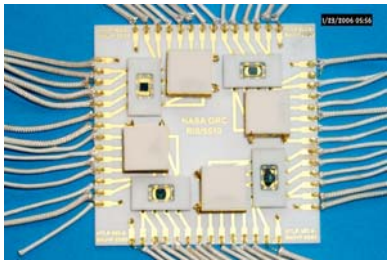

Fig. 5. The test assembly of 500°C amplifiers based on SiC MESFETs and aluminum oxide packaging system. The test assembly includes four amplifier circuits.

4. SENSOR TECHNOLOGY DEVELOPMENT

A range of sensor developments applicable to Venus missions is in progress at NASA GRC. The sensor development includes pressure sensors, thin film sensors, and chemical sensors. Each of these sensor types will be described briefly in the subsections that follow. A more detailed description is found in a separate paper presented at this conference [18].

4.1 High Temperature SiC Pressure Sensors

Conventional pressure sensors are temperature limited while SiC-based pressure sensors have a much wider temperature range and have the added benefit that high temperature SiC electronics can be integrated with the sensor. Progress has been made in both SiC pressure sensor micromachining and packaging [19]. The resulting sensors have demonstrated the capability to withstand high temperatures with improved reliability and operation up to 600°C [20]. These temperature ranges are more than adequate for Venus applications. Furthermore, the high temperature operation (600°C) of a SiC pressure sensor and anemometer has been previously demonstrated as separate discrete sensing devices. Ongoing research effort is geared towards integrating three functionalities by the utilization of advanced SiC MEMS Microsystems technology: a pressure sensor, an anemometer, and a fully passivated resistance temperature differential sensor [21].

4.2 Thin Film Physical Sensors

NASA GRC has an in-house effort to develop thin film sensors for surface measurement in propulsion system research. The sensors include those for strain, temperature, heat flux, and surface flow which will enable critical vehicle health monitoring of future space and air vehicles [22,23]. One area of development is a patented thin film multifunctional sensor which integrates into one "smart" sensor the designs of individual gauges that measure strain magnitudes and direction, heat flux, surface temperature, and flow speed and direction [24,25]. Various prototypes of the gauge have been bench tested on alumina substrates [25]. Future testing will include measuring all of the parameters simultaneously on a component to be tested in an engine environment. Thus, in one sensor system, a range of physical parameters regarding the immediate environment can be measured in Venus relevant environments.

4.3 Chemical Sensor Technology

The development of MEMS-based chemical microsensors to measure emissions in high temperature, harsh environments has been on-going for a considerable time for emission monitoring applications [26]. A first generation chemical microsensor array (High Temperature Electronic Nose) has been demonstrated on a modified automotive propulsion system. The High Temperature Nose showed the ability to detect nitrogen oxides (NO_x), oxygen (O_2), and hydrocarbons (C_xH_y). These results are qualitatively consistent with what would be expected for this type of engine. They also show the value of using sensors with very different response mechanisms in an electronic nose array: the information provided by each sensor was unique and monitored a different aspect of the engine's chemical behavior. These sensors have direct application in detecting multiple chemical species in Venus relevant environments. Overall, a potential chemical sensor array can be tailored for mission needs.

5. POSSIBLE VENUS APPLICATIONS

The preceding pages discuss a range of NASA GRC high temperature electronics and sensor technologies. While these electronics and sensors were intended for aeronautics applications, these devices and supporting technologies have significant application in Venus missions. One illustrative example of the use of the high temperature electronics and sensors is to enable a Venus Integrated Weather Sensor (VIWS) System. The purpose of this instrument would be to provide the base technology to characterize the surface of Venus *in situ* by simultaneously measuring pressure, temperature, wind velocity, seismic activities, and chemical species as well as local temperature and heat flux on the surface and above the surface of Venus. Thus, this instrument provides weather and surface climate information from a sensor system directly exposed to the environment and able to operate for extended durations. This instrument might include the following technologies:

Atmospheric Physical Sensors: The use of silicon carbide (SiC) to sense pressure changes (absolute pressure

sensor), wind velocity (cantilever based anemometer), and resistance temperature differential. These three functionalities are integrated on a single weather sensor chip to characterize atmospheric conditions.

Atmospheric Chemical Sensors: An extension of a MEMS High Temperature Electronic Nose to measure species including carbon monoxide, sulfur dioxide, hydrocarbons, nitrogen oxides, and oxygen. The approach is to use platform technology tailored to measure chemical gas species as required to characterize atmospheric constituents.

Surface Condition Physical Sensors: Multifunctional thin film sensors to measure surface temperature, strain, and heat flux in a single MEMS based sensor. This would enable monitoring of local thermal conditions embedded on a surface both to understand the surface conditions and also to provide information on vehicle conditions.

Therefore, this technology can very feasibly be incorporated into small and lightweight functional modules (without need for a cooling system), in order to help maximize scientific return while minimizing exploration vehicle size and weight. These multiple component technologies will be modularized onto a single platform. Thus, in a single sensing system, pressure, wind velocity, temperature, chemical species, as well as strain and heat flux can be measured. The approach would focus on integrating even more reliable and complex high temperature electronics and sensors into a small functional module to collect and transmit sensor data from the Venus surface for prolonged (as long as power can be supplied) durations.

The overall advantage of this approach is that using harsh environment electronics and sensors provides a multi-parameter weather and environment monitoring system which is able to operate *in situ* in Venus environments. The range of physical and chemical information available is broad and can significantly contribute to understanding the Venus environment. These ceramic MEMS sensing units and wide bandgap semiconductor electronics are operable in Venus environments without the need for a cooling system, and thus are small and lower in power consumption relative to conventional weather instruments. Other advantages include the fact that these systems are meant for engine operation and so the near chemical inertness of the starting materials, esp. SiC, makes them highly resistant to chemical attack. Being small and lightweight allows high resolution, broad terrain coverage, or distribution using Venus wind as a dispersal agent.

6. SUMMARY

NASA Glenn Research Center (GRC) is presently leading the development of electronics and sensors capable of prolonged stable operation in harsh 500°C environments. These technologies have the capability to enable new Venus missions without cooling of electronics and sensors while greatly improving the scientific return gained from Venus surface missions. One example of such improved capabilities is a possible Venus Integrated Weather Sensor (VIWS) System which can measure *in situ* a range of Venus atmospheric conditions as well as vehicle parameters in a miniature system. Further, with the inclusion of high temperature electronics and wireless communications, the data can be processed and wirelessly communicated enabling new Venus missions.

7. ACKNOWLEDGEMENTS

We gratefully acknowledge the contributions of those whose made this review paper and its contents possible: Dr. L. Matus, Dr. M. Zeller, T. Guo, J. Jordan, J. Xu, and E. Benavage of NASA GRC, C. Blaha, J. Gonzalez, D. Androjna, M. Artale, B. Osborn, P. Lampard, K. Laster, M. Mrdenovich of Sierra Lobo/NASA GRC, A. Trunek and D. Spry of OAI, Carl W. Chang and D. Lukco of QSS, A. Powell of SEST/NASA, O. Gregory of Rhode Island University, E. Savrun of Sienna Technologies, Inc., C.C. Liu of Case Western Reserve University, D. Makel and B. Ward of Makel Engineering, Inc., P. Dutta and B. Patton of the Ohio State University.

8. REFERENCES

1. Neudeck P. G., Beheim G. M., and Salupo C. S., 600°C Logic Gates Using Silicon Carbide JFET's, *Government Microcircuit Applications Conference Technical Digest*, 421-424, Anahiem, CA, 2000.

2, Hunter G. W., Wrbanek J. D., Okojie R. S., Neudeck P. G., Fralick G. C., Chen L.Y., Xu J., and Beheim G. M., Development and Application of High Temperature Sensors and Electronics for Propulsion Applications, accepted for publication for the Proceedings of the SPIE Defense and Security Symposium, 2006 Sensors for Propulsion Measurement Applications Workshop, 2006.

3. Spry D., Neudeck P., Okojie R., Chen L. Y., Beheim G., Meredith R., Mueller W., and Ferrier T., Electrical Operation of 6H-SiC MESFET at 500°C for 500 Hours in Air Ambient, 2004 IMAPS International High Temperature Electronics Conference, Santa Fe, NM, May 18-20, 2004.

4. Neudeck P. G., SiC Technology, in *The VLSI Handbook, The Electrical Engineering Handbook Series*, W.-

K. Chen, Ed., CRC Press and IEEE Press, Boca Raton, Florida, 2000.
5. Neudeck P. G., Okojie R. S. , and Chen L.-Y., High-Temperature Electronics- A Role for Wide Bandgap Semiconductors, *Proceedings of the IEEE*, Vol. 90, 1065-1076, 2002.
6. Neudeck P. G., Beheim G. M., and Salupo C. S., 600°C Logic Gates Using Silicon Carbide JFET's, Government Microcircuit Applications Conference Technical Digest, pp. 421-424, Anahiem, CA, 2000.
7. Okojie R. S., Lukco D., Chen L.Y., and Spry D. J., Reliability assessment of Ti/TaSi2/Pt ohmic contacts on SiC after 1000 h at 600°C, *Journal of Applied Physics*, Vol. 91, 6553-6559, 2002.
8. Chen L.Y., Spry D., and Neudeck P. G., Demonstration of 500°C AC Amplifier Based on SiC MESFET and Ceramic Packaging, presented at the 2006 HITEC Conference, Santa FE, NM, May 2006.
9. Schwartz, Z. D., Downey, A. N., Alterovitz, S. A., and Ponchak, G. E., "High-temperature RF probe station for device characterization through 500 º C and 50 GHz," *IEEE Trans. on Instrumentation*, Vol. 54, No. 1, pp. 369-376, Feb. 2005.
10. Schwartz Z. D., Ponchak G. E., Alterovitz S. A., Downey A. N., and Chevalier C. T., Measurement of Thin Film Integrated Passive Devices on SiC through 500°C, *Proceedings of the 34th European Microwave Conference*, Vol. 1, 313- 316, 2004.
11. Schwartz Z. D., Ponchak G. E., "1 GHz, 200 ºC, SiC MESFET Clapp Oscillator," *IEEE Microwave and Wireless Component Lett.*, Vol. 15, No. 11, pp. 730-732, Nov. 2005.
12. Levinshtein M. E., Rumyantsev S. L., Shur M. S., Gaska R., and Khan M. A., "Low frequency and 1/f noise in wide-gap semiconductors: silicon carbide and gallium nitride," *IEEE Proc.- Circuits Devices System.*, Vol. 149, No. 1, pp. 32-39, Feb. 2002.
13. Eddy Jr. C.R., Bassim N. D., Mastro M.A., Henry R. L., Twigg M.E., Holm R. T., Culbertson J.C., Neudeck P.G., Powell J.A., and Trunek A.J., Reduction of Defects in GaN Epitaxial Films Grown Heteroepitaxially on SiC, proceedings of the 2005 International Conference on Silicon Carbide and Related Materials, Pittburgh, PA , Sept. 18-23, 2005.
14. Salmon J. S., Johnson R. W., and Palmer M., "Thick Film Hybrid Packaging Techniques for 500°C Operation", Transactions of Fourth International High Temperature Electronics Conference (HiTEC), Albuquerque, New Mexico, June 15-19, 1998.
15. Chen L-Y., Okojie R. S., Neudeck P. G., and Hunter G., Material System for Packaging 500°C MicroSystems, MRS Proceedings, Symposium N: Microelectronic, Optoelectronic, and MEMS Packaging, San Francisco, CA, April 16-20, 2001.
16. Chen L-Y., Hunter G., and Neudeck P.G., Silicon Carbide Die Attach Scheme for 500°C Operation, MRS 2000 Spring Meeting Proceedings-Wide-Bandgap Electronic Devices (Symposium T), San Francisco, CA, April 10-14, 2000.
17. Chen L-Y. and Hunter G., Al2O3 and AlN Ceramic Chip-level Packages for 500°C Operation, 2005 International High Temperature Electronics Conference (HiTEN), Paris, France, September 6-8, 2005.
18. Hunter G. W., Okojie R. S., Oberle L., Krasowski M., Neudeck P. G., Beheim G. M., Fralick G., Wrbanek J., and Greenberg P., Microsystems, Instrument Electronics, And Mobile Sensor Platforms, Fourth Annual International Planetary Probe Workshop, Pasadena, CA, June 27-30, 2006.
19. Okojie R. S., Savrun E., Nguyen P., Nguyen V., Blaha C., Reliability Evaluation of Direct Chip Attached Silicon Carbide Pressure Transducers, 3rd IEEE International Conference on Sensors, Vienna, Austria, October 24-27, 2004.
20. Okojie R. S., Beheim G. M., Saad G. J., and Savrun E., Characteristics of Hermetic 6H-SiC Pressure Sensor at 600°C, AIAA Space 2001 Conference and Exposition, AIAA Paper No. 2001-4652, Albuquerque, NM, August 28-30, 2001.
21. Okojie R. S., Fralick G. C., Saad G. J., Blaha C. A., Adamczyk J. J., and Feiereisen J. M., A Single Crystal SiC Plug-and-Play High Temperature Drag Force Transducer", Digest of Technical Papers for Transducers '03, pp. 400-403, IEEE Catalog Number 03TH8664C, The 12th International Conference on Solid State Sensors, Actuators and Microsystems, Boston, MA June 8-12, 2003.
22. Lei J. F., Martin L. C., Will H. A., Advances in Thin Film Sensor Technologies for Engine Applications, NASA TM–107418, Turbo Expo '97, Orlando, FL, June 2-5, 1997.
23. Martin L. C., Wrbanek J. D., and Fralick G. C., Thin Film Sensors for Surface Measurements, NASA/TM—2001-211149, September 2001.
24. Lei J. F., Fralick G. C., and Krasowski M. J., Microfabricated Multifunction Strain-Temperature Gauge, US Patent 5,979,243, November 9, 1999.
25. Wrbanek J.D., Fralick G. C., Martin L. C., Blaha C.A., A Thin Film Multifunction Sensor for Harsh Environments, NASA TM-2001-211075, AIAA–2001–3315, July 2001.
26. Hunter G. W., Liu C. C., Makel D., *MEMS Handbook Second Edition, Design and Fabrication*, CRC Press LLC, ed. M. Gad-el-Hak, Boca Raton, Florida, Ch. 11, 2006.

5-1-2006

Extreme Temperature/Radiation Tolerant Crystal Oscillator for High Reliability Space Applications

Kouros Sariri
Frequency Management International Inc. (FMI)
15302 Bolsa Chica St.
Huntington Beach, CA 92649
714-373-8100 ksariri@fmi-inc.com

***Abstract*—**Chronos Technology (Div. of FMI, Inc.) is presently involved in an SBIR phase II effort to produce and deliver a comprehensive, practical and commercially available solution for a novel extreme temperature (both cold & hot), and radiation tolerant, compact radio frequency clock source (RTXO). Offering compelling features such as surface mounting, scalable configuration and miniature footprint, this innovative technology directly targets a wide range of requirements.

RTXO satisfies the critical requirements of NASA space programs such as Mars Science Laboratory (MSL), MER and future missions to Moon at both system and subsystem level with operating temperatures in the -180℃ to +120℃.

It also addresses the requirements of the extreme high temperature RTXO that could be utilized for the missions to Venus and other extreme environment space systems with highest operating temperature range to 460℃ and high ambient pressure to 90 Bar.

Furthermore, the RTXO enables and improves wide range of scientific, military & commercial space systems with its miniaturized footprint and rugged construction.

As for non space systems, it delivers a higher level of performance at smaller size to critical down-hole, nuclear process monitoring and very demanding geothermal applications.

Chronos Technology is the R&D division of Frequency Management International Inc. (FMI), a U.S. based, owned and operated company that offers high reliability frequency control products such as crystal resonators, crystal oscillators, VCXOs, and phase locked sources for applications ranging from high temperature down-hole and geothermal systems to commercial and scientific space. In addition to the scalable design, the proposed solution includes the electromechanical assembly and manufacturing processes to facilitate reliable and repeatable RTXO manufacturing. We have already fabricated and tested resonators for the extreme low temperature applications and completed the circuit design of the extreme low temperature RTXO using the thermal compliant and radiation tolerant elements.

We have already established the scalable designs for a wide range of crystal resonator frequencies in the single rotation miniature configuration for the extreme low temperature RTXO. The scope of progress so far offers a clear path to fabricating RTXO for extreme low and high temperature ranges.

We do expect that our solution will immediately and profoundly impact plans for the present and future space missions and for standard and other extreme environment space applications. RTXO brings new paradigm to resolve space systems design risk in terms of higher reliability and performance at significantly reduced size, weight and manufacturing time which all point to lower cost. This effort will yield innovations ranging from unique extreme temperature and high-Q resonator material, a unique matching integrated resonator driver amplifier/buffer based on Silicon Carbide (SiC) and the smallest surface mount high reliability, space level, radiation tolerant clock source.

EXTREME ENVIRONMENT ELECTRONIC PACKAGING FOR VENUS AND MARS LANDED MISSIONS

Linda Del Castillo[(1)], Donald V. Schatzel[(1)], Carissa Tudryn[(1)], Toshiro Hatake[(1)], Yuan Chen[(1)], Mohammad Mojarradi[(1)], and Elizabeth Kolawa[(1)]

[(1)]Jet Propulsion Laboratory, 4800 Oak Grove Drive, Pasadena, California 91109, USA, Email: Linda.DelCastillo@jpl.nasa.gov

ABSTRACT

Electronic packaging solutions for both Venus and Mars surface ambient conditions are determined by the lifetime and survivability of the material combinations selected, as well as by the dominant failure mechanisms for components subjected to such conditions. The results of various investigations on the reliability of packaged electronics for Venus and Mars ambient environments will be discussed in terms of the dominant failure mechanisms for the different configurations and environments.

1. ENVIRONMENTS AND MISSIONS

Future NASA Solar System exploration in-situ missions involve operation in extreme environments of temperature, pressure and radiation. The most challenging missions that will require operation in high temperature environments include Venus surface exploration missions and Venus sample return (480°C). On the low end of the temperature spectrum, Mars surface exploration missions require functionality from -120°C to +20°C for many cycles. Although the minimum Titan surface temperature (-180°C) is significantly lower than that on Mars, the development of packaging capable of surviving the wide temperature range and numerous cycles of the Martian environment is significantly more challenging than the development of packaging capable of sustained operation at -180°C. Just as with electronic devices, electronic packages intended for space applications are generally rated for operation within the military specified range of temperatures (-55 to +125°C). Therefore, packaged devices must either be maintained within this specified temperature range, or they must be designed for the ambient environment and evaluated under relevant operating conditions. A plot comparing each of these operating conditions is included in Fig. 1.

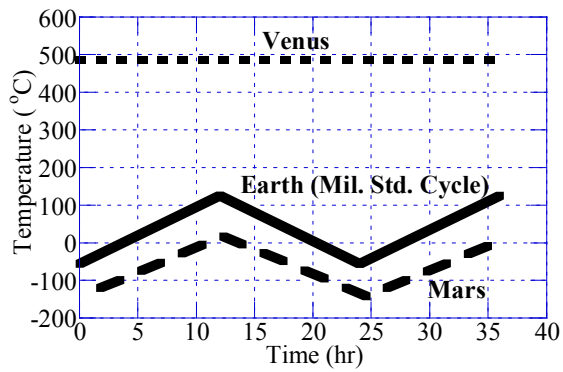

Fig. 1. Plot comparing the temperature cycles observed for electronics exposed to Venus and Mars surface ambient environments, as well as the military standard temperature cycle used for most space rated electronics.

Since current military and space rated electronics have typical application temperatures of -55 to 125ºC, electronic instruments and systems used for space exploration are traditionally maintained within protective environmental enclosures that allow them to function within their rated temperature ranges of operation, shielding them from the extreme temperatures, pressures and radiation levels of outer space or the target planetary ambient environments. Unfortunately, maintaining all of the electronics within this protective environment requires significant energy, and under several circumstances limits the mission's science return. Conversely, one could design the entire system to survive within the planet's ambient environment.

For Venus, the problem with this solution is that electronics capable of functioning at the desired operating temperatures (+480°C) do not possess the level of complexity available with standard Si electronics that operate within the military specified temperature range. Therefore, inconsistencies between the level of functionality available in current high temperature electronics capable of operating at 480°C and that required for the complete spacecraft in a Venus landed mission makes such an option unfeasible. Detailed

understanding of the capabilities and limitations of specialized high temperature electronic systems allows a third option, which is a craft that maintains high level, complex, low power electronics within the protective environmental enclosure, while allowing select subsystems to operate within the ambient environment of the planet. This option, as illustrated in Fig. 2, minimizes the cost and thermal load required to maintain a large volume of instrumentation at a significantly lower temperature than the ambient environment, while limiting the cost of high temperature electronic development efforts to critical subsystems that do not require complex circuitry.

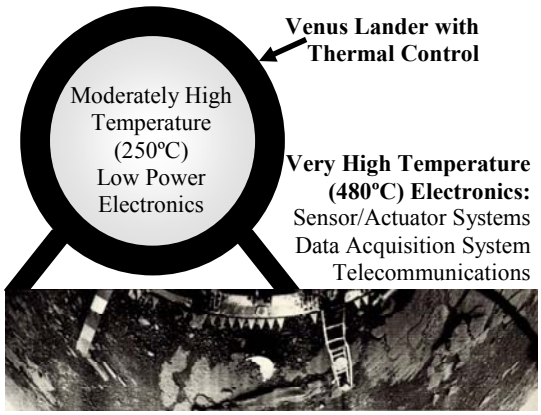

Fig. 2. Schematic of hybrid Venus Lander concept.

As illustrated in Fig. 2, there are several critical electronic subsystems, including sensor/ actuator systems, data acquisition systems and telecommunications. Regarding sensor, actuator and data acquisition subsystems, the goal is to maintain the required signal conditioning, signal amplification and control electronics close to the sensors and actuators with which they are associated. This reduces thermal leakage through the cabling port on the Lander as well as increasing the signal to noise ratio for the sensors. Much of the remaining electronics and instruments will need to be protected from the harsh Venus surface environment via a pressure vessel that is thermally controlled using either insulation alone or a combination of active cooling and insulation. Since maintaining heat generating electronic systems within the vessel greatly increases the amount of power required to maintain the desired internal temperature and reduces overall mission lifetime, the development of 500ºC electronics will allow the removal of high heat dissipating subsystems, such as signal transmitters for telecom, power converters, and actuator drive electronics from the pressure vessel.

As described for the Venus lander, the majority of the electronics required for a Mars rover would be held within the warm electronics box (WEB) that maintains the electronics within the military specified range of temperatures. Currently, sensor, actuator and data acquisition subsystems are kept within the WEB and are connected with their associated sensors through a complex network of heavy cables that run throughout the rover. Maintaining the required signal conditioning, signal amplification and control electronics close to the sensors and actuators with which they are associated would significantly reduce the weight and complexity of the system, while increasing the signal to noise ratio for the sensors.

2. ELECTRONIC PACKAGING

Electronic Packaging includes all of the passive components and materials used to connect integrated circuits (or individual devices) and sensors to each other and with the outside world. As shown in the Fig. 3 schematic, First-level packaging includes the signals directly connected to the device (within a package) and Second-level packaging includes the packaged active and passive devices as well as the printed circuit board that connects them. This paper will focus on the extreme environment challenges associated with First and Second Level Packaging.

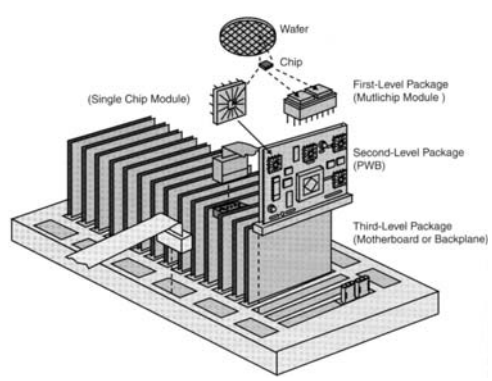

Fig. 3. Schematic illustrating the three levels of electronic packaging.[1]

Failure of electronic packaging for extreme environments can be separated into two different categories, over-stress and time-dependent failure mechanisms, as detailed in Fig. 4. Over-stress mechanisms are those that occur immediately upon exposure to the target environment and test conditions. Examples include plastic deformation, melting of materials, and change in resistance or capacitance with increasing temperature. Conversely, time dependent degradation of

electronic packages relate to processes that occur over many cycles or after extended exposure to the target operating conditions. Examples include fatigue, creep, diffusion, oxidation, changes in resistance or capacitance with time at temperature, and electromigration. The dominant failure mechanism for packages exposed to the Mars ambient environment is fatigue, which is influenced by phase transformations, embrittlement at these low temperatures, and especially the coefficient of thermal expansion (CTE) mismatch between the different materials. Due to the high temperatures of the Venus ambient environment, failure mechanisms of serious concern for electronic packages include material degradation, plastic deformation, creep, diffusion, oxidation, and electromigration.

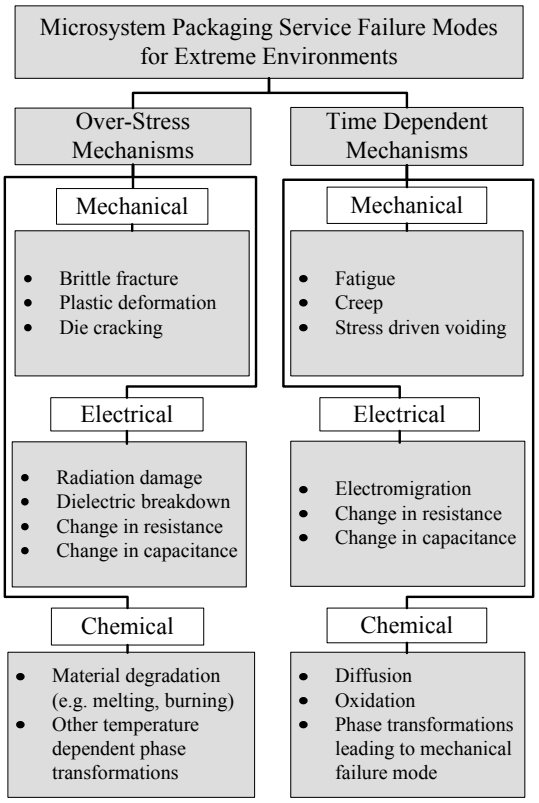

Fig. 4. Illustration describing failure mechanisms for electronic packages exposed to extreme environments.

3. MARS

Failure of electronic packages exposed to the low temperature thermal cycles of Mars is dominated by fatigue, which is the phenomenon of material failure under cyclic loading conditions. For electronic packaging, fatigue generally results from large temperature fluctuations and CTE differences between adjoining materials. As shown in Fig. 5, examples of sites at which fatigue becomes a problem are solder joints, die attachment points, and wirebonds. The room temperature fatigue life of gold as a function of stress amplitude is shown in Fig. 6. For electronic packages exposed to the Mars ambient thermal cycles, the fatigue life of the gold wirebonds is influenced by global and local thermal expansion mismatches between: (i) glob-top encapsulant and the silicon die, (ii) encapsulant and the wire, and (iii) encapsulant and the substrate assembly. For a wirebond chip-on-board assembly with a rigid encapsulant, the region above the ball bond has been found to be the predominant failure site.[2] This finding agrees well with the failed wirebond shown in Fig. 7, which was located on a chip on board assembly that was encapsulated with a rigid epoxy and thermal cycled from -125 to +85°C (a relevant Mars ambient condition).

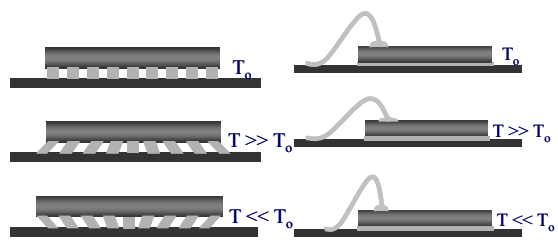

Fig. 5. Schematic illustrating the influence of temperature for materials with differing CTEs.

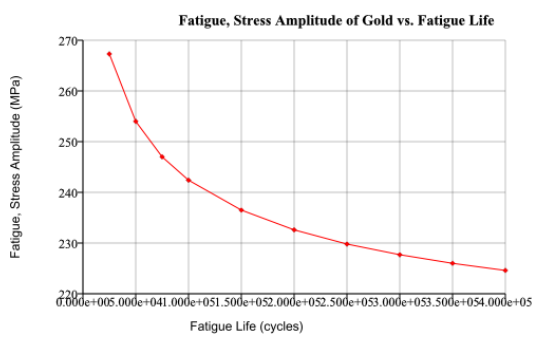

Fig. 6. Plot of room temperature fatigue strength as a function of cycles for gold.[3]

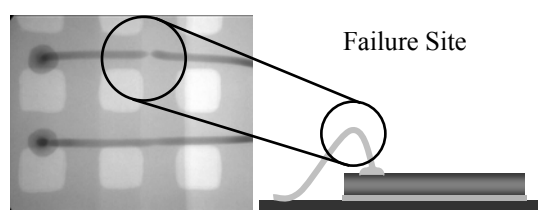

Fig. 7. An X-ray image of a failed wirebond and a schematic illustrating the location of failure.

Phase transformations that influence fatigue resistance, mechanical behaviour and electrical behaviour can also occur at the low temperatures of the Mars thermal cycle. Of particular concern are

the glass transition temperatures of the polymers used in the assemblies. This temperature can result in significant changes in the elastic moduli and CTEs of polymers.

4. VENUS

Due to the high temperatures of the Venus ambient environment, issues such as the degradation of materials with temperature, interdiffusion of metal layers, and oxidation become significant. Although the minimal thermal cycles experienced within the dense atmosphere of the Venus surface eliminates the issue of fatigue discussed previously, the CTE differences between the die and the substrate combined with the significant temperature differential observed during the single thermal cycle result in a sustained stress at the elevated temperature, which in turn causes problems such as high temperature tensile failure and creep. In addition, phase and microstructural changes combined with diffusion and oxidation influence the strength, ductility and conductivity of the different materials. Finally, all of these issues combined with the applied current can yield electromigration problems. The correct selection of materials for electronic packaging within the Venus environment can help minimize several of these issues, while in other cases trade-offs must be made between several competing mechanisms in order to promote the survival of the overall subsystem.

4.1 Melting and Degradation of Materials

Traditional microelectronic packaging relies heavily on the use of polymers for applications such as printed wiring boards, die attach and conformal coating. Since all of the traditional polymers used in electronic packaging degrade (melt or burn) below Venus surface temperatures, alternate materials and configurations must be used. In addition, various passivation materials used for thin film circuits may melt or soften, exposing the highly reactive materials underneath, as shown in Fig. 8 below.

As-received After Testing at 500°C

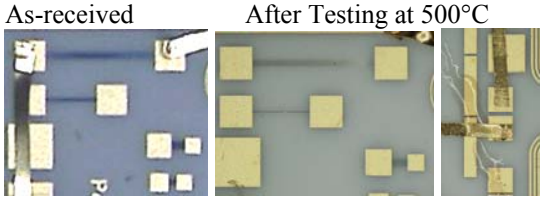

Fig. 8. Optical photograph of thin film resistors, before and after long term testing at 500°C.

With respect to die attach materials, which are used to attach the backside of a chip to the substrate that connects the device to other passive and active devices, most of those used for commercial applications on Earth melt at significantly lower temperatures than those required for Venus. A set of solder and braze considered for this application are summarized in Table 1, along with their melting temperatures. One of the techniques used to minimize temperature excursions during processing is to use lower melting temperature solders than the required application and rely on diffusion to modify the composition of the attach material. This will be discussed further in the following section.

Table 1. Maximum use temperatures for various die attach materials.

	Max. Temp. (°C)	Comments
Solders		
Au80Sn20	280	Eutectic
Au88Ge12	356	Eutectic
Au97Si3	363	Eutectic
Sn5Pb95	308	Solidus
Pb92In5Ag3	300	Solidus
Brazes		
82Au/18In	451	Solidus
45Ag/38Au/17Ge	525	Eutectic
72Ag/28Cu	780	Eutectic
82Au/18Ni	950	Eutectic
Other		
Au thick film paste	> 600	High firing temperature
Au thermo-compression bonding	> 800	Assumes Au to Au interface

4.2 Diffusion, Solid State Phase Transformation and Oxidation

Diffusion, the net transport of matter to minimize a concentration gradient or a free energy gradient, is significantly dependent upon temperature and time. This phenomenon is illustrated schematically in Fig. 9, which shows two different metals, Au and Ni, in intimate contact with each other, along with the associated concentration of Au, before and after extended exposure at an elevated temperature.[4] As mentioned in the previous section, this can be used advantageously for die attach materials as a means of modifying the composition of the alloy to that of one that is more amenable to the application. This process can be better described in relation to the phase diagram shown in Fig. 10. If Au-Sn solder of concentration C1 is placed in direct contact with pure Au, the composition of the alloy can change to C2 following extended exposure at elevated temperature. The amount of time required

for this concentration change is dependent upon the temperature of exposure and the respective diffusivities of Au and Sn.

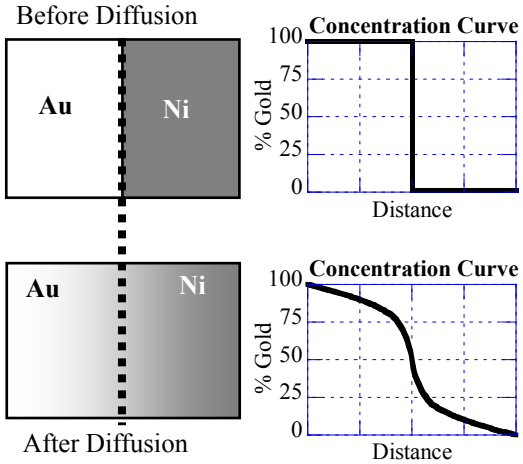

Fig. 9. Schematic illustrating interdiffusion of metals for Au-Ni diffusion couple.

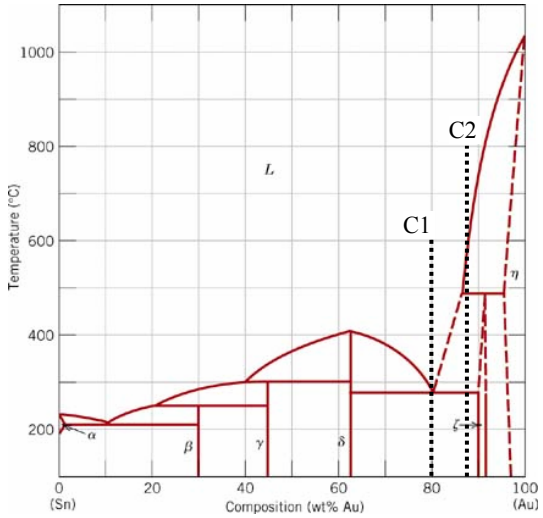

Fig. 10. Au-Sn binary phase diagram. [5]

Since there tend to be several different metal layers on both the die and the substrate, one must be careful to avoid the selection of attachment materials that will yield weak or brittle intermetallic phases following the solid state phase transformations that often accompany the interdiffusion of multiple metals. Fig. 11 exhibits the formation of secondary phases following the exposure of an assembly with a SiC device attached to a Cu-Ni-Au plated substrate using a Au-Ge die attach material to 500°C. Composition of the resulting brittle Ge-Ni intermetallic phase is shown in Fig. 12.

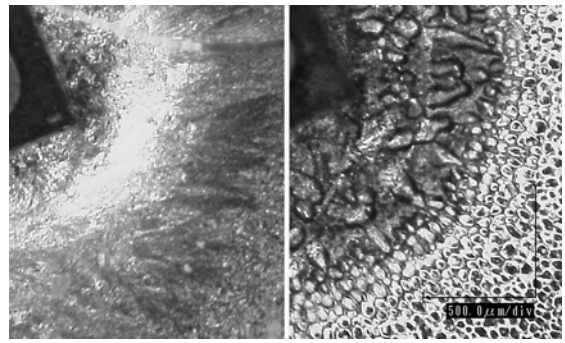

Fig. 11. Optical photograph of die attach material, before (left) and after (right) exposure at 500°C.

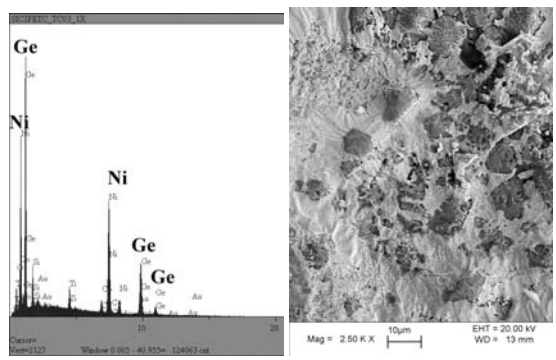

Fig. 12. EDS and SEM micrograph of GeNi phase.

The most dangerous diffusion-related failure mechanism for Venus electronics is the oxidation of metal to semiconductor contacts on the SiC devices. The diffusion of O_2 through the outer metal layers to the base metal forming the metal to semiconductor contact results in the oxidation of this base metal and a subsequent increase in the contact resistance. Development and implementation of diffusion barrier layers capable of minimizing oxidation along with device design optimization to minimize the effect contact resistance on circuit functionality are both required.

4.3 Elevated Temperature Deformation

Due to the many interfaces present within electronic assemblies, the stresses observed are closely related to the CTE, strength, and elastic modulus for each of the materials involved, along with environmental parameters, such as temperature excursions, and design parameters, such as die size. A plot of CTEs as a function of temperature for various materials used in high temperature assembly is provided in Fig. 13. Stress distributions between adjoining materials can be minimized by selecting materials with CTEs that are more closely matched over the entire range of exposure temperatures.

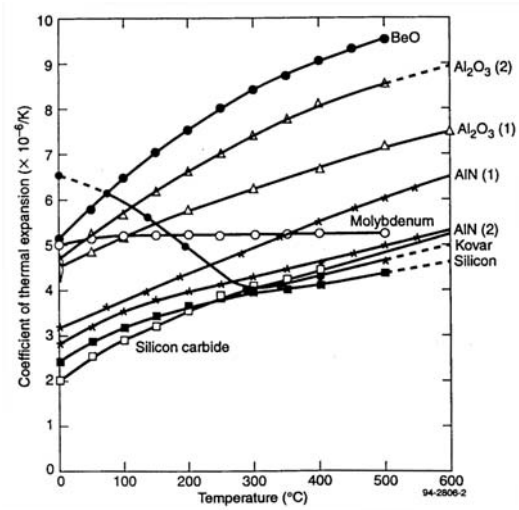

Fig. 13. Coefficients of thermal expansion as a function of temperature for various materials used in high temperature electronic assemblies. [6]

If the CTEs of the device and the substrate are not exactly matched, the stresses at the interface will steadily increase from a minimum at the center of the device to a maximum at its edges. As shown in Fig. 14, which summarizes the strength of various Pb-Sn solder alloys as a function of temperature, strength tends to reduce as temperature increases. In this application, this situation is exacerbated by the fact that the stresses within the die attach increase as a function of temperature as well. If the die attach is too weak it may fail following initial exposure.

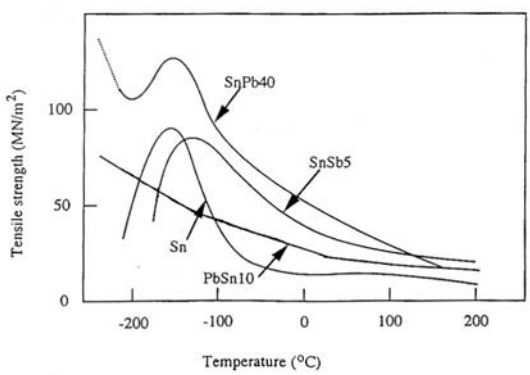

Fig. 14. Tensile strength as a function of temperature for various Pb-Sn solders. [6]

Assuming that the stresses are below the yield strength of the material, time and temperature dependent deformation, or creep, may still occur. Since creep is both time and temperature dependent, creep may occur at temperatures as low as 0.3 times the melting temperature (T_m) of the material; however, appreciable creep deformation within a reasonable amount of time is expected at temperatures above $0.5T_m$. The influence of temperature and applied stress on creep strain and time to failure is illustrated in Fig. 15. Creep of Au, which has a melting temperature of 1337K (1064°C), will become a significant concern above about 668K (395°C).

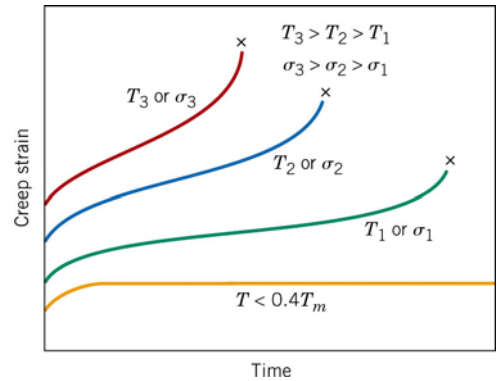

Fig. 15. Schematic illustrating the influence of temperature and stress on creep strain and time to failure. [4]

4.4 Electromigration

Due to the role of diffusion in electromigration and the fact that most active devices capable of working at elevated temperatures are power devices, electromigration becomes a considerable concern for high temperature electronic systems. Factors influencing electromigration include: current density, temperature, grain structure, temperature gradients, passivation coating selection (adhesion/degradation), surface structure and migration, stress distribution within the metal film, distribution and selection of metal layers, alloying effects, surface roughness, and CTE mismatch among the different layers. A schematic illustrating the influence of temperature and current density on electromigration is shown in Fig. 16.

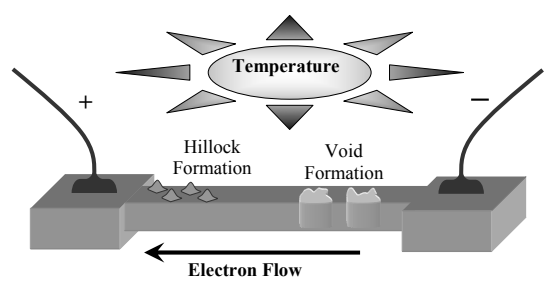

Fig. 16. Schematic illustrating the influence of temperature and current density on electromigration.

In addition to the previously mentioned temperature and device effects, exposure to Venus temperatures can result in grain structure and composition changes, passivation coating degradation, and increased stress within the metal layers. Careful selection of each of the different materials involved, along with the development of small signal devices, are critical to minimize electromigration problems.

5. SUMMARY AND CONCLUSIONS

NASA and ESA needs for electronics and electronic packaging are unique, with environmental requirements that are well outside the temperature ranges required for most terrestrial applications. However, the development of electronics capable of operating directly within the ambient environment of the target planetary environments will allow the incorporation of distributed electronics into future missions, potentially increasing the science return for such missions. The influence of environmental exposure of electronic subsystems on the behaviour of electronic packaging materials and configurations was discussed with respect to Mars and Venus. Proper selection of materials to minimize the effect of issues such as fatigue, creep, oxidation and electromigration, among others is critical to the performance of future distributed electronic systems.

6. REFERENCES

1. Tummala R., *Fundamentals of Microsystems Packaging*, McGraw-Hill, 2001.
2. Jinka K. K., *Thermo-Mechanical Analysis of Encapsulated Ball-Wedge Wire Bonds in Microelectronics, using Raleigh-Ritz Modeling*, Masters Thesis, University of Maryland, 2006.
3. McCammon R. D. and Rosenberg H. M., "The Fatigue and Ultimate Tensile Strengths of Metals Between 4.2 and 293 Degrees K," *Proc. Roy. Soc. London, A*, A242 (1229), pg. 203-11, 1957.
4. Callister, W. D., Jr., *Materials Science and Engineering: An Introduction, (7th Ed)*, John Wiley and Sons, Inc. 2007.
5. *Metals Handbook, 8th edition, Vol. 8, Metallography, Structures and Phase Diagrams, American Society for Metals*, Metals Park, OH, 1973.
6. McCluskey, F. P., Grzybowski, R., and Podlesak, T., eds., *High Temperature Electronics*, CRC Press, Boca Raton, 1997.

7. ACKNOWLEDGEMENTS

The research described in this paper was carried out at the Jet Propulsion Laboratory, California Institute of Technology, under a contract with the National Aeronautics and Space Administration.

EXTREME TEMPERATURE DESIGN TECHNIQUES FOR A VENUS EXPLORATION S-BAND TRANSMITTER

Robert H. Sternowski

Softronics Ltd., 6920 Bowman Lane NE, Cedar Rapids, IA 52402, USA, Email: bobs@softronicsltd.com

ABSTRACT

Softronics Ltd. was awarded a competitive NASA Small Business Innovation Research (SBIR) contract in 2004 for the analysis, design, and build of a transmitter for a Venus surface explorer craft. The novel aspect of the winning design was the ability of the S-band transmitter to operate continuously in the harsh 465°C, 90 barr CO_2 Venusian atmosphere *without cooling*. The transmitter is built from Silicon Carbide transistors and minimal other components constructed similar to early 20th century radios; no conventional electronic components or organic materials would survive the environment even briefly. This paper chronicles the development path to a successful design.

1. ORIGINS OF THE PROJECT

The Venusian transmitter project began in response to a NASA small business R&D solicitation. Based on prior military experience with new high-temperature Silicon Carbide transistors, as well as Softronics' experience in radio design and development, we set out to devise a strategy to win a competitive design award by offering a novel solution. In reviewing prior art, it was immediately obvious that past Venusian probes relied on a huge pressure vessel with closed cycle cryogenic cooling. The size, weight, and power of such probes were immediately targeted as candidates for a new approach. The strategy that was somehow creatively sparked was to offer a transmitter that would work in that environment without a pressure vessel or cooling system; the electronics would be exposed to and operated at the ambient 465°C atmospheric temperature.

The six-month Phase I study performed an analysis of how our approach would fare in the Venusian environment, along with conducting temperature tests on critical materials, components and circuits. In summary, that study and experimental output showed that our approach was feasible. That study in turn resulted in an invitation to propose a full-scale prototype for a Phase II contract; we did so, and were competitively awarded a second contract to build the prototype. The remainder of this paper describes much of the path travelled to a solution.

2. DESIGN APPROACH

Our primary concern was the environment, and we were given key guidance after contract award, to wit:

- We should design for constant 465°C operating ambient temperature
- We should design for constant 90 barr pressure
- We should design for 97% CO_2 atmosphere
- We should not be concerned with the acid, which is present only on atmospheric entry; the probe will be behind a shroud

After carefully comparing these environmental constraints against our proposed approach, we quickly realized that:

- The 465°C temperature was our primary driver for material selection and thermal design
- The pressure was irrelevant to our design
- The supercritical CO_2 atmosphere was actually beneficial to our cooling scheme
- Lack of acid opened the material choices

Additionally, it appeared that the only reason to have a case for the transmitter was to prevent any type of ambient material (jokingly dubbed "green Venusian slime") from accumulating on the microwave components and degrading their performance via one of a number of high frequency loss mechanisms. Thus it was determined that a closed (using a "leaky" gasket material) but not pressurized protective case was desirable.

Given a valid set of boundary conditions, we planned our effort, and broke it down into discrete tasks:

1. Transmitter architecture
2. Material selection
3. Thermal design
4. Circuit design
5. Component design
6. Environmental test

Each task is discussed in detail in the remainder of this paper.

3. TRANSMITTER ARCHITECTURE

While our original proposal had been based on a 10 watt transmitter at 2.2 GHz (S-band), sufficient to maintain a 50 kbps link to an orbital relay, we were asked to consider how we would build a direct Venus-Earth S-band transmitter with approximately 150 watts output power. Thus we broadened our approach to consider both possibilities, using a variable mix of common radio modules.

Because of the extreme temperature, only Silicon Carbide semiconductors were usable as active devices. Thus we could not build a conventional radio with crystals, frequency synthesizers, filters, etc., because none of those conventional components exist in high temperature forms. So we stepped backward one century to the early days of radio and the techniques of Marconi and other pioneers to find a solution, knowing that they too lacked a selection of sophisticated components. This led us to an old concept of a free-running power oscillator. This was easily implemented with an SiC transistor and a transmission line feedback network, plus two resistors, four capacitors, and three inductors. Testing showed that the frequency accuracy and stability was a function primarily of the [predictable] expansion coefficients of the feedback network, with only minimal impact from the transistors.

Our transistor of choice was the Cree Inc. CRF-24010, one of the few production SiC high frequency MESFETs available on the open market. This device had the frequency response, gain, dissipation, and size that we required. Further research into SiC MESFET characteristics revealed that such SiC devices were capable of high total dose radiation needed to survive the transit to Venus, and up to 1000°C temperatures. However, the commercial device was rated only at more "Earthly" temperatures, and so we undertook a test program to determine the high temperature performance. In summary, we saw 40% of 25°C RF gain at an operating temperature of 600°. This showed that we could expect about 7 decibels (db) of gain, and no more than 2.5 watts output at temperature. Unfortunately the commercial package would not survive, and so we saw that a custom mounting for the die would be required.

Given 2.5 watts output and 7 db of gain, we proceeded to develop an architecture that used two oscillators in a frequency-shift keying (FSK) scheme, one "mark" and the other "space", that would fail "softly" to an On-Off Keying (OOK) modulation scheme in the event that one oscillator failed. To obtain 10 watts output for an orbital relay, a number of 2.5 watt amplifiers were cascaded and combined with passive hybrid couplers to a single antenna output. To obtain 150 watts output, many more amplifiers were used in a classical hybrid "tree". While this at first looked unbelievably complex, we gradually realized that the fail-soft nature of this architecture, coupled with the very low parts count and ruggedness of the simple components, actually made it a simple and attractive approach. We now had to proceed to the next level of detailed design to determine HOW we were going to implement our system design.

4. MATERIAL SELECTION

The first implementation problem was determining what materials would survive the 465°C ambient. A great deal of research, and a significant pile of incinerated or melted materials from our lab furnace, revealed some simple truths:

- No organic materials would survive.
- Glass and ceramic were the only two usable insulating materials.
- Our metal choices were limited to select metals: copper and alloys, iron and alloys, gold, silver. Lightweight metals would fatigue at high temperatures.
- Electrical connections would have to be mechanical, welded, brazed, silver-soldered, or eliminated (single-piece multi-component)

Given that we required resistors, capacitors and inductors, some ingenuity would be required, and led us back to Marconi once again. Our structural needs would be met by the allowable materials.

5. THERMAL DESIGN

The next problem was to determine how we could "cool" our transistor to the ambient 465°C, given that we could stand 30-40°C rise in junction temperature. The problem turned out to be a complex fluid problem, owing to the supercritical CO_2 atmosphere. We started out using ANSYS for modelling and design, and evolved to a software heatsink model called "NATSINK" by Dr. Ake Malhammar. With Dr. Malhammar's assistance, the software was tailored to the high pressure environment from its normal Earth ambient. The Aerospace Engineering Department at Iowa State University calculated the CO_2 fluid constants for our temperature and pressure, and when plugged into NATSINK, allowed us to model the

thermal performance of various configuration heatsinks and dissipations in a simulated Venusian environment.

The output of the thermal design was not unexpected: we needed to conduct the heat rapidly out of the 1 square millimeter SiC die to a sufficient dissipating area. To do this, we needed high thermal conductivity materials for our heatsink. At our temperatures, that left only diamond, Silicon Carbide, Copper, and Silver. Silver and Copper are very close in conductivity, thus Copper was the winner in that pairing due to cost. Silicon Carbide was no better than Copper, and far more difficult to work with. Many of our heatsink analyses focused on diamond, and even coating a ceramic heatsink with diamond (which is easily done today). We were very disappointed to find that, at 465°C, diamond's thermal conductivity degraded to about that of Copper due to shifts in the crystalline structure with temperature. Thus we used Copper for our heatsink material, with black finish for black body radiation. Fig. 1 shows the modular heatsink design, swirled for structural strength. Electronic modules are mounted to the inside vertical rim onto the fin bases.

A key secondary thermal problem to be solved was attaching the SiC transistor die to the heatsink (none of the other components had any significant thermal issues). Conventional solder attach was grossly insufficient, with a limit of 250-300°C. We turned to Dr. R. Wayne Johnson, Auburn University, for help, and in summary, he developed an alternate die attach braze process that would survive up to at least 515°C. We are proceeding with this solution, with implementation and test planned in 2007.

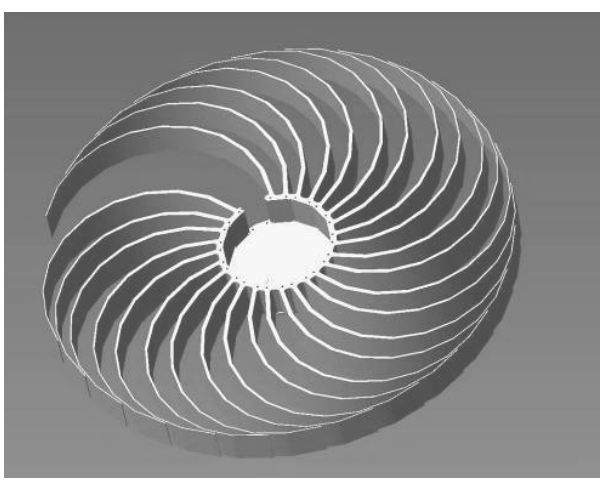

Fig. 1 – "Galaxy" Heatsink Design Has Circuit Boards Mounted On Inside Vertical Rim, With Interconnecting Power and Radio Quadrature Hybrids On A Top And Bottom Cover Disk

6. CIRCUIT DESIGN

From our system architecture design, we saw that the entire transmitter could be implemented with a series of 2.5 watt amplifier modules interspersed with quadrature combiners (also used as splitters). The oscillators were the common 2.5 watt amplifier module with a feedback network added, but were essentially the same design. Thus our effort focused on efficiently designing a common amplifier module and a quadrature combiner.

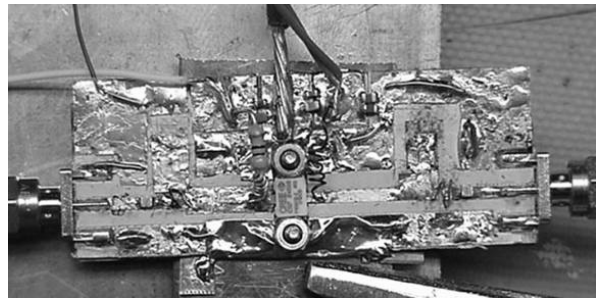

Fig. 2 – High Temperature 2.5W Amplifier Prototype

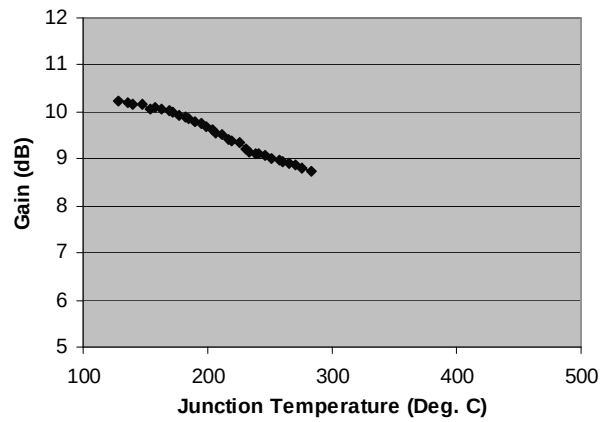

Fig. 3 – Gain vs Temperature Testing of Fig. 2 Amplifier

The amplifier circuit, after considerable modelling and experimentation, was selected to be a standard grounded-source MESFET amplifier. To improve DC power efficiency by approximately 100%, a negative grid bias (used as the keying signal) was selected in lieu of self-bias (e.g., a source resistor). To that circuit were added the necessary resistors, capacitors and inductors—approximately ten components per amplifier. Each amplifier or oscillator was to be implemented on a single ceramic circuit board.

The quadrature combiners/splitters were also extensively analyzed, and found to be easily

implemented as metallised traces on a ceramic circuit board, requiring no discrete components.

Fig. 2 shows one of our later breadboard amplifiers, and Fig. 3 the gain versus temperature test results. The final form amplifiers and oscillators will be built in 2007.

7. COMPONENT DESIGN

Our inspiration for component design was Marconi and his early transmitters. Given our limited material selection, we quickly converged on the following approaches:

- Resistors: either nichrome wire or fired ceramic paste wafers were buildable and survivable, and could be welded or brazed onto the ceramic circuit board; only two per amplifier were needed
- Capacitors: parallel plates or interdigitated fingers implemented as metallised traces on a ceramic circuit board were sufficient and easily implemented
- Inductors: at 2.2 GHz, inductors were simply transmission line metallised traces on our ceramic circuit boards

Wire used for power connections is fibreglass insulated copper. Coaxial cable—a unique problem—was designed by the project using copper semi-rigid 0.141 inch diameter cable but with the Teflon dielectric replaced by glass beads. Similarly, special high temperature SMA coaxial connectors were hand-built by replacing the Teflon dielectric insulator inserts with castable Aremco 586 ceramic.

8. SIMULATED VENUS TEST ENVIRONMENT

One of the key identified issues in the early stages of this project was just how we were going to prove the system would work in the actual [simulated] Venusian environment. The combination of temperature and pressure, plus supercritical CO_2, posed an interesting challenge. Once again, we turned to Iowa State University for assistance, and Dr. William Byrd, Director of NASA's Iowa Space Grant Consortium (ISGC, of which Softronics Ltd. is an industrial affiliate) came up with a novel and simple solution. Using the Ideal Gas Law, he observed that if we filled a sealed chamber with CO_2 at 25°C and 535 psi, then raising the temperature to 465°C would result in a pressure of 90 barr, equal to the Venusian pressure. Problem solved, neatly and simply.

With this solution in mind, we searched and found a small, used chemical reactor made by Autoclave Engineers that was capable of sustaining both the pressure and temperature simultaneously. The ISGC was awarded a subcontract to refit the chamber, instrument it, and conduct the final environmental tests on our transmitter circuits using this scheme.

Final testing will be done in the simulation chamber, although most of our testing is done in a laboratory furnace since pressure has little impact on our design.

9. SUMMARY

The high temperature Venus telemetry transmitter is well along in its design cycle. A significant number of material and architecture issues have been solved enroute to the final design, all using novel combinations of new technology and century-old radio construction techniques. The result will be a high temperature transmitter operating in the Venusian ambient that is directly heatsunk to the 465°C CO_2 atmosphere. Architectures for both orbital relay and direct Venus-Earth links have been developed, and are implementable with common modules.

The resulting extreme environment transmitter design and techniques are applicable to other applications, including general radio and circuit design in both hot and cold planetary probes, and military/commercial terrestrial applications in extreme environments.

Work on this project was performed under NASA SBIR contracts NNG05CA78C (Phase I) and NNC06CAC39C (Phase II).

Probe Radio Science in the Next Generation Deep Space Network

Sami Asmar and Robert Preston
Jet Propulsion Laboratory, California Institute of Technology

The end-to-end evolution of NASA's Deep Space Network (DSN) is driven by the need to significantly improve performance for spacecraft communications and navigation. The next generation network is likely to have advanced capabilities for Ka-band links augmenting X-band, increased effective receiving area and radiated power, and other features affecting the quality of radio-metric observables. The DSN is a world-class instrument for Radio Science research and has contributed to numerous scientific discoveries. The typical limitations to the Radio Science experiments are frequency stability, amplitude stability, signal-to-noise ratio, spacecraft and ground pointing stability, spacecraft non-gravitational forces, ground mechanical and electronic noises, intervening media, and navigation accuracy in predicting & reconstructing trajectory. In this paper, we discuss how the next generation Deep Space Network will impact the limitations to Radio Science experiments, most positively. A study of likely configurations of the next generation DSN and the expected performance of Doppler and range parameters relevant to Radio Science will be presented. We also discuss how future probe mission can benefit from the improvements to conduct experiments in atmospheric science as well as gravitation with improved received signal-to-noise ratio and improved interplanetary plasma and ionospheric and tropospheric calibrations.

Advances In Battery Technology Relevant For Planetary Probes

Chris Pearson[(1)], Andrea Bennetti[(2)], Rob Spurrett[(3)]

[(1)] *ABSL Space Products, 3617 E 8th Street, Long Beach, CA 90804, USA, chris.pearson@abslpower.com*
[(2)] *ABSL Space Products, F4Mezzanine, Culham Science Centre, Abingdon,OX14 3ED, United Kingdom, andrea.bennetti@abslpower.com*
[(3)] *ABSL Space Products, F4Mezzanine, Culham Science Centre, Abingdon,OX14 3ED, United Kingdom, rob.spurrett@abslpower.com*

ABSTRACT

This paper gives an overview of the advances in battery technology that have occurred in recent years, and are currently taking place, that are relevant for planetary probe missions. ABSL Space Products (ABSL) pioneered the current state of the art rechargeable battery technology, Lithium-ion, and has recently qualified a Lithium primary cell.

ABSL has supplied batteries for spacecraft destined to land on the planet Mars and a comet in deep space. Both of these missions drove unique battery requirements that were successfully solved by ABSL. Presently, ABSL is working on preliminary designs for batteries to power European and American planetary landers.

1. INTRODUCTION

ABSL has established the reputation as the industry leading supplier of rechargeable (secondary) battery technology utilizing the current state of the art: Lithium-ion. The first half of this paper explains the unique approach of ABSL of using commercial Lithium-ion cells, The Small-Cell Approach. The second half of the paper examines how ABSL is now able to offer cutting-edge primary cell technology, once more using commercially available cells.

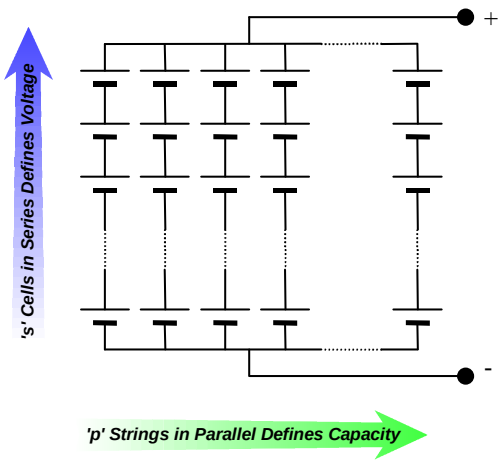

Fig 1 The ABSL Small-Cell battery configuration

2. THE ABSL SMALL-CELL APPROACH TO LITHIUM-ION

In the past, space batteries consisted of one or two strings of large capacity cells connected in series. This practice had been continued with advances in cell chemistries until the dawn of Lithium-ion. ABSL realized that there were huge benefits to the space industry in adopting smaller capacity Commercial Off The Shelf (COTS) Lithium-ion cells connected in a two-dimensional array as shown in Figure 1. ABSL term this concept the '***s-p***' topology. The battery voltage is determined by the number of cells connected in series ("s") and the battery capacity is determined by the number of such series "strings" connected in parallel ("p").

This unique utilization of small capacity cells arranged in arrays presents huge benefits for flexibility in battery configuration to meet capacity and volume layout to best meet mission demands. In the past (to optimize a battery for a particular program) the cost, risk and delay of a dedicated cell qualification program was necessary. However with ABSL concept by varying the "s" and "p" of the cell array, tailoring of battery performance became simpler and less costly.

The ABSL "Small-Cell" approach is similar in configuration to that of the Solar Array, and delivers two unique and invaluable benefits over large-cell battery options:

- ***Automatic Fault Tolerance***: - The in-built cell protection mechanisms, necessary to meet the safety demands of the consumer electronics market, ensure that a single-point failure in a cell leads to open circuit disconnection of a string. Combined with the small cell capacity used with the ABSL approach, this means almost negligible capacity reduction at battery level and no voltage level impact. The autonomous nature of protection and zero power dissipation deriving from ABSL proven approach are in strong contrast to dedicated cell by-pass electronics used in large cells battery systems. ABSL approach simplifies thermal design, and

eliminates problems associated with component stress following activation. The result is an exceptional level of reliability and robustness.

- ***Full Capacity Flexibility:*** - Capacity can be easily fine-tuned by altering the number of parallel strings without the cost, risk and schedule implications of a cell qualification program. Thus, our customers have scope to modify requirements early in the battery program, as a result of system-level technical development, without substantial risk, program delay and cost increase.

- ***Battery Simplicity:*** - Customers have consistently lauded the benefits of our battery simplification from the elimination of cell balancing electronics (essential on traditional Large-Cell batteries) as described in [1] as this reduces the complexity and cost of the power system, returning benefits at both technical and programmatic level. The checkout of cell balancing software can be notoriously costly and time consuming. Furthermore, the reduction in the number of telemetry channels and absence of telecommand requirement for safe battery monitoring and operation allows other subsystems to benefit.

Overall, the reduced risk of imperfection through utilizing small cells from modern, state-of-the-art production, compared to the traditional 'small batch' approach with large cells, has proven extremely valuable to customers ranging from small satellite manufacturers to major primes and national/international space agencies. Today, ABSL has received battery contracts for more sixty spacecraft and launch vehicles using the Small-Cell concept.

3. UTILIZING COTS LITHIUM-ION CELLS FOR SPACE APPLICATIONS

The maturity of commercial products and the consistency of their build standard are of primary importance for the use of such components in long-term space applications The ABSL 18650HC cell (the heritage spacecraft cell that has successfully clocked over 2,500 cell years of space operation without failure) has been in production since 1992. The raw materials, procedures and processes used have remained consistent and unchanged since 1996, when this cell was first released to market. These will continue in production unchanged so that it is expected our next generation cells will be offered to space customers alongside this heritage cell. The consistency associated to COTS cells provides crucial advantages over small-batch production cells for space applications:

- Performance measurements between cells, and indeed batches of cells, exhibit a very high level of uniformity.
- Security of supply of a cell with the necessary technical specification is crucial for space projects that can span long time durations. Customers are assured by the fact that ABSL holds a rolling stock of cells to satisfy the demands of the space market for a number of years in the future.

The performance uniformity and quality of COTS cells that are produced in vast quantities on highly automated production lines has been exploited in the ABSL space battery product, with the resulting benefits of a decreased cost and complexity for our customers. These benefits are derived from removing the need for charge management electronics, traditionally employed to balance differences in individual large-cell space batteries. Such management systems are complicated requiring cell-level monitoring devices in addition to the charge control functionality itself.

ABSL procures large batches (tens of thousands) of cells direct from commercial manufacturers and performs a strict Lot Acceptance Test (LAT) to ensure that the batch is suitable for use in space flight. The LAT procedure was originally developed for the ABSL 18650HC in cooperation with ESA using a similar process that is used for employing commercial capacitors for space use.

Fig 2 COTS Cell LAT and Screening Process

The exact details of the LAT procedure are sensitive proprietary information but an overview is presented below:

- A random subset of batch cells is selected for LAT testing.
- The electrical properties of cells are measured to ensure performance is within pre set limits.
- A number of the subset sample cells are subject to destructive physical analysis. (DPA), during which mechanical and chemical testing of cell components is performed

The remainder of the subset is split into three groups for endurance, abuse and environmental test.

- Endurance testing ensures that, following accelerated life-test, cell calendar and cycle life are within pre-set limits.
- The abuse group of test ensures the correct functionality of the cell protection devices.
- During the environmental group of tests vibration testing is performed on several cells. Following this test some of the cells are subject to DPA whilst the rest undergo rapid thermal cycling. Following cycling the cell seal is tested for integrity.

It is essential to understand that for ABSL to deem a LAT testing successful each individual test must be passed. The failure of a single cell during one of the tests leads to rejection of the entire batch. Following successful LAT testing, each cell in the batch is individually electrically tested and screened using high precision equipment for performance validation against pre-set limits. Individual cell test results are stored electronically on ABSL Database and record-matched against individual cell bar-codes. Using this information, when a specific number of cells are required for a flight program, a unique (proprietary) matching algorithm is used to select the group of cells that present the most closely matched performance characteristics. It is the rigor and proven maturity of this ABSL proprietary LAT, screening and matching process that eliminates the need for charge management electronics as described in [2].

4. ABSL SECONDARY LANDER BATTERIES

ABSL has delivered Lithium-ion batteries for the British National Space Centre (BNSC) Beagle 2 Mars lander and the French National Space Agency (CNES) Philae lander which aims to land on Comet 67P/Churyumov-Gerasimenko. Both landers adopted ABSL Small-Cell batteries as it was the ideal solution to the need to pack a high energy density battery within a tight mass and volume budget.

The Philae lander actually carries two lander batteries built by ABSL although both are mechanically identical and carry the same cell, the ABSL 18650HC. A photograph of one of the lander batteries is shown in Figure 3 where it can be seen that fourteen cells have been sandwiched between Glass Re-enforced Plastic (GRP) plates given additional structural support via Aluminium cross bracing. The battery also carries a thermofoil heater bonded to the upper side of the top GRP plate.

Fig 3 A 7s2p Rosetta Battery

Figure 3 shows that the distribution of the cells within the battery was not uniform and was actually staggered. Using this arrangement, ABSL was able to reduce the footprint of the battery over our traditional designs where cells are uniformly distributed by approximately 19mm.

In line with the two spacecraft power buses on Philae, two different battery designs were built: 7s2p and 2s7p. The nominal voltage of the ABSL 18650HC cell is 3.5V so that the nominal voltage of the batteries are 7V and 24.5V. Table 1 gives further information on the key performance parameters of the two batteries.

Parameter	2s7p	7s2p
Max Voltage	8.4	29.4
Min Voltage	5.0	17.5
Capacity (Ah)	10.5	3.0
Mass (kg)	0.72	0.72
Height (mm)	71	71
Footprint (mm)	118.5	63.2

Table 1 Philae Battery Performance

On 2nd March 2004, the European Space Agency (ESA) spacecraft Rosetta was launched carrying the Philae lander. Both spacecraft are powered by ABSL batteries (although Rosetta's are more than ten times bigger) and are currently en route to dock with Comet 67P/Churyumov-Gerasimenko. This journey will take over ten years finally reaching the comet on May 2014 after multiple gravity assists from both

Mars and Earth. The spacecraft will then slow to enter orbit around the comet at which point the lander Philae will be released to descend to the comet surface where it will operate for a number of weeks taking images, sampling the comet soil, its atmosphere and the changes it undergoes as the nucleus approaches the Sun.

The most challenging part of the mission is the extended hibernation phase during the ten-year journey to the comet before operations commence. Although spacecraft checkout has shown that the batteries are operating nominally on Philae, the real test will start after more than ten years in the harsh environment of deep space.

The Beagle 2 lander required a battery that would support both the nominal night-time operations on the cold Martian surface but also the power loads that had to be supported during the landing phase. For instance, sharp pulse loads had to be supported during the parachute deployment phase.

The Beagle 2 spacecraft was very much a custom lander design and had to pack a large array of instruments and electronics into a package of a similar size and shape to a trash can lid as shown in Figure 4.

Fig 4 The Beagle 2 Lander

The space available for the battery was a 'kidney-shaped' cavity and, to make use of the odd shape, it made obvious sense to a battery made of small cells to minimize redundant space. The Beagle 2 battery is shown in Figure 5 and the pillars on the top of the battery actually formed part of the greater spacecraft structure.

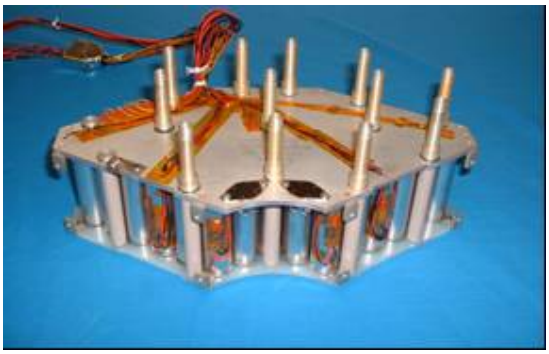
Fig 5 The Beagle 2 Mars Lander Battery

The performance of the Beagle 2 battery is shown in Table 3. This battery did not employ a heater and instead, to be able to operate in the harsh conditions of the Martian night, used the heat generated naturally during discharge to lift battery temperature and lower internal resistance. Even though the battery was designed to use this self-heating effect, it was still expected to operate with cells at a temperature around -30°C. During ground testing, ABSL even performed survival tests that proved the battery could still be used after being subjected to conditions of -50°C.

Parameter	6s9p
Max Voltage	25.2
Min Voltage	15.0
Capacity (Ah)	13.5
Mass (kg)	2.6
Height (mm)	66 (107 pillars)
Footprint (mm)	266x138 max

Table 2 Beagle2 Battery Performance

On 2nd June 2003, the ESA Mars Express spacecraft was launched towards Mars carrying the Beagle 2 spacecraft. As with Rosetta and Philae, both lander and host spacecraft were powered by ABSL Lithium-ion batteries. After a six-month cruise phase, Mars Express has been in a highly elliptical inclined Martian orbit performing a host of scientific experiments. The spacecraft has operated even better than planned with a mission extension already granted. Battery performance has been in line with software predictions as described at [3].

Just before Mars Express performed thruster firings to enter orbit around Mars, Beagle 2 was jettisoned towards Mars (on Christmas Eve 2003). Prior to jettison, checkout of Beagle 2 was successful and all systems appeared to be functioning nominally. The mission design called for no further communication with Beagle 2 until the lander had successfully landed and deployed solar panels and the communications antenna. Unfortunately no signal

was ever received from Beagle 2 and the reason for spacecraft loss remains unknown.

5. NEXT GENERATION LITHIUM-ION CELLS

ABSL lodged one of the original patents that allowed the commercialisation of Lithium-ion cell technology. As well providing an excellent revenue stream through various license and sub-license arrangements, it also cemented strong relationships with the leading commercial cell manufacturers that still exist today. Consequently, ABSL continually evaluates prototype COTS cells from around the world to assess their suitability for space applications. Importantly, due our presence in niche markets (such as space) we are not seen as a direct competitor but instead able to offer independent evaluation and advice.

In this way, ABSL has assembled a suite of Lithium-ion cells with exceptional performance for space applications. ABSL has also looked, wherever possible, to continue to utilize cells adopting the industry standard 18650 size (18mm diameter and 65mm high) so that existing space battery designs can be leveraged in a plug n play approach that minimizes Non Recurring Engineering (NRE) and hence battery cost.

There are two main drivers for performance in cells for space applications: energy density and power density. Energy density is basically a measure of the ability of a cell to store energy within a unit mass. For example, the ABSL 18650HC has a cell level energy density of 133Wh/kg. In contrast, at various levels of space qualification, ABSL has access to cells with energy densities ranging from 180Wh/kg to around 205Wh/kg.

These next-generation high energy density cells have the same dimensions as the ABSL 18650HC and so can be utilized in existing battery designs. It is therefore possible to accurately predict battery level energy density performance. In this way, ABSL can today provide batteries with an energy density in excess of 150Wh/kg and will soon be able batteries with an energy density approaching 180Wh/kg. It should be noted that these numbers include all parasitic mass (eg from wiring, connectors, structure etc).

The next generation of high energy density cells are already under lifetest and exhibit less degradation than the ABSL 18650HC. This means that batteries with these new cells could well be driven harder to higher Depth Of Discharge meaning that a lower Beginning Of Life (BOL) capacity is required - this further reduces the required battery mass.

Customers in both the USA and Europe are actively assessing these next generation cells for applications including planetary landers. In addition to high energy density, one cell also exhibits excellent low temperature performance with over 80% of nameplate capacity still available when subjected to capacity measurement at -40°C.

As already explained in the previous section, the surface exploration of Mars calls for operation in a harsh low temperature environment. Utilizing next generation Lithium-ion cells with their low temperature/low resistance electrolyte will be crucial for successful operation.

Recently, ABSL began to receive enquiries from a number of customers regarding the availability of high power density cells. Applications were emerging that required the delivery of high current pulses for short durations that were outside the scope of typical cells designed for high energy density.

In response to this need, ABSL last year qualified the ABSL 18650HR cell. This cell is now being used in a battery to power the Thrust Vector Control (TVC) system for the Korea Aerospace Research Institute (KARI) KSLV-1 program. This TVC battery will operate at a nominal voltage of 270V and is contains 168 ABSL 18650HR cells arranged in an 84s2p configuration.

Fig 6 The KSLV-1 ABSL 18650HR Based TVC Battery

Figure 6 shows a picture of the 84s2p battery. This battery was qualified for space in June 2006 following a full environmental qualification test program. The main risk area for ABSL during this qualification process was during thermal vacuum when the high voltage battery would be subjected to the conditions where critical Corona events can occur. The successful qualification showed that the design features incorporated by ABSL worked perfectly.

In addition to launch vehicles, ABSL has also received enquiries from customers interested in having a high rate capability on planetary lander spacecraft. Traditionally, surface mobility has been made possible using the traditional method of wheel and track drive. However, in order to extend the geographical zone of study, the use of hopping spacecraft is being actively explored. In this way, propulsion systems will be used to fly the spacecraft from one point of interest to another.

However, these propulsion systems required short bursts of high power. In this way the design drivers for the propulsion system can be very different from those of the rest of the spacecraft which require low-level loads over extended periods (such as night-time or crater operations which are shadowed).

For such applications, ABSL has traditionally offered customers two batteries: one employing the ABSL 18650HR cell and the other with a next generation high energy density cell. However, ABSL has performed internal research into the possibility of using a 'Hybrid' battery employing both high power and high energy density cells. Such a Hybrid would use the high energy density cells for the bulk of operations. However, when a high power demand occurs the voltage of these cells would drop below a threshold which would activate the high power cells to make up the required demand. Once this demand is over, the high energy density cells would once again take over.

Utilizing such a hybrid battery would reduce system level complexity as only a single set of interfaces (telemetry, charge control, PMAD etc) would be required. In addition there are also mass savings at battery level to be gained by using a single battery structure.

6. ABSL PRIMARY LANDER BATTERIES

In 2005, ABSL took our first contract to supply a primary battery for a space program, FOTON M3, from QinetiQ. FOTON M3 is the latest in a series of joint Russian and ESA science missions launching a capsule to perform science experiments in Low Earth Orbit (LEO) before returning to Earth after two weeks.

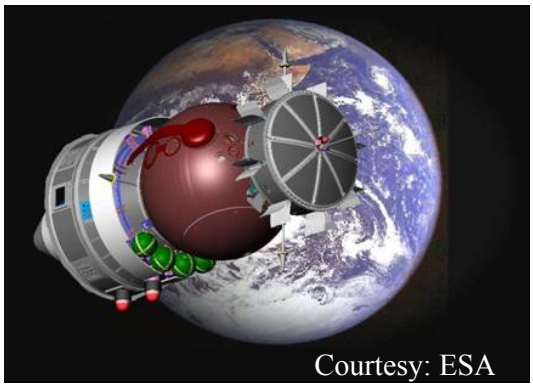

Fig 7 FOTON Capsule

Towards the end of the mission, as the capsule is commanded for the return to Earth, operators switch the power supply from the primary system and over to battery power. These batteries must then support the spacecraft during the descent until landing which is slowed by parachute and retro-rockets (activated by the battery). Following landing, the capsule switches to a low power emergency mode whilst the search for the vehicle by ground personnel is conducted.

This search can take from ten to twelve hours and during this period the battery must power essential systems such as the beacon transmitter. Due to the wide geographical area into which the capsule could fall, the battery might have to perform at temperatures as low as -20°C. As well as low temperature performance, in order to meet the mass budget for the capsule the battery must have an energy density in excess of 223Wh/kg.

ABSL was directed by QinetiQ to use a particular commercially available Lithium Sulphuryl Chloride DD cell. As reported in [4], QinetiQ performed a preliminary survey of commercially available primary cell technologies for the Mercury Surface Element (MSE) of the Bepi-Columbo mission. MSE was intended to spend a year on the ground before a 3.5year cruise phase to Mercury followed by seven days of surface operations.

Fig 8 DD Primary and 18650 Secondary cells

To perform science operations during the seven day period, a cell with a minimum energy density of 275Wh/kg was required. Additionally, the battery was needed to operate at cold temperatures down to -10°C. QinetiQ testing showed that the Lithium Sulphuryl Chloride cell was by far the best performing cell with a recorded energy density of 377Wh/kg at a temperature of 10degC (>480Wh/kg at 20°C and >500Wh/kg at 60°C). Following from the MSE work, QinetiQ realized that the same cell would be ideal for the FOTON M3 program.

The first part of the ABSL contract was to qualify the primary cell for space applications. A qualification program was executed on the cells including shock and vibration. Cells were successfully shock tested to 90g for 40ms and, in random vibration, withstood an input of $20g_{RMS}$. The cells were found to be exceptionally mechanically robust and therefore ideal for a planetary lander.

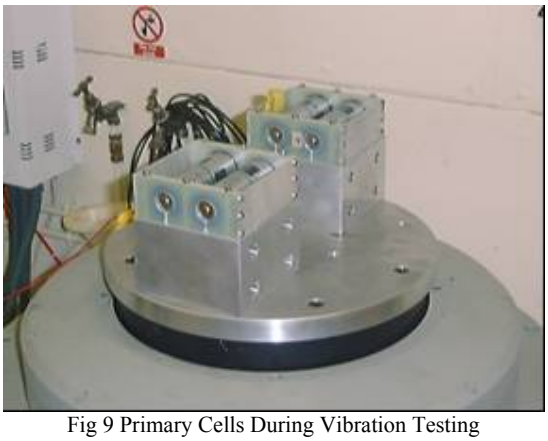

Fig 9 Primary Cells During Vibration Testing

The successful qualification of the primary cell allowed ABSL to begin formal design activities on the battery. To meet the needs of FOTON M3, 27 cells are connected in a 9s3p configuration. Figure 10 shows a CAD drawing of the battery and it should be clear that the basic battery design philosophy is very similar to our rechargeable secondary batteries.

Due to the very high energy density of the battery, safety is of paramount importance. Within the battery is fitted protection against short circuit via Positive Temperature Coefficient (PTC) devices that exhibit a large increase in resistance (reducing current flow) as temperature rises due to a high current short event. Also, primary cells must not be charged and so the battery is fitted with fuse and diode features to ensure that cells can only safely discharge.

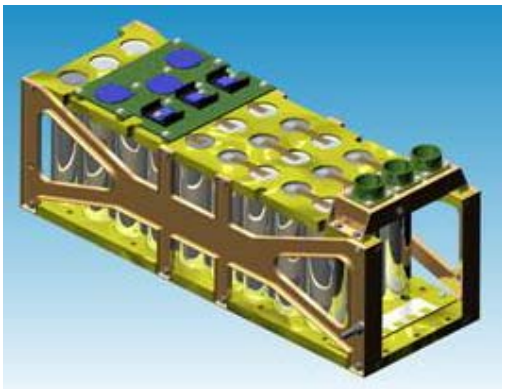

Fig 10 The 9s3p FOTON M3 Battery

It should be noted that this primary battery technology also holds great promise for high temperature applications, such as landing craft for Venus. The cell is rated to operate at temperatures as high as 90°C and ABSL is actively investigating whether, and how far, this temperature can be increased.

Despite the advances in rechargeable battery technologies for space applications, it is certain that the much higher energy density characteristics of primary cells will prove the technology of choice for some programs. This will probably remain particularly true for planetary landers where mass is absolutely critical and operations can take place over relatively short mission durations. However, for longer periods of operation and exploration the use of secondary batteries and solar arrays is mandatory.

7. CONCLUSION

ABSL has proven that the use of the Small-Cell concept has been of great gain to planetary probe missions. The flexibility of design is ideal for the custom nature of such missions where highly irregular battery envelopes can be the norm.

Batteries are available now that can offer battery level energy density over 150Wh/kg whilst being able to perform in the cold environments required for many planetary probes. It is also clear that the use of a combination of Lithium-ion high power and high energy density will be required as more complex missions are planned.

There will always be a need for primary batteries for one-off operational activities such as parachute deployment prior to touchdown. ABSL now has space qualified battery technology available so that a complete capability is now available.

8. ACKNOWLEDGEMENTS

ABSL would like thank our friends and colleagues at the British National Space Centre (BNSC), ESA and NASA for their support over the entire course of our space battery program.

9. REFERENCES

1. Spurrett R, Slimm M, Thwaite C., "The UK National Lithium-ion Spacecraft Battery Programme" Proceedings of the Fifth European Space Power Conference, ESA SP-416, 475-481, 1998.
2 Pearson, C., Thwaite, C., Curzon, D., Rao, G., "The long-term performance of small-cell batteries without cell balancing electronics", Proceedings of the 2004 NASA Battery Workshop, Huntsville, Alabama.
3 Pearson C., Ng K., Thwaite C., "Software Prediction of Battery Performance and Comparison with Operational Data" Proceeding of the 2005 Space Power Workshop, Manhattan Beach, California.
4. Green K., Bowles P., Ritchie A., Schautz M., Scholey N., "Development of high energy density primary battery" Proceedings of the 2005 European Space Power Conference in Stresa, Italy.

Evolving the Deep Space Network: Implications for Planetary Probes

by

Douglas S. Abraham, Leslie J. Deutsch, and Robert A. Preston
Jet Propulsion Laboratory, California Institute of Technology

Barry Geldzahler, Science Mission Directorate
National Aeronautics and Space Administration

NASA's Deep Space Network (DSN) is currently working to evolve its end-to-end link capability to better meet the communication and navigation needs of future robotic and human exploration missions. This end-to-end capability improvement encompasses the DSN ground system, flight instrumentation, evolution to Ka-band frequencies, and advances in data coding and compression. DSN ground system improvement efforts include increasing the effective receiving area, effective isotropic radiated power, and number of simultaneously supportable links. DSN flight-side technology improvement efforts include developing higher-power transmitters, larger deployable antennas, electronic beam steering antennas for in situ exploration, and lower mass, power, volume software-defined radios for relay-dependent in situ exploration elements. Together, these improvements can provide orders of magnitude increases in link capability. They can also enable lower cost planetary probe missions by eliminating the need for a spacecraft relay at the probe destination or helping reduce the telecommunications-related mass, power, and volume of both the relay and probe. The ability to use direct links from the probe to Earth can allow longer communication periods with probes, simultaneous tracking of multiple probes in one hemisphere, and improved probe position and velocity measurements (e.g., for winds). Hence, efforts to evolve the DSN's end-to-end link capability may translate into new mission concepts, lower costs, and more scientific capability for planetary probes or other in situ exploration craft (e.g., rovers, aircraft, and balloons).

DIRECT-TO-EARTH COMMUNICATIONS FOR OUTER PLANETARY ENTRY PROBE MISSIONS

Fourth International Planetary Probe Workshop
27 June – 30 June, 2006, Pasadena, California, USA

David H. Atkinson [(1)], Kamal Oudrhiri, Thomas R. Spilker, Kevin H. Baines, Sami Asmar[(2)], Bernie Bienstock, Steve Sichi [(3)]

[(1)] Dept. of Electrical and Computer Engineering, University of Idaho, Moscow ID 83844-1023, USA, email: atkinson@ece.uidaho.edu
[(2)] NASA/Jet Propulsion Laboratory 4800 Oak Grove Dr., Pasadena, CA 91109-8099,USA
[(3)] Boeing Satellite Systems, P.O. Box 92919, Los Angeles CA 90009-2919,USA

ABSTRACT

The giant planets represent time capsules of the solar system, each reflecting the different chemical and physical conditions existing at the epoch and location of formation. In particular, the record of the past is locked in the makeup of key diagnostic constituents, including (1) the noble gases and their isotopes, which can not be measured remotely, and (2) condensibles such as water and ammonia, which are largely hidden beneath the clouds that form in the colder reaches of the upper atmosphere. Descent probes carrying the appropriate sampling instrumentation are fundamental for assessing the requisite inventories noble gas and condensible of giant planets necessary to constrain theories of solar system origin and evolution. Although not currently feasible to conduct *in situ* exploration of the deepest (100's of bars and deeper) outer planetary atmospheres, significant science can still be obtained from shallow descent probes that reach levels no deeper than several tens of bars. One method proposed for *in situ* studies of the shallow to middle levels of outer planet atmospheres (0.01 to several tens of bars) incorporates Direct-to-Earth (DTE) communications from shallow probes. Although the DTE technique does not require a communications relay option in a carrier spacecraft, thereby significantly decreasing overall mission cost and operational complexity, this technique involves a number of mission design risks that nevertheless could increase overall mission risk and severely impact the science return.

1. INTRODUCTION

1.1 Overview

To understand the origin and evolution of planetary atmospheres and interiors requires the composition of the atmosphere be known. Remote sensing of planetary atmospheres can provide valuable information on atmospheric dynamics, meteorology, global circulation, and chemistry, in some cases reaching levels well below the visible cloud tops. However, to completely address questions regarding the origin, evolution, and processes of the giant planets and solar system, *in situ* studies are often necessary and, in some cases, the only means by which the deeper atmosphere can be studied [1].

Direct sampling of deep planetary atmospheres requires that a probe, instruments, and sensors be able to survive the pressure and temperature environment of the atmosphere, and be capable of returning the acquired data to Earth. Although not technologically feasible for a probe to survive to and return data from the deep (100's of bars and deeper) atmospheres of the outer planets, significant science remains within the realm of relatively shallow descent probes [2]. To return science data from a descending probe, two strategies are considered: 1) the use of a second spacecraft as a relay station to receive, store, and later transmit the probe science data to Earth, and 2) the implementation of Direct-To-Earth (DTE) communications between a probe and Earth antennas. The advantages of DTE communications are obvious - simplification of certain aspects of two spacecraft (probe and relay spacecraft) mission, simplification of the communications system with one less in-space communications link, and overall reduction of mission costs. However, the technique of DTE communications may severely impact mission design considerations, limit the total science return, and substantially increase overall risk.

1.2 Giant Planet Science and Measurement Objectives

The outer solar system, comprising the four giant planets, Kuiper Belt Objects and icy satellites, comets and asteroids, dust, magnetic fields, and plasmas, represents a complex, closely coupled system. Bound by origin, evolution, and interaction, this system not only offers a natural laboratory for understanding a variety of physical, chemical, and magnetospheric processes on bodies throughout the solar system,

including the Earth, but also offers a potential analog for studying both astrophysical phenomena and extra-solar planetary processes.

The giant planets represent a key element in tracing the origin, and chemical and dynamical evolution of the solar system. From both the remarkable similarities as well as the striking differences observed in their composition and overall structure, the giant planets provide fundamental clues to the chemical, thermal, and dynamical conditions at the time and location of their formation. In this regard, the giant planets represent time capsules of solar system formation, and, as described by Owen [1], as an ensemble can be considered "a Rosetta stone" for understanding the formation and evolution of the solar system. In particular, the elemental abundances and isotopic ratios found in the well-mixed deeper atmospheres can help discriminate between competing theories of giant planet origin and evolution.

Models of giant planet formation predict that relative to hydrogen, abundances of heavy elements in the outer solar system should be enriched as compared to the solar abundances. Furthermore, these models predict that this enrichment should increase from Jupiter outwards to Neptune. Particularly important are the abundances of noble gases and their isotopes, as well as other heavy elements including carbon, nitrogen, sulfur, and oxygen in the well-mixed deep atmosphere. Methane (CH_4), the primary reservoir of carbon in the outer solar system, is especially important since carbon is the only heavy element so far measured on all the giant planets. The ratio of carbon to hydrogen (C/H) is observed to increase from three times solar at Jupiter to 30x solar or more at Neptune [3]. Theory dictates that the other heavy elements should likewise increase in abundance from Jupiter to Neptune.

Many of the most diagnostic heavy elements are incorporated in volatile species such as water and ammonia that participate in photochemical reactions and haze- and cloud-forming processes in the upper atmosphere. Consequently, it is only in the deep atmosphere well below the condensation clouds that such species are expected to be well-mixed, so that their measured values are then true indicators of their bulk abundances [4]. As temperatures decrease with increasing solar distances, condensation clouds will generally form at greater depths, sequestering the well-mixed atmosphere to deeper levels as well. In the relatively warmer climes of Jupiter, equilibrium models predict an upper cloud of ammonia (NH_3), a second, slightly deeper cloud of ammonium hydrosulfide (NH_4SH), and either (or both) cloud(s) of water ice and water-ammonia mixture. The water cloud is expected to be the deepest cloud deck at Jupiter, with a base predicted to be at depths of 5 to 10 bars depending on values of O/H of 1 to 10 times solar [3]. Thus, measurements of the bulk planetary oxygen abundance require measurements beneath the 10-bar level on Jupiter.

The situation is even more adverse at Saturn. Assuming a heavy element enhancement of 10x solar, equilibrium thermodynamics predict that the deep atmosphere where water will be well-mixed can only be found beneath about 20 bars. Due to dynamical processes (e.g., convection, planetary waves) in the turbulent Saturn atmosphere, the well-mixed region could actually be pushed as deep as 50 to 100 bars in places [3].

In the most distant, colder regions of the solar system, water ice and water-ammonia solution clouds are expected to form at even deeper levels. Thermochemical equilibrium calculations suggest that the base of a Neptune water-ice cloud may be located at 50-100 bars for an O/H ratio of 30-50x solar, and the base of a water droplet (ammonia-water solution) cloud could be as deep as 370 bars and 500 bars, respectively, for O/H of 20-30x and 50x solar [4,5]. In addition, these planets are also expected to have ionic water-ammonia oceans at tens of kilobars which depletes the upper atmosphere of water [4,5]. Designing descent probes to reach and communicate from the deep-mixed levels on these planets is a truly formidable if not intractable problem.

However, given knowledge of the abundances of oxygen and nitrogen in the largest giant planets, Jupiter and Saturn, informative models of the formation of the ice giants, Uranus and Neptune, can be constrained without direct measurements there of the oxygen and nitrogen elemental abundances. Information gleaned on the amount of volatiles delivered to Jupiter and Saturn in the form of ices can then be extrapolated to Uranus and Neptune. Combined with measurements of a host of noble gases and their isotopes, $^{15}N/^{14}N$ and D/H, as well as the inventory of carbon from methane and other hydrocarbons, formation models of Uranus and Neptune can fortunately be meaningfully constrained. For these planets, additional constraints come from measurements of helium and neon [2,3]. These elements cannot be accurately measured in Jupiter and Saturn, because in these gas giants, atmospheric neon is expected to dissolve in helium droplets which then rain into the deep interior, thus depleting the measurable upper atmosphere of both of these elements. Such depletions are not expected to occur in either Uranus or Neptune as helium can not condense within them, and thus their original abundances at formation are preserved. Therefore, with the exception of measurement of oxygen (water) in the deep atmosphere of Saturn, compositional

science critical to the understanding of solar system origin and evolution, and giant planet formation, can be obtained from shallow descent probes reaching no deeper than several tens of bars.

The key measurement objectives addressing critical issues of giant planet origin, evolution, and processes are summarized in Table 1.

Table 1.

Outer Planet Probe Measurement Objectives

Primary

Abundances of noble gases & isotopes
Abundances of C, N, O, and S
Pressure & Temperature structure

Secondary

Cloud properties
Dynamics

To achieve the measurement objectives, a strawman instrument payload based primarily on the Galileo probe is assumed (Table 2).

Table 2.

Nominal Probe Instrument Complement

- Gas Chromatograph/Mass Spectrometer
- Atmospheric Structure Inst. (incl 3-axis accelerometry during entry)
- Nephelometer
- Doppler Wind
- Ortho/Para Hydrogen
- Analog Resistance Ablation Detector (ARAD)

2. MISSION DESIGN

The primary challenges of shallow probe DTE missions include (1) adequate communication link from depth in an absorbing atmosphere, (2) sufficient protection against the thermal heat of entry, and (3) sufficient observing time at depth. The role of the mission designer in entry probe mission communications is to craft a realizable geometry that allows useful communications from the probe to Earth, or to a relay spacecraft, or to whatever mission element is to receive the probe's transmissions. To enable DTE from a probe in a giant planet atmosphere, the mission design must place the probe in a location that is

1. Of sufficient scientific interest to justify the mission;
2. Accessible within technology (or other) constraints;
3. Amenable to communication with Earth.

Giant planets, especially Jupiter and Saturn, have deep gravity wells with significant ramifications for practical entry probe trajectories. With regard to point 2 above, entry probe speeds upon reaching the destination's atmosphere are extremely high, so the need to survive the entry with available technologies imposes a narrow entry corridor with the proper flight path angle with respect to the local horizontal. For a given destination there is a highly restricted set of possible entry sites, largely determined by the direction of the approach V_∞ vector, as shown in Fig. 1 below. A line from the planet's center in the V_∞ direction intersects the planet's reference surface at the *antipode*. For a spherical, non-rotating planet the set of possible entry site loci is a circle on the planet's "surface", centered the antipode with central angle θ as shown. Non-spherical shape and planetary rotation cause minor distortions (a small number of degrees or less) to the circle. Planetary rotation can cause part or most of these to violate entry speed limitations. For instance, Jupiter entry probes are limited to the short arc of the circle within 5-10 degrees of the equator, on the side of the circle that has the probe traveling prograde with respect to Jupiter's rotation.

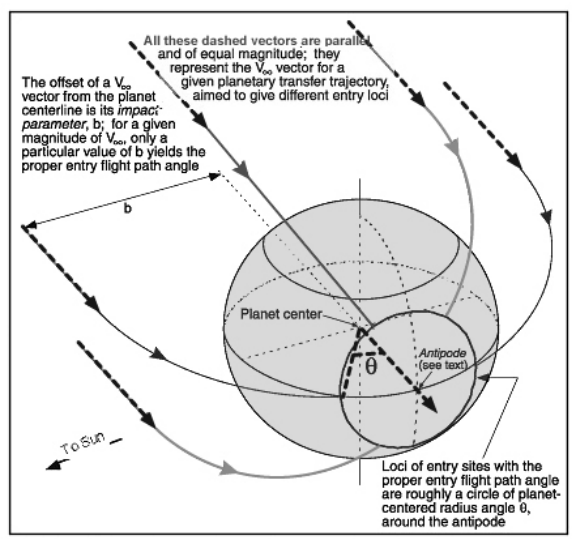

Fig. 1. Entry Trajectories

Without significant propulsive intervention, the transfer trajectory to the destination planet determines the approach V_∞ vector. Using Jupiter as an example as shown in Fig. 2, a tangential (minimum-energy) transfer trajectory to an outer planet yields an approach from the direction the planet is moving: the planet overtakes the slower-moving spacecraft. Angle θ for Jupiter is ~30 degrees (35-37 for Saturn), so the probe enters at a site ~30 degrees sunward of the dusk terminator. After entry

the planet rapidly rotates the entry probe past the planet's limb and out of view of Earth, as with the Galileo entry probe. Higher-energy variants of the transfer trajectory can adjust the trajectory-plane components of the V_∞ direction. But the inbound approach that moves the entry point toward the sub-Earth point, advantageous for DTE and "front-side" duration, adds years to the cruise duration to change the entry point longitude by only 20 degrees. Larger adjustments with this method add even more cruise duration, begin to increase the entry speed, and still cannot move the entry point to the sub-Earth longitude. Any significant additional entry location adjustments toward or past the sub-Earth longitude require larger angular rotations available only via propulsive maneuvers.

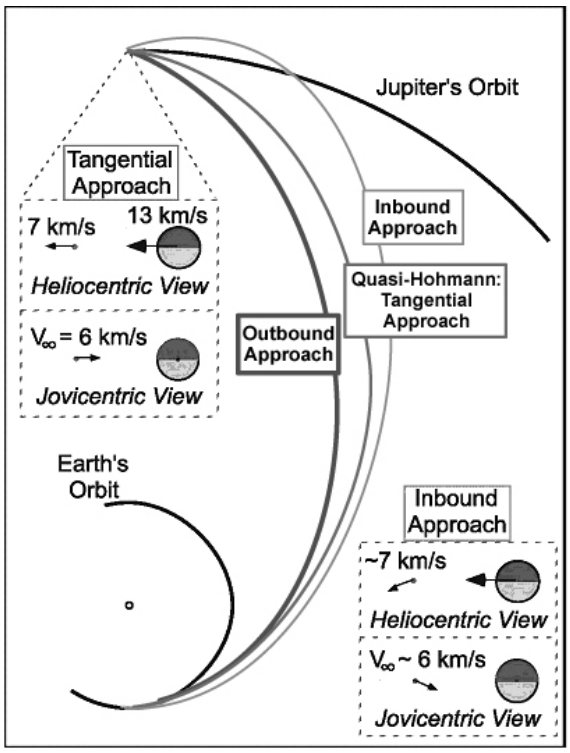

Fig. 2. Jupiter Trajectories

Fig. 3 shows a hyperbolic approach and entry from a tangential transfer trajectory, more nearly to scale than Fig. 1 and looking down on the planet's orbit plane. Fig. 4 is a closer look at the geometry near the planet, showing the Entry Offset Angle, which is the complement of angle θ in Fig. 1 and does not vary significantly with the magnitude of V_∞. This offset angle and the direction of V_∞ determine the Earth-referenced longitude of entry. As the direction of V_∞ changes the entire geometry of Fig. 3 rotates with it. Moving the entry point of Fig. 3 toward the sub-Earth point requires rotating the V_∞ vector clockwise, as seen in Fig. 5, where the 15-degree rotation is accomplished by use of an inbound approach. Further rotation to place the entry site at the sub-Earth point requires an additional 45-degree rotation of V_∞, requiring ~4 km/s of propulsive ΔV (Fig. 6). Greater rotation, necessary if the probe is to be near the sub-Earth point at the end of its mission, requires even larger ΔV.

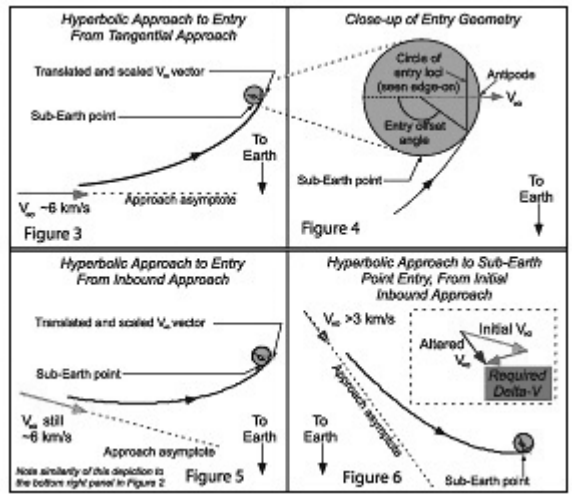

Figs. 3-6. Entry Trajectory Details

3. COMMUNICATIONS

In this section, the end-to-end communication link analyses from Saturn and Neptune probes to a ground-based receiving station on Earth are discussed.

The primary challenges of a non-coherent DTE downlink from a shallow descent probe are the losses due to antenna mis-pointing, atmospheric attenuation, and free-space propagation. Reliable signal detection requires 1) optimization of the probe communication subsystem to allow for maximum transmitted power, and 2) selection of the Earth station with the required antenna size and the desired pointing capabilities.

To further illustrate these challenges, an end-to-end analysis for both Saturn and Neptune descent probes is presented. A design similar to the Galileo probe is assumed with the exception of increasing the probe's transmitter peak power to 100 Watts. This is consistent with the recent improvements in solid state design and the increase in the overall efficiency of the power transmitter to the 50% mark. Using the Galileo probe as a baseline for the link analysis enables the evaluation and comparison of link budgets using variable antenna diameters on the ground while keeping the probe telecommunications parameters at fixed values.

At 30 AU range from Earth, a signal from a Neptune probe propagates through space and suffers very large space losses, posing serious design challenges for DTE communications. A preliminary end-to-end

analysis was conducted, including (1) arraying a single 70-meter diameter DSN antenna with two 34-meter diameter DSN antennas, and (2) utilization of non-DSN space antennas such as Arecibo with its 200 meter diameter. In each case it was found to be impossible to close the communications link at the required 128 bps data rate.

Table 3
Saturn and Neptune Probe

Transmitter Power	100 W
Peak Antenna Gain	9.8 dBi
Antenna Pointing Loss	6 dB

The remaining option was to consider the proposed Square Kilometer Array (SKA). Although still in its conceptual phase, when and if the SKA is implemented it could offer promising enhanced downlink signal gain capabilities. The current SKA design calls for large arrays comprising many small 12 m diameter reflector antennas. A total of 4400 proposed antennas will be combined to meet the required specifications and offer an enormous collecting area with an equivalent 800 meter antenna diameter.

With the much needed help from unparalleled SKA antennas, the issue of a probe antenna's mis-pointing during the descent phase can be addressed. Disturbances in the probe's attitude must be carefully considered in order to satisfy the objective of establishing preliminary bounds on the antenna beamwidth requirement necessary to support the entire critical descent period. The antenna beamwidth must accommodate the following considerations:

(1) Entry and initial link lock from a location significantly removed from the sub-Earth point;
(2) Planetary rotation that might carry the probe even farther from the sub-Earth point;
(3) Perturbations of the probe's spin axis away from the local vertical by such phenomena as aerodynamic buffeting and atmospheric turbulence, each tending to induce pendulum-style swinging, and the possible parachute flow instabilities.

Designing the link with a smaller antenna beamwidth (higher probe antenna gain) may result in serious signal detection outages and possibly even total loss of the science data. In the case of Saturn and Neptune probes, a 6 dB pointing loss equivalent to a beamwidth of 56 deg has been assumed for all link calculations.

The DTE link budget analyses for Saturn and Neptune probes were performed under the assumptions presented in Tables 3, 4, and 5. All parameters of the link budget were carefully selected in order to meet the required 128 b/s data rates. To optimize the link and ensure sufficient margins, different modulation and coding schemes were also explored. The summary of these computed margins is listed in Table 6 and should make it apparent that predicting the link performance of missions utilizing Direct to Earth communication strategies is a complex problem.

Table 4
DTE Link Assumptions

UHF Communications Band	401 MHz
Information Bit Rate	128 bps
Bit Error Rate	1.00e-5
Saturn Distance from Earth	9 AU
Neptune Distance from Earth	29 AU

For the case of a Neptune probe, many computations were carried out to determine the most suitable modulation and coding schemes capable of providing the optimal signal-to-noise ratio at the desired 128 b/s science data rate. Even under the best case link conditions (nominal noise temperature and SEP angles), all computations led to a DTE links with no margin or very poor margin. The case of the residual carrier with concatenated convolutional and Reed-Solomon codes still yielded a margin below the minimum DSN requirement of 3 dB above the threshold SNR needed for proper signal detection and data demodulation.

Table 5

Square Kilometer Array (SKA)	
Ground Antenna Elevation Angle	20º
SKA Collecting Area Diameter	800 m
Receiver Operating Temperature	25 K
Total Noise Temperature	45 K
Threshold Loop Noise BW (Blo)	10 Hz
Required Suppressed Carrier (BPSK) Threshold SNR in Blo	17 dB
Required Residual Carrier Threshold SNR in Blo	12 dB

The analysis is quite different for a Saturn mission. At a spacecraft-Earth range of 9 AU, the corresponding space losses for a Saturn DTE link are reduced by an order of 10 dB compared to the space losses for Neptune's missions. With margins above the 3 dB threshold, a Saturn DTE communications link performance is supportable at 128 bps data rate for atmospheric pressure levels no deeper than 20 bars. However, with its large scale height, presents new challenges as the need to descend deeper than 20 bars will result in significantly higher signal attenuation.

Table 6.
Direct to Earth Communications from Saturn & Neptune Probes
Assuming a Square Kilometer Array (Diameter=800 m)

Atmospheric Pressure			**2 Bars**	**5 Bars**	**10 Bars**	**20 Bars**
Saturn's Atmospheric Attenuation (dB)			**0.12**	**0.71**	**2.03**	**5.46**
Neptune's Atmospheric Attenuation (dB)			**4.63E-06**	**4.06E-04**	**9.48E-03**	**1.368**
Suppressed Carrier (BPSK) Conv (rate=1/2) MI = 1.57 (Rad/pk)	**Saturn**	Data Margin (dB)	11.44	10.85	9.52	6.02
	Neptune	Data Margin (dB)	**No_TLM**	**No_TLM**	**No_TLM**	**No_TLM**
Residual Carrier Turbo (rate=1/6) Blk Size 8920 MI = 0.9 (Rad/pk)	**Saturn**	Carrier Margin (dB)	11.46	10.87	9.55	6.12
		Data Margin (dB)	13.75	13.15	11.83	8.34
	Neptune	Carrier Margin (dB)	**No_Lock**	**No_Lock**	**No_Lock**	**No_Lock**
		Data Margin (dB)	**No_TLM**	**No_TLM**	**No_TLM**	**No_TLM**
Residual Carrier Conv (rate=1/6) + R/S (223/255) MI = 0.8 (Rad/pk)	**Saturn**	Carrier Margin (dB)	12.45	11.86	10.54	7.11
		Data Margin (dB)	12.29	11.7	10.37	6.91
	Neptune	Carrier Margin (dB)	2.44	2.44	2.43	1.07
		Data Margin (dB)	2.13	2.13	2.12	0.69

4. TECHNOLOGY ISSUES

The technology development challenges in designing, producing and testing a DTE probe are numerous. Certainly, the most difficult of these is the thermal design. To allow the carrier spacecraft to perform a deflection maneuver and avoid following the probe entry trajectory, a typical probe mission plan schedules probe separation from the carrier spacecraft some period of time before actual planetary entry,. The probe coast period can be anywhere from several weeks (e.g. 3 weeks for Huygens) to several months(e.g., 5 months for Galileo). During this time period, there is extremely low power dissipation within the probe to preserve battery life, and the thermal design for this mission phase must maintain the probe instrumentation, including sensors, electronics and mechanisms, above their thermal design limit.

Shortly before the probe enters the planetary atmosphere, the high power transmitter is turned on, dissipating substantial thermal energy. In addition, the probe deceleration generates external heat. These two factors drive the thermal design to maintain the probe elements below their upper thermal limits. Early probes used passive thermal blankets and high molecular weight gas to maintain hardware temperatures within acceptance ranges. Current probes have other techniques available for thermal control. Phase change materials, Aerogel and complex thermal blanket designs are other techniques used to implement the probe thermal design.

Batteries remain the only practical means of powering a probe following separation from the carrier spacecraft. Although nuclear sources and other techniques have been considered, probe mass limitations dictate the use of a compact battery. Recent planetary entry probes, including the Galileo and Huygens probes, used $LiSO_2$ batteries. This technology remains the most reliable and efficient probe battery chemistry. These batteries are characterized by extremely low self discharge levels and remain stable over the long duration mission phase between launch and first use just prior to probe separation.

Although the probe transmitter will certainly require the highest energy, evolving improvements in solid state designs can increase transmitter efficiency from 30% used in the TWTs on the Pioneer Venus and Galileo probes, to levels approaching 50% even at UHF bands. Low powered logic and power conditioning circuitry electronics minimize power draw from other housekeeping functions. Instrumentation power consumption too has benefited from circuitry improvements, miniaturization, and technology investment.

The probe telecommunications subsystem must also include an ultra stable oscillator (USO), to improve transmission quality and serve as the main part of a Doppler wind measurement. Inclusion of a transponder, although desirable to measure descent profiles and provide a coherent signal, may not be

possible due to power and mass budgets. Descent dynamics and aerodynamic forces are a big driver to antenna design and may limit physical size

The deceleration module design is critical to protect the sensitive instrumentation from the intense entry heat. Its mass fraction, as a percentage of the total probe separated mass, can be considerable, depending on the probe entry trajectory and planetary atmosphere. Table 3 summarizes deceleration mass fraction of recent planetary entry probes. The deceleration module separation system, required to allow instrumentation to sample and image planetary atmospheres for instrument access to planetary atmosphere, also adds to the deceleration module mass.

Table 7
Probe Deceleration Module Mass Fractions

Probe Mission	Mass Fraction (%)
Pioneer Venus	36
Galileo	63
Huygens	33

The heat shield thermal protection subsystem (TPS) design is critical to maintaining sensitive electronics within the probe below their thermal limits. An ablative design is optimal. Although fully dense carbon phenolic was the historic material used on Pioneer Venus and Galileo probes, it is no longer manufactured. However, TPS designs for entry probe descent missions may not require the use of the historic carbon phenolic material and can make use of other ablative materials, such as pica.

5. SUMMARY AND CONCLUSIONS

For Direct-to-Earth communications to be viable, the Earth must be in view of the probe throughout the period of the communication link. In most practical cases this limits the probe atmospheric entry to the west (retrograde or approaching) limb of the planet, with the probe trajectory swept across the sub-Earth meridian by the planet's rotation. Although a prograde entry on the west limb of the planet is certainly possible, prograde entries generally require a significant increase in ΔV and overall mission duration. Retrograde probe entries are more easily realized, but can severely impact the mission design, as well as thermal protection systems and, in consequence, total probe mass. Missions with multiple entry probes are even more severely constrained by the requirement of west-limb entry.

When a mission design relies on a DTE telecomm strategy, a number of other issues must be considered including: (1) increased probe transmitter power necessary to overcome the large initial probe-to-Earth aspect angle (due to the vertical descent of the probe near the west limb of the planet) resulting in lower off-axis gain; (2) proper phasing of the probe delivery with the Earth rotation such that the proper Earth-based antenna system(s) is (are) able to view the entire probe descent; (3) consideration of single point failure risks arising from an unfortunately timed occurrence of adverse weather or technical issues with the Earth antenna systems; (4) design of a communications link able to provide a data rate suitable to support the probe instrument payload and mission science floor; (5) limiting descent time to reach the target depth within the Earth visibility window; and (6) accommodating the TPS mass fraction needed to survive the entry conditions. In most practical cases this will be a retrograde entry.

Although the telecommunications aspect of the DTE technique is indeed challenging, the most critical issues are those associated with mission design and technology – delivering a probe to the approaching limb of a planet will generally require a retrograde entry, significantly increasing the TPS mass fraction. To complete a descent probe mission to a minimum depth defined by the science floor within the time constraints imposed by Earth visibility and the rotational period of the planet requires a rapid descent. For Saturn, with a large atmospheric scale height, an entry probe mission may need to be conducted without a parachute. Perhaps the most challenging aspect of an outer solar system DTE mission is the development of a system of Earth antennas capable of closing the link without the potential of a single point ground failure jeopardizing the science return. If an array of spatially-separated Earth antennas can be developed to maintain probe visibility throughout the descent, this issue will be largely alleviated. Unfortunately, such a system is not envisioned in the near future.

The Galileo and Huygens missions have demonstrated the viability and value of Direct to Earth communications for an outer planet descent probe mission. Indeed, the Huygens Doppler Wind measurement could not have been completed without DTE communications, this technique should be included as an important consideration in the design of future missions. A specific investigation that will continue to benefit from DTE is measurement of deep atmosphere dynamics by Doppler tracking of descent probes. Coupled with a probe-to-relay spacecraft communications link, the probe-to-Earth link provides a second Doppler component that allows the retrieval of a 2-dimensional wind vector.

Direct to Earth communications is a proven technique that should be maintained in mission planning, may be utilized in the definition of future outer planetary missions, and will continue to provide unique science opportunities. However, overall risk, mission and telecommunications link design, and current TPS

technologies are challenges that must be carefully weighed in designing missions that rely on DTE communications link as the only means of returning the entry probe data.

REFERENCES

1. Owen, T. "Atmospheric Probes: Needs and Prospects," *Proceedings of the International. Workshop, Planetary Probe Atmospheric Entry and Descent Trajectory Analysis and Science, Lisbon, Portugal, 6-9 October 2003*, ESA SP-544, February 2004, pp. 7-12.

2. Atreya, S.K, Bolton, S., Guillot, T, Owen, T.C., "Multiprobe Exploration of the Giant Planets – Shallow Probes," 3rd International Planetary Probe Workshop Proceedings, NASA/ESA Special Publication, 2006 in press.

3. Atreya, S.K., et al., "A Comparison of the Atmospheres of Jupiter and Saturn: Deep Atmospheric Composition, Cloud Structure, Vertical Mixing, and Origin," *Planetary Space Science*, 47, 1999, pp. 1243-1262.

4. Atreya, S.K, "SATURN PROBES: Why, Where, How?" 4th International Planetary Probe Workshop Proceedings, NASA/ESA Special Publication, 2006 in press.

5. Atreya, S.K. and Wong, A.S. "Coupled Clouds and Chemistry of the Giant Planets - A Case for Multiprobes," *Outer Planets* (R. Kallenbach, ed.) Kluwer Academic, 2004

DESIGN FOR RELIABILITY APPROACH FOR ELECTRONICS UNDER EXTREME LOW TEMPERATURE APPLICATIONS

Yuan Chen, Mohammad Mojaradi, Elizabeth Kolawa

Jet Propulsion Laboratory, California Institute of Technology
4800 Oak Grove Drive, Mail Stop 303-230, Pasadena, CA 91109
Email: yuan.chen@jpl.nasa.gov, Mohammad.M.Mojarradi@jpl.nasa.gov, Elizabeth.A.Kolawa@jpl.nasa.gov

ABSTRACT

We present a design for reliability approach for electronics under low temperature applications. The proposed approach does not require altering the semiconductor processes and is focused on device parametric characterization, failure criteria determination, device and circuit/system reliability correlation, as well as reliability extrapolation.

1. INTRODUCTION

Electronics in space applications are often required to operate in low temperature environments, such as in any *in-situ* exploration missions to Mars, Titan, Europa and Lunar surfaces. In this paper, we present a design for reliability (DFR) approach for electronics under extreme low temperature applications. This approach is a paradigm shift from current reliability assessment for low temperature electronics and it provides the design fundamentals to build electronics for low temperature applications.

In the area of low temperature electronics, the majority of the research activities have been concentrated on the performance evaluation of the electronics; very few focus on the long term reliability issue. Our approach is targeting to ensure the required electronics lifetime under extreme low temperature environments, which is a critical requirement for mission success.

The fundamental reliability challenges for electronics operating under extreme low temperatures come from a specific failure mechanism called hot carrier aging (HCA) effect or any mechanisms related to and/or triggered by ion impact ionization process from device physics point of view [1-6]. Because of this physics failure phenomenon, an electronic device designed with a 10-year hot carrier aging lifetime under a temperature range of 27°C to 125°C has a much decreased lifetime at low temperatures, such as -230°C for lunar surface exploration.

Our approach does not require altering the process and so is a cost-efficient way to design for reliability under low temperature applications.

2. DESIGN FOR RELIABILITY APPROACH

It consists of the following aspects:

1) Evaluate hot carrier aging evaluation across the entire operating temperature range. The parametric degradation, including drain saturation and linear currents, threshold voltage, transconductance and drain conductance, needs to be fully characterized to evaluate the hot carrier aging impact on circuit/system.

2) Determine appropriate device hot carrier aging failure criteria to translate the hot carrier aging lifetime into circuit/system lifetime. Device parametric failure criteria need to be established to reflect the critical circuit performance requirements of circuit/system.

3) Project hot carrier aging lifetime from testing conditions to operating condition. A hot carrier aging lifetime projection/extrapolation model has been proposed to take into account both the device bias configuration and operating temperature profile.

4). Establish design guidelines to design for reliability. The most applicable transistor sizes are determined in order to meet reliability requirements.

3. CASE STUDY

Future surface exploration missions to Mars, Moon, Europa, Titan, etc. can expose spacecrafts or probes to a local extreme environments with temperatures as low as –230°C and temperature ranges as wide as wide –130°C to +90°C. The traditional solution in extreme environments has been to keep the electronics operating in a limited temperature range by housing them in a "warm-electronics-box" (WEB); however, this is not

viable for next-generation robotics and rovers, where electronics are placed at the point of use or next to loads directly exposed to the environment.

The case study assumes for a Mars mission using 0.6-µm commercial CMOS semiconductor technology with 5.0 V nominal V_{dd} and a 5-year lifetime on its critical path under a temperature range of –120°C to +80°C.

3.1 HCA evaluation

Hot carrier aging (HCA) tests were performed on the 0.6-µm NMOS transistors at room temperature (RT), –100ºC, and –150ºC. At –100ºC and –150ºC, the bias conditions include V_{ds} = 6.5 V, 6.0 V and 5.5 V, with V_{gs} = 2.0 V, 2.2 V, 2.4 V, 3.5 V, and 5.0 V to cover both maximum and non-maximum I_{sub} conditions.

During hot carrier aging tests, the parametric characteristics, i.e. saturation current I_{dsat}, linear current I_{dlin}, threshold voltage V_{th}, transconductance g_m, and drain conductance g_{ds}, were extracted from the I_{ds} versus V_{ds} and V_{gs} curves. Fig. 1 shows the maximum transconductance shift during the hot carrier aging at room temperature and -150ºC, as an example of parametric shifting observed during the hot carrier testing.

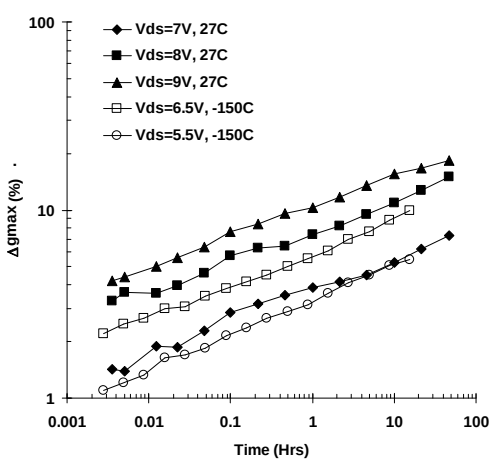

Fig. 1. g_{max} shift during hot carrier aging at room temperature and -150ºC.

3.2 Failure criterion determination

It has been demonstrated that the degradation of drain saturation current I_{dsat}, i.e., ΔI_{dsat} / I_{dsat} tracks and correlates with ring oscillator frequency degradation and a 10% I_{dsat} degradation typically yields a 5% frequency degradation [7-9]. Since drain saturation current I_{dsat} degradation on the NMOS transistors was found to be saturating around 2% to 5% both at room temperature and low temperatures, the digital circuitry does not appear to be the limiting factor for the low temperature circuit reliability.

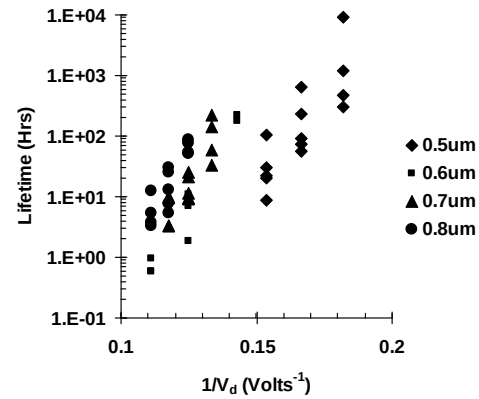

Fig. 2. Hot carrier aging tests at room temperature for NMOS transistors with different channel lengths.

For digital applications, the current drivability is the most significant device parameter, which can be described by I_{dsat}. In analog applications, the differential amplifier is one of the fundamental analog circuit building blocks; gain and offset voltage are the two most important performance parameters for the differential amplifier. The differential parameters transconductance g_m and drain conductance g_{ds} are essential, since the small-signal voltage gain, g_m/g_{ds}, is the maximum achievable single device amplification.

In the case of small-signal gain, a 75% small-signal gain corresponds to 15% maximum transconductance g_{max} change during the hot carrier aging [10]. Therefore, 15% g_{max} degradation was chosen as the failure criterion for the hot carrier aging lifetime for small-signal gain parametric.

In the case of offset voltage, 20 mV offset voltage was set as a failure criterion. This is equivalent to a 2% threshold change since the threshold voltage is approximately 1V. The relationship between the degradation of threshold voltage to that of maximum transconductance g_{max} indicated that a 2% threshold change was equivalent to a 10% maximum transconductance g_{max} change during the hot carrier aging [10]. Hence, 10% g_{max} degradation was chosen as the failure criterion for the hot carrier aging lifetime for fulfilling the offset voltage requirements.

3.3 Lifetime projection

Generally, worst-case hot carrier analysis has been used during process and technology qualification as well as product qualification [11]. This worst-case analysis usually only considers the N-channel metal-oxide semiconductor (NMOS) transistor hot carrier aging lifetime estimated under worst-case condition, i.e., maximum substrate current and minimum operating temperature. However, the worst-case hot carrier aging analysis approach typically gives a very conservative or, in some cases, an overly pessimistic prediction of NMOS lifetime. Therefore, a new methodology is desired and required to ensure the long-term reliability of electronics in low-temperature ranges.

Instead of using the worst-case analysis approach, which basically depends on the lowest temperature and maximum substrate current, we propose a new hot carrier aging lifetime extrapolation model that includes the temperature dependence of both substrate current and the hot carrier aging lifetimes. The extrapolation then becomes a function of transistor size and for the circuitry of interest, the target reliability requirement can be designed in by choosing the applicable transistor sizes along the critical paths. Please note that the applicable transistor size may not be the minimum channel length since, in some cases, transistors with longer channel length may have bias conditions which can generate more degradation due to hot carrier aging.

Assume 1) the degradation resulting from hot carrier aging is cumulative; 2) there is negligible annealing effect at higher temperatures, the input information to be determined is I_{sub} temperature dependence, I_{sub} profile, and operation temperature profile.

Substrate current is temperature dependent and since hot carrier aging lifetime is a function of substrate current, substrate-current temperature dependence is one of the most important factors needed, and is normally determined from experiments.

Typically, the expected hot carrier aging lifetime t_{50} is a function of substrate current I_{sub}.

Significant substrate current, and hot carrier aging, is present only during voltage transition. I_{sub} is not a constant value but changes over time. During each voltage transition, I_{sub} versus time is defined as an I_{sub} profile and can be determined by circuit simulation and/or experiments. Each I_{sub} profile can be divided into j small time intervals, where a constant substrate current I_{sub} is assumed during each time interval t_j.

During each time interval t_j, the NMOS transistor experiences a stress condition characterized by I_{sub}, and has a corresponding life time expectation of t_{50}, however, the transistor is biased under this I_{sub} only for a period of t_j. Therefore, the percentage of the NMOS transistor lifetime consumed during the time interval t_j is defined as $p(t_i)$ and can be then expressed as

$$p(t_i) = \frac{t_i}{t_{50}(I_{sub})} \tag{1}$$

t_{50} is the expected device hot carrier aging lifetime under the I_{sub} during the time interval t_j. The percentage of the device hot carrier aging lifetime consumed during one I_{sub} cycle is then $p(I_{sub})$ and is given by

$$p(I_{sub}) = \sum_{m=1}^{j} \frac{t_m}{t_{50}(I_{sub,m})} \tag{2}$$

The operating temperature profile shows the expected temperature changes over time under use conditions. The profile can be the temperature change over a day, a month, a year, or any time span.

Similar to the I_{sub} profile, the operating-temperature profile is divided into k intervals, where each interval is one I_{sub} profile cycle, assuming the I_{sub} cycle is typically very small since I_{sub} is a function of temperature**.** Again, a constant temperature can be assumed for each I_{sub} cycle and the percentage of the device hot carrier aging lifetime consumed during one operating temperature profile is $p(T)$, shown as follows:

$$p(T) = \sum_{n=1}^{k} \sum_{m=1}^{j} \frac{t_{m,n}}{t_{50}(I_{sub,m}, T_n)} \tag{3}$$

Assume the operating temperature profile is the temperature changes over a day and the reliability requirement of a circuit is D days; then the percentage of device hot carrier aging lifetime taken during D days is $p(D)$, given by:

$$p(D) = D * (\sum_{n=1}^{k} \sum_{m=1}^{j} \frac{t_{m,n}}{t_{50}(I_{sub,m}, T_n)}) \tag{4}$$

By setting (5) equal to one, we can determine the number days, given by (6), that the device can survive from the hot carrier aging point of view. Therefore, the minimum NMOS transistor channel length to satisfy the following expression with any desirable margin is:

$$D > (1/\sum_{n=1}^{k}\sum_{m=1}^{j}\frac{t_{m,n}}{t_{50}(I_{sub,m,}T_n)}) \qquad (5)$$

3.4 Design guidelines

Based on substrate current profile, temperature profile and channel length dependence, Fig. 3 gives the air temperature profile on Mars and Fig. 4 shows the projected hot carrier aging lifetime as a function of channel length under the Mars temperature profile.

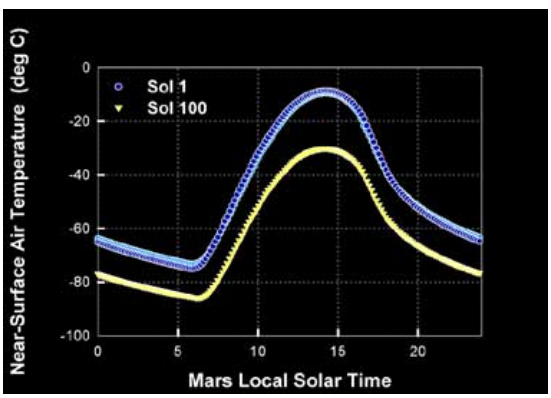

Fig. 3 Air temperature profile on Mars.

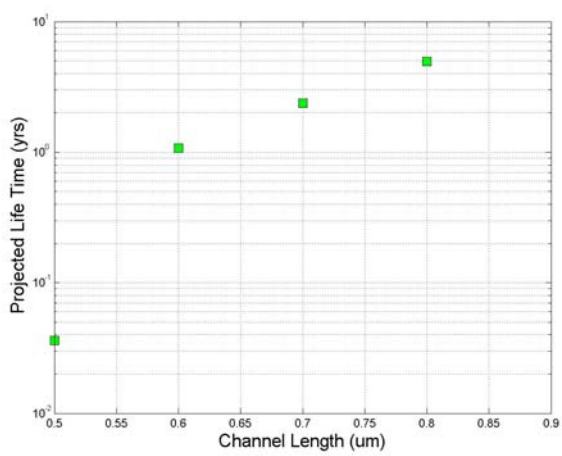

Fig. 4. An example of the projected NMOS hot carrier aging lifetime under a Mars temperature profile.

4. SUMMARY

A design for reliability approach for electronics under low temperature applications, which does not require altering the semiconductor processes, is presented. A case study has been used to demonstrate the approach on device parametric characterization, failure criteria determination, device and circuit/system reliability correlation, as well as reliability extrapolation.

5. ACKNOWLEDGEMENT

This work was carried out at Jet Propulsion Laboratory, California Institute of Technology, under a contract with the National Aeronautics and Space Administration.

6. REFERENCES

1. F. Balestra, G. Ghibaudo, “Device and circuit cryogenic operation for low temperature electronics,” Kluwer Academic Publishers, 2001.
2. S. L. Von Bruns and R .L. Anderson, “Hot-electron-induced interface state generation in n-channel MOSFET’s at 77K,” *IEEE Transactions on Electron Devices*, vol. ED-34, p. 75, 1987.
3. S. B. Bibyk, H. Wang and P. Borton, “Analyszing hot-carrier effects on cold CMOS devices,” *IEEE Transactions on Electron Devices*, vol. ED-34, p. 83, 1987.
4. A. Acovic, M. Dutoit, M. Ilegems, “A study of the increased effects of hot-carrier stress on NMOSFET’s at low temperature,” *IEEE Transactions on Electron Devices*, vol. ED-36, p. 2603, 1989.
5. M. Song, K. P. MacWilliams, J. C. S. Woo, “Comparison of NMOS and PMOS hot carrier effects from 300 to 77K,” *IEEE Transactions on Electron Devices*, vol. ED-44, p. 268, 1997.
6. J. Wang-Ratkovic, et al., “New understanding of LDD CMOS hot carrier degradation and device lifetime at cryogenic temperatures,” *IRPS*, 1997.
7. E.A. Vittoz, “The design of high-performance analog circuits on digital CMOS chips”, *IEEE Journal of Solid State Circuits*, Vol. 20, No. 3, March 1985.
8. K.N. Quader, E.R. Minami, W. Huang, P.K. Ko, C. Hu, “Hot carrier reliability design guidelines for CMOS logic Circuits”, *IEEE Journal of Solid State Circuits*, Vol. 29, No. 3, March 1994.

9. J.E.Chung, K.N. Quader, C.G. Sodini, P. Ko, C. Hu, "The effects of hot-electron degradation on analog MOSFET performance", *IEDM*, 1990.
10. JEDEC, "Foundry process qualification guidelines (wafer fabrication manufacturing sites", *JP001*, 2003.
11. Y. Chen, Lynett Westergard, Mohammad M. Mojaradi, Travis W. Johnson,, Raymond S. Cozy, Curtis Billman, Gary R. Burke, and Elizabeth A. Kolawa, "Design for ASIC reliability for low temperature applications", *IEEE Transactions on Device and Materials Reliability*, Vol. 6, No. 2, pp. 146-153, 2006.

HIGH TEMPERATURE ELECTRONICS (> 485 °C) FOR VENUS EXPLORATION

Edgar Cilio, John Garret, John Fraley, Jared Hornberger, Brice McPherson, Roberto Schupbach, Alexander Lostetter

Arkansas Power Electronics International,Inc.,700 Research Center Blvd Fayetteville, AR 72701 USA, Email: edgar@apei.net

Abstract – Venus is an extreme environment, with an average surface temperature in excess of 485 °C at 92 atmospheres of pressure, and a high concentration of sulphuric acid vapour at high altitudes. Venus robotic probes and landers would require motors and/or actuators (and their drivers) to perform a wide variety of functions in this environment, from moving and controlling robotic arms and drills, to providing traction for surface propulsion. Silicon carbide (SiC) has a theoretical junction temperature limit in excess of 600 °C, making it a prime semiconductor material for Venus exploratory electronics systems. APEI, Inc. is currently developing a high temperature SiC multichip power module (MCPM) electronic motor drive solution to address this requirement.

1. INTRODUCTION

Silicon Carbide (SiC) has a theoretical junction temperature limit in excess of 600 °C [1], which makes it a prime candidate semiconductor for severe environments. Developing a SiC power electronic motor drive that could be integrated with the casing of the DC motor would significantly reduce the weight of the required electronic environmental shielding and the complexity of the overall electronics system. SiC electronics not only could extend the life of a Venus atmospheric probe or lander beyond days or weeks, but would operate reliably through the implementation of simple passive thermal management strategies. Avoiding complicated advanced active thermal management strategies not only improves reliability, but significantly reduces the complexity, weight, and volume of the overall electronics systems. SiC power electronics offer other potential advantages over silicon as well, including 1/10th the switching losses, 10× the power density, 10× the breakdown voltage, and switching frequencies into the 10s of GHz range [2]. All of these advantages offer the potential to develop highly miniaturized, highly reliable, light weight extreme environment power electronics drive systems that can be integrated directly with DC motors or actuators.

The development of a SiC multichip power module (MCPM) motor drive for the exploration of Venus requires the addressing of several challenges:

1. SiC digital and power electronics that can survive the high-temperature ambient environments of ~ 500 °C with passive thermal management strategies.
2. Passive and magnetic components that can operate reliably within the required conditions.
3. Hermetically sealed electronic packages that can survive the high-temperature, high pressure, and chemical composition of the Venus atmosphere.

The paper is divided as follows: Section 2 presents the current state of the high temperature SiC devices, Section 3 describes high temperature passives, Section 4 shows the high temperature packaging approach, Section 5 describes other applications of this technology, and lastly, Section 6 describes ongoing work for extending component temperature ranges.

2. HIGH TEMPERATURE SIC DEVICES

APEI, Inc. has partnered with several SiC power switch manufacturers and tested the ability of the devices to operate at high temperatures. The results of the findings are presented next.

2.1 Power Devices

Two different device types, one from SemiSouth and one from SiCED were tested.

The SemiSouth 100V bare die JFET consisted of all gold metallization pads. The device was packaged into a gold plated beryllium oxide 3-pin package by APEI, Inc. The package is depicted in Fig. 1 without a lid. Both the package and the devices were tested successfully up to 500C. After 500 ºC, the adhesion of the die attach material was lost, resulting in die lift and caused loss of connection to the device, ultimately causing failure. The initial test setup used to capture switching curves is seen in Fig. 2. Fig. 3 and 4 displays the room temperature and the high temperature (500 °C) blocking voltages, respectively. In Fig. 3 and 4, channel 1 is a command signal generated by a function generator, channel 2 is the drain to source voltage, and channel 3 is the drain current.

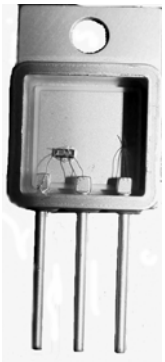

Fig. 1. APEI, Inc. packaged SemiSouth SiC JFET for high temperature operation

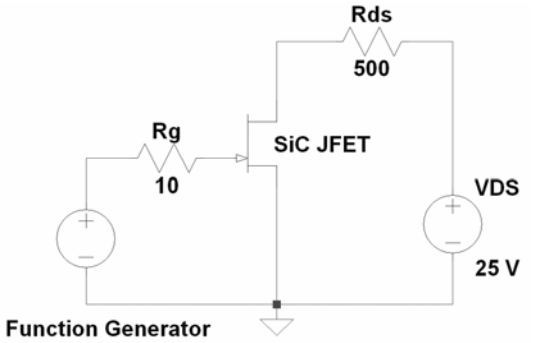

Fig. 2. Initial setup for temperature testing

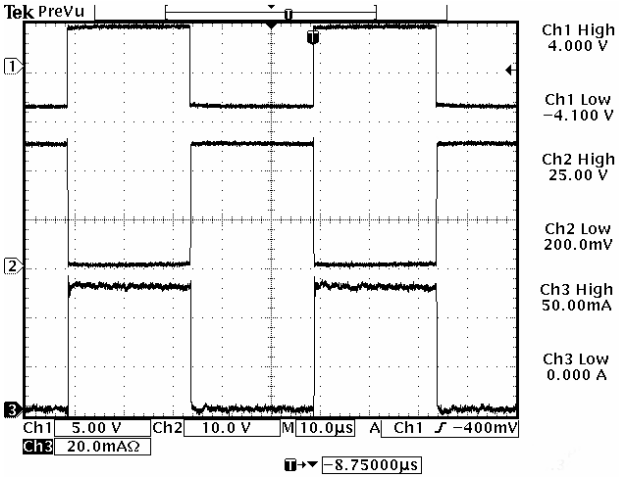

Fig. 3. Blocking voltage operation at 25 °C

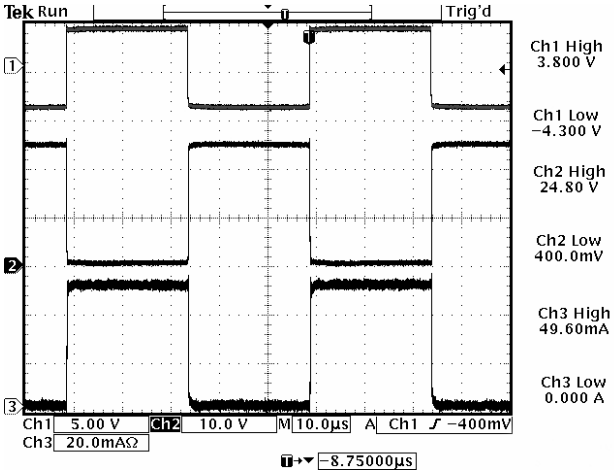

Fig. 4. Blocking voltage operation at 500 °C

Fig. 5 and 6 illustrate the on-state curves obtained at different temperature. As temperature increases, the on-resistance increases. For instance, at room temperature with a gate-to-source voltage (Vgs) of 3V and drain-to-source voltage (Vds) of 30V; the drain-to-source current (Ids) is 0.66A. At 350 ºC, the Ids is only 0.14 A at the same Vgs and Vds settings.

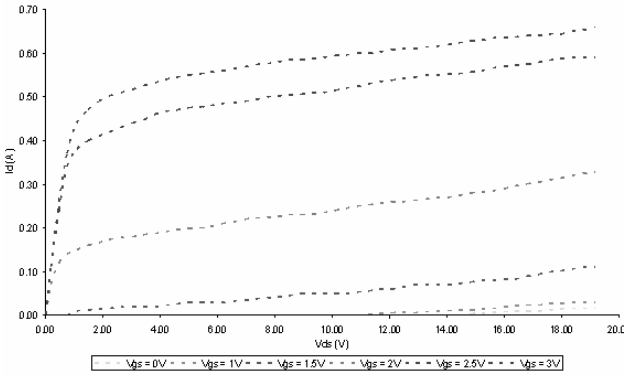

Fig. 5. On-state curve for the packaged SemiSouth SiC JFET at 25 ºC

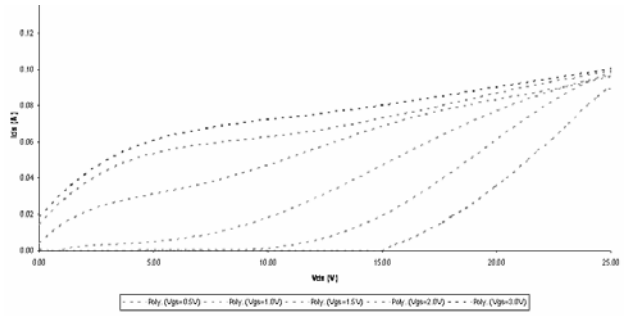

Fig. 6. On-state curve for the packaged SemiSouth SiC JFET at 350 ºC

APEI, Inc. also obtained and tested bare die SiC JFETs from SiCED. A device was attached to a direct bond copper (DBC) substrate using a high temperature epoxy and the source pads were attached with 8-mil power aluminum wirebonds. The gate terminal was bonded using 1 mil Al wire as seen in Fig. 7.

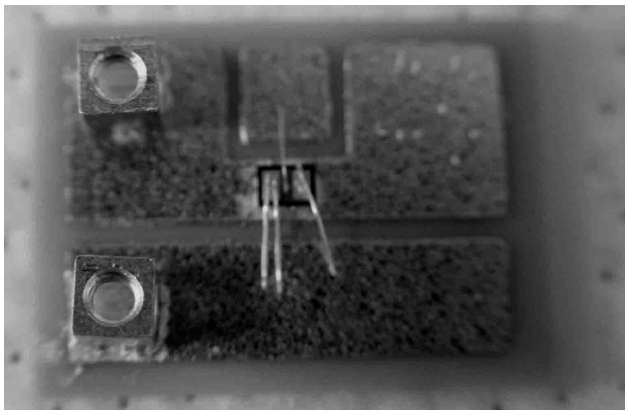

Fig. 7. APEI, Inc. packaged SiCED SiC JFET for high temperature operation

This packaged device was tested successfully to 400 °C as seen in Fig. 7. Fig. 8 illustrates the device switching at room temperature at a VDS of 100V. Note that the gate signal generated from an opamp is seen in channel 4, the command signal for the function generator is seen in channel 3, the VDS is channel 2 and channel 1 is the drain to source current. Fig. 9 shows the device switching at 100V at 400 °C.

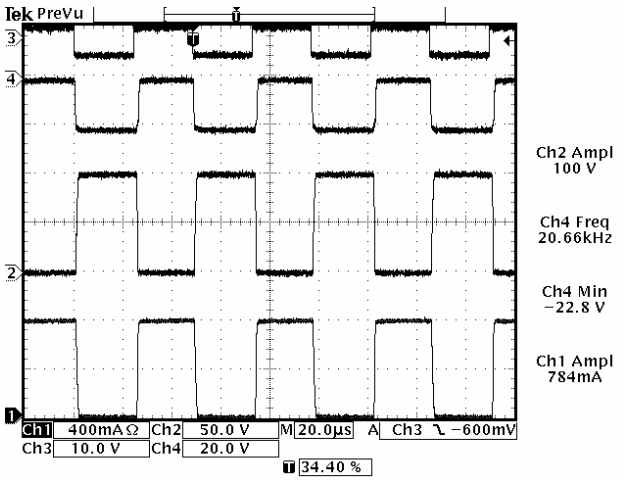

Fig. 8. Blocking voltage operation at 25 °C

The on-state curves are illustrated in Fig. 10 (room temperature) and 11 (350 °C). Note the voltage threshold is approximately -22.3 V and the on-state curves only go up to -20 V. As the temperature increases, the amount of Vgs it takes to turn the device off also increases.

APEI, Inc. has experimentally confirmed the ability of SiC devices to operate at very high temperatures (400 + °C).

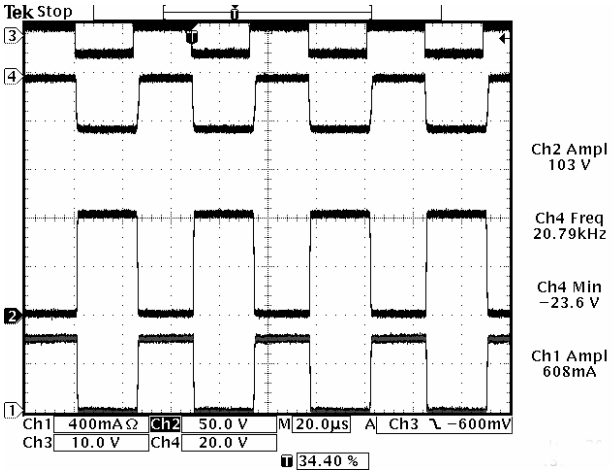

Fig. 9. Blocking voltage operation at 400 °C

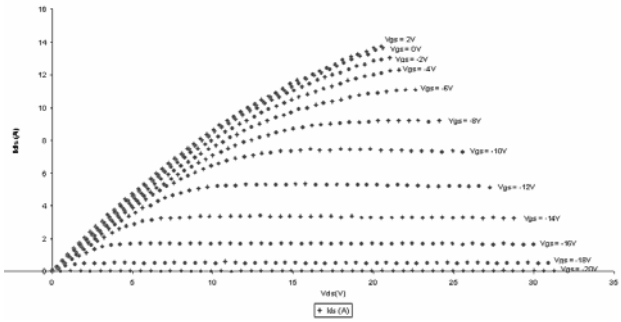

Fig. 10. On-state curves at 25 °C for SiCED SiC JFET using APEI, Inc. packaging technology

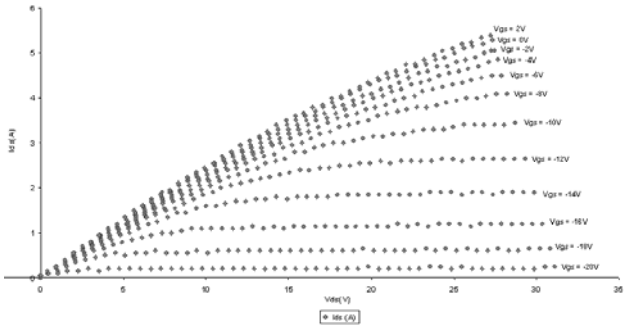

Fig. 11. On-state curves at 350 °C for SiCED SiC JFET using APEI, Inc. packaging technology

2.2 Digital Devices

The Lateral Trench Junction Field-Effect Transistor (LTJFET) from SemiSouth serves as a building block for

temperature-tolerant radiation-hardened fast SiC electronics that may include built-on-chip digital control circuitry and a power transistor with control levels compatible to 3.3 V CMOS or 3.3 V TTL (LVCMOS or LVTTL).

In order to show feasibility of the LTJFET ICs, simple logic gates have been built using discrete enhancement- and depletion-mode vertical power JFETs by SemiSouth. These circuits were tested by SemiSouth with a 2.75 V power supply and input levels of 0.25 V (LOW) and 2.75 V (HIGH). Fig.12 shows a truth table and measured waveforms of a hybrid SiC NOR gate, where enhancement- and depletion-mode vertical SITs were wirebonded on an alumina substrate.

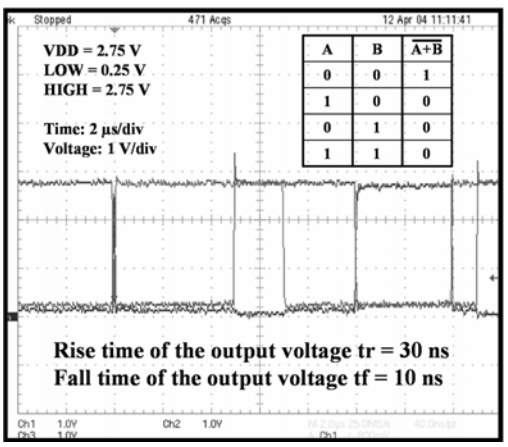

Fig. 12. Measured waveforms of a SiC logic gate (NOR) built with discrete SiC static induction transistors (SITs) (Courtesy of SemiSouth).

3. HIGH TEMPERATURE PASSIVES

3.1 Capacitors

Improvements in current dielectric materials and identification of new materials capable of operating reliably at high temperatures play a crucial role in the realization of high power density converters. APEI, Inc. has identified a number of high temperature capacitor technologies.

Twelve candidate materials were evaluated for high temperature operation The test results presented in Fig. 13 shows the relative change in capacitance over temperature under biased conditions (one-half the rated voltage or maximum of 25 V). The temperature testing was performed on various electrolytic, aluminium, Y5T, metallized polyester, polypropylene film, metallized polymer film, metallized film, tantalum, wet tantalum, X7R, NPO, and COG materials. It should be noted that the maximum applicable voltage was limited to 25 V due to the voltage restrictions of the RLC meter used to obtain data. The components were tested at room temperature before starting at 100 ºC. The temperature was raised with increments of 10 ºC with dwell times of ten minutes at each temperature.

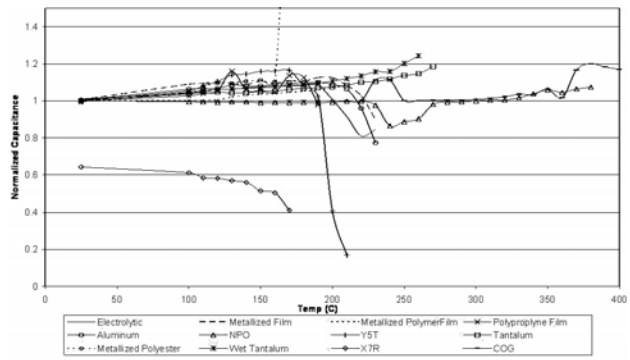

Fig. 13. Capacitor materials tested at 25 V vs. temperature

Electrolytic capacitors are normally rated to 125-150 °C; however, obtained data displays that operation at 230 °C can be maintained for short durations. Aluminium capacitors are grouped in the same family as electrolytic capacitors. Their characteristic behaviour mimics the curves seen in the electrolytic tests. These capacitors have poor long term reliability at extended temperatures.

Polypropylene has a high dielectric strength compared to polycarbonate and polyester films. These films also operated up to 230 °C as seen in Fig. 13.

Tantalum capacitors have proven to have high capacitance per unit volume. These capacitors render excellent performance with a high degree of reliability when properly used [3]. APEI, Inc. researchers observed these advantages of tantalum and wet tantalum capacitors as illustrated in Fig. 13.

The X7R becomes very unstable at higher temperatures and will not work for our application. However, the NPO and COG materials capacitors show excellent stability up to 500 ºC and have potential in being used for high temperature applications. However, these capacitors are seldom available larger than 0.22µF.

In conclusion, the NPO and COG materials capacitors show relative stability up to 500 ºC and potential for use in high temperature applications. The COG capacitors are the prime candidates to enable high temperature operation of the MCPM module.

Recent developments in dielectric technology have

demonstrated capacitors capable of operation beyond 400 ºC. Specifically the HT300 line of capacitors from TRS Electronics has been tested up to temperatures of 400 ºC.

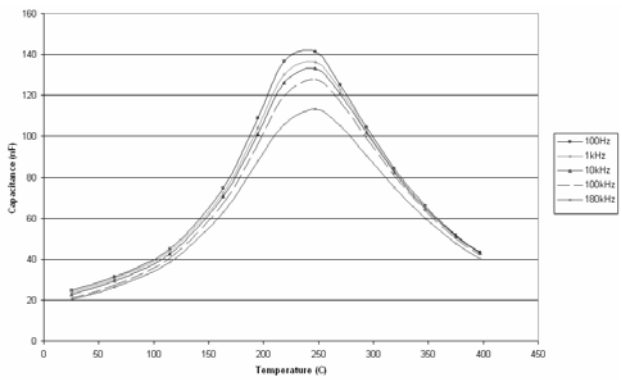

Fig. 14. Temperature dependence of the capacitance for a TRS 100nF/250V capacitor

The capacitor was characterized over temperature under different switching frequencies and is shown in Fig. 14. Further tests indicate that at 200 °C, the HT-300 dielectric operating at 500V outperforms the commercially available component by 10 times at 200 °C and over 100 times at 300°C [4].

3.2 Magnetic Design

It is well known that many magnetic materials do not have an extended temperature range of operation. APEI, Inc. has identified several types of magnetic cores, including powdered cores, tape-wound cores, and ferrite-based cores, that can operate at elevated temperatures when properly designed. Many of the properties of a magnetic core can be obtained from its hysteresis curve. The hysteresis curve, also known as the B-H curve, demonstrates the relationship between the induced magnetic flux density B and the magnetizing field strength H.

APEI, Inc. has tested a ferrite core over temperature. This core was selected because it offers an excellent combination of maximum saturation flux density (approximately 280 mT) and Curie temperature (420 °C). The characteristic B-H curve of this core at different temperatures is shown in Fig. 15 These B-H curves were extracted using an in house characterization circuit.

As expected, the saturation point of the magnetic core decreases when the temperature increases. Initially, the saturation flux density is 255 mT at T = 27 °C. If the temperature is increased to 270 °C, the saturation flux density decreases to 60 mT.

The transformer design is mainly determined by the signal applied to it. For an isolation transformer, it is important to avoid saturation, while maintaining the integrity of the pulse applied. This translates into having the highest possible magnetization inductance while staying below the saturation point at the maximum temperature of operation.

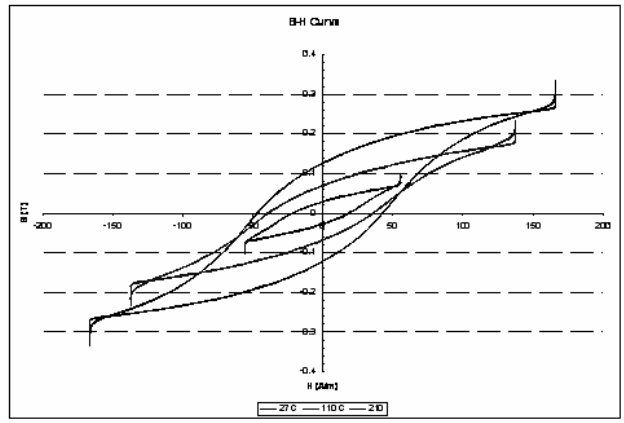

Fig. 15. B-H curves of the nickel-zinc ferrite L01-EA8X-75/1 at different temperatures.

The maximum magnetic flux Φ_{max} is obtained from observing the saturation point of the core at the desired temperature of operation. Based on Φ_{max}, the specific number of turns needed to keep the core from saturating at the desired temperature of operation is determined.

Fig. 16 shows a picture of a packaged high temperature transformer.

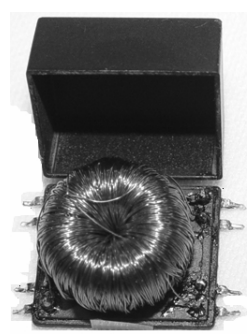

Fig. 16. APEI, Inc. high-temperature transformer

Fig. 17 and 18 show the operation of the transformer at two different temperatures. In these figures the transformer's input signal is displayed using channel 2 while the transformer's output signal is displayed using

channel 3. Fig. 17 shows the transformer operating at 150 °C while Fig. 18 shows the transformer operating at 400 °C. Fig. 17 and 18 show the transformer primary and secondary voltage signals operating at 15 kHz.

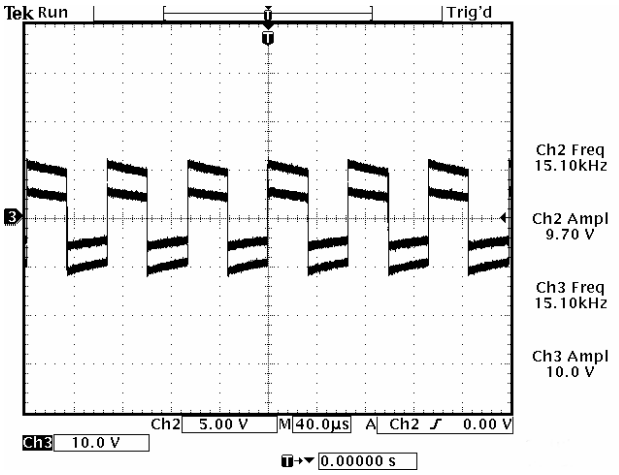

Fig. 17. Isolation transformer operating at 150 °C

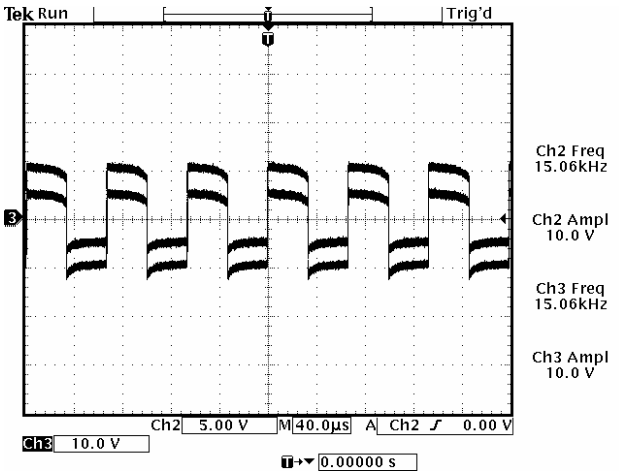

Fig. 18. Isolation transformer operating at 400 °C

This side-by-side comparison shows the output performance of the high temperature transformer in which only a slight degradation is seen at high temperatures.

4. HIGH TEMPERATURE PACKAGING

4.1 Substrates

The primary approach towards the development of a high temperature motor drive is to implement the power electronics in the form of a novel MCPM in which the substrate will be a SiC wafer.

This approach will be the most conducive to effectively securing the operational reliability of the package by minimizing CTE material mismatches throughout the power module. Matching the mechanical properties of the SiC wafer with the SiC electronics, and in turn matching those with a ceramic or MMC case will result in an overall module that minimizes thermal stresses.

The power module will be built upon a SiC wafer substrate utilizing bare die SiC control and power electronic components. The SiC based electronics will be functional to temperatures in excess of 500 °C. The SiC wafer substrate will allow close CTE matching between the case / substrate / electronics and thus improve thermal-stress response, reduce the chances of fracture, and improve package reliability. The module will be hermetically sealed within a ceramic housing to protect against possible corrosive effects from the atmosphere.

Figure 19 illustrates a cross-section of the proposed SiC based MCPM

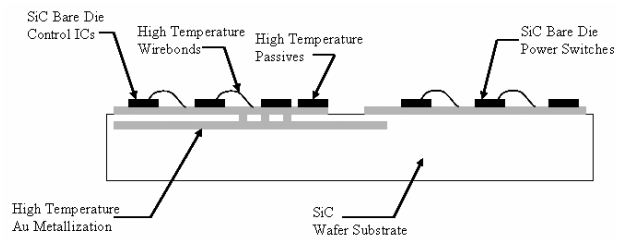

Fig. 19. SiC MCPM cross-section

4.2 Die attach

Die attachment is a major obstacle in realization of reliable high-temperature electronics, one which requires significant technological advances in both materials and in processing. The standard approach employing solder alloys becomes exceedingly difficult as the maximum use temperature of the electronics module is raised. The liquidus temperature of the solder must be higher than the operational temperature of the module, and this liquidus temperature generally must be exceeded by approximately 30-40 °C during processing to ensure a good bond. This exposes the assembly to temperatures higher than what is required during operation, instigating the formation of micro-cracks and defects in the packaging materials. These defects concentrate stresses and eventually may lead to a premature failure

Epoxies are an option under consideration, but offer substantial drawbacks. Conductive epoxies typically consist of an organic binder and a resin filled with metal powder or flakes in order to allow transmission of electrical and thermal energy. The binder is baked out

during the curing process, leaving a solid matrix that will remain solid until the resin liquefies.

APEI, Inc. is currently investigating a promising method of die attach, utilizing the process of diffusion to enhance or create a high-temperature bond. The method under investigation is using a Au/Sn solder alloy to initially create a bond, then proceeding to diffuse the Sn through a thick substrate metallization, reducing the ratio of Au to Sn, effectively increasing the melting temperature of the attach.

4.3 Overall System Integration

The final MCPM motor drive will be directly mounted on the motor. By integrating the highly robust power electronic systems at the point of operation within the environment, the weight and complexity of the lander or rover could be reduced. Fig. 20 illustrates one method in which these MCPMs could be integrated with motor systems in an exploration application (traction drives or other robotic appendages). Fig. 21 illustrates an exploded view of the integrated motor drive system.

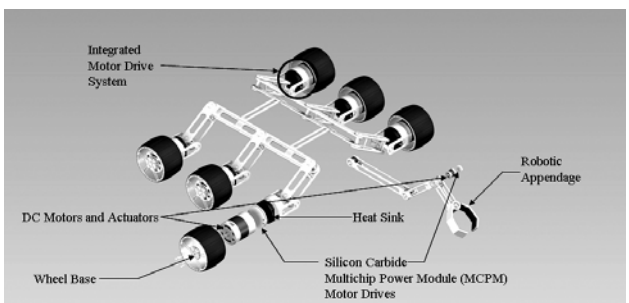

Fig. 20. Conceptual model of integrating high temperature SiC MCPMs with DC motors/actuators in extreme environment robotic landers

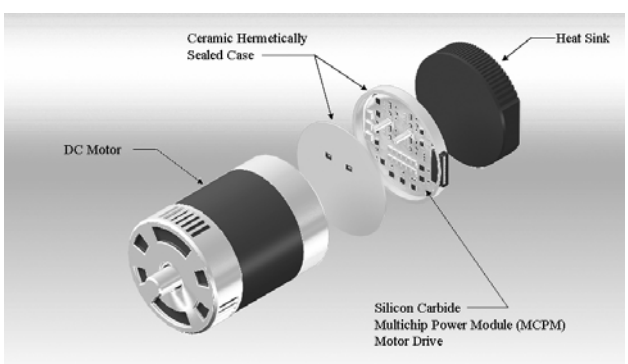

Fig. 21. Conceptual integrated motor drive system

5. OTHER APPLICATIONS OF THIS TECHNOLOGY

The technology currently being developed for a Venus lander/rover is also being developed for various other applications.

5.1 High Power Density Inverters

APEI, Inc. has built and tested a single-phase SiC-based 3 kW proof-of-concept inverter module achieving significant volume reduction (~85 % smaller) when compared with similar state-of-the-art commercially available Si-based single-phase inverter modules. APEI, Inc.'s SiC-based MCPM power inverter module has a power density of 0.67 W/cm^{3}[3] (using only passive cooling).

This power density was achieved primarily by the combination of a highly integrated module design constructed using APEI, Inc.'s MCPM approach and high-temperature operation. To operate at high temperature, the module utilizes SiC power devices in conjunction with high temperature active and passive control circuitry based on high-temperature silicon-on-insulator (SOI) MOS devices (HTMOS).

Fig. 22 shows the fully integrated MCPM inverter module where the control and power stages are attached to an AlSiC metal-matrix-composite (a ceramic matrix injected with a metal) heatspreader. This type of heatspreader offers excellent thermal conduction capabilities while simultaneously providing a close coefficient of thermal expansion (CTE) match to the DBC ceramic substrate.

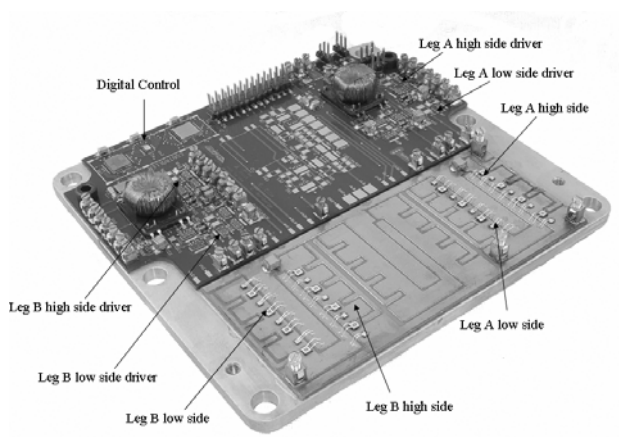

Fig. 22. Single-phase MCPM inverter module

5.2 High temperature RF Transmitters

APEI, Inc. is currently developing technology to allow for reliable RF transmission to be implemented in harsh environment conditions. Specifically, research into the field of high temperature telemetry is being pursued in order to relay information out of harsh environments experiencing temperatures upward of 400°C.

Reliable oscillator signals in the RF range have already been demonstrated at temperatures of up to 290°C. Fig 23 and 24 show a 30 MHz oscillator operating at 175 °C and 290 °C.

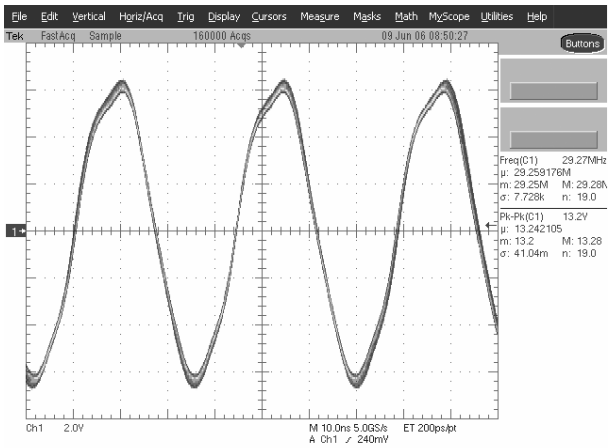

Fig. 23. 30 MHz oscillator operating at 175 °C

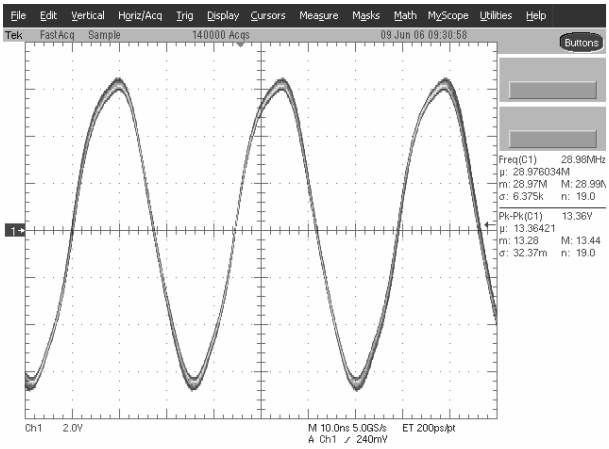

Fig. 24. 30 MHz oscillator operating at 290 °C

6. EXTENDING COMPONENT TEMPERATURE RANGES

There are only a handful of magnetic materials that operate beyond 400 °C, with which APEI, Inc. engineers have fabricated and tested isolation transformers to very high temperatures. These materials could potentially be pushed to 500 °C operation. High temperature capacitors are another area that will require investigation. APEI, Inc. researchers have tested several NPO/COG capacitor technologies up to 400 °C with relative stability. These technologies could potentially be pushed to operate up to approximately 500 °C. APEI, Inc. is teamed with TRS Technologies, a capacitor manufacturing company that specializes in R&D of high performance and high temperature dielectric materials. APEI, Inc. is currently in the process of testing TRS Technologies' HT300 Series prototype capacitors for very high temperature operation in power electronic applications.

7. CONCLUSION

The motor drive power module will be built upon a SiC wafer substrate utilizing bare SiC control and power electronic components. The SiC based electronics will be functional to temperatures in excess of 500 °C. The SiC wafer substrate will allow close CTE matching between the case / substrate / electronics and thus improve thermal-stress response, reduce the chances of fracture, and improve package reliability. The module will be hermetically sealed within a ceramic housing to protect against possible corrosive effects from the atmosphere.

The ability to integrate the motor drive electronics directly with the motors using the MCPM approach will significantly reduce the complexity and weight of the core electronics shielding system while improving the reliability of the mechanical robotic components.

8. REFERENCES

[1] T. Burke, et al., "Silicon Carbide Power Devices for High Temperature, High Power Density Switching Applications", Proc. of the IEEE Power Modulator Symposium, pp.18-21, June 1996.

[2] J. Hornberger, A.B. Lostetter, K. J. Olejniczak, S. Magan Lal, and A. Mantooth, "A Novel Three Phase Motor Drive Utilizing Silicon on Insulator (SOI) and Silicon-Carbide (SiC) Electronics for Extreme Environment Operation in the Army Future Combat Systems (FCS)," 37th International Symposium on Microelectronics (IMAPS 2004), Long Beach, CA, November 2004.

[3] Allison, W.; Bubriski, S.; Hazzard, H.; Millard, R.; "Symposium on Tantalum Capacitors", Component Parts, IRE Transactions on Volume 7, Issue 3, Sept 1960 Page(s):88 – 105.

[4] Stringer, C.J, et al., "High Temperature Ceramic Capacitors" 39th International Symposium on Microelectronics (IMAPS 2006), San Diego, CA, October 2006.

DERIVATION AND APPLICATION OF A METHOD FOR FIRST-ORDER ESTIMATION OF PLANETARY AERIAL VEHICLE POWER REQUIREMENTS

Jarret M. Lafleur

Georgia Institute of Technology, Daniel Guggenheim School of Aerospace Engineering
270 Ferst Drive, Atlanta, Georgia 30332-0150, United States of America
Email: jarret.m.lafleur@gatech.edu

ABSTRACT

One of the most fascinating options for the future of unmanned planetary exploration is the use of planetary aerial vehicles. From the perspective of endurance, it is preferable for such vehicles to rely on non-chemical forms of propulsion, meaning that power requirements estimation becomes particularly important in design.

Presented here is a primarily analytical (as opposed to empirical) method for first-order estimation of power requirements for planetary airplanes and rotorcraft. Equations are derived and applied to examples which provide an approximate basis for comparing difficulties of flying on Venus, Earth, Mars, and Titan. Results indicate a two-order-of-magnitude difference in power requirement between Mars and Titan aerial vehicles and at least a factor of two difference in power requirement between rotorcraft and airplanes in general. Highlighted is the importance of the planet-dependent parameter $g^{1.5}/\rho^{0.5}$. System implications for solar, radioisotope thermoelectric generator, and battery power options are also considered.

1. INTRODUCTION

Over the past few years, successes of planetary orbiters and landers have drawn considerable attention to unmanned planetary exploration. The future holds promise for unmanned exploration, and one of the most exciting options for the future is the use of planetary aerial vehicles. Whereas planetary orbiters are limited in the detail they gather and traditional landers are limited in range from their landing sites, aerial vehicles offer the unique combination of regional-scale range and detailed scientific measurements.

One aerial vehicle proposal, NASA Langley's ARES design [1], utilizes a rocket to power its flight. However, as designs become increasingly ambitious, it is likely that rocket propulsion will be replaced by electric propulsion due to the expendable nature of rocket propellant. An airplane powered by solar or nuclear energy, for example, could have a lifetime only limited by the wear and tear of its components. As soon as electricity is used in lieu of chemical energy, power consumption becomes as large a design issue as mass and volume constraints.

This paper presents a method for the first-order estimation of power requirements for planetary airplanes and rotorcraft. One method proposed by [2] has already detailed such power estimation based on purely empirical considerations. Presented here is a more analytical approach to the problem, originally developed as part of a study on Titan aerial vehicles in the Georgia Tech Space Systems Design Lab.

2. AIRPLANE POWER ESTIMATION

2.1. Airplane Power Equation

In this method, necessary installed power for an airplane is estimated using the condition of steady and level flight. For this condition, thrust power required is given by Eq. 1. [3] Here, D is drag and V is velocity:

$$P_{thrust} = DV \tag{1}$$

Clearly, this relationship alone is not sufficient to estimate the power requirement for a planetary aerial vehicle: Drag is entirely unknown and velocity may be any of a range of values. In addition, margin, efficiency effects, and non-propulsive terms are omitted.

Incorporating the terms P_{other} (for the non-propulsive power requirement), R_p (margin to account for power losses due to conversion and wire resistances), R_m (safety margin), and η (propulsive efficiency, including propeller, motor, and gearbox power losses):

$$P_{required} = (1+R_m)(1+R_p)\left[\frac{P_{thrust}}{\eta} + P_{other}\right] \tag{2}$$

Also note that the following substitutions can be made for the terms of P_{thrust} (here, m is airplane mass, g is the

gravitational constant, *L/D* is the steady flight lift-to-drag ratio, l_w is cruise wing loading, C_L is lift coefficient, ρ is atmospheric density, and S is wing planform area):

$$D = \frac{mg}{\frac{L}{D}}$$
$$V = \sqrt{\frac{2l_w}{C_L \rho}} = \sqrt{\frac{2mg}{SC_L \rho}} \quad (3)$$

In the end, required power for a planetary airplane can be estimated with Eq. 4:

$$P_{required} = (1 + R_m)(1 + R_p)\left[\frac{mg}{\eta \frac{L}{D}}\sqrt{\frac{2mg}{SC_L \rho}} + P_{other}\right] \quad (4)$$

Note that if drag or cruise velocity are known from the outset of a project, they can be substituted for their respective representations in Eq. 4. Also, it may occasionally prove more convenient to use the velocity expression involving wing loading as shown in Eq. 3.

2.2. Application of the Airplane Power Equation

Unfortunately, the equations developed here cannot be truly demonstrated since no airplanes have flown on other worlds to date. However, their results can be checked for reasonability, especially against the results predicted by [2]. To do so, power requirements will be estimated for a notional 300 kg aerial vehicle on Venus, Earth, Mars, and Titan.

2.2.1. Baseline Vehicle Parameter Estimation

The first step to sizing the airplane for this application is to determine wing parameters. If low-speed flight is assumed, educated guesses for certain wing parameters for this generic 300 kg airplane will lead to definitions of S, *L/D*, and C_L. If it is assumed that this airplane has a wing planform area (S) of 20 m²,[1] a reasonable wing aspect ratio (AR) of 7,[2] and a reasonable cruise lift coefficient (C_L) of 0.8, then the induced drag coefficient C_{Di} can be calculated (as in Eq. 5 from [3]) and lift-to-drag ratio (*L/D*) can be roughly estimated if it is assumed that parasitic drag is equal to induced drag[3] plus a modest 25% margin. The calculation of induced drag also depends on the spanwise efficiency factor e, which will be taken as 0.98.[4]

$$C_{Di} = \frac{C_L^2}{\pi \cdot AR \cdot e} \quad (5)$$

Making the assumptions above, C_{Di} is 0.0297, C_{Dp} is found to be 0.0371, and thus *L/D* is found to be 12.0.

The final assumptions that need to be made are those of the efficiency and margin factors in Eq. 4 and the non-propulsive power requirement. Here, a propulsive efficiency factor of 0.70 is assumed (that is, if 0.90 is taken as motor efficiency [5], if 0.90 is taken as gearbox efficiency [5], and if 0.87 is taken as propeller efficiency [6]), power loss margin is taken as 25% (which includes losses due to power converters and wiring [7]), power safety margin is taken at a realistic 50%, and the non-propulsive power requirement (for flight computers, sensors, payloads, etc.) is assumed to be 150 W for this class of vehicle[5].

A summary of these assumptions is shown in Table 1. Recall that most of these parameters use notional values for a vehicle that is hardly defined (in fact the only thing defined at the outset was its mass). If further information is known about a given design problem, the appropriate parameters can certainly be replaced. Here, the information will be used to make comparisons between flight power requirements on different worlds and, later, to determine the difference between rotorcraft and airplane power requirements.

---

[1] This is the same as the wing area of an early design for a 300 kg Mars airplane in [4].

[2] While a large aspect ratio would indeed be desirable, this estimate is somewhat conservative to account for anticipated aeroshell packaging constraints which will likely be present for any missions in the near future.

[3] Essentially, this assumes that the airplane is cruising at the speed for minimum drag; in other applications, it may be desirable to estimate parasitic drag independently based on the airplane geometry as described in [3]. For applications requiring high-speed flight (such as with Mars), drag due to compressibility would also need to be accounted for. In this paper, this rough drag assumption is made for the purposes of demonstration and rough comparison.

[4] Reference [3] indicates that this factor is typically between 0.98 and 1.00 for unswept wings of most practical planforms.

[5] This 150 W estimate is a variant of a non-propulsive power budget for a 300 kg Titan helicopter designed by the Georgia Tech Space Systems Design Lab. Here, 50 W is notionally allotted for payload, 60 W for attitude determination and control, and 40 W for communications and command and data handling.

Table 1. Example Airplane Parameter Assumptions.

m	300 kg	R_m	0.50
L/D	12.0	R_p	0.25
S	20 m²	η	0.70
C_L	0.8	P_{other}	150 W

2.2.2. Power Requirements on Different Worlds

Now the only parameters missing from the equation are density and gravitational constant, which vary with the planet or moon in question. This data is shown in Table 2. For purely the purposes of comparison, flight is assumed to occur at an altitude of 500 m on all worlds.

Table 2. Conditions at 500 m Altitude on Different Worlds. *Superscripts indicate source of given data.*

	Venus	Earth	Mars	Titan
Density (kg/m³)	63.2[5]	1.17[8]	0.015[9]	5.34[10]
Gravity (m/s²)	8.93[5]	9.81	3.73[5]	1.35[5]

When these final values, plus the values in Table 1, are plugged into Eq. 4, final power requirements are generated. These data are shown by the dark bars in Fig. 1. The light bars represent the purely empirical results of applying the appropriate equation from [2].[6]

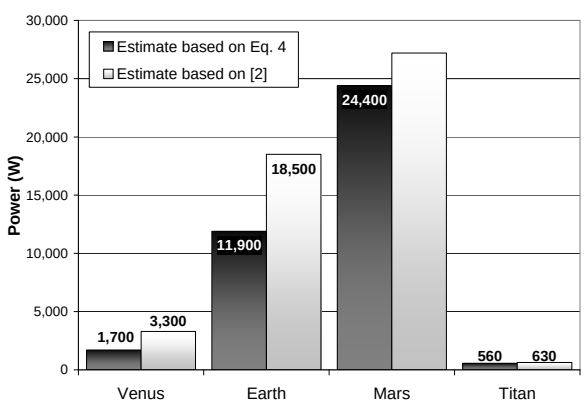

Figure 1. Approximate Power Requirements for 300 kg Airplanes.

[6] To apply the proper equation from [2], velocity must be known and is given by Eq. 3. The variable n in the Ref. [2] equation is set to 0 to represent no changes in propeller efficiency due to density (i.e. propeller disk area is scaled to compensate for density changes).

While the values differ somewhat between the two estimates (recall again that there are no real data points to verify either), it is clear that the trends are the same. The important fact to recall is that the estimate from [2] is purely empirical based on Earth aircraft (plus adjustments for gravity and atmospheric density) and the estimate from Eq. 4 is based on an analytical equation. Thus, with Eq. 4, the engineer has complete insight into the factors controlling the power estimate, whereas with [2], many factors are "black-boxed" by the method's empirical nature.

3. ROTORCRAFT POWER ESTIMATION

3.1. Rotorcraft Power Equation

With this methodology, necessary installed power for rotorcraft is estimated based on ideal actuator disk theory [3][11] for hover conditions. According to ideal actuator disk theory, the power required by a rotor is:

$$P_{thrust} = T\sqrt{\frac{T}{2\rho A}} \tag{6}$$

In Eq. 6, T is thrust, ρ is density, and A is disk area. Substituting ¼ π d^2 for A (where d is rotor diameter) and fulfilling the hover condition with $T = mg$ (where m is mass and g is gravitational acceleration):

$$P_{thrust} = \frac{mg}{d}\sqrt{\frac{2mg}{\rho\pi}} \tag{7}$$

While this is a reasonable estimate for required hover power, it is recognized that the desired installed power estimate will also consist of non-propulsive power requirements, propulsive cruise power, and margin. Since the factor of propulsive cruise power is not as simple to estimate for rotorcraft as it is for airplanes, the final assumption in this rotorcraft methodology is an empirical one: According to [2], "Most conventional helicopters appear to have installed powers ~100% larger than predicted [by actuator disk theory applied to hover], the difference being due to rotor drag, fuselage blockage, and tail rotor power requirements, and that practical aircraft must do more than merely hover." This observation is accurate based on the data in [2] on 64 rotorcraft, shown in Fig. 2. To be more precise, this data yields a mean ratio of installed power to ideal hover power of 2.36.

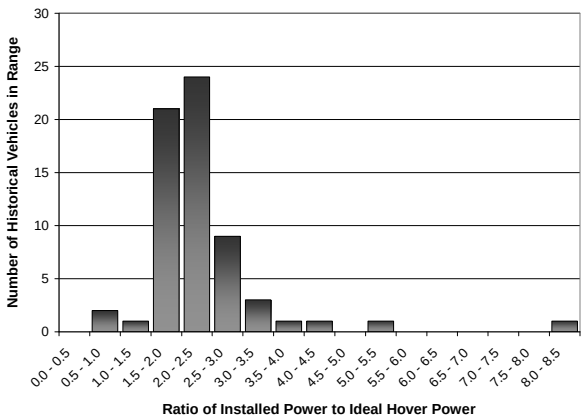

Figure 2. Historical Distribution of Rotorcraft Installed Power to Ideal Hover Power Ratios. [2]

Thus, multiplying the estimate of Eq. 7 by the empirical factor B, taken here as 2.36:

$$P_{required} = B\frac{mg}{d}\sqrt{\frac{2mg}{\rho\pi}} = 2.36\frac{mg}{d}\sqrt{\frac{2mg}{\rho\pi}} \qquad (8)$$

3.2. Application of the Rotorcraft Power Equation

As before, the equations developed here cannot be truly verified since no rotorcraft have flown on other worlds to date. However, they can be checked for reasonability, especially against the results predicted by [2]. To do so, power requirements will be estimated for a 300 kg rotorcraft on Venus, Earth, Mars, and Titan.

3.2.1. Baseline Vehicle Parameter Estimation

Compared to Eq. 4, Eq. 8 involves few parameters. The mass of the rotorcraft is defined up front in this application, and g and ρ are properties of the world on which the craft flies. Thus, the only parameter that requires discussion is d, or rotor diameter.

Clearly there are structurally-driven upper bounds to the diameter of a rotor; however, Eq. 8 lends no insight into those bounds. If Eq. 8 is taken alone, required power can be brought to zero by increasing rotor diameter to infinity. What is desired is some relationship between rotor diameter and vehicle mass. This is provided in part by [2]: "Regression indicates that the rotor diameter scales as $m^{0.4}$". In symbols (in which K is a proportionality constant):

$$d = Km^{0.4} \qquad (9)$$

Using the 64 data points provided in [2], the best-fit constant K is found to be 0.449 m/kg$^{0.4}$. About 72% of the historical data points fall within a K-value of 0.40-0.55 m/kg$^{0.4}$ (see Fig. 3). Based on the best-fit K, the diameter d is chosen as 4.4 m for this vehicle. Note that based on the typical range of K mentioned above, rotor diameters of 3.9 - 5.4 m may also be reasonable. Of course, if rotor diameter is known up-front for a particular design, it may be entered into Eq. 8 and this empirical rotor diameter estimation can be bypassed.

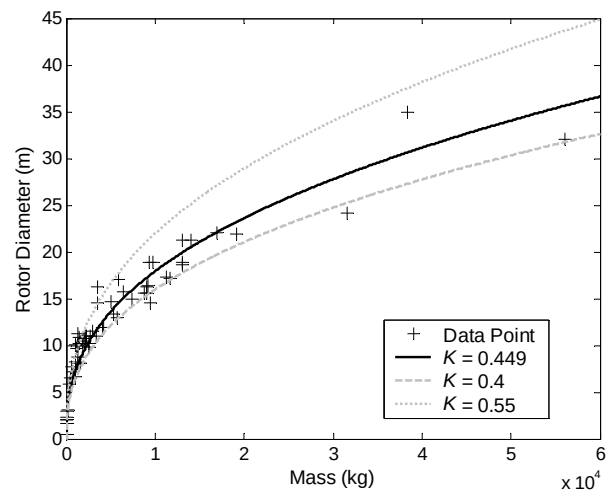

Figure 3. Historical Helicopter Rotor Diameter vs. Vehicle Mass. [2]

3.2.2. Power Requirements on Different Worlds

Using the 300 kg mass and 4.4 m rotor diameter assumption, the only parameters missing are density and gravitational constant, which are given in Table 2. In Fig. 4, dark bars indicate the results of applying Eq. 8, and light bars indicate the results of the same vehicle evaluated using the appropriate equation from [2].

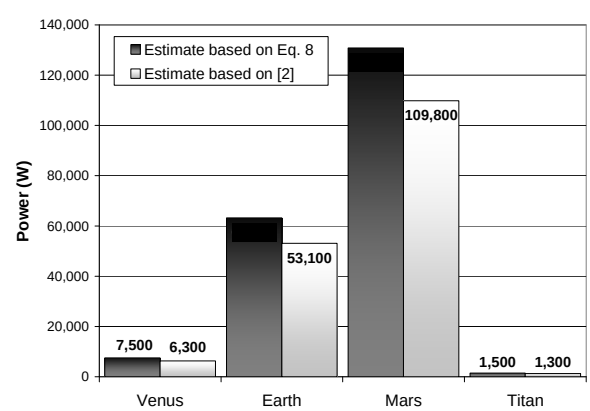

Figure 4. Approximate Power Requirements for 300 kg Rotorcraft.

While the values differ between the two estimates, it is clear that the trends are the same. Again, the estimate from [2] is purely empirical based on Earth aircraft and the estimate from Eq. 8 is based on a more analytical equation. Here, Eq. 8 has "un-black-boxed" the parameter of rotor diameter.

4. IMPLICATIONS

4.1. Comparison of Flight on Different Worlds: The Importance of $g^{1.5}/\rho^{0.5}$

In Figs. 1 and 4, clear trends exist in regards to power requirements on different worlds. Whether the vehicle is an airplane or rotorcraft or whether the estimation is analytical or empirical, the trends are remarkably similar: At 500 m on Venus, required power is about 14% of that required on Earth. On Mars, required power is about 190% of that on Earth, and on Titan the number is 3.2%. From a power standpoint, Mars is the worst choice for flight and Titan the best (to the extent that Titan is nearly 60 times easier than Mars).

The reason for this consistency in power differences among worlds is evident upon inspection of Eqs. 4 and 8. As P_{thrust} grows much larger than P_{other} in Eq. 4, airplane power varies as $g^{1.5}/\rho^{0.5}$. From inspection of Eq. 8, it is clear that rotorcraft power also varies as $g^{1.5}/\rho^{0.5}$. Very similar relationships are present in [2]. On Mars, atmospheric density is about 1% that of Earth's, but gravity is still 38% of Earth's. This results in a very large "ratio" of g to ρ. However, on Titan, density is 360% greater than on Earth and gravity is only 14% that of Earth. Fig. 5 shows the value of $g^{1.5}/\rho^{0.5}$ at 500 m altitude on Venus, Earth, Mars, and Titan. As can be seen, the trends clearly reflect those in Figs. 1 and 4.

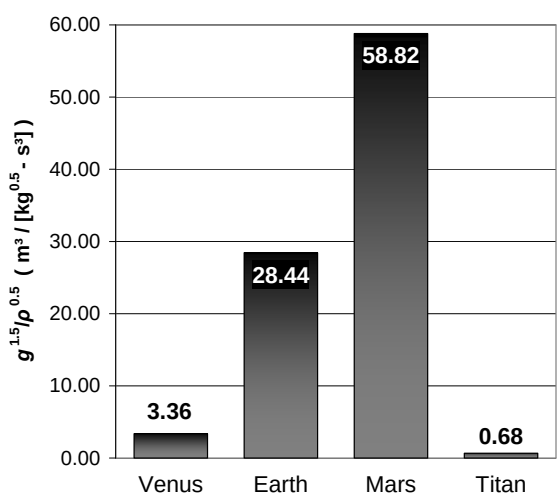

Figure 5. Magnitude of $g^{1.5}/\rho^{0.5}$ at 500 m Altitude

Note, of course, that certain practical factors are not taken into consideration in the estimates in Fig. 1 and Fig. 4. For example, the temperature at 500 m altitude on Venus is about 460 degrees Celsius[5] and the pressure is about 88 times that at sea level on Earth. This is not to say that flight on Venus is impossible; in fact, more recent Venus airplane designs have sought to fly at altitudes of 71-76 km [12]. At such altitudes, the quotient of g and ρ would be much higher due to the decreased density and virtually unchanged gravitational constant. The flight conditions would effectively become more Earth-like.

To illustrate the fact that a range of $g^{1.5}/\rho^{0.5}$ values exist on any world with an atmosphere, Fig. 6 shows the relationship between $g^{1.5}/\rho^{0.5}$ and altitude on Venus, Earth, Mars, and Titan.[7] As can be seen, to reach an Earth-sea-level-like power requirement on Venus, an aerial vehicle must fly at about 55 km altitude. Interestingly, on Titan, such a power requirement is not reached until 185 km altitude (not shown in Fig. 6). Mars-like power requirements could be simulated on Earth at an altitude of approximately 13 km.

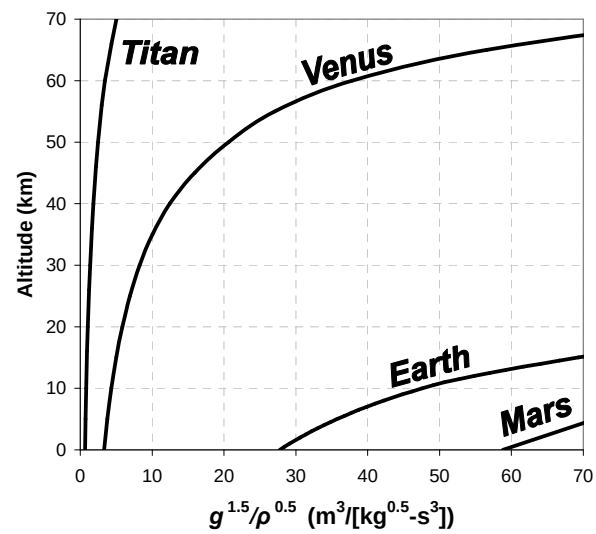

Figure 6. Relationship between Altitude and $g^{1.5}/\rho^{0.5}$

4.2. Wings or Rotors?

Common sense suggests (correctly) that it generally takes less power to fly an airplane than a helicopter. The thrust-to-weight ratio of a helicopter is necessarily greater than one, while, in contrast, the installed thrust

[7] Density profiles for Venus, Earth, Mars, and Titan are from [13], [3], [9], and [10], respectively. Though small, gravity variation with altitude is also included.

to weight ratio of a Boeing 747-400 is approximately 0.27 [14]. Figs. 1 and 4 allow benefits of planetary airplanes versus rotorcraft to be quantified.

As is clear from Fig. 7, differences exist between this paper's method and [2] in the calculation of the relative advantage of airplanes over rotorcraft. However, in both cases it is clear a significant advantage exists: In almost every instance, the rotorcraft requires at least twice as much power as the airplane. In some scenarios this may mean the difference between using a battery for limited-duration flights and using solar power for continuous flight. In others it may mean an airplane flying twice as long as a rotorcraft on the same battery.

As before, however, a design must be based on more than power requirements. An airplane will raise operational problems involved with landings and takeoffs that a rotorcraft could easily solve. The designer must weigh the alluring power advantage of an airplane against its operational disadvantages.

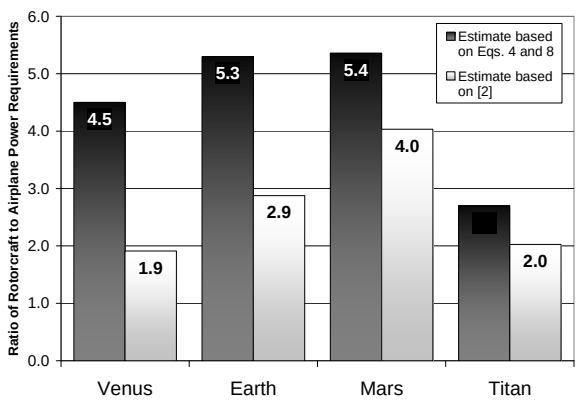

Figure 7. Relative Advantages of using Airplanes over Rotorcraft

4.3. System Implications

A valuable perspective to this study is that of what the power requirements estimated here mean in terms of the requirements and capabilities associated with the planetary aerial vehicle system. To put the example 300 kg aerial vehicle requirements into perspective, solar, radioisotope thermoelectric generator (RTG), and battery power subsystem options are sized using mass relationships from [7] and [15].

4.3.1. Solar Power Option

The sizing of the solar power option involves accounting for solar arrays, batteries, a power control unit, regulators and converters, and wiring. Solar arrays are sized taking into account solar intensity differences due to distance from the Sun and atmospheric opacity.[8] An optimistic 15% solar cell efficiency is assumed as well as an optimistic end-of-life specific performance of 47 W/kg [7]. In the cases of Earth and Mars, airplanes and rotorcraft both require regulator and converter systems which are much more massive than the vehicle itself. In the case of Titan, power requirements are very small, but the required solar array areas are on the order of a football field (see Fig. 8). Only in the case of Venus is a solar power solution nearly feasible; however, the prohibitive solar array size due to the very low 500 m altitude selected prevents this case from proving truly feasible. It should be noted, however, that in the case of Venus, higher altitudes may be selected which may increase the solar intensity by a factor more than the increase in $g^{1.5}/\rho^{0.5}$. For example, flight at 20 km altitude increases $g^{1.5}/\rho^{0.5}$ by about 77% but increases solar flux by approximately 226% relative to the 500 m values. Higher altitudes on Venus also afford a more benign thermal environment, which was not taken into account in the sizing of this system. Thus, a solar-powered aerial vehicle on Venus is not outside the realm of possibilities. Because of the very long periods of sunlight on Venus (a solar day lasts 116.8 Earth days [20]), an aerial vehicle may even be designed for a mission lasting continuously for months.

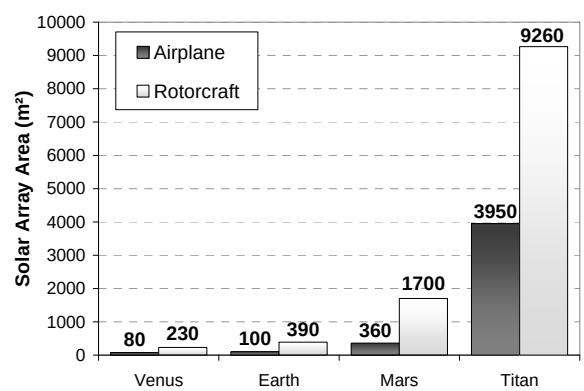

Figure 8. Required Solar Array Area for Continuous Solar Operation.

4.3.2. RTG Option

The sizing of the RTG power system option accounts for RTGs, radiators, regulators and converters, and wiring. The end-of-life output of the high-performance

[8] Solar intensity data is derived from [13], [16], [17], [18], and [19].

second-generation SRG (Stirling RTG) is assumed, and mass and power data is taken from [15]. As with the solar power option, airplanes and rotorcraft on Earth and Mars require regulator and converter systems more massive than the vehicle itself. For Venus, the number of RTGs required for continuous operation exceeds the vehicle mass for both airplane and rotorcraft. For Titan, however, it is found that an airplane is feasible and a rotorcraft is nearly feasible on RTG power alone. The power system mass breakdown for the airplane is shown in Table 3. Batteries are not included in this first-order mass budget since the vehicle can fulfill its power needs via RTGs alone. Additionally, a 50% safety margin is included in the original power estimate, and the seven SRGs actually provide 70 W more than the estimated requirement. The rotorcraft is considered nearly feasible on RTG power because its total power system mass is found to be 280.4 kg. It will be shown that this mass can be reduced via the use of batteries.

Table 3. RTG-Powered Titan Airplane Power System Mass Breakdown.

Component	Mass (kg)
RTGs (7 SRGs)	98.0
Radiator (20.8 m² area)	13.9
Regulators and Converters	14.8
Wiring	6.0
Total Power System Mass	132.7

4.3.3. Battery Options

In this final analysis, batteries are considered in combination with RTG and solar options to determine whether mission capabilities may be enhanced. Power system mass is limited to 150 kg (half the vehicle mass) and battery life is assessed. Nickel-hydgrogen batteries are assumed with a 100% depth of discharge and 45 W-hr/kg ratio of battery capacity to mass. [7]

As with the solar-only and RTG-only power options, airplanes and rotorcraft on Earth and Mars require regulator and converter systems more massive than the vehicle itself. Thus, regardless of battery mass, no 300 kg Earth or Mars aerial vehicle with the specifications given earlier will result in a closed design.

In the case of Venus, it is found that a battery-powered rotorcraft is infeasible. However, an airplane is found to be feasible, and a batteries-only power system outperforms solar-plus-battery and RTG-plus-battery systems. The resulting maximum duration for this system is found to be 90 minutes with a 12.5 km range. The mass breakdown of this power system is in Table 4.

Table 4. Battery-Powered Venus Airplane Power System Mass Breakdown.

Component	Mass (kg)
Batteries (3710 W-hr cap.)	82.4
Regulators and Converters	61.6
Wiring	6.0
Total Power System Mass	150.0

In the case of Titan, it is found that a battery-only power system is feasible for both airplane and rotorcraft. This results in a 3.5 hour rotorcraft duration and 9.8 hour airplane duration (with an 81.4 km range). These vehicles' power system mass breakdowns are shown in Tables 5 and 6. In both cases, it is found that the addition of solar arrays has a positive but negligible (less than 0.4%) effect on mission duration due to the low solar intensity at Titan. The addition of RTGs drives the airplane to the RTG-only solution but drives the rotorcraft to the battery-only solution shown below.

Table 5. Battery-Powered Titan Airplane Power System Mass Breakdown.

Component	Mass (kg)
Batteries (5810 W-hr cap.)	129.2
Regulators and Converters	14.8
Wiring	6.0
Total Power System Mass	150.0

Table 6. Battery-Powered Titan Rotorcraft Power System Mass Breakdown.

Component	Mass (kg)
Batteries (4920 W-hr cap.)	109.3
Regulators and Converters	34.7
Wiring	6.0
Total Power System Mass	150.0

5. CONCLUSIONS

The prime goal of this paper has been the presentation of a method for prediction of planetary aerial vehicle power requirements. While at least one comprehensive method has been published [2], it leaves many design parameters hidden because of its empirical roots. This paper attempts to "un-black-box" those parameters so the engineer may more fully understand the relationships involved in power estimation. The reduction of empirical considerations may also help the engineer avoid potential bias introduced from necessarily Earth-based empirical data.

In the case of airplane power estimation, this method has succeeded in removing all empirical variables: Eq. 4 is based solely on efficiencies, margins, and variables with physical meaning. For rotorcraft, empirical data is still used, but the design engineer can now observe the effect of rotor diameter in addition to that of mass, gravity, and density variations. Ideally, the rotorcraft equation would also avoid such empirical parameters.

The power estimation equations derived here represent a simple but useful method for conducting top-level studies and comparisons of planetary aerial vehicles. Two of the most important results that can be drawn from these equations involve the quantification of the power advantages to using airplanes instead of rotorcraft and to flying on Titan instead of Mars, Earth, or Venus. Unlike purely empirical equations, these equations are flexible in the sense that the designer has the freedom to change vehicle parameters to essentially adjust his vehicle design to modify his power requirement. From this power requirement, power sources can be selected, battery life can be determined, and mission capabilities can be estimated. This adds notably to the tools available to the engineer involved in preliminary planetary aerial vehicle design.

6. ACKNOWLEDGMENTS

The author would like to thank Dr. Robert Braun and the Georgia Tech Space Systems Design Lab Planetary Aerial Vehicles Team under the lead of Ravi Prakash for their continued support of this work.

7. REFERENCES

1. Guynn, M.D., Croom, M.A., Smith, S.C., Parks, R.W., and Gelhausen, P.A. "Evolution of a Mars Airplane Concept for the ARES Mars Scout Mission," AIAA 2003-6578, San Diego, 15-18 Sept. 2003.
2. Lorenz, R.D., "Flight Power Scaling of Airplanes, Airships, and Helicopters: Application to Planetary Exploration," *Journal of Aircraft*, Vol. 38, No. 2, March-April 2001, pp. 208-214.
3. Shevell, R.S., *Fundamentals of Flight*, 2nd ed., Prentice Hall, Upper Saddle River, 1989.
4. Clarke, Jr., V.C., Kerem, A., and Lewis, R. "A Mars Airplane…Oh Really?" AIAA 79-0067, New Orleans, 15-17 Jan. 1979.
5. Colozza, Jr., A. "Evaluation of an Airship for Planetary Atmospheric Exploration," AIAA 2004-6475, Chicago, 20-23 Sept. 2004.
6. Florida International University Aeronautics Learning Laboratory for Science, Technology, and Research Network, *Aircraft Engine Thrust Calculations – Level 3* [online], URL: http://www.allstar.fiu.edu/aero/Propulsion2.htm [cited 11 June 2006].
7. Larson, W.J., and Wertz, J.R. (ed.), *Space Mission Analysis and Design*, 2nd ed. Microcosm, Inc. and Kluwer Academic Publishers, Torrance, 1992.
8. Stanford University Aircraft Aerodynamics and Design Group, *Standard Atmosphere Computations* [online], URL: http://aero.stanford.edu/StdAtm.html [cited 11 June 2006].
9. Justus, C.G. and Johnson, D.L., "Mars Global Reference Atmospheric Model 2001 Version (Mars-GRAM 2001) Users Guide", NASA/TM-2001-210961, April 2001.
10. Yelle, R.V., Strobell, D.F., Lellouch, E., and Gautier, D. "Engineering Models for Titan's Atmosphere," ESA SP-1177, 1997, pp. 243-256.
11. Newman, S., *The Foundations of Helicopter Flight*, Halsted Press, New York, 1994.
12. Colozza, A. "Feasibility of a Long Duration Solar Powered Aircraft on Venus," AIAA 2004-5558, Providence, 16-19 Aug. 2004.
13. Landis, G.A., LaMarre, C., and Colozza, A. "Atmospheric Flight on Venus," AIAA 2002-0819, Reno, 14-17 Jan. 2002.
14. NASA Glenn Research Center, *Glenn Learning Technologies Project* [online], URL: http://www.grc.nasa.gov/WWW/K-12/BGP/Donna/t_w_ratio_answers.htm [cited 11 June 2006].
15. Levine, J.S. and Wright, H.S. "Titan Explorer: The Next Step in the Exploration of a Mysterious World," NASA Vision Mission Study Final Report (NRA-03-OSS-01), 10 June 2005.
16. U.S. Dept. of Energy, *Solar Energy Technologies Program: Light and the PV Cell* [online], URL: http://www1.eere.energy.gov/solar/pv_cell_light.html [cited 17 May 2006].
17. Landis, G.A. "Solar Cell Selection for Mars," *NASA Glenn Research Center Photovoltaic & Space Environments Branch* [online], URL: http://powerweb.grc.nasa.gov/pvsee/publications/wcpec2/cells4mars.html [cited 17 May 2006].
18. Lorenz, R., "Exploring Titan From A Helicopter," *SpaceDaily* [online], 15 July 2000, URL: http://www.spacedaily.com/news/future-00i.html [cited 11 June 2006].
19. National Aeronautics and Space Administration, *Cassini Launch Press Kit*, Oct. 1997.
20. NASA Goddard Space Flight Center, *National Space Science Data Center Planetary Fact Sheet* [online database], URL: http://nssdc.gsfc.nasa.gov/planetary/factsheet/ [cited 11 June 2006].

Silicon-Germanium (SiGe) Technology
For Europa and Enceladus Lander or Probe Missions

Fourth Annual International Planetary Probe Workshop

Leora Peltz, William Atwell, and Robert Frampton, Boeing

A Europa mission has been designated by the Decadal Study as the highest priority flagship mission for the next decade, and the Europa Geophysical Explorer (EGE), is likely to be the next large mission to the outer planets after Cassini. A Europa mission would likely include landers and/or surface probes.

Enceladus has recently captured the headlines after NASA's Cassini spacecraft returned images showing icy jets and towering plumes that might be erupting from near-surface pockets of liquid water.

Europa has extreme environmental conditions, with a surface temperature varying from a low of 50 Kelvin, up to 125 Kelvin, with a mean temperature of around 100 Kelvin. The surface of Enceladus is dominated by ice blocks at temperatures of 74 Kelvin to 80 Kelvin, with hot spots topping 100 Kelvin. Europa also has a high radiation environment: 20 Mrad per month at the surface. The Ice provides effective radiation shielding; the radiation dose at 10 cm depth into the ice is ~5 Krad per month.

These are harsh and challenging environments for electronics circuitry. SiGe technology is particularly suited to answer these demands. The performance characteristics of SiGe devices vary gracefully over this extreme temperature range, with no evidence of abrupt "killer" phenomena. The structure of SiGe devices also confers a "free perk" - multi-Mrad total dose hardness, with no intentional hardening.

Boeing is part of a NASA funded team, led by Dr. Cressler from Georgia Institute of Technology, which is developing SiGe Integrated Electronics for Extreme Environments. This university-NASA-industry team includes Georgia Institute of Technology, Jet Propulsion Laboratory, Auburn University, the University of Tennessee, Vanderbilt University, the University of Maryland, BAE Systems, IBM, and Lynguent Inc. The team focuses on versatile mixed-signal circuits, applicable to distributed interface, data acquisition, and control interfaces, which operate over a very wide range of temperatures: down to 43 Kelvin (-230 degC) without "warm boxes", and up to 398 Kelvin (+125 degC) in normal operation. Parallel spinoffs of this activity include the development of Si-Ge micro-controller and FPGA for these harsh environments.

In this paper we show the predicted (modeled) electron and proton flux environments encountered by a spacecraft at various orbital inclinations, and on the surface of Europa and Enceladus, in comparison to the Lunar environment. We then present the SiGe technology for Extreme Environments, and the design considerations for a SiGe electronic module in a lander or a probe on Enceladus, or in the harsh environment of Europa.

Radio Opacity Estimates for Giant Planet Atmospheres

Thomas R. Spilker

Jet Propulsion Laboratory, California Institute of Technology
4800 Oak Grove Dr., Pasadena, CA 91109-8099,USA

ABSTRACT

Estimating radio opacities in giant planet atmospheres is an interdisciplinary effort involving spectroscopy, planetary atmospheric science (both physics and chemistry), and geometry. Spectroscopy provides quantitative estimates of radio absorption by appropriate species, given their environmental conditions. Planetary science provides estimates, for each location of interest in an atmosphere, of the quantity of these absorbers and the environmental conditions. Then geometrical considerations allow integrating to yield the total opacity along a given signal propagation path. Uncertainties in both the spectroscopy and the atmospheric science combine to yield fairly sizeable uncertainties in opacity estimates, but nonetheless allow placing bounds on those opacity estimates that are useful for engineers designing telecommunications systems for entry probe missions. This paper discusses calculation of microwave opacity estimates and presents the preliminary results for Jupiter, Saturn, and Neptune.

1. Introduction and Background

There is strong scientific motivation for *in situ* sampling of our solar system's giant planets' atmospheres[1]. Among the science objectives currently considered best addressed by *in situ* sampling are vertical abundance profiles of primary volatiles, isotopic ratios of noble gases and other key constituents, atmospheric structure (temperature and pressure as a function of altitude), cloud density profiles and particle characteristics, radiant heat flow as a function of altitude, and abundance profiles of "diagnostic species" such as carbon monoxide that tell of conditions in inaccessible locations.

Analyses to determine the mission requirements stemming from the various science objectives reveals penetration depth requirements ranging from "shallow", 5-10 bar levels, to "very deep", deeper than 1000-bar levels. Unofficially, the breakpoint between relatively shallow and relatively deep involves water, the most abundant of the volatiles in giant planet atmospheres: above a given planet's water cloud is considered shallow, below its base is considered deep. But planet-to-planet environmental variation precludes any absolute definition of shallow and deep. "Below the typical water cloud base" at Jupiter includes pressure levels that are above the expected water cloud top at Neptune.

Returning high-priority science data from entry probes within giant planet atmospheres, especially deep within those atmospheres, depends critically on reliable knowledge of the RF propagation characteristics of the overlying atmosphere. Although refraction and scintillation can be important in some instances, absorption is usually the primary source of atmosphere-related relay signal attenuation. The science community usually refers to the absorptive aspect of a propagation medium as *opacity*, often expressed in units of *optical depths*, while radio engineers typically refer to *attenuation* in *decibels* (dB). This presentation uses the two interchangeably, but note that in both cases the reference signal characteristic is power, not electromagnetic field strength. An opacity of one optical depth produces the same signal attenuation as an opacity of $10\log_{10}e$ (~4.343) dB.

Estimating radio opacities in giant planet atmospheres is an interdisciplinary effort involving spectroscopy, planetary atmospheric science (both physics and chemistry), and geometry. Spectroscopy provides quantitative estimates of radio absorption by appropriate species, given their environmental conditions. Planetary science provides estimates, for locations of interest in an atmosphere, of the quantity of these absorbers and the environmental conditions. Then geometrical considerations allow integrating to yield the total opacity along a given signal propagation path. Uncertainties in both the spectroscopy and the atmospheric science combine to yield fairly sizeable uncertainties in opacity estimates, but nonetheless allow placing bounds on those opacity estimates that are useful for engineers designing telecommunications systems for entry probe missions.

At pressure levels up to at least a few hundred bars the microwave radio opacity behavior of giant planet atmospheres stems mainly from two chemical species in those atmospheres: ammonia (NH_3) and water (H_2O). Both species, especially ammonia, have presented challenges to researchers attempting to describe quantitatively the opacity due to these species under appropriate conditions, namely

temperature, partial pressures of these species, and partial pressures of line-broadening gases such as hydrogen (H_2) and helium (He). Where many gases are fairly well described by formalisms derived from simplified quantum mechanical treatments, water and ammonia are "problem children" in spectroscopy, resisting such treatments. So far, formalisms for them are hybrids of theoretical predictions with significant empirical modifications[2]. Laboratory data from a number of researchers have allowed steady progress over the years, shrinking absolute error bars from factors of two or greater in the 1970's to tens of percent.

JPL has funded an internal task under which the most recent formalisms for ammonia and water opacity have been coded as subroutines and incorporated into software that, given an atmospheric model, calculates estimates of total vertical opacities vs. altitude in giant planet atmospheres. Similar software is found in the radiative transfer modeling codes used to interpret radio astronomical data, but the new software is intended primarily as an engineering tool. The atmospheric models must specify the partial pressures of the absorbing and broadening species, as well as temperature, as a function of altitude. Since there are uncertainties in atmospheric thermal models, and fairly large uncertainties in the absorber abundance profiles, no single model captures the uncertainty in vertical opacities. The new software allows quickly generating estimates for a range of physically plausible atmospheric models, thereby bounding the communications problem, to the extent that the atmospheric models capture the worst-case conditions.

Opacity estimates have been calculated using example atmospheric models for Jupiter and Saturn, and most recently for Neptune. Those results suggest that data relay from deep probes, especially at Neptune, will be difficult for single-hop relay links.

2. Structure of Planetary Tropospheres

Pressures, temperatures, and mass densities increase with depth for tropospheres in equilibrium. The local rate of the increase in pressure P is given by the *scale height*, H,

$$H = \frac{RT}{mg} \qquad (1)$$

where R is the universal gas constant, T is temperature, m is the average atmospheric molecular mass, and g is the local effective gravitational acceleration. At a given pressure level, temperatures at Saturn are somewhat lower than at Jupiter, but g at Saturn is about a third that of Jupiter, so Saturn's H is more than twice Jupiter's. Thus radio signals at a given pressure level at Saturn travel significantly farther to emerge. Figure 1 shows the T and P structure of those two tropospheres.

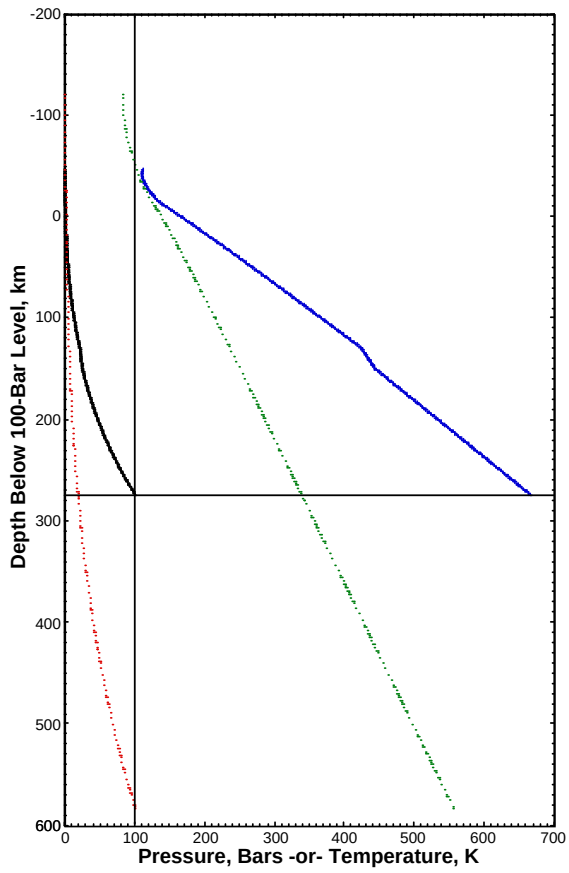

Figure 1. Tropospheric temperatures and pressures as a function of altitude at Jupiter and Saturn. The black and blue curves are pressure and temperature, resp., at Jupiter, and the red and green curves are for Saturn. The abrupt dogleg in the Jupiter curves is an artifact of appending deeper theoretical results to the Galileo Probe's observed data.

As temperature increases, atmospheric constituents that condense out of the cold upper levels are no longer limited by vapor pressure saturation, and can reach their deep abundances. Some such constituents, notably ammonia and water, are strong radio absorbers. The planet-to-planet variation of H and T profiles prevents generalizing opacity calculations from one planet to another.

3. Radio Signal Absorption by Gases

Most gases absorb radio-frequency electromagnetic radiation due to rotational or vibrational absorption lines in the infrared. This makes them weak absorbers

at radio frequencies, in the far low tails of those absorption lines. But absorption lines can be greatly broadened by frequent molecular collisions, and higher pressures greatly increase this effect. Figure 2 illustrates the "pressure broadening" of a line, broadened only by Doppler broadening in the left panel, then mildly pressure-broadened (note the drop in amplitude at the peak, increase in the wings) in the center panel, then more severely pressure-broadened. Note that in the right panel the frequency scale is compressed, and asymmetry of the line, a natural effect of severe pressure broadening, is now evident.

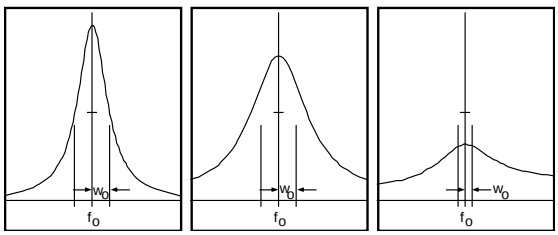

Figure 2. Progressive pressure broadening of an isolated absorption line.

Ammonia and water are notable because they have fairly strong absorption lines at radio frequencies (but those lines are still weak compared to the powerful IR lines), and they are relatively abundant in giant planet atmospheres, so they dominate radio opacity in those atmospheres. The three panels of Figure 3 illustrate the change in ammonia's absorption spectrum with increasing pressure broadening, from an essentially un-broadened line spectrum to one dominated by the low tails of the IR lines.

4. Calculated Radio Opacity Estimates

The new software used to calculate these opacity profiles consists of two primary elements. One is a set of absorptivity calculation subroutines that calculate the radio absorption coefficients for each of the absorbing gases under given conditions of temperature, pressure, *etc*. The other is an atmosphere integrator that calculates the vertical opacity in each 1-km interval from the top of the atmosphere, *i.e.* the level at which the overhead opacity is essentially zero, down to the level of interest, and sums those opacities over the vertical interval. This software currently does not calculate opacity due to clouds or absorbing species other than water, ammonia, and hydrogen. Atmosphere models used in the calculations are not fully accurate and are intended to show general tendencies only, so they are not yet appropriate for use in space mission detailed design.

Jupiter

Figures 4-7 are charts of vertical radio opacity at two different frequencies: 401 MHz, in the UHF part of the radio spectrum, and 1.3 GHz, near the Galileo Probe radio relay link frequency in the "L-band" part of the spectrum. Note the large differences in scales of the opacity axes. Figures 4 and 5 are based on atmosphere models whose deep abundances of both water and ammonia are the same as solar abundances of oxygen and nitrogen, respectively. Figures 6 and 7 models have deep water and ammonia abundances 5 times the solar values. Jupiter's powerful radiation belts, unique among the giant planets, influence the

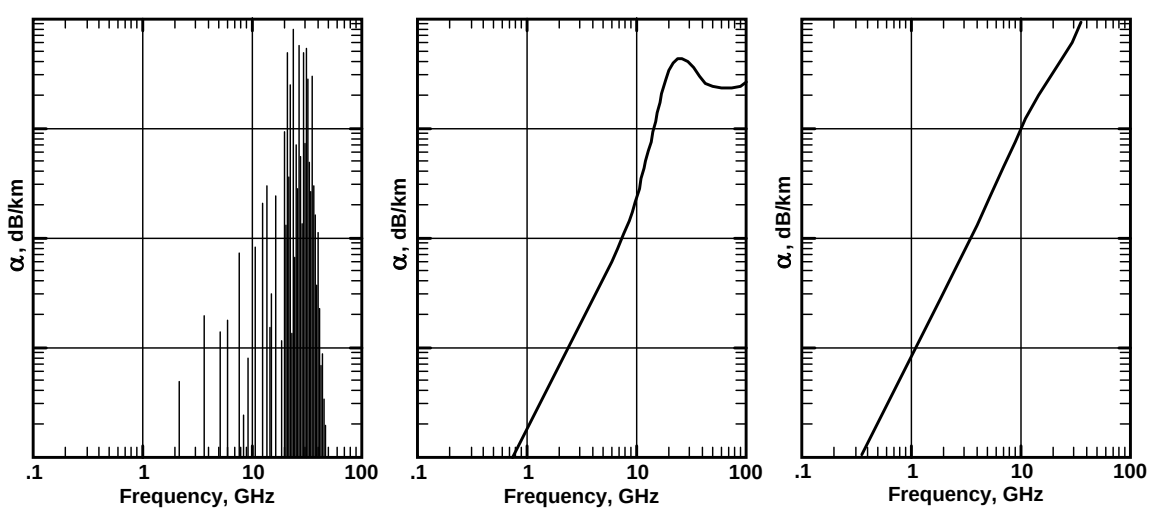

Figure 3. Progressive pressure-broadening effects on ammonia's microwave absorption spectrum.

choice of relay link frequency by adding synchrotron radiation noise to the situation. That noise increases rapidly as frequency decreases from ~2 GHz to its peak at ~300 MHz, so the best SNR occurs in L-band, not at lower frequencies where atmospheric opacity is smaller.

Saturn

Figures 8-11 mirror the Jupiter charts in radio frequencies and absorber abundances. Again, note the large differences in scales of the opacity axes, in this case nearly two orders of magnitude. Figure 12 is a vertical opacity profile from an atmospheric model with the ammonia deep abundance the same as solar nitrogen but the water abundance 5 times that of solar oxygen. This hybrid model can be viewed as a simulation of the "solution cloud" situation, where ammonia dissolves in water cloud droplets, causing its abundance above the water cloud to be less (possibly much less) than its deep abundance. Compare this profile with the part of Figure 11 above the 20-bar level. Note that at 10 bars this model's opacity is about a fifth that of Figure 11, consistent with an ammonia abundance between the ammonia and water clouds that is a fifth of that model. But below the top of the water cloud, water opacity causes the total opacity to increase more quickly.

Neptune

Recently models of Neptune's atmosphere have been adapted for use by the new software, and preliminary results calculated. Note in Figure 13 how Neptune's colder atmosphere pushes the radio-absorbing species deeper into the atmosphere, but below their saturation (cloud-forming) levels the opacity increases quickly. Compare the opacity at the 100-bar level to those at Jupiter and Saturn at similar frequencies.

5. Summary and Conclusions

At radio frequencies useful for entry probe communications, calculated vertical opacities at the various giant planets' 100-bar levels range from ~10 dB to over 100 dB (at Neptune). When the opacity exceeds ~15-20 dB it is difficult to envision probes as currently implemented being able to return useful data to an overhead spacecraft, not to mention directly to Earth. *In situ* measurements of the deep abundances of some important volatiles would require radically new entry probe architectures, such as "staged probes" that leave sub-probes at higher altitudes, for communications relay and perhaps science measurements focused on the upper troposphere. That particular architecture is attractive because it allows the shallow element, with its higher relay link data rate, to fold in the lower-rate deep probe data in parallel with its own shallow data.

If volatile abundances are less than anticipated -- which would be a surprise, but cannot be ruled out as yet -- the prospect of deep probes penetrating the water clouds at Jupiter and Saturn is better, but still difficult. Such missions would be hampered by low data rates.

Further work can include the full range of plausible atmospheres for Jupiter and Saturn, and extension to Uranus and Neptune. Also, opacity estimation routines for less abundant absorbers such as hydrogen sulfide (H_2S) and phosphine (PH_3, the phosphorus-centered equivalent of ammonia) can be added.

6. Acknowledgments

This work was funded by and performed at the Jet Propulsion Laboratory, California Institute of Technology.

7. References

1. "New Frontiers in the Solar System: an Integrated Exploration Strategy," National Academies Press, Washington DC, 2003.
2. "Laboratory Measurements of Microwave Absorptivity and Refractivity Spectra of Gas Mixtures Applicable to Giant Planet Atmospheres," Stanford University Ph.D Dissertation, 1990.

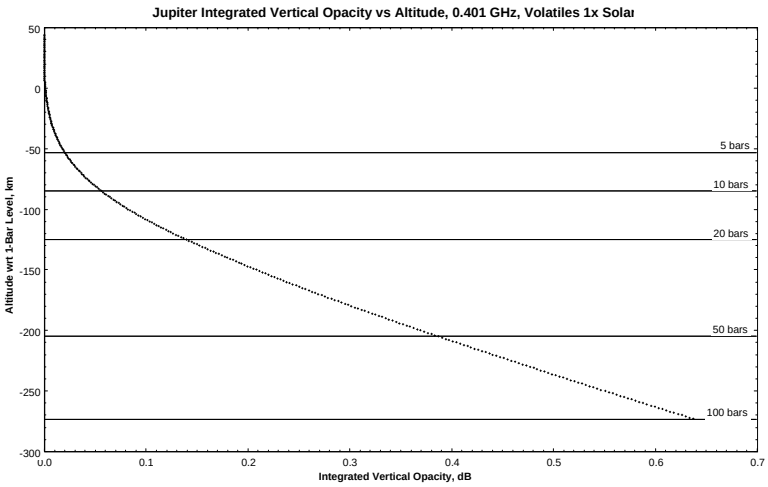

Figure 4. Jupiter vertical opacity profile at 401 MHz, solar absorber abundances.

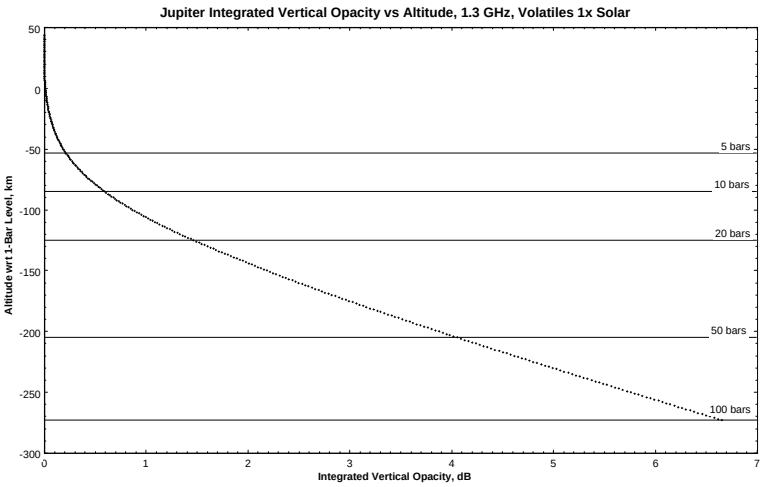

Figure 5. Jupiter vertical opacity profile at 1.3 GHz, solar absorber abundances.

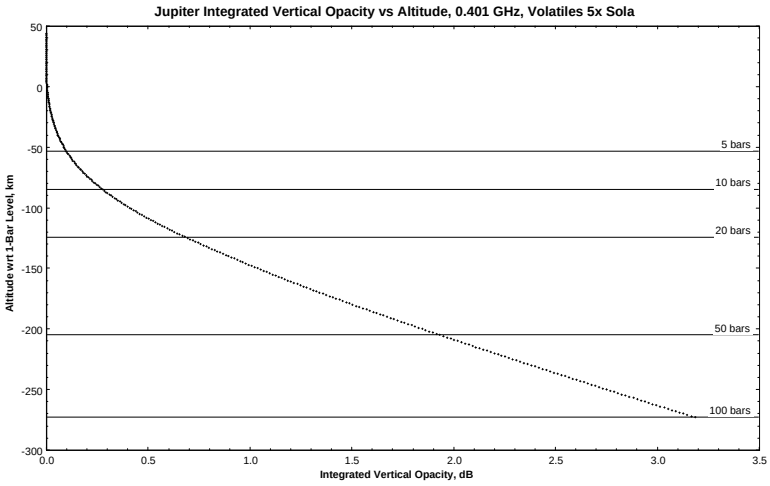

Figure 6. Jupiter vertical opacity profile at 401 MHz, five times solar absorber abundances.

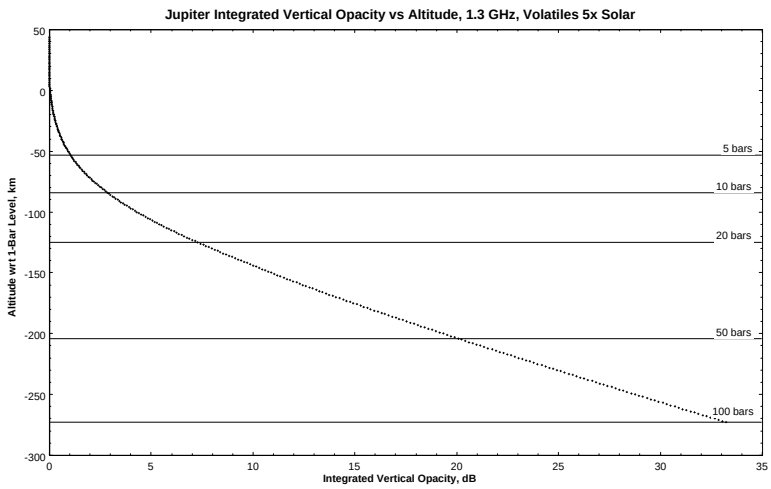

Figure 7. Jupiter vertical opacity profile at 1.3 GHz, five times solar absorber abundances.

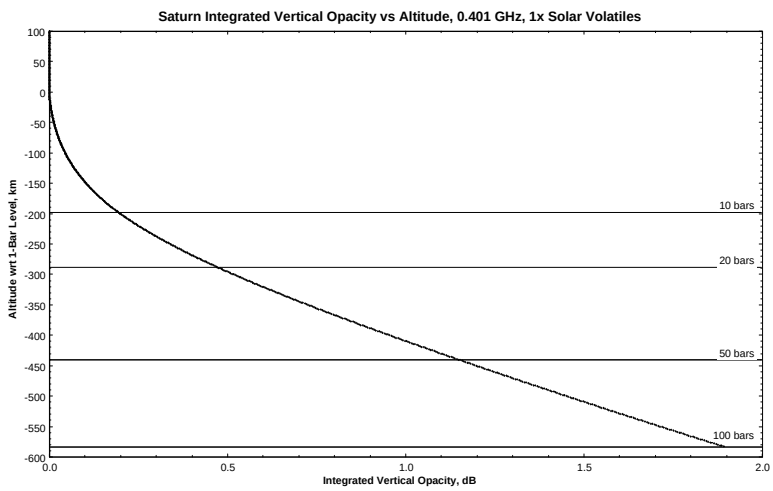

Figure 8. Saturn vertical opacity profile at 401 MHz, solar absorber abundances.

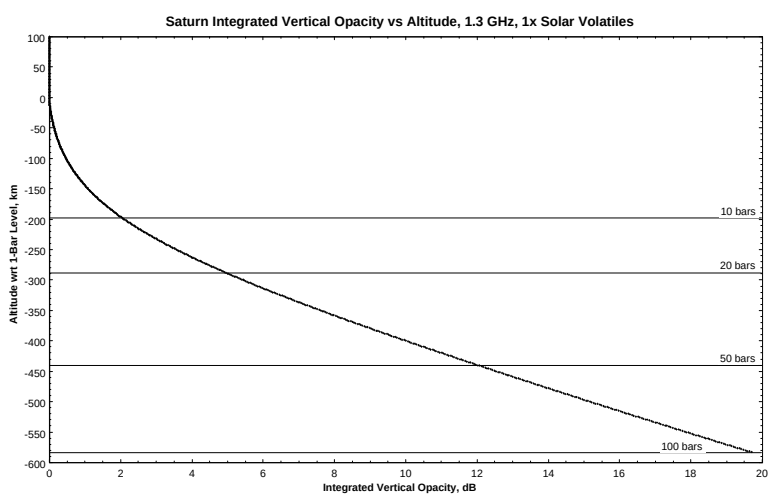

Figure 9. Saturn vertical opacity profile at 1.3 GHz, solar absorber abundances.

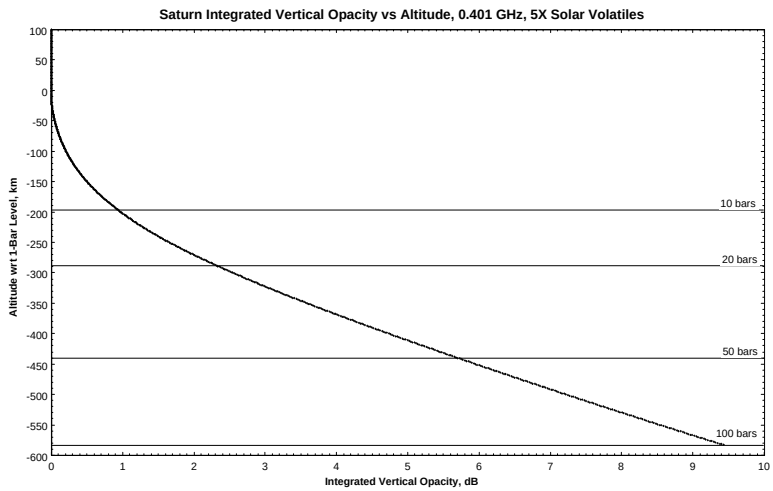

Figure 10. Saturn vertical opacity profile at 401 MHz, five times solar absorber abundances.

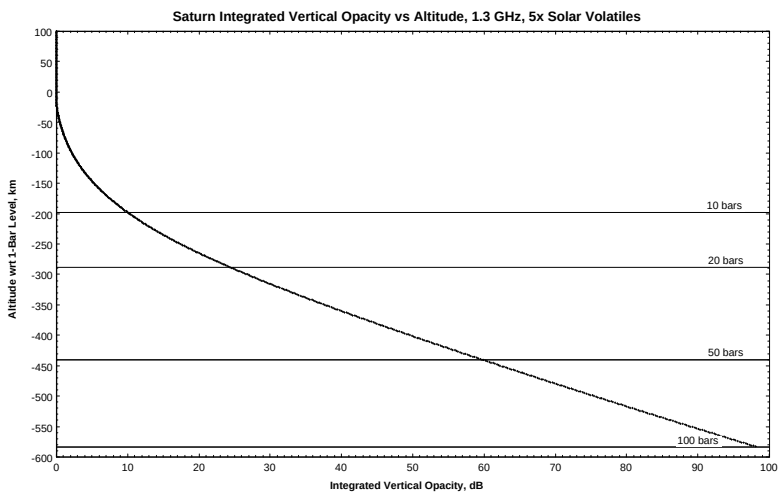

Figure 11. Saturn vertical opacity profile at 1.3 GHz, five times solar absorber abundances.

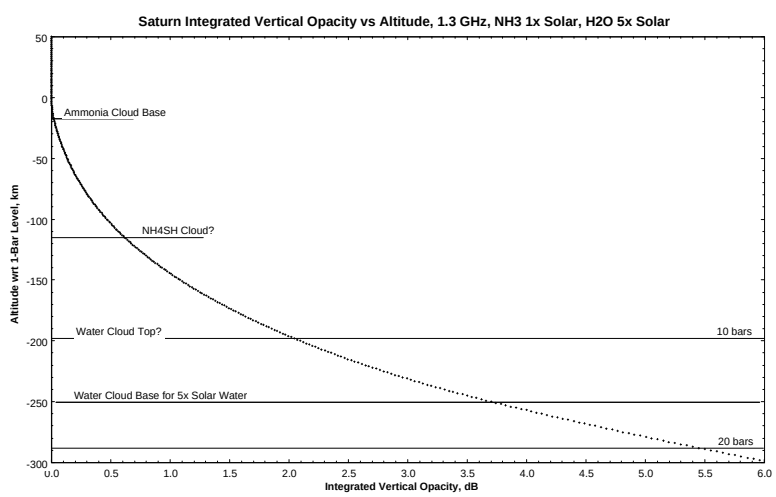

Figure 12. Saturn vertical opacity profile at 1.3 GHz, solar-abundance ammonia, five times solar water.

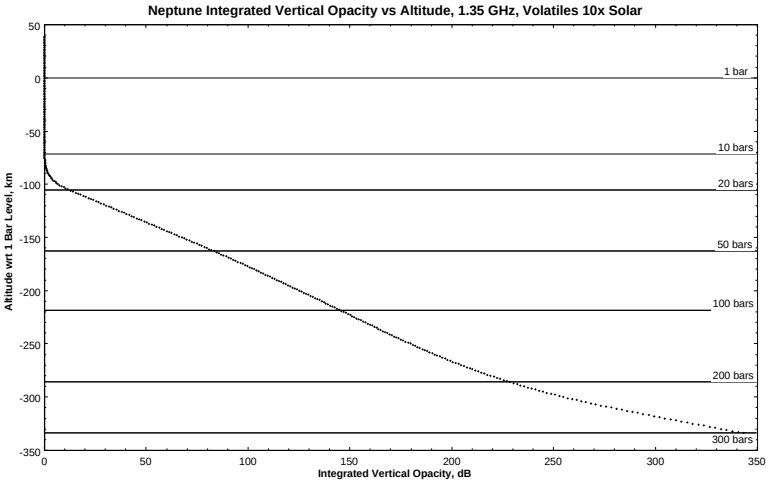

Figure 13. Neptune vertical opacity profile at 1.35 GHz, ten times solar absorber abundances.

SESSION 8

ENTRY, DECENNT AND MOBILITY SYSTEMS

Chairs:
Ed Martinez, ARC, USA (ermartinez@mail.arc.nasa.gov)
Kerry T Nock, Global Aerospace Corp., USA (kerry.t.nock@gaerospace.com)

AEROCAPTURE TECHNOLOGY DEVELOPMENT FOR PLANETARY SCIENCE – UPDATE

M. M. Munk, In-Space Propulsion, Mail Stop VP51, NASA-MSFC, Huntsville, AL 35812,
Michelle.M.Munk@nasa.gov

Introduction: Within NASA's Science Mission Directorate is a technology program dedicated to improving the cost, mass, and trip time of future scientific missions throughout the Solar System. The In-Space Propulsion Technology (ISPT) Program, established in 2001, is charged with advancing propulsion systems used in space from Technology Readiness Level (TRL) 3 to TRL6, and with planning activities leading to flight readiness. The program's content has changed considerably since inception, as the program has refocused its priorities. One of the technologies that has remained in the ISPT portfolio through these changes is Aerocapture. Aerocapture is the use of a planetary body's atmosphere to slow a vehicle from hyperbolic velocity to a low-energy orbit suitable for science. Prospective use of this technology has repeatedly shown huge mass savings for missions of interest in planetary exploration, at Titan, Neptune, Venus, and Mars. With launch vehicle costs rising, these savings could be the key to mission viability. This paper provides an update on the current state of the Aerocapture technology development effort, summarizes some recent key findings, and highlights hardware developments that are ready for application to Aerocapture vehicles and entry probes alike.

Description of Investments: The Aerocapture technology area within the ISPT program has utilized the expertise around NASA to perform Phase A-level studies of future missions, to identify technology gaps that need to be filled to achieve flight readiness. A 2002 study of the Titan Explorer mission concept showed that the combination of Aerocapture and a Solar Electric Propulsion system could deliver a lander and orbiter to Titan in half the time and on a smaller, less expensive launch vehicle, compared to a mission using chemical propulsion for the interplanetary injection and orbit insertion. The study also identified no component technology breakthroughs necessary to implement Aerocapture on such a mission. Similar studies of Aerocapture applications at Neptune, Venus, and Mars were studied in 2003 through 2005. All showed significant performance improvements for the missions studied. Findings from these studies were used to guide the technology development tasks originally solicited in a 2002 NASA ROSS Research Announcement. The tasks are now in their final year and have provided numerous improvements in modeling and hardware, for use in proposals or new mission starts.

Major Accomplishments: Since validation of the Aerocapture maneuver requires a space flight, ground developments have focused on modeling and environment prediction, materials, and sensors. Lockheed Martin has designed and built a 2-meter Carbon-Carbon aeroshell "hot structure." The article utilizes co-cured stiffening ribs and advanced insulation to achieve large scale, and up to a 40% reduction in areal density over the Genesis probe construction. This concept would be an efficient solution for probes that experience heat rates near 800-1000 W/cm^2, such as at Venus and Earth. Applied Research Associates has extensively tested a family of efficient ablative TPS materials that provide solutions for a range of heating conditions. These materials are being applied to high-temperature structures built by ATK Space Systems, led by Langley Research Center. One-meter aeroshells will be thermally tested to validate construction and demonstrate higher bondline temperatures, which can lead to mass savings of up to 30% over traditional heatshields. Ames Research Center has developed aeroshell instrumentation that could measure environmental conditions and material performance during atmospheric entry. Instruments to measure TPS recession, heat flux, and catalycity could be combined with traditional sensors to provide a "plug-and-play" system for minimal mass and power, that would acquire flight data for model improvement and risk reduction on future missions. Improved atmospheric and aerothermodynamic models have also been a major focus of the program.

Next Steps: Aerocapture is one of five technologies in competition for a flight validation opportunity through the New Millennium Program. If selected, a fully autonomous vehicle will perform an Aerocapture at Earth in 2010, and flight data will be used to validate the guidance system and the TPS material for science mission infusion.

Ablative thermal protection systems for entry in Mars atmosphere. A presentation of materials solutions and testing capabilities

4th International Planetary Probe Workshop - June 27 – 30, 2006 – PASADENA, CALIFORNIA, USA

Jean-Marc BOUILLY [(1)], Francine BONNEFOND [(1)], Ludovic DARIOL [(1)], Pierre JULLIEN [(1)], Frédéric LELEU [(1)],

[(1)] EADS SPACE Transportation - BP 11, 33 165 SAINT-MÉDARD-EN-JALLES Cedex, France

jean-marc.bouilly@space.eads.net

ABSTRACT

EADS SPACE Transportation aims at providing the aeroshell, as part of the Entry Descent and Landing System (EDLS), for the ExoMars Descent Module. ExoMars is the first Aurora flagship mission to Mars for ESA in the continuation to Mars Express. With the aim to bring safely a rover and a Geophysical and Environmental Package (GEP) to the Martian surface in order to study biological environment, the aeroshell is a key element to guarantee mission success.

The reference material for the thermal protection system (TPS) of ExoMars is the Norcoat-Liege, a flight proven cork powder and phenolic resin based ablator. In addition to its original use for launchers, the Norcoat-Liege was previously used for two re-entry programs, namely the Atmospheric Re-entry Demonstrator (ARD) that performed a guided and controlled re-entry on Earth in 1998, and the Beagle 2 probe that entered Mars atmosphere in 2003. For the latter use, the material was for instance adapted to comply with stringent planetary protection requirements.

The paper will present an overview of the background on this material, including the most recent outcomes from R&D studies, aiming at a refinement of the material knowledge.

In addition to the material itself, most of the skills required to achieve the development of the whole TPS are available at EADS-ST. These key proficiencies are heat shield engineering and design, material fine modeling, high temperature testing capabilities that include plasma wind tunnel with dust injection and CO2 environment, and assembly facility with clean room conditions.

Finally, possible alternative uses for the material will be outlined (Titan, aft body thermal protection, assessment of growth potential). The Norcoat-Liege will be compared to other ablators such as the EADS-ST Picsil developed for LEO servicing missions, and the AQ60 used for the Huygens EDLS.

1. EXOMARS MISSION OVERVIEW

1.1 ExoMars mission objectives

The ExoMars mission is devoted to the outstanding scientific question of establishing the existence of life on Mars: it will thus search for traces of past and present life, characterize the Mars geochemistry and water distribution, and improve the knowledge of the Mars environment and geophysics.
ExoMars is the first flagship mission within the Aurora program of ESA, and will also by the way have a role of preparation for future robotic or human exploration missions. ExoMars will thus demonstrate the safe Entry, Descent and Landing of a large size spacecraft on Mars [1], the surface mobility and access to subsurface, forward Planetary Protection and identify possible surface hazards to future human exploration missions.

The spacecraft will be composed of a Carrier Module (CM) and a Descent Module (DM) (Fig. 1) that will be released in order to allow safe landing of two elements on the Martian surface, that will support the ExoMars scientific mission: a high-mobility Rover and a fixed station — the Geophysics / Environment Package (GEP).
The ExoMars Rover will carry the Pasteur Payload devoted to exobiology and geological research and will ensure a regional mobility (several kilometers) over its planned 6-months lifetime.
The Geophysics/Environment Package (GEP) will be accommodated on the DM and is designed to be in operation for more than 6 years. It will be the first item of a network aiming at the long-term study of Martian geophysics and ambient conditions.

In addition, sensors on the DM heatshield will provide an opportunity to perform vital "entry and descent science" measurements. Today, the only existing atmospheric sounding data sets for Mars stem from the twin 1976 Viking mission.

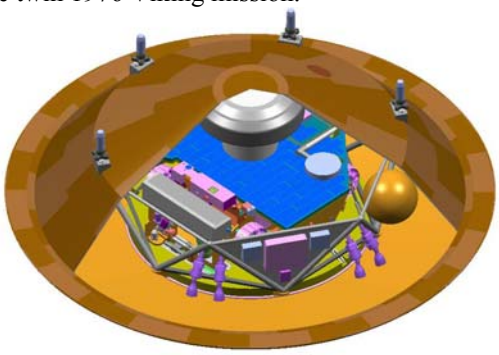

Fig. 1. ExoMars Descent Module architecture (as of phase A)

1.2 Programmatics and schedule

It is currently scheduled by ESA to launch the ExoMars mission in 2011, with a possible back-up launch date foreseen in 2013.

The project started in 2003 and three parallel phase A studies were conducted in the time-frame 2003/2005. Following these studies, the ExoMars Phase B1 activities are expected to consolidate the mission and system requirements, design and interfaces, including the GEP and the Rover with the Pasteur Payload set of instruments, to a level of detail which will allow the start of the following phases B2 and C/D. As much as possible, available and proven technologies shall be selected in order to minimize uncertainties and project risks and thus to guarantee the success of the mission. The ExoMars Phase B1 is planned to be finalized by March 2007.

1.3 Descent Module Architecture

The study of the aeroshell was one of the contributions of EADS-ST during phase A. A Viking-like aeroshape was selected (Fig. 2).

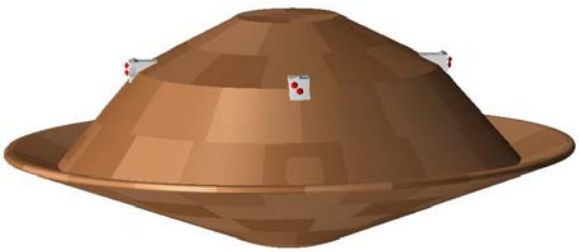

Fig. 2. Descent Module aeroshape (as of phase A)

Both Frontshield and Back-Cover designs rely on a robust lightweight solution made of a sandwich structure (aluminium honeycomb + CFRP skins) covered with Norcoat-Liege thermal protection implemented under the form of panels or tiles (Fig. 3) glued onto the underlying structure.
It is worthwhile to highlight that Norcoat-Liege was selected as baseline solution independently by each of the three teams contracted for ExoMars phase A.
Table 1 summarizes the main characteristics of the ExoMars TPS and shows that Norcoat-Liege provides a mass effective solution, with limited TP mass fraction.

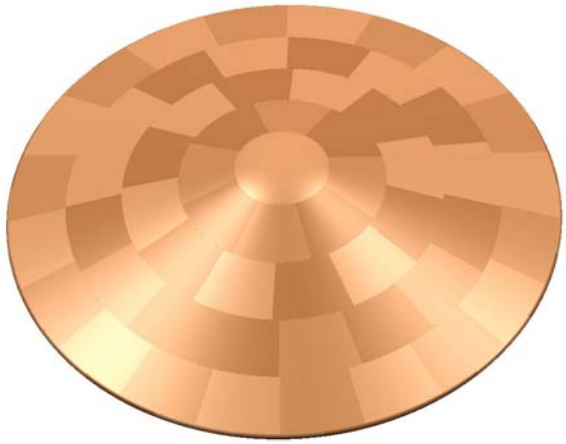

Fig. 3. ExoMars Frontshield TPS arrangement

Table 1 - Main characteristics of ExoMars TPS

Frontshield	T.P. material	Norcoat-Liege
	Density	d = 0.47
	Thickness	10 mm
	T.P. mass	90 kg (including glue and periphery on rear face)
	T.P. mass fraction	7.5 %
	T.P. arrangement	~ 60 large panels (4 rows) + 50 smaller tiles (shoulder area)
	Structure	CFRP honeycomb
Back-Cover	T.P. material	Norcoat-Liege
	Density	d = 0.47
	Thickness	6 mm
	T.P. mass	45 kg
	T.P. mass fraction	3.7 %
	T.P. arrangement	~ 80 panels
	Structure	CFRP honeycomb
Whole Entry Module	Max. diameter	3.80 m
	Total mass of the vehicle	1200 kg

1.4 TPS trade-off

For application on ExoMars, Norcoat-Liege was preferred to alternative solutions, such as AQ60 or Picsil.
AQ60 was the low density silica / phenolic material used for Huygens heatshield (Fig. 4) [9].
Norcoat-Liege allows a simpler design, an easier implementation and a slightly lower mass budget.

Fig. 4. AQ60 tiles on HUYGENS heat shield

Picsil (Fig. 5) is the low density silicone-based ablator developed in 1995-96 within ESA's MSTP program [10]. This material was finally selected as baseline for the European CTV studies.
It is however less optimized than Norcoat-Liege for a mission to Mars, for which the thermal solicitations are less severe. In addition, maturity of Norcoat-Liege was higher.

Fig. 5. PICSIL technological demonstrator

2. PRESENTATION OF NORCOAT-LIEGE

2.1 Composition and manufacturing

Norcoat-Liege is made of hot-pressed cork particles and phenolic resin. This material is a very good insulator with a density of 0.47.
Three types of Norcoat-Liege can be achieved:

- the standard material called Norcoat-Liege F,
- the fire proof material called Norcoat-Liege FI,
- the fire and water proof material called Norcoat-Liege FIH.

Large panels (1200x700 mm²) with a wide range of thicknesses (from 1 up to 150 mm) are industrially produced.
This material is easily machinable (boring, spotfacing, routing) in order to cope with the numerous geometrical constraints (access doors and hatches, dismountable covers over the back cover pyro nuts, back cover venting and break-out patch, antennae, etc…). It can also be easily formed to a desired simple geometric shape, if necessary.

It is then bonded onto various types of structure with a space-grade silicone based glue. The same glue is also used to seal the junction lines between panels.

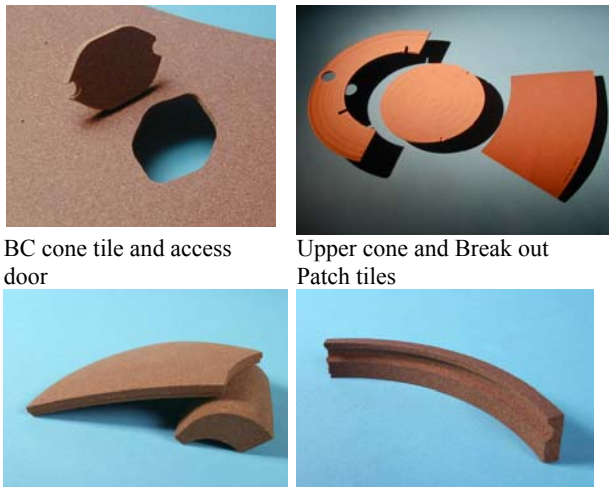

BC cone tile and access door

Upper cone and Break out Patch tiles

Fig. 6. Norcoat-Liege Tiles for Beagle 2: various shapes obtained after forming and /or machining

2.2 Heritage

Norcoat-Liege was developed in the seventies for application on launchers. It was used first for deterrent force, then on Ariane 4.
Its first application on a re-entry vehicle was for the Atmospheric Reentry Demonstrator [2] that successfully flew on October 21st 1998.
Norcoat-Liege panels 19 mm thick protected the rear cone structure and the back cover of the ARD capsule. It must be highlighted that many singularities could easily be implemented in these areas (thrusters, TPS experiments, measurement devices, antennas, access doors, etc…)
The first analysis and inspection after recovery showed and demonstrated the perfect behavior of this kind of material after the atmospheric reentry (Fig. 7).

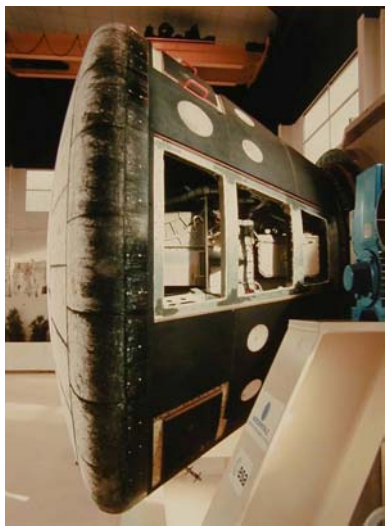

Fig. 7. ARD after flight

Norcoat-Liege also equipped the Frontshield and Back-Cover of the Beagle 2 probe (Fig. 8). This probe [3] aimed at delivering at the surface of Mars a scientific payload devoted to study chemical composition of soil and atmosphere. Unfortunately, the mission failed on December 25th 2003. However, the Beagle 2 ESA / UK Commission of Inquiry stated in April 2004 that 'the entry thermal protection is not a likely cause for the Beagle 2 loss'.

Fig. 8. Beagle 2 heat shield in assembly workshop

Beside its application on entry probes, the main use of Norcoat-Liege is for launchers (Ariane 5 and French deterrence force), and the material is regularly and continuously produced for these applications, with secured and perennial procurement source for raw materials.

2.3 Adaptation to space missions

In order to meet requirements specific to Mars entry missions, the standard Norcoat-Liege required some adaptations [4].
The first one was the thermal treatment devised to cope with outgassing requirements, after several evaluations with variation of the following parameters:

- A temperature level chosen to be in accordance with the maximum temperature seen by the material during the tiles fabrication process.
- A vacuum level imposed by the available vacuum pumps which are likely to be used during the fabrication process.
- A duration of the cycle fitted in order to meet the targeted outgassing properties.

After application of the abovementioned thermal treatment, the obtained outgassing properties for the Norcoat-Liege are given in Table 2.

Total Mass Loss (TML)	4.05%
Collected Volatile Condensable Material (CVCM)	0.09%
Recovered Mass Loss (RML)	0.72%
Water Vapor Released (WVR)	3.33%

Table 2 - outgassing properties of Norcoat-Liege FI after thermal treatment

Though a still high mass loss mainly due to water release, these properties were deemed acceptable for application on Mars entry heatshields.

The second adaptation was required in order to comply with planetary protection constraints and regulations, established to avoid contamination:

- of the outer space planets with terrestrial organisms carried by spaceships,
- of the Earth with alien organisms brought back by return re-entry vehicles or samples

The manufacturing and the integration of the Beagle 2 Mars lander have required to work in stringent cleanliness conditions and therefore to set up appropriate decontamination / sterilisation methods.
The work began by screening different decontamination / sterilisation methods mainly based on medical experience, and then a trade-off allowed selection of the most appropriate method.

- For the frontshield, bonding operation in class 100 000 clean room (Fig. 9), then packing in double bio bags and sterilization

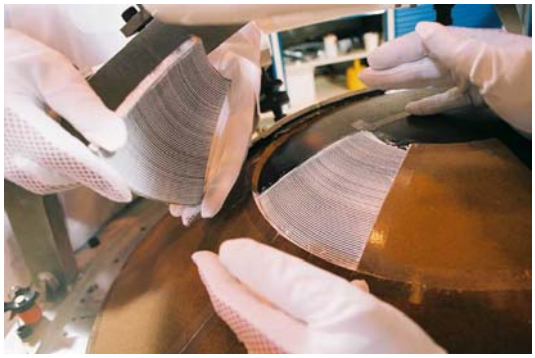

Fig. 9. Bonding of a FS tile in class 100000 clean room

- For the back cover, individual sterilization of structure and TP elements, then bonding operation in class 100 clean room (Fig. 10) and finally packing in double bio shields inside this room.

Fig. 10. Bonding of Back Cover tiles in class 100 clean room

3. THERMAL QUALIFICATION TESTS

Norcoat-Liege was extensively characterized and qualified for Mars entries including with CO2 environment during plasma testing. This was carried out in the framework of the abovementioned Beagle 2 program and also of CNES' NetLander EDLS project, for which phase B was completed in 2002, as well as in the framework of in-house R&D activities conducted in parallel to these two programs. COMETE and SIMOUN facilities of EADS-ST were upgraded [5] to allow simulation of anticipated aerothermal environment.

3.1 Synthesis of plasma tests results

Plasma tests were carried out in different test centers (EADS-ST, IPM in Russia, VKI in Belgium). The various following parameters were investigated:

- Plane board and stagnation point configurations
- Air and CO_2 atmospheres, with some tests allowing direct comparison
- Different heat flux missions on tangential flow tests: ~800kW/m² for Beagle2, up to ~1600kW/m² for Netlander plus some supplementary tests with a (not measured) value estimated to 1800 ± 100 kW/m².
- Heat flux up to 2000 kW/m² in stagnation point
- Validation of TPS architecture (including joints, steps and gaps)
- Instrumented samples, allowing detailed exploitation and elaboration of a thermal model

It must be highlighted that the experienced values of heat flux were the qualification levels required for the considered programs. The capability of the material is certainly significantly higher and further exploration is recommended to assess it more completely. Anyhow, the robustness for the ExoMars application is already ensured based on available results.

3.2 Stagnation point plasma tests

As mentioned above, Norcoat-Liege was tested up to 2000 kW/m² in stagnation point configuration. Numerous tests were performed in different test centers. Fig. 11 to Fig. 13 show pictures of Norcoat-Liege samples after the most severe tests carried out for each facility.

Fig. 11. COMETE sample (air - ~2000 kW/m²)

Fig. 12. sample tested at IPM (CO2 - ~1100 kW/m²)

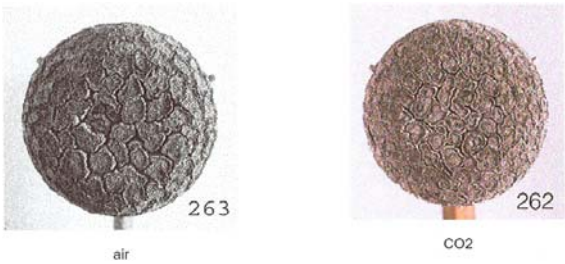

Fig. 13. samples tested at VKI
(comparison air-CO2 - ~2000 kW/m²)

These tests proved the good behaviour of the material both in air and CO_2 atmospheres. No influence of the atmosphere composition was noticeable during these tests. This contributed to validate the qualification approach on flat samples, for which the highest levels could be reached only in air.

3.3 SIMOUN plasma tests

In parallel, several tests were carried out in tangential flow configuration on the SIMOUN facility of EADS-ST (Fig. 20). This plasma arc heater allows good heat flow homogeneity on large samples of ~150 x 300 mm, together with a simulation of shear loads. The tests were performed either in air, or in CO_2.

Fig. 14 to Fig. 16 show pictures of Norcoat-Liege specimens after tests in different conditions.

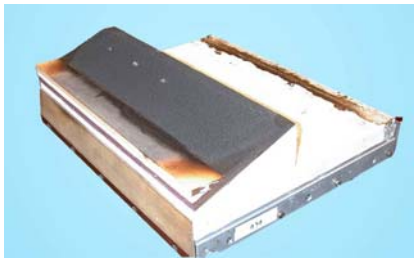

Fig. 14. SIMOUN sample after test
(Netlander – air – 1600 kW/m²)

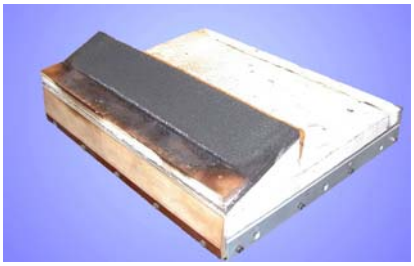

Fig. 15. Sample after test (Netlander complement - air – ~1800 kW/m²)

Fig. 16. A SIMOUN sample before and after test (Beagle 2 – CO2 – 700 kW/m²)

These tests allowed demonstrating the good behavior of the material itself, when submitted both to heat flux and aerodynamic shear. They also permitted to qualify some particular points simulating potential manufacturing defects, such as empty or wide joints, steps or local repairs.
Furthermore, these tests proved the satisfactory thermal performance of the material. Thanks to the quite complete instrumentation implemented for those qualification tests, good quality thermocouple data were obtained, which were then used for detailed exploitation and elaboration of thermal model (cf § 3.4).

3.4 Characterization and thermal model

Based on a combination of elementary characterization tests as well as on the exploitation of instrumented arc jet tests, a complete thermal model including pyrolysis and ablation effects has been established for Norcoat-Liege. This model is operated at EADS-ST for accurate and reliable design and mass-effective dimensioning (Fig. 17).

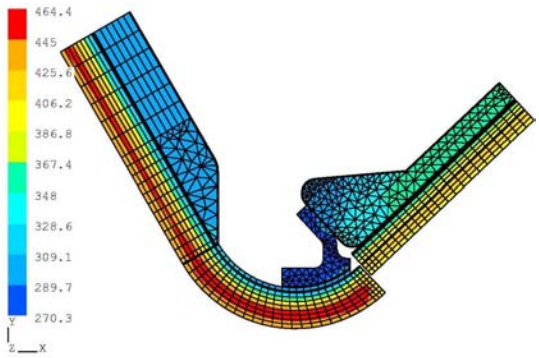

Fig. 17. 2D results for Beagle2 using Norcoat-Liege thermal model.

4. DUST EROSION

4.1 Overview

Due to periodical dust storms in Mars atmosphere, solid particles can remain in suspension for a long time. According to their high velocities, when reentry vehicles cross such dust clouds, even small particles can induce significant damage to the TPS, due to the high kinetic energies involved. Various effects can be encountered by the TPS and need modelling for a comprehensive assessment of dusty flows.

- Shock layer / particle interaction
- Particle / TPS interaction
- TPS charred layer erosion
- Increased heat flux

Ref [6] details the theoretical aspects of this theoretical and experimental combined approach defined jointly by CEA/CESTA and EADS-ST.

4.2 Test facilities

Ref [7] presents the test facilities used for experimental side.
The first step of the approach was based on the adaptation of an existing torch so-called AQTIL (Fig. 18). This Huels-type arc jet facility can be used with different gas mixtures (air, N2, N2+H2). The stagnation point heat flux level can reach 2.5 MW/m² on a standard ESA shape model (Φ50mm) with a working pressure equal to 1 atm.

The first experimentations were dedicated to the study of alumina particles impact effects on TPS in the framework of distancing rockets used on Ariane 5 boosters. Many difficult points have been solved during this AQTIL seeded plasma generator development in 2003.
Some parameters such as, carrier gas mass flow rate, number of injectors, their location and injection angle have been defined thanks to theoretical and experimental results.

Fig. 18. AQTIL Huels plasma torch

A specific injection device (Fig. 19) has been designed, based on four injectors settled up on a ring and located at the exit of the downstream electrode.
This allows a precise control of the mass flow rate of both particles and carrier gas.

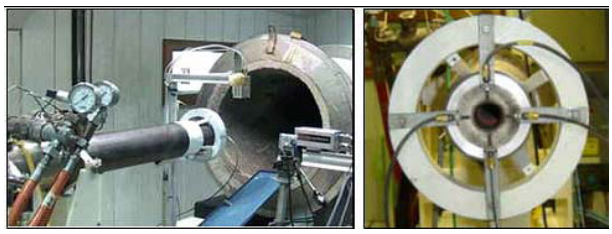

Fig. 19. AQTIL particle injection adaptation

Once the seeded plasma flow obtained, several diagnostic techniques have been implemented to obtain a precise control of the test conditions such as the homogeneity of the seeded flow, the particle velocity and status (solid, melt,...).
This injection technique with its adjustment was patented in year 2005. The AQTIL facility is now available and fully qualified for TPS characterisation under particle impingement, including simulation of dust particles erosion encountered during Mars atmospheric entry.

The second step of the development of seeded plasma test facilities has been initiated (as an internal R&D development) and a validation test campaign is scheduled in 3rd quarter of 2006.
The power injection will be implemented on SIMOUN (Fig. 20), based on the experience gained during former AQTIL development. The same injection method and diagnostic techniques will be used and validated in hypersonic flow.

As a first approach, the stagnation point configuration will be used with the 50 mm diameter ESA standard sample combined to axisymetric injection particles at nozzle exit.

The foreseen next step is to evaluate the use of SIMOUN facility in flat plate configuration, thus with combination of shear stress and particles erosion effects. This will be the last point to fully complete the excellent simulation capability of SIMOUN for Mars atmospheric entries.

Fig. 20. SIMOUN plasma test facility

5. R & D results and growth potential

Norcoat-Liege has been proven to be a TPS material with outstanding properties. As its main component is natural cork, it induces a relatively complex composition. In order to get a better understanding of the behavior of the material, thorough analyses and characterization work [12] were performed during the past last years in cooperation with universities and labs, particularly CRPP from CNRS.

Two main points were analysed:
- Influence of main organic (families of) molecules constituting the material
- Analysis of degradation process

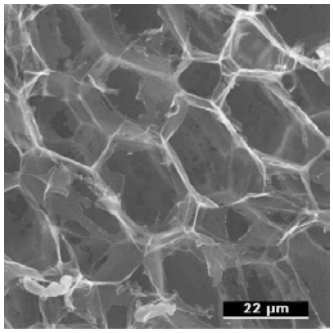

Fig. 21. Norcoat-Liege after carbonization @ 2000°C

This produced very interesting results, showing among others a very good stability of the carboneous cells at high temperature (Fig. 21).
Moreover, the better understanding of the role of each constitutive type of molecules provides a basis for a more detailed theoretical modeling, as well as for future tailored improvements of the material.
The two following perspectives are deemed quite attractive, and should enable to enlarge the use of this type of material to a wider domain:
- Inclusion of a mechanical reinforcement in the material, in order to strengthen the char layer. This is expected to allow use for more demanding missions, with higher heat fluxes than those encountered during Mars entries.

- Search for a lightened material, in view of application on aft body of entry probes, where the low density is a key parameter

6. CONCLUSION

EADS-ST is ready to bring a significant contribution to ExoMars development and future success, in particular through the different following topics, among which those mentioned in this paper:

- Thermal protection design and assembly
- High temperature testing facilities
- All the disciplines required for atmospheric entry (Aerodynamics, Aerothermodynamics,…)

These technologies and techniques can obviously also serve any future scientific mission with atmospheric entry probe [11, 13].

7. ABBREVIATIONS

CM	Carrier Module
CNRS	Centre National Recherche Scientifique
CRPP	Centre de Recherche Paul Pascal
CTV	Crew Transportation Vehicle
DM	Descent Module
EDLS	Entry Descent and Landing System
MSTP	Manned Space Transportation Programme
TP	Thermal Protection
TPS	Thermal Protection System

8. REFERENCES

1. P. Régnier, C. Koeck, R. Slade, P. Tran, Assessment of landing system concepts for the ExoMars mission, IAC-05-A5.2.04, IAC Fukuoka, Japan, 2005

2. J.M. Bouilly, S. His, J.L.Macret, The ARD Thermal Protection System, 1st International Symposium on ARVS, Arcachon, France, March 1999.

3. Bertrand J, Labaste V., Mignot Y., The Beagle 2 Thermal Protection System, 3rd International Symposium on ARVS, Arcachon, France, 24-27 March 2003

4. Labaste V., Bertrand J, Dariol L., Mignot Y., Adaptation of Thermal Protection to a Martian mission, 2nd International Symposium on ARVS, Arcachon, France, March 2001

5. Conte D, Labaste V., Mignot Y, Tran Ph., SIMOUN Aerothermal test facility for Netlander reentry, 3rd International Symposium on ARVS, Arcachon, France, 24-27 March 2003

6., Montois I., Pirotais D., Conte D., Sauvage N., Chazot O., Overview of dust effects during Mars Atmospheric entries : Models, Facilities and design tools, 4th International Planetary Probe Workshop, Pasadena, California USA, 27-30 June 2006.

7. Sauvage N, Montois I., Tran P., study of particles impact effect on ablative material properties. Application to Mars Reentries, 5th European Workshop on TPS and Hot Structures, ESTEC Noordwijk, May 17-19, 2006.

8. Labaste V., Mignot Y., EADS Launch Vehicles Main Achievements for Planetary Exploration Missions, 4th European Workshop on Thermal Protection Systems, Palermo, 2002

9. Bouilly J-M, Thermal protection of the HUYGENS probe during TITAN entry: last questions. 2nd International Planetary Probe Workshop, NASA Ames Moffett Field, California USA, 23-26 Aug. 2004

10. Labaste V, Bouilly J-M, Conte D., Mignot Y., PICSIL, a New Low Density Ablative Material Family for Future Space Probes, 3rd European Workshop on Thermal Protection Systems – ESTEC Noordwijk – March 1998

11. Ablative thermal protections for atmospheric entry. An overview of past missions and needs for future programmes, 5th European Workshop on TPS and Hot Structures – ESTEC Noordwijk – 17-19 May 2006

12. Reculusa S., Trinquecoste M., Dariol L., Delhaès P., Formation of low-density carbon materials through thermal degradation of a cork-based composite, Carbon Journal n° 44, (2006), pp 1298-1352

13. B. Laub, Y.-K. Chen, Updated TPS Requirements for Missions to Titan, 3rd International Planetary Probe Workshop, Anavyssos, Greece, 27-30June 2005

70 MW PLASMA WIND TUNNEL UP-GRADES FOR ESA AURORA TPS TESTING

4th INTERNATIONAL PLANETARY PROBE WORKSHOP, 27 June – 30 June, 2006, Pasadena, California, USA

F. De Filippis [(1)], A. Del Vecchio [(1)], A. Martucci[(1)], E. Trifoni[(1)], L. Marraffa[(2)], R. Savino[(3)], D. Paterna[(3)]

[(1)]CIRA, via Maiorise, Capua 81043 (CE), Italy,
Email: f.defilippis@cira.it; a.delvecchio@cira.it; a.martucci@cira.it; e.trifoni@cira.it;

[(2)] ESA/ESTEC, Aerothermodynamics Section, Keplerlaan 1, PO Box 299, 2200AG, Noordwijk, NL,
Lionel.Marraffa@esa.int;

[(3)]Department of Space Science and Engineering (DISIS)
University of Naples "Federico II", 80125, Naples, Italy
Email: rasavino@unina.it; paterna@unina.it;

ABSTRACT

The SCIROCCO facility is a high enthalpy hypersonic Plasma Wind Tunnel developed by CIRA in collaboration with ESA. With an electrical power available at the arc heater of 70 MW, SCIROCCO is the World's most powerful ground test facility, able to simulate hypersonic air flows encountered during re-entry into Earth atmosphere and to test innovative large scale TPS (Thermal Protection System) for spacecrafts. In the frame of ESA Aurora Exploration Programme, Mars and Earth atmospheric re-entries represent critical issues. Ground tests simulating the reentry conditions encountered by space vehicles are required to validate TPS concepts and to ensure the feasibility of interplanetary missions.

The objective of this work is to identify the necessary upgrades to the SCIROCCO facility to make it able to reproduce hypersonic flows representative of Mars and Earth super-orbital atmospheric re-entries. For the Earth super-orbital re-entry, the work consists in properly changing the configuration of the facility to extend its experimental envelope towards higher stagnation heat flux and pressure values. To reproduce Mars atmospheric entry conditions, the facility must be able to provide a high enthalpy hypersonic flow of a gas mixture representative of the red planet atmosphere; As a consequence, a number of difficulties arise that have been addressed and investigated.

1. INTRODUCTION

This paper summarizes the activities performed in the framework of the ESA AURORA exploration program to extend the SCIROCCO Plasma Wind Tunnel capabilities to deal with Mars atmospheric entry and Earth super-orbital re-entry.

The hypersonic Plasma Wind Tunnel SCIROCCO is a 70 MW arc-heated facility developed to test Thermal Protection Systems of vehicles re-entering the Earth atmosphere. With this facility it is possible to reproduce hypersonic flows on 1:1 scale models with total enthalpies up to 45 MJ/kg and total pressures up to 17 bar.

Figure 1 shows a simplified scheme of the present facility configuration, with the main components.

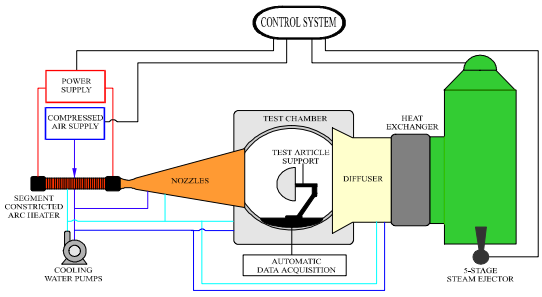

Fig. 1. The SCIROCCO schematic diagram

A number of modification are necessary to upgrade the facility for TPS tests of interest in the framework of the exploration programme.

For an interplanetary mission, the spacecraft that approaches the re-entry has a velocity quite higher than for a "Return From Orbit" one (11-12 km/s instead of 7 km/s). This implies that during the re-entry phase the aero-thermo-dynamic conditions will be more critical due to the higher specific total enthalpy. Moreover, to reproduce the conditions encountered on space vehicles during entry in the atmosphere of the Mars planet, a number of

modifications are necessary to simulate an atmosphere essentially composed by CO_2 (95%).
In this paper we analyze the main results of this feasibility study. Section 2 deals with the requirements and the technical solutions found to simulate superorbital reentry in the Earth atmosphere. Section 3 is dedicated to the feasibility study of the SCIROCCO upgrade with the objective to simulate the aerothermodynamic environment during hypersonic entry in the Mars atmosphere. The conclusions are presented in Section 4.

2. SUPER-ORBITAL EARTH RE-ENTRY

A feasibility study has been carried out to upgrade SCIROCCO in order to reproduce aerothermal conditions of interest for interplanetary return to earth. The facility requirements, the necessary modifications, the new facility performances, the time scheduling are briefly reported in the following paragraphs.

2.1 Requirements

The main requirement for the proposed upgrade is the possibility to reproduce the aero-thermal loads on the TPS materials of the *Earth re-entry Vehicle Demonstrator* during its Earth re-entry phase.
Table 1 summarizes the specific ESA requirements.

Table 1

Test 1			
Stagnation Heat Flux	Stagnation pressure	Test time	Test sample size
18800 [kW/m^2]	130000 Pa	About 6 s	25 mm

Test 2			
Stagnation Heat Flux	Stagnation pressure	Test time	Test sample size
21000 [kW/m^2]	150000 Pa	About 20 s	25 mm

Test 3			
Stagnation Heat Flux	Stagnation pressure	Test time	Test sample size
13900 [kW/m^2]	80000 Pa	About 20 s	50 mm

Test 4			
Stagnation Heat Flux	Stagnation pressure	Test time	Test sample size
8900 [kW/m^2]	42000 Pa	About 20 s	100 mm

All the conditions represented in Table 1 require an extreme design configuration of the facility. In fact, the stagnation point heat fluxes (in the order of 10-20 MW/m2) can be obtained on large models only if the throat section of the facility is directly connected to the Test Chamber. This introduces a number of problems, that will be analyzed in the following paragraphs.

2.2 Facility performances

As discussed in the introduction, the typical velocity of a spacecraft at the atmospheric entry interface, when the vehicle re-enters from LEO is about 8 [Km/s]. For the hyperbolic trajectory described by the spacecraft in the case of direct reentry from an interplanetary mission, this velocity is about 11-12 [Km/s]. Since the stagnation point pressure and heat flux are roughly proportional to the square and to the cube of the velocity, they dramatically increase.
In the present configuration SCIROCCO can be used with different nozzles; indeed the conical nozzle is divided in several parts that, assembled in the correct way, provide different configurations. Figures 1(a,b,c,d) show how the facility is assembled when it is used with the nozzles C, D, E and F respectively.

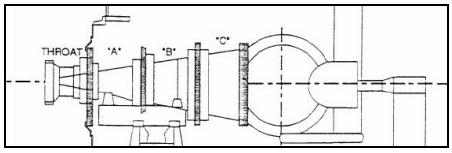

Fig. 1a. Nozzle C

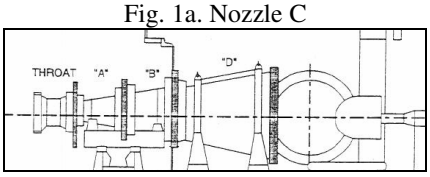

Fig. 1b. Nozzle D

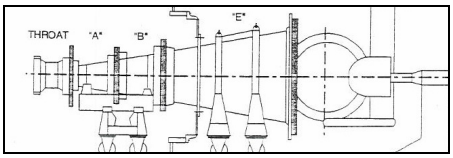

Fig. 1c. Nozzle E

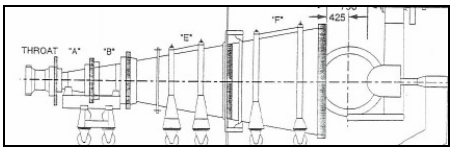

Fig. 1d. Nozzle F

Figures 1 show that it is possible to change the conical nozzle exit area by changing the configuration. Four configurations (C, D, E, F) are now available; however, also other configurations (e.g. throat 0, A, B) have been investigated.

Table 1 shows the diameters of the different exit sections, in mm, and the correspondent geometrical (nominal) *Exit Section-Throat Section* area ratio. The throat section diameter is the same in any case (75 mm).

Table 1

Conf.	**0**	**A**	**B**	**C**	**D**	**E**	**F**
Diam.	187	430	670	900	1150	1350	1950
A/A*	6.2	32.8	79.8	144	235	324	676

For each configuration, the conditions at the nozzle exit section have been computed using one-dimensional theory, according to the equation:

$$\left(\frac{A}{A^*}\right)^2 = \frac{1}{M^2}\left[\frac{2}{\gamma+1}\left(1+\frac{\gamma-1}{2}M^2\right)\right]^{\frac{\gamma+1}{\gamma-1}} \quad (1)$$

Where A is the area of the cross section, A* is the throat area and γ is the specific heats ratio. Experimental data fitting formulas and CFD computations fitting formulas have been utilized to evaluate the stagnation point heat fluxes and pressures on the available hemispherical probe (with radius R=5 cm). This probe is water-cooled and made by copper, so that it is assumed to have a fully catalytic behaviour.
The performances in terms of stagnation pressure and stagnation heat flux are summarized in Figure 2. It is evident that it is possible to meet the requirements of Table 1 only using the configuration "throat 0".

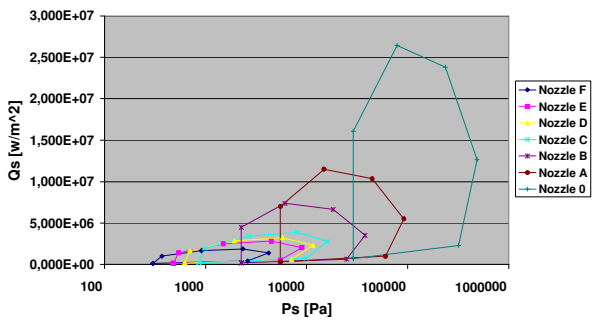

Fig. 2 Facility performances in terms of stagnation point heat flux and pressure

2.3 Description of the modifications

The modifications to make SCIROCCO able to simulate these more critical conditions include modifications to the nozzle (that, as seen before, must be shorter than in the present available configurations), to the test-chamber interface and to the model support system. Indeed, because of the higher stagnation heat fluxes the available calibration probe cannot be used. Moreover, it is not possible to utilize the available model support system, for the reasons explained below.

Test Chamber interface walls

As discussed in paragraph 2.2, the requirements reported in Table 1 can be satisfied only with the shortest configuration of the nozzle (throat 0). In order to use this configuration, a new model support system is necessary to keep the model near enough to the nozzle exit section. In addition, a technical solution is required to connect the throat section to the test chamber. Let us consider Figure 3, where a zoom of the configuration C of Fig. 1a is shown in the region of the Test Chamber interface wall.

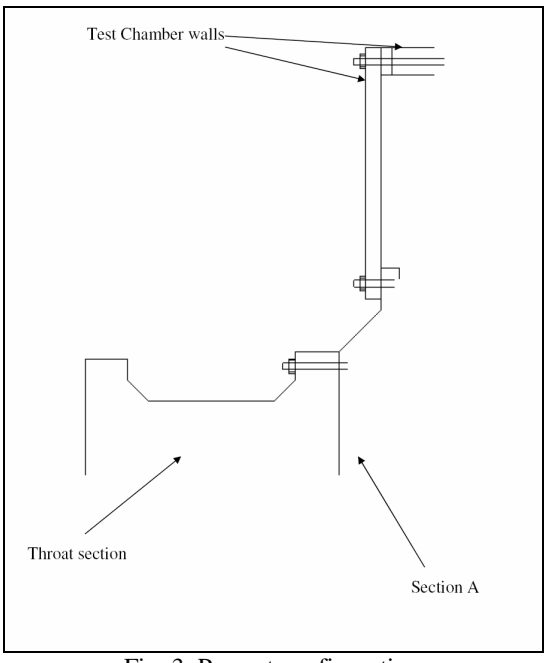

Fig. 3. Present configuration

It is possible to notice how in the present design the section "A" is joined to the test chamber. To directly connect the throat section to the test chamber a new component will be mounted between the test chamber and the throat section, as shown in Figure 4.

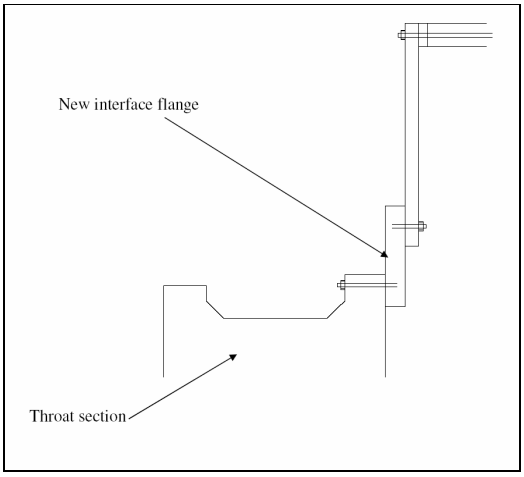

Fig. 4. Future configuration

Model Support System

Figures 1(a-d) show the position of the model in the test chamber in the present configurations. The minimum distance from the throat section is about 2.4 m, for the configuration C (Fig 1a). If the throat section is directly connected to the test chamber, a new model support system is necessary to place the model in the correct position.
Under the assumption of correct flow expansion in the nozzle, so that the velocity downstream the exit section is parallel to the nozzle contour (see Figure 5) the flow properties and the corresponding values of the stagnation point heat flux and pressure on the probe, at different distances from the exit section, have been computed using equation (1). The results pointed out that, in order to satisfy the ESA requirements, the distance from the exit section cannot exceed 3 cm.

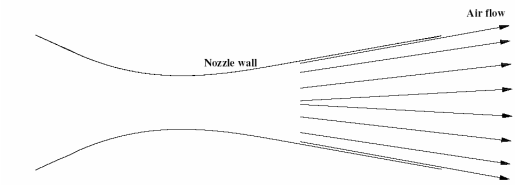

Fig. 4.

Under this assumption the Mach number on the axis, in a generic point not too far from the nozzle exit, can be evaluated through a numerical solution of the equation (1).
Moreover, in order to introduce both the probe and the model during a specific test, the new model support system will be able to sustain simultaneously two different holders that will be translated (along two orthogonal axes) as illustrated in Figure 5.

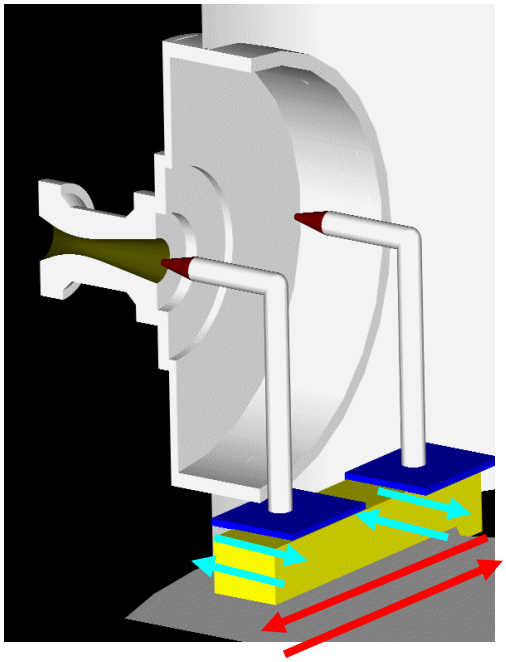

Fig. 5. The new Model Support System

2.4 Instrumentation

The required new instrumentation is related to the higher values of the stagnation pressure, to the higher stagnation point heat fluxes and to the different location of the model. In its present configuration, the facility operates with stagnation point pressures of the order of magnitude of 10^3 (maximum 10^4) Pa, and maximum stagnation point heat fluxes of 3 MW/m^2 on the previously described copper probe. The Gardon Gage cooled sensor is able to make accurate measurements of heat fluxes not exceeding 3 MW/m^2
In the modified configuration of the facility, for the simulation of super-orbital Earth re-entry, the stagnation point pressure will rise to values of the order of 10^5 Pa and heat fluxes will be larger than 10 MW/m^2. For this reason, a new probe will be developed to fulfil the new requirements. The estimated time for design, procurement, manufacturing and verification is 6-9 months.
Moreover, the locations of all the optical diagnostic instruments (thermography, spectroscopy, pirometry) as well as the cameras used for videorecording of the tests are optimized for a field of view centered in the actual Scirocco test chamber. In particular, in the present configuration, a side view of the test model is possible but it is not possible to look at the region very close to the model stagnation point. A number of optical components can be utilized including mirrors optimized for dedicated techniques, i.e. in the visible, in the infrared for pirometry or for thermography, in the UV for spectroscopy. In this

case, a careful analysis for the evaluation of the dependence of the mirror reflectance with temperature is necessary due to the relatively high temperature caused by hot air recirculation and/or radiation from hot model surfaces under test.
Finally, a more precise air mass flow meter will be considered for its importance in the measurement of the specific total enthalpy.

3. MARS ENTRY FEASIBILITY STUDY

In this section, all the modifications needed to extend and/or improve the SCIROCCO capabilities to deal with Mars atmosphere entry are described. The expected facility performances are evaluated and compared to the ESA requirements.

3.1 Facility requirements for Mars atmosphere entry

The upgraded facility should be able to simulate the conditions of the ExoMars mission. The ExoMars capsule is shown in Figure 6 [1]. The stagnation point heat flux and pressure values corresponding to relevant conditions pertaining to two ExoMars trajectories [2], denoted as M1 and M2, are reported in Table 3.

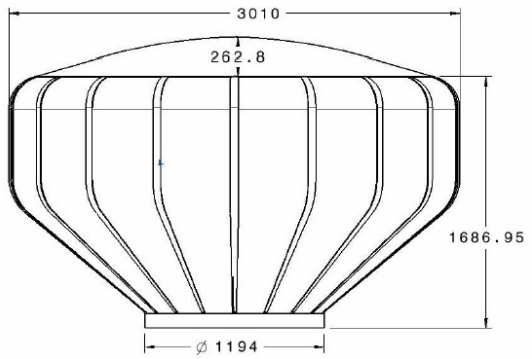

Fig. 6. The Exomars Descent Module

Table 3

Test	Heat Flux [MW/m^2]	Stagnation Pressure [Pa]	Time [s]
M1	2.09	8014	46
M2	1.3	6415	48

The Martian atmosphere mass composition is [2]:

CO_2 = 96.8%; N_2 = 1.7%; Ar = 1.5%

Additional ESA requirements deal with the mass flow rate, the duration of the tests, the refill time and the pressure (Table 4). Assuming that the maximum mass flow rate for the mixture is 2.066 Ks/s, including 2 kg/s of CO_2, 0.035 kg/s N_2 and 0.031 kg/s Ar, the required mass and volume have been estimated.

Table 4

	Species	Mass flow rate [kg/s]	Mass cons. [kg]	Volume cons. [Nm^3]
CO_2	**98.30%**	**2.000**	**1800**	**911**
N_2	**1.70%**	**0.035**	**31.5**	**27**
CO_2 + N_2		**2.035**		
Test duration	**15 minutes = 900 seconds**			
Refill time	**24 hours**			
Pressure	**87 bar**			

3.2 Description of the facility modifications

Based on these system requirements, a number of modifications and changes have been identified that can be summarized as follows:

- Realization and installation of a CO_2 – N_2 gas management system and of an interface to the facility
- Electrical heat tracing of the compressed air system piping
- Reduction of hoses to the arc heater
- By-pass of the DeNOx system
- Realization and installation of a CO combustion system
- Appropriate modification of the control system
- Acquisition of instruments and procedures for people safety

These specific aspects are analyzed below.

CO_2 – N_2 Gas Management System

A feasibility study has been carried out in order to identify a technical solution for the gas management system for the CO_2 - N_2 mixture, since an Argon system is already available at the facility SCIROCCO.
To satisfy the requirements reported in Table 2, two different technical solutions have been investigated:

Technical Solution #1

- 5 m^3 cryogenic tank of liquid CO_2 at 17 bar_g and -25°C
- CO_2 vaporizer
- 160 Nm^3 cylinder pack of gaseous N_2 at 200 bar_g
- N_2 pressure reducer
- CO_2-N_2 mixer at 8 bar_g
- 200 bar_g compressor for 50 Nm^3/h of CO_2-N_2 mixture
- 10 m^3 total capacity tanks of gaseous CO_2-N_2 mixture at 200 bar_g and controlled temperature
- pressure controller

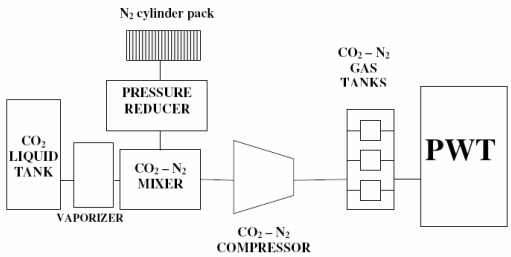

Fig. 7 Technical solution 1

Technical Solution #2

- 10 m^3 cryogenic tank for the storage of liquid CO_2 at 17 bar_g and -25°C
- cryogenic pumping system, designed for mass flow rate of 7200 kg/h CO_2
- CO_2 vaporizer, fed by 1.4 t/h of super heated water steam at 250°C and 28.5 bar_g
- gas delivery pressure (87÷100 bar_g) and temperature (75÷100°C) control system
- 160 Nm^3 cylinder pack of gaseous N_2 at 250 bar_g
- N_2 pressure reducer
- N_2 mass flow controller

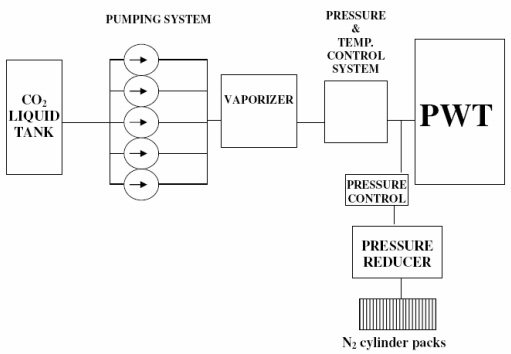

Fig. 8 Technical solution 2

Compressed Air Supply System

The function of the Compressed Air System is to distribute the air to the arc heater. Even if this subsystem is quite complex, it can be simply described with the scheme of Figure9, where we can notice that there are two main valves (PCV-033A and PCV-033B) and downstream three distribution lines, each provided with a distribution valve, up to the column of the arc heater.

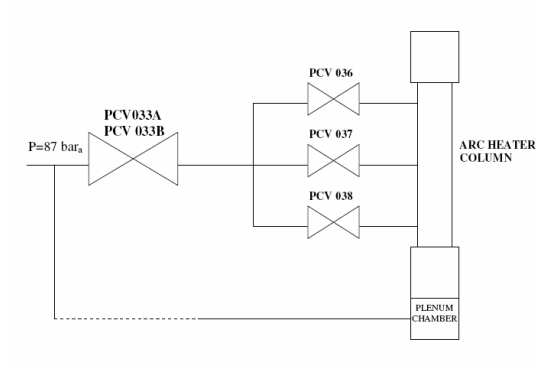

Fig. 9. Compressed air system

Downstream the three distribution valves, and upstream the arc heater, the pressure is high enough to have a choked flow upstream the column, and small pressure drops occur along the three lines. A pressure drop of about 8-10 bar occurs in the three valves PCV 036, PCV 037, PCV 038, and another great pressure drop takes place in the main valves PCV 033A and PCV 033B. Upstream the compressed air supply system a pressure of 87 bar_a is required. The design temperature of the compressed air system is 50 °C; therefore, in order to avoid the CO_2 condensation during its expansion, all the piping must be electrically heat traced, carrying the temperature of the system around a value of 50°C.

Pressure drops in the valves and in the lines, when using CO_2, have been computed and they are of the same order of magnitude compared to the air case. However, when using CO_2, a lower number of gas distribution hoses should be utilized.

The software of the control system should be properly regulated to be used with CO_2 – N_2 mixtures. Moreover, the facility should be able to operate at relatively low specific total enthalpies, because there is the possibility to inject CO_2 – N_2 into the plenum chamber through a line that is positioned upstream the two main valves but downstream arc heater column (see Figure 9). In fact the gas, after its passage into the arc heater, reaches relatively high specific total enthalpy (at least 10 MJ/kg). In order to reduce its specific

energy content cold gas can be injected downstream.

Vacuum System

The vacuum system should be able to properly operate using a gas mixture with the same composition of the Mars atmosphere.
No chemical problems (such as corrosion) are foreseen. The effects of CO_2/CO on the metallic parts of the vacuum system should be negligible. The carbonic acid formed due to the presence of water at the vacuum condenser is in fact less aggressive than the nitric acid formed during usual operations with air.
On the other hand, there are some consequences on the system performances, represented by the "vacuum level" the vacuum system is able to reach, i.e. by the pressure that it is possible to provide. Of course, lower is this pressure, better is the performance. The performances of this system working with air are available, and a preliminary analysis has been carried out for the mixture with the Mars composition, simply scaling the performances with air with the CO_2/air density ratio. The results are shown in Figure 6, where the pressure provided by the vacuum system is reported versus the mass flow rate. The pressure is always higher when using Mars atmosphere in comparison to Air.
Figure 10 includes two curves (red lines) representing the maximum allowed pressures. It is possible to notice that the facility is able to satisfy the requirements.

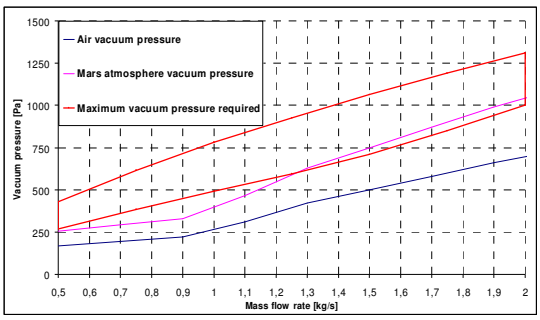

Fig. 10 Vacuum system performances

Carbon Monoxide Combustion System

It is well known that at the very large specific total enthalpy established in the arc heater column, the CO_2 is almost completely dissociated, according to the reaction:

$$CO_2 \rightarrow CO + ½\ O_2$$

Other chemical reactions occur between the different chemical components but a large amount of Carbon Monoxide is generally present. The chemical compositions of the different species remain typically frozen in the diverging part of the nozzle, so that they are still present in the diffuser downstream the test chamber, where the flow field slows down from hypersonic to subsonic.
A study developed in [3] has shown, for instance, that in the worst case at the total pressures of 0.001, 1 and 10 atm, at the temperatures of 4000, 5000 and 7000 K, respectively, the equilibrium CO molar fraction is 0.5 and thus its mass fraction is about 0.64. This means 1.3 kg/s of CO emission at the maximum CO_2 mass flow rate of 2 kg/s.
For safety reasons, CO leakages must be prevented in all components of the facility, and a number of CO and CO_2 detectors should be placed in different points of the facility.
In addition, safety procedures and systems will have to be considered and used by people working at the facility.
In order to reduce the CO concentration at the values allowed by the Italian law (10^{-4} kg/ m^3), a combustion system must be installed downstream the vacuum system by-passing the $DeNO_x$ (see Figure 11). The DeNOx system has the function to reduce the NO_x concentration in the gas flow during air operations.

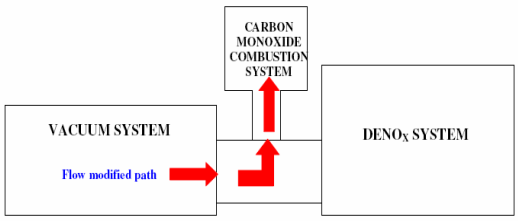

Fig. 11. Carbon monoxide combustion system

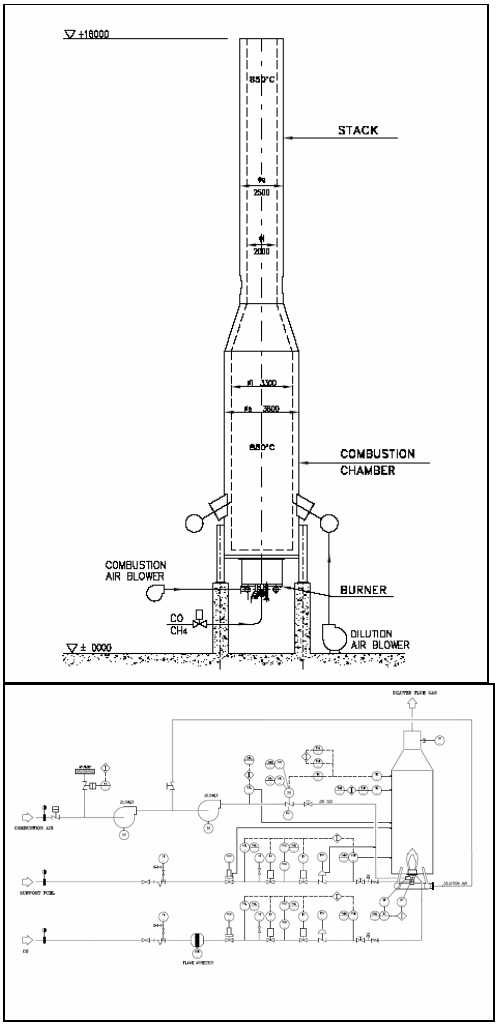

Fig. 12, CO combustion system

When using the facility SCIROCCO with Mars atmosphere, the amount of N_2 in the gas (less than 0.035 kg/s) is negligible if compared with normal operations of the facility with air (up to 3.5 kg/s composed by 77% of N_2); for this reason one can assume that during SCIROCCO operations with Mars atmosphere the concentration of NO_x in the gas flow will be negligible and the DeNOx system will be not necessary.

If we consider the facility working with air, we have, a gas saturated with water steam at a pressure of about 1.06 bar_a and 65 °C. Assuming at the exit of the last condenser of the vacuum system a pressure of 1.06 bar_a, a temperature of 65 °C (typical values for operation with air) a CO concentration of 1 kg/m^3 of discharged gas can be evaluated. Therefore, it is necessary to reduce the carbon monoxide emissions of about four orders of magnitude. A technical solution for this purpose is provided by a dual fuel burner (Figures 12a,b) characterized by a 13.2 MWt carbon monoxide nominal power plus 1 MWt of support methane; to guarantee the required CO reduction it needs a residence time of 2 seconds at a temperature of 850°C; thus the system results to be a 18 m tower made by a 3.8 m diameter combustion chamber followed by a 2.5 m diameter stack. The combustion reaction is sustained by a 3.61 kg/s combustion air fan (30 kWe) and by a 10.55 kg/s dilution air fan (22 kWe).

3.3 Instrumentation

Non intrusive optical diagnostic methods analyzing and describing the chemical-physical properties of the plasma gas are of particular interest in arc-heated wind tunnels, due to the non equilibrium aspects. For this reason the Diode Laser Absorption Spectroscopy (DLAS) is going to be developed in the SCIROCCO Plasma Wind Tunnel. Since its introduction in the mid 90's, the DLAS has been used in hypersonic facilities like ONERA-F4 hot shot facility, DLR-HEG shock tube and ONERA-S4 wind tunnel. This technique is based on measuring the absorption intensity of a fast wavelength tunable laser beam passing through the free-stream (Fig. 13). Velocity, translational temperature and species concentration measurements can be retrieved from the recorded spectral profiles.

The measurements are made at repetition rates up to 10 kHz. Conventional diode lasers in the infrared domain (5 µm) are used to acquire the fundamental and therefore the most intense absorption lines of heteronuclear species such as NO, CO, CO_2 and H_2O. The main advantages of this technique in the context of the Scirocco Arc-Heater Plasma Facility include: a)characterization of the composition of the plasma flow (free stream and shock layer in front the test article); b) cross check with CFD results and possibility to validate and/or to improve the models and capabilities of the CFD analyses; c) optimization of the diagnostic technique, due to the experimentation operation time of Scirocco wind tunnel.

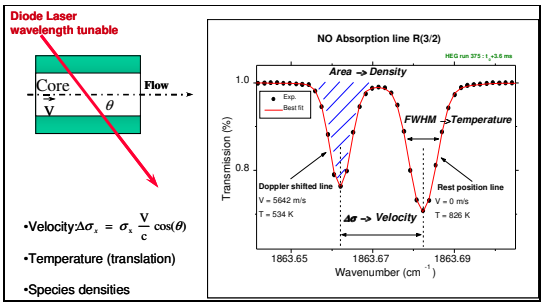

Fig. 13.

The system to be implemented in the SCIROCCO facility is initially optimized to operate with NO. The instrumentation setup can be upgraded in order to make it able to work with CO and CO2 using a dedicated laser source and some properly designed optical accessories such as prisms, mirrors and power meters.
The modification/upgrading of the DLAS technique will require a preliminary design (about 2-3 months), then the procurements of the components (3-5 months) and, finally, the configuration set-up and the modifications to the software (about 5 months)to take into account the new components and the properties of the species under investigation (CO and CO_2).
As discussed at the end of Section 2, an additional, more precise gas mass flow meter will be considered for its importance in the evaluation of the specific total enthalpy. In the present configuration of the facility, this important parameter is measured with a system developed and calibrated only for use with dry air.
As discussed before, in the Aurora projects, different gas mixtures are expected to be used as Co and CO_2. For this purpose a new system will be specifically calibrated for use not only restricted to air but also extended to the additional gas components. This can be realized with a variety of off-the-shelf components now available on the market and specific calibration can be required during the procurement phase.

3.4 Numerical simulation of the SCIROCCO performances with CO_2 flows

Numerical simulations of the aero-thermo-chemical flowfield in the SCIROCCO facility, considering CO_2-based mixtures in thermochemical non-equilibrium, have been carried out. A number of test conditions has been considered to study the flowfield in the SCIROCCO nozzle type "F", and around the hemispherical probe in the test chamber. As discussed before the probe radius is R=5 cm and a fully catalytic material is considered.
Examination of data from literature shows that Air and CO_2-N_2 mixture transport properties (viscosity, equilibrium thermal conductivity, equilibrium specific heats and electrical conductivity, radiation absorption coefficients) are similar at different temperatures and pressures. This suggests that the arc performances should be similar for Air and Carbon Dioxide mixtures, and therefore, in order to evaluate the SCIROCCO performances with CO_2-based mixtures, the same specific total enthalpies and total pressures as in Air (at the same arc electric power and mass flow rate) have been assumed at the SCIROCCO nozzle inlet.
A number of conditions, almost uniformly distributed in the SCIROCCO operating envelope, have been selected (Fig. 14).

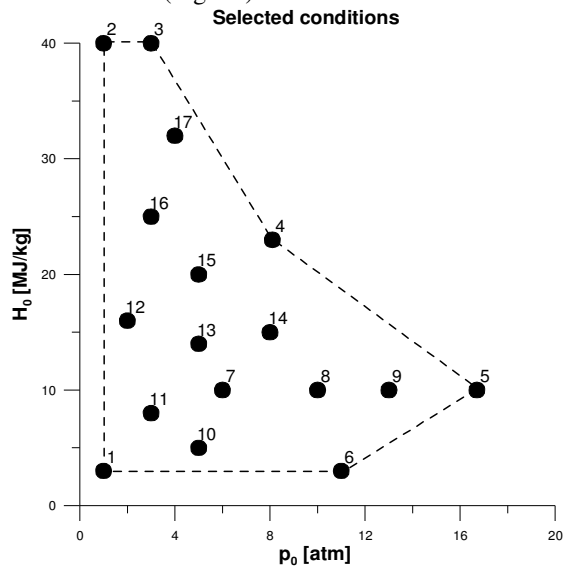

Fig. 14 – Selected conditions in SCIROCCO operating envelope

Thermochemical computations of the equilibrium composition of CO_2-N_2-Ar mixtures have been performed using the validated NASA software CEA2 [4], and, accordingly, only the nine-species with non negligible compositions (Ar, CO_2, CO, C, O, O_2, O, NO , N , N_2) have been taken into account. Each species of the mixture is assumed to behave as a thermally perfect gas where translational-rotational and vibrational-electronic degress of freedom are characterized by different temperatures. Vibrational-translational energy exchanges have been modeled according to the Landau-Teller model and the vibrational relaxation time is derived from the Millikan-White formula, with Park [5] correction for high temperatures. Chemical kinetic model is taken from Park [6-8]. Only the most relevant reactions are taken into account. The fluid-dynamics equations have been numerically solved in the computational domain (nozzle + test chamber). Convective fluxes are computed according to Roe's Flux Difference Splitting scheme. Integration of the equations is performed implicit in time, until steady state is achieved, solving the linearized system of equation by the multigrid technique. The solver has been used in this work in combination with a number of "ad hoc" developed user defined functions to model hypersonic flows in chemical and vibrational nonequilibrium.

The flowfield inside the nozzle type “F” and test chamber and around the hemispherical test model has been computed for all the selected SCIROCCO conditions (see for instance Figures 15 and 16 referring to the condition n. 5 in Figure 14).

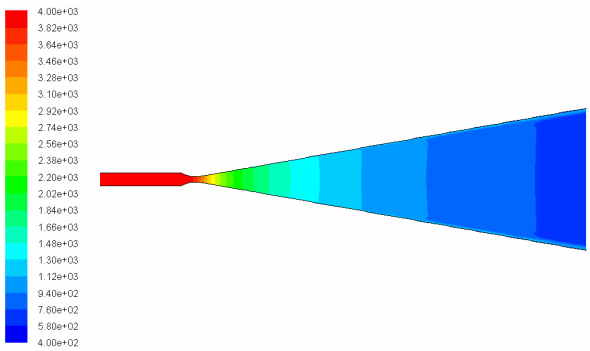

Fig. 15 – Translational temperature distribution in the nozzle (P_0=16.7 bar, H_0=10 MJ/kg)

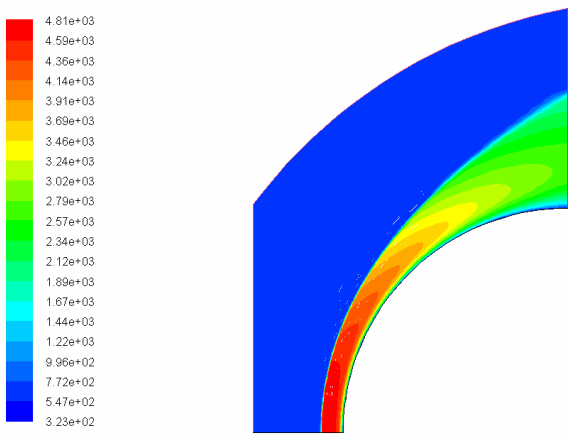

Fig. 16 – Temperature distribution around the spherical model (P_0=16.7 bar, H_0=10 MJ/kg)

The stagnation point pressures and heat fluxes on a fully catalytic test model have been evaluated for each simulation. The numerical results show that including Argon in the mixture does not change the flowfield distribution in an appreciable way. Furthermore, including thermodynamic nonequilibrium effects does not affect the computed surface heat flux distribution on the test model, unless the model wall is assumed to be adiabatic with respect to vibrational energy (Fig.17). In that case, since not all the fluid energy is released to the wall, heat flux can be up to 15% lower.

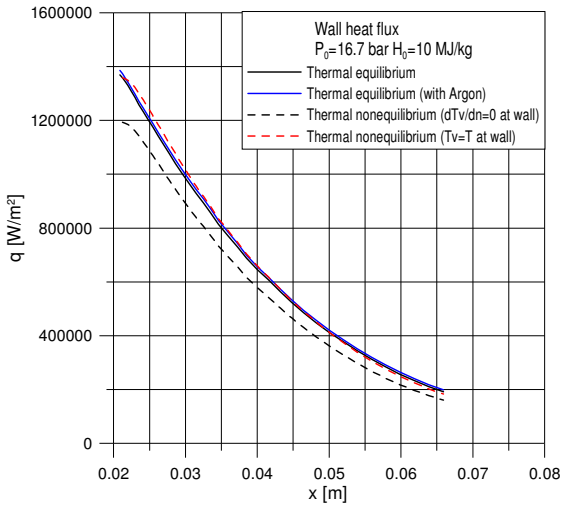

Fig. 17 – Surface heat flux (P_0=16.7 bar, H_0=10 MJ/kg)

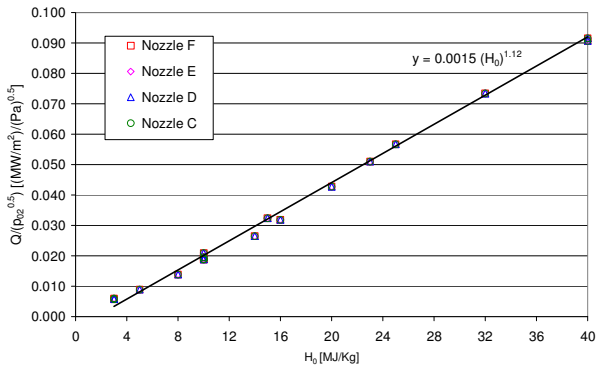

Fig.18 – $Q/p_{02}^{0.5}$ vs H_0 at the exit section of the nozzle F for any selected condition

Suitable correlation formulas have been found for both the stagnation point heat flux as function of the total enthalpy, and for the stagnation point pressure as function of the total pressure, that could be used in future analyses (Figures 18 and 19).
The results have also been extended to the other SCIROCCO nozzles (types “C”, “D”, “E”) by scaling laws.

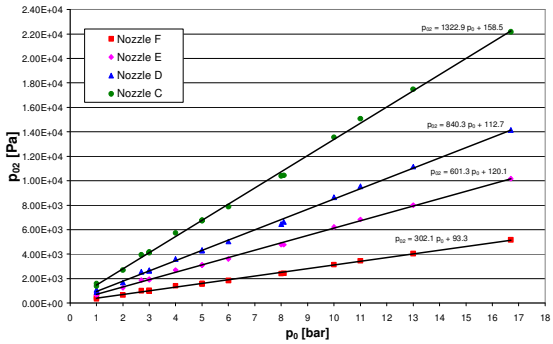

Fig. 19 – p_{02} vs p_0 at the exit sections of the different nozzles for any selected condition

4. CONCLUSIONS

In the present paper, the facility modifications requested in order to have Scirocco Plasma Wind Tunnel ready to be the main on-ground test facility for Aurora ESA Program are presented and discussed. Both goals, i.e. to have a big facility simulating the Mars entry conditions and the Earth super-orbital re-entry conditions, are achievable through a set of engineering modifications and solutions of which the impacts and the costs and the time schedule have been identified.

Actually the ESA Agency is evaluating the feasibility study and results, the relative costs and the schedule. A decision for the following operative phase resulting in the realization of the modification judged necessary and mandatory will be taken within short time.

5. REFERENCES

1. ExoMars09 DM, *Mars Exobiology Descent Module, CFD Study report*, CFD-14(C), ESA-ESTEC, December 2002.

2. ESTEC Contract No 19501/05/NL/EK.

3. Vincent Marieu, Philippe Reynier, Lionel Marraffa, Evaluation of SCIROCCO's capabilities to entry simulations in CO_2 atmospheres.

4. NASA-GLENN CHEMICAL EQUILIBRIUM PROGRAM CEA2, McBride B. J. and Gordon S., May 21, 2004.

5. Park C., "Nonequilibrium Hypersonic Aerothermodynamics", John Wiley & Sons, 1990.

6. Park C., "Review of Chemical-Kinetic Problems of Future NASA Missions, I Earth Entries", Journal of Thermophysics and Heat transfer, Vol. 7, No 3, pp 385-398, 1993.

7. Park C., Howe J. T., Jaffe R. L., Chandler G. V., "Review of Chemical-Kinetic Problems of Future NASA Missions, II Mars Entries", Journal of Thermophysics and Heat transfer, Vol. 8, No 1, pp 9-23, 1994.

8. Park C., Jaffe R. L., Partridge H., "Chemical-Kinetic Parameters of Hyperbolic Earth Entry", Journal of Thermophysics and Heat Transfer, Vol. 15, No 1, January-March 2001.

RE-ENTRY DYNAMICS OF UNCONTROLLED MARS PROBE

S. Skorokhod
Moscow Institute of Physics and Technology,
Dolgoprudnij, Moscow region 141700, Russia
skorohod-sergey@yandex.ru

Landing of the number of small probes on the surface of Mars is the great opportunity to explore his geology and atmosphere on big territory simultaneously. These probes should be simple enough to decrease the project expenses.
Therefore it looks reasonable to use uncontrolled ballistic descent during the probes' landing. But in this case it is necessary to understand well the re-entry dynamics and, in particular, the features of the probe's attitude motion.

Taking into account, we investigated the uncontrolled ballistic descent of probe with the special emphasis on its attitude dynamics. It was supposed that the mass distribution inside and the shape of the probe are axially symmetrical, the aerodynamic damping is negligible.

In general the probe's angular motion can be described as the regular precession with imposed oscillations (so called nutational oscillations). To specify the regular precession it is convenient to use the quantities (W, Θ), where W is the angular velocity of probe's axis of dynamic symmetry, Θ is the angle between this axis and the velocity vector of the probe's mass center. One more motion parameter is the amplitude of the nutational oscillations c.

The influence of aerodynamic torque causes the evolution of the attitude motion parameters. To study this evolution we applied semianalytic approach, based on numeric integration of mass center motion equations and analytic treatment of the averaged attitude motion equations.

As an example we presented in Fig. 1 the deformation of the grid in the space of the regular precession parameters. This grid has regular structure at the initial moment of time and the shown complex structure at the moment of maximum of aerodynamic torque. The regions where an increase of amplitude of nutational oscillations takes place are shaded.

The developed semianalytic approach allows to accelerate substantially the studies of uncontrolled re-entry dynamics.

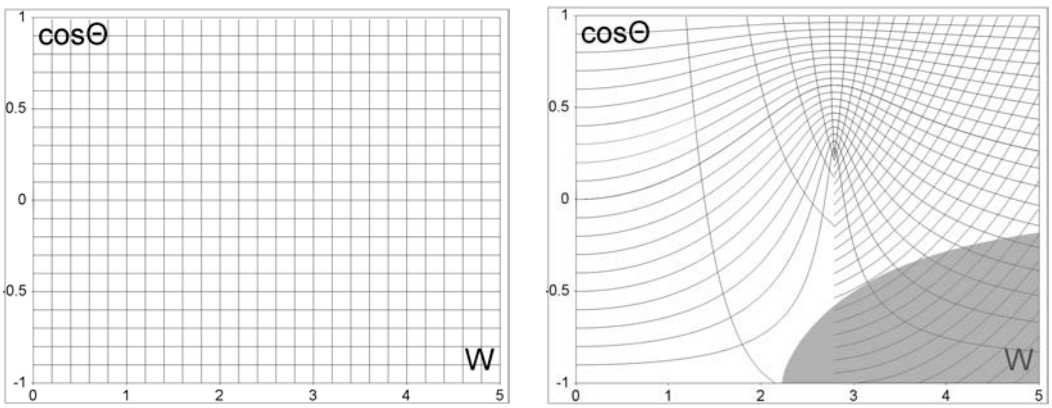

Fig. 1.

Summary of Ultralightweight Ballute Technology Advances

Jim Masciarelli (Ball Aerospace & Technologies Corp., 1600 Commerce St., Boulder CO 80301, 303-939-5146, jmasciar@ball.com)

Kevin Miller (Ball Aerospace & Technologies Corp., 1600 Commerce St., Boulder CO 80301, 303-939-6550, klmiller@ball.com)

Ultralightweight ballutes offer the potential to provide aerodynamic deceleration for space science and exploration missions that require entry or aerocapture at without high heating rates on the host spacecraft, and with much lower mass than traditional technologies. This innovative concept involves deployment of a large, lightweight, inflatable aerodynamic decelerator (ballute) whose large drag area allows the spacecraft to decelerate at very low densities high in the target planet's atmosphere with relatively low heating rates. Because the vehicle using the ballute decelerates at much higher altitude, the peak heating rate is significantly lower than for entry using a traditional lunar return capsule. The lower heating rates experienced during atmospheric entry allows the use of lightweight construction techniques for the ballute, resulting in significant mass performance advantages.

Key technical challenges associated with ultralightweight ballute technology include materials survivability, techniques for ballute construction, packaging, and deployment, flow stability, aeroelastic stability, and trajectory control. A team consisting of Ball Aerospace, ILC Dover, Georgia Tech, NASA Langley, NASA JSC, and the Jet Propulsion Laboratory has been working to advance this technology over the past few years under funding provided by NASA's In-Space Propulsion Program, and NASA's Exploration Systems Research and Technology Program. This presentation summarizes the work accomplished to advance this technology.

AN APPROACH TO SIZING A DUAL-USE BALLUTE SYSTEM FOR AEROCAPTURE, DESCENT, AND LANDING

Kristin L. Gates Medlock[(1)] and James M. Longuski[(2)],
[(1)] *Doctoral Candidate, Purdue University, Aeronautics & Astronautics, West Lafayette, IN 47907-2023, USA*
Email: gatesk@purdue.edu
[(2)] *Professor, Purdue University, Aeronautics & Astronautics, West Lafayette, IN 47907-2023, USA*
Email: longuski@ecn.purdue.edu

ABSTRACT

A dual-use ballute system for aerocapture and descent at the atmosphere-bearing planets and at Titan may provide significant performance benefits. The ballute's large area-to-mass ratio allows the vehicle to stay high in the atmosphere where the heating rate is low. Once the desired velocity change is achieved, the ballute is released allowing the orbiter to continue on its capture orbit, while the ballute/lander (or ballute/probe) descends to the denser regions of the atmosphere.

Sizing of the dual-use ballute is driven by several factors including the target orbit, ballute material limits, and the planetary atmosphere. Using Vinh's analytic theory for aerocapture and ballistic fly-through trajectories, we present an expression for the maximum heating rate as a function of velocity, atmospheric density, scale height, nose radius, and ballistic coefficient. Once we specify a capture trajectory, the maximum heating-rate expression is used to determine the approximate size (i.e. the ballistic coefficient) of the ballute. We test the accuracy of our sizing algorithm for aerocapture and descent trajectories at Mars, Titan, Neptune, and Earth.

NOMENCLATURE

A	=	aerodynamic reference area, m^2
C_B	=	ballistic coefficient, kg/m^2
C_D	=	aerodynamic drag coefficient
g	=	gravitational acceleration, m/s^2
h_e	=	reference (entry) altitude, m/s^2
m	=	mass, kg
Q	=	heating rate, W/cm^2
R	=	radius of the atmosphere, km
R_n	=	nose radius, m
r	=	radial distance, km
t	=	time, s
v	=	speed, km/s
v_c	=	circular speed, km/s
v_e	=	entry speed, km/s
x	=	non-dimensional speed variable
Z	=	non-dimensional altitude variable
α	=	non-dimensional speed ratio parameter
β	=	inverse scale height, km^{-1}
ϕ	=	non-dimensional flight path angle variable
γ	=	flight path angle, deg
ρ	=	atmospheric density, kg/m^3
ρ_e	=	reference atmospheric density, kg/m^3

1. INTRODUCTION

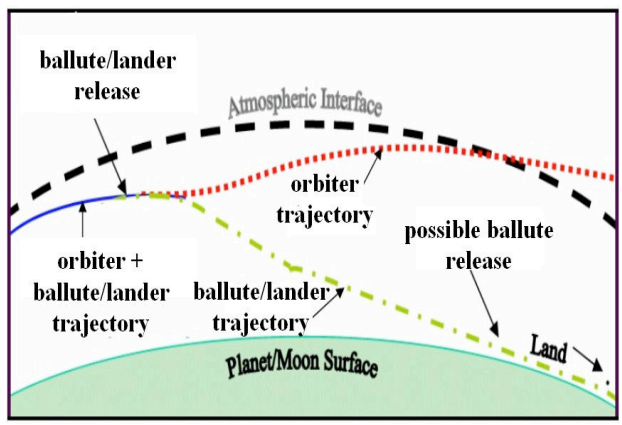

Fig. 1. Dual-Use Ballute Schematic

Because of performance advantages and mass savings potential, a significant amount of research has been carried out to investigate the feasibility of different ballute systems and missions. A systems level study of ballutes for aerocapture at several planetary bodies has been conducted by McRonald [1,2] and an extensive review of ballute technology is provided by Hall [3]. K. Miller et al. [4] characterize and refine the use of ballutes for future aerocapture missions and the Inspace Propulsion group at Marshall Spaceflight Center has published a paper on inflatable decelerator investments [5]. Recent studies by Lyons and McRonald [6] and Medlock et al. [7] present preliminary studies on the feasibility of using dual-use ballute systems at Mars, Titan, and Neptune.

2. VINH'S SECOND-ORDER THEORY FOR BALLISTIC AEROCAPTURE TRAJECTORIES

We make use of Vinh's second-order theory for ballistic aerocapture trajectories [8] to analyze dual-use ballute trajectories. To size the ballute, we derive a transcendental expression for the maximum heating rate as a function of ballistic coefficient and entry trajectory.

Dual-use ballute studies have shown that the ballute/lander is typically released shortly after peak conditions (i.e. when heating, deceleration, and dynamic pressure have already reached their maximums). Because the descent trajectory does not produce heating rates larger than those prior to release, we do not examine the trajectory after release. Instead, we employ Vinh's capture theory for (a worst-case) analysis of the entire dual-use ballute system. Next we present a brief review of the analytical capture theory, details of which can be found in Refs.8 and 9.

Vinh et al. [8,10] give the following planar equations of motion for a non-rotating planet:

$$\frac{dr}{dt} = v\sin\gamma \tag{1}$$

$$\frac{dv}{dt} = \frac{-D}{m} - g\sin\gamma \tag{2}$$

$$\frac{d\gamma}{dt} = -\frac{1}{v}\left(g - \frac{v^2}{r}\right)\cos\gamma \tag{3}$$

The atmosphere is assumed the be locally exponential and is given by

$$d\rho = -\beta(r)\rho dr \tag{4}$$

The assumptions given in Eqs. (5)–(6) are applied to Eqs. (1)–(3),

$$\begin{aligned} g(r) &\approx g(R) \\ \frac{v^2}{r} &\approx \frac{v^2}{R} \end{aligned} \tag{5}$$

$$-g\sin\gamma = 0 \tag{6}$$

resulting in the simplified equations of motion presented in Eqs. (7)–(9).

$$\frac{dr}{dt} = v\sin\gamma \tag{7}$$

$$\frac{dv}{dt} = \frac{-\rho S C_d v^2}{2m} \tag{8}$$

$$\frac{d\gamma}{dt} = -\frac{1}{v}\left(g - \frac{v^2}{R}\right)\cos\gamma \tag{9}$$

Vinh uses the non-dimensional variables given in Eqs. (10)–(12), representing altitude, flight path angle, and speed, respectively.

$$Z = \rho S C_D m^{-1}\left(R/\beta\right)^{1/2} \tag{10}$$

$$\phi = -\left(\beta R\right)^{1/2}\sin\gamma \tag{11}$$

$$x = \log\left(v_e^2/v^2\right) \tag{12}$$

An additional non-dimensional variable, α, specifies the type of entry orbit (i.e. hyperbolic: α < 0.5, parabolic: α = 0.5, elliptic: α > 0.5).

$$\alpha = gR/v_e^2 = v_c^2/v_e^2 \tag{13}$$

Dividing the time derivatives of Eqs. (10) and (11) by the time derivative of Eq. (12) and applying the small angle approximation in Eq. (14),

$$\left(\cos\gamma \approx 1\right) \tag{14}$$

provide equations of motion

$$\frac{dZ}{dx} = \phi \tag{15}$$

$$\frac{d\phi}{dx} = \left(\alpha e^x - 1\right)Z^{-1} \tag{16}$$

with initial conditions

$$\begin{aligned} &x = 0, \\ &Z(0) = \varepsilon = \rho_e S C_D m^{-1}\left(R/\beta\right)^{1/2}, \\ &\phi(0) = c = -\left(\beta R\right)^{1/2}\sin\gamma_e \end{aligned} \tag{17}$$

To facilitate integration by use of Poincare's method of artificially inserting a small parameter, a final change of variables is made,

$$y = Z/\varepsilon \tag{18}$$

$$\tau = x/\varepsilon \tag{19}$$

$$d(\ )/d\tau = (\ )' \tag{20}$$

to get Eqs. (21) and (22),

$$y' = \phi \tag{21}$$

$$\phi' = \left(\alpha e^{\varepsilon\tau} - 1\right)/y \tag{22}$$

with initial conditions,

$$\tau = 0,\ \ y(0) = 1,\ \ \phi(0) = c \tag{23}$$

Using drag parameter ε, we look for solutions of the form:

$$\begin{aligned} y &= y_0 + \varepsilon y_1 + \varepsilon^2 y_2 + \ldots \\ \phi &= \phi_0 + \varepsilon\phi_1 + \varepsilon^2\phi_2 + \ldots \end{aligned} \tag{24}$$

with initial conditions

$$\begin{aligned} &y_0(0) = 1,\ \ y_1(0) = y_2(0) = \ldots = 0 \\ &\phi_0(0) = c,\ \ \phi_1(0) = \phi_2(0) = \ldots = 0 \end{aligned} \tag{25}$$

Substituting Eq. (24) into Eqs. (15) and (16) and equating like terms of ε, gives the following system of equations:

$$y_0' = \phi_0 \tag{26}$$

$$\phi_0' = -(1-\alpha)\, y_0^{-1} \tag{27}$$

$$y_1' = \phi_1 \tag{28}$$

$$\phi_1' = (1-\alpha)\, y_1 y_0^{-2} + \alpha\tau y_0^{-1} \tag{29}$$

$$y_2' = \phi_2 \tag{30}$$

$$\begin{aligned} \phi_1' = {} & (1-\alpha)\, y_2 y_0^{-2} - \alpha\tau y_1 y_0^{-2} \\ & + \frac{1}{2}\alpha\tau^2 y_0^{-1} - (1-\alpha)\, y_1^2 y_0^{-3} \end{aligned} \tag{31}$$

After some labor, solutions for the 0th, 1st, and 2nd order systems are obtained. (See references 1 and 2 for details).

1.1. Zero-Order Analytic Solutions

The independent variable ϕ_0 (representing the zero-order flight path angle) monotonically increases from its initial value c. The zero-order solution for the altitude variable, y, is

$$y_0 = \exp\left[\left(c^2 - \phi_0^2\right)/\delta\right] \tag{32}$$

where

$$\delta = 2(1-\alpha) \tag{33}$$

represents the entry speed. The analytical expression for τ, representing the speed variable is

$$\tau = \sqrt{\frac{\pi}{\delta}}\exp\left(\frac{c^2}{\delta}\right)\left[erf\left(\frac{c}{\sqrt{\delta}}\right) - erf\left(\frac{\phi_0}{\sqrt{\delta}}\right)\right] \tag{34}$$

where the error function is defined as

$$erf(x) = 2\pi^{-1/2}\int_0^x e^{-t^2}\,dt \tag{35}$$

1.2. First-Order Analytic Solutions

The first-order solution coefficients for y and ϕ are

$$y_1 = 2\alpha\delta^{-2}\phi_0 + 2\alpha\delta^{-2}k\left(y_0 - \phi_0\tau\right) \tag{36}$$

$$\phi_1 = \alpha\delta^{-1}(k\tau - 1)\, y_0^{-1} + \alpha\delta^{-1}\left(y_0 - \phi_0\tau\right) \tag{37}$$

where,

$$k = (1-\alpha)\tau - c \tag{38}$$

1.3. Second-Order Analytic Solutions

The second-order solution coefficients for y and ϕ are

$$\begin{aligned} y_2 &= 2\alpha\delta^{-3}\left(y_0-\phi_0\tau\right)\left[\left(1+\alpha\right)+\left(1-\alpha\right)\tau^2\right] \\ &+\alpha\delta^{-3}\phi_0\tau\left[\alpha+\left(\delta/6\right)\left(\alpha+2\right)\tau^2\right] \\ &-\alpha\delta^{-3}\left(\alpha+2\right)y_0^3-\alpha^2\delta^{-3}\left(k\tau-1\right)^2 y_0^{-1} \\ &+\alpha\delta^{-2}ky_1-6\alpha\delta^{-4}\left(\alpha+2\right)\phi_0\left[K\left(\phi_0\right)-K\left(c\right)\right] \end{aligned} \tag{39}$$

$$\begin{aligned} \phi_2 &= 2\alpha\delta^{-2}\left(y_0-\phi_0\tau\right)\tau \\ &+\alpha\delta^{-3}\phi_0\left[\alpha+\left(1+\alpha\right)\left(\alpha+2\right)\tau^2\right] \\ &+\left(\delta/6\right)\delta^{-2}\tau y_0^{-1}\left[3\left(\alpha+2\right)+\left(1-\alpha\right)\left(4-\alpha\right)\tau^2\right] \\ &+\alpha^2\delta^{-3}\left(k\tau-1\right)^2\phi_0 y_0^{-2}+\left(\alpha/2\right)\delta^{-1}y_1+\alpha\delta^{-2}k\phi_1 \\ &-2\alpha^2\delta^{-3}\left(k\tau-1\right)y_0^{-1}\left[k+\left(1-\alpha\right)\tau\right] \\ &+3\alpha\delta^{-3}\left(\alpha+2\right)y_0^{-1}\left[K\left(\phi_0\right)-K\left(c\right)\right] \end{aligned} \tag{40}$$

where,

$$K\left(\phi_0\right)=\left(\delta\pi/12\right)^{1/2}\exp\left(3c^2/\delta\right)erf\left[\left(3/\delta\right)^{1/2}\phi_0\right] \tag{41}$$

3. THE HEATING CONSTRAINT

Stagnation-point heating rate during atmospheric flight is calculated by,

$$Q_{stag}=\frac{C\rho^{Nstag}v^{Mstag}}{\sqrt{R_n}} \tag{42}$$

(similar to the Sutton-Graves convective heating equation [11]). In Eq. (42), N_{stag} and M_{stag} are the density and velocity coefficients (typical values of N_{stag} = 0.5 and M_{stag} = 3.0 are used for this study), and C is the stagnation point heating coefficient. The stagnation-point heating coefficient (C) varies according to the planet. We use 9.748 x 10^{-5}, 9.80 x 10^{-5}, 9.00 x $10^{-5}$and 3.54 x 10^{-5} $kg^{0.5}/m$ for Earth, Mars, Titan and Neptune, respectively. The R_n of the ballute/lander is calculated assuming a spherical ballute.

Eq. (42) can be written as

$$Q_{stag}=C_H\left(\frac{\rho}{\rho_e}\right)^{1/2}\left(\frac{v}{v_e}\right)^3 \tag{43}$$

where

$$C_H=C\left(\frac{\rho_e}{R_n}\right)^{1/2}v_e^3 \tag{44}$$

From Eqs. (10), (12), (18), and (19), we see that,

$$\frac{\rho}{\rho_e}=y \tag{45}$$

and

$$\frac{v}{v_e}=e^{-\tau\varepsilon/2} \tag{46}$$

Substituting Eqs. (45) and (46) into Eq. (43) gives an expression for stagnation point heating rate as a function of the nondimensional variables y, τ, and ε (representing altitude, speed, and ballistic coefficient, respectively):

$$Q_{stag}=C_H y^{1/2}e^{-3\tau\varepsilon/2} \tag{47}$$

To evaluate conditions at the point of maximum instantaneous heating rate, we differentiate Eq. (47) with respect the speed variable τ .

$$\frac{d\left(Q_{stag}\right)}{d\tau}=0=\frac{C_H}{2}\left[y'y^{-1/2}e^{-3\tau\varepsilon/2}-3\varepsilon y^{1/2}e^{-3\tau\varepsilon/2}\right] \tag{48}$$

Recalling that $y'=\phi$, Eq. (48) simplifies to

$$\phi=3\varepsilon y \tag{49}$$

Eq. (49) provides the key that relates the speed variable, flight path angle variable, and ballistic coefficient at the point of peak heating. Substituting this equation into the nondimensional heating rate expression, in Eq. (47), gives an equation for maximum heating rate as a function of ϕ_0 :

$$Q_{stag,\max}=C_H\left(\frac{\phi}{3\varepsilon}\right)^{1/2}e^{-3\tau\varepsilon/2} \tag{50}$$

In order to solve for ϕ in Eq. (50), we derive an expression for ϕ_0, at the point of peak heating. Using Eq. (49) and the zero-order solution for y given in Eq.

(32), we obtain an implicit (or transcendental) expression for ϕ_0:

$$\phi_0 = 3\varepsilon y_0 = 3\varepsilon y_0 \, \mathrm{e}^{c^2/\delta} \, \mathrm{e}^{-\phi_0^2/\delta} \tag{51}$$

Using the approximation,

$$\mathrm{e}^{-\phi_0^2/\delta} \approx 1 - \frac{\phi_0^2}{\delta} \tag{52}$$

we obtain an explicit expression for ϕ_0:

$$\phi_0 = \frac{-\delta}{6\varepsilon}\left[\mathrm{e}^{-c^2/\delta} - \sqrt{\mathrm{e}^{-2c^2/\delta} - \frac{36\varepsilon}{\delta}}\right] \tag{53}$$

We can now use Eq. (53) with Eqs. (32)–(41) and Eq. (24) to obtain 0th, 1st, and 2nd order solutions for y and ϕ at the point of peak heating in terms of the ballistic coefficient (represented by ε) and the entry conditions (α, representing entry speed, and c, representing entry flight path angle). Depending on the desired accuracy, any order of the ϕ solution can be used in Eq. (49) to determine the appropriate ballute size (ε value) for a given maximum heating rate limit.

4. NUMERICAL RESULTS

In this section we consider the problem of sizing the ballute for missions at Earth, Mars, Titan , and Neptune [4,12-16] with a wide range of entry conditions and allowable heating rates. Although the analysis depends on the ballistic coefficient, we provide (in Table 1) some specific values for a typical dual-use ballute system in which the ballute area may range from 500-3000 m^2.

Table 1 Vehicle Parameters for Dual-Use Ballute Simulations at Earth, Mars, Titan and Neptune.

Parameter	Orbiter	Ballute/Lander
m	400 kg	100 kg
C_D	1.37	1.37
A	2 m^2	500–3000 m^2 *
R_n	0.8 m	15.5 m
C_B	$m/(C_D A)$	0.730–0.122 kg/m^2

* Representative of the ballistic coefficient range used.

The range of entry speeds examined at Earth, Mars, Titan, and Neptune are adapted from previous studies [6, 12–15] and are displayed in Table 2.

Table 2 Entry Conditions and Atmospheric Constants at Earth, Mars, Titan, and Neptune.

Condition	Earth	Mars	Titan	Neptune
βR	900	350	56	441
reference density, kg/m^2	2.22e-8	4.73e-10	7.52e-10	1.48E-14
Entry/Exit Altitude, km	120	150	1025	1500
Inertial Entry Speeds, km/s	12.9	5.75–11	6.5–10	23.6

For this particular study, we are concerned only with the segment of the trajectory prior to release of the ballute/lander (this is the time during which the maximum heating rate occurs).

We choose an entry flight path angle that targets a circular orbit at exit (assuming the ballute/lander is not released). Because the target apoapsis altitude of the orbiter is higher than that of the chosen circular exit orbit, the ballute/lander will be released inside the atmosphere and continue its descent. This method allows the vehicle to dive deep enough to accommodate navigation and atmospheric uncertainties while maintaining a high enough trajectory to keep the heating rates low.

The altitude variable is represented by the dimensionless density y, normalized with respect to the density at the entry altitude (ρ_e). The variation of the linear altitude h is provided through y:

$$\beta\left(h - h_e\right) = \beta\Delta h = -\log y \tag{54}$$

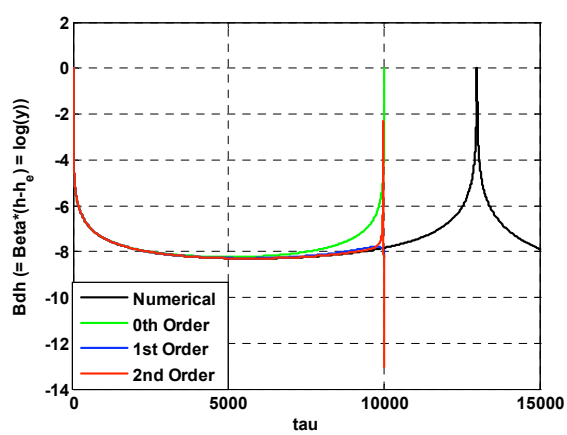

Fig. 1. Variation of Linear Altitude vs. Representative Speed Variable (τ).

In our first case we consider a Martian entry with an entry velocity of 5.75 km/s. The analytic solutions in Fig. 1 show excellent agreement (with the numerical integration of Eqs. (15) and (16)) through the critical segment of the trajectory, but underestimates the total velocity lost prior to exiting the atmosphere . This discrepancy is partially attributed to the small angle approximation made during derivation of the analytic solutions, and is expected to increase with the steepness of the entry angles.

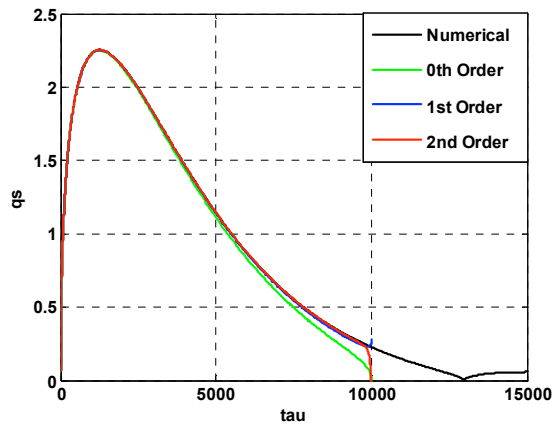

Fig. 2. Stagnation Point Heating Rate vs. Representative Speed Variable, τ, at Mars with v_e = 5.75 km/s.

Fig.2 displays the heating rates continuously calculated using the 0th, 1st, and 2nd order analytic solutions along with the heating profile obtained through numerical integration. Again, the analytic solutions show excellent agreement throughout the crucial portion of the trajectory, just slightly underestimating the peak heating rate.

Next, we evaluate the accuracy of Eqs. (50) and (53) in predicting the maximum heating rate. Tables 3–7 provide errors for the predicted heating rate for varying entry speeds at both Mars and Titan. As entry speed, at either planet, increases (resulting in a steeper entry) the percent error of the analytic heating expression increases due in part to the truncation error in Eq. (52). (Here we note that a more accurate prediction may be possible by solving the transcendental Eq. (51) for ϕ_0, where the explicit solution Eq. (53) provides a useful first guess.) We show only the 0th order heating rate errors in Tables 3–7 because the higher order errors are nearly indistinguishable from the 0th order. For example, in Table 5 for the case C_B = 0.12 kg/m^2, the heating rate errors for 0th, 1st, and 2ne order ar 11.83%, 11.80%, and 11.80%, respectively. (Again, a better prediction may be obtained by solving the transcendental expression in Eq. (52).

Table 3 Zero-Order Heating Rate Error for Mars, v_e= 5.75 km/s, α= 0.37, m = 500 kg, C_D= 1.37

C_B [kg/m^2]	A [m^2]	R_n [m]	ε *10^{-4}	γ_e [deg]	Heating Rate Error %
0.73	500	12.6	1.23	-9.50	2.60%
0.49	750	15.5	1.84	-9.23	2.59%
0.36	1000	17.8	2.46	-9.04	2.60%

Table 4 Zero-Order Heating Rate Error for Mars, v_e= 7.00 km/s, α= 0.25, m = 500 kg, C_D= 1.37

C_B [kg/m^2]	A [m^2]	R_n [m]	ε *10^{-4}	γ_e [deg]	Heating Rate Error %
0.49	750	15.5	1.84	-10.40	4.24%
0.36	1000	17.8	2.46	-10.20	4.28%
0.24	1500	21.9	3.69	-9.91	4.28%

Table 5 Zero-Order Heating Rate Error for Mars, v_e= 11.0 km/s, α= 0.10, m = 500 kg, C_D= 1.37

C_B [kg/m^2]	A [m^2]	R_n [m]	ε *10^{-4}	γ_e [deg]	Heating Rate Error %
0.49	750	15.5	1.84	-11.88	11.62%
0.24	1500	21.9	3.69	-11.36	11.64%
0.12	3000	30.9	7.37	-10.83	11.83%

Table 6 Zero-Order Heating Rate Error for Titan, v_e= 6.75 km/s, α= 0.06, m = 500 kg, C_D= 1.37

C_B [kg/m^2]	A [m^2]	R_n [m]	ε *10^{-4}	γ_e [deg]	Heating Rate Error %
0.49	750	15.5	7.43	-29.28	16.91%
0.24	1500	21.9	14.9	-27.70	16.97%

Table 7 Zero-Order Heating Rate Error for Titan, v_e= 10.0 km/s, α= 0.02, m = 500 kg, C_D= 1.37

C_B [kg/m^2]	A [m^2]	R_n [m]	ε *10^{-4}	γ_e [deg]	Heating Rate Error %
0.49	750	15.5	7.43	-30.66	25.88%
0.36	1000	17.8	9.91	-30.00	25.85%
0.24	1500	21.9	14.9	-29.05	25.77%
0.12	3000	30.9	29.7	-27.39	25.77%

Fig. 3 plots the ballistic coefficient (calculated using the area of the ballute) plotted against the maximum stagnation point heating rate of the ballute (calculated

using an R_n that varies with the ballute size). Similarly, Fig. 4 provides values for the orbiter (R_n = 0.8 m^2). Assuming a maximum heating limit of 5 W/cm^2 on the ballute, Fig. 3 indicates that any of the ballute sizes shown will work (the most cost effective, of course, being the smallest). However, applying the same heating limit to the orbiter, Fig.4 shows that only the lowest of the entry velocity cases at Mars and Titan stay within the limit (for the sizes plotted), suggesting that a thermal protection system (TPS) may be required on the orbiter. It is interesting to note that the cases for Titan with v_e = 6.50 km/s and Mars with v_e = 5.75 km/s follow nearly the same contour.

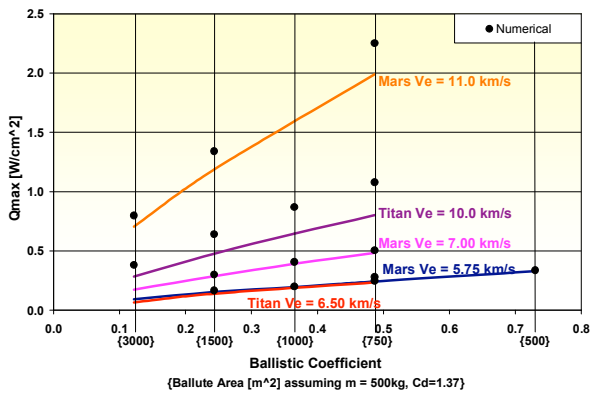

Fig. 3. Maximum Stagnation Point Heating Rate (on Ballute) vs. Ballistic Coefficient

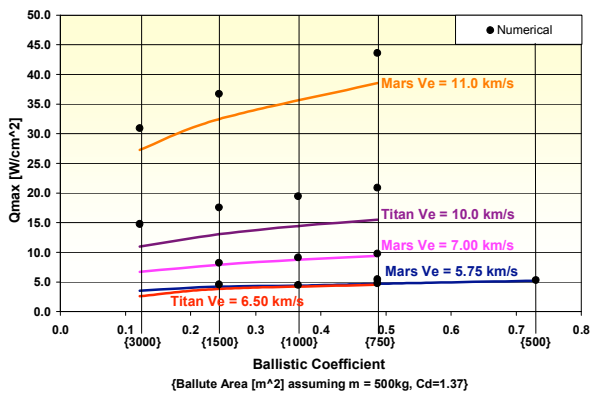

Fig. 4. Maximum Stagnation Point Heating Rate (on Orbiter) vs. Ballistic Coefficient

Numerical and analytical results for missions to Neptune and return missions to the Earth (e.g. from the Moon) indicate heating error trends similar to those at Mars and Titan. For instance, a case at Neptune (v_e = 23.6 km/s) with an entry angle of -10° has less than 1% error, whereas a case with the same entry velocity and an entry angle of -11° has a 15% error.

5. CONCLUSIONS

It appears that the zero-order theory gives adequate results to predict the maximum heating rate, when compared to the first- and second-order results. Using the analytic solution in the zero-order theory, we found an underestimation ranging from -0.002 W/cm^2 (best Mars case) to -0.120 W/cm^2 (worst Titan case) for heating on the ballute and from -0.140 W/cm^2 to -4.41 W/cm^2 for heating on the orbiter (with A = 2 m^2). The less hyperbolic the entry speed (and likewise, the shallower the entry angle for a specified target orbit), the more accurate the explicit theory is. It is expected that the implicit expression will provide more accurate results.

For practical ballute sizes, dual-use ballute concept appears feasible at Mars, Titan, and Earth. As shown in earlier work, dual-use ballute aerocapture and descent at Neptune is highly challenging in that a very large ballute for a given mass, may be required.

Overall, the dual-use ballute concept promises tremendous potential for exploration of atmosphere bearing bodies in the Solar System.

6. ACKNOWLEDGEMENTS

The work described in this paper was funded by NASA's Graduate Student Research Program (GSRP) awarded by Marshall Space Flight Center in Huntsville, Ala. We would particularly like to thank Bonnie James at MSFC for her support. Also, we would like to thank Mohammad Ayoubi (a doctoral candidate at Purdue University) for his assistance.

7. REFERENCES

1. McRonald, A. D., "A Light-Weight Inflatable Hypersonic Drag Device for Planetary Entry," Association Aeronautique de France Conf. at Arcachon France, March 16-18, 1999.

2. McRonald, A. D., "A Light-Weight Hypersonic Inflatable Drag Device for a Neptune Orbiter," AAS/AIAA Space Flight Mechanics Meeting, Clearwater, FL, AAS Paper 00-170, Jan. 23-26, 2000.

3. Hall, J. L., "A Review of Ballute Technology For Planetary Aerocapture," 4th IAA Conference on Low Cost Planetary Missions, Laurel, MD, May 2-5, 2000.

4. Miller, K. L., Gulick, D., Lewis, J., Trochman, B., Stein, J., Lyons, D. T., and Wilmoth, R., "Trailing

Ballute Aerocapture: Concept and Feasibility Assessment," 39th AIAA/ASME/ASEE Joint Propulsion Conference and Exhibit, Huntsville, AL, AIAA Paper 2003-4655, July 20-23, 2003.

5. Richardson, E. H., Munk, M. M., James, B. F., Moon, S. A., "Review of NASA In-Space Propulsion Technology Program Inflatable Decelerator Investments," 18th AIAA Aerodynamic Decelerator Systems Technology Conference and Seminar, Munich, Germany, AIAA Paper 2005-1603, May 23-26, 2005, pp.1-6.

6. Lyons, D. T., and McRonald, A. D., "Entry, Descent and Landing using Ballutes," Presentation at 2nd International Planetary Probe Workshop, NASA Ames Research Center, Moffet Field, CA, Aug. 2004.

7. Medlock, K. Gates, Longuski, J. M., and Lyons, D. T., "A Dual-Use Ballute for Entry and Descent During Planetary Missions," 3rd International Planetary Probe Workshop, Attica, Greece, June 27-July 1, 2005.

8. Vinh, N. X., Johannesen, J. R., Longuski, J. M., and Hanson, J. M., "Second-Order Analytic Solutions for Aerocapture and Ballistic Fly-Through Trajectories," The Journal of the Astronautical Sciences, Vol. 32, No. 4, Oct.-Dec. 1984.

9. Medlock, K. L. Gates, Ayoubi, M. A., Longuski, J. M., and Lyons, D. T., "Analytic Solutions for Aerocapture, Descent, and Landing Trajectories for Dual-Use Ballute Systems," To be presented at the AIAA/AAS Astrodynamics Conference, Keystone, Colorado, American Institute of Aeronautics and Astronautics, AIAA Paper 2006-6026, Aug. 2006.

10. Vinh, N.X., Busemann, A., Culp, R. D., "Hypersonic and Planetary Entry Flight Mechanics," The University of Michigan Press, Ann Arbor, MI, 1980.

11. Sutton, K. and Graves, R. A., Jr., "A General Stagnation Point Convective Heating Equation for Arbitrary Gas Mixtures," NASA TR R-376, NASA Langley Research Center, Hampton, VA, Nov. 1971.

12. Lyons, D. T. and Johnson, W. R., "Ballute Aerocapture Trajectories at Neptune," AIAA Atmospheric Flight Mechanics Conference and Exhibit, Providence, RI, AIAA Paper 2004-5181, Aug. 16-19, 2004.

13. Lyons, D. T. and Johnson, W. R., "Ballute Aerocapture Trajectories at Titan," *Advances in the Astronautical Sciences*, Vol. 116, Suppl. pp. 1-20, 2004.

14. Hall, J. L. and Le, A. K., "Aerocapture Trajectories for Spacecraft with Large, Towed Ballutes," 11th Annual AAS/AIAA Space Flight Mechanics Meeting, Santa Barbara, CA, AAS 01-235, Feb. 11-15, 2001.

15. Westhelle, C. H. and Masciarelli, J. P., "Assessment of Aerocapture Flight at Titan Using a Drag-only Device," 2003 AIAA Atmospheric Flight Mechanics Conference and Exhibit, Austin, TX, AIAA Paper 2003-5389, Aug. 11-14, 2003.

16. Vaughan, D., Miller, H. C., Griffin, B., James, B. F., Munk, M. M., "A Comparative Study of Aerocapture Missions with a Mars Destination," 41st AIAA/ASME/SAE/ASEE Joint Propulsion Conference & Exhibit, Tucson, AZ, AIAA Paper 2005-4110, July 10-13, 2005, pp. 1-16.

Submitted to Proceedings of the 4th International Planetary Probe Workshop, Pasadena, CA, June 25-29, 2006

FIELD TESTING AND DYNAMIC MODEL DEVELOPMENT FOR A MARS TUMBLEWEED ROVER*

R. Lorenz[1,3], A.Behar[2], F. Nicaise[2], J.Jonsson[2], M. Myers[1],

[1]Lunar and Planetary Laboratory, University of Arizona, Tucson, AZ 85721, USA.
[2]Robotic Vehicles Group, NASA/Jet Propulsion Laboratory, M/S 107-102, 4800 Oak Grove Dr., Pasadena CA 91109, USA. (3) Now at : Space Department, Johns Hopkins University Applied Physics Lab, 11100 Johns Hopkins Rd., Laurel, MD 20723-6099. email: Ralph.lorenz@jhuapl.edu

ABSTRACT

We present field measurements of the mobility performance of a tumbleweed rover (an instrumented wind-blown sphere) at Willcox Playa, Arizona. Video and GPS data are used, with meteorological stations deployed close enough to correlate motion with the wind. In the thin boundary layer of a desert playa, the drag coefficient is determined to be <0.2. Rolling and bouncing motions are discussed, and the performance of sphere-mounted flexible solar panels is evaluated.

.

1. INTRODUCTION

A Tumbleweed rover [1,2,3,4] is a quasi-spherical vehicle intended to traverse a planetary surface (nominally Mars) with a rolling and/our bouncing motion driven by the wind, much as the 'tumbleweed' or Russian Thistle is driven across the desert (figure 1).

Figure 1. A terrestrial Tumbleweed, highly evolved for mobility. Note that barbed-wire fences are unlikely to be an obstacle on Mars.

* *This work was performed by the Jet Propulsion Laboratory, a division of California Institute of Technology, under contract to NASA.*

As such, its trajectory is largely uncontrollable, but it offers the potential for much longer range surveys than conventional rovers. Two origins have been cited for the concept – inspiration from the bouncing motion of Pathfinder during its airbag landing, and the rapid wind-blown movement of a spherical wheel that had been removed from a rover under test on a playa.

The conventional configuration (figure 2) is spherical by inflation, with an equipment package suspended in the center by tension cords, although we have also explored other arrangements (electronic equipment mounted on the spherical surface). Other workers have explored non-inflated concepts with rigid elements arranged to give a near-spherical shape such as the Dandelion and Kite (e.g. [5]).

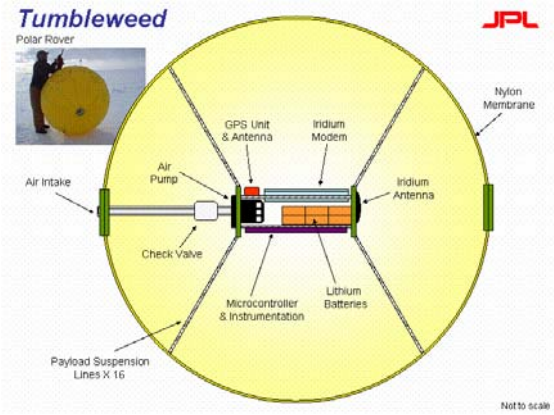

Figure 2. The Tumbleweed configuration used in field tests to date.

2. PRIOR FIELD TESTS AND RATIONALE FOR PRESENT WORK

Previously, several Tumbleweed rovers (e.g. [6]) have been deployed in polar regions, and have demonstrated a level of (unguided) mobility that surpasses that of conventional rovers by several orders of magnitude.

Deployment area, lifetime and distance travelled are as follows:

August 2003, Greenland, 9 days, 131 km
January 2004, South Pole, 7 days, 134 km
May 2004, Greenland, 7 days, 200km

These distances and times indicate an impressive average speed of ~0.3 m/s – almost a factor of 20 lower than the wind speed. Inspection of the GPS data (figure 3) shows that this is because the motion is strongly episodic – once the rover gets moving it moves quickly for a while, then stops, perhaps upon encountering an obstacle. (Additional deployments, not optimised for mobility evaluation, have included an air-drop deployment test in Antarctica.)

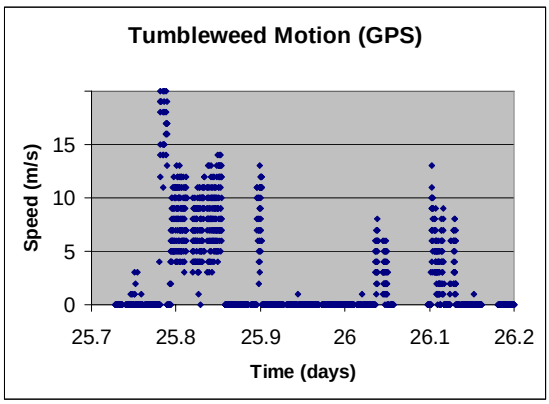

Figure 3. Part of the motion record of the South Pole tumbleweed rover from GPS data. The record is strongly intermittent, with periods of stasis interspersed with rapid movement.

It can be further seen (figure 4) that the episodic nature of the motion is not apparently due to the wind. Several factors confound the correlation of the launch site wind record and the motion history. First, the rover may respond to gusts of a duration too small to be captured in the low-time-resolution meteorological record (which is after all not acquired for this purpose). Second, as the rover moves away from the launch site, a lead or lag-time will be introduced – a gust front moving at, say, 5 m/s will take several hours to traverse the distance between the met station and the rover. Third, local variations in wind due to terrain blockage etc may occur, and slopes will also affect the motion directly. Finally, the inertia of the rover and the thresholding of the motion (perhaps relating to bouncing as well as rolling) introduce nonlinearities in the relation of instantaneous wind and motion speed. It is these issues that we aim to confront with the present tests.

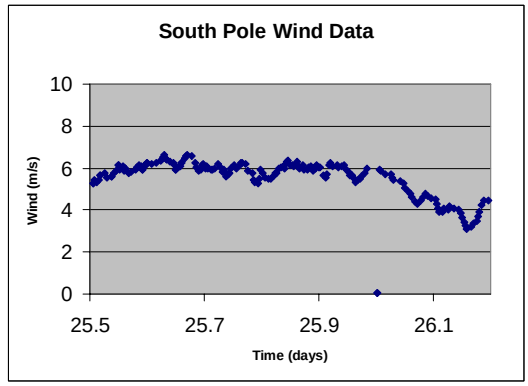

Figure 4. Wind measurements at the South pole, contemporaneous with the motion shown in figure 3. The winds are apparently much more steady than the motion record would indicate.

3. FIELD TESTS

3.1 Field Site

Field Tests were conducted at the Northwestern end of Willcox Playa in Eastern Arizona, about 1hr drive from the University of Arizona. Tests were conducted in February 2006. Our tests were conducted in the northwestern part managed by the Bureau of Land Management.

The site provides easy access, and a large area for rolling. It is of note that natural tumbleweed are found there in abundance.

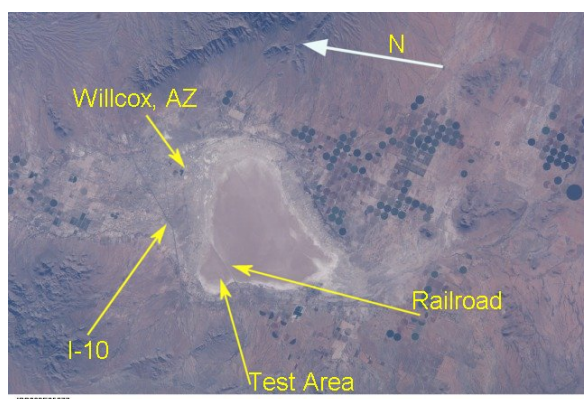

Figure 5. Annotated version of digital image from the International Space Station (image ISS009-E-5677 courtesy of http://eol.jsc.nasa.gov). The majority of the playa is used for military training and is not readily accessible.

3.2 Rover and Mass Properties

Figure 6. Rover in the field. Left to right are authors Nicaise, Behar, Lorenz and Jonsson.

The rover used in the field tests comprises a spherical shell of ballistic nylon with a diameter of 1.83m and a mass of 7.25kg. Its moment of inertia I is therefore 4.05 kgm^2. Suspended on a set of cords is a cylinder (35cm long by 16.5cm diameter) carrying the rover instrumentation and pumps. This cylinder, with a mass of 8.15kg, has axial and transverse moments of inertia of 0.03 and 0.09 kgm^2 respectively. Taking the two items together gives vary similar total moments of inertia of 4.08 and 4.15 kgm^2 - these are sufficiently close that there is no strong preference for axis of rotation : small deformations of the shell can cause larger deviations in I than this difference. Total mass m is 15.4 kg.

The moment of inertia is not negligible in the partitioning of energy between rotational and translational motions. If rolling without skid ($V=\omega R$, R=0.91m) then the translational kinetic energy ($0.5mV^2$) is $7.7V^2$, while the rotational kinetic energy $0.5I\omega^2 = 2.5V^2$ – or in other words the vehicle has ~30% more energy in total than can be attributed to translation alone.

3.3 Meteorological Measurements

We installed two meteorological monitoring instruments in the field, about 50m apart and close to the rolling area of the rover (in one case the rover collided with the monitor). First was a Davis anemometer and weathervane on a tripod, with data sampled by a microcontroller and stored on-board for later download. The second was a three-anemometer array, with anemometers at logarithmically-spaced heights to measure the thickness of the boundary layer.

Experience is such as to recommend as much redundancy in field measurements as is reasonably possible, to accommodate unanticipated effects and attrition in the field. A handheld anemometer was also used, and by reading the display aloud could be captured in the video record to facilitate timetagging. Wind noise on the video record (including a periodic flapping of the tethered wind cap) correlated with wind speed, although a quantitative calibration of this effect has not been attempted as yet.

The anemometer data (with a resolution of a few seconds) correlate well with each other, and thus may be expected to correlate well with the motion of the rover. Careful time-tagging is essential – notice that there is a ~10m periodicity in the windspeed (figure 7).

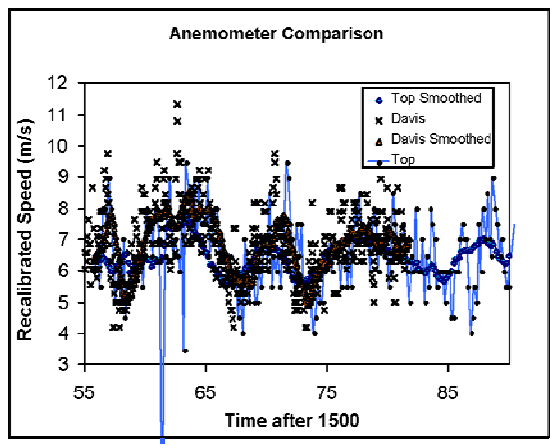

Figure 7. Anemometer records about 50m apart – good correlation is seen. Typical wind speed is ~6.5 m/s.

A plot of the windspeed versus logarithmic height (figure 8) permits a regression of the aerodynamic roughness length, which approximately corresponds to the scale of roughness of the surface. For the playa this is rather small – our data indicate ~0.5cm. (For comparison, the roughness measured the same way at the rocky Pathfinder landing site was some ten times larger. [7])

Thus, in the present experiment, the wind field experienced by the rover can be considered uniform – the boundary layer is so thin that there is only a small (~20%) variation in windspeed from the center of the rover to the top. In rougher environments this will not be the case, and the wind gradient may lead to several effects which may be rather important in influencing the rover's

motion – some aerodynamic lift may be generated, and the shear may cause a rolling moment that may assist the motion.

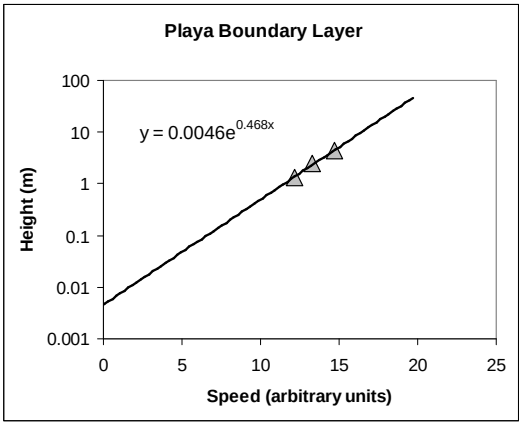

Figure 8. Windspeed vs height, indicating an aerodynamic roughness of only 0.5cm.

3.4 Video Measurements

Although GPS is ideal for large-scale motion studies, on very short timescales a more convenient tracking technique is to use video. A commercial camcorder was set up on a tripod and the onset of Tumbleweed motion was monitored. Video also permits documentation of effects such as whether the vehicle is rolling or bouncing. While the difference in accelerometer readings is very clear [8] between these two modes of travel when data is acquired at ~ 10 times a second, the instrumentation in our field deployments was not sampled as fast).

The video tape was digitized with a USB frame grabber. The resulting windows movie file (.wmv) was converted into a sequence of individual frames (.avi) with Videoconverter software. The .avi sequence was then analyzed with Videopoint software which creates an excel file of pixel positions by clicking a cursor on features to be tracked (this has been previously used by RL to monitor attitude motions of a parachute-borne model of the Huygens probe – [9]) In the fast rolling sequence (1626hrs) the 6ft Tumbleweed was 30 pixels across, yielding a pixel scale of ~6cm/pixel (the motion was essentially orthogonal to the line of sight so the pixel scale did not change). Once it began moving, the Tumbleweed crossed the field of view of the camera in about 15 seconds.

Figure 9. Screenshot from Videpoint software, showing manually-digitized locations in each frame – the acceleration towards the right is evident.

Several different tests were performed, over a period of two days. These include sequences of rolling and bouncing motion, although the latter have not been studied in much detail as yet.

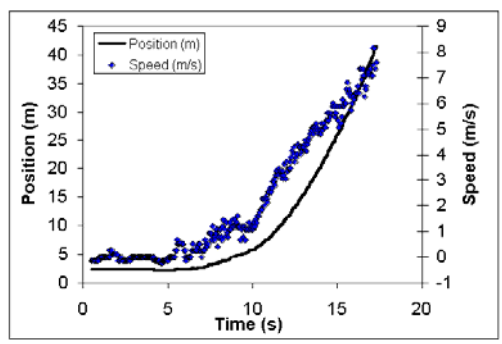

Figure 10. Position vs time, and velocity derived by differencing the positions at each frame step yielding a slightly noisy but high-time-resolution speed record.

It is evident from the appearance of the velocity plot as approximate line segments that there are two distinct phases – the first with a gentle acceleration of 0-1.2 m/s in the first 4.5 seconds of motion (an acceleration of 0.027g), while over the following 7 seconds the acceleration is much higher (0.09g), reaching 7.5 m/s. The speed determined by video agrees rather well with the GPS-determined speed (figure 11).

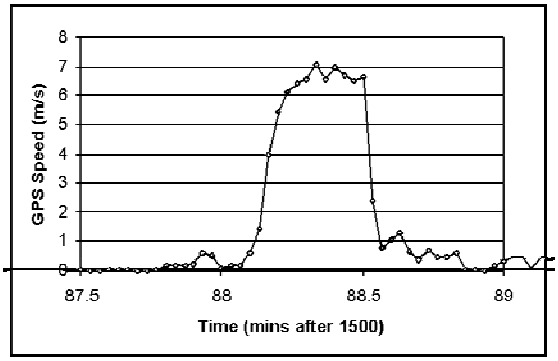

Figure 11. The Tumbleweed translation speed recorded by GPS. The steady-state speed is very close to the ambient windspeed, indicating very low rolling friction. The data have a much lower time resolution (~0.5s) than the video (0.04s).

4. DRAG COMPUTATION

The acceleration determined above allows the determination of the extraction of momentum from the wind to the rover i.e. the drag. If only translational motion is assumed, the drag on the tumbleweed must therefore be 4N and 13.6N. The anemometer record appears to indicate winds of 4-5 m/s rising to 9 m/s : the relative velocities would therefore be about 4-5 and 8 m/s respectively.

Taking the cross-section area as 2.6 m^2, and air density as 1.1 kg/m^3, (Willcox Playa is at 4100ft elevation) the drag coefficient for the faster phase of motion is therefore 0.14. However, if the vehicle is rolling without skid, as was apparent in the video, then the drag force coefficient must be augmented by 30% to account for the additional energy extracted from the airstream used to supply rotational kinetic energy – this correction yields C_d=0.19. The slower speed segment indicates a slightly smaller drag coefficient after rotation correction of C_d=0.14. In all cases these are lower limits, in that they do not account for any possible frictional losses.

At a flow speed of 2 m/s, the Reynolds number is 2.4×10^5, and the drag force on a smooth sphere would be expected to be of the order of 0.4 (e.g. see the Java C_d calculator at http://www.fluidmech.net/jscalc/cdre01.htm). At a flow speed of 7 m/s, the Reynolds number is 8.4×10^5 and the C_d, now in the turbulent regime, is only 0.1.

Thus the experimental results suggest a typical value between these two extremes, perhaps closer to the lower value of drag coefficient – not surprising given that the flow in the open air is likely to be somewhat turbulent.

Thus, following previous work [6], it seems probable that the performance of a Tumbleweed could be enhanced by drag augmentation devices on the surface, or an architecture like that of the natural Tumbleweed, where the flow in part goes through, not around, the plant [10].

5. SOME REMARKS ON BOUNCING

The onset of bouncing was clearly facilitated by the presence of surface roughness elements. However, once bouncing began, it often grew, suggesting bouncing may be a preferred mode of locomotion.

It was observed that the rover tended to bounce and rotate about a short axis of the central cylinder. This is obviously the axis of maximum moment of inertia, although some investigation of whether the position and tension of the suspension cords plays a role in defining the preferred spin axis would be worthwhile. The axis of maximum moment of inertia is of course the dynamically favoured (lowest energy) axis for spin.

Careful study of video records of bouncing (e.g. figure 12) shows an unexpected effect – the vehicle tends to spin forwards at a rate such that it bounces exactly twice per rotation (i.e. it bounces repeatedly on two opposite points on the sphere). Again, whether this is a purely dynamical effect, or is influenced by cord tension or friction effects would be worth exploring.

Figure 12. Action shot of the rover bouncing (note the shadow) The plane of rotation is roughly in the image plane – the short axis of the spheroid is the long axis of the internal cylinder and thus the axis of maximum moment of inertia.

In one sense, bouncing is an inefficient mode of transport, in that without roll, the vehicle experiences friction during the contact phases of bouncing, whereas in pure roll, there is no relative motion and thus no friction. However, the friction tends to promote rolling, leading to the combined bounce/roll described above.

In a thin boundary layer, this may be the end of the (simple) story. However, in a thick boundary layer with a significant wind gradient with height, bouncing may allow the rover to access faster winds above the ground.

Clearly, future work should consider, model and perhaps optimize, the bouncing performance of a vehicle of this type.

6. MOTION THRESHOLD

We measured the windspeed at which our rover began to move. This threshold of course depends on the level of inflation – to begin rolling, the net force of wind drag and weight (minus lift, if any) must be sufficiently forward of the central contact point to cause a net moment.

At rest, the internal pressure excess of the ball, multiplied by the contact area, will equal the weight: as the inflation pressure is decreased, the contact area increases, and thus the drag force and wind speed required to initiate motion will increase. The influence of inflation pressure on rolling/bouncing performance is of course well-known to soccer players. The data we obtained indicates an approximately inverse relationship between threshold wind speed and the inflation pressure (see table 1 below).

Level of inflation %	Wind speed m/s
100	4.5
80	5.5
70	7.0
50	9.5

Table 1. Rolling threshold wind speed as a function of inflation.

7. SURFACE-MOUNTED FLEXIBLE SOLAR CELLS

Until now, Tumbleweed rovers have been purely battery powered. In order to achieve a mission duration in excess of a few days, an alternative power source is required, with solar power being an obvious choice. Traditional crystalline cells are fragile, but amorphous silicon cells are now available which are fabricated onto a flexible substrate. Here we show a proof-of-concept experiment on the ability of such cells to develop power even after rolling in a dusty environment.

A thin-film solar cell was installed on the side of a PVC sphere (figure 13). The short-circuit current was measured aiming the cell at the sun. The sphere was then kicked around on a dusty field to simulate windblown rolling and bouncing and the short-circuit current measured after 10,30,100 and 300m of travel. It was noted that while the cell became somewhat dusty after a very short interval, the dustiness did not increase – soon the rate of dust removal by abrasion matches the rate of dust accumulation and a near-steady state is reached.

Figure 13. Tefzel-coated solar cell at start (above) and after 300m of rolling (below).

The short-circuit currents (and thus the power outputs) stabilized at about 70% of the dust-free case (figure 14). There was no obvious difference in dust obscuration for a cell coated with a cellulose tape and one with a UV- abrasion-resistant Tefzel coat, although something like the

latter would probably be preferred for long-duration use.

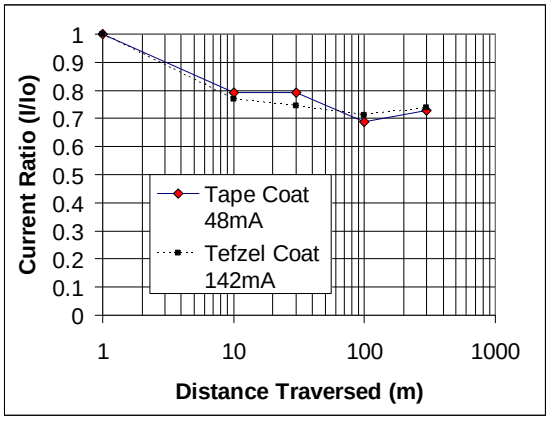

Figure 14. Short circuit current performance of flexible array as a function of distance traversed over a rough surface.

This experiment shows promise that an effective vehicle could use lightweight solar cells on its perimeter to provide power in all orientations. The large area available means that even with the modest loss in capacity due to dust obscuration ample power to support science measurements and data return.

8. CONCLUSIONS

Study of GPS data from polar field deployments suggests a poor correlation of the motion of a Tumbleweed rover with the meteorological record from the launch site. The motion is strongly episodic, suggesting the influence of short-period variations in windspeed and threshold effects on motion.

A short program of field tests with on-site documentation of the winds have permitted the quantitative measurement of the drag and rolling performance. As expected, the drag coefficient is rather low and could be improved.

Close observation of the motion in real-world conditions indicates some aspects of the bouncing motion (which may be the dominant mode of travel) which may allow rather superior performance than pure rolling.

Future work should explore this motion in more detail, and investigate the performance of a rover on terrain with a larger aerodynamic roughness.

Some simple tests show that flexible solar cells mounted on the exterior of a tumbleweed may be able to provide adequate power, dust accumulation becoming self-limiting after ~30% obscuration.

9. REFERENCES

1. G. Hajos, J. Jones and A. Behar, M. Dodd, An Overview of Wind-Driven Rovers for Planetary Exploration, AIAA-2005-0244, 43rd AIAA Aerospace Sciences Meeting and Exhibit, Reno, Nevada, Jan. 10-13, 2005

2. J. A. Jones, Inflatable Robotics for Planetary Applications, 6th International Symposium on Artifical Intelligence, Robotics and Automation in Space I-SAIRAS, Montreal, Canada, June 19-21, 2001.

3. J. Antol, Philip Calhoun, John Flick, Gregory A. Hajos, Richard Kolacinski, David Minton, Rachel Owens and Jennifer Parker, Low Cost Mars Surface Exploration: The Mars Tumbleweed, NASA/TM-2003 212411, August 2003 – see also http://centauri.larc.nasa.gov/tumbleweed/

4. Lorenz, R D, J Jones and J Wu, Mars Magnetometry from a Tumbleweed Rover, IEEEAC paper #1054, IEEE Aerospace Conference, Big Sky Montana, March 2003

5. S. Rose, C. Moody, D. James, and A. Barhorst, Drag Measurement and Dynamic Simulation of Martian Wind Driven Sensor Platform Concepts, AIAA-2005-249, 43rd AIAA Aerospace Sciences Meeting and Exhibit, Reno, Nevada, Jan. 10-13, 2005

6. A. Behar, F.rank Carsey, J. Matthews, J. Jones, NASA/JPL Tumbleweed Polar Rover, IEEE Aerospace Conference, Big Sky Montana, March 2004 – see also http://robotics.jpl.nasa.gov/ ~behar/JPLTumbleweed.html

7. Sullivan, R. et al., Results of the Imager for Mars Pathfinder windsock experiment, Journal of Geophysical Research Vol. 105, (E10), pp. 24,547–24,562, 2000

8. R. D Lorenz, Miniaturized Testbeds for Planetary Probes : Tumbleweed and Frisbee, IEEE Aerospace Conference, Big Sky, Montana, March 2005

9. R D Lorenz, J M Dooley and K Brock, Dynamics and Measurements of a Scale-Model

Huygens Probe parachute-dropped from a model aircraft, 3rd International Planetary Probe Workshop, Anavyssos, Greece, June 2005

10. R. D. Lorenz, Spinning Flight : Dynamics of Frisbees, Boomerangs, Samaras and Skipping Stones, Copernicus-Springer, 2006

10. ACKNOWLEDGEMENTS

The authors acknowledge the support of a JPL DRDF grant.

SURVIVING THE ACID TEST: INITIAL PERFORMANCE OF A BALLOON FOR LONG DURATION STUDIES OF THE ATMOSPHERE OF VENUS

V. Kerzhanovich, J.Hall, K. H. Baines,S. Stephens, A. Yavrouian, Jet Propulsion Laboratory, California Institute of Technology, Pasadena, CA, USA, E-mail: Viktor.V.Kerzhanovich@jpl.nasa.gov,
M.Said, D.Fairbrother, NASA Wallops Flight Facility, Wallops Island, VA, USA
C.Willey, C.Sandy, J. Ware, T. Frederickson, ILC Dover Inc, Frederica, DE, USA

After many years, Venus has again become a focus of interest for planetary science missions. Since April 11, the Venus Express spacecraft has been orbiting the planet, the first new orbiter to assess the Venusian atmosphere and climate in over 25 years. On a daily basis, Venus Express has been acquiring near-infrared views of the surface as well as three-dimensional measurements of winds, temperatures, and several important reactive species, to name just a few measurement goals of the mission. Yet such a remote sensing mission does not effectively address many high priority science objectives of the National Research Council Decadal Survey. For example, these missions are unable to measure noble gas abundances, key to understanding the origin and early evolution of the planet. Only *in-situ* missions can address such key goals by providing the requisite measurements of noble gases and their isotopes, and the isotopes of light elements. Long-lived balloon–borne missions provide additional powerful and unique capabilities to assess the planets dynamics, meteorology, and reactive chemistry at very fine scales. As one example, such missions can provide precise measurements of local variations in vertical motions and heat transport, thus providing new insights into the nature of (1) topographically-forced gravity waves, (2) large-scale planetary waves, and (3) convection.

In this paper we describe the approach, design and expected performance of a balloon capable of carrying a 40-50 kg instrumented gondola for extended duration, globe-encircling flights in the sulfuric cloud atmosphere of Venus near the 55-km level. We show the results of recent testing of both (1) our Venus balloon material and of (2) a full-scale, flying, balloon prototype. The results show that the material properties and balloon performance are close to the design predictions and more than fulfill mission design requirements. High material strength and low gas permeability ensure that such a balloon will be able to circumnavigate Venus several times at any latitude.

MONTGOLFIERE AEROBOTS FOR TITAN

Jack A. Jones[(1)] and Jiunn Jenq Wu[(2)]

[(1)]Mail Stop 157-316, Jet Propulsion Laboratory, 4800 Oak Grove Dr., Pasadena, CA, U.S.A. 91109 Email: Jack.A.Jones@jpl.nasa.gov

[(2)]Mail Stop 157-307, Jet Propulsion Laboratory, 4800 Oak Grove Dr., Pasadena, CA, U.S.A. 91109, Email: Jwu@jpl.nasa.gov(2)

ABSTRACT

Montgolfieres, commonly known as "hot air balloons," are balloons that are filled with heated ambient atmospheric gas. These balloons appear very promising for large-scale scientific exploration of the atmosphere and surface of Saturn's moon, Titan. Titan was once geologically and chemically very similar to the early warm Earth when life first appeared, although Titan became literally frozen in time. Analysis at JPL has shown that a double-hull Montgolfiere heated by a radioisotope power source (RPS) could travel safely with the winds at 10 km altitude and could make numerous circumnavigations of the Moon during a multi-month mission.

Altitude control of small unmanned Montgolfieres has been demonstrated on Earth and has shown that Montgolfieres can be controlled to take numerous surface samples for scientific analysis. Mission lifetimes lasting many years may be possible, since the RPS power source has a half-life of about 88 years, and turbulent weather is extremely rare. Also, small leaks do not impair performance of ambient-gas-filled Montgolfieres. The primary scientific goal of this type of mission would be to look for evidence of ancient biotic or prebiotic activity in the atmosphere or in the frozen surface water ice.

1. INTRODUCTION

Montgolfieres, which are balloons that are filled with heated ambient atmospheric gas, were first flown over two centuries ago by the Montgolfier brothers in France. The original Montgolfiere used burning wool to heat air inside a balloon, while present commercial hot air balloons more commonly use burning propane. Other types of Montgolfieres that have flown on Earth include solar-heated Montgolfieres and radiant-heated Montgolfieres.

Since the 1970s, the French Centre National d'Etudes Spatiales (CNES) has flown over forty Montgolfieres in the Earth's upper stratosphere, which is similar to the Martian atmosphere, for periods of up to 69 days [1]. The Montgolfieres were generally 40-m diameter or larger and fabricated from 12-micron (0.0005-in.) Mylar and polyethylene. Heated by the Sun during the day, they rose to an altitude in the stratosphere corresponding to about 10 mbar pressure. At night, the Montgolfieres were warmed by radiant Earth heat and descended to an elevation with a pressure of about 40 mbar.

Since Montgolfieres are relatively impervious to small leaks and since the stratosphere is generally a very benign environment, the primary failure mechanism after successful deployment has been the occasional presence of high-altitude cold clouds at nights. This has caused the balloons to lose buoyancy and descend to Earth.

2. MARS MONTGOLFIERES

The Jet Propulsion Laboratory (JPL) has been involved in the testing of solar-heated Montgolfieres for Mars since 1997. These balloons could potentially be used as lightweight parachutes to more gently land small payloads on Mars, or they could be used for multi-month missions during the polar summers (Fig. 1), which are about 6 months long. JPL deployed many dozens of low altitude 3–5 meter diameter solar Montgolfieres during 1997–1998. These balloons had a small opening at the bottom of the balloon that allowed them to fill while falling. All balloons that had a means to hold the bottom hole open were successfully deployed (Fig. 2). Stratospheric deployment soon followed, in order to simulate the deployment in Mars' cold thin atmosphere. Although most of the thin Mylar balloons failed due to ripping, three out of four thin, polyethylene balloons (10- to 15-m diameter) survived deployment. The fourth polyethylene Montgolfiere failed to open due to the fact that it was top-heavy, and the top fell below the bottom before the balloon could fill. The deployment of larger polyethylene Montgolfieres (as large as 30-m diameter) has met with mixed results, and further testing is underway in a joint program between JPL, NASA Wallops Flight Facility (WFF), and GSSL, a private balloon-development

company in Tillamook, Oregon. The first joint deployment of a 20-m Montgolfiere at 36 km altitude ((230 K, 0.006 bar pressure) was successful for the first minute of operation, but it failed when the separated parachute later collided with the slowing Montgolfiere (December 2005). Gliding parachutes are planned for future flights in order to avoid future collisions.

Fig. 1. The Mars Montgolfiere can be used to perform science from various altitudes, to soft-land payloads, or to take surface samples.

It should be mentioned that all large stratospheric Montgolfiere deployments are using very thin (10 micron) polyethylene balloon envelopes since heavier Montgolfieres would not float in Mars' thin atmosphere (220 K, 0.006 bar). The materials that have been developed and tested for balloon applications on Titan are over 100 times stronger, since Titan's atmosphere is about 400 times as dense as Mars, and thus stronger and heavier composite materials can be used.

3. TITAN MONTGOLFIERES

Various aerial vehicle missions to Saturn's moon, Titan, have been envisioned which take advantage of Titan's thick nitrogen atmosphere (1.46 bar, 93 K, more than four times as dense as the atmosphere on Earth). One of the simplest altitude-controlled atmospheric missions for Titan is that of a radioisotope power source (RPS)-heated Montgolfiere. For this mission, the RPS would be held inside the lower portion of the balloon, thus allowing nearly all of the waste heat to warm the internal ambient nitrogen atmosphere (Fig. 3, [2]).

Altitude control could be maintained by opening and closing a vent at the top of the balloon. Just as commercial hot air Montgolfieres can hover close to the ground (Fig. 4), so have our unmanned altitude-controlled solar Montgolfieres (Fig. 5). Altitude control of RPS-heated Montgolfieres on Titan can allow cruising with the Titan winds at 10 km altitude, as well as allow numerous samplings of water ice or methane lakes on the surface.

(a) Preparing to deploy

(b) Fully deployed from hot air balloon

Fig. 2. Deployment of solar Montgolfiere from a commercial hot-air Montgolfiere

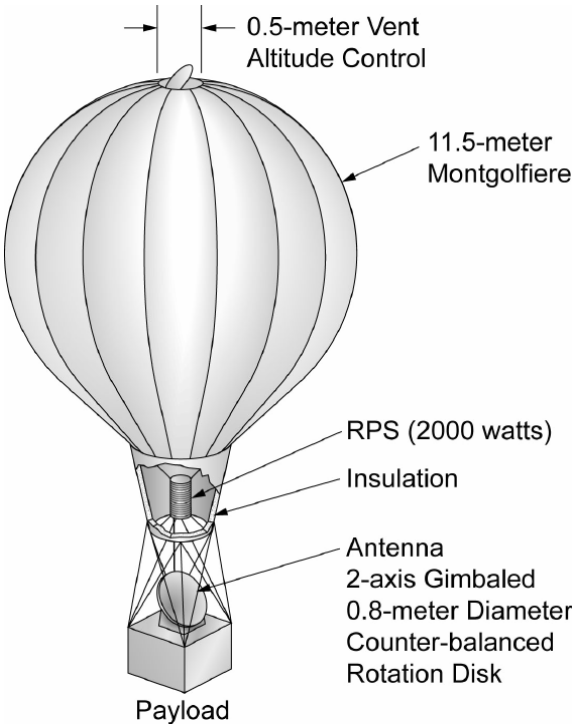

Fig. 3. Titan RPS Montgolfiere with altitude control

Fig. 4. Commercial hot air Montgolfiere descending and hovering over Lake Tahoe, California

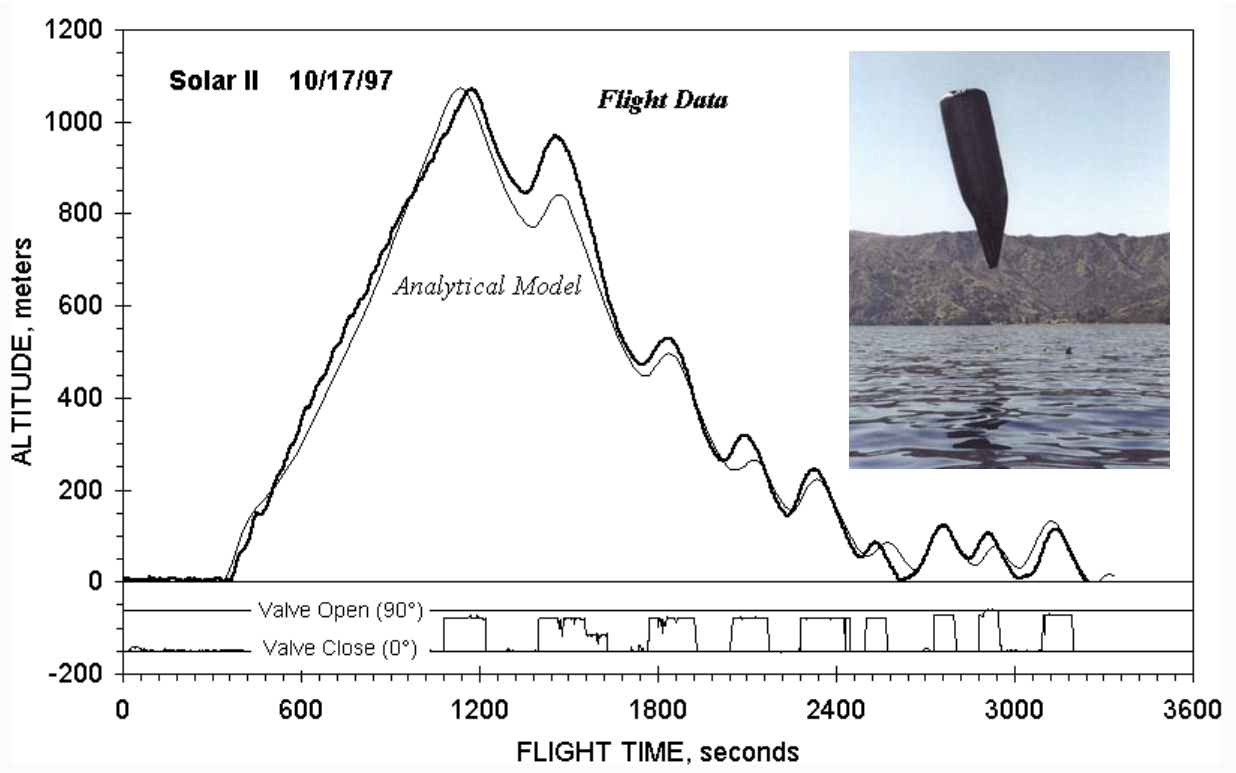

Fig. 5. The solar Montgolfiere can also hover over water. The performance closely matches thermal analyses.

3.1. Thermal Analysis

A number of thermal analyses have been performed to determine the expected performance of RPS-heated Montgolfieres in the Titan atmosphere. As discussed in [2], cold Titan Montgolfieres require only about 1% of the heat required by warmer Earth Montgolfieres. This is due to a combination of reduced cryogenic radiation, reduced convection heat transfer, and buoyancy inversely proportional to the square of absolute temperature. Two independent thermal modeling techniques, using Engineer Equation Solver (EES) and Computational Fluid Dynamics (CFD) have confirmed this with remarkably similar results. Furthermore, the EES thermal analysis [3] has been confirmed with actual test measurements of Earth solar Montgolfieres.

From simple Archimedes principles, an 11-m diameter Montgolfiere is required to float a 160-kg payload at 10 km altitude on Titan, assuming an envelope aerial density of 100 gm/m^2. The first transient analyses performed were to determine the transient heating of the Montgolfiere as it descended. It was found that 2000 W was insufficient to allow time for the Montgolfiere to heat up before hitting the Titan surface. The diameter was then increased somewhat, and the Montgolfiere was seen to almost have enough time to heat up before hitting the surface (Fig. 6). When the diameter was increased a bit more, the Montgolfiere could heat up before reaching 10 km altitude, and it could actually attain a ceiling of about 18 km (Fig. 7), well above the planned 10-km ceiling, which is safely below the Titan methane ice clouds. With the upper vent valve partially open, the balloon could descend to near the surface and maintain an altitude of about 100 $\pm$20 m (Fig. 8). The large bobbing effect is due to the rapidly changing external convection heat transfer coefficient that varies significantly with relative velocity.

In order to minimize the bobbing effect, a double-walled Montgolfiere was analyzed next. Double-walled balloons have been used in various competition balloons, such as Rozier balloons, which are a combination of helium and hot air, as well as in Aerostar double-walled competition Montgolfieres (Fig. 9). The planned double-walled design for the Titan Montgolfiere consists of an inner porous wall, surrounded by a ballooning outer wall (Fig. 10). The middle gap acts as an insulation layer to minimize heat leaks as well as to minimize effects of large changes in the external heat transfer coefficient.

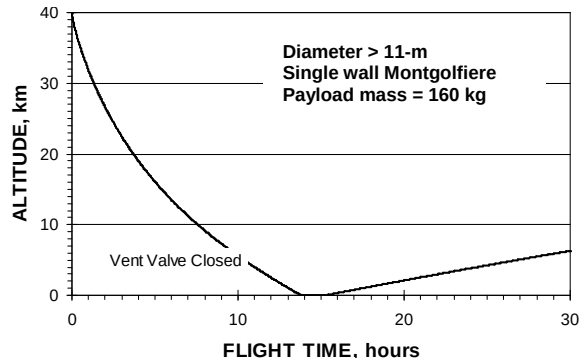

Fig. 6. Montgolfieres tend to require significant time to heat up on Titan. Smaller diameter Montgolfieres may require sitting on the surface for hours before they can lift off. This can be avoided by increasing the size of the Montgolfiere.

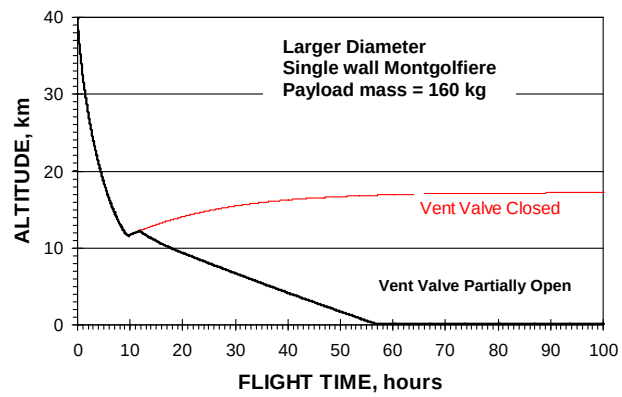

Fig. 7. Larger diameter Montgolfieres can obtain positive buoyancy before they hit the ground and maximum altitude is higher, unless the upper vent is open.

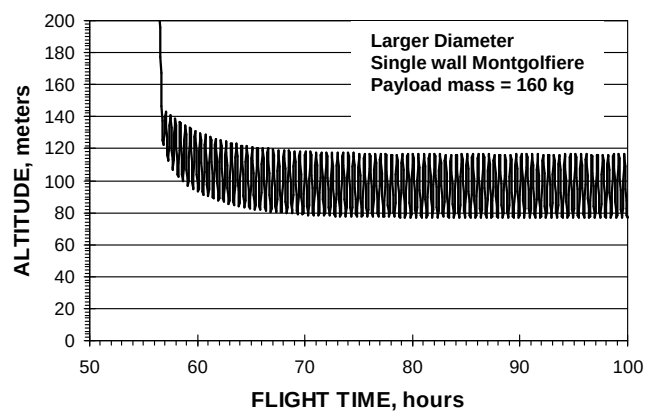

Fig. 8. This larger diameter Montgolfiere can be held to 100-m altitude $\pm$20-m, and it requires constant corrections that are a function of both altitude and velocity.

(a) Rozier balloons

(b) Aerostar International competition Montgolfieres

Fig. 9. Examples of double-walled balloons

Use of a small-gap, double hull increased the maximum ceiling of a larger Montgolfiere from 18 km to about 27 km, even accounting for a heavier total balloon envelope of 150 gm/m^2. Double-walled Montgolfieres were also found to be capable of holding much greater altitude control within ±2 m for 100-m altitude control (Fig. 12). To determine obstacle collision avoidance capability, a double-walled larger Montgolfiere analytically closed its upper vent when neutrally buoyant, and the balloon ascended at a rate of about 1 km/hr (Fig. 13). With a maximum anticipated surface wind of 1 m/sec, this corresponds to a 15º climb angle, which is considered to be quite safe, considering Titan's generally very flat surface.

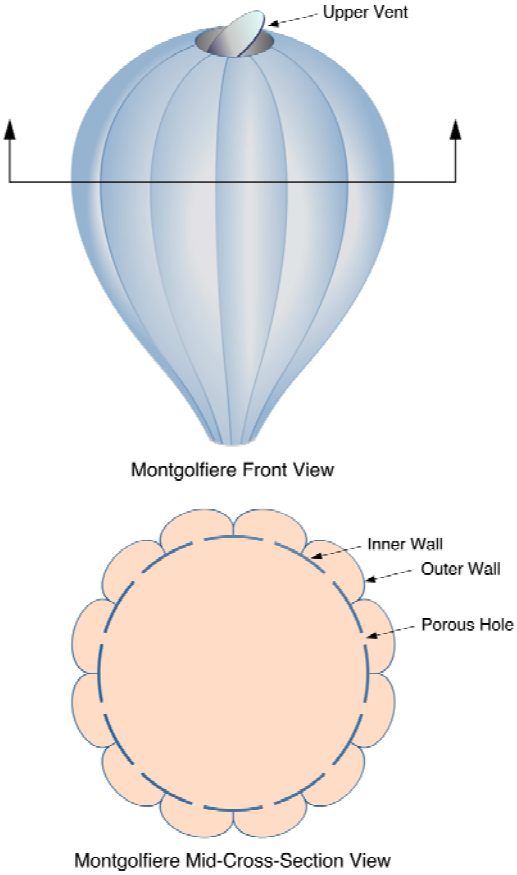

Fig. 10. The double wall of the Titan RPS-heated Montgolfiere would be similar to the Aerostar design and would have an inner porous balloon, surrounded by a larger diameter balloon, which keeps an insulating gas layer in between.

3.2. Mission Scenario

A preliminary schematic of a possible entry vehicle configuration is shown in Fig. 14. The pliable Montgolfiere envelope would be tucked to two sides in the entry vehicle to allow for last-minute placement of the RPS inside the entry vehicle prior to launch. The system would contain at least two parachutes, supersonic and subsonic, and all RPS heat rejection during cruise would be out the back lid of the entry vehicle, similar to Mars Science Laboratory (MSL).

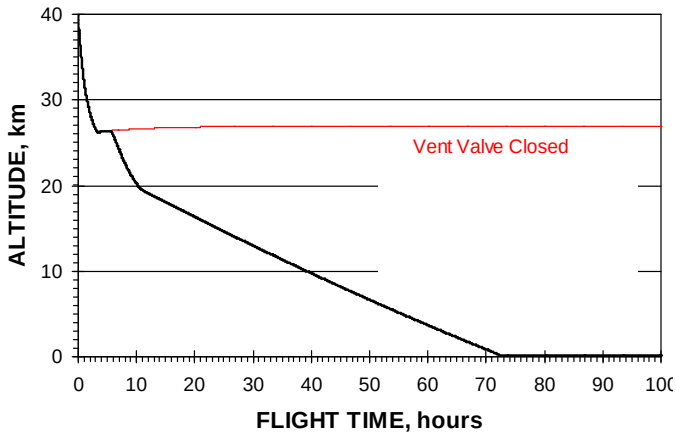

Fig. 11. An insulated, or double-walled, Montgolfiere heats up much faster and can attain much higher altitudes if the upper vent is fully closed.

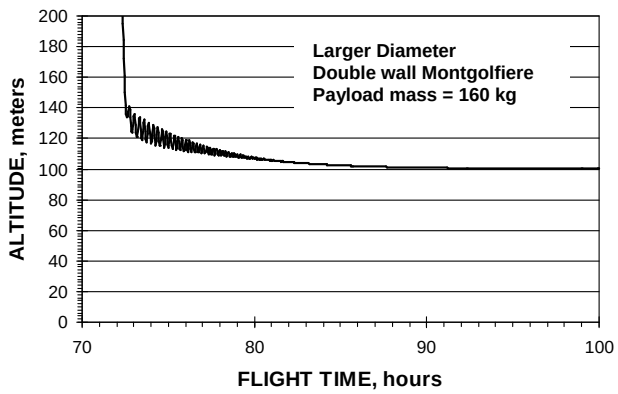

Fig. 12. The double-walled Montgolfiere can obtain a much more stable altitude, since its temperature and buoyancy are much less affected by vertical motion.

Figure 15 shows a possible deployment scenario, based on the Huygens entry. After entering the atmosphere, a supersonic pilot chute is deployed. Then a subsonic chute is deployed, followed by dropping of the heat shield. The Montgolfiere then deploys while falling under the parachute, similar to JPL's numerous Mars-simulation Montgolfiere deployments. After filling and stabilizing, the Montgolfiere descends to about 100-m altitude, which allows tethered sampling of the frozen ice surface (Fig. 16). The vehicle may be able to take advantage of anticipated reverse directional winds at lower altitude so that it can retrace its path to an area of interest seen while cruising at 10-km altitude.

Floating lifetimes are anticipated to be many years, since small leaks do not impair performance. Leaking gas is rapidly replaced and heated at the bottom of the balloon. Furthermore, turbulent weather is extremely rare on Titan, and is likely predictable. Ample RPS heating should last many decades, since the half-life of the RPS power source is about 88 years.

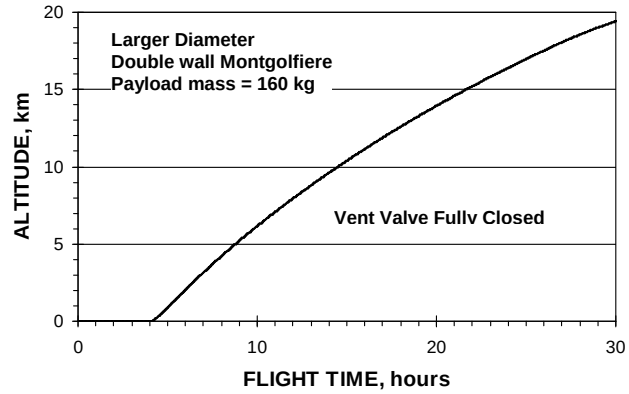

Fig. 13. If the upper vent valve is fully closed, it takes about 1 hour to climb to 1000-m altitude. With a surface wind of 1 m/sec, this corresponds to a 15º climb angle. For a descending balloon, the allowable safe descent rate has been calculated to be at least 1 km/hr.

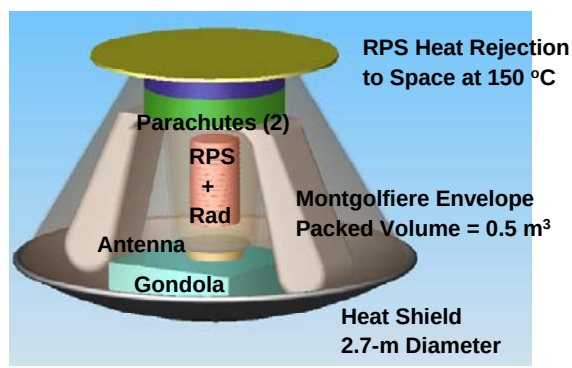

Fig. 14. The Montgolfiere envelope would be tucked to two sides to allow for last-minute placement of the RPS inside the entry vehicle prior to launch.

Titan was at one time geologically and chemically very similar to the early warm Earth when life first appeared. Both had warm liquid water oceans and thick nitrogen/methane atmospheres. Life on Earth changed the methane portion of the atmosphere to oxygen and carbon dioxide, but Titan cooled quickly and became literally frozen in time. The primary scientific goal of this global aerobat mission is to look for evidence of ancient biotic or pre-biotic activity in the atmosphere and in the frozen surface water ice of Titan. The aerobot is also expected to use wind currents to reach specific scientifically intriguing areas, such as the recent Cassini-discovered active volcano (possible present biotic activity) and the apparent liquid methane lake near the south pole.

4. FUTURE PLANS

JPL is presently developing and testing various sample acquisition and handling devices that can be used on a balloon platform, such as on the Titan Montgolfiere Aerobot. We are also developing test plans to perform thermal verification testing of double-hulled Montgolfieres in a cryogenic nitrogen atmosphere. Other development activities may include refinement of present cryogenic Montgolfiere envelope materials and testing of balloon-borne directional communications systems to confirm the ability to communicate directly from the Titan Montgolfiere to Earth.

5. REFERENCES

1. P. Maleterre, "Long Duration Balloon Flights in the Middle Stratosphere," *Adv. Space Res.*, Vol. 13, no. 2, pp. 107–114, 1993.
2. Jack A. Jones, James A. Cutts, Jeffery L. Hall, Jiunn-Jenq Wu, Debora Ann Fairbrother, and Tim Lachenmeier, "Montgolfiere Balloon Missions for Mars and Titan," *IPPW*, Athens, Greece, June 2005.
3. Jiunn-Jenq Wu and Jack A. Jones, "Performance Model for Reversible Fluid Balloons," *11th Lighter-Than Air Systems Technology*, AIAA-95-1608-CP, 2005.
4. Jonathon Lunine et al., "Titan Planetary Exploration Study," JPL Final Report, Pasadena, CA, May 2006.

6. ACKNOWLEDGMENTS

This research was carried out at the Jet Propulsion Laboratory, California Institute of Technology, under a contract with the National Aeronautics and Space Administration.

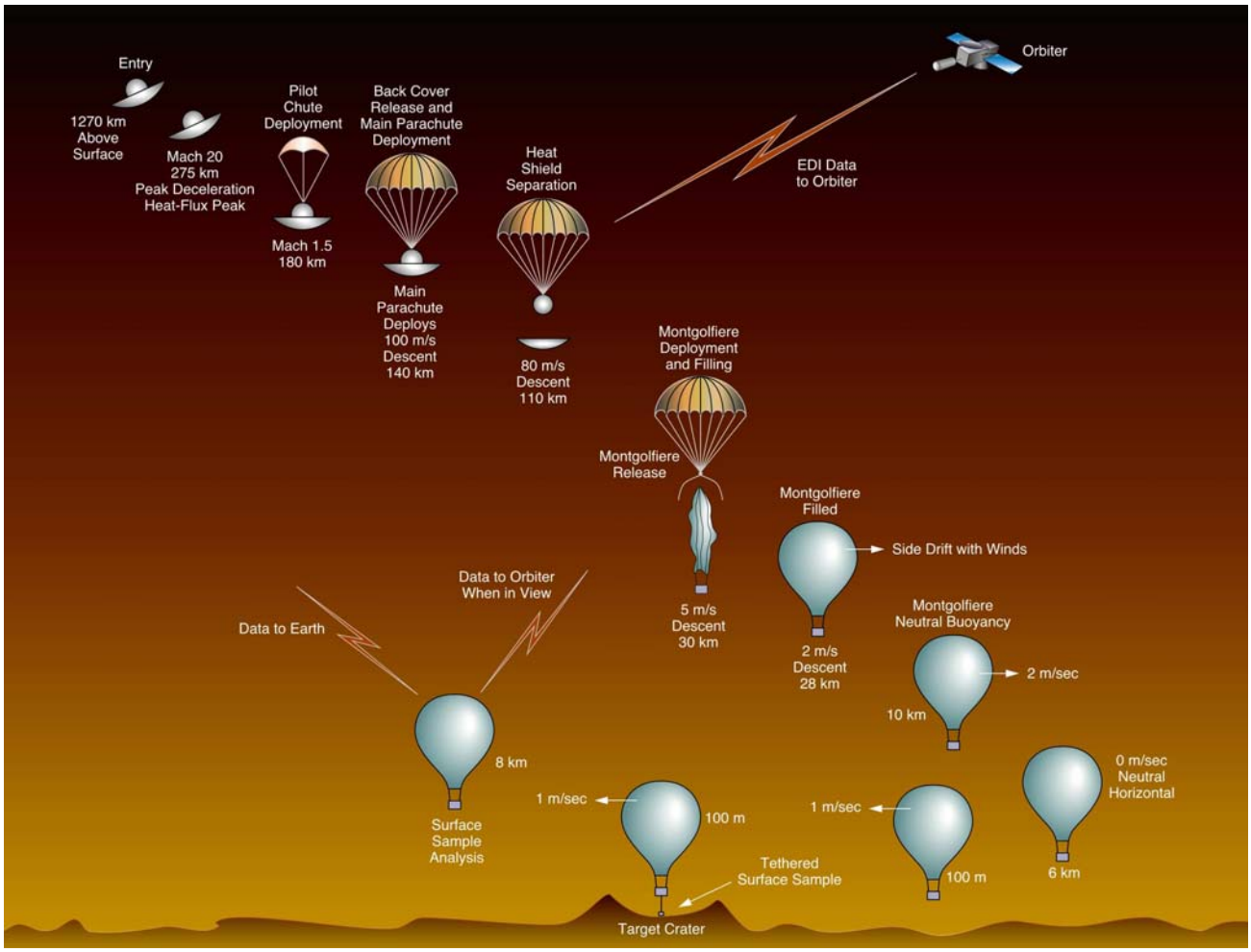

Figure 15. Titan Montgolfiere entry, descent, and inflation (EDI) scenario [4]

Fig. 16. A tethered sampling device will be used to acquire ten samples (1-2 grams each) of surface ice from 100-m altitude above the Titan surface. The samples will be pulled back up to the gondola for scientific analyses.

Experimental results for Titan aerobot thermo-mechanical subsystem development

J. L. Hall (1), J. A. Jones (1), V. V. Kerzhanovich (1), T. Lachenmeier (2), P. Mahr (3), J. M. Mennella (1), M. Pauken (1), G. A. Plett (1), L. Smith (3), M. L. Van Luvender (1), A. H. Yavrouian (1)

(1) Jet Propulsion Laboratory, California Institute of Technology, Pasadena, CA, United States
(2) GSSL Inc., Tillamook, OR, United States
(3) Lamart Corp, Clifton, NJ, United States

This paper describes experimental results from a development program focused in maturing Titan aerobot technology in the areas of mechanical and thermal subsystems. Results from four key activities are described: first, a cryogenic balloon materials development program involving coupon and cylinder tests and culminating in the fabrication and testing of an inflated 4.6 m long prototype blimp at 93 K; second, a combined lab experiment and numerical simulation effort to assess potential problems resulting from radioisotope thermal generator waste heat generation near an inflated blimp; third, an aerial deployment and inflation development program consisting of laboratory and helicopter drop tests on a near full scale (11 m long) prototype blimp; and fourth, a proof of concept experiment demonstrating the viability of using a mechanically steerable high gain antenna on a floating blimp to perform direct to Earth telecommunications from Titan. The paper provides details on all of these successful activities and discusses their impact on the overall effort to produce mature systems technology for future Titan aerobot missions.

BALLUTES: LAUNCHING AEROBOTS WITHOUT COMPROMISES

Julian Nott

Consultant Scientists, 704 Chiquita Road, Santa Barbara CA 93103 USA, ScienceConsulting@nott.com

ABSTRACT

There is great interest in exploring Solar System destinations, particularly Titan, using aerobots, robotic balloons and blimps. But how will they be launched? If they are filled under a parachute there is a vertical slipstream. If they are filled on the surface, the terrain may be unsuitable and there may be surface wind.

This paper proposes to avoid all these problems with a ballute, a "BALLoon parachUTE". The ballute fills like a parachute and is then heated, becoming a hot air balloon. Once floating it is an ideal launch platform: there is no wind and it is away from the surface.

The following notes focus on Titan but ballutes also appear useful for Venus and Mars.

NOTE This ballute is quite different way from those for aerobraking which are inflated in space.

1. THE PROBLEM - LAUNCHING AEROBOTS

There is great interest in flying aerobots, robotic balloons and blimps, over several Solar System bodies, particularly Titan [1]. The aerobot would arrive from space in an aeroshell. But how will it be launched?

The aerobot could be extracted from the aeroshell at altitude and inflated while descending under a parachute. This is problematic because:

- Time is limited.
- The fabric will flap in the slipstream, risking damage. Fabrics may be more vulnerable at Titan's low temperatures.
- There may be damage as large or heavy components move at random.
- As the aerobot become buoyant, the parachute will continue down and might collapse over the aerobot.

Alternatively inflating on the surface is problematic:

- The surface may be rough at the landing place.
- It may be windy.

While inflation on the surface might be possible at the Huygens landing location, it appears impossible on the steep slopes in the "highlands region" about 5 km to the North. Even if average winds are light, it might be windy at landing time. The craft would have to wait on the surface for calm, risking further uncertainty.

Although inflation and launch take little time, it is a crucial period. Inflating balloons in anything other than calm conditions is always precarious and to date blimps have invariably been inflated inside hangars.

2. THE SOLUTION – UTILIZE A BALLUTE

Using a ballute "BALLoon parachUTE" eliminates all of these problems. The kind of ballute proposed here is a cross between a parachute and a hot air balloon. As it falls through the atmosphere it fills like a parachute. It is then heated and floats like a hot air balloon.

At the destination the system enters the atmosphere and decelerates in an aeroshell. At an appropriate altitude a drogue extends the ballute from the aeroshell, Fig. 1:

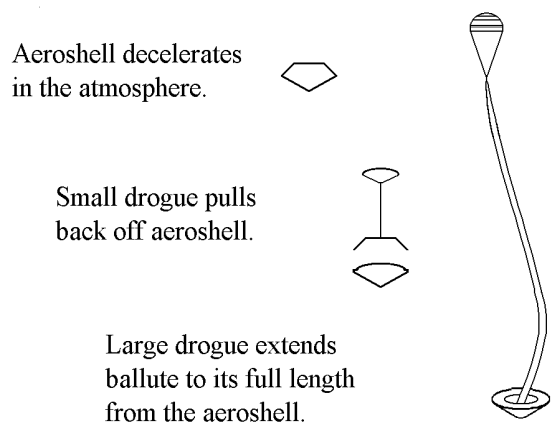

Fig. 1. Atmospheric entry and initial deployment.

Once clear of the aeroshell and pulled down by the payload, dynamic pressure is greatest at the bottom of the ballute, the mouth, which is forced open, forcing the ballute to inflate. When it is full, heat is supplied by burning a few kilograms of solid propellant and it flies level as a hot air balloon, Fig. 2. Conditions are now extraordinarily tranquil, hard to appreciate without firsthand experience of hot air balloons, Fig 3.

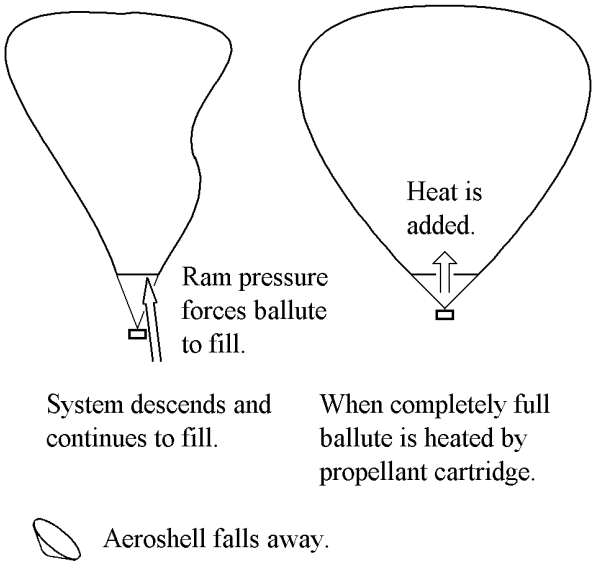

Fig. 2. Ballute fills and is heated.

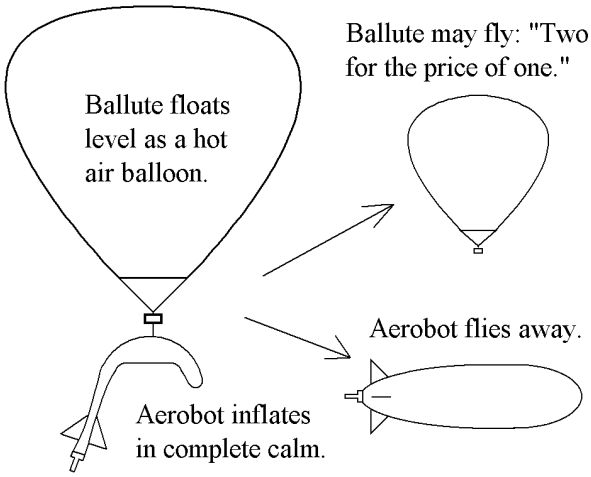

Fig. 3. After heating, the ballute flies level. A blimp or balloon can be inflated in perfect calm.

Helium now flows into the aerobot, which fills in perfectly calm conditions. As the ballute cools hot air lift is lost but helium lift increases. The gas flow is regulated to keep perfect equilibrium. In Titan's conditions the time constants are tens of minutes or longer.

This method completely avoids surface hazards.

During filling, flexing may cause fabric pinholes, but hot air balloons are highly tolerant of pinholes.

Because the heat required in Titan conditions is low, a solid propellant cartridge could support a ballute for long periods. Vertical motion can be detected with a pressure transducer and easily regulated. With only one axis of control, hot air balloon autopilots are simple. Many examples have been successfully flown.

A ballutes has other advantages. It usually deploys much slower than a parachute because it fills through the small mouth. This reduces opening shock. If correctly proportioned, a ballute is extremely stable without the swinging common with many parachute types.

3. EXISTING EXPERIENCE

Wide experience shows every aspect is practical.

Ballutes are very widely used in personal parachutes and to decelerate weapons dropped from high-speed aircraft. Fig. 4

Fig. 4. Ballute inflation during munition release at high speed. Photo Irvin Aerospace.

The Huygens parachutes were fully effective. The numerical methods used to design them have advance greatly in the years since. These methods are equally applicable to the inflation of a ballute.

Aerostar [Raven] completed practical demonstrations deploying several types of systems in which ballutes were launched at altitude, filled and then heated to float level. Fig. 5 to 7 shows a typical sequence, in this case to float an airborne electronics jammer.

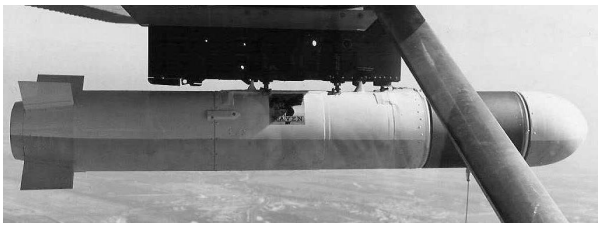

Fig. 5. System canister at altitude below aircraft wing before drop. A ballute can be packed in any shape, for instance an aeroshell. Photo Rekwin Achieve.

Fig. 6. Falling and inflating. Note systems canister below mouth of ballute. Photo Rekwin Achieve.

Fig. 7. Ballute fully inflated, heated & flying level. Photo Rekwin Achieve.

The author easily stopped a 15,000 meter terminal [burner off] descent in a hot air balloon in 200 meters, Fig. 8. Indeed stopping a descent is so easy that every student is now required to make a terminal descent in training to receiving a balloon pilot license.

4. MAJOR DESIGN ADVANTAGE

If an aerobot is inflated under a parachute it must be designed to survive this dynamic situation as well as normal flight. But if a ballute is used, the aerobot need only be designed for normal flight. This simplification is a major benefit.

5. SIMPLIFIED TERRESTRIAL TESTING

The calm conditions under a ballute mean the actual inflation will be easier. In addition testing on Earth is much simpler. Physically simulating inflation falling under a parachute is difficult. A vertical wind tunnel cooled to 90K is conceivable, but would be a major facility. By contrast a simple static chamber cooled to near the boiling point of nitrogen provides an excellent facility to simulate static inflation under a ballute.

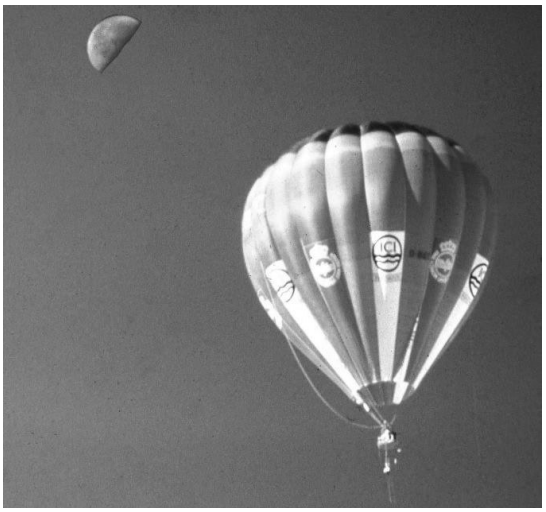

Fig. 8. The author easily stopped the terminal descent of this balloon after falling 15,000 meters.

6. TWO FOR THE PRICE OF ONE

An attractive possibility is that the ballute would not be discarded but would itself fly away as a hot air balloon heated by a radioisotope heat source. This launches two complementary craft with a single entry vehicle.

7. OTHER SOLAR SYSTEM DESTINATIONS

A ballute would be ideal at altitude above Venus and may be applicable over Mars.

REFERENCES AND ACKNOWLEDGEMENTS

1. Hall, J. L. et al, "An aerobot for global in situ exploration of Titan" 35th COSPAR Scientific Assembly, Paris, France, July 18-25, 2004.

The author would particularly like to thank James Winker, Rekwin, for photographs and information and also to thank Dr James Rand, Winzen Engineering, Eric Frische, Space Data, Robert Sinclair, Irvin Aerospace and Luke Brooke, Tensys.

A METHOD FOR PLANETARY BALLOON FLIGHT PATH GUIDANCE

K. M. Aaron, K. T. Nock, M. K. Heun, A. A. Pankine
Global Aerospace Corporation, Altadena, CA, 91001, kim.m.aaron@gaerospace.com

ABSTRACT

In this paper, we describe the operation, performance, and benefits of a Balloon Guidance System (BGS) for operation at Mars. Balloon guidance systems have been under development by Global Aerospace Corporation (GAC) for use in NASA's scientific balloon program. In addition, several NASA-funded studies have explored the use of BGSs for guiding scientific balloons on Earth, Mars, Venus and Titan. A scaled flight test validated the aerodynamics, stability, control, and operation of a balloon guidance system for high-altitude scientific balloon applications. These tests were carried out in a relevant environment giving high confidence that a full-scale system will perform as expected on stratospheric Earth balloons. In addition, scale model testing along with performance analysis provides assurance that planetary balloon guidance systems will perform well in the relevant atmospheres.

1. INTRODUCTION

Systems capable of modifying the trajectory of high altitude scientific balloons at Earth have been under development by GAC since about 1997 [1-4]. In 2002, GAC began developing concepts for guiding planetary balloon platforms [5, 6]. One embodiment of a Balloon Guidance System (BGS) uses a wing suspended several kilometers below the balloon on a very long tether. In planetary atmospheres, there is generally a vector wind difference between balloon and wing altitudes (separated by a few kilometers) that results in a relative wind at the wing, allowing it to generate a lift force. This lift force can be directed horizontally across the natural flight path of the balloon. This force is transmitted by the tether to the balloon, causing the balloon to drift across the winds at its altitude. This force, acting over long durations (days), can cause the balloon to depart hundreds to thousands of kilometers away from its natural drift trajectory. In the next several sections, we will discuss the aerodynamics, performance modeling, design, and simulation of a low-cost, low-risk, passive, planetary balloon flight path guidance concept with a focus on the Mars application.

2. SYSTEM CONCEPT OF OPERATION

In the past, the inability to control the path of planetary balloons had limited their usefulness and, therefore, scientific interest in their use. This statement is particularly true for Mars: without flight path guidance technology, a Mars balloon cannot observe desired regions of interest, and it has a high probability of impacting mountainous territory. The BGS vastly expands the capabilities of balloons for Mars exploration by providing the means to control their balloon trajectories in the Martian atmosphere to observe regions of interest, to drop surface probes in desired targets, and to reduce the risk of mission failure by avoiding terrain with high topography.

2.1 Principle of Operation

A BGS exploits the natural wind field variation with altitude to generate passive lateral control forces on a balloon using a tether-deployed aerodynamic surface below the balloon. A lifting device, such as a wing on end, is suspended on a tether well beneath the balloon to take advantage of this variation in wind velocity with altitude. The wing generates a horizontal lift force that can be directed over a wide range of angles. A BGS consists of an aerodynamic system or "BGS wing" (e.g. near vertical wing, support boom, and rudder) below the balloon, a kilometers long tether and a winch system for lowering and, sometimes raising, the BGS wing. A variety of concepts for the aerodynamic system have been studied including kites, dual wing airfoils, and whirligigs [1]. Fig. 1 illustrates the principle of operation of a single-wing BGS. For the Mars application, the balloon would typically be at 10 km altitude and the BGS main wing at 3 km altitude. Generally there is a wind difference between altitudes that translates to a relative wind on the BGS wing as it is dragged along by the balloon. This relative wind can generate a lift and drag force at the wing, resulting in a horizontal force. Changing the angle of attack of the wing by use of the rudder can modify the direction and magnitude of this force. This force, transmitted to the balloon by a tether, alters the balloon's path providing a bias velocity of a few meters per second to the balloon drift rate.

A BGS enables a balloon to fly over surface targets for high-resolution reconnaissance or for deployment of microprobes, to steer around mountains to avoid collisions, to sample the atmosphere to map the abundance of trace gases that could lead to locating possible surface sources of these gases, and to explore a planet on regional and global scales. No longer are planetary balloons completely at the mercy of the winds.

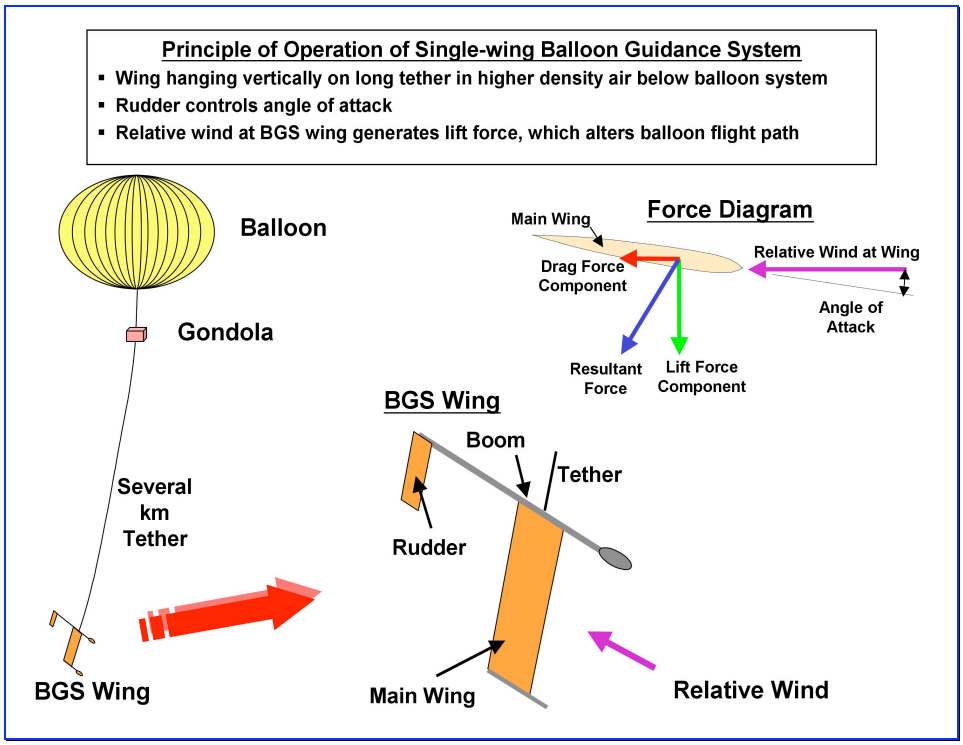

Fig. 1. Principle of operation of single-wing balloon guidance system.

Features of a BGS include the ability to:

- Passively exploit natural wind conditions
- Operate day and night
- Control direction of balloon flight path in various wind conditions
- Be made of lightweight materials and inflatable structures
- Operate with very little power and without consumables

In usual wind circumstances with conventional designs, a balloon with a BGS cannot keep station over a given location. However, advanced BGS design concepts being studied by Global Aerospace can station-keep stratospheric airships.

2.2 Physics of Operation

Fig. 2 shows a vector diagram illustrating the wind vectors and dominant forces during operation of the BGS. The definitions of the various vectors are described in Table 1. The view is looking down from above the balloon and the BGS and is not to scale. The BGS (represented as an airfoil section) is at a much lower altitude than the balloon (represented by the circle). For illustration purposes, the BGS wing is shown much larger than it would be in proportion to the balloon. The upper portion of the figure shows expanded views of some small vector details.

Table 1. Notation for vectors in shown in Fig. 2.

V_{10}	Wind Velocity (relative to the ground) at Balloon altitude (~10 km on Mars)
V_3	Wind Velocity at BGS altitude (~3 km on Mars)
V_B	Velocity of Balloon relative to the ground = Velocity of all parts of the system
V_{DRIFT}	Drift Velocity of the balloon due to action of the BGS = V_B - V_{10}
V_{REL}	Relative Wind Velocity at the BGS = V_B – V_3
V_{DF}	Vector Difference between Winds at Balloon and at BGS = V_3 - V_{10} (used in an even simpler analysis, but not used here)
V_{CT}	Cross-Track Velocity Component of V_{DRIFT} (perpendicular to V_{10})
V_{BT}	Back-Track Velocity Component of V_{DRIFT} (parallel to V_{10})
F_L	Lift Force on BGS (acts horizontally and is perpendicular to V_{REL})
F_D	Drag Force on BGS (acts horizontally and is parallel to V_{REL})
F_R	Resultant force on BGS = F_L + F_D ~ Drag force on balloon
F_{DRIFT}	Drag Force on balloon due to V_{DRIFT} ~ F_R

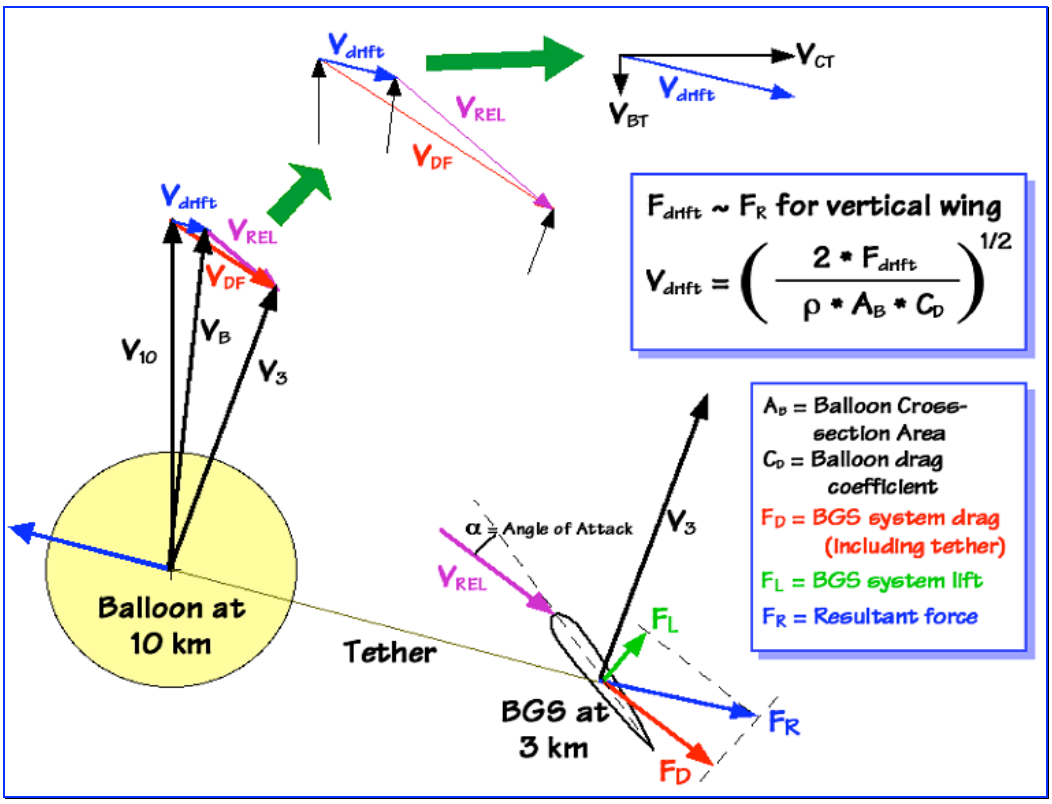

Fig. 2. Balloon guidance system vector wind and force diagrams at Mars.

Many simplifying assumptions are present in Fig. 2; however, the complex models that have been developed to characterize and simulate the BGS behavior do not share these limitations. For example, the tether is shown here as a straight line. In reality, due to the variation in relative wind and atmospheric density along its length, the drag forces on the tether will cause it to have a gentle curvature. The detailed models include this effect by breaking the tether down into shorter segments over which conditions are treated as being constant. In Fig. 2, the tether drag force is shown to act at the BGS. This is not a bad assumption since the drag on the lower 10% or so of the tether dominates the rest of the tether because the atmospheric density is greatest and the relative wind is also greatest here. The wing is assumed to be exactly vertical so the lift and drag forces act in a horizontal plane. In actual operation, the wing will hang with some tilt to the side and backwards. Our detailed models resolve the forces in three dimensions and include this effect.

The system is assumed to be in equilibrium, so the vector sum of the forces must equal zero. In the vertical direction, the buoyancy force provided by the balloon exactly equals the weight of the system. These vertical forces are not shown. The aerodynamic drag force on the balloon is equal to and opposite to the resultant aerodynamic force on the BGS (including the tether drag force). With this simplification, one can calculate the drift velocity of the balloon (inset box in figure) in which A_B is the projected area of the balloon (as viewed from the side), C_D is the drag coefficient of the balloon (for flow from the side), and ρ is the atmospheric density at the altitude of the balloon. The angle of attack, α, of the BGS wing is controlled by adjusting the incidence angle of the rudder (not shown), and is usually arranged to produce close to the maximum lift coefficient for the wing as this typically produces maximum useful control effect for the system. A small amount of iteration is required to determine the drift velocity vector that balances the forces, thereby making the system self-consistent or in equilibrium. The diagram in Fig. 2 is drawn to illustrate an equilibrium solution.

3. SCALE MODEL TESTING

To gain confidence in the ability of the BGS to perform properly for NASA stratospheric balloon applications we carried out two scale model tests. We built and tested a 1/4-scale model (see Fig. 3) of the BGS wing assembly. The scale model BGS uses a 0.31-m chord by 1.41-m long, NACA 0015 airfoil for its main wing. The rudder used a scaled down version of the same airfoil. It was scaled down from a full-scale system intended for

operation in the Earth's stratosphere. The scale model actually tested is lighter and has lower moments of inertia than an ideal dynamically-scaled model making it more responsive than an ideal scale model, thus emphasizing any instabilities that might exist in the design.

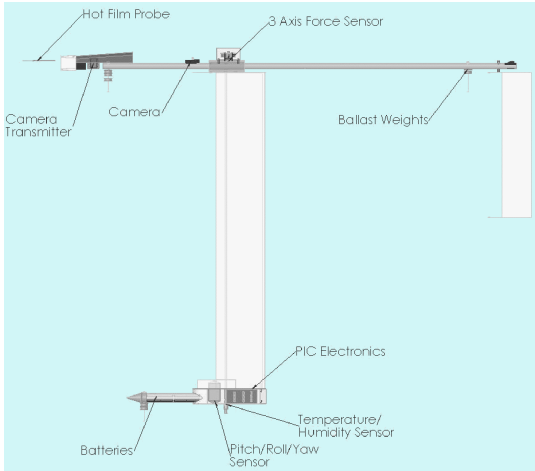

Fig. 3. Scale model BGS configuration.

In April 2001, GAC conducted the second of two scale model flight tests from a tethered blimp at El Mirage Dry Lake in California, which is discussed below.

3.1 Test Objectives

The objectives of this test were to acquire quantitative data to verify aerodynamic performance predictions, to investigate effects of center of gravity (CG) location on dynamic behavior, validate stability and control requirements, and to gain experience with instrumentation applicable to full-scale test.

3.2 Scale Model Instrumentation

We carried an array of instruments aboard the scale model to make measurements of its performance and behavior. These instruments included:

- Hot Film X-probe (velocity and alpha)
- 3-axis tether force transducer (strain gage)
- Accelerometer-based Pitch Roll sensor
- Magnetometers
- Temperature and humidity
- Rudder position encoder
- On board video camera

In addition, we had an onboard data acquisition and transmission system that sent data to a laptop computer for real-time evaluation.

3.3 Dynamic Scaling

In the 2001 testing, we matched full-scale aerodynamic parameters as well as possible, including Reynolds number (Re). The 1/4 scale prototype system simulated the performance of the full-scale system, which has a 5-m long wing, at 20 km altitude in the Earth atmosphere. During scale model testing, the Reynolds number varied, due to wind speed changes, between 38,000 and 227,000. This range encompasses much of the operating range of the Earth full-scale system. The average Re throughout the test was about 72,000 versus the nominal 69,000 expected for the full-scale system at 20 km altitude for one likely set of wind conditions (Latitude –24° in January). This fit of average Re is really quite a good match for scaled experiments. And, we collected many data points on either side of Re =69,000.

3.4 Results of Scale Model Testing

Data from scale model testing indicates that the horizontal lift force was somewhat better (10-20%) than expected. Analysis of the data (see Fig. 4) indicates that the maximum lift coefficient point, 1.2 at an angle of attack (α) of about 12°, was obtained when the Re was 45,000, which is somewhat lower than the test average (72,000). This result indicates that the measured lift coefficient underestimates the expected performance at full-scale flight altitudes in higher winds. The scale model tests occurred at low altitude where turbulence is expected to improve apparent performance, which means that the performance of the full-scale system could have been overestimated by 10-20%. Note, the BGS tested was not just a single airfoil; i.e. the boom, forebody, and rudder all contribute to the lift, which means that the measured lift coefficient could easily be greater than the airfoil alone.

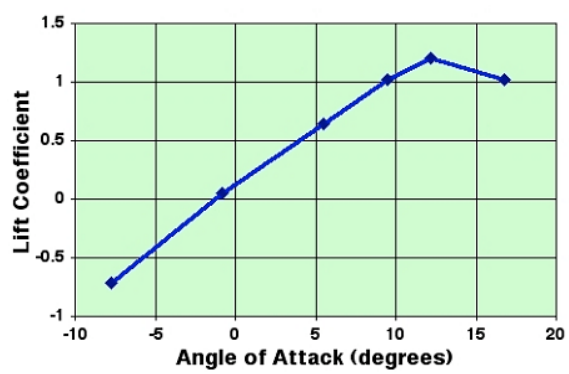

Fig. 4. Scale model lift coefficient as a function of angle of attack.

Over the Reynolds number range flown, we did not observe any changes in flight characteristics nor was any instability encountered despite attempts to induce instabilities by (a) significant shifts in the CG location both behind and above its preferred location and (b) by driving large-amplitude oscillations that could excite unstable dynamics in the system.

In this, the instrumentation worked perfectly which set the stage for development of instrumentation for full-scale tests and operational flights. This scale model testing gives us high confidence that the full-scale version will perform well at Earth. In addition, this test suggests that BGSs will be able to provide the needed guidance for balloon missions on most planets. Mars is a special challenge, however, as we discuss in the next section.

4. MARS BALLOON GUIDANCE SYSTEM

In this section we discuss low Reynolds number airfoils, their performance in real Martian winds, and conceptual Mars BGS system designs.

4.1 Low Reynolds Number Airfoils

In this section we discuss (a) low Reynolds number airfoils, their performance in Martian winds and (b) conceptual Mars BGS system designs.

4.2 Low Reynolds Number Airfoils

The aerodynamic surface of a Mars BGS will be operating at low Reynolds numbers (Re the order of ~1000). For example, during seasons near an Ls of 150°, BGS Re will typically vary, globally, between 400-6000 for wind differences between 4 and 10 km [7]. For these low Reynolds numbers, drag coefficients are significantly higher and maximum lift coefficients are a little lower than for higher Reynolds number operation (e.g. above 50,000). In recognition that operation in the Martian environment would result in fairly low Reynolds numbers, we reviewed existing literature on wings designed for low Re operation. Although there have been some studies in this regime, there are far fewer sources of data or modelling results than for the higher Reynolds numbers typical of normal aircraft flight. It is clear that for these low Reynolds numbers, drag coefficients are higher and maximum lift coefficients are a little lower than for higher Reynolds number operation, as studied by Sunada in 2002 [8].

The reduced lift-to-drag ratio (L/D) during low Re operation is quite a challenge for flight systems, such as airplanes, that use aerodynamic lift to support system weight and provide thrust to overcome the drag. However, for a BGS, the weight is supported by buoyancy and thrust is not required to overcome drag. The "lift" from the wing is directed close to horizontal and predominantly across the flight path of the balloon. The drag acts mostly to slow down the balloon, and is relatively unimportant to the operation of the BGS. In fact, tether drag is typically much greater than BGS wing drag. The forces generated by the BGS are very low (of order 1 N). However, the drag on even a large balloon moving at only 1 m/s in the Martian atmosphere is also very small.

In Fig. 5, airfoils #5-12 (red boxes) are likely candidates for the Mars BGS wing design.

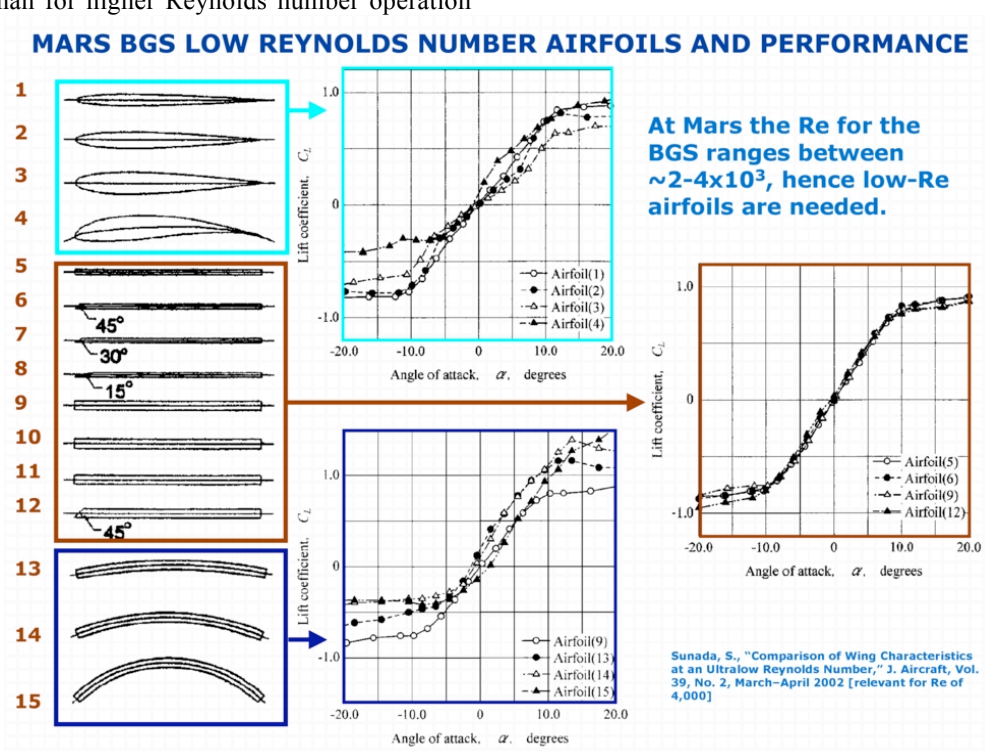

Fig. 5 Low Reynolds number airfoils and their performance.

4.3 BGS Performance in Mars Winds

The difference in winds at different altitudes in the atmosphere creates a relative wind at the altitude of the wing (stronger winds are usually found at higher altitudes on Mars). An example of a wind profile at Mars is shown on Fig. 6 (from Mars-GRAM 2001 [9]) for southern mid-latitudes at an Ls = 150°. This wind profile shows the high relative winds available during this season and latitude.

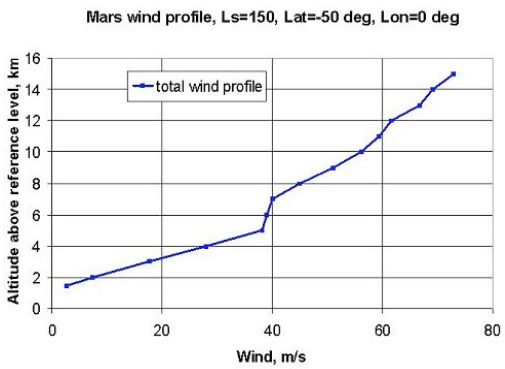

Fig. 6. Mars atmospheric wind profile.

The horizontal component of the total force produced by the wing can be used to change the path of a balloon in the winds. For this example wind profile, the wind at 10 km altitude, where the balloon would be floating, is about 56 m/s while the wind at 3 km, where the BGS would be situated, is about 18 m/s. The resultant relative wind is therefore 38 m/s. This level of relative wind could apply a cross-wind delta-V to the balloon of the order of 4 m/s for an 8 m^2 wing operating with a lift coefficient of 0.8.

Having developed and tested the numerical model of the BGS, a study was carried out of its performance in different wind regimes characterized by strong or weak vertical wind gradients, varied tether length and balloon sizes. The model solves for the equilibrium solution that maximizes the cross-track velocity of the balloon (the velocity in the direction perpendicular to the direction of the prevailing winds).

Example of model solutions are illustrated in the next two figures. The model run for the first case shown in Fig. 7 takes place at about equinox (Ls=6°). The corresponding date is August 13, 2013 – within a month of the 2013 Mars arrival window of opportunity for a Mars Network Emplacement Mission.

The location of the model run is on the southern edge of the zonal jet in the northern hemisphere. The action of the BGS in this case changes the velocity of the platform by 2.5 m/s. The BGS velocity vector is close to the southwest direction. The solution for the tether configuration and the relative winds are shown in Fig. 7. Note the different scales in the U (zonal) and V (meridional) directions. And the scales in U and V directions are different from the vertical scales to better illustrate the tether shape. The deflection of the tether from the straight down configuration in the U direction is due to the drag of the tether in the strong relative U wind. The deflection from the vertical configuration in the V direction is primarily due to the sideways lifting force generated by the BGS.

The platform continues to be embedded into the zonal flow (ground speed U=45.7 m/s) with a slight southward drift more than 50% of which is due to the action of the BGS (ground speed V=-2.7 m/s, BGS U=-1.84 m/s, BGS V=-1.83 m/s).

For the weak flow case shown in Fig. 8, the relative wind at the wing altitude is much smaller than before – just about 1 m/s in the zonal direction. Interestingly, the total BGS velocity is of the same order of magnitude as the relative wind at the altitude of the wing ~9 m/s. The tether deflection shown in the figure is due to the tether drag (note different spatial scales on all three plots). This analysis illustrates the worst case for the BGS performance – in low relative wind at the wing altitude, the cross-track component of the BGS velocity is negligibly small. However, the conditions described in this analysis do not persist long at Mars. Simulations for a different longitude at the equator at the same time (different local time, not shown) show an increase in relative wind and a corresponding increase in the cross-track component of the BGS velocity (1 m/s for relative wind of 9 m/s). Hence, our analysis indicates that the BGS will enable balloon steering capabilities for the wide range of atmospheric conditions that can be encountered at Mars.

4.4 Example Mars Balloon Guidance System

The Mars BGS consists of the main wing, the winch system at the gondola and the long tether. An example Mars BGS wing system design is displayed in Fig. 9. It is characterized by a long, vertical wing below which is a support boom and rudder. The Mars BGS is attached to the gondola via a very strong, 3-8 km long tether. The BGS requires very little power (about 1 W on average) to operate, when it is not being reeled up to avoid terrain obstacles, and it can be made very light. This Mars BGS is expected to incorporate low-Reynolds number airfoil designs. The science payload could be split between the gondola and the BGS, e.g. the BGS in Fig. 9 illustrates cameras attached to it just below the large wing structure. Also shown is the narrow solar array on the top of the boom that supplies power to the BGS systems.

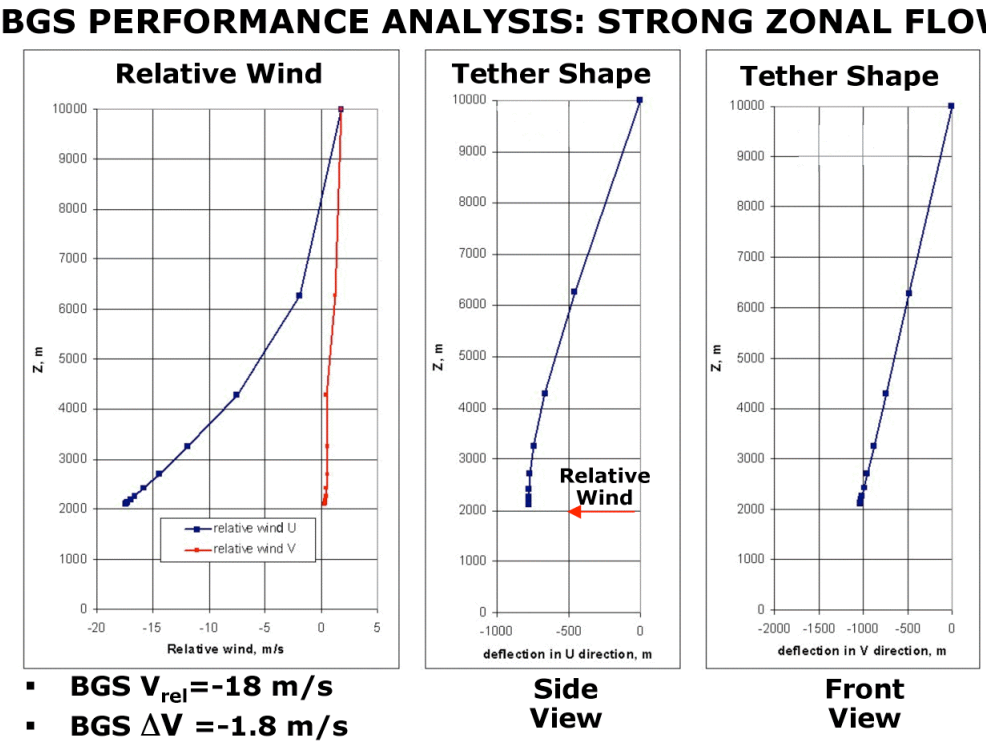

Fig. 7. BGS Performance in strong zonal flow.

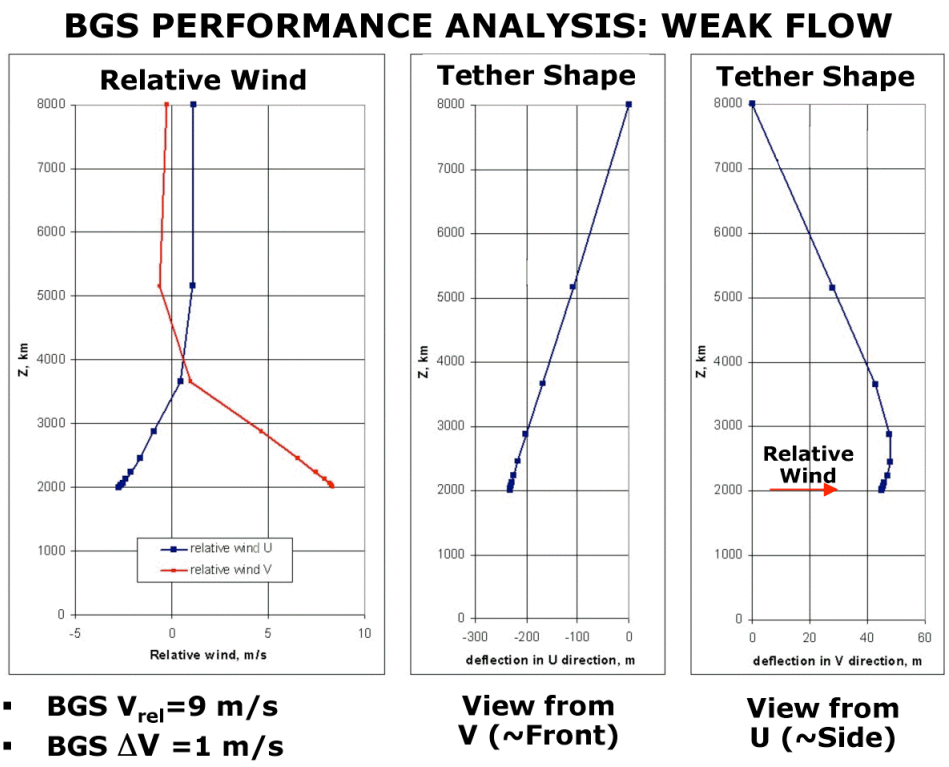

Fig. 8. BGS Performance in weak wind flow.

In this example, the main wing is 8 m in length and 1 m in chord for a total of 8.0 m^2 in wing area. The assumed wing coefficient of lift is 0.8 with a corresponding drag coefficient of 0.2. The estimated mass of this wing system, including the support boom, rudder, and power and computer elements is 8.7 kg. The tether mass is estimated at 1.0 kg (only 125 g/km) while the winch mass is estimated at 2.0 kg. The total suspended mass of the BGS system is therefore only 11.7 kg. Designing a lightweight BGS can easily be achieved by the use of advanced structures technology including inflatable structures [7].

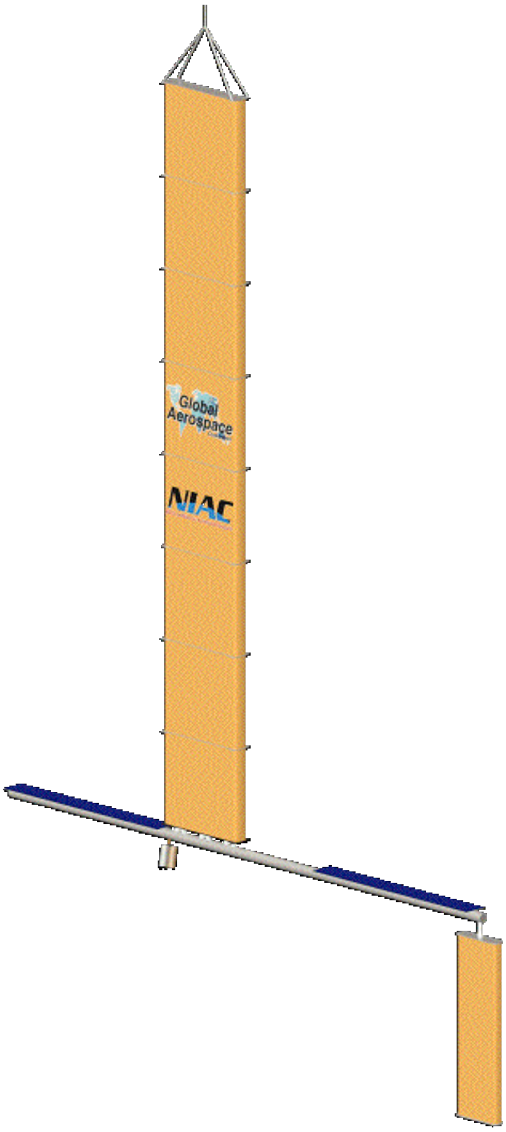

Fig. 9. Example BGS main wing system design.

5. SUMMARY

A Balloon Guidance System (BGS) provides flight path control so that balloons can be directed instead of being completely at the mercy of the prevailing winds. A BGS can be designed and fabricated out of very light materials, including inflatable structures. Earth-based scale model BGS testing provides high confidence in operation in relevant atmospheric conditions. Flight operations have been simulated at Mars using comprehensive aerodynamic and atmospheric models. In addition, the BGS concept is appropriate for near-term applications at Mars and other planets with atmospheres.

A BGS enables a number of science capabilities not otherwise available to Mars explorers. Global planetary coverage from within the atmosphere is possible. Targeted overflight of surface sites and more accurate delivery of science probes can occur. High-resolution imaging, elemental, magnetic and gravity surveys not possible or very challenging from orbit are enabled. Finally, robotic and crewed landing sites can be investigated at close range and navigation beacons deployed.

6. REFERENCES

1. Aaron, K. M., United States Patent No. 6,402,090, Balloon trajectory control system, Filed: June 29, 1998, Issued: June 11, 2002.
2. Aaron, K. M., M. K Heun and K. T Nock, "Balloon Trajectory Control," AIAA paper 99-3865, AIAA International Balloon Technology Conference, Norfolk, VA, July 1999.
3. Aaron, M. K. Heun, K. T. Nock, "A Method for Balloon Trajectory Control," COSPAR, Warsaw, Poland, July 2000.
4. Aaron, K., M. Heun, and K. Nock, "Advanced Technologies for Extended Flight Stratospheric Balloon Missions," 15th ESA Symposium On European Rocket and Balloon Programmes and Related Research, Biarritz, France, May 2001.
5. Pankine, A., K. Aaron, N. Barnes, and K. Nock, "Sailing the Planets: Planetary Science from Guided Balloons," 17th ESA Symposium On European Rocket and Balloon Programmes and Related Research, Sandefjord, Norway, May 2005.
6. Pankine, A., K. Aaron, N. Barnes, and K. Nock, "Guided Mars Balloon Platforms", 4th International Planetary Probe Workshop, Pasadena, CA, July 2006.
7. Pankine, A., NIAC Phase II Final Report, "Sailing the Planets: Science from Directed Aerial Robot Explorers (DARE)," April 14, 2006.
8. Sunada, S., "Comparison of Wing Characteristics at an Ultralow Reynolds Number," J. Aircraft, Vol. 39, No. 2, March–April 2002.
9. Justus, C. and D. L. Johnson, "Mars Global Reference Atmospheric Model (Mars-GRAM) 2001: Users Guide", NASA/TM-2001-210961, April 2001.

PRACTICAL NAVIER-STOKES COMPUTATION OF FLOWFIELDS WITH ABLATION PRODUCTS INJECTION

Daniele Bianchi[1], **E. Martelli**[2], **and M. Onofri**[3]

[1]*University of Rome "La Sapienza", 00184 Rome, Italy, daniele.bianchi@uniroma1.it*
[2]*University of Rome "La Sapienza", 00184 Rome, Italy, emanuele.martelli@uniroma1.it*
[3]*University of Rome "La Sapienza", 00184 Rome, Italy, marcello.onofri@uniroma1.it*

ABSTRACT

CFD codes typically treat fluid/solid boundary conditions in a simplified manner such as constant prescribed temperature or heat flux with zero mass transfer. However, thermal protection materials strongly interact with the flow so that simple CFD surface boundary conditions cannot realistically be used for TPS design. In order to obtain a better estimation of the wall heat flux over an ablating surface, a two-dimensional axisymmetric full Navier-Stokes equation solver is used coupled with surface mass balance and an ablation model. The wall composition is computed basing on equilibrium reactions with the solid phase (graphite) and the species are not allowed to react with each other as they diffuse across the boundary layer. The effect of gas injection in the boundary layer is studied focusing the attention on the wall heat flux and its reduction due to the blowing effect. Flat plate tests are presented. Results are compared with the most commonly used blowing rate correction equations.

NOMENCLATURE

B'	normalized mass blowing rate
C_h	Stanton number for heat transfer
C_m	Stanton number for mass transfer
D	diffusion coefficient
h	enthaply
h_r	recovery enthalpy
h_0	total enthalpy
j	diffusive mass flux
k	thermal conductivity
Le	$Lewis$ number
$\dot{m}$	blowing mass rate
p	pressure
q_{cond}	heat conduction into the solid
q_{rad}	radiative flux to the surface
T	temperature
u	streamwise velocity
v	velocity component normal to surface
y	mass fraction
$\alpha_{k,i}$	mass fraction of element k in species i
ϵ	surface emissivity
η	outward normal coordinate
λ	blowing correction parameter
ρ	density
σ	Stefan-Boltzmann constant
ω	mass flux due to surface chemical reaction

Subscript

e	outer edge of boundary layer or freestream
i	species
k	element
s	solid
w	wall

Superscript

r	surface reaction

1. INTRODUCTION

Usually CFD codes use simple surface boundary conditions (i.e. zero mass transfer) and cannot be realistically used to predict the aerothermal heating for the design of thermal protection systems (TPS). An appropriate boundary condition should include energy and multispecies mass balances with surface-kinetics or equilibrium models and surface ablation.
Current methods used to predict the aerodynamics and heatings of reentry vehicles focus their attention on some aspects of the problem at the expense of others. Thus aerodynamic methods concentrate on the flowfield, and rely on other methods to provide material-response characteristics such as surface temperature and ablation rates. On the other end, material-response methods concentrate on the physical and chemical processes associated with surface ablation and heat conduction in the interior of the heat shield in order to predict surface temperature, ablation rate, and internal temperatures, using correlation or highly simpified approaches to provide the aerothermodynamic heating acting on the surface of the vehicle. However, in reality all these phenomena are highly coupled.
The heat flux to the ablating surface is usually computed based on the input non-ablating heat transfer coefficients

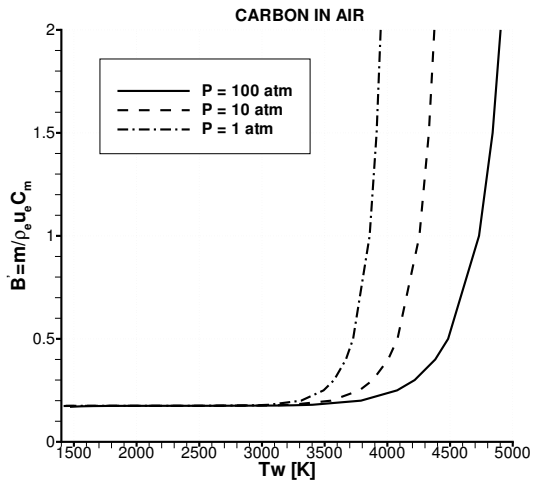

Figure 1. Dimensionless ablation rate for carbon. Full equilibrium surface thermochemistry.

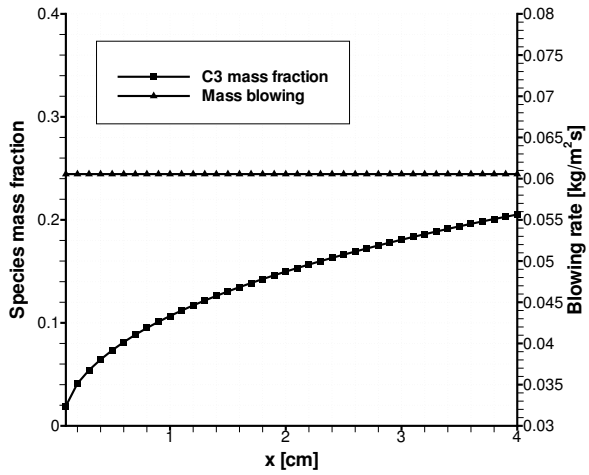

Figure 2. Case 1: Helium. Mass blowing rate (imposed) and C_3 mass fraction at wall.

and empirical blowing reduction parameters. The uncertainty in this estimated ablating surface heat flux is high, and consequently the predictions of surface blowing rate and temperature are somewhat inaccurate. Thus, in order to improve the estimation of the heat flux over an ablating surface, a flow solver with ablating surface conditions becomes a requirement. This goal can be achieved by considering that the surface energy and mass balances, coupled with an appropriate ablation model, provide complete thermochemical boundary conditions for a solution of the fully coupled fluid-dynamics/ solid mechanics problem. A significant increase of prediction capability in aerothermal computational fluid dynamics is possible by uniting CFD methodology with surface thermochemistry boundary conditions. However, none of the available Navier-Stokes solvers include complete boundary conditions to realistically determine aerothermal heating and surface ablation rates and a certain amount of decoupling is always performed.
In this study, a general surface boundary condition with mass balance and surface thermochemistry effects is developed for equilibrium gas states adjacent to a noncharring (graphite or carbon-carbon) ablating suface. Based on this formulation, a surface thermochemistry procedure is developed and integrated with a multispecies turbulent Navier-Stokes solver. Radiation and turbulent effects may be important in an ablating flowfield; however, they are not included in this paper.

2. NUMERICAL APPROACH AND SURFACE BOUNDARY CONDITIONS

The analysis of ablative flowfields is performed via a 2-D axisymmetric time-accurate multispecies reacting Reynolds averaged Navier-Stokes solver, ReVMBF (Reacting Viscous Multi-Block and shock-Fitting), based on the approach described by Nasuti & Onofri (1996) and Nasuti (2003). The main features of this method are to discretize the convective terms according to the lambda scheme and to handle shock discontinuities by a fitting technique developed by Moretti (1987). For the present calculations, the thermodynamic and transport properties of the single species are described by the curve fits of Gordon & McBride (1994). Mixture properties for conductivity and viscosity are derived from the Wilke's rule. The diffusion model used is limited to binary diffusion. The binary diffusion coefficients are specified using a constant Lewis number.
The general boundary conditions for a chemically reacting, noncharring ablating surface can be written as:

$$k\frac{\partial T}{\partial \eta}+\sum_i h_i \rho D_i \frac{\partial y_i}{\partial \eta}+q_{rad} = \rho v h_w - \dot{m} h_s + \epsilon \sigma T^4 + q_{cond} \tag{1}$$

which is the surface energy balance (SEB), and:

$$\rho D_i \frac{\partial y_i}{\partial \eta} = \rho v y_i - \dot{m} y_{s,i} + \sum_r^{N_r} \omega_i^r \tag{2}$$

which is the surface mass balance (SMB).
ω_i^r is the mass flux of species i due to surface reaction r, and $y_{s,i}$ is the mass of species i produced in the ablation gas per mass of TPS material ablated. The $y_{s,i}$ are positive for ablation products, negative for atmospheric species which are consumed in the ablation process and sum to unity. For charring (pyrolyzing) TPS materials, additional terms with pyrolysis gas flux have to be considered in the above boundary conditions. Equations 1 and 2 can also be applied on a non-ablating surface, if $\dot{m}$ and ρv are set to zero.
A summation of Equation 2 over all the species yields: [1]

$$\rho v = \dot{m} \tag{3}$$

[1] the summation made over the diffusive and chemical terms is zero because of mass conservation

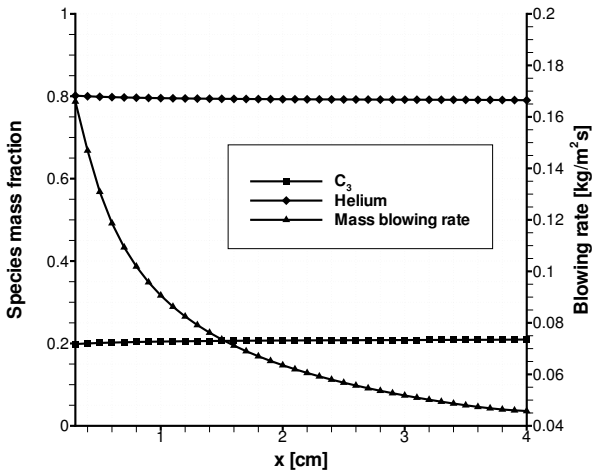

Figure 3. Case 1: Helium. Mass blowing rate and species mass fraction (imposed with equilibrium relations) at wall.

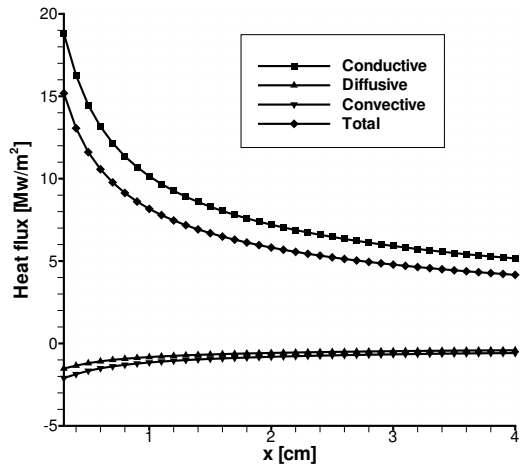

Figure 4. Case 1: Helium. Wall heat fluxes.

where ρ and v are the density of the gaseous mixture at the wall and the gas-phase convection velocity, respectively.
Making use of Equation 3 and neglecting the radiative and reradiative terms, the surface energy balance Equation 1 becomes:

$$k\frac{\partial T}{\partial \eta} + \sum_i h_i \rho D_i \frac{\partial y_i}{\partial \eta} + \dot{m}(h_s - h_w) = q_{cond} \quad (4)$$

In Equation 4 the terms on the left side account for the heat conduction to the surface, the diffusive chemical energy flux to the surface, and the convective energy flux due to blowing and injection. The term on the right side accounts for heat conduction into the solid. The conduction term q_{cond} is indeterminate from the CFD analyses, unless a numerical or semianalytic CSM (Computational Solid Mechanics) solution is also computed.
If the diffusion coefficients D_i of all species are assumed to be equal, then a summation of the SMB Equation 2 yields a balance equation for each element k, and consequently eliminates the surface reaction term:

$$\rho D \frac{\partial y_k}{\partial \eta} = \dot{m}(y_k - y_{s,k}) \quad (5)$$

where y_k is the elemental mass fraction of the gaseous mixture at the wall and $y_{s,k}$ is the elemental mass fraction of the TPS material.
The use of the elemental mass balance equation (5) instead of the species mass balance equation (2) permits to bypass the entire discussion about governing processes and intermediate steps concerning the number of species, reaction mechanisms, and the associated reaction rates, especially for the complex flowfields with ablation. The advantage of using Equation 5 instead of Equation 2 lies in the fact that the source term due to chemical reactions vanishes in the elemental approach. For what concerns the elemental composition of the ablation material (the term $y_{s,k}$) it is easy to determine because it depends only from the material while its species' counterpart composition (the term $y_{s,i}$) depends also from the reaction mechanism with the atmosphere and the atmosphere itself.

3. ABLATION MODEL

In a hypersonic heating environment, noncharring TPS materials, such as carbon-carbon and silica, lose mass only by ablation and melt/fail mechanisms. Detailed modeling of the performance of such TPS materials involves a CSM (Computational Solid Mechanics) and a CFD analysis coupled with surface mass and energy balance (SMB and SEB) and ablation modeling. Coupling the CSM and CFD via the surface energy balance yields the surface temperature. With the surface temperature, the surface mass balance, and a suitable ablation model, CFD analyses yield the wall heat transfer rate (conductive, diffusive and eventually radiating terms).
For TPS materials, the so called thermochemical ablation is the most general and widely applicable ablation model. This model was developed by Kendall et al. (1968) and by Kendall & Rindal (1968). Thermochemical ablation models are obtained from a solution of the equations for thermodynamic equilibrium or nonequilibrium between the TPS material and the atmosphere of interest, coupled with surface mass balance and boundary-layer transfer coefficients. With the boundary layer transfer coefficient approach the diffusional mass flux to the surface can be expressed as:

$$\rho D \frac{\partial y_k}{\partial \eta} = \rho_e u_e C_m (y_{k,e} - y_k) \quad (6)$$

where C_m is a dimensionless mass transfer coefficient and $y_{k,e}$ is the elemental composition at the edge of the

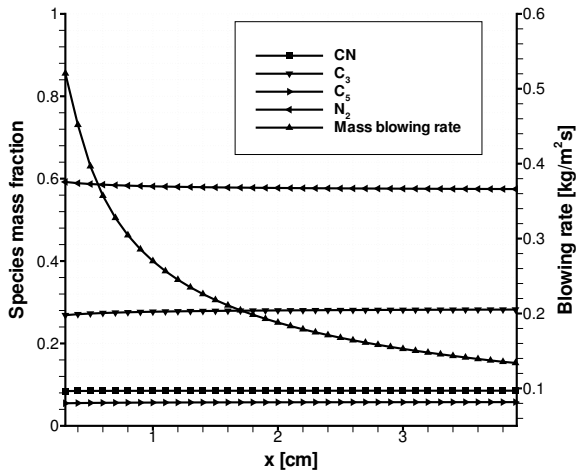

Figure 5. Case 2: Nitrogen. Mass blowing rate and species mass fraction (imposed with equilibrium relations) at wall.

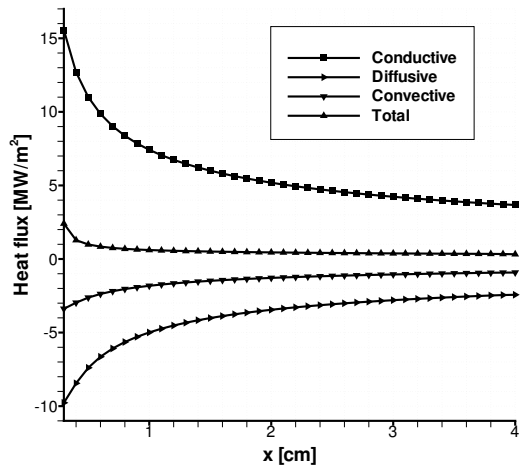

Figure 6. Case 2: Nitrogen. Wall heat fluxes.

boundary layer. With the use of Equation 6, the surface mass balance Equation 5 becomes:

$$\rho_e u_e C_m (y_{k,e} - y_k) = \dot{m}(y_k - y_{s,k}) \tag{7}$$

Introducing the dimensionless mass flux $B^{'} = \dot{m}/\rho_e u_e C_m$ Equation 7 becomes:

$$y_{k,e} + B^{'} y_{k,s} = (1 + B^{'}) y_k \tag{8}$$

which, fixing a value for $B^{'}$, permits to find the wall elemental composition (edge elemental composition $y_{k,e}$ and material elemental composition $y_{k,s}$ are known):

$$y_k = \frac{y_{k,e} + B^{'} y_{k,s}}{(1 + B^{'})} \tag{9}$$

Once the wall elemental composition is known, assigning the pressure and assuming that the gas is in chemical equilibrium with the wall material (or using kinetic rate-limited reactions between gas species and surface species) the surface temperature can be determined. The net result of the calculations is a set of thermochemical tables relating surface temperature and pressure to a dimensionless surface mass flux owing to ablation. These tables numerically represent a general ablation function $F(T, p, B^{'}) = 0$ for a specific TPS material, such as carbon, and a specific boundary layer edge gas, such as air. The shape of the $B^{'}$ curves depends on the material elemental composition, the choice of allowable surface and gas phase species, the atmospheric elemental composition, and whether or not kinetically limited reactions occur.

Figure 1 shows $B^{'}(T, P)$ for pure [2] thermochemical ablation of carbon in air. As the pressure is increased, a higher surface temperature is needed to reach the same dimensionless ablation rate. For any pressures, at the highest ablation rates, carbon sublimation is the primary mass loss mechanism, and C_3 is the predominant ablative species. However, below $B^{'} = 0.2$, surface oxidation reactions dominate, and CO is the major species leaving the surface.

The advantage of using these tables is that, once they have been generated, they are applicable over a wide range of aerothermal heating conditions. The disadvantage is that they are obtained with a very simplified boundary layer approach based on transfer coefficients (represented by the term C_m) to model species diffusion across the BL. In order to obtain the dimensional mass blowing rate we use the following expression, from the definition of $B^{'}$:

$$\dot{m} = B^{'} \rho_e u_e C_m \tag{10}$$

It is clear that the diffusion coefficient C_m then plays a dominant role in determining the surface ablation rate, and thus the uncertainty in this estimated mass blowing rate can be high. The coefficient C_m is in fact usually obtained via the convective heat transfer coefficient C_h and semi-empirical relations (Spalding, 1963) such as:

$$C_m = C_h Le^{2/3} \tag{11}$$

Sometimes they are even taken as simply being equal (Kuntz et al., 1999).

4. PRESENT APPROACH AND COUPLING TECHNIQUE

The important fact which is explained by the thermochemical ablation model, as shown by Figure 1, is that there is a unique relation between temperature and mass blowing rate. Even modern approaches rely on the use of

[2] no mechanical erosion or spallation

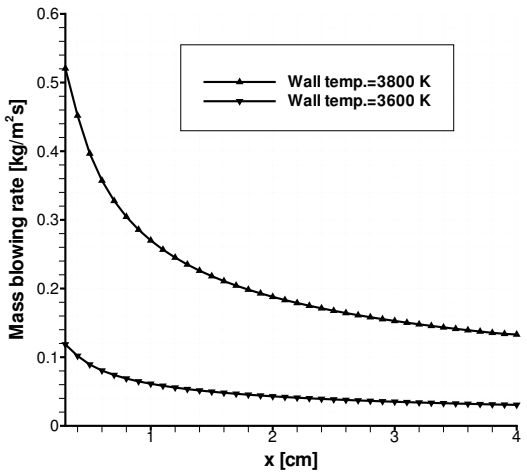

Figure 7. Case 2: Nitrogen. Effect of wall temperature on mass blowing rate.

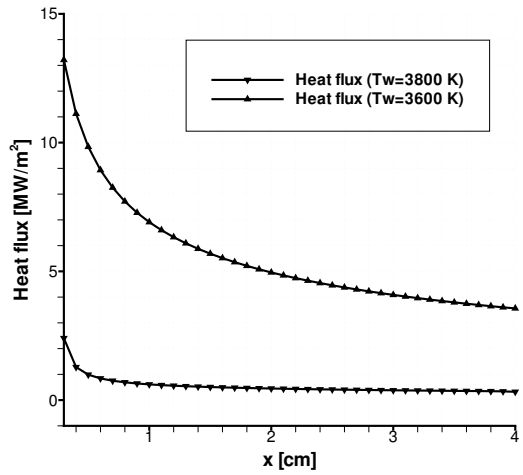

Figure 8. Case 2: Nitrogen. Effect of wall temperature on total wall heat flux.

such tables because of the difficulty of imposing directly the mass balance equation as boundary condition for the CFD code. The design and analysis of a TPS involves transient CSM (Computational Solid Mechanics) analyses of the material and a sequence of steady-state CFD analyses to determine the time-history of the aerothermal heating and coupled mass and energy balance boundary conditions, as reported in the work of Chen et al. (1995) and Olynick et al. (1999). When a coupling with a transient CSM code is not included in the analysis the steady-state ablation is commonly assumed as in the work of Bhutta & Lewis (1992) and Gupta (2000).

In all of these approaches the flowfield boundary conditions at the wall consist of a specified surface ablation rate $\dot{m}$ and a specified wall temperature T_w. When the procedure is coupled with a transient CSM analysis, wall temperature and mass blowing rate come from the material code (which makes use of thermochemical tables); when the procedure is based on the steady-state assumption, the mass blowing rate comes from the energy equation (Equation 1) written in the steady-state form, while temperture can be the sublimation temperature (Gupta, 2000) or is simply assigned to an arbitrary value (Bhutta & Lewis, 1992).

Assigning both temperature and mass blowing rate as boundary conditions can be misleading especially when the steady-state assumption is made; in this case, in fact, the steady-state wall temperature depends on the flowfield and it can be difficult to assign it beforehand (Bhutta & Lewis, 1993). When the wall temperature is specified, and with the wall pressure coming from the flowfield solution, the thermochemical ablation model dictates that there is a unique mass blowing rate coming from mass balance and from thermochemical equilibrium or nonequilibrium reactions between the gas mixture adjacent to the wall and the wall material. Therefore, assuming a fixed wall temperature, the mass blowing rate should be an output instead of an input. When temperatures and blowing rates come from a CSM code, the relation between blowing rate and temperature is guaranteed by the use of thermochemical tables. As we have seen, however, these tables rely on a very simplified boundary layer model and the error in the estimation of the mass transfer coefficient C_m to calculate the dimensional mass blowing $\dot{m}$ can compromise the accuracy of the following full Navier-Stokes solution (which has the calculated mass blowing rate as boundary condition).

In this work, efforts have been made in order to bring the process at the base of the thermochemical ablation model inside the CFD code. The advantage of using pre-generated tables is lost but the simplified boundary layer transfer-coefficient approach has been totally removed.

Coupling Technique

Assuming chemical equilibrium between the wall mixture of gases and the solid TPS material, with the pressure coming from the flowfield [3] and with the wall temperature assigned, the chemical composition at wall can be obtained using a free energy minimization procedure[4]. From the known wall species composition, the wall elemental composition is easily obtained with the relation:

$$y_k = \sum_i \alpha_{k,i} y_i \tag{12}$$

where $\alpha_{k,i}$ is the mass fraction of element k in species i. Also the diffusive mass flux of element k can be obtained with:

$$j_k = \rho D \frac{\partial y_k}{\partial \eta} = \sum_i \alpha_{k,i} \rho D \frac{\partial y_i}{\partial \eta} \tag{13}$$

[3] assuming zero pressure derivative in the normal direction: $\frac{\partial p}{\partial \eta} = 0$

[4] elemental composition of the environmental gas and of the wall material are assigned

Finally, with the elemental composition and the elemental diffusive mass flux at wall, the mass blowing rate can be evaluated using Equation 5:

$$\dot{m} = \frac{j_k}{(y_k - y_{s,k})} \tag{14}$$

Among the N_k (number of elements of the system[5]) equations of this type there are $N_k - 1$ relations[6] so that (obviously) they are not independent and there is only one mass blowing rate. Therefore the mass blowing rate can be obtained from Equation 14 using any of the elements of the system.
During the computational transitory the mass blowing rate boundary condition and the wall chemical composition[7] are continuously updated until the steady-state condition is reached. Mass blowing rate must be uptaded continuosly because it depends on the boundary layer solution (via the diffusive mass fluxes) and at the same time it affects its development. When steady-state (convergence) is reached, the mass blowing rate is everywhere consistent with the mass balance Equation 2 and the wall composition is in chemical equilibrium with the wall material at the wall pressure and temperature.

5. RESULTS AND DISCUSSION

The procedure described above is applied to a flat plate made up of pure carbon (graphite). Solutions with different environmental gases and boundary conditions are presented in this study to examine their effects on the predictions of flow structure and surface conditions. Chemical reactions between the wall material and the environmental gas are considered to determine the composition of the mixture of gases at wall. Once this composition has been calculated the species are not allowed to further react with each other as they are diffusing across the boundary layer.

Case 1: Helium environment

First, the case with an inert environmental gas made up of pure helium was analyzed. Two kind of wall boundary conditions are investigated. The first with assigned temperature and mass blowing rate and the second with assigned temperature and chemical composition. In the last case the composition at wall is the one in chemical equilibrium with the solid material (graphite) at the temperature and pressure of the wall. Since pressure is varying during the computational transitory, the wall composition is constantly updated. The respect of the elemental mass balance Equation 5 is invoked in both cases. In the first case the mass balance is used to compute the elemental composition, while in the second case it is used to compute the corresponding mass blowing rate. The freestream conditions are expressed in table 1. The wall temperature is kept constant and equal to $3500\ K$. At this temperature and for pressures near 1 bar the primary ablation product is gaseous C_3 (85%)[8]. The equilibrium assumption is acceptable because the wall temperature is sufficiently high (Kendall & Rindal, 1968). Figure 2 shows the C_3 mass fraction at wall along the x direction, with mass blowing rate imposed as boundary condition. As in the work of Bhutta & Lewis (1993), the ablation species (C_3) shows a gradual buildup in the streamwise direction and then asymptote to some value which is less than 1. Figure 3 instead, is obtained imposing the composition at wall to be in chemical equilibrium with the solid material (graphite) at the temperature and pressure of the wall. Wall composition is almost constant because the wall pressure is weakly varying. Mass blowing rate instead, is strongly varying in the streamwise direction according to the growing of the boundary layer. Higher mass blowing rates are experienced near the leading edge of the flat plate where the diffusional mass fluxes are higher. Imposing the wall composition is surely a more adequate boundary condition because it ensures a physical relation between the wall mixture of gases at wall and the solid material. Figure 4 shows the wall heat fluxes computed according to Equation 4. The diffusive and convective heat flux are negative in accordance to the fact that the mechanism of ablation reduces the total wall heat load.

Table 1. Freestream condition for Test Case 1

Freestream Conditions	
pressure:	1 [bar]
temperature:	4500 [K]
Mach number:	1.8
Composition:	100% He

Table 2. Freestream condition for Test Case 2

Freestream Conditions	
pressure:	1 [bar]
temperature:	5000 [K]
Mach number:	3.5
Composition:	100% N_2

Case 2: Nitrogen environment

[5] both material and environmental gas

[6] the elemental composition of the environmental gas is known and fixed as well as the elemental composition of the protection material; the only unknown is their relative amount at the wall

[7] the wal temperature is assigned and fixed but pressure can vary

[8] for higher temperatures also the production of C_5 becomes important

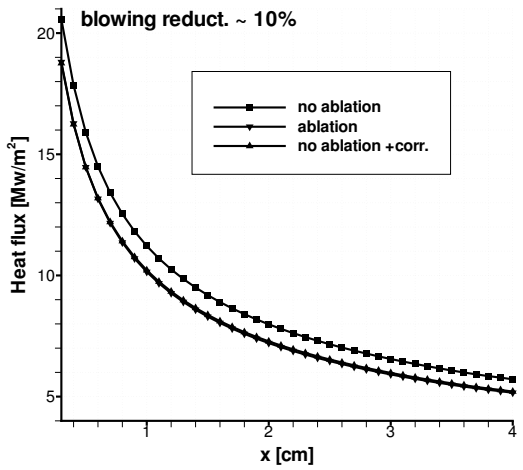

Figure 9. Case 1: Helium. Conductive wall heat flux with and w/o ablation: blowing effect and use of correction equation.

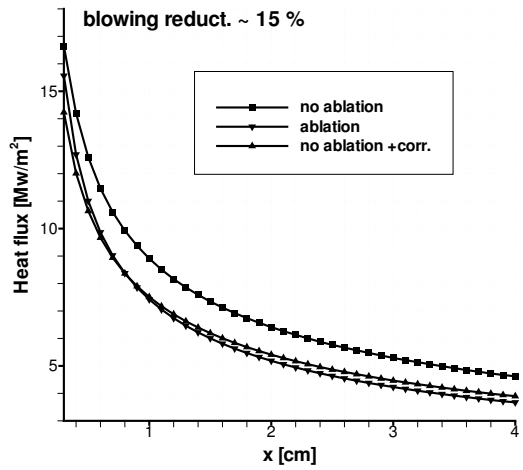

Figure 10. Case 2: Nitrogen. Conductive wall heat flux with and w/o ablation: blowing effect and use of correction equation.

In this case the environmental gas is molecular nitrogen and the ablation products considered are C_3, C_5, and CN. With the use of a non-inert environmental gas there are also reactions between the solid material and the gas itself (e.g. nitridation of carbon). The freestream conditions are expressed in table 2. The wall temperature is kept constant and equal to $3800\ K$. In this case freestream conditions and wall temperature are more severe in order to produce a higher ablation rate. The equilibrium composition between gas phase and solid phase is imposed at wall. The four species considered (C_3, C_5, CN, and N_2) make up more than 95% of the equilibrium mixture for the actual condition of pressure and temperature. Species with minor concentrations have been negleted. Figure 5 shows the composition at wall and the mass blowing rate. In this case the blowing rate is more intense because of the higher wall temperature and freestream Mach number. The higher wall temperature increases the ablation products' mass fraction at wall and, together with the higher freestream velocity, increases the species' gradients inside the boundary layer and consequently the diffusional mass fluxes. Figure 6 shows the wall heat fluxes. In this case the heat absorption due to the ablation process is much more evident and the total (conductive + diffusive + convective) heat flux is highly reduced. The same test case has been repeated with the same freestream conditions and a lower wall temperature of $3600\ K$. Figures 7 and 8 show the effect of a reduction in wall temperature on the mass blowing rate and total heat flux, respectively. A 5% reduction in wall temperature produces an average mass blowing reduction of approx. 75% and an average total heat load increase of approx. 85%. This is because wall temperature is close to the sublimation temperature. Looking at the thermochemical table of Figure 1 it can be seen that, in the knee region of the curve, a slight temperature variation causes a great mass blowing variation.

Comparison with blowing correction equation

In some cases, CSM and CFD codes are loosely coupled, and the thermal response solution is obtained using the nonablating heat flux with assumed blowing reduction parameter. Using a convective transfer coefficient approach the conductive heat flux from the gas to the surface can be expressed as (Chen & Milos, 1999, 2001):

$$q_c = \rho_e u_e C_h (h_r - h_{e,w}) \tag{15}$$

where $h_{e,w}$ is the enthalpy of edge gases evaluated at wall temperature and h_r is the recovery enthalpy which, for the laminar case, is expressed as:

$$h_r = h_0 - \frac{u^2}{2}(1 - \sqrt{Pr}) \tag{16}$$

In Equation 15 the term C_h is the transfer coefficient ($Stanton$ number) for heat transfer. A blowing correction allows for the reduction in transfer coefficient due to the transpiration or blowing effect of gases being injected into the boundary layer. The most commonly used blowing rate correction equation is (Chen & Milos, 1999, 2001):

$$C_h = C_{h_0} \frac{2\lambda B_0{}'}{\exp 2\lambda B_0{}' - 1} \tag{17}$$

where λ is a blowing redution parameter, C_h is the heat transfer coefficient for the ablating surface, C_{h_0} is the heat transfer coefficient for the nonablating surface, and $B_0{}'$ is the dimensionless mass flux evaluated with the nonablating transfer coefficient:

$$B_0{}' = \dot{m}/\rho_e u_e C_{m_0} \tag{18}$$

With $\lambda = 0.5$ Equation 17 reduces to the classical laminar-flow blowing correction.

Using Equations 15 and 16 to evaluate the unblown $Stanton$ number C_{h_0}, and Equations 18 and 11 to evaluate the dimensionless mass flux $B_0^{'}$, Equation 17 can be used to compute the corrected heat transfer coefficient. With the corrected heat transfer coefficient the ablative surface heat flux can be evaluated via Equation 15.
Figures 9 and 10 show the computed conductive heat fluxes for Test case 1 and 2 with and without ablation. Results are compared with the corrected nonablating heat flux using the methodology above mentioned. For Test case 1 the conductive heat flux is reduced approximately by 10% and the corrected curve shows a perfect agreement with the computed one. For Test case 2, with a more intense blowing, the reduction is approximately of 15% and the agreement between computed and corrected heat flux is slightly worse. The blowing reduction equation seems to work better in case of lower ablation rates, as one would easily expect.

6. CONCLUSIONS

The general surface boundary conditions with mass balance of chemically equilibrated gas adjacent to an ablating surface were derived. A computer procedure based on these surface conditions was developed and integrated with a two-dimensional axisymmetric full Navier-Stokes equation solver. Solutions with various surface boundary conditions were obtained to study the effects on surface composition and ablation rate. The solutions indicate that, when imposing mass blowing rate as boundary condition, the wall composition is regulated by boundary layer development and has no relations with the solid phase. Imposing the wall composition to be in equilibrium with the material solid phase, instead, allows to find the correct axial distribution of mass blowing rate which satisfies the mass balance equation. Mass blowing rates, wall species compositions, and surface heat fluxes were obtained for two different environmental gases over a flat plate. Results for blowing and nonblowing surfaces were compared with the most commonly used blowing rate correction equation.

7. AKNOWLEDGEMENTS

Attendance to the workshop was funded through the IPPW4 student scholarship programme.

REFERENCES

Nasuti F., Onofri M., "Analysis of Unsteady Supersonic Viscous Flows by a Shock Fitting Technique", *AIAA Journal*, Vol. 34, No. 7, July 1996, pp. 1428-1434

Nasuti F., "A Multi-Block Shock-Fitting Technique to Solve Steady and Unsteady Compressible flows", *Computational Fluid Dynamics 2002*, edited by Armfield S., Morgan P., Srinivas K., Springer-Verlag, Berlin, 2003, pp. 217-222

Moretti G., "A Technique for Integrating Two-Dimensional Euler Equations", *Computer and Fluids*, Vol. 15, No.1, 1987, pp. 59-75

Gordon S., McBride B. J., "Computer Program for Calculation of Complex Chemical Equilibrium Compositions and Applications", *NASA RP-1311*, October 1994

Kendall R. M., Bartlett E. P., Rindal R. A., Moyer C. B., "An Analysis of the Chemically Reacting Boundary Layer and Charring Ablator. Part I: Summary Report", *NASA CR-1060*, June 1968

Kendall R. M., Rindal R. A., "An Analysis of the Chemically Reacting Boundary Layer and Charring Ablator. Part V: A General Approach to the Thermochemical Solution of Mixed Equilibrium-Nonequilibrium, Homogeneous or Heterogeneous Systems", *NASA CR-1064*, June 1968

Chen Y. K., Henline W. D., Tauber M. E., "Mars Pathfinder Trajectory Based Heating and Ablation Calculations", *Journal of Spacecraft and Rockets*, Vol. 32, No. 2, March-April 1995

Olynick D, Chen Y. K., Tauber M. E., "Aerothermodynamics of the Stardust Sample Return Capsule", *Journal of Spacecraft and Rockets*, Vol. 36, No. 3, May-June 1999

Bhutta B. A., Lewis C. H., "New Technique for Low-to-High Altitude Predictions of Ablative Hypersonic Flowfields", *Journal of Spacecraft and Rockets*, Vol. 29, No. 1, Jan-Feb 1992

Bhutta B. A., Lewis C. H., "Low-to-High Altitude Predictions of Three-Dimensional Ablative Hypersonic Flowfields", *Journal of Spacecraft and Rockets*, Vol. 30, No. 4, July-August 1993

Gupta R. N., "Aerothermodynamic Analysis of Stardust Sample Return Capsule with Coupled Radiation and Ablation", *Journal of Spacecraft and Rockets*, Vol. 37, No. 4, July-August 2000

Chen Y. K., Milos F. S., "Ablation and Thermal Response Program for Spacecraft Heatshield Analysis", *Journal of Spacecraft and Rockets*, Vol. 36, No. 3, May-June 1999

Chen Y. K., Milos F. S., "Two-Dimensional Implicit Thermal Response and Ablation Program for Charring Materials", *Journal of Spacecraft and Rockets*, Vol. 38, No. 4, July-August 2001

Kuntz D. W., Hassan B., Potter D. L., "Iterative Approach for Coupling Fluid/Thermal Predictions of Ablating Hypersonic Vehicles", *AIAA Paper*, 99-3460, June 1999

Spalding D. B., "Convective Mass Transfer, an Introduction", *Edward Arnold*, London, 1963

The Effect of Forebody Geometry on Turbulent Heating and Thermal Protection System Sizing for Future Mars Mission Concepts

James L Brown, Ph.D.
Reacting Flow Environments Branch, MS230-2
NASA Ames Research Center
Moffett Field, CA 94035
jameslbrown@mail.arc.nasa.gov

Abstract

Past Mars entry missions have made extensive use of 70° sphere-cone forebody heatshields. This shape was chosen for its aerodynamic stability during direct entry, either ballistic or low L/D trajectories. Historic missions, including Viking in 1976, Pathfinder in 1997, and Mars Rover in 2004, have provided a large aerodynamic and aerothermodynamic database for the 70° sphere-cone shape that perpetuates continued use for future Mars missions. Using 3D Real-Gas Navier-Stokes simulations, we show that once turbulent heating occupies a significant portion of the mission trajectory, undesireable aerothermodynamic properties arise associated with the 70° sphere-cone heatshield geometry. As an additional consideration, the pitch angle to achieve high L/D of a Mars aerocapture trajectory mitigates the stability justification for the 70° sphere-cone. This suggests that alternative forebody geometries should be considered for future Mars missions.

Introduction

Future Mars mission concepts now include the use of larger diameter entry vehicles capable of aerocapture maneuvers. Associated with large diameter Mars vehicle concepts is the issue of heatshield boundary layer transition to turbulence early in the aerocapture maneuver. High heating levels associated with turbulent flow are expected throughout most of the atmospheric portion of the trajectory. We find that the 70° sphere-cone heatshield geometry[1-3], with a pitch angle set to accomplish aerocapture, to be particularly ill-behaved with respect to heat levels once turbulent transition occurs. On the leeside of the heatshield, the turbulent heating bump factor can reach as high as 6, causing the leeside turbulent heating to exceed even the heating level at the laminar stagnation point. This turbulent heating behaviour for the 70° sphere-cone is seen both in Navier-Stokes solutions for the present work and in experiments carried out in the Cal Tech T5 facility in support of the Mars Science Lab mission, see Wright, et.al.[4].

In this paper, we consider the origins of the observed excess heating associated with turbulent flow over the leeward 70° sphere cone heatshield and, furthermore, examine an alternative ellispoidal heatshield geometry chosen so as to match the 70° sphere-cone diameter and aerodynamic lift and drag. For the latter geometry, transition to turbulence occurs predominantly over the leeside of the heatshield leaving the stagnation point laminar, but with turbulent heating bump factor on the leeside reaching only approximately three. As a consequence, a significant potential reduction in forebody heatshield TPS mass can be achieved relative to that required for a 70° sphere-cone.

Discussion

As an example of this turbulent heating effect, Fig. 1 depicts heatshield surface results obtained using the DPLR Real-Gas Navier-Stokes code[4] for the peak heating time of a trajectory characteristic of a Mars aerocapture mission. Fig. 1 includes pressure contour lines in black and surface streamlines in red. For this trajectory point, the 70° sphere-cone is at a 16° angle of attack and a 0.24 aerodynamic L/D (Lift/Drag). Navier-Stokes solutions were obtained for both laminar and turbulent flow over the heatshield, using an 8-species Mars atmosphere chemistry model. All heating results in this paper are normalized by Qref, the peak laminar heating for this 70° sphere cone at this trajectory point. Fig. 2 shows the boundary layer momentum thickness for the laminar solution. Using as a criterion for turbulence transition as occuring when the laminar boundary layer momentum thickness Reynolds number, Reθ, exceeds 200, we see that the stagnation point and windward portion of the heatshield remain laminar, while the leeside of the heatshield becomes turbulent. Fig. 1 shows both the laminar (the

figure's left half) and turbulent (the figure's right half) heating levels obtained from the Navier-Stokes solver. As can be seen, turbulent peak heating actually occurs on the leeward-most shoulder far in excess of the stagnation point heating level, with a turbulent heating bump factor, defined as (turbulent Qw)/(laminar Qw), approaching 6 along the leeward centerline.

This turbulent heating effect associated with the 70° sphere-cone geometry suggests that when turbulent transition occurs early in the trajectory, a search for an alternative heatshield geometry may yield a more benign design heating pulse, both integrated and peak levels, with a possibility for relatively lighter density TPS materials and lower forebody TPS mass.

In order to explore this potential, we consider a family of ellipsoid heatshield geometries with parameterization configured so as to match the diameter and aerodynamic lift and drag properties of the 70° sphere-cone heatshield at hypersonic velocities for the Martian atmosphere. The matching of hypersonic aerodynamics was accomplished using a modified Newtonian method for both the 70° sphere-cone and the prototype ellipsoidal shape. Fig. 3 shows the height variation with radius of the resulting axisymmetric ellipsoidal shape as compared to the 70° sphere-cone.

Fig. 4 depicts the ellipsoidal heatshield heating obtained by the DPLR Navier-Stokes solver for the same trajectory conditions as for the 70° sphere-cone heating shown in Fig. 1. Fig. 4 includes pressure contour lines in black and surface streamlines in red. Fig. 5 shows the boundary layer momentum thickness for the ellipsoidal heatshield at this trajectory point.

For the ellipsoidal heatshield, transition occurs on the leeward side of the heatshield similar to the 70° sphere-cone. The laminar heating levels for the 70° sphere-cone and the ellipsoidal heatshield are comparable. However, the peak turbulent heating for the ellipsoid heatshield is at a much reduced level relative to the 70° sphere-cone. The turbulent peak heating for the ellipsoidal heatshield is at a Qw/Qref of 1.63 compared to 3.23 for the 70° sphere-cone, a reduction of nearly 50%.

The high leeside turbulent heating for the 70° sphere-cone appears related to a stronger than expected turbulent viscous-inviscid interaction that occurs for this shape on the heatshield leeside. For a thin boundary layer, inviscid regions are insensitive to growth of the boundary layer. Once boundary layer growth begins to affect the pressure field imposed by the inviscid flow over the viscous region, a viscous-inviscid interaction is said to have occurred. Typical interaction regions include separated regions and shock/boundary layer interactions where wall shear stress and heating can be significantly affected by the interaction. The exact nature of the present interaction is not fully understood, but observations can be made.

To examine the effects of this viscous-inviscid interaction, Fig. 6 and 7 show the boundary layer thickness color contours for the 70° sphere-cone and the ellipsoidal heatshields, respectively. Both laminar and turbulent results are given in these figures. The single black contour line in each figure gives the trace of where the boundary layer edge Mach number, Me, equals 1. Note in Fig. 6, for the leeward portion of the 70° sphere-cone heatshield, that the turbulent Me=1 contour line is changed in position significantly relative to the laminar Me=1 contour line. This corresponds to where the turbulent boundary layer thickness has considerably increased over the laminar thickness. However, Fig. 7 shows this effect on the Me=1 contour line as much less dramatic for the ellipsoidal heatshield.

Fig. 8 through 11 explores the differing strength of this effect for the 70° sphere-cone compared to the ellipsoidal heatshield. These plots give the variation of the boundary layer edge Mach number, wall pressure, boundary layer thickness and convective heating along the centerline, Y=0, of the two heatshields. Obvious is that there is a significant change in the turbulent relative to the laminar solution along the leeward side of the 70° sphere cone heatshield, but this is not true for the ellipsoidal heatshield. There are virtually no differences in the edge Mach number and wall pressure plots for the laminar vs turbulent ellipsoidal heatshield solutions. And yet, the small difference in the wall pressures along the leeward side, turbulent vs laminar, of the 70° sphere-cone is associated with a very substantial change in edge Mach number.

The unusual centerline heating results of Fig. 11, in particular, has experimental support in that similar results for laminar vs. turbulent heating were also obtained for the 70° sphere-cone in the T5 tunnel of CalTech as reported by Wright, et.al.[4] where the turbulent heating bump factor also approached 6 on the leeside centerline of the 70° sphere-cone being tested.

These several observations are manifestations of the unexpected sensitivity of an interaction ocurring between the viscous turbulent boundary layer and the thin inviscid region between the boundary layer and the bow shock in this region for the 70° sphere-cone.

The effects manifest in the viscous-inviscid interaction along the 70° sphere-cone leeside originate for two reasons. The first is that along the leeward centerline the turbulent boundary layer thickness is a significant fraction of the shock standoff distance. The second is the turbulent boundary layer in this region is efficiently entraining, or "swallowing", an energetic entropy layer that occupies much of the inviscid region between the boundary layer and the bow shock. The entropy layer, of course, is an inviscid but rotational region that arises in the presence of a curved bow shock.

Fig. 12 presents, for the leeward centerline (Y=0, Z>0) pitch plane of the 70° sphere-cone, color-shaded contours of the total enthalpy, along with the approximate bow shock position depicted by a solid black line. Both laminar and turbulent solutions are given. The viscous boundary layer region shows clearly in the total enthalpy color contours, since the total enthalpy does not change across the shock nor in the freestream. Fig. 13 supplements Fig. 12 with individual profiles at a typical station, (Y=0, Z/R~3/4), along this same 70° sphere-cone leeside centerline, of the laminar and turbulent normalized velocity, $U/U\infty$ and normalized total enthalpy, $(H-H_{wall})/(H\infty-H_{wall})$ as a function of the distance from the wall, Yn/R. Fig. 12 and 13 show the turbulent boundary layer in this region to be considerably thicker than the laminar boundary layer, but is very full with a steep gradient near the surface and with an extensive "wake" region. The turbulent boundary layer edge is best found in Fig. 13 by examination of the normalized total enthalpy at Yn/R~0.018. The turbulent solution bow shock is at Yn/R~0.06. The turbulent boundary layer occupies 30% of the bow shock standoff distance. The bow shock is actually closer to the surface for the turbulent relative to the laminar solution by approximately 7%. Also, the entropy layer edge can best be seen in the velocity profiles of Fig. 13 at Yn/R~0.028, about 47% of the bow shock standoff distance. The turbulent boundary layer is in the process of entraining the rotational entropy layer. The vorticity inherent to an entropy layer is favorable to rapid production of turbulent kinetic energy. As the turbulent structures span the boundary layer, this energizes the inner portion of the boundary layer, leading to a full velocity profile, a higher wall shear stress and higher heat transfer.

The observed increase in turbulent boundary layer edge Mach number for the 70° sphere-cone leeside occurs, not as a result of acceleration, but because the turbulent boundary layer edge moves outwards into the higher Mach number entropy layer as part of the entrainment process. This entrainment process is rapid, being nearly complete by the time the leeward shoulder is reached.

Fig. 14 shows contours of the normalized wall shear stress and reinforces the observation that the wall shear stress and heat transfer undergo a significant increase in this leeside centerline region of the 70° sphere-cone as a result of the entropy swallowing process.

These unusual effects are not observed to occur with the ellipsoidal heatshield. Although there is an increase in thickness for the turbulent boundary layer relative to the laminar boundary layer (Fig. 10), no discernible difference in the wall pressures (Fig. 9) are seen for the turbulent vs. laminar ellipsoid heatshield, and the edge Mach numbers (see Fig. 8) are unaffected as well. Further, the turbulent heating bump factor over most of the ellipsoidal heatshield remains at a level of approximately 3, more characteristic of an "acreage" or weak interaction turbulent heating bump factor. Unlike the 70° sphere cone, the bow shock for the ellipsoidal heatshield stands considerably further off the surface, so that the increase in turbulent boundary layer thickness does not lead to the types of viscous-inviscid interaction effects seen with the 70° sphere-cone.

To compare thermal protection system, TPS, sizing for the baseline 70° sphere-cone and the alternative ellipsoid heatshield, the heat pulse for a typical 70° sphere-cone Mars aerocapture trajectory shown in Fig. 15 is used in conjunction with the FIAT material response code, see Chen and Milos[5]. Loomis suggests in [6] a convenient curve fit procedure where the form $q=a\rho^m V^n$ is assumed and the coefficients a,m and n are found from fitting a limited number of heat transfer solutions along a specified trajectory. Loomis fits for the heating pulse for both the 70° sphere-cone and the ellipsoidal heatshields are shown based on the same vehicle atmospheric entry trajectory. The same trajectory (velocity and altitude vs time) would appy to both heatshields since the ellipsoidal heatshield was configured to match the aerodynamic lift and drag of the 70° sphere-cone heatshield.

Due to the high heating level for this trajectory of the 70° sphere-cone, PICA (Phenolic Impregnated Carbon Ablator, see Tran, et.al.[7]) is chosen as a suitable baseline TPS material. A simplified constant thickness TPS approach is used for the baseline heatshield giving an unmargined mass of 232 Kg for the PICA baseline 70° sphere-cone heatshield. For the 70° sphere-cone, proper center-of-gravity placement is aggravated by the leeside peak turbulent heating were variable thickness heatshield to be used.

TPS sizing was also carried out for the ellipsoid heatshield. The approximately 50% lower peak heat transfer enabled consideration of lighter TPS materials such as SLA-561v (see Covington, et.al.[8]) for the ellipsoid heatshield. Further, the lower heating pulse appropriate to the ellipsoidal heatshield shown in Fig. 15 is used for the ellipsoidal heatshield TPS sizing. TPS sizing for the SLA-561v ellisoid heatshield gives an unmargined forebody heatshield TPS mass of 64 Kg. Fig. 16 compares this estimate for unmargined mass of the SLA-561v ellipsoidal heatshield with the 232 Kg for the unmargined mass for the PICA baseline 70° sphere-cone heatshield.

The considerable saving in TPS mass for the ellipsoidal heatshield relative to the 70° sphere-cone is the consequence not only of the reduction in thickness of the heatshield but also that a switch to the lighter density SLA 561v was enabled due to the much lower peak heating level. The reduction in peak heating by approximately 50% for the ellipsoidal heatshield relative to the 70° sphere-cone thus leads to forebody heatshield with only 27% of the TPS mass.

This particular example emphasizes both the non-linearity of TPS mass sizing with applied heat load and the importance of heatshield shape in reducing the entry integrated heat load.

Concluding Remarks

A more thorough aerodynamic stability and aerothermodynamic analysis of the ellipsoid heatshield, followed by experimental validation, would be required before its use could be confidently recommended for a Mars mission. We stress that no optimization of the ellipsoidal heatshield geometry was attempted, only that the hypersonic lift and drag levels were matched to the baseline 70° sphere-cone heatshield.

Clearly demonstrated in this paper is that with an increase in probe size anticipated for future Mars missions, once the flow over the 70° sphere-cone heat shield becomes turbulent, a significant penalty in excessive heating is associated with the 70° sphere-cone geometry. This appears to be associated with a weak viscous-inviscid interaction arising from the "swallowing" of the entropy layer over the leeside heat shield by the turbulent boundary layer leading to energizing the inner portion of the turbulent boundary layer, with consequent high wall shear stress and heat transfer. This problem is seen not to occur with at least one alternative heatshield shape, that of a modified ellipsoid. As a result, demonstrated in this brief analysis, there is sufficient potential to justify further exploration of heatshield geometries that are alternatives to the classic 70° sphere-cone for use in future Mars missions.

Acknowledgements

This work was supported by Michelle Munk of the NASA In-Space Propulsion program. The TPS sizing reported in this paper for the 70° sphere-cone and ellipsoidal heatshield were accomplished by Y.-K. Chen and S. Sepka of Ames Research Center.

References

1. Viking Lander System, Primary Mission Performance Report, NASA CR-145148, Martin-Marietta, April 1977.
2. Milos, F.S. and Chen, Y.-K., Mars Pathfinder Entry Temperature Data, Aerothermal Heating, and Heatshield Material Response, *Journal of Spacecraft and Rockets*, Vol. 36, No. 3, May-June 1999.
3. Roncoli, R.B., and Ludwinski, J.M., Mission Design Overview for the Mars Exploration Rover Mission, AIAA 2002-4823.
4. Wright, M.J., Olejniczak, J., Brown, J.L., Hornung, H.G. and Edquist, K.T., Computational Modeling of T5 Laminar and Turbulent Heating Data on Blunt Cones, Part 2: Mars Applications, AIAA 2005-0177, Jan. 2005.
5. Chen, Y.-K., and Milos, F.S., Ablation and Thermal Response Code for Spacecraft Heatshield Analysis, *Journal of Spacecraft and Rockets*, Vol. 36, No. 3, May-June 1993.
6. Olynick, D., Loomis, M., Chen, Y.-K.,

Venkatapathy, E. and Allen, G., New TPS Design Strategies for Planetary Entry Vehicle Design, AIAA 99-0348, Jan. 1999.

7. Tran, H.K., Johnson, C.E., Rasky, D.J., Hui, F.C.L., Tsu, M.-T. and Chen, Y.-K., Phenolic Impregnated Carbon Ablators (PICA) for Discovery Class Missions, AIAA 96-1911, June 1996.

8. Covington, M.A., Heinemann, J.M., Goldstein, H.E., Chen, Y.-K., Sailinas, T.-S., Balboni, J.A., Olejniczak, J., and Martinez, E.R., Performance of a Low Density Ablative Heat Shield Material, AIAA 2004-2273, June 2004.

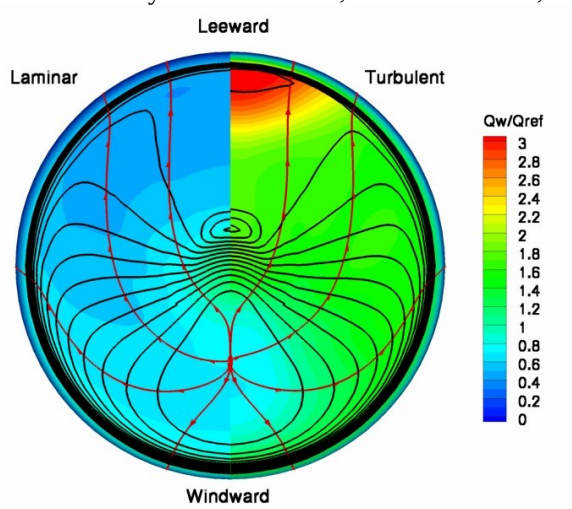

Fig. 1. Convective Heat Transfer for 70° Sphere-Cone Heatshield. 16° angle of attack, L/D=0.24, Peak Heating Trajectory Point. Surface streamlines in red. Pressure contour lines in black.

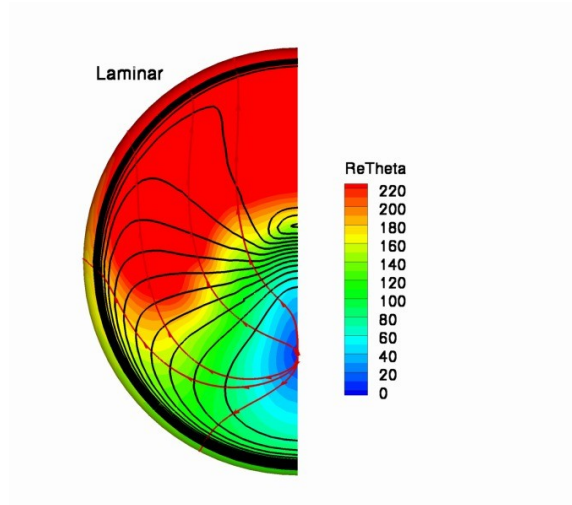

Fig. 2. Laminar Boundary Layer Momentum Thickness for 70° Sphere-Cone Heatshield.

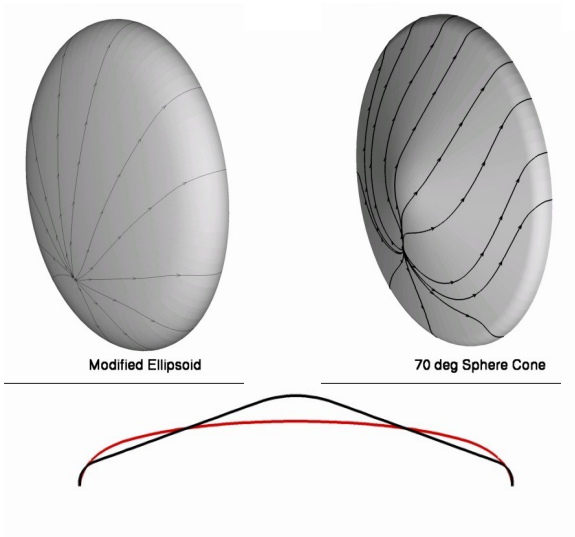

Fig. 3. Ellipsoidal (red) Heatshield Shape Comparison with 70° Sphere-Cone (black).

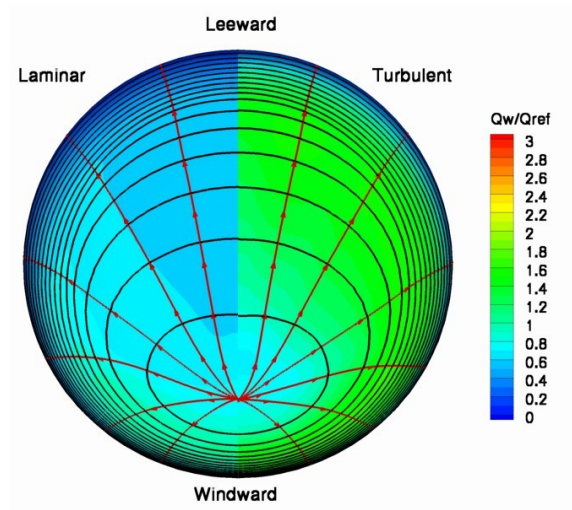

Fig. 4. Convective Heat Transfer for Ellipsoidal Heatshield, 16° angle of attack, L/D=0.24, Peak Heating Trajectory Point.

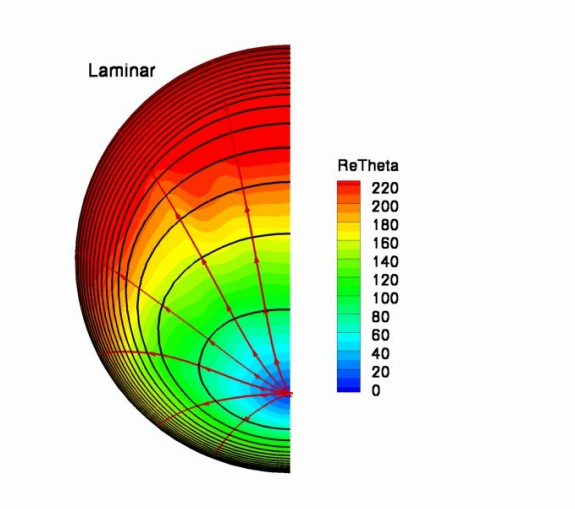

Fig. 5. Laminar Boundary Layer Momentum Thickness for Ellipsoidal Heatshield.

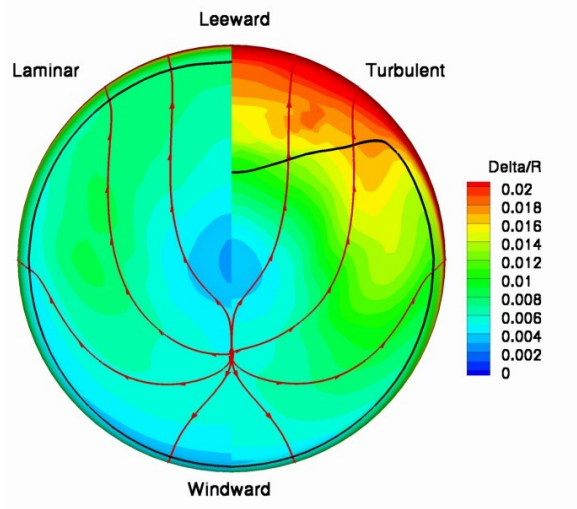

Fig. 6. Boundary Layer Thickness for 70° Sphere-Cone Heatshield. Mach 1 contour line in black, Surface Streamlines in red.

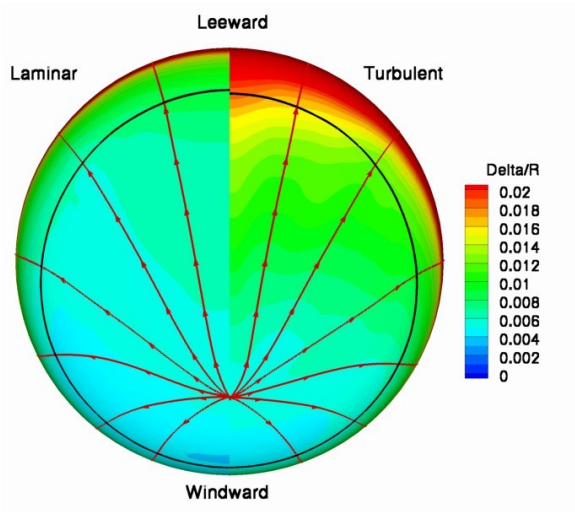

Fig. 7. Boundary Layer Thickness for Ellipsoidal Heatshield. Mach 1 contour line in black. Surface Streamlines in red.

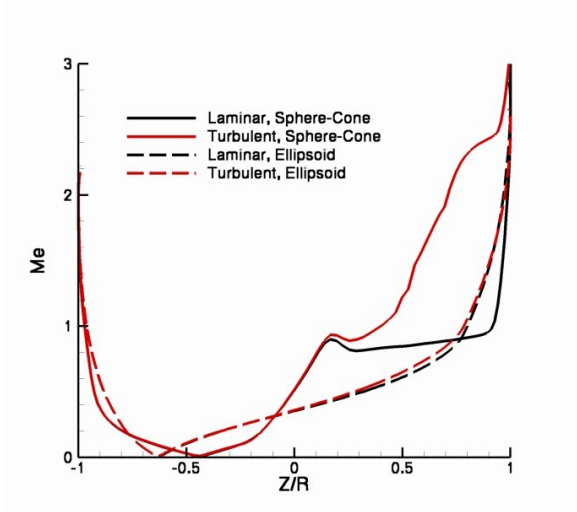

Fig. 8. Boundary Layer Edge Mach number variation along the Y=0 centerline for the 70° Sphere-Cone and Ellipsoidal Heatshields.

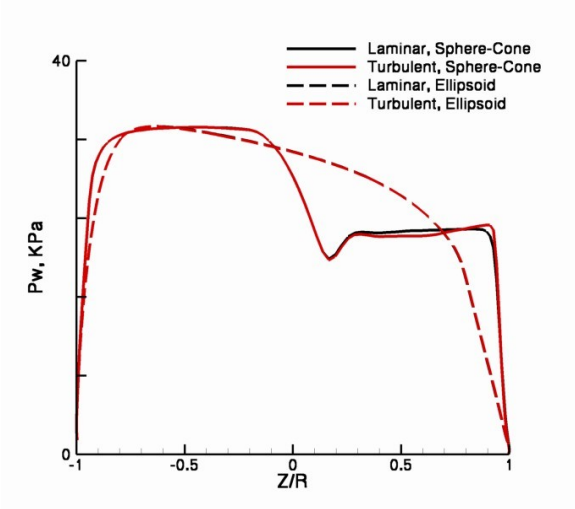

Fig. 9. Wall Pressure variation along the Y=0 centerline for the 70° Sphere-Cone and Ellipsoidal Heatshields.

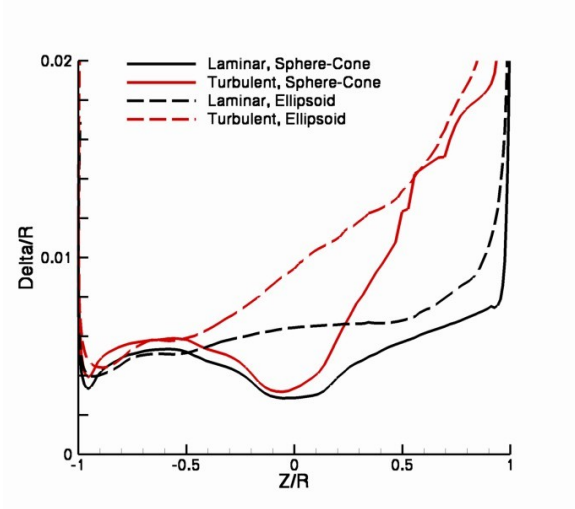

Fig. 10. Boundary Layer Thickness variation along the Y=0 centerline for the 70° Sphere-Cone and Ellipsoidal Heatshields.

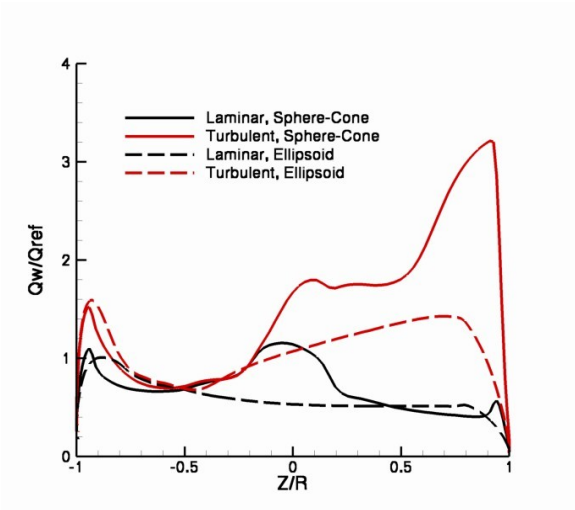

Fig. 11. Convective Heat Transfer variation along the Y=0 centerline for the 70° Sphere-Cone and Ellipsoidal Heatshields.

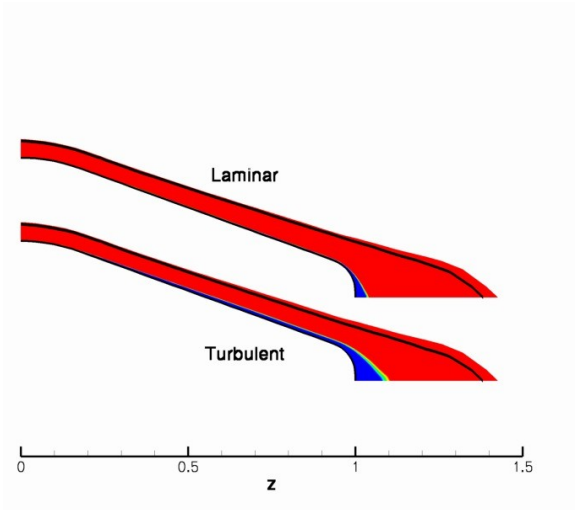

Fig. 12. Total Enthalpy Color Contours for Laminar and Turbulent Leeward Pitch Plane of 70° Sphere-Cone Heatshield. Bow shock location is depicted by black line.

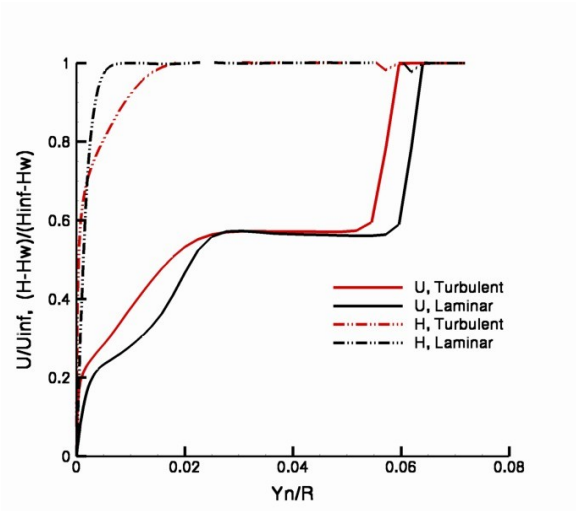

Fig. 13. Normalized Velocity and Total Enthalpy profiles for 70° Sphere-Cone leeward centerline (Y=0, Z/R=3/4)

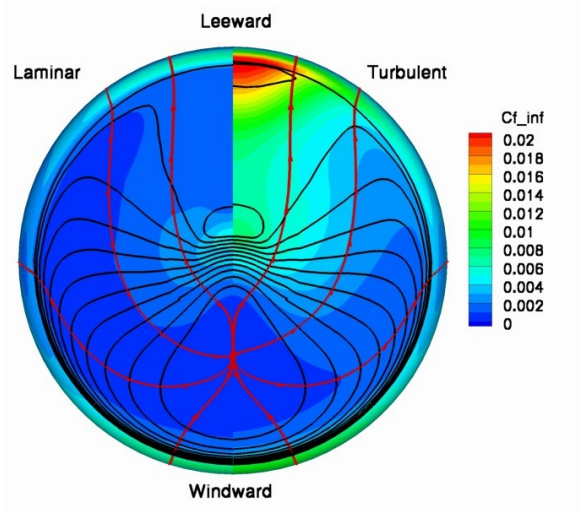

Fig. 14. Surface Shear Stress distribution for 70° Sphere-Cone. Normalized by $0.5(\rho U^2)\infty$.

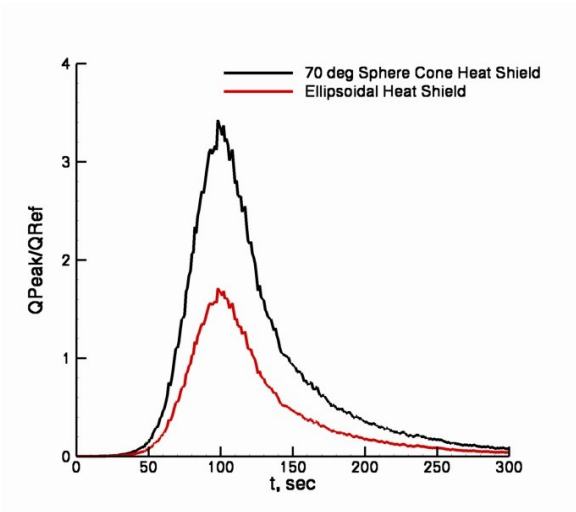

Fig. 15. Peak Heating Pulse for Ellipsoidal and 70° Sphere-Cone Heatshields, including turbulence, Mars Aerocapture Trajectory.

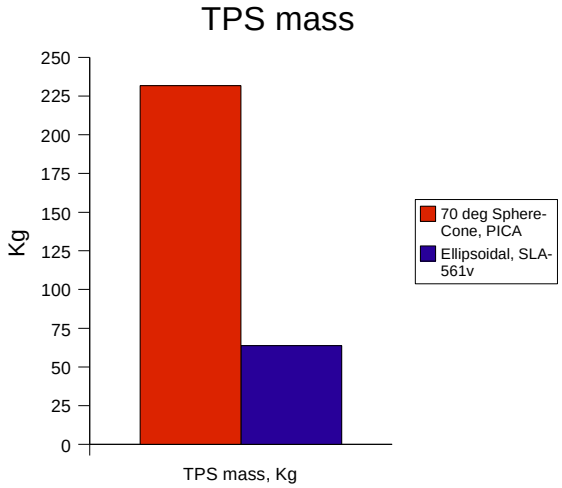

Fig. 16. TPS Sizing for Ellipsoidal vs 70° Sphere-Cone Heatshield.

Airship Simulation Models for Planetary Exploration Using Darts/Dshell

Jonathan Cameron, J. Balaram, Abhi Jain
Jet Propulsion Laboratory
4800 Oak Grove Drive
Pasadena, CA 91109
818-354-1189
Jonathan.M.Cameron@JPL.NASA.Gov

Robotically controlled airships and balloons are being considered for a wide range of planetary missions. In light of recent discoveries about Titan, the possibility of an airship mission to Titan is promising and exciting. Using an airship for planetary exploration presents unique challenges because its motion is very dependent on its environment. With landed rover missions, complete understanding of the interaction of a rover exploration vehicle and its environment is not as critical as with an airship. If problems arise with a rover, the system can go into a "safe" mode and do nothing until ground controllers can analyze the problem and decide how to deal with it. High-quality physical simulations of airships are important to develop a good understanding of how airships will interact with the environment in order to design airship configurations, develop control strategies, and create and test flight software.

At NASA's Jet Propulsion Laboratory (JPL), we have developed an airship simulation based on the *Darts/Dshell* high-fidelity dynamics simulation framework. This airship simulation model implements all of the key physical and aerodynamic features of airships including virtual mass effects, aerodynamic lift and drag forces of the main airship envelope and all attached fins, controllable thrusters, buoyancy effects, and more. The simulation includes a full model of the "ruddervator" tail fins including fixed and controlled surfaces.

Darts/Dshell Airship Simulation

In the airship simulation, the motion of the bodies involved is computed using the *Darts* high-fidelity multi-body dynamics simulation code. The "*Dshell*" part is used to model components that generate forces corresponding to aerodynamics, buoyancy, and thrusters. These forces are then applied to the bodies in the *Darts* multi-body simulation. The simulation also includes models of the environment of user-selectable fidelity developed for *DSENDS* (the entry and descent simulation for the MSL 2009 mission). In order to represent the terrain surface under the airship simulation uses the *SimScape* terrain modeling software library developed for Roams (rover simulation). *SimScape* allows the airship simulation to emulate instruments such as range finders that are needed by the onboard control software.

The simulation also includes a graphical visualization toolkit called "*Dspace*". The figure above shows the three dimensional view of the airship simulation. *Dspace* enables the simulation of views from cameras attached to the airship to simulate capturing images for science and control purposes.

The airship simulation can be run in several different modes. In one mode, the user can pilot the simulated airship as if it was an RC aircraft with controls to vary thrust, tilt the thrusters, and turn the movable control surfaces. The airship simulation can also be controlled from a non-human external source, such as receiving commands from emulated flight software or from scripts.

In the paper we will describe the features above in detail and describe how the airship simulation is being used at JPL to develop concepts for exploration of Titan using airships.

Autonomy Capability Development for a Titan Aerobot

Alberto Elfes, Jeffery L. Hall, Eric A. Kulczycki, Arin C. Morfopoulos,
James F. Montgomery, Daniel S. Clouse, David S. Bayard, Jonathan M. Cameron, Richard J. Machuzak,
Lee J. Magnone, Charles F. Bergh, Gerald J. Walsh

Jet Propulsion Laboratory
Pasadena, CA 91109, USA

Exploration of the planets and moons of the Solar System has up to now relied on remote sensing from Earth, fly-by probes, orbiters, landers and rovers. Remote sensing probes and orbiters can only provide non-contact, limited resolution imagery over a small number of spectral bands; landers provide high-resolution imagery and in-situ data collection and analysis capabilities, but only for a single site; while rovers allow imagery collection and in-situ science across their path. The fundamental drawback of ground-based systems is limited coverage: in past or planned exploration missions, the rover range has varied from approximately 130m for the 1997 Sojourner mission, to currently 4.0 km for the Mars Exploration Rovers, to tens of kilometers for the teleoperated Lunokhod rovers.

There is currently a strategic gap in robotic exploration technologies for systems that combine extensive geographical coverage with high-resolution data collection and in-situ science capabilities. For planets and moons with an atmosphere, this gap can be addressed through aerial vehicles. In the Solar System, in addition to Earth, the planets Venus and Mars, the gas giants (Jupiter, Saturn, Uranus and Neptune) and the Saturn moon Titan have substantial atmospheres. Aerial vehicles that have been considered for planetary exploration include airplanes and gliders, helicopters, balloons [Kerzhanovich 2002] and airships. Flight time for gliders depends heavily on wind and updraft patterns, which in turn constrain their surface coverage, while airplanes and helicopters expend significant energy resources simply staying airborne [Elfes 2001, Elfes 2003].

Lighter-than-atmosphere (LTA) systems provide significant advantages for planetary exploration due to their potential for extended mission duration, long traverse, and extensive surface coverage capabilities. Robotic airships, in particular, are ideal platforms for airborne planetary exploration. Airships have modest power requirements, and combine the extended airborne capability of balloons with the maneuverability of airplanes or helicopters. Their controllability allows precise flight path execution for surveying purposes, long-range as well as close-up ground observations, station-keeping for long-term monitoring of high-value science sites, transportation and deployment of scientific instruments and in-situ laboratory facilities across vast distances to key science sites, and opportunistic flight path replanning in response to the detection of relevant science sensor signatures. Furthermore, robotic airships provide the ability to conduct extensive surveys over both solid terrain and liquid-covered areas, and to reconnoiter sites that are inaccessible to ground vehicles.

The main challenges for aerobot exploration of Titan include: *large communication latencies*, with a round trip light time of approximately 2.6 hours; *extended communication blackout periods* with a duration of up to 9 Earth days, caused by the rotation of Titan and its orbital occlusion by Saturn; *extended mission duration*, currently projected to be on the order of six months to one year; and o*peration in substantially unknown environments,* with largely unknown wind patterns, meteorological conditions, and surface topography.

These challenges impose the following capability requirements on a Titan aerobot: *vehicle safing*, so that the safety and integrity of the aerobot can be ensured over the full duration of the mission and during extended communication blackouts; *accurate and robust autonomous flight control*, including deployment/lift-off, long traverses, hovering/station-keeping, and touch-and-go surface sampling; *spatial mapping and self-localization* in the absence of a global positioning system and probably of a magnetic field on Titan; and *advanced perceptual hazard and target recognition, tracking and servoing,* allowing the aerobot to detect and avoid atmospheric and topographic hazards, and also to identify, home in, and keep station over pre-defined science targets or terrain features.

In this paper, we present an aerobot autonomy architecture that integrates accurate and robust vehicle and flight trajectory control, perception-based state estimation, hazard detection and avoidance, vehicle health monitoring and reflexive safing actions, vision-based localization and mapping, and long-range mission planning and monitoring. We also discuss the development of a highly accurate aerodynamic airship model and its validation, as well as an initial implementation of the flight control system and the results obtained from autonomous flight tests conducted in the Mojave desert.

REUSABLE LAUNCH VEHICLE AEROSHELL MANUFACTURING CONCEPT

S. Ferretti[(1)], **G. Mazzoni**[(2)]

[(1)] University of Bologna, Faculty of Engineering, DIEM - Viale Risorgimento, 2 – 40100 Bologna, Italy
email: stefano.ferretti@mail.ing.unibo.it

[(2)]Technologies & Laboratories Manager, Alcatel Alenia Space, Strada Antica di Collegno, 253 - Turin, Italy
email: guido.mazzoni@aleniaspazio.it

ABSTRACT

Innovative Reusable Launch Vehicles concepts pose several challenging manufacturing issues, which have been considered during a feasibility study conducted recently at Alcatel Alenia Space. One of these aspects is related to the manufacturing of a light aeroshell structure, high temperatures resistant, affordable in a strict time schedule with a cost effective approach.
A conservative approach was taken into account in the final design, implementing some reliable technologies to ensure short development time and available know-how to avoid long term investments planning.
The main issue is related to the construction of a quite large structure, requiring innovative manufacturing facilities and complex research tools. The manufacturing and forming of large Titanium honeycomb panels, with very complex shapes, represents itself a challenge. A special vacuum oven brazing process was selected and a dedicated study on filler metals researches offered the chance to design a suitable product for this application.
The final assembly of the panels to manufacture the aeroshell is planned using laser welding technology. In this case the very small thickness of the skins, the difficult accessibility of the parts to be joined and the strict dimensional tolerances required by the final product for aero-thermodynamic reasons, represents interesting aspects which have been investigated.
The aeroshell manufacturing design implements technologies like Cutting, Forming and Descaling of titanium thin skins and honeycomb, Brazing of titanium honeycomb and skins to obtain sandwiches, Laser welding on sandwiches to obtain assemblies.
The paper offers an innovative perspective on re-entry vehicles aeroshell system, including the principles of design for manufacturability and technology transfer as key points to reduce mass, delivery time and costs of the final product.

1. INTRODUCTION

Space exploration requires safe, reliable, and affordable systems for the development of future Reusable Launch Vehicles (RLV).
Significant efforts have been conducted internationally in the technology development of advanced manufacturing techniques and joining processes.
The application of special metallic heat resistant materials in hot load carrying structures, like the aeroshell structures, has been investigated, facing the several challenges of the manufacturing.
The present feasibility study has been performed recently at Alcatel Alenia Space with the aim of preparing a manufacturing plan for a light aeroshell structure, high temperatures resistant, affordable in a strict time schedule with a cost effective approach.

2. THE AEROSHELL

The aeroshell's main purpose is to protect the capsule inside from the intense heating of the entry into the planetary atmosphere.
The aeroshell is covered with a Thermal Protection System (TPS), acting as a heat shield which protects from the heat and sustain the aerodinamic drag (Fig.1).

Fig. 1 - Spirit entering Mars atmosphere
(©NASA)

The concept presented takes into account the implementation of some reliable technologies to ensure short development time and available know-how to avoid long term planning.

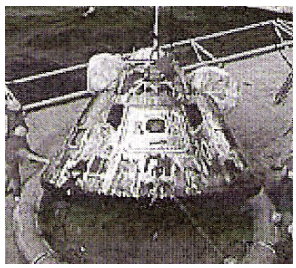

Fig. 2 – Apollo honeycomb heat shields
(©AERONCA)

The aeroshell here considered is made of a titanium honeycomb sandwiched between titanium face sheets using a brazing process, and consists of several panels assembled together with a laser welding process in three main parts: apex cone, central airframe, lower airframe.
These three assemblies are then integrated on the primary structure with mechanical fastening, taking care that appropriate insulation is provided between the two structures.

3. THE MANUFACTURING TECHNOLOGIES

The manufacturing of the aeroshell structure can be achieved implementing several different materials and technologies. A trade off among them suggested to keep the overall process highly reliable adopting well know processes, as the brazing one.
Considering the fact that there are some issues related to the relatively large dimension of the structure, it has been considered an investment in innovative facilities and advanced process simulation tools.
Also the forming of large Titanium honeycomb panels with a double curvature represents itself a challenge, and two options have been investigated.
In summary the technologies involved in the manufacturing process are:

Cutting, Forming and Deoxidizing
(on titanium skin and honeycomb).

Brazing
(on Ti honeycomb/skins
to obtain sandwiches)

Laser welding
(on Ti sandwiches
to obtain assemblies).

4. CUTTING, FORMING, DEOXIDIZING

The sandwiches are made of titanium skins and honeycomb which have to be prepared to assure appropriate shape, tolerances and cleanliness for the following brazing process.
All the materials, honeycomb and skins, require the deoxidizing for which it is needed a pool able to accommodate 3 m X 1.2 m panels.
Titanium skins don't need forming as they have a thickness of only 0,2 mm.
Titanium honeycomb (Ti3Al2.5V) is available in foils of the needed dimension, as it is possible to purchase 3mX2m foils. Honeycomb can be found already formed with double curvature, ensuring high mechanical properties, precise tolerances and a cell always perpendicular to the skin.

Fig. 3 – Titanium honeycomb (©INNOVENT)

In this case it is possible to purchase honeycomb which is produced on the base of our design requirements. It is obtained joining small machined pieces with special welding processes. Conical shapes can be provided for the upper and middle stage, more complex ones, to be used for the lower stage, have to be produced developing a process with the supplier.
A second option is to procure flat honeycomb and then to form it, developing an in house ad hoc forming processes.

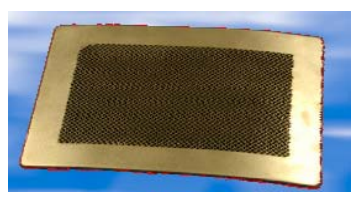

Fig. 4 – Titanium honeycomb panel (©INNOVENT)

Activies undergoing will provide information on some honeycomb samples (size: 50 mm X 50 mm, cells dim: 1/32" ÷ 1") to verify the brazing process and the mechanical properties of different cell size and configurations. In this case the honeycomb is furnished electrochemically polished.
The honeycomb panels have then to be cut to perfectly fit the final shape, as the brazing process requires an high level of precision on the contact surfaces to ensure that the bonding occurs at the border of each cell.

5. *BRAZING*

The joining processes like welding produce a melting and solidification of the base metal to create the connection between two parts.
The brazing process instead maintain the two parts in the original status and sees the melting of a filler, which with capillarity phenomena distribute itself in the gap between the pieces.
The main advantage of this process is that it works at lower temperature than the welding one, and it doesn't decrease the mechanical properties of the base metal.
The brazing process can be performed locally or globally, depending on the requirements and on the extension of the joints. Several methods can be applied, but it is considered the global brazing method in oven.
The driving factor in this case is that the global brazing process ensures a more uniform temperature distribution in the volume and produces a more precise joint geometry on large panels. The brazing in oven usually works in a controlled atmosphere (with an inert gas, e.g. Argon) or in vacuum.

Fig. 5 - Brazed Sandwiches

5.1 Brazing process

The aeroshell manufacturing requires a brazing process that has been designed to fulfil the following requirements:

1. *compatibility* of materials and filler metal
2. strict *tolerances (*minimum gap allowable for appropriate brazing is 0.25 mm)
3. high *degassing*
4. appropriate *thermal cycle*

The skins and the honeycomb are made of Ti 3Al 2.5V alloy, so it is recommended to apply a Ti based filler metal, to ensure homogenous joints and to produce a high rate of solidification, avoiding brittle behaviour.
To maintain strict tolerances during brazing it is important to perform the brazing of both the honeycomb surfaces at the same time, and the gap between surfaces have to be lower than ¼ mm.

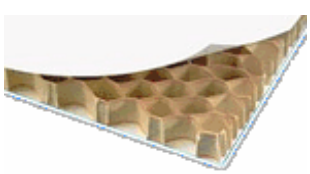

Fig. 6 – Titanium sandwich

The wall of the honeycomb cell has to be thick as much as possible, and at least 0.5 mm, because the filler metal can be chemically aggressive on the surfaces, producing distortions which can lower the mechanical properties.
It is required that the honeycomb used for Space application allows an high level of degassing and this is even more important in case of a brazing process is used for the manufacturing of the sandwiches.
The thermal cycle is crucial to obtain high performance brazed panels. Some other details have then been investigated to better define the eutectic temperature of the filler, cooling temperature available on the oven, mass of panels and tools, configuration of the overall system in the oven.

5.2 Filler metals

The composition of the filler metal depends on the materials involved in the process (Ti3Al2.5V) and on the temperature range determined by:

- operational temperature of the aeroshell: ~ 300 ºC
- β transformation temp of titanium alloy ~ 900 ºC

Several alloys have been considered in different forms: paste, powder, foils. Foils have been excluded for the very complex shape of the brazed joint and the difficulties to maintain tolerances. In the other forms some have been selected for a preliminary investigation:

- PASTE: Ag Cu (~ 780 ºC) and Ag Cu Ti (~ 900 ºC)
- POWDER: *Ti 37.5 Zr 15 Cu 10 Ni* (~ 850 ºC), US.

The brazing filler metal would be applied according to the physics, in fact the paste brazes thanks to capillarity. It is placed on the surface of the materials manually or with an automatic injector, then the assembly is dried at almost ambient temperature and finally the sandwich is placed into the oven for brazing. This solution ensure precise tolerances on the distribution of the filler and on the final joint geometry.

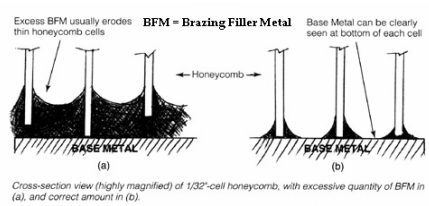

Fig. 7 – Effect of filler on the brazed joint

Another option considers instead the use of a brazing powder, which is placed on the pieces after having distributed the adhesive. This solution is largely adopted in aerospace components brazing and a compound for Ti alloys is already commercially available.

5.3 Oven

It is possible to realize the brazing process in oven having an Argon atmosphere or in vacuum, depending on the quality of the joints which are required by the specific applications.
The vacuum maintain a better clean condition and produces very high quality joints at level $>10^{-5}$ bar. For this reason the vacuum oven brazing was chosen as the ideal solution for this specific application.
The cooling after brazing has been recommended to occur in a convective environment, to increase the control of the oven parameters and the temperature gradient. This is obtained with the rapid insufflation of Argon in the chamber when filler has already reached the solidus temperature. For the development phase it is possible to use in house facilities which allow to perform testing on 1.5 m X 1.5 m panels.

Fig.8 – Brazing oven (©COFI)

6. LASER WELDING

The final assembly of the panels to manufacture the three part of the aeroshell is planned using a welding technology. The YAG laser welding has been identified as the most suitable process to assemble the Titanium brazed sandwiches, because it is compatible with requirements like the very small thickness of the skins, the difficult accessibility of the parts to be joined and the strict dimensional tolerances required by the final product for aero-thermodynamic reasons. Moreover the laser has a great advantage over other welding processes as it concentrate the energy in a very narrow path, reducing the thermal affected zone to the minimum, ensuring higher mechanical properties of the airframe.

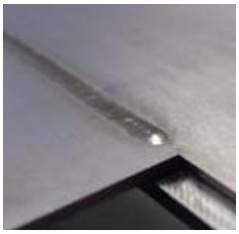

Fig. 9 – Laser welded sample

In fig. 8 are shown specimens 1mm thick which have been welded with 1 Kw YAG laser for preliminary tests, which proved that this process has the lowest thermal dispersion, producing at 10 mm from the weld seam a temperature of ~ 250 ºC. The low temperature is also very important to avoid damages to the brazed joints which have been created in the step before.
It is also known that the mechanical properties of the titanium skins at 0,1 mm from the welding are comparable to the base metal.

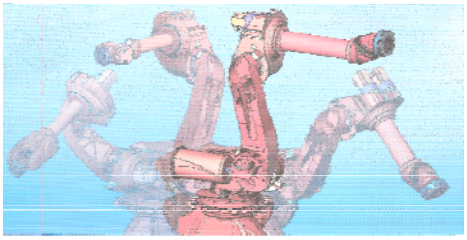

Fig. 10 – Laser welding facility (©COMAU)

Another advantage of the laser process is its flexibility, as it works transmitting the power through optical fibers. For this reason it offers the possibility of multiple welding and just changing the optics it can be used for laser cutting.

7. TESTS AND CONTROLS

The concept is suited for aerospace applications, especially for the ones in which a high temperature and strength-to-weight ratio is required. Brazed structures have also a good energy absorption capability and can withstand combinations of aerodynamic, acoustic, and thermal loads. To validate the processes described it is advisable that a test campaign might develop and validate control methods for the overall aeroshell and its subsystems. The "technologies and processes" laboratory is dedicated to characterize sandwich panels through:

Non Destructive Inspections

- Ultrasonic inspection
- Eddy currents
- X-Rays

Destructive tests

- Metallurgical characterization
- Tensile tests
- Susceptibility to stress corrosion cracking

The panels has to be checked with NDI to verify eventual cell deformations, while the brazed joints has to be examined to exclude partial disbonding. Destructive tests are more focused on the laser welded joints to determine the eventual presence of volume defects, cracks and inclusions.
The "structures" laboratory characterizes, through macro tests (Modal analysis, mechanical properties of the structure, etc..), the final assembly and validates the final configuration of the flight unit.

8. CONCLUSION

Honeycomb structures are widely used in Space engineering thanks to their unique characteristics of strength and mass. The efficiency of the honeycomb depends upon the material, cell form, and technological processes. Therefore new method of honeycomb structures' optimization, honeycomb filler specially made for each structure, and technology of efficient skin-to-honeycomb bonding allow to implement new possibilities of the honeycomb structures' weight reduction.

This aeroshell manufacturing design implements technologies like Cutting, Forming and Descaling of titanium thin skins and honeycomb, Brazing of titanium honeycomb and skins to obtain sandwiches, Laser welding on sandwiches to obtain assemblies.

The aeroshell manufacturing concept presented might then offers an innovative perspective on re-entry vehicles system, including the principles of design for manufacturability and technology transfer as key points to reduce mass, delivery time and costs of the final product.

9. REFERENCES

1. A.A. Ivanov, S. M. Kashin, V. I. Semenov, *New generation of honeycomb fillers for aviation and space engineering*. - N.: Energoatomizdat, 2000. – 436 pages.

2. OEM design, *Designing with titanium: welding brazing and typical applications.*

3. Collin, Launais, Dubois, Aubry, *Robotised YAG laser welding of complex aerospace motor components in INCO718 or TA6V*, Metal fabrication and welding technology, Nottingham 2003

SUBSONIC DYNAMIC STABILITY TESTS OF A SAMPLE RETURN ENTRY VEHICLE

C. Michael Fremaux[(1)] and R. Keith Johnson[(2)]

[(1)] Senior Research Engineer, Flight Dynamics Branch, MS 308, NASA Langley Research Center, Hampton, Virginia, U.S.A, 23681, c.m.fremaux@larc.nasa.gov

[(2)] Aerospace Engineer, Exploration Systems Engineering Branch, MS 489, NASA Langley Research Center, Hampton, Virginia, U.S.A, 23681, r.k.johnson@larc.nasa.gov

ABSTRACT

An investigation has been conducted in the NASA Langley 20-Foot Vertical Spin Tunnel (VST) to determine the subsonic dynamic stability characteristics of a proposed atmospheric entry vehicle for sample return missions. In particular, the effects of changes in aft-body geometry on stability were examined. Free-flying tests of a dynamically scaled model with various geometric features were conducted, including cases in which the model was perturbed to measure dynamic response. Both perturbed and non-perturbed runs were recorded as motion time histories using the VST optical data acquisition system and reduced for post-test analysis. In addition, preliminary results from a static force and moment test of a similar model in the Langley 12-Foot Low Speed Tunnel are presented. Results indicate that the configuration is dynamically stable for the baseline geometry, but exhibits degraded dynamic behavior for the geometry modifications tested.

1. SYMBOLS

C_m	body axis pitching moment
C_{mo}	zero-lift static pitching moment coefficient
$C_{m_{\hat{q}}} + C_{m_{\dot{\alpha}}}$	sum of damping derivatives due to pitch rate and time rate of change of angle of attack, rad^{-1}
$\overline{C}_{m_{\hat{q}}}$	pitch damping derivative; approximation of $C_{m_{\hat{q}}} + C_{m_{\dot{\alpha}}}$, rad^{-1}
d	model or vehicle maximum diameter, ft
I_{xx}, I_{yy}, I_{zz}	moment of inertia about model or vehicle x, y or z body axis, respectively, slug-ft^2
M	Mach number
m	mass, slugs
q	pitch rate about model y axis, rad/s
$\hat{q}$	reduced pitch rate, qd/2V
$\overline{q}$	free-stream dynamic pressure, $1/2\rho V^2$, lb/ft^2
r_n	nose radius, ft
r_{sa}	aft radius of shoulder, ft
r_{sf}	forward radius of shoulder, ft
Re	Reynolds number, $\rho Vd/\mu$
S	reference area, $\pi d^2/4$, ft^2
t	full-scale time, s
V	full-scale sink rate, ft/s
X, Y, Z	coordinates in tunnel-fixed reference system, in
x, y, z	coordinates in model or vehicle body-fixed reference system, with x coincident with model axis of symmetry, in
α	true (aerodynamic) angle of attack, deg
$\dot{\alpha}$	time rate of change of angle of attack, deg/s
$\overline{\alpha}$	$\theta + 90$; approximately equal to model or vehicle angle of attack, deg
$\overline{\alpha}_T$	total pitch angle calculated from model attitude time history estimates, deg
ϕ	roll angle; angle between y body axis and an arbitrary reference, measured in a horizontal plane, deg
μ	absolute viscosity, lb sec/ft^2
ρ	air density, slugs/ft^3
σ	standard deviation
θ	pitch angle; angle between x body axis and horizontal, measured in a vertical plane. Equals -90 for model or vehicle nose pointing straight down, deg

ψ yaw angle; angle between y body axis and horizontal. Equals 0 for model or vehicle pointing straight down, deg

2. INTRODUCTION

2.1 Background

Several free-flying model tests were used to determine the dynamic behavior of a proposed sample return vehicle in vertical free-fall at terminal velocity. This vehicle concept enters the atmosphere passively without a parachute, which is typically used to provide deceleration and stability over the subsonic flight regime. Without a parachute, maintaining aerodynamic stability and proper orientation for landing is critical. The model was originally flown in the NASA Langley 20-Foot Vertical Spin Tunnel (VST) in its baseline configuration in 2004, and it was noted that its dynamic behavior was relatively benign compared to that of a generic model with a similar forebody shape [1] that had been tested in the late 1990s. Based on this difference in behavior, a second test entry was planned to help understand why the dynamic behavior of the current model was superior to that in [1]. Two backshell modifications were designed and fabricated for the current model in an attempt to emulate some of the geometric features of the earlier model [1]. It was hypothesized that these features might be promoting unsteady flow on the backshell, resulting in a dynamic instability. Re-running the tests with the modifications installed showed that they did influence the behavior of the current model by making it less dynamically stable, or even unstable (i.e., divergent) in some cases. In a related effort, static force and moment tests of a full-scale model were conducted in the Langley 12-Foot Low Speed Tunnel (12-Foot) to quantify the static stability characteristics of the configuration. The backshell modifications were also tested on the static model. Results from the VST test will be discussed in detail in a later section. Results from the 12-Foot test will be summarized and used to augment the analysis of the VST results where appropriate.

2.2 Wind Tunnel

The dynamic stability tests were performed in the Langley 20-Foot Vertical Spin Tunnel (VST). In operation since 1941, the VST is an atmospheric, low-speed, annular return tunnel with a closed, twelve-sided test section that is 20 feet across and 25 feet tall. A cross-sectional sketch of the facility is shown in Fig. 1. Maximum tunnel dynamic pressure ($\bar{q}$) is approximately 9 lb/ft^2 at a speed of 87 ft/s (Re = 0.55 x 10^6/ft, M = 0.08). Upper and lower nets prevent models from getting drawn into the fan or falling through the flow straightening "honeycomb", respectively. The test section walls are padded to minimize model damage due to impact, but a "safety tether" was used during these tests in order to further reduce the likelihood of model damage and reduce downtime due to model repair. The tether consists of lightweight braided nylon line attached to the model with a ball-bearing swivel. It was kept slack during data runs, but was tightened to prevent impact by an operator using an electric winch if the model drifted near a wall. A series of cameras around the test section provide video coverage for visual documentation of the test as well as input to an optical data acquisition system (to be discussed in the next section). The VST has a long history of testing aircraft models, primarily for determining spin and spin-recovery characteristics, but there have been numerous dynamic stability and drogue parachute sizing tests for atmospheric entry vehicles over the years, including Mercury [2], Gemini [3], Apollo [4], Pioneer Venus [5] and several proposed planetary entry vehicles in addition to more recent tests of the Stardust [6] and the generic configuration previously mentioned.

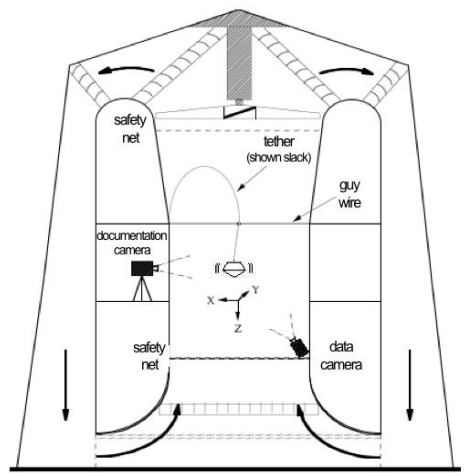

Fig. 1 Cross-section of 20-Foot Vertical Spin Tunnel

2.3 Data acquisition system

An optical data acquisition system is used to obtain 6 degree-of-freedom (6-DOF) motion time histories of models during dynamic tests. The VST Model Space Positioning System, or MSPS [7], is a non-intrusive, workstation-based system that uses three single-camera views of retro-reflective targets on a model to generate post-test estimates of model attitude (ψ, θ, ϕ) and spatial position (X, Y, Z) with respect to an earth-fixed test-section axis system (Fig. 1) at a sample rate of 60 Hz. At the start of data acquisition, test section state (dynamic pressure, flow velocity, temperature, etc.) is recorded on a separate system and time-correlated for post-test processing. Numerical differentiation of the attitude time histories is used to calculate angular rates. Comparisons to a reference at known attitudes indicate

that angles reported by MSPS are accurate to within ±1 degree.

2.4 Model

A 53%-scale model of the proposed sample return vehicle in the baseline configuration was fabricated at the NASA Langley Composite Model Shop using a rapid prototyping technique to significantly reduce cost and fabrication time compared to earlier sample return models tested in the VST (e.g., [1], [6]). A sketch of the geometric features of the baseline configuration is shown in Fig. 2, and a photo of the model flying in the VST is shown in Fig. 3.

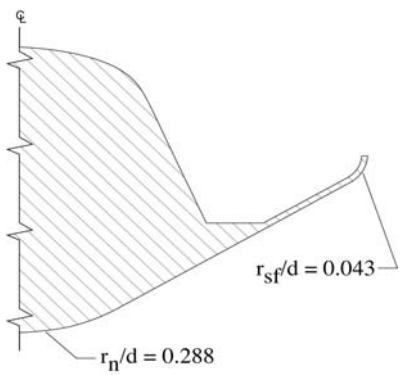

Fig. 2. Baseline configuration geometric features

Fig. 3. 53%-scale sample-return model in the VST

The vehicle features a spherically-blunted cone forebody with a 60-degree half angle and a nose radius that is 28.8% of the maximum (base) diameter (note that the model referred to in [1] had a slightly different nose radius of 25%, and is referred to as the "6025" model in that paper). The model was ballasted (using lead weights) to achieve model-to-vehicle similitude of inertial and gravitational forces using the dynamic scaling laws [8] (i.e. maintaining constant Froude number and vehicle-to-atmosphere relative density factor). For a dynamically scaled model, not only are the geometric characteristics similar to the full-scale vehicle, but the mass, center of gravity (c.g.) and moments of inertia are scaled as well. Adherence to the dynamic scaling laws allows direct conversion of the model linear and angular rates to full-scale, with the assumption that Reynolds number (Re) and Mach number (M) effects are not significant. For the 53% scale model, the factor for converting time from model-scale to full-scale is approximately 1.37, i.e., rates during the model tests are 1.37 times faster than full-scale.

Two modifications to the backshell were also fabricated as "appliqués" that could be attached to the model. These modifications were designed to approximate some of the backshell features of the 6025 model tested in [1]. The first modification (Mod 1) consisted of a ring that covered the sharp rear-facing corner of the forebody-backshell juncture with a relatively large radius shoulder (Fig. 4). The second modification (Mod 2) used the same radius shoulder as Mod 1 but faired it into a flat plate that covered the concave portion of the backshell (Fig. 5).

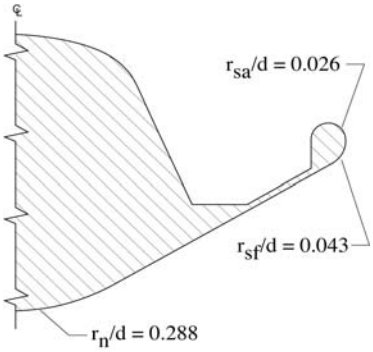

Fig. 4. Mod 1 geometric features (shoulder installed)

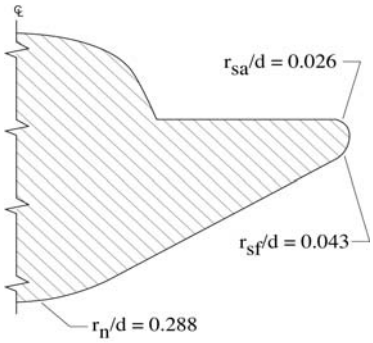

Fig. 5. Mod 2 geometric features (shoulder + backplate installed)

Regardless of configuration, the model was ballasted to obtain dynamic similarity to the full-scale entry vehicle at an altitude of 5000 ft ($\rho = 2.04 \times 10^{-3}$ slug/ft^3 based on the 1976 Standard Atmosphere [9]). The target mass, moments of inertia (MOI), and center of gravity location used during the dynamic test (based on the full-scale vehicle) appear in Table 1.

Table 1. Full-Scale Mass Properties of Proposed Sample-Return Vehicle

parameter	target value	comment
m	0.795 slugs	
Ixx	0.143 slug-ft^2	roll MOI
Iyy	0.098 slug-ft^2	pitch MOI
Izz	0.099 slug-ft^2	yaw MOI
c.g. location	0.23d	x = 5.198 inches aft of nose and on axis of symmetry (y = 0, z = 0)

Model mass properties were measured prior to testing (and any time the model configuration was changed) on a "swing rig" [10]. The accuracy of the mass property measurements (based on calibration standards traceable to National Institute of Standards) is summarized in Table 2.

Table 2. Accuracy of Mass Property Measurements

parameter	accuracy
m	$\pm$0.1%
Ixx	$\pm$0.25%
Iyy	$\pm$0.25%
Izz	$\pm$0.25%
c.g.	$\pm$0.001d

2.5 Test technique

For the dynamic model tests, the model was "free-flying" in the tunnel (with the exception of lightweight tether described in section 2.2). For each test run, the model was attached to the tether and lowered into the test section. Any residual movement of the model was damped out with a long-handled hook that can grasp the tether anywhere along its length. The tunnel operator brought the test section velocity up to a point where the weight was taken off of the tether and the model was free-flying (i.e., model average drag equals model weight). A technician ensured that the tether was kept slack by making adjustments to the electric winch if required. Once the model was stabilized in the test section, the MSPS data acquisition system was activated for a pre-determined amount of time to capture the motion of the model. The length of each data record was dependent on the amount of time the model stayed in the field of view of the MSPS cameras, and is thus variable from run to run. In some cases, the technician perturbed the model by striking one side with the hook so as to cause the model to oscillate. While there is no way to precisely control the amount of initial displacement, efforts were made to be as consistent as possible. Both types of tests (perturbed and non-perturbed) were conducted for all of the model configurations (baseline, Mod 1, and Mod 2).

3. RESULTS AND DISCUSSION

3.1 Motion time histories

Several runs were made for each combination of model geometry and test type (i.e., perturbed or non-perturbed). Time history plots of total pitch angle ($\overline{\alpha}_T$), with the model results converted to full-scale, are presented in this section. In this paper, a representative run for each combination will be presented to save space. While variations in model dynamics existed run-to-run, the overall character was generally similar and thus useful for comparing and contrasting the behavior resulting from geometric changes. The time history plots in the next section are plotted as continuous curves instead of discreet data points for clarity. The scale of the vertical axes was chosen to accommodate the largest amplitude oscillations observed and thus highlight differences among the results. The length of the time scales (horizontal axes) was allowed to vary depending on the length of the data record. Periodically, the MSPS loses track of a model due to occlusion of the targets or glints on the model that confuse the system. Loss of track by MSPS is reflected as gaps in the curves. An unbroken line indicates that the system tracked at the full 60 Hz (model scale) sample rate.

3.1.1 Baseline configuration

Results for the baseline configuration appear in Fig. 6 (unperturbed) and Fig. 7 (perturbed). For the unperturbed run, the total pitch angle ($\overline{\alpha}_T$) is seen to vary in a "limit cycle" oscillation. This type of behavior is typical of blunt entry vehicles at subsonic conditions. Note that compared to "classic" limit-cycle behavior in aircraft flight dynamics (such as wing rock), the cycle-to-cycle peak amplitude varied significantly with time. While wing rock is primarily a 1-DOF motion about an airplane's roll axis, axisymmetric blunt-bodies tend to oscillate about the pitch and yaw axes simultaneously, often in a pattern that prevents both the pitch and yaw angles from crossing through zero. Small disturbances (such as variations in test section flow field) can trigger the initial oscillations, but they are often self perpetuating due to the aerodynamic behavior of a particular vehicle (e.g., statically stable but marginal or

even negative dynamic damping near zero angle of attack). The peak amplitude reached during the run as about 11 degrees, but was significantly less than 10 degrees for most of the run.

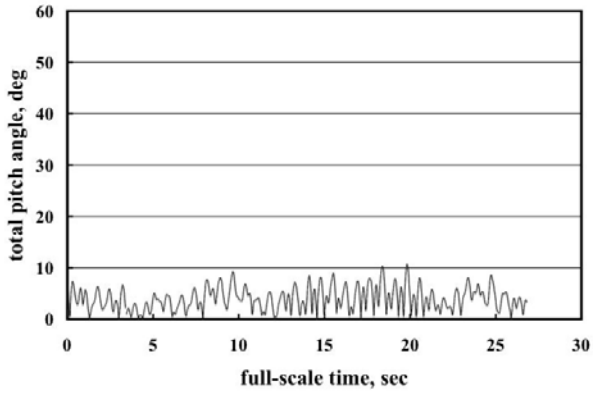

Fig. 6. Baseline configuration, unperturbed

When perturbed, the baseline configuration exhibited clear damping, as illustrated in Fig. 7.

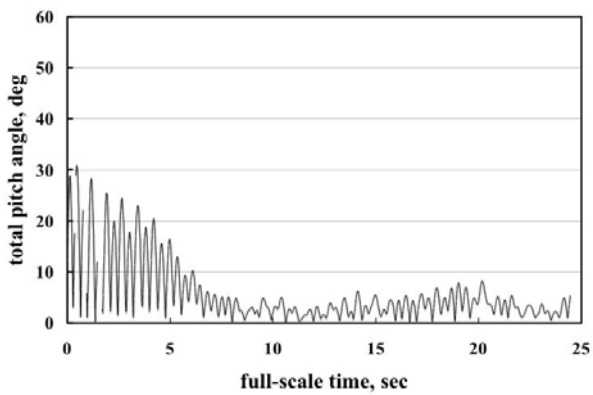

Fig. 7. Baseline configuration, perturbed

The MSPS began sampling just after the model heeled over, with an initial displacement near 30 degrees. A near-linear reduction in cycle-to-cycle amplitude is evident for the first five seconds, with a steeper drop thereafter until a limit cycle is established at between seven and eight seconds. This is in contrast to the results from [1], in which limit-cycle amplitudes in the range of 25 to 30 degrees were sustained after perturbation, with no evidence of decay during the run. Note that the model in [1] was ballasted to the same c.g. location. This difference in behavior was the motivation for examining the effect of geometry modifications to the current model (Mod 1 and Mod 2), to be presented in the next section.

3.1.2 Mod 1 configuration

As noted earlier, the Mod 1 configuration consisted of a ring that was installed over the relatively sharp forebody-backshell juncture of the baseline configuration. It was postulated that installing a large radius shoulder similar to that used in [1] might promote attached flow on the backshell, in contrast to the sharp trailing edge of the baseline configuration, which likely forces the flow to separate cleanly. In Fig. 8, the results for the unperturbed model are shown. In contrast to the baseline, the amplitude of the limit-cycle rocking is significantly larger, with the total pitch angle varying between about 10 degrees and 17 degrees during most of the run (with one spike of nearly 20 degrees). Since the mass properties, test conditions, and geometric features (other than the rounded shoulder) of the Mod 1 test were similar to that of the baseline, the different dynamic behavior appears to be caused by the difference in geometry.

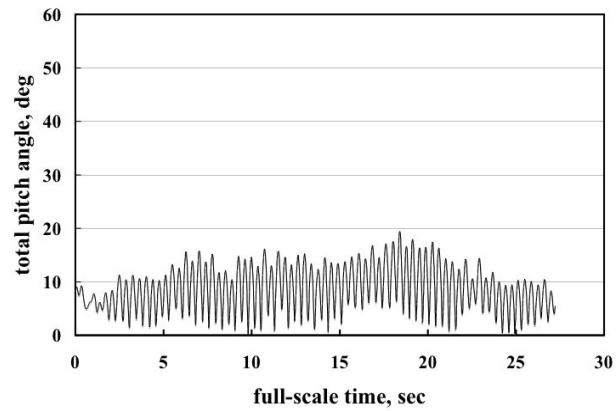

Fig. 8. Mod 1 (shoulder added) configuration, unperturbed

When the Mod 1 was perturbed (Fig. 9), the steep drop off in amplitude noted for the baseline is not evident, even though the initial displacements were similar (about 32 degrees in this case).

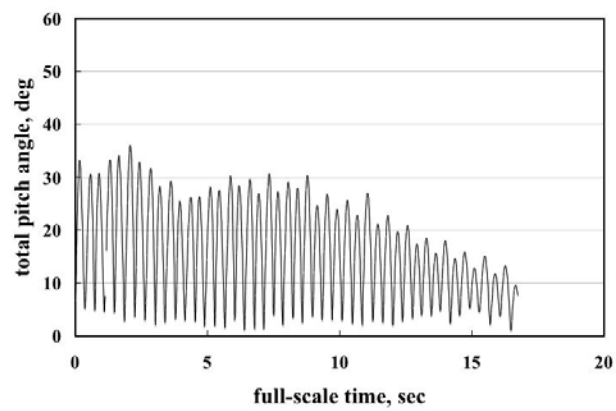

Fig. 9. Mod 1 (shoulder added) configuration, perturbed

In fact, the amplitude tended to grow for over several cycles before beginning to decay. A second interval of growth is noted before the oscillation envelope begins a final gradual decay. In this case, the run ended prior to a

clear limit cycle being re-established, but the final amplitude is within the range displayed in Fig. 8. As with the unperturbed results, changing the sharp, aft-facing corner to a relatively large-radius shoulder appears to have affected the dynamic response of the model in otherwise similar test conditions.

3.1.3 Mod 2 configuration

The Mod 2 configuration added a flat plate, or disk, to the back of the model (faired into a corner with the same radius as the Mod 1 shoulder) that covered the concave backshell of the model. This configuration was the most similar (in terms of outer mold line) to the 6025 model in [1]. When perturbed only by the tunnel flow, the model exhibited limit-cycle behavior that displayed features noted in the previous two cases, i.e., alternating periods of relatively large amplitudes of up to 13 degrees and oscillations in the 5 degree range (Fig. 10).

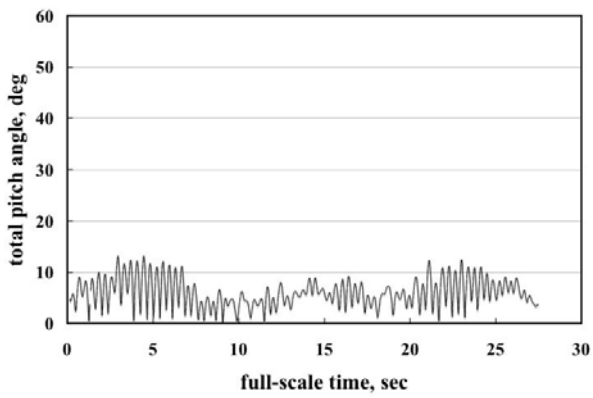

Fig. 10. Mod 2 (shoulder + backplate added) configuration, unperturbed

When the Mod 2 was perturbed (Fig. 11), the behavior of the model was significantly more dynamic than in the earlier cases.

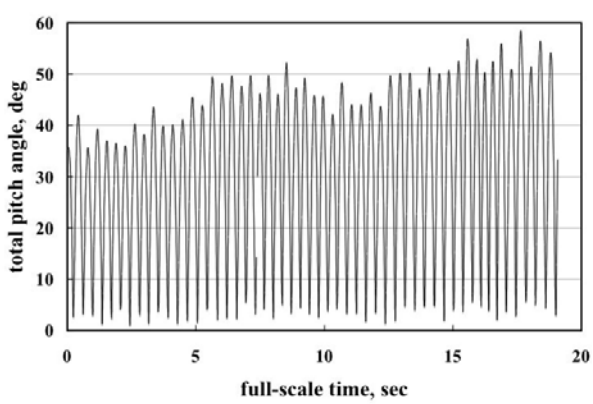

Fig. 11. Mod 2 (shoulder + backplate added) configuration, perturbed

3.2 Static and dynamic stability estimates

The initial perturbation of about 35 degrees (~3 degrees more than the Mod 1 case) resulted in the model entering a divergent oscillation. While the peak values of $\overline{\alpha}_T$ grew or decayed cycle-to-cycle, the overall trend was a clear growth in the oscillation envelope. The peak value reached near the end of the test record was nearly 60 degrees. While the model did not flip over during the test, other models (e.g., [1], [6]) did begin tumbling soon after reaching pitch angles of this magnitude. It is possible that longer test times would have allowed the amplitude to build up to a point that the model pitch angle diverged.

As mentioned earlier, a static force and moment test was conducted in the Langley 12-Foot Low Speed Tunnel on a full-scale model, including the Mod 1 and Mod 2 configurations. The static stability level of the vehicle will be estimated from the results of the 12-Foot test. Likewise, a measurement of dynamic stability (in a linear sense) is the pitch damping derivative $\overline{C}_{m_{\dot{q}}}$. Pitch damping will be estimated from the time histories that were presented in section 3.1

3.2.1 Static stability

A plot of pitching moment coefficient (resolved about the vehicle target c.g. location 0.23d aft of the nose and on the axis of symmetry) for all three configurations appears in Fig. 12. These data were taken at a dynamic pressure ($\overline{q}$) of 2 psf ($Re_d \approx 0.49 \times 10^6$). In contrast, the dynamic pressure during the VST tests was on the order of 6 psf, but due to the 53% scale of the dynamic model relative to the (full-scale) model tested in the 12-Foot tunnel, the Reynolds number based on maximum diameter (d) during the two tests was approximately the same.

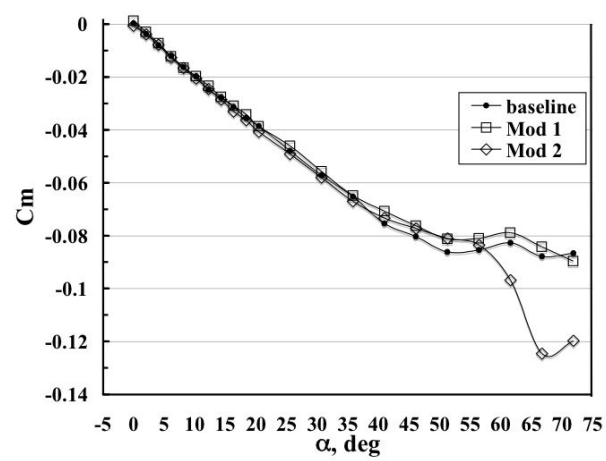

Fig. 12. Pitching moment coefficient from 12-Foot Low Speed Tunnel tests

Though there are slight variations in pitching moment coefficient for a given angle of attack among the three

configurations, the curves are quite similar and linear to angle of attack of 35 degrees. Arbitrarily choosing an angle of attack range of 0 to 8 degrees and calculating the slope results in the static stability estimates ($C_{m\alpha}$) shown in Table 3. Note that negative values of $C_{m\alpha}$ indicate static stability.

Beyond α=50 degrees, the pitching moment characteristics of all three configurations become non-linear, with the baseline and Mod 1 experiencing moderate unstable breaks (i.e. change in slope from negative to positive), while Mod 2 exhibits a very large stable break at 55 degrees before again breaking unstable at about 67 degrees. This large stable break likely is a driving force in the large amplitude oscillations noted in Fig. 11, i.e., Mod 2 has a stiffer "spring" to force the vehicle toward lower angles of attack. If this stiff static system is coupled with very small (or even negative) damping, dynamic motions may exhibit limit-cycle or divergent oscillations. Presumably, the ability of the flow to "turn the corner" and remain attached to the backshell (due to the presence of a large-radius corner coupled with a flat, surface) was the driver for the significantly different pitching moment characteristics exhibited by Mod 2 at large angles of attack. The large-radius corner of the Mod 1 configuration did not have a significant impact on the static pitching moment relative to the baseline. It is likely that the large turning angle due to the concave backshell prevented extensive flow attachment in spite of the presence of the shoulder.

It should be noted that the 12-Foot tests were conducted using pitch sweeps that progressed from the low to high angles of attack, but did not take data as the angle of attack was reduced from maximum. Therefore, it is not known if static hysteresis is present in the pitching moment characteristics of any of the configurations examined. Static hysteresis has been linked to the aircraft wing rock phenomenon (e.g., [11]) and could be a driver for the motions observed during the present dynamic tests.

Table 3. Static Stability Parameter Estimates
(12-Foot LST data; slope computed between $\alpha=0^o$ and $\alpha=8^o$)

configuration	$C_{m\alpha}$, deg^{-1} (static test)
Baseline	-0.116
Mod 1	-0.124
Mod 2	-0.112

3.2.2 Dynamic stability

The time histories of Figs. 7, 9, and 11 were used to estimate the dynamic damping-in-pitch ($\overline{C}_{m_{\hat{q}}}$) of the three configurations. Two different methods were used to extract approximations of this parameter as outlined next.

A simple hand calculation can be performed to get an initial assessment of pitch damping. With some simplifying assumptions, the 1-DOF pitch equation of motion

$$C_{m_{total}} = C_{m_o} + C_{m_\alpha}\alpha + \overline{C}_{m_{\hat{q}}}\hat{q} = \frac{Iyy}{\bar{q}Sd}\ddot{\theta} \qquad (1)$$

(i.e., a classic spring-mass-damper system) can be used to calculate the total (i.e., static-plus-dynamic) aerodynamic pitching moment from the calculated angular acceleration and dynamic pressure during a test, measured MOI, and model reference area and diameter. Calculating the $\Delta C_m/\Delta\hat{q}$ at a given angle of attack for the positive and negative pitch rate during each cycle and averaging over several cycles gives an estimate for $\overline{C}_{m_{\hat{q}}}$. For the present work, motion time histories from Figs. 7, 9, and 11 were used with Eq. 1 to calculate the total pitching moment value each time the model crossed α=0 (noting that $\alpha=\theta$ due to kinematics associated with the 1-DOF motion assumption). Since the model is axisymmetric, the static aerodynamic contribution to the total pitching moment vanishes at zero angle of attack and any non-zero pitching moment is assumed to be a function of angular rate only. These C_m values were plotted against their respective positive or negative $\hat{q}$ values to calculate $\Delta C_m/\Delta\hat{q}$ for each half cycle of the oscillation. Regardless of the configuration, the pitch damping estimated using this method was on the order of -0.35, which indicates significant damping. Based on the different dynamic responses for the three configurations noted in Figs. 7, 9, and 11, it is clear that a single-point estimate at α=0 is not adequate to describe the damping characteristics of the vehicle if there is appreciable deviation from α=0. It is likely that damping varies widely with angle of attack during an oscillation cycle.

The second method used involved the use of a parameter identification (PID) technique. The SIDPAC [12] software package consists of a suite of MATLAB® scripts for modeling flight data and extracting aerodynamic coefficients. Again assuming 1-DOF and a linear model of the aerodynamic coefficients (i.e., Eq. (1)), the three time histories were run through a 1-DOF aerodynamic extraction program built using SIDPAC. While assuming a constant value of pitch damping is likely not adequate to fully model the motion (as there may be linear or even non-linear dependencies on angle of attack, amplitude, rates, etc.) it is reasonable to start

with a linear model before moving to more complex models. The PID approach used here calculates a single value of $\overline{C}_{m_{\hat{q}}}$ that best represents the response (within the limitations of the linear model) over the entire range of motion, not just a single point. A sample of the modeling results is shown in Fig. 13, where pitching moment coefficient is plotted versus time. Input for this calculation was a truncated version of Fig. 7 with only the cycles of clearly decreasing amplitude retained.

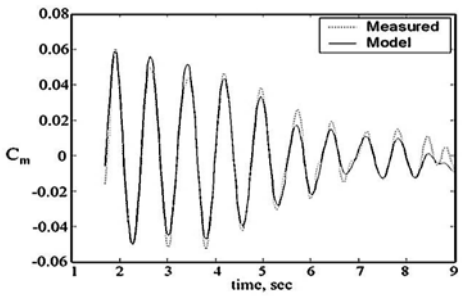

Fig. 13. Pitching moment coefficient from 20-Foot VST test using PID technique for baseline configuration

The "Measured" curve (dashed line) represents the total (1-DOF) pitching moment calculated directly from the RHS of Eq. (1). The "Model" curve (solid line) represents the linear buildup of the estimated aerodynamics from SIDPAC, which does a reasonable job of capturing the overall character of the motion, but misses the peak values (overshooting or undershooting) for several of the cycles. Average damping derivative estimates for the three configurations are presented in Table 4, along with the 2σ (95% confidence) bounds from SIDPAC. Also in Table 4 are the estimated values of static stability, $C_{m\alpha}$, based on the PID modeling. Note that the static stability levels from the 12-Foot test (Table 3) and VST test are in reasonable agreement.

In Table 4, there is a clear progression from damped (-.047) for the baseline, to near neutral dynamic stability (-0.007) for Mod 1, to slightly propelling (+0.008) for Mod 2. The trend in these results is in agreement with the that observed for the three configurations.

Table 4. Static and Dynamic Stability Parameter Estimates (PID estimates from 20-Foot VST time histories)

Configuration	$C_{m\alpha}$, deg^{-1} (from dynamic tests)	$\overline{C}_{m_{\hat{q}}}$, rad^{-1} (+/- 2σ)
Baseline	-0.137	-0.047 +/-0.018
Mod 1	-0.132	-0.007 +/-0.018
Mod 2	-0.137	+0.008 +/-0.009

4. CONCLUSIONS

1. The baseline configuration, at the center of gravity location and scaled mass properties of the test, will be statically and dynamically stable at low mean angles of attack, with a limit-cycle amplitude of 10 degrees or less.

2. Excursions in total angle of attack as large as 30 degrees will damp out to a small-amplitude limit cycle once the excitation causing the excursions ceases.

3. Differences in aft-body geometry, notably the sharpness or bluntness of the forebody to aft-body juncture and the total turning angle created by the corner will affect the level of pitch damping, possibly resulting in a dynamically unstable configuration.

4. Oscillatory motion over an appreciable angle of attack range will not be adequately described using a single-point estimate of pitch damping at α=0, but can be modeled reasonably well using a pitch damping value that is estimated while taking the entire range of motion into consideration.

5. REFERENCES

1. Mitcheltree, R. A., Fremaux, C. M., and Yates, L. A., Subsonic Static and Dynamic Aerodynamics of Blunt Entry Vehicles, AIAA 99-1020, 1999.

2. Bowman, J. S., Dynamic Model Tests at Low Subsonic Speeds of Project Mercury Capsule Configurations with and without Drogue Parachutes, NASA TM X-459, 1961.

3. Bowman, J. S., Dynamic-Model Investigation of a 1/20-Scale Gemini Spacecraft in the Langley Spin Tunnel, NASA TN-D-2191, 1964.

4. Lee, H. A., and Burk, S. M., Low-Speed Dynamic Model Investigation of Apollo Command Module Configurations in the Langley Spin Tunnel, NASA TN-D-3888, 1967.

5. McCloy, R., Entry Dynamics Performance Predictions for Pioneer Venus Probes, AIAA-1978-1370, 1978.

6. Mitcheltree, R. A. and Fremaux, C. M., Subsonic Dynamics of Stardust Sample Return Capsule, NASA TM 110329, 1997.

7. Snow, W. L., Childers, B. A., Jones, S. B., and Fremaux, C. M., Recent Experiences with Implementing a Video Based Six Degree of Freedom Measurement System for Airplane Models in a 20-Foot Diameter Vertical Spin Tunnel, *Proceedings of the SPIE Videometrics Conference*, Vol. 1820, 1992, pp. 158-180.

8. Wolowicz, C. H., Bowman, J. S., and Gilbert, W. P., Similitude Requirements and Scaling Relationships as Applied to Model Testing, NASA TP 1435, 1979.

9. United States Committee on Extension to the Standard Atmosphere: *U.S. Standard Atmosphere*, 1976.

10. Boynton, R., and Wiener, K., A New High Accuracy Instrument for Measuring Moment of Inertia and

Center of Gravity, Society of Allied Weight Engineers SAWE Paper No. 1827, 1988.

11. Nguyen, L., Yip, L., and Chambers, J., Self-Induced Wing Rock of Slender Delta Wings, AIAA 81-1883, 1981.

12. Morelli, E., System IDentification Programs for AirCraft (*SIDPAC*), AIAA paper 2002-4704, 2002.

THE INTERACTION DYNAMICS OF PULSED RETRO-ROCKET PLUMES WITH THE GROUND DURING SPACECRAFT DESCENT ON MARS

Manish Mehta [1†], Nilton O. Renno [1‡], Peter G. Huseman [2], Douglas S. Gulick [2] and Aline Cotel [3§]

(1) Atmospheric, Oceanic & Space Sciences, Univ of Michigan Ann Arbor MI 48109 USA, manishm@umich.edu
(2) Aerophysics, Lockheed Martin Space Systems Company, Littleton, CO 80125 USA
(3) Civil & Environmental Engineering, Univ of Michigan Ann Arbor MI 48109 USA

ABSTRACT

This study focuses on the impingement dynamics of pulsed supersonic plumes with the ground at Mars atmospheric conditions. Experimental results show that large transient pressure peaks with amplitudes between 35 and 42 kPa (4.5-5.2 psi), and durations between 10 and 18 msec develop at the surface during pulsed supersonic jet impingement at a motor frequency of 10 Hz. These transient pressure peaks are superimposed on "quasi-steady" pressure perturbations with amplitudes of about 5 kPa (0.87 psi) and duration of 55 msec. This interaction corresponds to a 20 Hz ground shock frequency. Numerical and experimental data show that the transient pressure spikes are caused by the formation and collapse of plate shocks (normal reflected shocks) due to the startup and shutdown cycle of pulse-modulated thrusters. These pressure perturbations may cause soil liquefaction and gas-soil bursting which can lead to substantial soil erosion. Our goal is to understand the dynamics of pulse jet impingement during terminal descent and quantify crater formation, dust lifting, and spacecraft stability at low ambient pressure. This study is the first step in this direction.

1. INTRODUCTION

Future landed missions to Mars and the Moon need reliable and well understood landing systems. Economical soft landing systems are important to turn the US vision for space exploration into reality [1]. The understanding of the interactions of thruster plumes with the surface, plume/thruster feedbacks caused by these interactions, and the quantification of dust lifting are important for assessments of lander stability and its contamination by dust lifted during terminal descent. Thus, these studies are extremely important not only for the engineering but also for the science of future missions [1].

Entry, descent and landing (EDL) systems have been a high risk area of landed space missions. It is extremely challenging to safely land a spacecraft in a poorly known environment. The understanding of the fluid dynamics of the impingement of thruster plumes on planetary surfaces is very important to the success of future missions. Previous investigations of plume interactions with the surface were conducted mostly by NASA researchers in the 1960s and 70s. These past studies focused on steady-state rocket plumes such as those produced by the Viking and Apollo descent engines [1]. *Studies of pulsed rocket plumes such as the ones produced by the Phoenix (PHX) spacecraft engines are virtually non-existent*. Phoenix is the first scout mission to Mars, and the first to explore its northern polar region [1]. Today's technology and analysis techniques allow us to easily study pulsed jets and expand on earlier studies of the interaction of steady-state rocket plumes with the ground. There are three main areas of concerns to mission planners related to plume-ground interaction: 1. Control authority deterioration; 2. Surface alteration and crater formation; and 3. Dust lifting during landing [1].

Control authority of lander's descent needs to be fully understood, so that it can be accurately included in Guidance, Navigation and Control (GNC) systems. Ground effect and lift-loss, in particular in the presence of topographical features, can cause asymmetric loadings on spacecrafts during descent [1]. This leads to undesirable torques which may cause destabilization of the spacecraft. *Rigorous GNC models of these processes for pulse-modulated thrusters during terminal descent do not exist.* In order to minimize the risks to landings, these processes must be understood and incorporated into Lander Simulators *(LanderSim/POST) [2].The impingement of supersonic plumes with the ground can excavate the surface during landing. Once the bearing capacity of the soil is exceeded by shear stress due to plume impingement pressure perturbations, ground failure occurs [1]. This failure can lead to site-alteration, crater formation and the lifting of large quantities of sand and dust. The main reason for concern is that this may lead to lander instability, damage of its underside, and alteration of the surface of scientific interest. Dust

‡ AOSS Associate Professor; † AOSS Graduate Student; § CEE Assistant Professor

lifting and settling on the lander can cause instrument contamination and failure [1]. This could also have serious effects on the overall power available to the spacecraft because of the settling of lifted dust on solar panels. *Investigations of site alteration by supersonic pulsed jets and dust lifting and deposition during spacecraft landings do not currently exist.*

The necessity for improvements in the understanding and technology of descent systems for soft Lunar and Martian landers cannot be understated. The landing ellipsis of NASA's Viking and Apollo missions was in excess of 250 km by 250 km [2]. Safe landings on scientifically interesting sites require much more precise landings. Simple and cost effective soft precision landings might be achieved with pulse-modulated engines such as the ones employed by the Phoenix spacecraft. The Phoenix engines use pulse frequency and duty cycle control to dynamically adjust thruster power during descent [3]. If these pulse-modulated engines are successful and well understood through adequate testing and modeling, they could be safely employed in future missions to the Moon, Mars and beyond.

2. EXPERIMENTAL COLD FLOW TEBSTED (CFTB)

An experimental testbed has been developed to study the impingement dynamics of supersonic pulsed jets with the surface at Mars ambient pressure (Figure 1). Various quantitative diagnostics have been installed into the CFTB to record important physical quantities. The quantitative diagnostics are composed of: 8 Freescale ground pressure sensors (with 1 msec response time and pressure range between 0 and 53 kPa), 1 OMEGA thruster Pc transducer (0-3.44 MPa), 1 MKS Baratron 627 B absolute pressure sensor (0-700 Pa), and various Analog Devices thermocouples. The ground pressure sensors and thermocouples are placed in a radial fashion along a clear acrylic impingement plate (Figure 1). To obtain supersonic flow through the nozzle, a general contour of the MR107 converging-diverging nozzles employed on the Phoenix terminal descent engines have been implemented. Half-scale model tests have been conducted to reduce the mass flow and the interactions of the thruster plumes with the chamber walls. A motor has been developed to control the pulse width (PW), thruster chamber stagnation pressure (Pc), thrust and motor frequency. Dry compressed nitrogen has been used as our test gas to simulate the specific heat ratio of hydrazine by-products. From past studies, we determined that the temperature effects are second order and do not significantly alter the flow. Past tests and numerical modeling have confirmed these results [3].

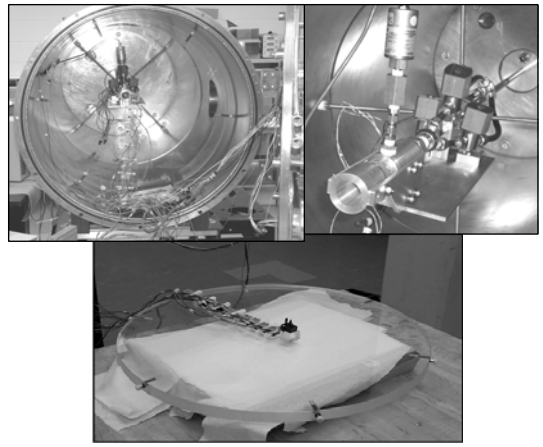

Fig. 1. Experimental Cold Flow Testbed

The test model is inserted into our Mars vacuum chamber, and its temperature and pressure are monitored. Our CFTB system has achieved all performance requirements necessary to simulate the jet plumes of the Phoenix (PHX) pulse modulated Terminal Descent Engines (TDE) (Figure 2 & Table 1). The performance requirements set by the PHX TDE during the constant velocity descent phase are: 10 Hz Pulse-Width Modulation (PWM) Frequency; 1.26 MPa maximum Pc, and 151.7 MPa/s Pc rates during engine startup/shutdown cycles. The pressure at the nozzle inlet (Pc) and the ground impingement pressures are

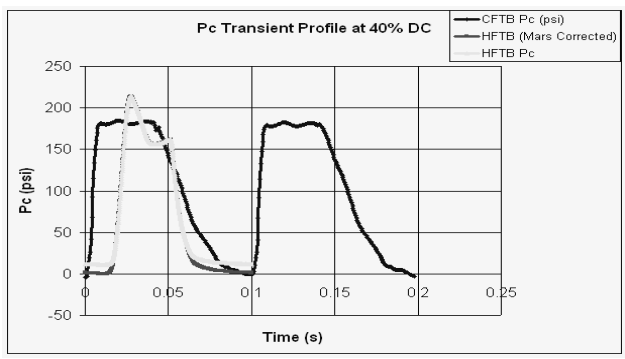

Fig. 2. CFTB-HFTB Pc profile comparison [3]

transiently monitored with a USB 6009 DAQ unit with a total sampling rate of 48 kHz. To understand the physics of plume-ground interactions for spacecraft altitudes ranging from 10 to 0.5 m from the surface, an adjustable altitude system has been developed. All hardware components have been either fabricated at the University of Michigan or obtained from commercial vendors.

Table 1. CFTB Performance Comparison

PARAMETER	CFTB	Full-Scale[4]
Nozzle Area Ratio	20.9	20.9
Pc (MPa)	1.26	1.26
Pc rise/fall time (msec)	12/25	14/18
Pulsed Frequency (Hz)	10	10
Gamma (test gas)	1.4	1.3
Tc (K)	298	1100
P ambient (Pa)	690.0	690.0
H/D Range	8.4- 21	8.4-48

3. FLOW VISUALIZATION

For transient shock structure observation, a single pass-mirror reflectance shadowgraph imaging system has been developed. The light beam passes through the vacuum chamber test section, and the beam is reflected off of a flat mirror within the chamber. To visualize the transient shock structure, a 1534 Strobotac AB that pulses the light beam at a frequency of 25 kHz has

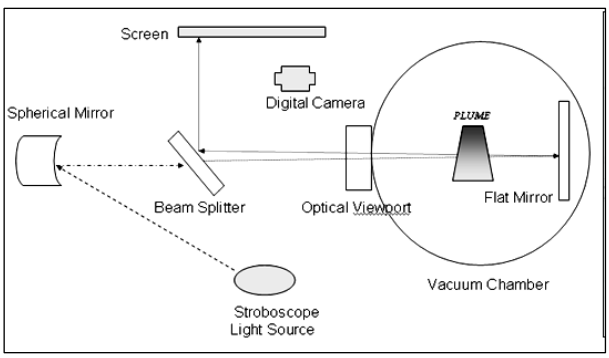

Fig. 3. Schematic of Single-Pass Reflectance Shadowgraph Imaging System [3]

been incorporated. A parabolic-mirror collimates the light beam and a 50/50 beam splitter directs the shadowgraph image on a Da-Lite High-contrast screen (Figure 3). The shadowgraph image is captured with a 7.0 MPx Nikon Digital camera.

4. COMPUTATIONAL ANALYSES

Axi-symmetric computational models have been developed for the pulsed plume-ground interactions at low ambient pressure at various altitudes in collaboration with Lockheed Martin's Aerophysics Department (LM). Both GASP (performed by LM) and FLUENT (performed by the University of Michigan) computational models were designed to study these complex flow interactions. The computational analyses done at The University of Michigan were performed at two specific heights: 0.53 meters (PHX touchdown altitude) and 1.73 meters. The Pc pressure time-series profile obtained from the PHX hot fire testbed (HFTB) was incorporated as a boundary condition to the models. The Pc pressure profiles were averaged over the 12 PHX engine tests to provide an average profile for our analyses [3]. The Pc profiles obtained from the CFTB experiments were also incorporated into the CFD models.

5. RESULTS

5.1 Pressure Measurements

Preliminary cold flow test data of experiments at Phoenix's touchdown altitude (0.53 m) of H/D=8.4, show two, centerline, transient ground pressure peaks of average amplitudes between 24 and 42 kPa, and duration ranging between 10 and 18 msec (Figure 4a and 6). This correlates to a ground shock frequency of 20 Hz. A quasi-steady state region with ground pressure amplitude of 5 kPa develops for 55 msec. Within the quasi-steady state region, we observe minor pressure perturbations with frequencies ranging between 0.5 and 1.8 kHz. We also observe these transient pressure spikes at higher altitudes where H/D=11.98 (0.762 m), but with smaller amplitudes. The maximum pressure peak have amplitudes between 22 and 26 kPa with duration of approximately 10-18 msec and a quasi-steady pressure amplitude of 4.4 kPa for 40 msec [5].

Ground pressure profiles were also modeled by CFD, and the results were compared with the experimental results (Figure 7).

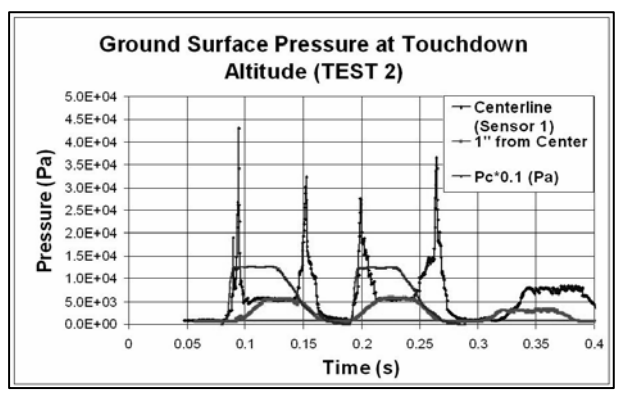

Fig 4a. Experimental ground pressure/Pc temporal profiles at touchdown altitude [5]

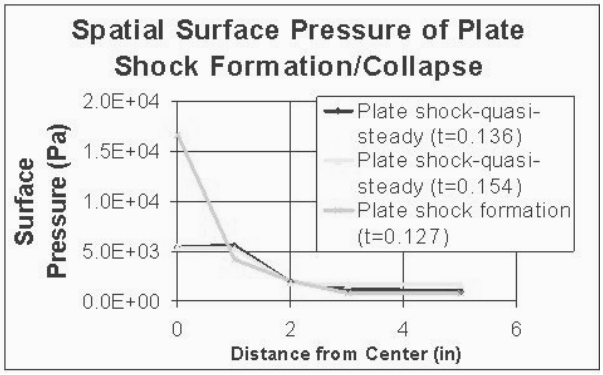

Fig. 4b. Experimental spatial pressure profile at touchdown altitude [5]

During plate shock formation, the centerline pressure amplitude is 15 kPa and at quasi-steady state regime, the pressure amplitude decreases to 5 kPa (Figure 4b). From the surface pressure profile graph at quasi-steady state regime (t=0.136s), two small characteristic ground pressure peaks of 5.54 kPa are observed at +/- 0.8 D_e (nozzle exit diameter) (Figure 4b). Higher spatial resolution is required.

5.2 Flow Visualization Data

Near-field flow visualization of cold, steady-state supersonic jets produced by the PHX thruster have been obtained (Figure 5). However, the visualization of shock-ground interactions caused by pulsed, under-expanded jets is still in progress. *Our main goal is to visualize the plate shock formation/collapse dynamics seen in the numerical simulations.*

Numerical simulations of the transient plume shock structure at 1.73 m provide us with an initial model of the ground interaction physics.

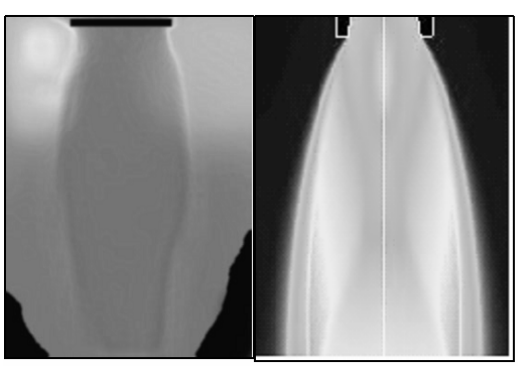

Fig. 5. Shadowgraph (LEFT) and CFD (RIGHT) near-field flow comparison [5]

6. DISCUSSION

6.1 Transient Ground Pressure Profile Analyses

There is close agreement between Pc and the rate of change of Pc in transient profiles obtained with the HFTB and our CFTB, with a PWM of 40 msec (Figure 2). Water-hammering effects at the TDE valves cause an asymmetric double pressure peak at 50 msec in the HFTB data [2]. During cold flow testing, water hammer effects were negligible. This causes a slight disparity in the data from these two tests (Figure 2).

CFD studies show that ground pressure peaks are caused by the formation and collapse of a plate shock. These processes are caused by the engine's startup and shutdown cycle. The transient peaks form when an under-expanded shock wave strikes the surface. When the wave is reflected by the surface, a plate shock parallel to the ground plane forms [7]. When the nozzle chamber pressure cannot provide the energy necessary to sustain the plate shock, it collapses. Our CFD simulations show that the maximum diameter of the plate shock is approximately 1.25 D_e (nozzle exit diameter). The plate shock is a convex structure at a standoff distance of 0.23 times the nozzle altitude (Figure 7). We believe that the amplitude of the pressure peaks depend on the rise/fall rate of the thruster chamber pressure (Pc), the plate shock strength (Mach number), and the thruster altitude. The spreading of these transient peaks may be related to the Pc rise/fall times. The amplitude of the quasi-steady state ground pressure profile may depend on the ambient pressure, the nozzle altitude, and the strength of the plate shock. High frequency pressure oscillations develop during the quasi-steady regime, because of fluctuations in the plate shock perpendicular to the ground (Figure 6) [7]. These oscillations are caused by Hartman's fundamental modes [6]. The flow physics in the impingement zone is quite unsteady [7]. There is good agreement between CFD and experimental data of these transient processes (Figure 6).

In preliminary studies of steady state under-expanded jets, under similar boundary conditions, the ground pressure is approximately constant with time with only minor oscillations of amplitude +/-0.05% of Pc. No transient pressure spikes were noticed during steady-state flow testing.

6.2 Spatial Ground Pressure Profile Analyses

The spatial pressure profiles at the centerline and the point 1 inch adjacent to it show different pressure profiles during normal shock formation and the quasi-steady state regime (Figure 4b). This same behavior is observed during plate shock collapse. A decrease in ground pressure is observed after shock formation. This may be caused by flow recirculation in the post-shock regime. The generation of the stagnation bubble produces small-scale spatial pressure variations in the quasi-steady state flow at the external boundaries of the plate shock (Figure 4b) [7].

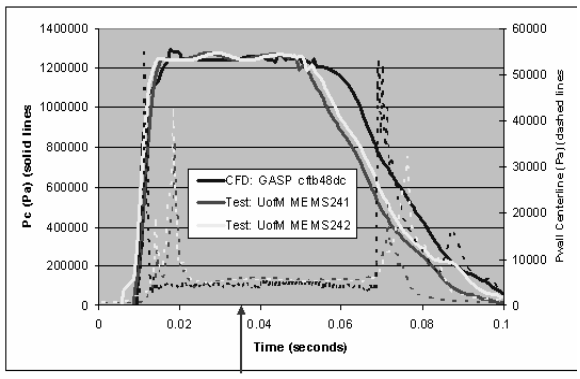

Fig. 6. LM CFD & UM test data comparison [5]

6.3 Flow Structure Analyses

Preliminary shadowgraph images confirmed that our laboratory system produces the desired supersonic plumes and has the flow visualization capabilities necessary for studying the dynamics of jet impingement. Preliminary shadowgraph images are comparable with results from CFD simulations (Figure 5). It shows that the jet is moderately under-expanded with an expansion ratio of approximately 4.2. The expansion ratio is determined by the ratio of ambient pressure to nozzle exit pressure. According to one-dimensional nozzle theory, the PHX nozzle exit Mach number is 4.5 and the exit pressure is 2.8 kPa for both the sub-scale cold flow test model and full-scale TDE. Further optimization is necessary to improve the flow visualization such as time synchronization of the image with cycling of the motor valve. We are currently increasing the field of view of our shadowgraph system to capture both the near-field flow and the plate boundary interaction.

The plume structure is collimated (Figure 7). This occurs because the Mars back pressure (ambient pressure) is relatively large. The plume structure for a lunar spacecraft during terminal descent has a larger plume diameter and expansion ratio because of the low back pressure (the near vacuum lunar atmosphere) [8].

After the jet impinges on the surface, it diverges in a radial fashion at speeds of Mach 2.1 (Figure 7). This high speed wall jet causes significant increase in the shear stress at the surface that can lead to large ground erosions.

7. FUTURE WORK

This study will provide data for accurate characterization of the ground interaction physics due to pulsed jet impingement in support of the Phoenix EDL Validation and Verification Program. It will also help the Phoenix Science Team and future NASA mission planners understand the potential contamination and site-alteration problems caused by dust lifting during landing, and if necessary it will help the team develop mitigating strategies for reducing the effects of pulsed rocket plume-soil interaction [3]. The main goals of this investigation are:

1. To provide physical and analytical models that can be used to predict the effects of plume-soil and plume-surface interactions.
2. To determine the ground pressure profiles and ground site-alteration as a function of altitude and soil properties, as well as the conditions that leads to soil liquefaction and gas-soil bursting.
3. To quantify dust particle lifting as a function of plume and soil characteristics.
4. To study the effects of terrain asymmetry such as slopes and idealized craters on surface-plume interaction.
5. To develop shadowgraph/Schlieren images of transient pulsed jets for model validation.

7.1 Phase I: Plume-Surface Interaction Dynamics

We are currently in the initial stages of optimizing our shadowgraph system to visualize the plume shock structure during pulsed firing. Our goal is to develop a system capable of characterizing flow impingement via transient pressure measurements at the ground plane and visualizations of the shock-ground interaction. In particular, we plan to determine the dynamics of vortices formed between the free stream shock structure and the wall jet. We will use a Particle Image Velocimetry (PIV) available to our group to study the behavior of these vortices and their impact on dust particle transport. This approach will provide us with

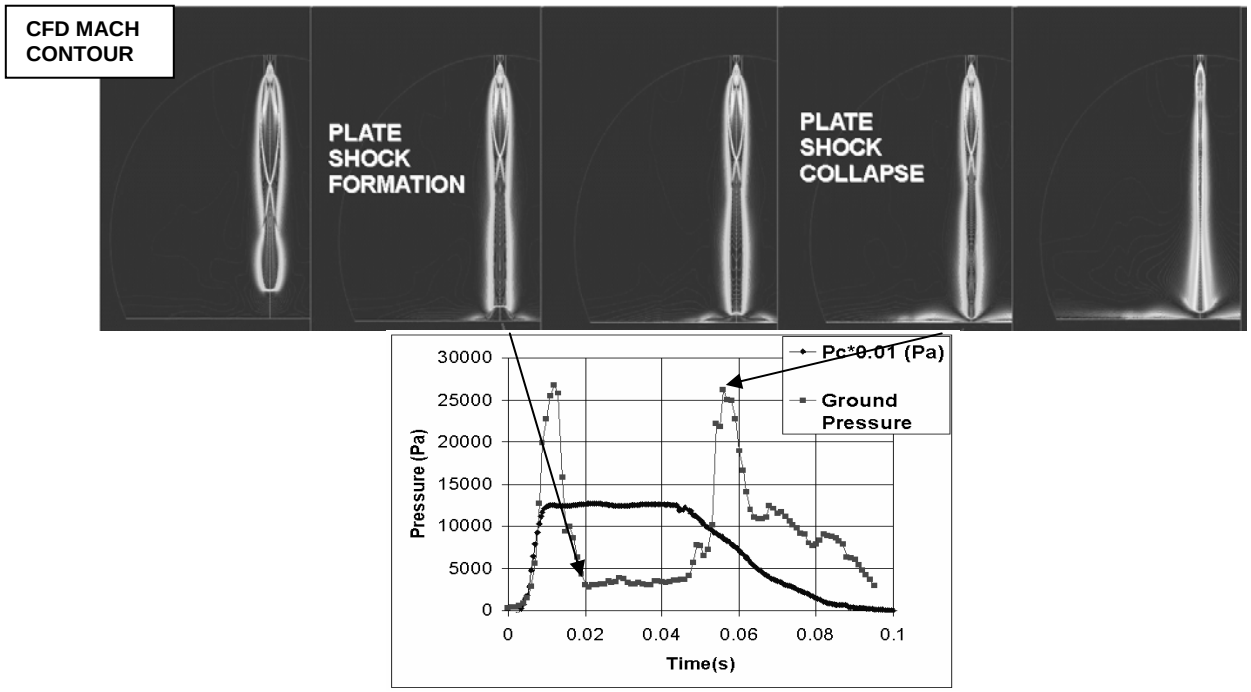

Fig. 7. Plate shock formation-collapse processes for a full-scale PHX TDE at 1.73 m altitude [5]

quantitative and qualitative data on pressure impingement, plume structure, and dust particle transport.

7.2 Phase II: Plume-Soil Interaction Dynamics

Once we complete the studies of pulsed supersonic jet impingement, we plan to study the effects of pulsed rocket exhaust on simulated Martian and lunar soils at NASA-Ames Planetary Aeolian Laboratory (PAL) and possibly at NASA-JPL [5]. Currently, we are working on the preliminary design of these experiments with other Phoenix Team members. The main goal of this second phase is to study the effects of transient perturbations on "cratering" and dust lifting. An important concern is that soil liquefaction may occur because of high pressure ground disturbances caused by the pulsed jets. Ground shock vibrations caused by large pressure perturbations may disrupt the soil and reduce particle-to-particle cohesive forces. This decreases the bearing capacity of the soil and eventually may lead to ground failure and crater formation [9]. The extent of ground failure is dependent on non-linear interactions between the jet plume and the ground as well as the soil's physical properties [9]. We have matched the pressure footprint and the exhaust flow field with full-scale TDE, but non-dimensional analysis is necessary to study the dynamics of plume-soil interactions. The non-dimensional parameters that need to be similar in both the CFTB and the full scale models are: hypersonic similarity term, aerodynamic to soil restraining shear stress ratio, density ratio of testgas to soil, and Reynolds/Froude number. This analysis will allow us to build simple scaling models of soil excavation and dust lifting due to pulsed rocket plumes.

8. CONCLUSION

From CFTB and CFD data that match the characteristics of the Phoenix MR107 motor, we observe a ground shock frequency of 20 Hz with maximum average pressure amplitudes of 35 kPa and an average "quasi-steady" pressure perturbation of 5.0 kPa near touchdown altitudes. *Experimental and computational data show good agreement with each other.* The large pressure amplitudes are strongly correlated to the plate shock formation and collapse processes of an under-expanded jet. These events have been observed to take place between altitudes of 1.73 m and 0.53 m, but further studies at higher altitudes are still necessary. The ground shock perturbations may cause soil liquefaction and gas-soil bursting which

could lead to large lateral ground erosion and an increase in the amount of dust lifting.

9. ACKNOWLEDGEMENTS

This study was the result of collaboration between the University of Michigan (UM), Lockheed Martin Aerophysics Department and NASA-Jet Propulsion Laboratory (JPL). Valuable insight and support were provided by NASA-GSRP Technical Advisor Rob M. Grover of JPL, Erik S. Bailey of JPL, Robb Gillespie of UM and Timothy A. Priser of Lockheed Martin. Undergraduate students, Cody Martin and Loy Xing Tai, were instrumental to our research activities.

10. REFERENCES

1. Romine GL, Reisert TD et.al. "Site alteration effects from rocket exhaust impingement during a simulated Viking Mars landing: Nozzle development and physical site alteration". *NASA Contractor Report NASA CR-2252*. Denver CO 1973.
2. Grover MR, Priser TA, et.al. Phoenix EDL Critical Design Review Report. *NASA-JPL PHX EDL CDR Meeting,* Pasadena CA 2005.
3. Mehta M, Renno NO, Gulick DS, Huseman, PG. Plume-Soil Interaction Progress Report. *Plume-Soil Working Group (PSWG) PHX EDL TIM*. Lockheed Martin, Denver CO 2005.
4. Huseman PG, Bomba, J. "CFD Analysis of Terminal Descent Plume Impingement for Mars Landers." *34th AIAA Thermophysics Conference AIAA 2000-2501*, Denver, CO 2000.
5. Gulick DS, Mehta M, Huseman PG, Renno NO. Plume-Soil Interaction Study Presentation. *Sub-Phase Terminal Descent PHX EDL TIM.* Lockheed Martin, Denver, CO 2006.
6. Powell A, Henderson B. "On the Tones of Round Choked Jets Impinging on Normal Flat Plates" *AIAA 13th Aeroacoustic Conference AIAA 90-3985*, Talahasee FL 1990.
7. Lamont PJ, Hunt BL. "The Impingement of Underexpanded Axisymetrical Jets on Perpendicular and Inclined Flat plates". *Journal of Fluid Mechanics*, Vol. 100, 1980. pp. 471.
8. Grossman RL. "Characteristics of Particles Blown by Exhaust Jet Impingement on a Lunar Surface". *Summer Meeting AIAA 63-199*. Los Angeles, CA 1963.
9. Vitton S, et.al. Liquefaction and Flow Failure During Seismic Exploration. *Journal of Geotechnical Engineering*. Vol. 116, no. 12, pp. 1881-1899. 1990

INCREASED OUTER PLANET SCIENCE PAYLOAD USING HYBRID BALLUTE/AEROSHELL ENTRY SYSTEMS

A. D. McRonald
Global Aerospace Corporation
Email: angus.d.mcronald@gaerospace.com

Half of the Galileo entry probe mass was heat shield ablation material that was required to safely decelerate the science payload. For future outer planet entry probe missions it is desirable to increase the fraction of science payload mass. A hybrid entry system that could achieve this performance is discussed. A hybrid entry system will be discussed that would use a ballute to reduce the entry system performance requirements for Jupiter, Saturn and Neptune entry probes. An entry probe system is assumed similar in mass to the Jupiter Galileo probe. The premise is that a ballute, as part of the entry system, can decelerate the probe at a lower atmospheric density to a lower velocity before substantial probe convective and radiative heating occurs, which can result in an increased mass of science payload as a fraction of the entry systems mass. In addition, the design of the probe, ballute, heat shield and descent package can possibly be optimized using reduced performance technologies for the same entry mass. Entry trajectories will be explored for a range of ballute size, entry angle, and release point. Convective and radiative heating, based on Galileo probe predictions and results, will be evaluated. The corresponding heat shield requirements and ballute and entry probe system mass will be evaluated, and the design and implementation will be discussed.

TITAN - THE ULTIMATE DESTINATION FOR AEROBOTS

Julian Nott
Consultant Scientists, Santa Barbara CA 93103 USA, ScienceConsulting@nott.com

ABSTRACT ***TITAN: NOT GOOD, PERFECT***

Aerobots, robotic balloons and blimps have been proposed for exploring Titan for many years. However what is not appreciated is that Titan is not merely a place where aerobots are possible but rather has better conditions for aerobots by several orders of magnitude than any other location in the entire solar system.

The low gravity and a dense atmosphere are obviously helpful. But the thermal environment and fabric life, both dominant considerations in the design of balloons and blimps are orders of magnitude better than on Earth. This means aerobots can fly for years or decades over Titan, limited only by the weather. And entirely new configurations are possible such as Montgolfier "Infinity Balloons" lifted only by surplus heat from radioisotope power sources.

This paper looks at the conditions in detail and proposes several new kinds of aerobots.

1. TITAN: EXTRAORDINARY POSSIBILITIES

Aerobots, robotic blimps and balloons, were first proposed for Titan in 1978 by the remarkable Jacques Blaumont. Alan Friedlander wrote a detailed proposal for a Titan balloon in 1986 [1]. Even before the Huygens probe landed on Titan, aerobots appeared very suitable, see for instance the comprehensive 2004 paper Hall [2]. But with Cassini, Huygens, Keck and other data, Titan emerges as not only suitable for aerobots but, in almost every regard, orders of magnitude better than any other Solar System destination. Aerobots are not merely suitable for Titan: Titan is their perfect home.

Basic factors are all ideal. Gravity is low and atmospheric density very high. Surface winds, the bane of all buoyant craft, appear to be very light.

But critical factors are dramatically better. Firstly the change in solar heating between day and night is usually the single most important factor for terrestrial balloon designs. But below Titan's clouds this factor is so small as to be unimportant. Second, ultraviolet and diffusion limit the life of existing balloons but are vastly reduced on Titan. A third and crucial factor is the low temperatures. For terrestrial balloons the majority of heat transfer is by thermal radiation. But radiation obeys Stefan's Law, depending on the fourth power of absolute temperature. Titan's temperature is so low that radiation is very small so another critical factor for terrestrial balloons is vastly more favorable. This alone opens up novel possibilities. Finally the dense atmosphere and low absolute temperature mean that change in lift gas temperature generate much greater change in lift than for terrestrial equivalents. This is summarized in Fig 1.

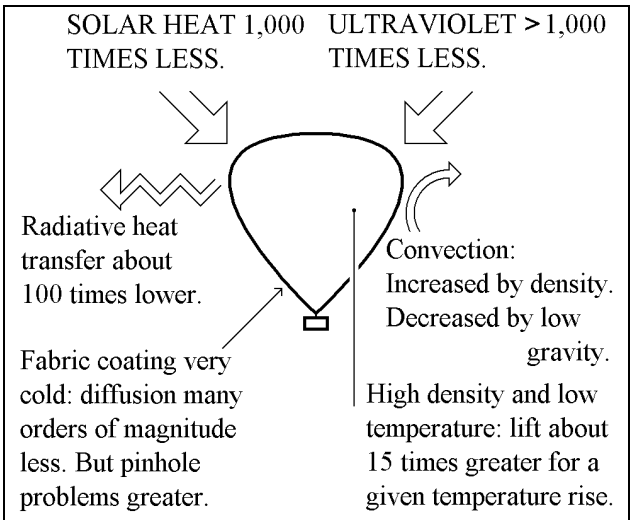

Fig 1. Dramatic decrease of factors important to balloon design on Titan relative to Earth.

While surface rovers move precisely, the terrain they can cross is limited. Even if rovers could operate on Titan's surface, their range is limited. While aerobots have less precise control, they can cover great distances: a craft could alternate between flying near or even touching the surface, and flying at altitude to move substantial distances in upper winds. Wind steering, steering only by changing altitude has become well developed and is useful for any aerobot. Balloons are less maneuverable than blimps but can still make many kinds of observations. And their remarkable simplicity implies great reliability

These factors permit extraordinary possibilities. The most striking is that a radioisotope power source, RPS, provides enough "waste" heat to fly Montgolfiers, "hot air balloons". Such craft could be very simple with

corresponding high reliability and could fly for years or decades.

2. THERMAL CONDITIONS & HEAT BALANCE

The temperature of the lifting gas is fundamental to the behavior of any balloon so understanding heat transfer is essential to design and operation.

2.1 Day / Night Variation

For most terrestrial balloons by far the most important factor limiting the length of flight is solar heating. When the sun heats a classic balloon the gas and expands and gas must be vented. When heating stops, the gas lost must be made up by ballasting. Designers have been trying to overcome this fundamental limitation throughout the two hundred and twenty years of ballooning. Many concepts have been proposed including controlling gas temperature [Rozier Balloons] and making up lift with cryogenic helium [AN balloons]. These types work well but have specific limitations. Preventing expansions of the gas [Superpressure Balloons such as GHOST and ULDB] appear attractive but no design has yet been fully successful except very small versions, several of which have flow for two years.

But below Titan's clouds the incident energy from the sun is a thousand times less than on Earth. Instead of being the dominant factor in balloon design it becomes almost insignificant.

2.2 Thermal Radiation

Another startling difference concerns thermal radiation. With terrestrial balloons radiation typically accounts for two thirds or more of the heat transfer. This is not just for hot air balloons: in designing high altitude helium balloons, convection is often neglected completely. Radiative heat transfer can be estimated with some confidence from first principles because it obeys Stefan's law. Since the law involves the fourth power of the absolute temperatures, it is self-apparent that radiative heat transfer in the Titan environment will be extremely small compared to Earth.

As with solar heating, at Titan thermal radiation goes from a factor that dominates design to a minor concern.

2.3 Convection & need for physical modeling

With low radiation, the main heat transfer mechanism between the lifting gas and the environment will be convection. Unfortunately numerical modeling of free convection is difficult. For reliable estimates it will be essential to make measurements on physical models. A model could be of similar size to an actual Titan craft reducing scaling concerns. Titan's low gravity reduces buoyancy forces, which will reduce convection. Experience shows that simple model balloons can be very useful. And modest models can be very valuable in exposing unforeseen problems at very low cost. The author has used physical models three to five meters in diameter to develop heat transfer software, Fig 2. This software works with full sized balloons and has proved central in allowing the author to set 79 world ballooning records and valuable for many other projects.

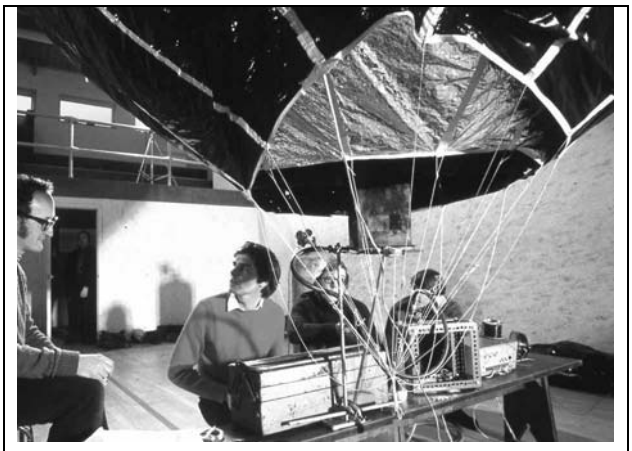

Fig 2. The author has made wide use of instrumented models. This is a double-hulled Montgolfier balloon.

3. EXTRAORDINARY FABRIC BEHAVIOR

Nearly all the critical processes that limit fabric life for buoyant craft are not merely better on Titan, but orders of magnitude better than on Earth.

3.1 Fabric: ultraviolet & chemical deterioration

Ultraviolet it is very damaging to terrestrial balloons. But below Titan's clouds sunlight is a thousand times less intense than on Earth. Shorter wavelengths are scattered even more by Titan's atmosphere so ultraviolet will be even more attenuated. The longest flights by terrestrial balloons, in strong ultraviolet at 12,000 meters altitude, exceed 2 years. With a thousand times less intensity, a Titan balloon's fabric should not fail from ultraviolet for 2,000 years!

Damage by ultraviolet depends on the energy of individual photons and is proportional to intensity. But

many chemical processes depend on thermal activation energy and their speed halves with every 10K drop in temperature. Between 60C, a typical hot air balloon fabric temperature, and Titan's 90K, reaction speeds will fall by many orders of magnitude and many chemical processes will be insignificant.

Discoloration of terrestrial balloons over time is a concern because more heat is absorbed from the sun. But if fabrics darken by chemical processes or the accumulation of organic compounds, this will not matter over Titan because solar heat is so small.

3.2 Gas diffusion & pinhole leaks

Like the chemical processes referred to in the previous section, diffusion of helium through fabric is controlled by thermal activation energy and similarly drops by orders of magnitude at Titan temperatures. It will not be important even for small balloons, Fig 3.

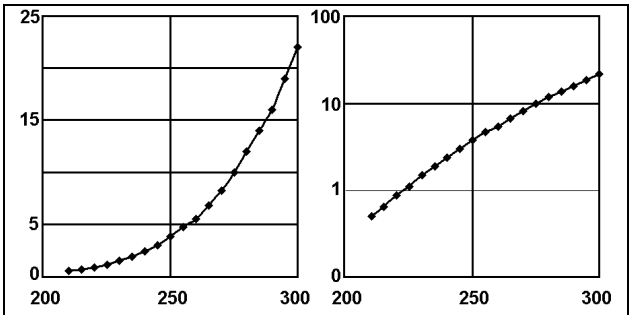

Fig 3. Left, relative permeability of helium through Mylar, 210K to 300K, right with logarithmic scale.

BUT THIS DOES NOT APPLY TO PINHOLES, which are likely to be significant for long-life Titan aerobots. Indeed one of the few factors that will be worse on Titan is that any fabric coating will be stiffer and more prone to pinhole formation.

But this might be solved by completely reconsidering coating materials. Some materials are not considered for balloons because they do not hold gas well at room temperatures. But with reduced diffusion at Titan temperatures they might have adequate gas holding. Simultaneously mechanical properties might be better than conventional materials. Silicones come to mind: they do not hold gas well at terrestrial temperature but on Titan might hold gas adequately. And they have excellent mechanical properties at low temperature. It would be valuable to review materials popular in the cryogenics industry from this perspective.

4. TOPOGRAPHY

In light winds terrestrial balloons can easily negotiate up and down across steep terrain: "Contour Flying" is a popular pilot pastime. Gradients that are impossible for surface rovers are no barrier to Aerobots. The “Highlands Region” about 5 km North of the Huygens landing looks impassable to rovers. But these steep valleys may often have light winds making them ideal for aerobot visits, and scientifically interesting material have likely washed into them.

The highest terrain has to be considered: the height of Olympus Mons is significant for Mars balloons. But if Titan is similar to Ganymede with maximum elevations of a few thousand meters, this is not a concern.

5. WEATHER VERSUS CLIMATE

With the ubiquitous cloud cover and haze, solar heat at Titan’s surface is modest suggesting benign conditions. On earth there is nothing a balloon pilot likes more than full cloud cover because tranquil conditions can be expected.

But almost the first thing a designer considered for any lighter than air project is not climate but weather, wind, rain, turbulence, lightning, microbursts, aggressive wave, drafts: there is a very long list. No aircraft, even the most robust fighter jet, can survive all weather on Earth. Long flights over Titan need a meticulous understanding of weather extremes and strategies to avoid them.

A simple example of weather extremes can be found near Pasadena at the famous Tustin Blimp Hangars, an important lighter than air center. They are in an ideal location with year-round average winds of merely 1.9 meter per second. Nonetheless, gusts routinely exceed 20 meter per second and the strongest gust in the last twenty years exceeded 30 meters per second.

5.1 Extrapolation from terrestrial experience

Titan’s weather has clear similarities to Earth, including convection, possible highs and lows, and the methalogical cycle. Several tens of millions of weather balloons have sounded the earth's atmosphere, yet new weather features are constantly observed. By contrast there has been one sounding of Titan's atmosphere by Huygens. It is essential to be careful extrapolating, but there is much to learn from terrestrial balloon experience. Several meteorologists now have a brilliant understanding of how weather influences

balloons, combining a great depth of scientific knowledge with long practical experience. It would be valuable to involve them in any Titan aerobot project at an early stage.

Unusual winds sometimes occur in valleys and balloon meteorologists have a unique understanding of them.

5.2 Wind Steering

These same meteorologists understand “wind steering”. Remarkable success is now achieved steering balloons solely by changing altitude to enter favorable winds. Skilled pilots can arrive within a meter of a pre-assigned target after flying ten kilometers. Sport balloons routinely cross the continental United States using wind steering alone, yet avoid mountains, bad weather and prohibited areas. Of course they use vast meteorological services. But the understanding learned on earth could be useful on Titan where goals could be much simpler, such as remaining in a particular hemisphere or avoiding areas of convection.

Wind steering is not restricted to balloons. It can be very valuable for blimps. A balloon can only climb or descend at its exactly location limiting the winds it can enter. But a blimp can move under power and potentially moving a short distance may allow it to be enter significantly different winds.

A Titan craft must use wind steering autonomously. Ever more structure, particularly variations in wind direction with modest changes in height, is constantly discovered in the Earth’s winds and similar structure seems likely over Titan. It is possible an aerobot might navigate with simple instructions such as "Cycle altitude slowly until you find a wind with a component towards the Equator. When you find it fly level". This could only be fully tested in situ over Titan. But the instruments, controls and processing likely to be included in any aerobot would allow this to be attempted with no penalty except the cost of programming the instructions.

5.3 Icing and Rain

It is generally believed that some long duration balloon in the GHOST and EOLE programs were bought down by icing. Flying at levels below those at which methane melts, icing is not a problem. And if a balloon descends as soon as it collects light icing it will likely melt at lower levels.

6. AEROBOT TYPES: INFINITY BALLOONS

Balloons for Titan can be designed with well-established fabrics. And interesting new fabrics being developed for stratospheric blimps may be very useful.

Since others have covered blimps in detail, these notes focus on balloons. It appears that Montgolfier and Rozier balloons heated only by the surplus heat from an RPS could fly over Titan for years or even decades. Nothing lasts forever: nonetheless the name INFINITY BALLOON has been coined for any balloon able to fly much longer than a terrestrial equivalent.

Looking at these in detail:

6.1 Montgolfier Infinity Balloon

A Montgolfier balloon has great advantages. It does not need helium for inflation. Numerous pinholes in the fabric are of no importance. The fabric does not flex when changing altitude so it can wind steer indefinitely without reducing fabric life. The only movement will be in gusts or turbulence or when the gondola touches the surface. Assuming the communication antenna has no moving parts such as a phased array, the only moving part in the craft is a control valve. A very simple valve is needed to control balloon temperature. This could take several forms. The valve does not even need to seal tightly when closed: minor leakage is not important. With these fabric advantages and extreme mechanical simplicity such balloons could fly for extraordinary periods.

This type of balloon has the greatest flexibility to descend to the surface repeatedly. Some designers have been reluctant to consider allowing a balloon gondola to touch the surface. However in light winds it is common practice in sport balloons to make "intermediate landings" on the surface to change passengers or take on fuel. As Titan conditions become better understood, there seems no reason why balloons should not touch the surface repeatedly. Presumably the largest, most interesting organic molecules are on the surface.

6.2 Double-hulled and double-gored Montgolfiers

An excellent way to improve the performance of this type of balloon is to use an envelope with two layers. A variety of multi-layer envelopes have been used for specialist balloon projects over many years.

The simplest arrangement is to fly one balloon inside another, a double-hull. This allows for a large gap

giving good installation. But for a number of reasons the most suitable for Titan is probably a balloon with double gores. This is a balloon with a single set of vertical load tapes but with two layers of fabric. Both layers meet at the tapes but there is a gap in the centre center of the gore. The installation is less effective but there are important operational advantages.

The author has designed and built both double-hulled and double-gored balloons.

6.3 Quantitative estimate of heat loss

The author has developed mathematical models over many years to estimate heat transfer for balloons. These are well tested in the terrestrial environment and are central to the author's successfully establishing 79 world balloon records.

These models have been used for the preliminary design of a Titan Montgolfier Infinity Balloon. As explained is section 2.2 thermal radiation can be estimated from first principles with some confidence and is clearly very low compared to terrestrial balloons. But convection is much more problematic. Keeping this caution in mind these models show that it is well within the capability of an RPS to heat this kind of balloon.

A practical Montgolfier must be have more heat than is needed for level flight, particularly to stop a decent. Further modeling is needed but it appears radioisotopes can provide sufficient heat.

6.4 Rozier Infinity Balloon

The author CURRENTLY believes that a Montgolfier Infinity Balloon is the best approach. However new data about Titan is pouring in from Cassini. If weather conditions are not tranquil enough for a Montgolfier, for the same payload a Rozier is substantially smaller and better able to survive weather hazards. A Rozier, a combination balloon, gets most of its lift from hydrogen or helium but controls altitude by regulating the temperature of this gas.

Minor fabric damage is not significant for Montgolfiers but even pinholes will cause significant gas loss for a Rozier. Pinholes are a universal concern for balloon especially with light fabrics. In a Rozier the fabric flexes with every change in altitude, encouraging pinhole formation. But it is still better than a blimp that constantly pitches and rolls. The shape of the ballonets in a blimp is always a compromise but the ballonet or ballonet equivalent in a Rozier can be symmetrical with smoother motion.

Any valve to control gas must seal meticulously, always a concern for long-term operation.

6.5 Quantitative thermal analysis

Because incident sunlight is so weak, the heat absorbed by a Titan Rozier will only be tens of watts. So at night only tens of watts are needed to maintain the temperature of the lifting gas and hence maintain level flight, likely a small fraction of the heat from an RPS.

6.6 Superpressure Balloons

Superpressure balloons have flown for over two years, about 20 times longer than any other type. But only a few balloons from a large fleet managed achieved this. The others were presumably brought down by weather, pinholes or fabric deterioration. In principle Titan superpressure balloons could fly for astonishing periods. But they must remain free of pinholes and avoid bad weather, both major challenges.

The drawback of superpressure balloons is that they cannot change altitude for wind steering or to reach the surface for observations.

Various superpressure types have been flown which incorporate compressors to allow flight at different levels. These include the pumpkin balloon the author designed and piloted, making the first balloon crossing of Australia. A promising new development is the Voss CMET, **C**ontrolled **MET**eorological balloon. Although any compressor is only needed when changing altitude, it is still a reliability issue for very long flights. Also when altitude changes the fabric flexes introducing pinhole concerns.

6.7 Launch

A novel method of launching aerobots which might minimize pinhole formation is described in a companion paper "Ballutes: Launching Aerobots Without Compromises". [3]

7. IMPROVING USEFULNESS & SUCCESS

7.1 A fleet

When the next mission goes to the Saturn system, understanding of Titan's weather will still be incomplete, so there is a strong case for sending a fleet,

perhaps one large craft and several much smaller "pilot balloons". Presumably many very interesting scientific opportunities are on the surface. With only one craft there would be reluctance to take even small risks by flying low. With a fleet, the loss of a small balloon would be disappointing but not disastrous and subsequent operations would learn from the mishap.

7.2 An orbiter

An orbiter enormously enhances the possibilities for Titan aerobots. High data rates would be possible with much lighter, low powered communications equipment. Much smaller balloons would be viable. As an example of what is currently possible based around commercial components, Paul Voss's long duration CMET balloons include a pumping system for altitude control and a two-directional Iridium satellite link all in craft with a total mass of 750 grams. [4]

An orbiter would be invaluable for balloon location, function exactly as the terrestrial ARGOS system.

7.3 Accidental ground contact

Any aerobot gondola should be able to survive accidentally hitting the ground. This is a common and harmless occurrence with sport balloons.

7.4 Operation after landing

Any aerobot is likely to land before its RPS stops providing any power. Aerobots should be designed to operate after landing. Titan would be left with a long-lasting weather station[s] that would provide invaluable data for third generation Titan explorers. Even if an aerobot envelope tears in flight, the low gravity and thick atmosphere will mean a low terminal velocity. It should be possible to design components to survive the impact.

REFERENCES

1. Friedlander, Alan L., "Buoyant Station Mission Concepts for Titan Exploration," Acta Astronautica, Vol 14, pp 233-242, 1986.

2. Hall J. L, Kerzhanovich, V.V, Yavrouian, A. H., Jones, J.A. et al "An aerobot for global in situ exploration of Titan" 35th COSPAR Scientific Assembly, Paris, France, 2004.

3. Nott, J, IPPW 4 2006, "Ballutes: Launching Aerobots Without Compromises".

4. Voss, P.B., E.E. Riddle, and M.S. Smith, Altitude Control of Planetary Balloons, American Institute of Aeronautics and Astronautics (AIAA) Journal of Aircraft, 43 (2), 478-482, 2005

ACKNOWLEDGMENTS

The author would particularly like to thank Dr James Rand, Winzen Engineering, Jack Jones, NASA Jet Propulsion Laboratory, Eric Frische, Space Data, and Luke Brooke, Tensys.

ROBOTIC SUPPLY OF SUPPORT EQUIPMENT FOR CREWED MISSION TO MARS

M.B. Velante[1,2], K. Schreck[1,2], N. Djordjevic[1], E. Ortiz[2], A.H. Djamshidpour[2], V. Shum[2], R. Brill[2]

(1)*Lockheed Martin Space Systems Company, 1111 Lockheed Martin Way, Sunnyvale, California, USA, 94089*
matthew.b.velante@lmco.com, nik.djordjevic@lmco, keith.r.schreck@lmco.com
(2)*San Jose State University, Department of Mechanical and Aerospace Engineering,*
One Washington Square, San Jose, California, USA, 95152-0087
ortize@slac.standford.edu, aminh110@yahoo.com, vshum12@gmail.com, rjbrill@pacbell.net

ABSTRACT

This paper addresses robotic aspects for Mars missions in preparation for a Crewed Mission to Mars Program, based upon requirements defining a mission emphasizing use of the International Space Station as a major resource in execution of the mission [1,2].

The system-level solution for this mission is described in three phases. Focusing on the first phase, two robotic missions will deliver to the Martian surface supplies and support equipment for the mission duration. The departure of the two robotic missions will take place at the ISS.

The staging of two robotic missions relies on proven technology and lessons learned in trans-Mars injection, aero-breaking, descent, and Earth re-entry technologies. Trade studies for executing a multi-year, multi-element, international, mission to Mars were performed based upon optimum performance parameters, and technology readiness levels.

Emphasis is placed upon reliable and proven techniques for mission success for human landings on Mars.

1. INTRODUCTION

New initiatives by President George W. Bush and the Commission on Implementation of United States Space Exploration Policy has made human and robotic exploration of space a priority for NASA and the international space community [3]. The Crewed Mission to Mars Program (CMMP) is designed to address these initiatives and provide a total system solution for a future manned mission to Mars.

1.1 Crewed Mission to Mars Program (CMMP)

CMMP was designed to provide the international space community with viable options for sending a crew to the Martian surface to conduct science and Martian base operations. Implementing proven techniques with robust technology provides a margin of safety for the crew and the mission.

2. MISSION CONCEPT OF OPERATIONS

Many concepts for missions to Mars have been proposed under a variety of mission requirements and timeframes. Detailed in section 2.1 are the requirements and mission specifications for the CMMP.

2.1 CMMP Mission Requirements

The baseline requirements for this mission are outlined in the six following points:

1. The crew must land on Mars within 10 years of the authority to proceed date of Jan 1, 2015.
2. Six person crew to consist of three men and three women.
3. Crew shall be capable of safe living on the surface of Mars for a minimum of 62 Earth days.
4. Crew shall be capable of safely returning to Earth at any point during the mission.
5. Crew shall be capable of two way communication to Earth at all times during the mission. Allowances of two hours per day communications blackout due to trajectory characteristics are allowed.
6. Crew shall be capable of safe meaningful scientific exploration, including water and ice, in addition to others. Crew shall have access to locations within 500 km radius of the base of operations.

These primary mission requirements were utilized and additional considerations that placed limitations or constraints on the primary requirements are presented here.

1. Use of International Space Station (ISS) on-orbit and ground support hardware, software, operational procedures, Mission Operations (including Ground Control facilities), training facilities, Program Management teams and engineering personnel.
2. Overall cost of the mission, which shall be minimized to the greatest extent possible.
3. Safety of the crew shall be maximized to the greatest extent possible.

4. Maximize simplicity, robustness, and reusability of concept, hardware and software.
5. All technology implemented in mission design must achieve Technology Readiness Level (TRL) 7 by year 2015 [4].

Use of, and level of involvement of the ISS in the planning, development and operation of this mission is left as an open requirement in the mission. To minimize overall system cost and to develop a robust system use of common elements is being considered of highest priority to rapidly mature planetary technology.

The CMMP is a three-phase mission to successfully land a crew on Mars, stay for a period of time and return them safely to Earth. The first phase is of primary interest in this paper as it establishes the structure and the outline of the mission process. This paper will cover the events critical to this phase of the mission and cover main points for Phases 2 and 3.

2.2 Phase 1: Robotic Supply Mission to Mars

In Phase 1 of the mission, all of the major components of the entire system are combined together and prepared for the entire mission. This phase incorporates the supply and support elements; Mars habitat and laboratory, planetary power reactor (PPR), Mars Ascent Vehicle (MAV), communications satellites, rovers, propellant, and supplies for the duration of the mission. All these elements will be staged to launch to the ISS at regular intervals atop four Energia boosters each with 100 metric ton launch capabilities. The cargo carriers for these elements from Low Earth Orbit to a Trans-Mars Injection (TMI) orbit are two Bimodal Nuclear Thermal Rockets (BNTR) vehicles. To ensure safe operation and handling of the nuclear engines, fuel cores will be launched separately from the reactor and only inserted into the vehicle in orbit at the ISS after full vehicle check outs and system tests have been performed.

Fig. 1. Proposed Energia Heavy Lift Launch Vehicle with Prototype CTV Elements [5]

The ISS plays the keystone of the entire mission. In its completed state by the launch window for this mission, the station will be able to service, test and assemble many of the mission elements to ensure operation before launch of the cargo elements. As the assembly and testing proceed new techniques that are crucial to future missions can be evaluated including, construction, testing, and repairing the elements needed for the long mission.

Launching of the elements is on a staggered timetable from their launch site at Baikonur. Assembly of the mission elements can occur on the ground, however larger elements such as the BNTR's must be assembled on orbit at the ISS. All components can then undergo rigorous final testing to ensure they survived the harsh launch conditions before committing them to this multiyear mission.

After final verification of all systems on each craft the two cargo vehicles will depart Earth's orbit September 14, 2022. The BNTR engines will provide high thrust propulsion and power to transport all these elements to Mars. Arrival occurs on October 2, 2023, where cargo elements will separate from the BNTRs and prepare for direct aerocapture to the landing site using parachutes and liquid oxygen/methane reaction control thrusters.

Upon determination of successful landing of the habitat and MAV, two small robotic trucks will deploy and travel a minimum of 500 meters away from the base camp. Integrated with each truck is an 80 kW nuclear power plant, which will provide the needed power for the habitat and laboratory, the in-situ propellant development facilities and the MAV, and provide power for high bandwidth data transfer with the satellites and the crew. One satellite will be deployed and phased with the communication elements on each Cargo Launch Vehicle (CLV) and take up orbit around the planet to provide continuous communications coverage amongst the astronauts on the surface and Earth.

Two un-pressurized rovers with autonomous capabilities will deploy from the vehicles and begin scouting the area around the base camp for signs of water and marking locations of scientific relevance for the crew to investigate later. Once the power plants have been confirmed operational, the in-situ propellant development will begin. This process will generate the propellant for the MAV to return to orbit upon completion of the crews' surface stay. The propellant development will also generate propellant to refuel the rovers used to transport the crew over the surface. The activities of all these components will be closely monitored via the communication network. The crew launch in late 2024 will not commence until all of the mission sequence events here have been completed.

As the base camp is being established on Mars, the power generators begin operations, propellant generation begins, and the rovers begin to explore, preparation on Earth will continue to ready the supplies and prepare another BNTR to transport the six person crew to Mars in late 2024.

2.3 Phase 2: Crew Transit To Mars

Phase (2) begins with the launch of the six crewmembers. In this phase a launch vehicle (e.g. Soyuz) transports the crew to the ISS. The third BNTR elements will be launched on two additional Energia boosters to rendezvous with the ISS in early 2024 for on orbit assembly and checkout. The Transit Habitat joins with the Mars Transfer Vehicle for a departure on October 17, 2024. In the 180-day transit to Mars, the BNTR provides thrust for all burns and electrical power. The nominal arrival date is April 15, 2025. Upon arrival to Mars, a propulsive burn puts the vehicle into orbit. The crew performs a rendezvous maneuver with the Mars Habitat/Lander waiting in orbit, then a propulsive burn de-orbits the lander and it parachutes down to the Mars landing site where the crew will stay for 535 Earth days. Constant Earth and Mars base communication is provided by communication satellites, and travel around the site is made easier by one pressurized rover that also serve as a “safe haven” if needed.

Once the crew arrives, they find all the needed supplies waiting and the return vehicle prepared to launch if necessary. The crew will then begin scientific measurement of the local terrain searching for signs of water in the vicinity. With the arrival of the supply vehicles from Phase 1, two rovers were deployed and sent to explore the region. The rovers marked sites of interest, and the astronauts can explore the surface with these vehicles. The astronauts will collect samples and explore the region until the time of the return trip to Earth.

2.4 Phase 3: Crew Transit Return to Earth

Phase (3) consists on the return of the crew to Earth. In this phase the crew members, with return samples, board the MAV and depart Mars surface to rendezvous with the Transit Habitat left in Mars orbit. The crew will then depart on a 180-day journey to Earth. Mars orbit departure is nominally on October 2, 2026. Upon arrival at Earth orbit, the crew could either perform a ballistic entry to Earth, or dock at the ISS for systems and crew checkout prior to Earth entry. Earth arrival date is expected on March 31, 2027 translating into a nominal 895-day mission for the crew.

3. PHASE 1 SYSTEM COMPONENTS

The main robotic section of the mission is in Phase 1 where various systems perform either autonomous or remote operations in orbit and/or on the surface of Mars.

3.1 Habitat/Lander

The habitat can land using an autonomous landing sequence or with manual control to the Martian surface. Serving as research center, storage space, exercise room and general living space, the habitat is a multi-functional facility that the crew will call home for the mission duration.

The first floor is mission oriented, with storage, exercise, scientific laboratory, and interplanetary and Martian communications areas. Upper floor is the individual crew living quarters with a common meeting area, totaling approximately 900 m^3.

Structurally, the habitat will appear vertically cylindrical in external appearance with a diameter of 7.5m.

3.2 Communication Elements

Every crewmember will have two-way voice and data communication capability with the habitat and any location on the Martian surface. For this to occur, every rover, environmental suit and the MAV will have powered communication equipment.

For communication with Earth, the habitat communication will relay relevant information to one of the on-orbit communication elements. Included with the CLV element is a communication satellite dedicated to transmitting information to Earth. Phased with the two empty CLVs, placed in highly elliptical Molniya orbits as additional data relays, communication blackouts with Earth will be minimized. These high power satellites will provide the power to support mega-bit/second data transfer rates from Earth to Mars. The orbit phasing of these satellites will ensure one is located over the base camp at all times with a 25 degree orbital inclination will be able to maintain a constant contact with Earth and NASA’s Deep Space Network.

Communications and scientific data collection is of crucial note for this mission with an emphasis on looking for signs of water. The communications network will monitor all the elements here and provide a high data rate conduit for all future astronaut communications.

3.3 Crew Comfort Requirements

Although crew comfort may seem secondary to mission objectives, it is critical to maintain crew moral and well-being. Including essential living requirements, the crew will have access to a couple luxuries that serve not only recreational purposes but also supplement the mission at hand.

Each crew member will have access to the following amenities: galley and food, clothing, sleep accommodations, crew health care, personal hygiene, waste collection, housekeeping, operations, maintenance, recreation and photography [2,6].

3.4 Nuclear Power Option

The TMI elements and habitats require a large power supply to operate at the levels needed for this mission. To ensure a short travel time to Mars a high power propulsion system is required to transport the mission elements. In designing the power systems for this mission several options were investigated. For the propulsion systems onboard the space craft both chemical and nuclear power were considered. To provide electrical power to the spacecraft and during the planetary stay on Mars chemical, nuclear, and solar systems were considered. In order to minimize the zero gravity exposure time for the crew a high power system is need to keep the travel time to 180 days. Chemical propulsion methods were considered as a long standing proven technology for interplanetary travel. In design of the mission it was realized that an enormous amount of propellant would be needed for the required maneuvers. Propellant consumption rates would be very high requiring the vehicle to keep empty tanks for a large portion of the mission. Additionally this method would only provide propulsion for the craft; an additional system would be needed to power the communications equipment. In comparison, use of the BNTR element would reduce the amount of needed propellant for the required maneuvers and also provide the high power necessary for data transmission. Use of the BNTR for all the mission elements builds additional levels of reliability in the system and matures the technology from the cargo supply to the crew launch. Nuclear power was chosen here as it provides a low maintenance system to provide the needed power. Solar panels are also capable of generating the needed power, however to develop a system to generate this much, would require a giant solar farm area on Mars, that is unfeasible to develop.

For the TMI of the cargo and later crewed components, chemical propulsion methods were considered as a long standing proven technology for interplanetary travel. In design of the mission it was realized that an enormous amount of propellant would be needed for the required maneuvers. Propellant consumption rates would be very high requiring the vehicle to keep empty tanks for a large portion of the mission. Additionally this method would only provide propulsion for the craft, an additional system would be needed to power the communications equipment. In comparison, use of the BNTR element would reduce the amount of needed propellant for the required maneuvers and also provide the high power necessary for data transmission.

Mission requirements for the crew establish very high power needs to operate all the scientific equipment propellant generation systems and communications system. Chemical systems would require a significant amount of additional propellant for the mission timeline. Nuclear power on Mars will deliver the required power, generate the mission propellant supply and provide for the astronauts needs.

3.5 Bimodal Nuclear Thermal Reactor Design

The design for the BNTR's to deliver the cargo and manned elements to Mars is based on Fusselman's design [7]. The key design parameters used in the sizing of this system are summarized in Table 1. Each CTV will consist of three BNTR's to allow for system redundancy in case of an "engine out" failure. This configuration will deliver the needed power for high thrust propulsion, TMI maneuvers, course corrections, and electrical power for the communication satellites.

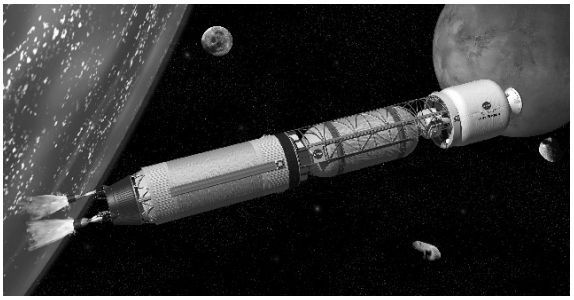

Fig. 2. NASA Glenn Research Center Concept for BNTR Vehicle [8]

For the propulsion element of the Crew Transfer Vehicle design, it has been proposed to use Bi-Modal Nuclear Thermal Rockets (BNTR). A common BNTR design capable of producing 15klbf and 50 kilowatts of electrical power is used for both the supply and the crewed Mars flight. Use of the BNTR for the cargo mission validates the concept and reduces overall program cost through use of a common space propulsion system. The BNTR used for the manned crew also includes additional radiation shielding. The BNTR provides the thrust for the TMI & TEI maneuvers, all mid course corrections and electrical power during transit.

The bimodal core stage is a closed Brayton cycle power conversion system that uses one 25 kW Brayton

rotating unit for each of three reactors. Each reactor is operated at 2/3 capacity to ensure the mission can be accomplished with one "engine-out". High pressure hydrogen propellant is used for active cooling of the reactor, and then to drive the turbine for electrical power. The exhaust is routed through the reactor core's fuel elements absorbing energy released by fissioning uranium atoms. The superheated propellant is expanded out a supersonic nozzle for thrust.

Table 1. BNTR Design Parameters

Parameter	Value
NTR Thrust	15,000 lbf
Core Thermal Power	313.2 MWt
NTR Specific Impulse	863.7 sec
Brayton Cycle Net Power	37 kWe
BNTR Mass each	6,744 lbm (3,059 kg)
BNTR Length	448" (11.4 m)
NTR Nozzle Exit Diameter	54" (1.4 m)

3.6 Mars Terrestrial Power Supply

Once on Mars the astronauts will need a robust power supply, to power the high power elements needed in this mission. This includes the Mars habitat/ laboratory, in-situ propellant for the MAV, light trucks, and communications system. NASA mission requirements for this class of mission require a minimum of 100 kWe for all the elements [9]. CMMP mission concept will employ two 80 kWe nuclear power generators meet the high power mission requirements and be able to operate at a slightly reduced capacity should a power unit fail during the mission. The high power requirements of the propellant generation device make the use of nuclear power plant the best option for this mission.

3.7 Martian In-Situ Propellant Development

Propellant resources are a precious commodity on Mars and will be generated for In-Situ Resource Utilization plant (ISRU) [10]. This plant will run off of a nuclear power plant deployed a distance away and generate methane fuel using the CO_2 in the Mars atmosphere and hydrogen delivered with the supplies; the process will also produce water and oxygen. The methane production shall be completed within twelve months, before the crew mission begins, as a safety precaution.
The methane fuel provided by the ISRU will be used for the light trucks and MAV, as well as oxygen and water for human consumption. The ISRU process is based upon the Sabatier reaction and is expressed as followed:

$$CO_2 + 4H_2 \rightarrow CH_4 + 2H_2O \qquad (1)$$

The consumables for this process are Hydrogen brought from Earth (about 5 % of the total generated consumable weight) and the abundant Carbon Dioxide in the Martian atmosphere. Electrolysis, decomposes water into $2H_2$ and O_2. This can be combined with the original Sabatier reaction to yield a final ISRU decomposition:

$$3CO_2 + 6H_2 \rightarrow CH_4 + 2CO + 4H_2O \qquad (2)$$

yielding an Oxygen to Methane output ratio of 4:1 and therefore giving a propellant mass leveraging of 18:1 along with a large quantity water as a bi-product. When combined with hydrogen from Earth, the Martian environment will be able to provide propellant for the Mars Ascent Vehicle (MAV) to return to orbit and fuel for the light trucks to transport the crew over the surface of Mars. The propellant generation process will be remotely started upon the arrival of the cargo to Mars. Propellant generation will be monitored from Earth and be completed prior to the crew launch to Mars. This process will take approximately one year and is a high power draw mission element, thus the need for the supplemental planetary power supply.

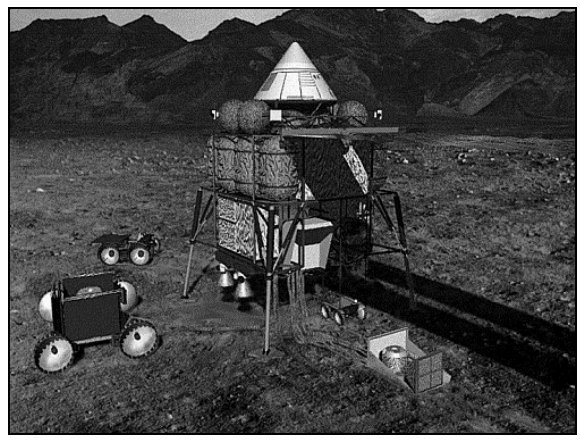

Fig. 3. MAV and Integrated ISRU [5]

Martian planetary propellant generation will yield a significant mission weight benefit. Propellant for the return mission will not need to be carried to Mars first reducing the launch payload. Setup of a Martian propellant generation facility will allow future missions to build on from the basic facilities here. Only future re-supply of the hydrogen reactant is needed to generate more propellant reserves on Mars.

3.8 Mars Transportation Supply

All orbital assembly and packaging will be done in the proximity of the ISS for human supervision and assurance. The vehicle orbiting Mars will be the surface habitat that will also serve as the Mars Lander when the crew arrives. The vehicle landing on mars will carry the bulk of the supplies including a MAV and what has become a staple of sorts in current Mars mission concepts, an ISRU. The MAV is an Apollo type spacecraft capsule that returns the crew to the CTV from the Martian surface. Initially this vehicle is an

integral part of the ISRU. As the ISRU generates methane, it is pumped directly into the MAV fuel tanks eliminating dangerous human interaction to transfer fuel from the ISRU to the MAV. The ISRU/MAV interface structure allows the MAV to launch from directly on top of the ISRU platform without damaging the ISRU's operational capability.

The Cargo Lander (CL) landing will position the ISRU un-fueled MAV combination, feedstock, nuclear power integrated on top of its robotic truck, and two un-pressurized rovers near the planned human landing site. The robotic truck will drive the power plant several hundred meters from the base, connected by flexible cabling.

Included in the Cargo Supply mission is an atmospheric blimp. It will inflate on the surface and fly over the Martian terrain. Attached to the blimp is a mini-rover with a small science package that is capable of air, soil, and liquid measurements. This blimp will explore the region around the habitat and report back any sites of interest to Earth that the crew can later explore upon arrival in more detail. Activated at arrival of the cargo elements the blimp will be able to scout 1km^2 per day and will operate for the entire mission lifetime continuously investigating the Martian surface.

A baseline 535 day stay emphasizing in search for water/ice either sub-surface or on the surface, additionally intensive scientific research in geological, atmospheric, biochemistry and human-medical areas will be conducted by the entire crew. Following the 535 day mission, the crew and return samples will board the MAV and prepare to rendezvous with the CTV (same vehicle used in the outbound leg). Once docked, the crew will transfer to the habitat module in the Earth Return Vehicle (ERV) and begin the Trans-Earth Injection (TEI) phase. Before arrival at Earth, the crew transfers into the MAV and separates from the ERV.

3.9 Rovers

Three Martian rovers, each capable of traversing more than 500 kilometers radius from the base, will be used to explore the surrounding area for existence of water, proof of past or present life forms, and general geological and atmospheric studies. Two will be un-pressurized similar to the original moon rovers, with the third rover being pressurized for further missions from base camp and can be used by the crew as a temporary safe haven. Range can easily be improved by adding additional fuel storage. Each Rover weighs approximately 0.55 metric tons and uses an internal combustion engine, generating 65 horsepower. The engines run on methane fuel, generated from the ISRU, with an inert buffer of carbon dioxide. Fuel consumption is on the order of 0.5kg bi-prop per kilometer.

Fig. 5. Conceptual Rendering of Pressurized Martian Rover Docked to Habitat [5]

4.0 TRADE STUDIES

Several trade studies were performed to optimize system drivers derived from mission requirements.

4.1 Mission System Mass Breakdown

The elements used in this mission were sized from reference numbers in *NASA Reference Mission* [9]. Major system components have been includes here to give scope to the sizes and payload requirements needed for this mission.

Table 2. Mission System Masses

Cargo Transfer Vehicle 1 Mass Breakdown		
Cargo Lander Payload Mass	**50024**	**kg**
Mars Ascent Capsule	4829	kg
ISRU plant	3941	kg
Hydrogen feedstock	5420	kg
3 teleoperable science rovers	1500	kg
Entry System Masses	**23333**	**kg**
Total BNTR Mass	**23400**	**kg**
TMI Propellant Mass	**54931**	**kg**
TOTAL INITIAL MASS (IMLEO)	**156947**	**kg**
Cargo Transfer Vehicle 2 Mass Breakdown		
Habitat Element	**29105**	**kg**
80 kW nuclear power plant	5713	kg
Unpressurized rover	550	kg
Crew Vehicle Payload Mass	**37591**	**kg**
Landing System Masses	**4204**	**kg**
NTR Propulsion System	**23400**	**kg**
TMI Propellant	**48922**	**kg**
TOTAL INITIAL MASS (IMLEO)	**139778**	**kg**

4.2 Mission Trajectories

Both cargo and crew vehicles will use conjunction type trajectories between Earth and Mars. These minimum energy trajectories are constrained so that the arrival entry speed at Mars for both vehicles does not exceed 8.7 km/s (corresponds to a hyperbolic excess velocity of 7.167 km/s) and that the crewed transfer vehicle does not have an arrival entry speed at Earth exceeding 14.5 km/s (corresponding to a hyperbolic excess velocity of 9.36 km/s). The crewed trajectories are further optimized to a maximum transit time of 180 days. Due to the synodic period between Earth and Mars, the minimum time between transits requires that the crew remain on the surface of Mars for nearly one-and-a-half Earth years. However, this relatively long stay time can be used to maximize the potential for scientific return.

4.3 Landing Site

Both the cargo vehicles and the crewed vehicle arriving two years later will enter orbit at Mars while the southern hemisphere is in its winter. Based upon NASA Ames Mars General Circulation Model (MGCM) simulation of the Martian atmosphere, the winter hemisphere develops a strong polar jet stream which drives that hemisphere to have relatively higher wind speeds on a large scale, while the opposite hemisphere is relatively quiescent near the pole [11]. Winds in portions of the middle northern latitudes may also exceed landing criteria as a result of persistent climatological circulations as the season progresses.

The declinations for the arrival trajectories favor a more equatorial landing site, while the criteria for finding water favors a landing site above 50° N latitude based upon the Gamma Ray Spectrometer (GRS) data. However, planetary protection constraints may preclude visiting sites, which may provide viable habitats for Earth organisms.

The tentative landing site selected is near the resting place of the Viking 1 Lander on Chryse Planitia (22.5^o W, 47.8^o N). This site was selected because a large amount of data has been accumulated on it from Viking 1 and other unmanned probes. Since the site's environmental characteristics are well understood, its choice provides a greater measure of crew safety, as well as opportunity to perform well-conceived science. The area is also considered to have great historical and public interest value because of Viking 1 remains.

As the data from current and future Mars missions are analyzed and the current design is further refined, it is expected that alternative landing sites will be developed.

4.4 International Space Station

The International Space Station is a keystone for this mission. With its completion by the retirement of the Space Shuttle, the fully functional station will be able to serve as a stepping-stone to the planets and beyond. Exploration of the solar systems cannot be achieved by a single nation. With the ISS many countries will be able to contribute to the future exploration of space. For the CMMP the ISS will serve as the launching point from Earth, complex launch systems will be tested, evaluated, and undergo final assembly before being launched to Mars. The hardest part of the launch process getting off the surface is already complete and from there interplanetary vehicle can re-supply at the ISS before departing. Materials can be supplied to the ISS in small launches and assembled in orbit to develop future spacecraft. Research into new construction techniques and materials can be developed in the near zero- gravity environment. Further understanding of the effects of long term space exposure can be better understood and treated to keep our astronauts safe for long interplanetary missions. As a fully operational space station the ISS can serve as a permanent docking station for all future missions and allow the crew to launch to and from Earth as necessary. Acting as a bridging point between the chemical launch vehicles from Earth and the high power nuclear vehicles needed for long duration space missions, the ISS will be a key component in all future missions.

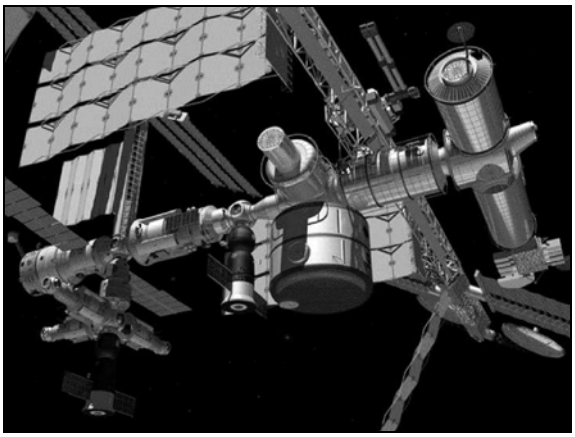

Fig. 6. NASA Design Reference Mission Mars Habitat Concept Rendering at ISS [5]

5.0 CONCLUSION

As a system level solution, CMMP can enable future interplanetary explorers with the tools, techniques, and technology to reach other planetary bodies within the solar system, provide insight into its origin, and possibilities for the future of humanity.

Please note that all images of vehicles and equipment are conceptual artists' renderings and are not representations of the final product for this mission.

6.0 REFERENCES

1. Team Olympus. *Crewed Mission to Mars Program*. N.p., n.d. (2003).

2. Spartan Martian Team. *Crewed Mission to Mars Program - Augmented*. N.p., n.d. (2005).

3. Bush, G. W, *President's Statement on the Commission on Implementation of United States Exploration Policy*, The White House. Office of the Press Secretary, 2004.

4. NASA. Office of Space Access and Technology. (1995). *Technology Readiness Levels*. [Online]. http://www.hq.nasa.gov/office/codeq/trl/trl.pdf. (2006, June 12).

5. The Mars Society. NASA Design Reference Mission charts. [Online]. http://www.marssociety.org/interactive /art/nasa_charts.asp (2006, June 7).

6. Stilwell, D., Boutros, R., and J. Connolly. *Human Spaceflight Mission Analysis and Design*. New York: McGraw Hill Companies, 1999.

7. Fusselman, S., et al. *NERVA-Derived Concept for a Bimodal Nuclear Thermal Rocket*, Space Technology and Applications International Forum – *STAIF 2005*, American Institute of Physics 0-7354-0230-02/05, 2005.

8. Zona, K. (2006, June 5). NASA Glenn Research Center: Our contributions to Exploration Systems. [Online]. http://www.nasa.gov/centers/glenn/projects/ exploration.html. (2006, June 7).

9. Hoffman S. J., and Kaplan D.I., Eds. *Human Exploration of Mars: The Reference Mission of the NASA Mars Exploration Study Team*, NASA Special Publication 6107. 1997.

10. Sanders, G.B. et al. *Common In-Situ Consumable Production Plant for Robotic Mars Exploration*. Concepts and Approaches for Mars Exploration. 6177. (2000, July 20). [Online]. http://www.lpi.usra.edu/ meetings/robomars/pdf/6177.pdf (2006, June 14).

11. Haberle, R. (2004, August 30). Mars General Circulation Modeling Group @ NASA Ames. [Online]. http://www-mgcm.arc.nasa.gov/MGCM.html. (2006, June 5).

NUMERICAL SIMULATIONS OF UNSTEADY FLOW AROUND AN ENTRY CAPSULE

Axelle Viré[1]

[1] *Université Libre de Bruxelles, Avenue F.D. Roosevelt 50, 1050 Brussels, Belgium, Email: avire@ulb.ac.be*

ABSTRACT

Unsteady near-wake characteristics of a sphere-cone bluff body in incompressible flow are investigated numerically, using a hybrid spectral/finite element solver. Direct Numerical Simulations (DNS) are performed at a Reynolds number Re=1000. Comparison with experiments at higher Re [1] confirms that results are independent of the Reynolds number for Re>1000. Solutions also seem to support the hypothesis of F.Y. Wang, *et al.* [2]: oscillations of the wake closure point could be responsible for the appearance of additional swirl structures in the wake. Moreover, simulations indicate the existence of an unsteady lateral force at a 15° angle of attack.

Key words: Unsteady flow; reentry; wake; flow visualization; DNS.

1. INTRODUCTION

At low speeds, before the splashdown (or touchdown), the turbulent flow field around an entry capsule induces unsteady forces on the capsule. In particular, even if the capsule geometry is axisymmetric, the flow field is not because of three-dimensional effects which manifest themselves as ring vortices in the azimuthal direction. The understanding of these phenomena is essential to ensure both static and dynamic stability. In addition, parachute deployment plays an important role in the stabilization of the capsule. The aim of the present study is to analyse the flow field around an entry capsule at low Reynolds numbers numerically, using a hybrid spectral/finite element solver. Apollo is chosen as the representative geometry. Results are compared qualitatively with water tunnel experiments at low speeds and quantitatively with literature at higher Reynolds numbers.

2. MODEL

The scaled drawing of the model is shown in Fig. 1. The heat shield forward position corresponds to the zero angle of attack and incidences increase in the clockwise direction.

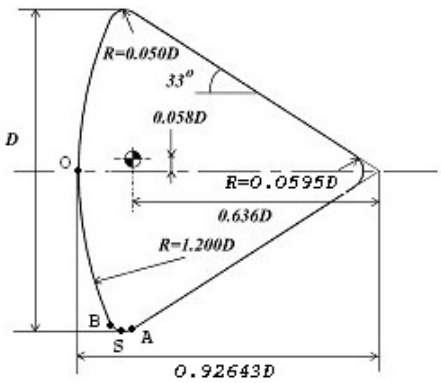

Figure 1. Apollo capsule model.

3. WATER TUNNEL VISUALIZATIONS

A preliminary experimental study is conducted in the WT1 water tunnel of the Von Kármán Institute for Fluid Dynamics (VKI). The periodicities of the eddies in the near wake are deduced from the video recordings and no quantitative measurement device is used. The maximum speed in the 240mm x 120mm section of the tunnel is 0.15 m/s. Two small-scale models are used. Both are characterized by a heat shield diameter d=50mm but they differ from the dye injection holes position. The first model, equiped with dye injection holes at the junction between the spherical and the conical part, is used to visualize the shear-layer instability. The shear-layer is characterized by a pseudo-periodic motion of ring vortices (Fig. 2). The pairing of two or three vortices can be observed as illustrated in Fig. 3. Using the heat shield diameter as the non-dimensional length, the Strouhal

number St of this Kelvin-Helmoltz instability is approximately equal to 2.1.

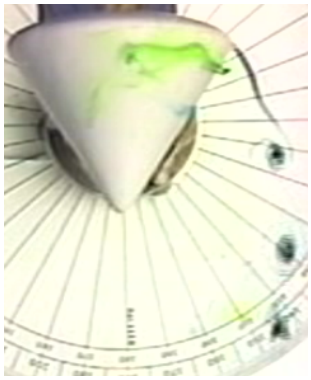

Figure 2. Shear-layer instability (Re=3700).

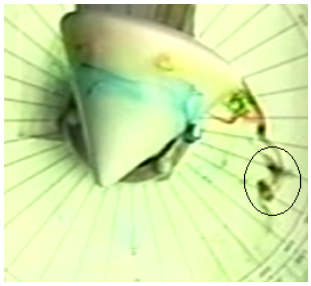

Figure 3. Pairing of two vortices (Re=3000).

The second small-scale model allows the visualization of the "fish tail motion" downstream of the wake. The Strouhal number evaluation is quite difficult due to rapid dispersion of coloured liquid. However, St=0.19 constitutes a good approximation. The periodicity of this oscillation motion in the vicinity of the wake closure point is one order of magnitude smaller than that of the shear-layer instability.

4. NUMERICAL SIMULATIONS

Numerical simulations are performed using a hybrid spectral/finite element solver developed for Direct Numerical Simulations (DNS) of incompressible turbulent flows around axisymmetric geometries. A Fourier series is used to represent flow variations in the azimuthal direction whereas a finite element discretization of the equations is applied in the meridional plane. As a consequence, the resolution of a three-dimensional problem is decomposed into a series of two-dimensional problems.

Two angles of attack are studied, 0° and 15°, at a Reynolds number Re=1000. Computations simulate 100 seconds (real time). Results are compared with experimental data available in the literature [1] at higher Reynolds numbers in terms of periodicities, pressure distributions, force and moment coefficients.

4.1. Mesh

The domain is a cylindrical box. The heat shield center is located at 5d downstream of the inlet surface. The domain length equals 26d and the domain height with respect to the capsule axis of rotation is 6d as shown in Fig. 4. The mesh contains 26,000 nodes and 51,452 triangular elements.

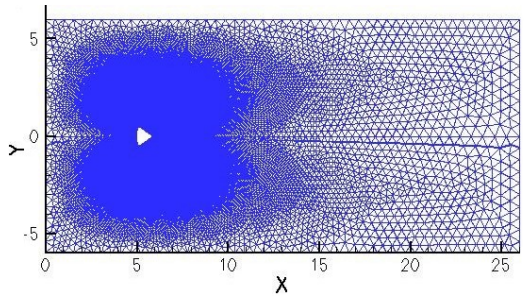

Figure 4. Mesh.

4.2. Periodicity

Numerically, the Strouhal number of the low frequency mode is estimated to be St=0.165-0.200 whereas mesh cells are not sufficiently small to capture the high frequency shear-layer instability.

4.3. Pressure distribution

The pressure distribution is maximum at the heat shield stagnation point and decreases in streamwise direction as illustrated in Fig. 5. Its sign changes to negative before the end of spherical part. On the conical part, the distribution is uniform. Pressure coefficient C_p is compared with literature experimental data [1] obtained at $2.10^5 \leq Re \leq 1,2.10^6$.

4.4. Aerodynamic coefficients

The convention chosen for aerodynamic coefficients is depicted in Fig. 6, where the x-axis coïncides with the capsule axis of rotation. D

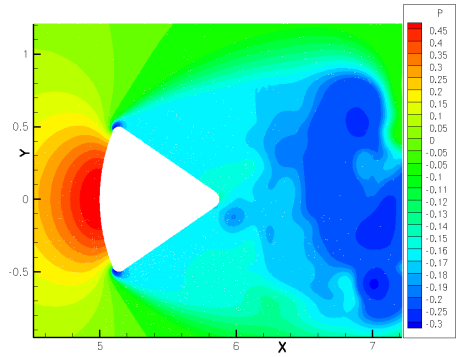

Figure 5. Pressure distribution $P - P_\infty$ at 0°

stands for the drag, L the lift, Fz the lateral force, Cx the rolling moment, Cy the yawing moment and Cz the pitching moment (positive for a nose-up configuration).

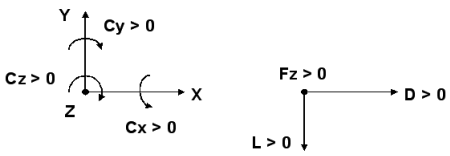

Figure 6. Aerodynamic coefficients convention.

At a zero angle of attack, the configuration is symmetric which is why perturbations are initially added to allow three-dimensional effects to start. The analysis of the perturbations influence confirms that asymptotic values of aerodynamic coefficients are quite unsensitive to the perturbations. However, at a zero angle of attack, if no perturbation is introduced, the flow field is two-dimensional and the drag coefficient is twice smaller than in a flow in which three-dimensional effects appear due to the addition of perturbations (three-dimensional flow field). Moreover, in a three-dimensional flow field, aerodynamic coefficients experience unsteady variations which suggest that three-dimensional effects are responsible for a deterioration of aerodynamic characteristics of the capsule and also influence its stability.

For a three-dimensional flow field, non-dimensional force coefficients are compared with experimental data at Re=60,000 from the literature [1]. Numerical simulations indicate that, at a 15° angle of attack, unsteady phenomena also appear in the lateral direction, along the z-axis, and this has not been observed during the wind tunnel experiments [1]. In fact, the lateral force coefficient equals zero during 25 seconds before starting to oscillate. In Fig. 7, the dotted line concerns a 345° angle of attack whereas the other one is obtained for the symmetric case (15°). Even if the oscillations amplitude is small, to the author's knowledge, this phenomenon has never been referred in the literature. Further simulations should be conducted at different incidences in order to support the present solutions.

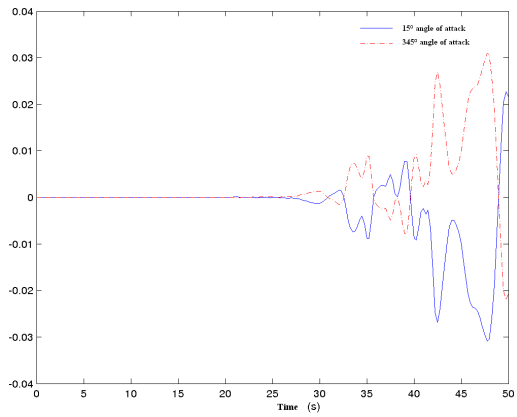

Figure 7. Lateral force coefficient.

Non-dimensional moment coefficients are compared with experimental data obtained in the literature at Re=110,000 [1]. Both rolling and yawing coefficients with respect to the theoretical center of gravity position are equal to zero. The pitching moment analysis confirms that a 15° angle of attack corresponds to the trim position when the heat shield faces the stream.

4.5. Flow visualizations

A movie was made based on numerical visualizations. This approach allows the comparison with experimental flow visualizations in water tunnel. Large recirculation regions are observed in the near-wake. Also, after the destruction of the vortex rings, a part of the vortices rolling-up in the upper portion moves into the near-wake and becomes part of the flow convected on the lower portion of the capsule. As suggested in [3], this phenomenon may disturb the vehicle stability by introducing an amplification of the incidence oscillation magnitude. Furthermore, instantaneous numerical visualizations illustrate large oscillations of the wake closure point and the apparition of additional swirl structures which do not belong to vortex rings. F.Y. Wang, *et al.* [2] suggests that these vortices could be the consequence of the capsule experiencing unsteady lift. In fact, the "fish tail" motion of the wake closure point influences forces that act on the body and a new starting vortex is subsequently deposit into the wake. This study seems to support the proposed mechanism.

5. CONCLUSIONS

Unsteady flow around an Apollo capsule has been computed in Direct Numerical Simulations (DNS) using a new hybrid spectral/finite element solver. Results show very good agreement with the quantitative wind tunnel and qualitative water tunnel experiments. The study also confirms that the flow around the Apollo capsule is largely independent of Reynolds number for Re$>$1000, as the flow separation is determined by the geometry. The implementation of Large-Eddy Simulations (LES) subgrid models could allow simulations to be performed at higher Reynolds numbers.

Moreover, this study reveals interesting conclusions concerning unsteady phenomena which act on the body. An unsteady force in the lateral direction is shown for the first time by the present direct numerical simulations. A more detailed analysis should be done to confirm these observations and to study their influence on the capsule stability.

Apollo was chosen as the representative geometry to compare results with those in the literature. Good agreements with the literature give us the sufficient confidence to apply similar simulations to other capsule shapes such as the Huygens. The impact of external perturbations such as wind gust loads could also be the subject of further studies.

6. ACKNOWLEDGMENTS

The numerical study has been done at the Université Libre de Bruxelles (Belgium) as part of a student final year research project. The Experimental work has been conducted in Von Kármán Institute for Fluid Dynamics (Belgium). I thank Professor Gérard Degrez and Yves Detandt who supervised my work at the university and Sébastien Paris, research engineer at the Von Kármán Institute. Special thanks to Dr. Özgur Karatekin for the interest he took in my work.

REFERENCES

1. Karatekin Ö., *Aerodynamics of a planetary entry capsule at low speeds*, PhD. Thesis Université Libre de Bruxelles / Von Kármán Institute for Fluid Dynamics, 2002.
2. Wang F.Y., Karatekin Ö. and Charbonnier J.-M., An experimental study of the flow-field around an Apollo capsule at low speed, *In AIAA 36th Aerospace Sciences Meeting and Exhibit*, Reno (NV), USA, 1998.
3. Karatekin Ö., Wang F.Y., Charbonnier J.-M., Aerodynamic stability of planetary entry capsules in subsonic flow, *International Symposium on Atmospheric Reentry Vehicles and Systems*, Arcachon, France, 1999.
4. Carati D., *Large-eddy simulation for turbulent flows: from mathematical fundations to practical applications*, Thèse d'agrégation ULB, 2001.
5. Charbonnier J.-M., *Plans de la capsule Apollo: sonde oscillante - ensemble et bouclier*, Von Kármán Institute for Fluid Dynamics, 1997.
6. de la Llave Plata M., *Flow field investigation behind a re-entry capsule in VKI-WT1 water tunnel*, Stagiaire report, Von Kármán Institute for fluid dynamics, 1998.
7. Erre A., *Experimental and numerical investigation of a low Reynolds number flow around a 2D Apollo capsule*, Stagiaire report, Von Kármán Institute for fluid dynamics, 1999.
8. Karatekin Ö., Wang F.Y. and Charbonnier J.-M., Terminal aerodynamics of a planetary entry capsule, *2nd Ankara International Aerospace Conference*, Ankara, Turkey, 1998.
9. Karatekin Ö., Wang F.Y. and Charbonnier J.-M., Aerodynamic stability of planetary entry capsules, *3rd European Symposium on Aerothermodynamics for Space Vehicles*, ESTEC, Noordwijk, The Netherlands, 1998.
10. Karatekin Ö., Wang F.Y. and Charbonnier J.-M., Visualisation of an unsteady wake, *In 8th International Symposium on Flow Visualization*, Sorrento, Italy, 1998.
11. Karatekin Ö., Wang F.Y. and Charbonnier J.-M., Near-wake of a three-dimensional bluff body at angles of attack, *In ASME Paper FEDSM98-5185, Proceedings 1998 ASME Fluids Engineering Division Summer Meeting*, Washington DC, 1998.
12. Karatekin Ö., Wang F.Y. and Charbonnier J.-M., Characterisation of a bluff body wake using LDV and PIV techniques, *9th International Symposium on Applications of Laser Techniques to Fluid Mechanics*, Lisbon, Portugal, 1998.
13. Karatekin Ö., Voets R., Charbonnier J.-M. and Wang F.Y., Incompressible aerodynamics of a planetary entry capsule, *17th International Congress on Instrumentation in Aerospace Facilities*, Toulouse, France, 1999.
14. Sagaut P., *Large eddy simulation for incompressible flows - An introduction*, 3rd edition, Springer, 2005.
15. Viré A., *Étude de l'écoulement autour des capsules spatiales*, Mémoire de fin d'études, Université Libre de Bruxelles, Brussels, Belgium, 2006.
16. Wang F.Y., Charbonnier J.-M., Karatekin Ö. and Paris S., The utilization of low speed facili-

ties in transonic stability of reentry vehicles research - An evaluation, *In AIAA 16th Applied Aerodynamics Conference*, Albuquerque (NM), USA, 1998.
17. Wang F.Y., Karatekin Ö. and Charbonnier J.-M., Low-speed aerodynamics of a planetary entry capsule, *Journal of Spacecraft and Rockets*, 36(5):659-667, 1999.
18. Wang F.Y., Karatekin Ö., Charbonnier J.-M. and Paris S., Utilization of low-speed experiments in transonic capsule stability research, *Journal of Spacecraft and Rockets*, 36(5):774-776, 1999.